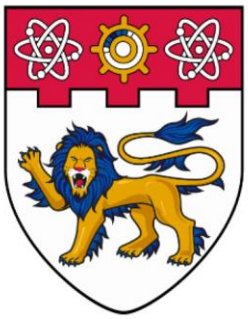

NANYANG TECHNOLOGICAL UNIVERSITY
SINGAPORE

DEVELOPMENT OF VANADIUM COMPLEXES FOR SELECTIVE PHOTOCATALYTIC CARBON-CARBON BOND CLEAVAGE

MILOŠ ĐOKIĆ

School Of Physical And Mathematical Sciences

2018

DEVELOPMENT OF VANADIUM COMPLEXES FOR SELECTIVE PHOTOCATALYTIC CARBON-CARBON BOND CLEAVAGE

MILOŠ ĐOKIĆ

School of Physical And Mathematical Sciences

A thesis submitted to the Nanyang Technological University in partial fulfillment of the requirement for the degree of Doctor of Philosophy

2018

Abstract

Activation of carbon-carbon single bonds remains a long-standing pursuit in synthetic chemistry due to their high stability. However, the ability to selectively break down C-C bonds under mild conditions and with inexpensive catalysts would be beneficial for rapid development of complex molecules as well as for valorizing neglected feedstocks such as biomass and plastics. To address this issue, we have prepared a series of vanadium photocatalysts that are able to effect highly selective C-C bond activation in aliphatic alcohol substrates under exceptionally mild conditions and visible light irradiation.

Improving on our group's initial catalyst **VO-10**, we began with the systematic tuning of electronic properties of the ligand backbone by introducing strong electron-withdrawing groups at specific ligand sites. This approach led to the development of new photocatalysts with significantly enhanced reactivity. Detailed kinetics studies of photodegradation of representative non-phenolic, β-O-4-containing lignin model substrates **5** and **25** revealed **VO-14** as the fastest catalyst, performing up to 7 and 17 times faster than the original **VO-10,** with respective substrates. Furthermore, the computational DFT studies supported our initial hypothesis that stabilization of the HOMO level of the complex could significantly improve the catalytic rate of the C-C bond cleavage.

In the subsequent work, we have been able to apply this unique reactivity of catalyst **VO-14** to a wide range of substrates. Alcohols that generate highly stabilized benzyl radicals upon C-C bond cleavage were especially suitable. Additionally, mechanistic screening and substrate modifications revealed that various functional groups are well tolerated under optimized reaction conditions. Moreover, even simple, commercially available alcohols, which generate less stabilized tertiary, secondary, and even primary radicals underwent C-C bond cleavage under photocatalytic conditions. Remarkably, in some instances, a second C-C bond cleavage of the initially formed alcohol product occured, indicating a possibility of applying a cascade-type C-C bond activation in specific substrates.

Lastly, the ease of preparation of hydrazone-amide ligands and their corresponding complexes allowed us to synthesize a significant number of new vanadium catalysts

with various functional groups on the ligand. This work shows that fine-tuning the ligand design can effect distinct structural, as well as photophysical properties in the resulting vanadium complexes. Depending on the type, and the position of ligand substitution, complexes with different reactivity, as well as distinct light absorbing, and emitting properties may be obtained.

Acknowledgments

First, I would like to thank my supervisor, Dr Soo Han Sen, for his continuous support and guidance throughout my Ph.D. studies. His advices and suggestions helped me become a better, more objective researcher. In addition, his constant involvement with my projects helped me keep track of my progress and eased the preparations of manuscripts, as well as writing this thesis. For this, I am most sincerely grateful. Thank you, Han Sen.

I would also like to express my gratitude to Dr Sarifuddin Gazi, our former group member, who was always there for me from the very first stages of my Ph.D. studies. His passion for chemistry and research always inspired me to pursue new projects, and new possibilities. Thank you very much for your help Gazi.

I thank Prof. Hajime Hirao and his team for performing computational studies for our project. Their invaluable knowledge helped us improve our work and gain much needed insights regarding our chemical systems.

I also thank Dr Rakesh Ganguly and Dr Li Yongxin for their help with X-Ray crystallographic analyses, and Miss Goh Ee Ling for assistance with NMR spectroscopy. Their assistance has been much appreciated.

I am very grateful to the Nanyang Technological University (NTU) and the Agency for Science, Technology, and Research (A*STAR) for awarding me the scholarship, which enabled me to embark on this magnificent journey through the world of academic research. It has been a wonderful experience studying and conducting research at the state-of-the-art laboratories and facilities of NTU, while also enjoying a friendly, multicultural environment.

All my research would not have been possible without the cheerful and extremely helpful bunch of amazing people in our group. From experienced postdocs to summer research students and volunteers just starting their academic pursuits, my life has been enriched by all of them. I thank my dear friends Ng Kia Sheun Leonard and Hong Zonghan for their immense help I received since my first day at NTU. I also thank them for their sincere friendship during my stay in Singapore. My appreciation also goes to Dr Lim Jia Hui, Dr Shao Hai Yan, Dr Siva Prasad Das, Dr Subas Kumar Muduli, Dr

Kee Jun Wei, Dr Wang Jingyi, Dr Chin Kek Foo, Miss Yik Yie, Mr Dwaipayan Ghosh, Mr Ho Xian Liang, and Mr Ng Yun Ru Andrew for their endless assistance and friendship.

Most importantly, I thank my dear mum Vesna, dad Novica, my nana Gordana, and my girlfriend Michelle for always being there for me during my struggling times when I needed reassurance, motivation, love, and support. Without you guys I would not have succeeded in achieving my dream. Thank you so much!

Permissions for Content Reproduction

- The material for **CHAPTER 1** was reproduced from Đokić, M; Soo, H. S. *Chem. Commun*., **2018**, *54*, 6554-6572, with permission of the Royal Society of Chemistry (http://pubs.rsc.org/en/content/articlelanding/2018/cc/c8cc02156b#!divAbstract)

- The material for **CHAPTER 3** was reprinted with permission from Gazi, S.; Đokić, M.; Moeljadi, A. M. P.; Ganguly, R.; Hirao, H.; Soo, H. S. *ACS Catal*. **2017**, *7*, 4682−4691. Copyright 2017 American Chemical Society (https://pubs.acs.org/doi/abs/10.1021/acscatal.7b01036)

List of Publications

1. “Artificial Photosynthesis by Light Absorption, Charge Separation, and Multielectron Catalysis”, **Đokić, M**.; Soo, H. S. *Chem. Commun*., **2018**, *54*, 6554-6572.

2. “Kinetics and DFT Studies of Photoredox Carbon−Carbon Bond Cleavage Reactions by Molecular Vanadium Catalysts under Ambient Conditions”, Gazi, S.; **Đokić**, **M**.; Moeljadi, A. M. P.; Ganguly, R.; Hirao, H.; Soo, H. S. *ACS Catal*. **2017**, *7*, 4682−4691.

3. “Selective Carbon-Carbon Bond Cleavage by Earth Abundant Vanadium Compounds Under Visible Light Photocatalysis”, Soo, H. S.; Gazi, S.; **Đokić**, **M**. WO/**2016**/126207, (patent).

Table of Contents

Symbols and Abbreviations

$\Delta E^{\ddagger}$	activation energy from the ground state
δ	NMR chemical shift (ppm)
ε	extinction coefficient (M^{-1} cm^{-1})
λ_{max}	wavelength of maximal absorbance
µL	microliter
Φ	quantum yield
Ψ	torsion angle
°	degree
°C	degree Celsius
Å	Angrstrom
C_0	initial concentration
C_t	concentration at a given time
d	doublet
dd	doublet of doublets
E_0	formal electrode potential
$E_{1/2}$	half-wave potential
h^+	photogenerated hole
J	coupling constants
m	multiplet
q	quartet
s	singlet
S_0	singlet ground state
S_1	singlet excited state
t	triplet
tt	triplet of triplets

T_1	triplet excited state
1,4-CHD	1,4-cyclohexadiene
9,10-DHA	9,10-dihydroantracene
AP	artificial photosynthesis
Ar	aryl (substituted aromatic ring)
Boc	*tert*-butyloxycarbonyl
CD_3CN	deuterated acetonitrile
$CDCl_3$	deuterated chloroform
CV	cyclic voltammetry/cyclic voltammogram
DBAD	di-*tert*-butyl azodicarboxylate
DFT	density functional theory
dmFc	decamethylferrocene
DMSO-d_6	deuterated dimethyl sulfoxide
DSPEC	dye-sensitized photoelectrochemical cell
DSSC	dye-sensitized solar cell(s)
Et	ethyl
et al. (*et alia*)	and others
EtO	ethoxy
EtOAc	ethyl acetate
EtOH	ethanol
eq.	equivalent
eV	electronvolt
ESI-MS	electrospray ionization-mass spectrometry
EWG	electron-withdrawing group(s)
Fc^+/Fc	ferricenium/ferrocene redox couple
FT-IR	Fourier transform infrared spectroscopy

h	hour
HAT	hydrogen atom transfer
HMF	5-hydroxymethylfurfural
HOMO	highest occupied molecular orbital
HRMS	high resolution mass spectrometry
Hz	Hertz
in situ	on site
Int	intermediate
*i*Pr	*iso*-propyl
*i*PrO	*iso*-propoxy
kcal mol^{-1}	kilocalorie per mole
LED	light-emitting diode
LMCT	ligand-to-metal charge transfer
LUMO	lowest unoccupied molecular orbital
M	concentration (mol/L)
Me	methyl
MeCN	acetonitrile
MeO	methoxy
MeOD	deuterated methanol
MeOH	methanol
mg	milligram
MHz	megahertz
min	minute(s)
mL	milliliter
mmol	millimole
mol %	mole percent

mpg-C_3N_4	mesoporous graphitic carbon nitride
m/z	mass to charge ratio
$NADP^+$	nicotinamide adenine dinucleotide phosphate
NADPH	reduced form of $NADP^+$
NBS	*N*-bromosuccinimide
nm	nanometer
NMR	nuclear magnetic resonance
OLED	organic light-emitting diode
PCET	proton-coupled electron transfer
Ph	phenyl
PIDA	phenyliodine(III) diacetate
PL	photoluminescence
ppm	parts per million
Q-TOF	quadrupole-time of flight
RC	reactant complex
ROS	reactive oxygen species
SET	single electron transfer
TEMPO	(2,2,6,6-tetramethylpiperidin-1-yl)oxy
tert-Bu	*tert*-butyl
THF	tetrahydrofuran
TLC	thin layer chromatography
TM	transition metal
TON	turnover number
TS	transition state
TW	terawatt
UV-vis	ultraviolet-visible

UV-vis DRS	UV-visible diffuse reflectance spectroscopy
V	volt(s)
XPS	X-ray photoelectron spectroscopy

CHAPTER 1

INTRODUCTION

PREFACE

The content of this chapter has been reproduced from the article "Artificial Photosynthesis by Light Absorption, Charge Separation, and Multielectron Catalysis", **Đokić, M.**; Soo, H. S. *Chem. Commun.*, **2018**, *54*, 6554-6572, with permission of the Royal Society of Chemistry. Both authors contributed to the preparation of the final manuscript.

1.1 Artificial Photosynthesis

The "terawatt (TW) challenge" was coined in 2005 by the late Nobel laureate, Richard Smalley, to contextualize the scale of our energy requirements in the near future.[1] Currently, over 80% of global energy needs are satisfied by fossil fuels,[2] and the total energy demand is expected to increase by about 20% from 19 to 23 TW in 2030.[3, 4] Furthermore, fossil fuels are limited, and the additional strain from pollution and global climate change due to fossil fuel combustion has led to an impending energy and environmental crisis.[5, 6]

Nature has provided a blueprint and inspiration for averting and overcoming these energy and pollution crises.[3, 4, 7-9] On average, solar energy reaches the Earth's surface at a rate of 120 000 TW, which is at least three orders of magnitude above what the global population uses now and will need in the foreseeable future.[3, 10] To exploit this virtually unlimited resource, natural photosynthesis worldwide currently stores solar energy at a rate of around 120 TW.[3, 4, 10] Photosynthetic organisms have evolved sophisticated biological processes, using exclusively earth-abundant elements available in disparate ecosystems, to capture solar energy and store it in reduced carbon compounds.[3, 4] In so doing, they have simultaneously achieved multiple functions that should instruct us, including the following aspects:

(i) The storage of diffuse sunlight over a panchromatic spectral range into energy dense fuels. Although solar energy is plentiful, it is distributed over a broad surface area and electromagnetic spectrum.[3, 4, 9] Yet photosynthetic organisms have been able to concentrate this energy into energetic small molecules.

(ii) The spatial and temporal separation of energy collection versus energy use. The available sunlight varies with the location, season, time of the day, and the weather. By storing the energy within the chemical bonds of small molecules, Nature circumvents the need to manage or match the solar flux with utilization, as usually required in photovoltaics.[10, 11]

(iii) The one-directional multielectron charge separation across an interfacial membrane *via* thermodynamically and kinetically favorable and well-matched chemical processes. The chlorophyll chromophores absorb single photons and undergo single charge separation events, but are coupled with energetically downhill charge transfer

reactions that kinetically outcompete undesired recombination processes.[3, 4, 7, 8] Natural photosynthesis operates essentially with a molecular diode.

(iv) The indirect energy storage on the reductive half-reaction in the form of partially reduced carbon (instead of nitrogen) compounds *via* kinetically more facile proton reduction processes. The primary light driven process in the reductive Photosystem I half-reaction is the generation of "hydride" equivalents from water to convert $NADP^+$ to NADPH, which is subsequently employed in carbohydrate synthesis in the dark Calvin cycle.[3, 4, 7, 8] The two-electron reduction of $NADP^+$ and subsequent reduction of CO_2 are all kinetically accessible reactions with numerous stable intermediates.

(v) The concurrent generation of an oxygenic atmosphere to support their own survival and those of other aerobic organisms in an equally productive and critical oxidative half-reaction. Energy is stored during water oxidation to O_2, which can subsequently be released during aerobic respiration.

Nature has thus created a self-sustaining system from which we can derive insights and adapt to our contemporary demands.

Commensurate with the scale of the TW challenge, inter-university and even international consortiums have dedicated research efforts to the development of artificial photosynthesis (AP), with the intention of mimicking green plants to produce solar chemicals and ultimately solar fuels.[12] However, the term AP is traditionally often synonymous with solar fuels or water splitting, which may be unnecessarily restrictive. As the term suggests, AP is the invention of man-made (artificial) chemical or biological processes to harness light (photo) to produce fuels and chemicals (synthesis). To differentiate between photosynthesis and photocatalysis, we can consider a convention based on thermodynamics and kinetics.[13] Photocatalysis involves light as an energy input to accelerate rates by overcoming the kinetic barrier for reactions that are already thermodynamically downhill reactions, whereas photosynthesis requires light to drive reactions that are otherwise thermodynamically uphill. In other words, we use photosynthesis to refer to redox processes that will store energy overall across two half-reactions.

Tremendous progress has been reported in the field of AP, although the research has largely focused on solar fuels production through water splitting by semiconductor

materials.[14-17] On the other hand, molecular systems offer the advantages of systematic ligand design and modification, better product selectivity, and more comprehensive characterization.

Inspired by natural photosynthesis, our research group has adopted an engineering "plug-and-play" concept to create AP constructs based on combining the functions of individual components (Figure 1.1). A number of researchers have been exploring a more general perspective to use light to make chemicals, beyond H_2 and O_2 from water splitting.

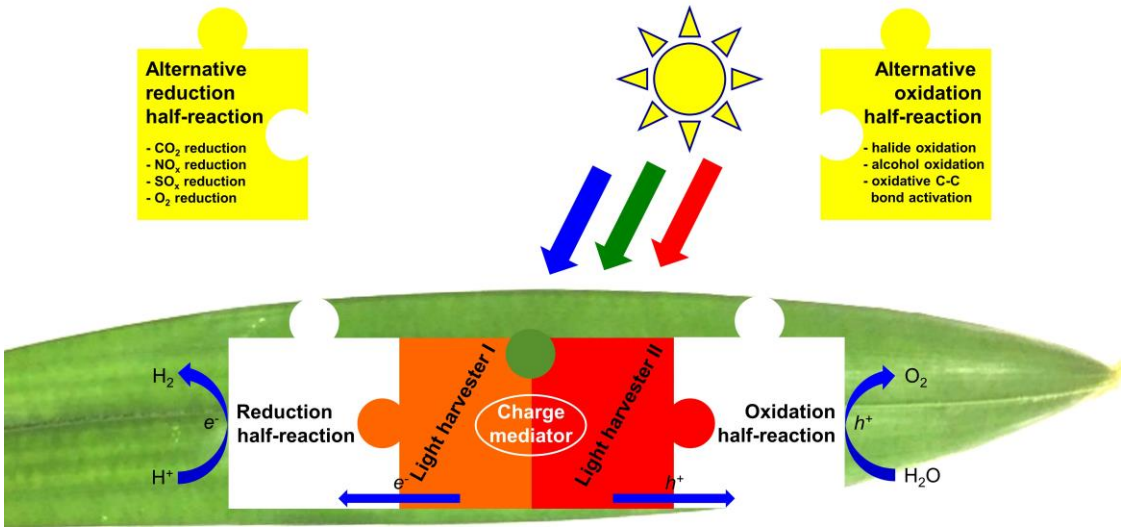

Figure 1.1. Proposed general "plug-and-play" system for AP to encompass a more inclusive range of catalytic processes that can store sunlight in the form of chemical bonds in solar fuels and value-added solar chemicals.

In general, photosynthetic systems possess elements to enable the following essential processes:

(i) The productive absorption of sunlight, especially with panchromatic chromophores.

(ii) The effective charge separation and interfacial chemistry to achieve a more systematic flow of reducing and oxidizing equivalents.

(iii) The multielectron catalytic reduction of substrates to produce fuels.

(iv) The multielectron catalytic oxidation of substrates to produce similarly value-added chemicals other than the atmospherically abundant O_2.

With the aim of developing new, and applicable AP systems, the focus of this thesis will be to examine alternative photocatalytic oxidation reactions that would lead to production of synthetically more useful chemicals than O_2, which is commonly generated by solar water splitting. Specifically, the elusive oxidative carbon-carbon (C-C) single bond activation reaction will be explored. Given the abundance of C-C bonds in organic compounds, their selective activation would be a useful tool in synthetic chemistry.

1.2 Alternatives to Water Oxidation Reaction

The envisioned plug-and-play concept allows for a highly modular system in which a variety of oxidative and reductive half-reactions can be combined into suitable AP systems. Apart from the water oxidation reaction, which has been an integral part of many water splitting AP units, we aim to investigate other photo-oxidative transformations that can supply electrons for the reductive half-reaction and result in value-added solar chemicals production. Discussed in this section are the photocatalytic oxidation processes that generate solar chemicals, with an emphasis on the use of earth-abundant constituents.

The water oxidation half-reaction is kinetically and thermodynamically challenging since it involves multiple electron and proton transfers, and usually produces O_2, an abundant gas with limited commercial value. Hence, there have been some efforts to develop scalable oxidative half-reactions commensurate with the electron demand for solar fuels production. For instance, Meyer and co-workers have been adapting their dye-sensitized photoelectrochemical cell (DSPEC) architecture to target the oxidation of earth-abundant halides, namely bromide and chloride (Scheme 1.1).[18, 19] They employed cationic, visible light absorbing Ru^{II} polypyridyl photosensitizers and complexes to form ionic donor-acceptor interactions with halide ions and bring them in close proximity to the catalytic center.[20] After the halide photooxidation reaction, the X_2 molecules would be released due to the absence of Coulombic interactions.[20] In the case of chloride oxidation, the reaction product was indirectly determined to be chlorine atoms *via* the use of 2,3-dimethyl-1,3-butadiene as a halogen trap.[19]

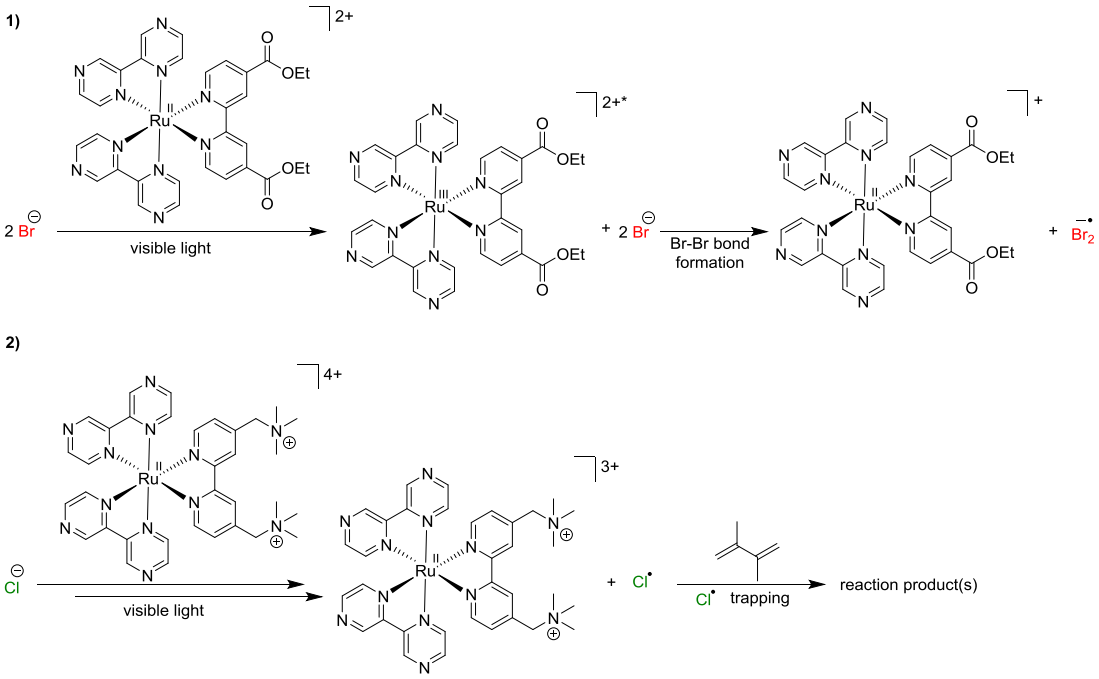

Scheme 1.1. Work of Meyer and co-workers on photooxidation of 1) bromide and 2) chloride in presence of ruthenium polypyridyl photocatalysts.[18-20]

They have also applied their DSPEC for HBr splitting en route to the simultaneous generation of H_2 as a solar fuel and Br_2 and Br_3^- as solar chemicals.[21] Notably, however, the DSPECs predominantly comprise Ru photosensitizers and catalysts, which will offer future opportunities for replacement with earth-abundant variants instead.

As another alternative to water oxidation, Reisner and co-workers have reported a system that replaced water oxidation with alcohol oxidation, and coupled it with H_2 production to form an AP unit with concurrent solar chemicals and solar fuel generation.[22] They employed a cyanamide surface-functionalized melon-type carbon nitride as the light harvester that oxidizes 4-methylbenzyl alcohol to the corresponding benzaldehyde through the photogenerated holes, while electrons are funneled to a $[P_2N_2]Ni^{II}$ catalyst, which performs as the H_2 evolution catalyst.[22] This study represents an outstanding integrated catalytic redox cycle free of expensive noble metals with almost 100% atom economy and yields value-added products for both half-reactions, showcasing the feasibility of accomplishing functional and effective AP using exclusively earth-abundant elements.[22]

In some novel developments lately, there has been greater political and economic pressure to reduce our dependence on finite fossil fuels and harness the under-utilized but sizable quantities of biomass as renewable sources of carbon. Biomass is often

treated as fuel currently, which destroys the inherent valuable functional groups in the original form. Moreover, the biomass-derived feedstocks produced in large scale often possess low value, which can be increased in further transformations. Thus, they represent suitable substrates for the oxidative half-reaction in AP constructs.

In a recent study, Reisner and Kuehnel discussed the use of biomass lignocellulose for H_2 production at room temperature and light irradiation in a photoreforming process.[23, 24] Although the reduction half-reaction generates H_2 cleanly as a fuel, the biomass oxidation half-reaction is unselective and predominantly yields CO_2, which also presents opportunities to develop new processes to obtain more value-added feedstocks from non-food biomass.[23,24] For example, Sun and co-workers reported the oxidation of furfuryl alcohol and 5-hydroxymethylfurfural (HMF) coupled with a H_2 evolution half-reaction using earth-abundant electrocatalysts.[25, 26] The reaction was conducted under strongly alkaline conditions and carboxylate products were obtained, of which 2,5-furandicarboxylic acid is a promising replacement for terephthalic acid in polyamides, polyurethanes, and polyesters.[26] Their subsequent visible-light induced oxidative valorization of furfuryl alcohol and HMF over Ni decorated ultrathin CdS nanosheets in neutral water resulted in selective formation of value-added aldehyde or acid products, depending on the reaction conditions.[27] Unfortunately, aldehydes appeared to inhibit the Ni/CdS catalyst, which led to incomplete conversion of HMF.[27] Nonetheless, their work is an important demonstration that biomass derived feedstocks can be upgraded to value-added aldehydes or acids, which are commonly used in the pharmaceutical and fragrance industries. This oxidative half-reaction produces more valuable solar chemicals than O_2 from H_2O.

Bearing the versatile plug-and-play concept in mind, we have been exploring the oxidation of non-food biomass lignin as another half-reaction in an AP system. Lignin, a sizable constituent of non-food biomass, is especially attractive since it represents one of the only renewable sources of aromatic compounds on Earth. However, although much effort has been devoted to the valorization of lignin into fuels through thermal and microbial reactions, majority of the valuable aromatic units and functional groups are destroyed. In our group's work on lignin model compounds, Soo and co-workers have uncovered a unique vanadium(V) photocatalyst that is able to induce a highly selective and unprecedented C-C single bond scission in aliphatic alcohols under visible light irradiation and ambient, atmospheric conditions.[28] Surprisingly, the more common

alcohol oxidation to ketones is not competitive since it occurs only at temperatures exceeding 80 °C.[28] The obtained reaction products are valuable aryl aldehydes and formates, which contain a synthetically useful carbonyl moiety. This remarkable photooxidation reaction catalyzed by the earth-abundant vanadium-containing complexes is a suitable half-reaction for highly modular AP systems that would generate solar chemicals. Development of vanadium complexes that effect such unprecedented C-C bond cleavage in aliphatic alcohols under visible light irradiation and ambient conditions will be discussed in more detail in the following chapters of the thesis.

References

1. Smalley, R. E. *MRS Bull*., **2005**, *30*, 412–417.
2. Styring, S. *Faraday Discuss*., **2012**, *155*, 357–376.
3. Hambourger, M.; Moore, G. F.; Kramer, D. M.; Gust, D.; Moore, A. L.; T. A. Moore, *Chem. Soc. Rev*., **2009**, *38*, 25–35.
4. Moore, G. F.; Brudvig, G. W. *Annu. Rev. Condens. Matter Phys*., **2011**, *2*, 303–327.
5. Fischer, E. M.; Knutti, R. *Nat. Clim. Change*, **2015**, *5*, 560–564.
6. Lesk, C.; Rowhani, P.; Ramankutty, N. *Nature*, **2016**, *529*, 84–87.
7. Calvin, M. *Photochem. Photobiol*., **1983**, *37*, 349–360.
8. Gust, D.; Moore, T. A.; Moore, A. L. *Acc. Chem. Res*., **2009**, *42*, 1890–1898.
9. McConnell, I.; Li, G. H.; Brudvig, G. W. *Chem. Biol*., **2010**, *17*, 434–447.
10. Lewis, N. S.; Nocera, D. G. *Proc. Natl. Acad. Sci. U. S. A*., **2006**, *103*, 15729–15735.
11. Lewis, N. S. *Science*, **2016**, *351*, aad1920.
12. Faunce, T. A.; Lubitz, W.; Rutherford, A. W.; MacFarlane, D. R.; Moore, G. F.; Yang, P. D.; Nocera, D. G.; Moore, T. A.; Gregory, D. H.; Fukuzumi, S.; Yoon, K. B.; Armstrong, F. A.; Wasielewski, M. R.; Styring, S. *Energy Environ. Sci*., **2013**, *6*, 695–698.
13. Osterloh, F. E. *ACS Energy Lett*., **2017**, *2*, 445–453.
14. Fujishima, A.; Honda, K. *Nature*, **1972**, *238*, 37–38.
15. Khaselev, O.; Turner, J. A. *Science*, **1998**, *280*, 425–427.
16. Reece, S. Y.; Hamel, J. A.; Sung, K.; Jarvi, T. D.; Esswein, A. J.; Pijpers, J. J. H.; Nocera, D. G.; *Science*, **2011**, *334*, 645–648.
17. Wang, Q.; Hisatomi, T.; Jia, Q. X.; Tokudome, H.; Zhong, M.; Wang, C. Z.; Pan, Z. H.; Takata, T.; Nakabayashi, M.; Shibata, N.; Li, Y. B.; Sharp, I. D.; Kudo, A.; Yamada, T.; Domen, K. *Nat. Mater*., **2016**, *15*, 611–615.
18. Li, G. C.; Ward, W. M.; Meyer, G. J. *J. Am. Chem. Soc*., **2015**, *137*, 8321–8323.
19. Wehlin, S. A. M.; Troian-Gautier, L. Li, G. C.; Meyer, G. J. *J. Am. Chem. Soc*., **2017**, *139*, 12903–12906.
20. Li, G. C.; Swords, W. B.; Meyer, G. J.; *J. Am. Chem. Soc*., **2017**, *139*, 14983–14991.

21. Brady, M. D.; Sampaio, R. N.; Wang, D. G.; Meyer, T. J.; Meyer, G. J. *J. Am. Chem. Soc*., **2017**, *139*, 15612–15615.

22. Kasap, H.; Caputo, C. A.; Martindale, B. C. M.; Godin, R.; Lau, V. W. H.; Lotsch, B. V.; Durrant, J. R.; Reisner, E. *J. Am. Chem. Soc*., **2016**, *138*, 9183–9192.

23. Kuehnel, M. F.; Reisner, E. *Angew. Chem., Int. Ed*., **2018**, *57*, 3290–3296.

24. Wakerley, D. W.; Kuehnel, M. F.; Orchard, K. L.; Ly, K. H.; Rosser, T. E.; Reisner, E. *Nat. Energy*, **2017**, *2*, 17021.

25. You, B.; Jiang, N.; Liu, X.; Sun, Y. J. *Angew. Chem., Int. Ed*., **2016**, *55*, 9913–9917.

26. You, B.; Liu, X.; Jiang, N.; Sun, Y. J. *J. Am. Chem. Soc*., **2016**, *138*, 13639–13646.

27. Han, G. Q.; Jin, Y. H.; Burgess, R. A.; Dickenson, N. E.; Cao, X. M.; Sun, Y. J. *J. Am. Chem. Soc*., **2017**, *139*, 15584–15587.

28. Gazi, S.; Ng, W. K. H.; Ganguly, R.; Moeljadi, A. M. P.; Hirao, H.; Soo, H. S. *Chem. Sci*., **2015**, *6*, 7130–7142.

CHAPTER 2

LITERATURE REVIEW

2.1 Thermal and Photoredox Carbon-Carbon Bond Cleavage Reactions

The C-C bonds are among one of the most pervasive covalent interactions in nature. Given that formation of such bonds typically leads to the increase of a molecule's complexity, methods that enable C-C bond construction are highly sought after in synthetic chemistry. However, in some instances, C-C bond cleavage processes may also yield synthetically useful compounds that cannot be obtained by other means. Unfortunately, selective, catalytic C-C single bond cleavage has been a formidable problem that is yet to be overcome. Several challenges include the poor selectivity of C-C bond activation over reactions in other functional groups, the lack of thermodynamically compensating bond formation processes, and the kinetic inertness of the non-polar C-C bond. Hence, thermal conditions are typically employed to induce the C-C bond activation reactions in specialized substrates with specifically constructed functional groups to prevent undesired decomposition.

In one recent example, Sarpong *et al*. demonstrated a deconstructive fluorination of cyclic amines.[1] The reaction encompasses a $C(sp^3)$-$C(sp^3)$ bond cleavage with a concomitant $C(sp^3)$-F bond formation in presence of Selectfluor and silver catalyst under thermal conditions (Scheme 2.1).[1] The commercially available cyclic amines are converted into fluorinated acyclic analogues with potential application in pharmaceutical or agrochemical industry *via* a two-step process.[1] First, in the presence of Ag(I) salt, the cyclic amine is oxidized to the iminium ion, which then reacts with water to form a hemiaminal.[1] In the second step, the hemiaminal undergoes a ring-opening with the aid of the Ag salt yielding the primary alkyl radical in the process.[1] Subsequently, a fluorine atom transfer furnishes the desired fluorinated amine product.[1] Notably, this work showcases the possibility of utilizing cyclic amines as synthons for amino alkyl radical intermediates that could undergo coupling reactions with other radicals.[1] Furthermore, the deconstructive fluorination was applicable to cyclic amines containing unstrained rings and was even demonstrated in several examples of di- and tripeptides as a tool for rapid drug discovery.[1] Additionally, the reaction tolerated various functionalities, allowing for fluorination in a number of substituted piperidines.

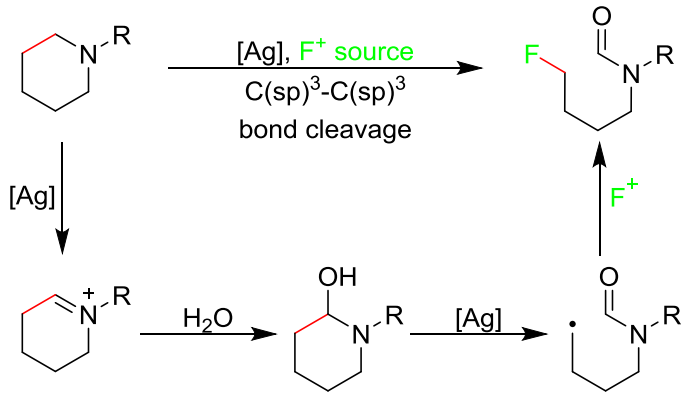

Scheme 2.1. Deconstructive fluorination of cyclic amines demonstrated by Sarpong *et al.*[1]

In another report, Li *et al*. used a silver(I) catalyst under thermal conditions and oxygen environment to perform a highly selective C-C bond cleavage of 1,2-diols (Scheme 2.2) and obtained corresponding carboxylic acids as products.[2] Both terminal and internal diols were examined, and the reaction showed good tolerance to various functional groups.[2] Furthermore, the authors reported several examples of cyclic diols and natural products that could be converted into carboxyl acid derivatives.[2] The procedure could even be applied to gram-scale reactions with satisfactory conversion and product yields.[2] To investigate the reaction mechanism behind this transformation, the authors utilized $^{18}O_2$ as the sole oxidant and proposed that the 1,2-diol is firstly oxidized to a 1,2-dicarbonyl intermediate, which then undergoes a Baeyer-Villager-type cleavage to give the final products.[2]

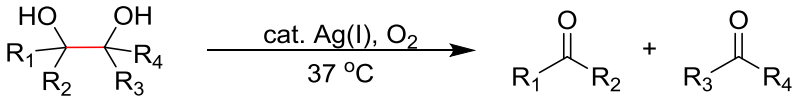

Scheme 2.2. General reaction conditions for oxidative C-C bond cleavage in 1,2-diols proposed by Li *et al.*[2]

A recent review paper by Dong and co-workers summarized the "cut and sew" concept of transition metal (TM) catalyzed C-C bond activations in strained systems under thermal conditions.[3,4] Generally, the TM oxidatively adds into the C-C bond leaving the terminal carbons exposed for functionalization in subsequent migratory insertion and reductive elimination steps with unsaturated moieties such as alkenes, alkynes, CO, or other polar multiple bonds (Scheme 2.3). The procedure is mainly applicable to highly strained three- or four-membered rings, while the instances of unstrained systems are rare and usually require presence of directing groups.

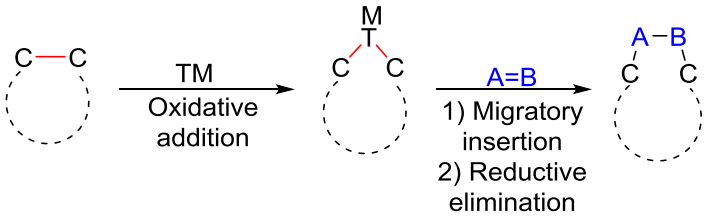

Scheme 2.3. The "cut and sew" concept of C-C bond activation by TM catalysts.[3] The C-C bond depicted in red undergoes activation, while the dashed circle represents a ring-type substrate of arbitrary size.

Additional to thermal processes, photoredox C-C bond activation chemistry has mainly relied on the release of ring strain in small cyclic organic molecules such as cyclopropane, cyclobutane, and even cyclopentane rings. For instance, Zheng and co-workers have reported annulation reactions of cyclopropyl- and cyclobutylanilines with unsaturated systems to give amine-functionalized ring-expanded products (Scheme 2.4).[5,6] The ring- opening is facilitated by the oxidation of the aniline to a transient amine radical cation by the photoexcited $*Ir^{3+}$ catalyst, which is in turn reduced to Ir^{2+}.[5,6] The following ring-opening generates a radical iminium ion, which can then react with phenylacetylene in a intermolecular fashion to yield the vinyl radical.[5] Subsequently, the vinyl radical undergoes an intramolecular addition to the iminium ion, giving rise to a six-member ring and an amine radical cation.[5] Finally, the radical cation is reduced by Ir^{2+}, which regenerates to Ir^{3+} completing the cycle.[5] As reported by the authors, both mono- and bicyclic cyclobutylanilines could react with terminal and internal alkynes to give rise to amine-functionalized six-member cyclic products.[5] Furthermore, the reaction showed significant tolerance to various functionalities incorporated on the cyclobutylaniline, including the presence of heterocycles.[5]

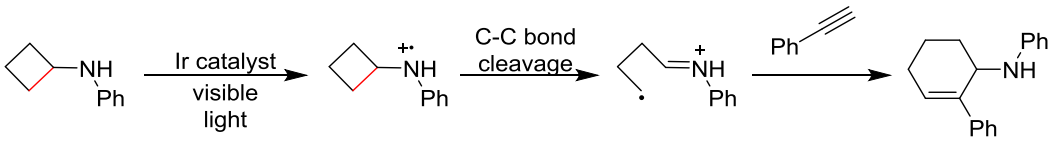

Scheme 2.4. Visible light induced [4+2] annulation of cyclobutylaniline with alkynes proposed by Zheng and co-workers.[5,6]

In a related study, Knowles *et al*. demonstrated a photocatalytic isomerization of cycloalkanols to acyclic ketones *via* C-C bond cleavage.[7] Their mechanistic studies suggest that the key alkoxy radical intermediate is formed during the intramolecular proton-coupled electron transfer (PCET) (Scheme 2.5).[7] The alkoxy radical subsequently weakens the proximal C-C bond and causes the ring-opening *via β*-

scission. The formed alkyl radical is finally trapped and reduced by a hydrogen atom donor.[7] The reaction proceeded with cyclic substrates of different sizes, indicating that the ring-strain is not required for this transformation. Furthermore, the C-C bond scission was possible in bicyclic systems as demonstrated in several examples of natural product derivatives. Finally, the authors also explored the possibility of functionalizing the alkyl radical with various halogen atoms further supporting the versatility of this C-C bond activation strategy. Though the work demonstrates an unusual C-C bond deconstruction *via* PCET and *β*-cleavage, the procedure relies on expensive iridium photosensitizers and is limited to cyclic alcohols.

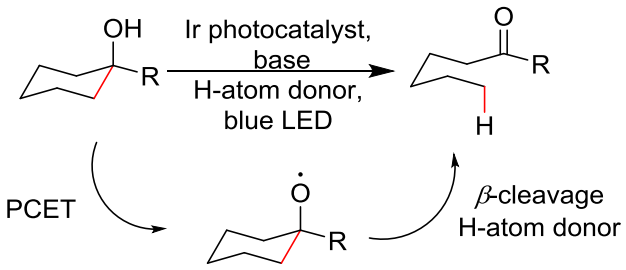

Scheme 2.5. Visible-light induced ring-opening in cycloalkanols *via* alkoxy radical intermediate reported by Knowles *et al*.[7]

On the other hand, the group of Zuo has combined the photoredox catalytic ring-opening of unstrained secondary cycloalkanols with amination of the transient alkyl radicals by utilizing cerium trichloride ($CeCl_3$) as the catalyst (Scheme 2.6).[8] Cerium(III) compounds are known for their luminescent properties, but have not been used in photoredox catalysis prior to this work.[8] Here, the authors propose that Ce(III) undergoes a photoexcitation to *Ce(III), which by single-electron transfer (SET) would generate Ce(IV).[8] The highly oxidizing Ce(IV) species then promotes a *β*-cleavage, similarly to what was observed in the work of Knowles, to yield a Ce(III)-coordinated carbonyl intermediate and an alkyl radical.[8] The resulting alkyl radical is finally functionalized by di-*tert*-butyl azodicarboxylate (DBAD). The authors noted that analogously with the report of Knowles and co-workers, ring-strain of the substrate was not a pre-requisite for *β*-scission. Additionally, the C-C bond cleavage/amination proceeded with both secondary and tertiary cycloalkanols, and various functional groups, as well as sterically demanding substrates were tolerated. Furthermore, the authors demonstrated a possibility of using this procedure for the preparation of pharmaceutically important compounds by incorporating the diazepine pharmacophore in the reaction products.

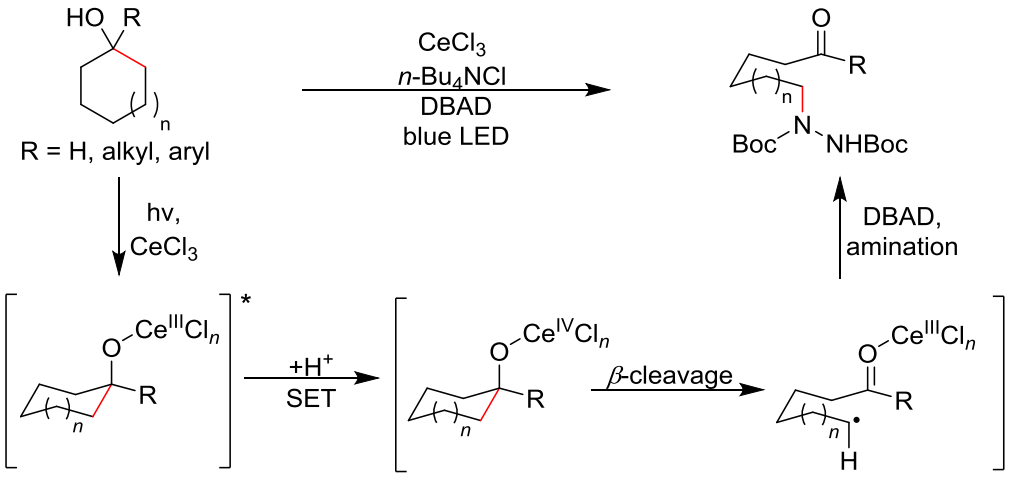

Scheme 2.6. Cerium(III) catalyzed C-C bond cleavage with subsequent amination in unstrained cycloalkanols reported by Zuo *et al*.[8]

Another study pertaining to the ring-opening of unstrained cycloalkanols under mild conditions was reported by Zhu and co-workers.[9] In their work, the authors used iridium-based photocatalyst to perform a C-C bond cleavage of medium- and large-sized cycloalkanols followed by a bromination to yield distally brominated alkyl ketones (Scheme 2.7).[9] The authors proposed that in the presence of light, the photoexcited $*Ir^{III}$ is generated, which is subsequently oxidatively quenched by *N*-bromosuccinimide (NBS) to form Ir^{IV}.[9] However, the Ir^{IV} complex is not able to oxidize the cycloalkanol to the corresponding alkoxy radical *via* SET.[9] Instead, the alkoxy radical is presumably generated *via* PCET in the presence of Ir^{IV} and a weak base, such as succinimide anion.[9] The alkoxy radical may alternatively form from the homolytic cleavage of the O-I bond formed *in situ* by the reaction of alcohol with phenyliodine(III) diacetate (PIDA).[9] Subsequently, the alkoxy radical undergoes *β*-cleavage to yield the alkyl radical and a carbonyl product.[9] The alkyl radical is finally trapped by NBS to furnish the brominated ketone.[9] The authors also demonstrated that the reaction products could be further functionalized to give a variety of useful compounds for organic or medicinal synthesis.[9] Furthermore, the procedure was applicable to ring-opening cyanation and alkynylation reactions of unstrained rings to a certain extent showcasing the prospect of C-C bond cleavage followed by distal C-C bond formation.[9]

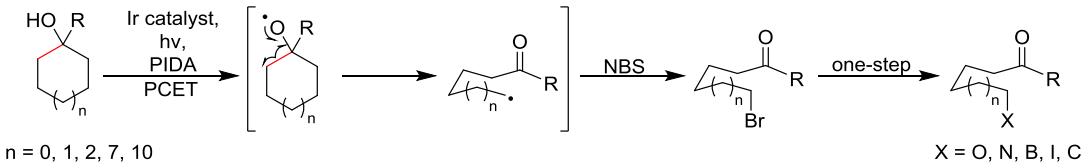

Scheme 2.7. Photoredox C-C bond cleavage in unstrained cycloalkanols reported by Zhu *et al*.

The group of MacMillan has been especially active in exploring the photoredox catalysis.[10-15] Their work has mainly been noted for successfully merging the photoredox and nickel-based catalysis to combine the C-C bond cleavage *via* decarboxylation of carboxylic acids, followed by a C-C or C-heteroatom bond formation processes (Scheme 2.8).[13] Typically, the acid substrate is deprotonated, the carboxylic acid anion reduces the photoexcited *Ir(III) catalyst and forms the alkyl radical upon decarboxylation. Subsequently, the alkyl radical is coupled with an alkyl bromide in the presence of a nickel catalyst to form a C-C cross coupled product.[13] Their work has been applied to a large number of substrates, including amino acids,[16] and they demonstrated good tolerance to various functionalities.

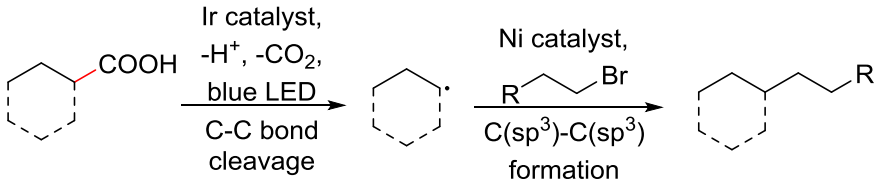

Scheme 2.8. The merger of photoredox and nickel catalysis for C-C bond formation proposed by MacMillan *et al*.[13] The dashed line represents an arbitrary size of the substrate.

Most of the reported procedures for photoredox C-C bond activation involve small, and often strained molecules, while its application for selective breakdown of macromolecules remains scarce. In a formative study, Wang *et al*. employed a heterogeneous, mesoporous graphitic carbon nitride (mpg-C_3N_4) catalyst for photo-oxidative C-C cleavage in β-O-4- and β-1-containing lignin model compounds under mild conditions and room temperature through π-π stacking interactions.[17] The authors proposed that upon light absorption, C_3N_4 would undergo charge separation, and the photogenerated holes (h^+) in the valence band were the active species to mediate the C-C bond cleavage process of β-O-4 lignin model **1** in the presence of O_2 (Scheme 2.9) as

supported by the experiments involving active species scavengers as well as DFT calculations.[17]

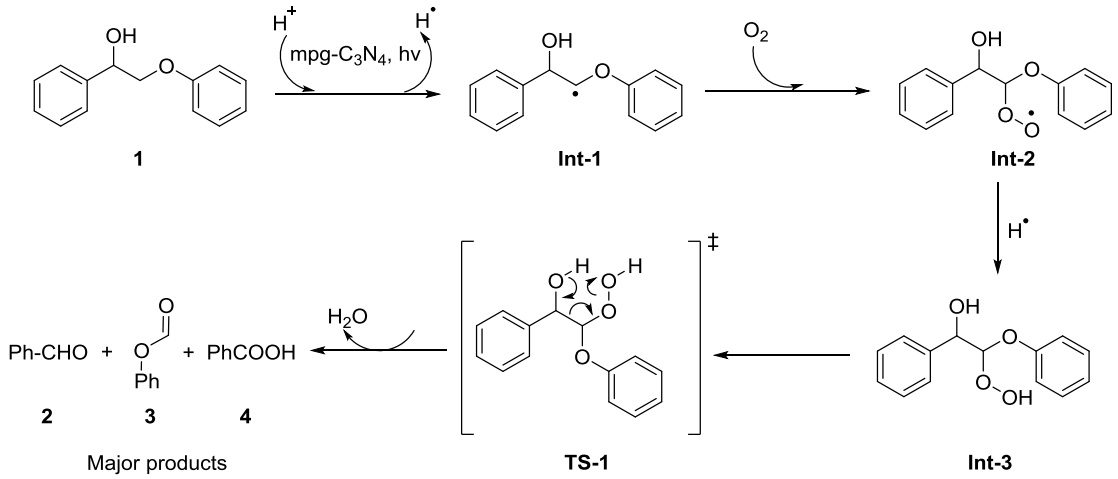

Scheme 2.9. Mechanism for photocatalytic C-C bond cleavage in **1** by mpg-C_3N_4 proposed by Wang and co-workers.[17]

The obtained major reaction products included synthetically valuable benzaldehyde (**2**), phenyl formate (**3**), and benzoic acid (**4**), while small amounts of the benzyl alcohol oxidation product were also noted.[17] The authors attributed the significant photocatalytic reactivity of the mpg-C_3N_4 partly to the low charge recombination efficiency and the high specific surface area (206.5 $m^2 g^{-1}$). This study indicates the potential of photoredox catalysis in selectively breaking down polymeric feedstocks to useful, platform chemicals.

2.2 Vanadium-based Catalysts for C-C Bond Cleavage

As previously discussed, application of photoredox catalysis for C-C bond activation has been significantly limited, either by the high price of photocatalysts, or by the narrow choice of substrates, which is mainly limited to small, ring-strained compounds. To fully utilize the potential of photoredox catalysis in late-stage functionalization of intricate molecules, or in valorization of feedstock macromolecules, more affordable, yet selective photocatalysts need to be developed.

As an earth-abundant transition metal, vanadium has attracted significant attention in catalysis.[18] High oxidation state vanadium catalysts are known to catalyze aerial oxidations of benzylic, allylic, and propargylic alcohols.[19-21] In addition, vanadium-based catalysts have been used for aerobic oxidative kinetic resolution of α-hydroxy

acids,[22] esters,[23] amides,[24] and ketones.[25] With the ever-growing human population, increased consumption of the fossil fuels, and the negative environmental effects associated with their usage, the topic of biomass valorization has become very prominent among the academic society. The selective bond cleavage of macromolecular biomass constituents, such as lignin, would generate useful platform chemicals that can be used as pharmaceutical precursors or in synthetic chemistry.[26] To that end, several research groups have been developing vanadium catalysts for selective bond scission in lignin models.

While investigating the selective breakdown of lignin model compounds, the group of Toste has reported vanadium catalysts that effect benzylic alcohol oxidation and a unique C-O bond cleavage in diol-containing lignin model compounds under thermal conditions.[27-28] Their vanadium complexes (**VO**-(**1**-**7**)) depicted in the Figure 2.1 exhibited different reactivity with a representative, dimeric lignin model, (1*R*,2*S*)-1-(4-ethoxy-3-methoxyphenyl)-2-(2-methoxyphenoxy)propane-1,3-diol (**5)**, which contains the *β*-O-4 linkage that is also found in native lignin.

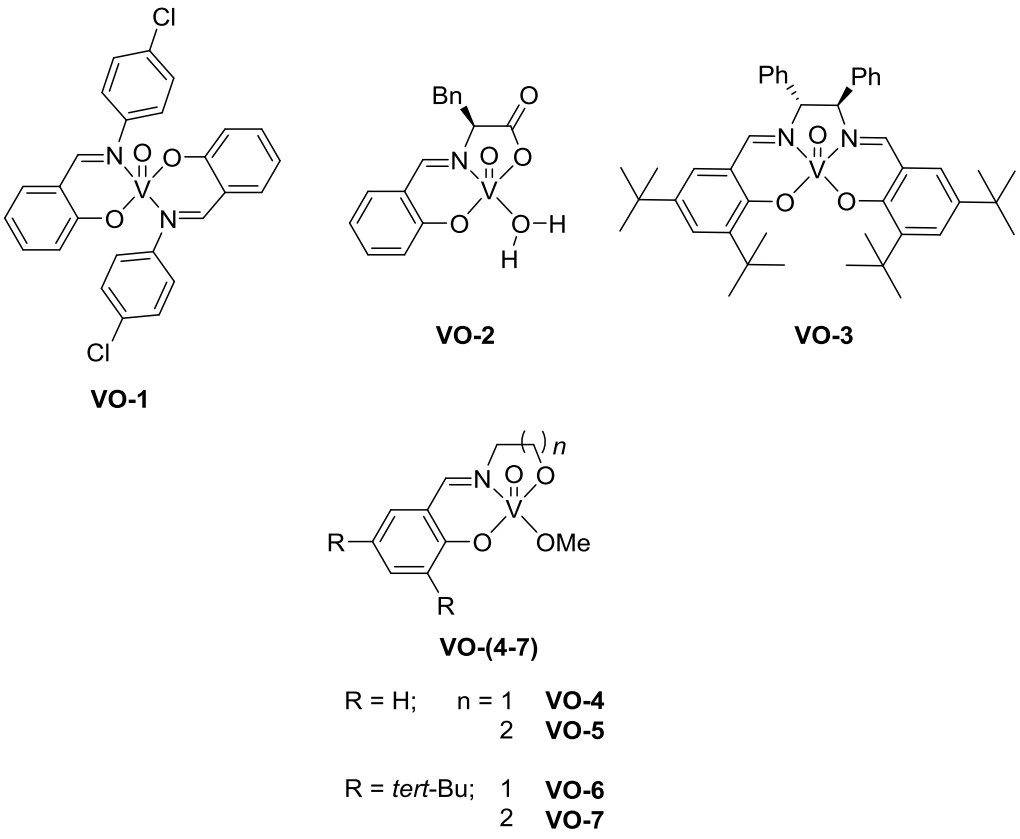

Figure 2.1. Vanadium oxo complexes for benzylic alcohol oxidation and C-O bond cleavage in lignin models reported by Toste *et al*.[27]

The authors discovered that although all the complexes yielded C-O bond cleavage products 1-(4-ethoxy-3-methoxyphenyl)prop-2-en-1-one and guaiacol (**6** and **7**, respectively) to some extent besides the ketone product **8** (Scheme 2.10), typical benzylic alcohol oxidation was particularly suppressed when catalysts with a tridentate Schiff base, large bite angle ligand were used (**VO-4** and **VO-6**).[27] In addition, the catalyst **VO-7** bearing *ter*t-butyl (*tert*-Bu) groups on the ligand was believed to have increased catalytic rate due to the inability to form insoluble aggregates because of its steric bulk.[27]

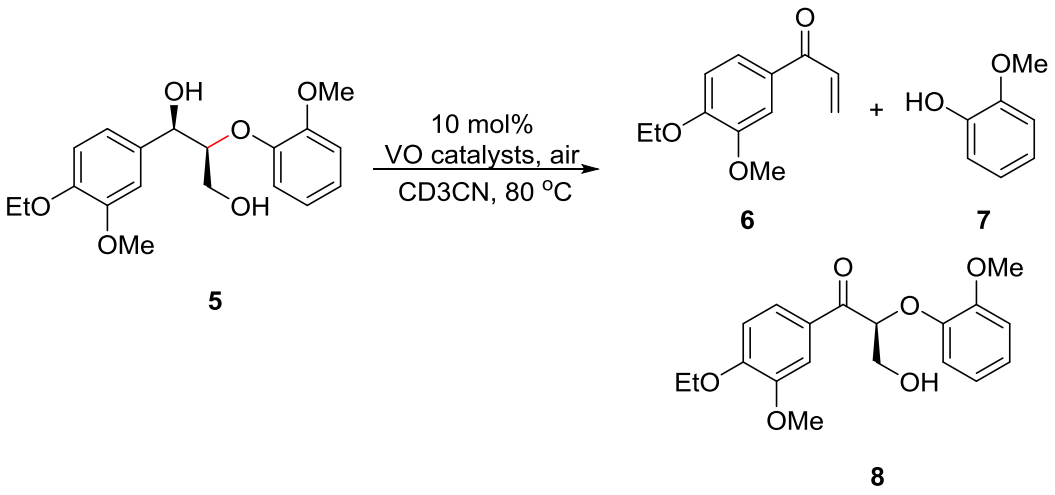

Scheme 2.10. Thermal reactivity of vanadium complexes reported by Toste *et al.* with **5**.[27] The C-O bond depicted in red is cleaved.

Furthermore, this overall redox-neutral process does not require O_2 to proceed, but its presence accelerated it.[27] The authors proposed that the reaction proceeds with the generation of the ketyl radical (**TS-2**) formed by hydrogen atom abstraction from the benzylic position, followed by the elimination of the aryloxy radical and the formation of the enolate (**Int-4**).[27,28] The enolate finally converts to the enone product **6**, while generating a V^{IV} species (**Int-5**).[27,28] The catalyst is finally re-oxidized by the previously formed aryloxy radical.[27,28] This proposed mechanism is depicted in Scheme 2.11 below.

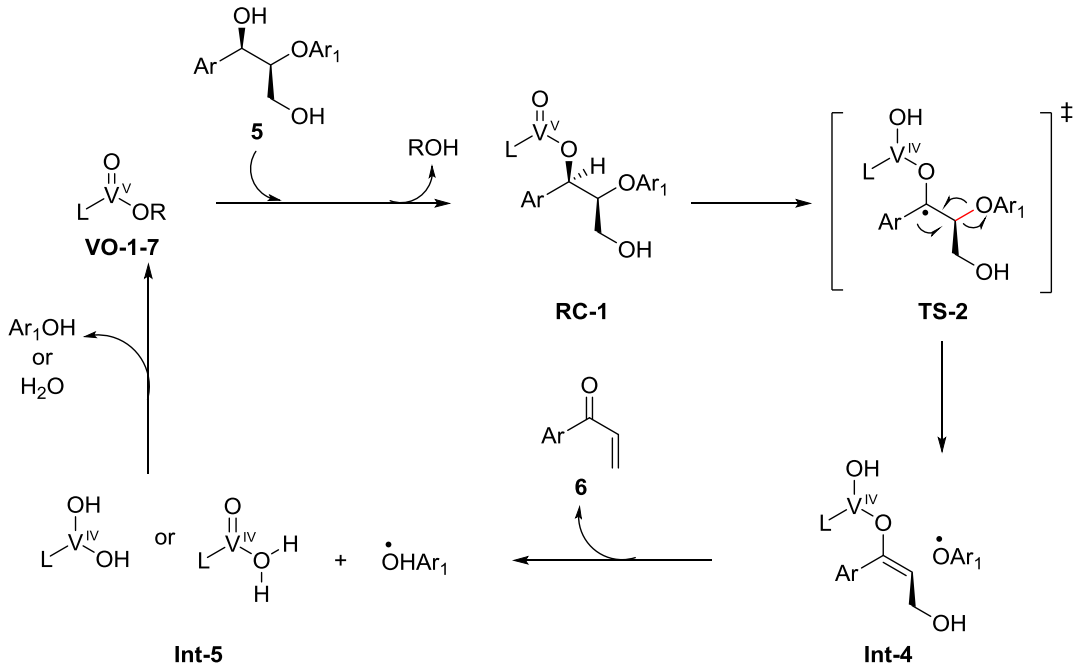

Scheme 2.11. Catalytic cycle for thermal C-O bond cleavage in **5** proposed by Toste and co-workers.[27] Symbol L represents the ligand of the vanadium catalyst.

The studies conducted by Toste and co-workers demonstrate that careful tuning of the ligand bound to the vanadium metal center can lead to drastically different reactivities. Although it was C-O, and not C-C bond cleavage that the authors observed, their work provides valuable insight into various catalytic applications of vanadium complexes.

On the other hand, in their work with lignin models, Hanson and Silks have revealed vanadium(V) oxo complexes with dipicolinate (**VO-8**), and 8-quinolinate (**VO-9**) ligands (Figure 2.2) that are capable of inducing C-C bond cleavage in several lignin model compounds.[29-32] Similarly to the work of Toste *et al.*, the reactions proceed under thermal conditions.

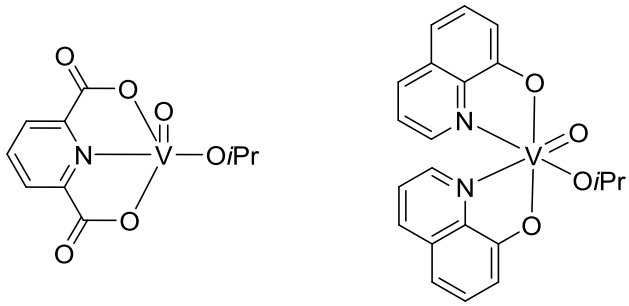

VO-8 **VO-9**

Figure 2.2. Vanadium(V) catalysts with dipicolinate (**VO-8**) and 8-quinolinate (**VO-9**) ligands for selective C-C bond cleavage in lignin models reported by Hanson *et al.*[31]

When reacted with a simple lignin model benzoin methyl ether (**9)** (Scheme 2.12.1), and a phenolic *β*-O-4 lignin model (**11)** (Scheme 2.12.2), vanadium catalysts **VO-8** and **VO-9**, respectively, exhibited unprecedented C-C bond cleavage.[29,30] Although it was shown that **9** would undergo a C-C bond activation without the vanadium catalyst, the presence of **VO-8** enhanced the reaction's rate as well as the yields of **4** and methyl benzoate (**10**).[29] In the presence of **VO-9**, substrate **11** underwent a remarkable C(alkyl)-C(phenyl) bond cleavage uncommon for vanadium catalysts, yielding 2,6-dimethoxybenzoquinone (**12**), acrolein derivative **13** and a ketone **14**. To probe the influence of phenolic groups on this unprecedented reactivity, a non-phenolic analogue of **11** (**15**) was tested. Surprisingly, no C-C bond cleavage was observed with substrate **15** (Scheme 2.12.3).[30] This interesting find indicated that the phenoxy radical intermediate could be formed during the reaction and the formation of superoxo vanadium species by means of H-atom abstraction from the lignin model was proposed (Scheme 2.12.4).[30] However, the more conclusive mechanistic details remain unknown. The work of Hanson and co-workers thus highlights that not only the design of ligands, but also the choice of substrates will have a great effect on the catalyst's selectivity.

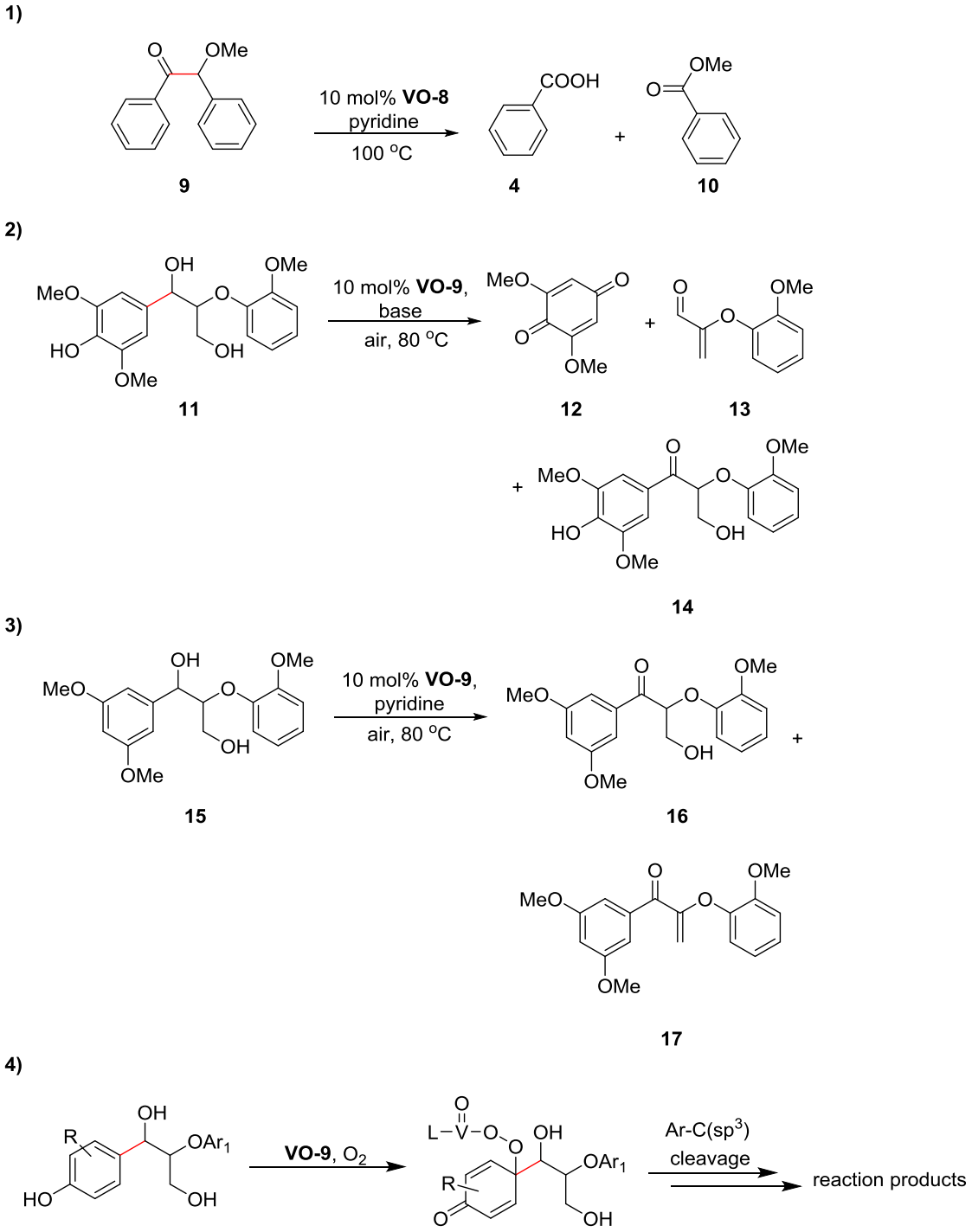

Scheme 2.12. Vanadium-catalyzed C-C bond cleavage in 1) **9** with **VO-8** and, 2) **11** with **VO-9** reported by Hanson and co-workers. 3) No C-C bond cleavage was observed with **15**. 4) General reaction pathway for C-C bond cleavage in phenolic lignin models. The C-C bonds colored in red undergo scission. Symbol L denotes the ligand of the vanadium catalyst.[29,30]

Encouraged by the work of Toste and Hanson on lignin model disassembly by molecular vanadium complexes, Fu and co-workers have undertaken a thorough experimental and DFT computational study to further elucidate the working

mechanisms behind these remarkable transformations and bring unidentified elements to light.[33] The authors provided comparative mechanisms for C-O and C-C bond cleavage in **11** with Toste's Schiff base catalysts (**VO-1-VO-7**) and Hanson's quinolinate catalyst **VO-9** (Scheme 2.13).[33]

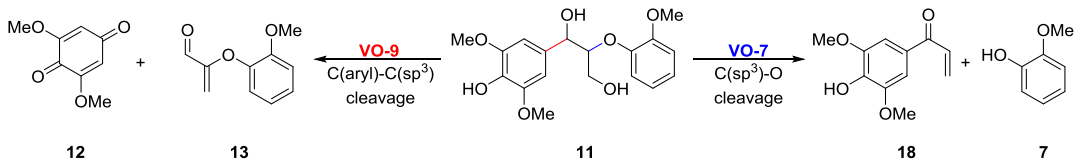

Scheme 2.13. Comparison of different reactivities of **VO-7** and **VO-9** with substrate **3b**.

In the case of C(sp^3)-O bond cleavage catalyzed by Toste's complexes, the authors proposed a V^V-V^{IV}-V^{III}-V^{IV}-V^V cycle (Scheme 2.14).[33] The cycle initiates with the ligand exchange of the alkoxy ligand of V^V catalyst for the benzyl alcohol of **11** (**RC-2**). Subsequently, a hydrogen transfer occurs generating V^{IV} (**Int-6**), which quickly isomerized into V^{III} species (**Int-7**) *via* spin crossover.[33] Afterwards, the C(sp^3)-O bond cleaves and forms V^{IV} intermediate (**Int-8**), from which the re-oxidation of the vanadium catalyst occurs through another spin crossover to regenerate the V^V state (**Int-9**).[33] Lastly, the active V^V catalyst is reformed by the release of **18** and hydroxyl group elimination from **Int-9,** followed by the ligand exchange from **Int-10**.[33]

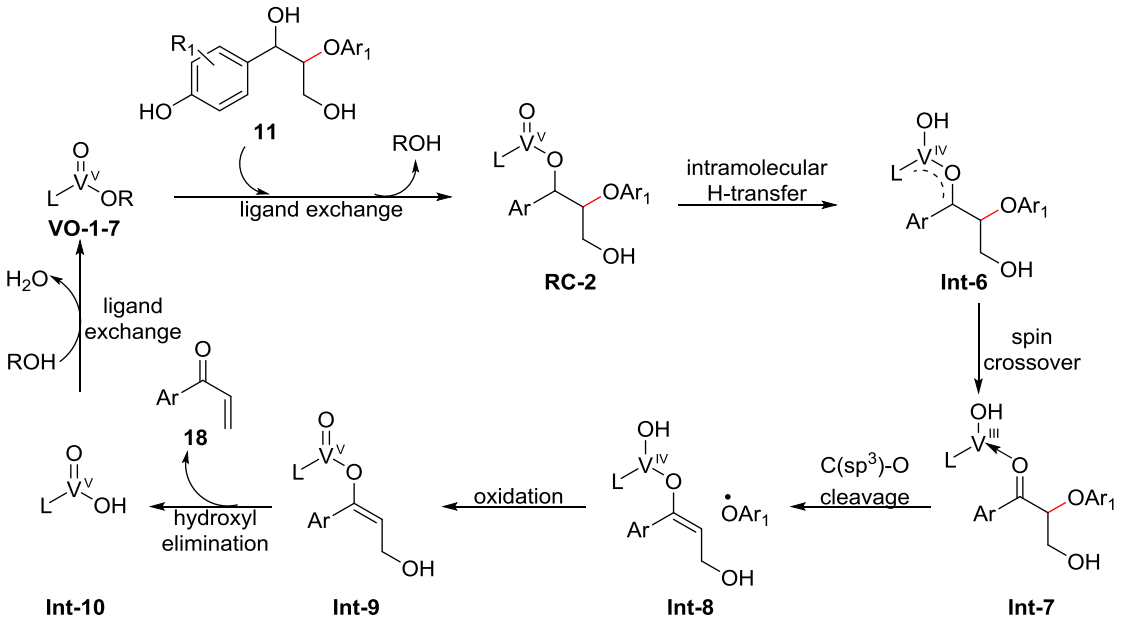

Scheme 2.14. Reaction mechanism for C-O bond cleavage in **11** with Schiff base vanadium catalysts proposed by Fu *et al*.[33] Symbol L denotes the ligand of the vanadium catalyst.

On the other hand, for the C(aryl)-C(sp^3) bond cleavage in **11** with quinolinate **VO-9**, Fu and co-workers proposed a V^V-V^{IV}-V^V catalytic cycle (Scheme 2.15).[33] The cycle begins with the spin crossover-related intermolecular H-atom transfer from the benzylic alcohol of **11** to the oxo ligand of **VO-9**.[33] Consequently, V^{IV} intermediate (**Int-11**) and a phenoxyl radical (**Int-12**) are generated.[33] The V^{IV} intermediate undergoes a proton transfer *via* proton shuttle mechanism to form an alcohol-ligated V^{IV} species (**Int-13**), which then reacts with oxygen and the phenoxyl radical to form a superoxo vanadium intermediate (**Int-14**) with the concomitant release of alcohol.[33] Subsequently, **Int-14** undergoes a stepwise O-O cleavage to yield **Int-15** and **Int-16**, and a C(aryl)-C(sp^3) cleavage, followed by a radical coupling that yields a *gem*-diolate vanadium intermediate (**Int-17**) with concomitant release of **12**.[33] In the final step, the active V^V catalyst and the β-hydroxyaldehyde (**19**) are formed by intramolecular H-atom transfer and ligand exchange from **Int-18**.[33] Dehydration of **19** by **Int-18** aided by a base results in the formation of product **13**.

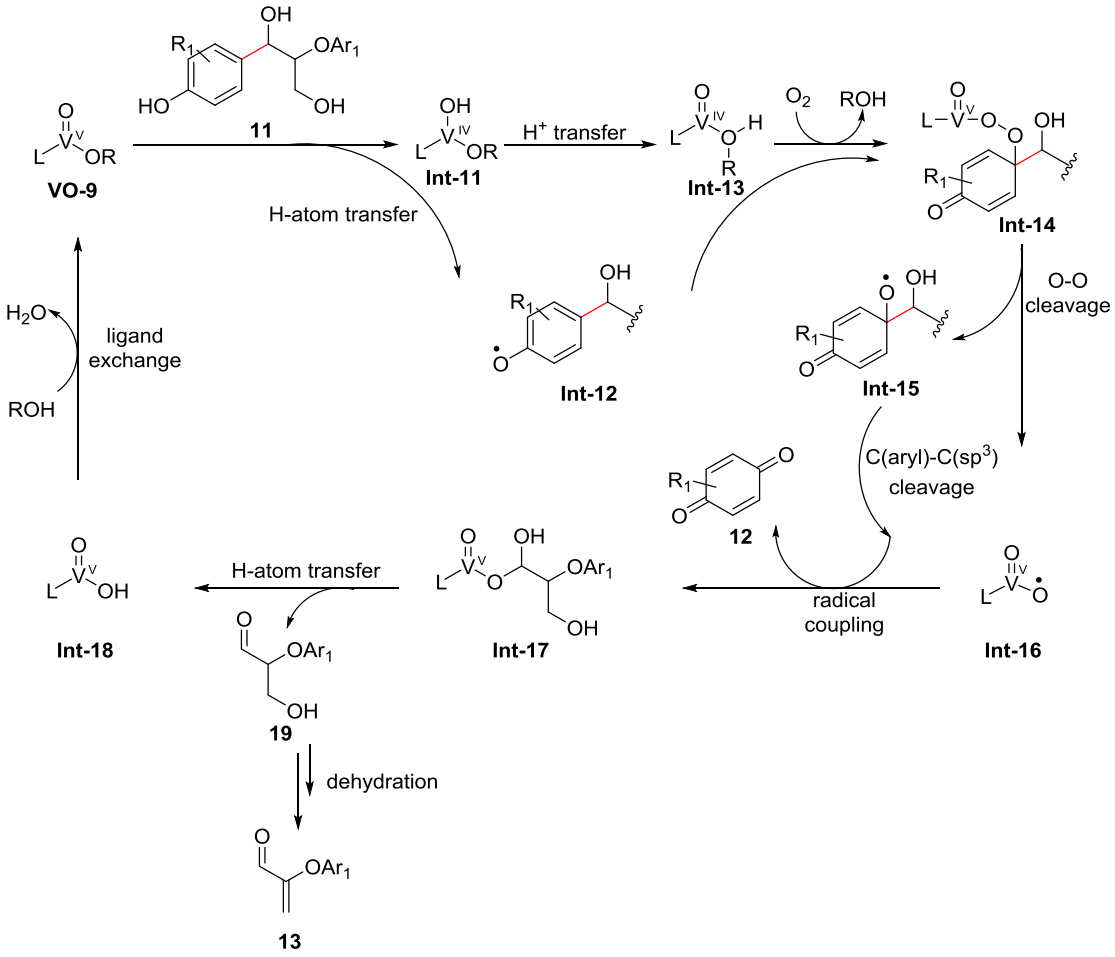

Scheme 2.15. Reaction mechanism for C(aryl)-C(sp^3) bond cleavage in **11** with **VO-9** proposed by Fu *et al*.[33] Symbol L denotes the ligand of the vanadium catalyst.

Even though the work of Toste and Hanson on selective lignin model disassembly showcases remarkable reactivities induced by vanadium complexes, they still rely on thermal conditions, while the photoredox processes remain unknown. Inspired by these studies, our group has recently reported the first vanadium(V) oxo photocatalyst for oxidative C-C bond cleavage in aliphatic alcohols under ambient conditions.[33] The catalyst **VO-10** reported by Soo and co-workers is supported by the redox noninnocent hydrazone-amide ligand **L-1**.[34] Their structures are shown in the Figure 2.3 below.

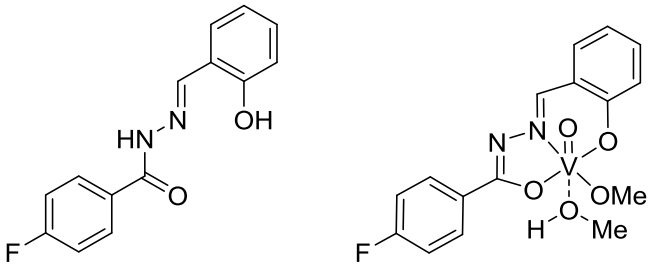

L-1 **VO-10**

Figure 2.3. Structures of the hydrazone-amide ligand **L-1** (left), and the vanadium complex **VO-10** supported by the hydrazone-imidate tautomer of **L-1** (right).[34]

The complex **VO-10** exhibited an octahedral geometry with the equatorial methoxy ligand, and a weakly coordinated methanol in the axial position.[34] Interestingly, **VO-10** is a brownish solid that was found to absorb visible light up to about 500 nm, with the UV-vis absorption maximum (λ_{max}) in the near-UV region centered around 396 nm.[34] The computational density functional theory studies (DFT) conducted by Soo and co-workers suggested that **VO-10**'s visible light absorbing properties could stem from a ligand-to-metal charge transfer (LMCT) transition occurring in this d^0 vanadium(V) species.[34] The catalyst showed remarkably unique reactivity with representative lignin models as substrates. These aliphatic alcohols would undergo a highly selective C-C bond cleavage under visible light irradiation of a 300 W solar simulator, with catalytic amounts of **VO-10**, and under air.[34] As reported by the authors, compound **5** had undergone full conversion in 24 h in presence of **VO-10** to give rise to 4-ethoxy-3-methoxybenzaldehyde (**20**) and 2-methoxyphenyl formate (**21**) as the major cleavage products (Scheme 2.16).[34] In addition, formic acid (**22**) and **7** were generated from *in situ* hydrolysis of **21**, while the oxidation of a small amount of aldehyde **20** to the corresponding acid (**23**) was also observed.[34] Furthermore, a trace amount of formaldehyde (**24**) that was expected to form after the initial C-C bond cleavage was observed in the ^{1}H NMR spectrum of the reaction mixture. Gratifyingly, the benzyl alcohol oxidation was not observed at temperatures below 80 °C, contrasting the previous reports on lignin model degradation under thermal conditions.[34]

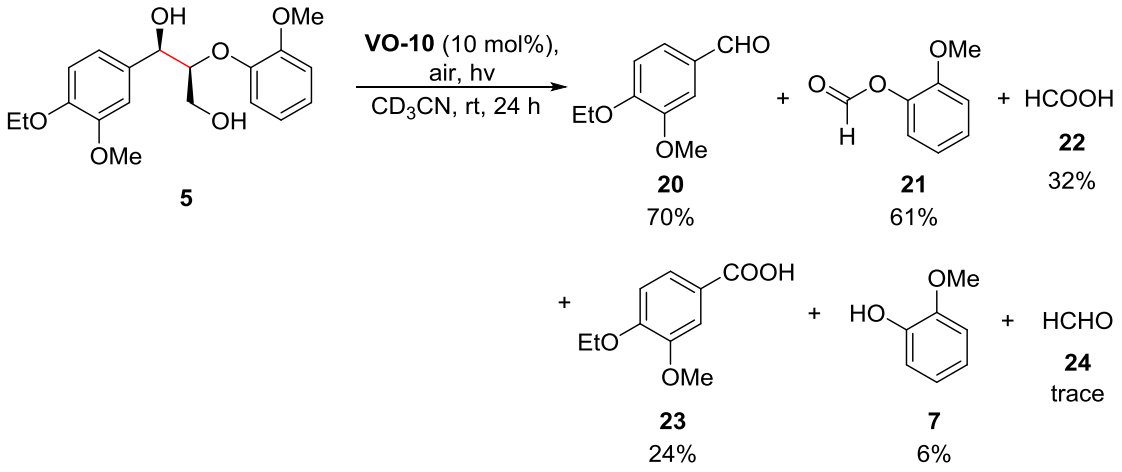

Scheme 2.16. The photocatalytic C-C bond cleavage in lignin model **5** in presence of **VO-10** as reported by Soo *et al*. The C-C bond depicted in red undergoes cleavage.[34]

To provide a possible mechanism for this unprecedented reactivity, the authors conducted isotope labeling and DFT studies.[34] The product analyses of the photocatalytic experiments with isotopically labeled lignin models **5-C1** (^{13}C labeled), **5-D1** and **5-D2** (^{2}H labeled) revealed no proton scrambling and indicated a pathway for a direct C-C bond activation following the initial photoexcitation (Scheme 2.17).[34]

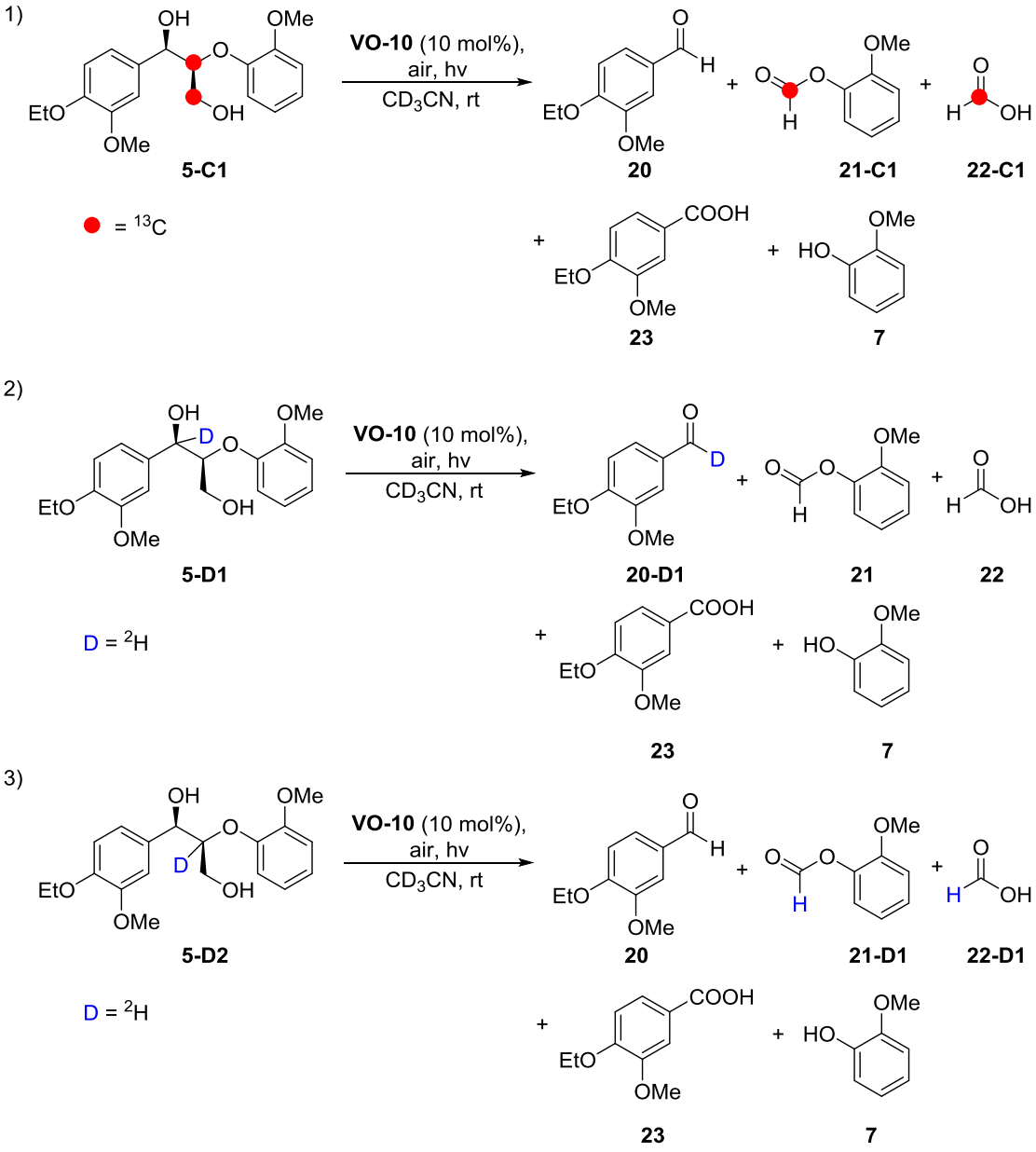

Scheme 2.17. Distribution of products after the photocatalytic C-C bond cleavage in 1) ^{13}C-labeled lignin model **5-C1**, 2) ^{2}H-labeled **5-D1** at the benzylic carbon, and 3) ^{2}H-labeled **5-D2** at the alkyl carbon of the *β*-O-4 linkage.[34]

The experimental observations were further supported by the DFT calculations and the simplified proposed mechanism is depicted in Scheme 2.18 below. After the initial ligand exchange of the methoxy group of **VO-10** with the alkoxy of the substrate, the reactant complex (**RC-3**) undergoes a photoexcitation *via* LMCT.[34] The LMCT triggers a cleavage of the C-C bond proximal to the alcohol group of the substrate in the transition state (**TS-3**), leading to the formation of **20** that is bound to the catalyst, and a transient alkyl radical intermediate (**Int-19**).[34] The radical is expected to react with aerial oxygen to form a peroxo radical (**Int-20**), which will re-oxidize the initially

formed V^{IV} back to V^{V} with concomitant release of **20**.[34] The vanadium peroxo species (**Int-21**) can then undergo a concerted heterolytic cleavages of O-O and C-C bonds from **TS-4** from the S_0 state with an energy barrier of about 20 kcalmol^{-1} to furnish the remaining reaction products **21** and **24**.[34] Alternatively, **Int-21** can undergo another photoexcitation and complete the reaction in an almost barrier-free approach *via* two subsequent homolytic cleavages of the O-O and then C-C bond (**TS-5**) in the T_1 state to yield the same reaction products.[34] The proposed mechanism also indicates that although V^{V} is temporarily reduced to V^{IV}, at the end of the cycle, the catalyst is regenerated, and O_2 plays a crucial role in this process (**Int-20**, Scheme 2.18).[34] This was verified by the fact that the reaction proceeded in the absence of O_2 only with the consumption of catalyst **VO-10** since the alkyl radical would then react with oxygen of the V=O bond leading to catalyst depletion.[34] Furthermore, the necessity of light was confirmed with the control reaction in the dark that yielded no cleavage products.[34] Finally, the intermediacy of organic radical species was verified by employing the stable radical (2,2,6,6-tetramethylpiperidin-1-yl)oxy (TEMPO) as a trap for the transient alkyl radical generated by C-C bond cleavage.[34]

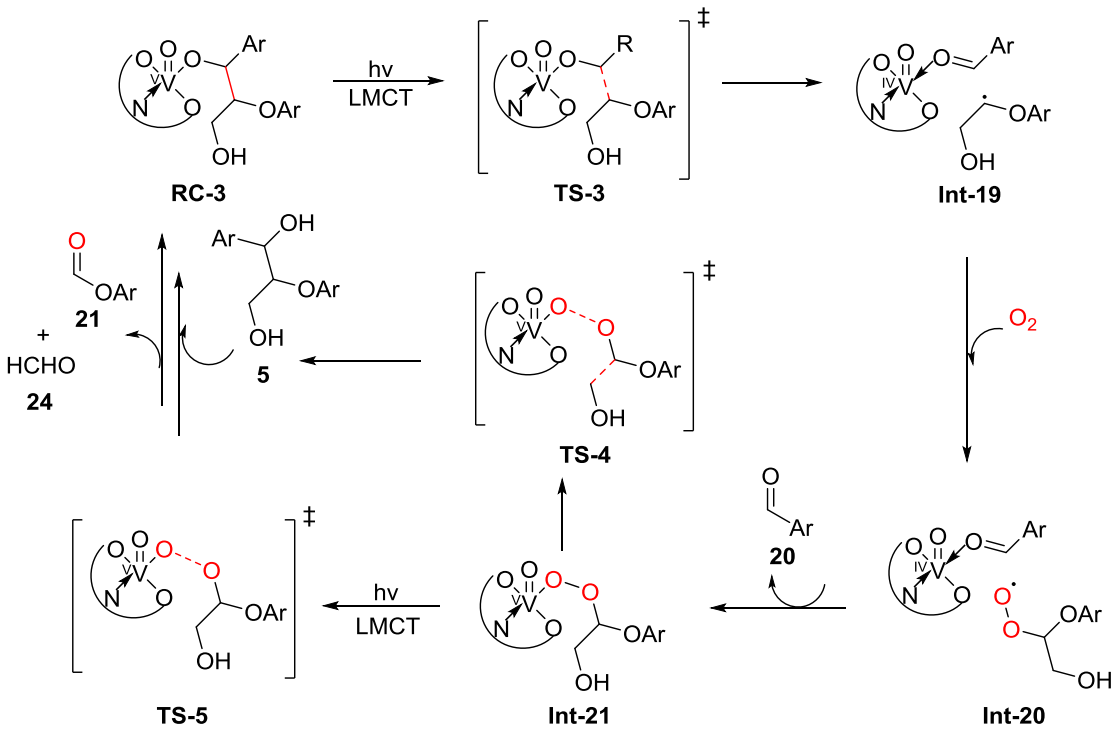

Scheme 2.18. Simplified reaction mechanism for photocatalytic C-C bond cleavage in **5** proposed by Soo and co-workers.[34]

The DFT calculations also provided insights into the incompatibility of **VO-10** with phenols, which was experimentally observed by Soo and co-workers.[34] The higher acidity of the phenolic group compared to aliphatic alcohols, allows it to bind strongly to the vanadium center.[34] Unfortunately, for such substrates, DFT calculations did not indicate a possible C-C bond cleavage pathway neither through S_1 or T_1 excited states.[34] These findings reaffirm the requirement to passivate phenolic groups of native lignin if such a photocatalytic system is to be used for biomass valorization.

2.3 Aims of Thesis

Photoredox carbon-carbon bond activation under mild conditions and with inexpensive catalysts has been a long-standing problem in the field of synthetic chemistry. Furthermore, the selective C-C bond cleavage could be potentially used to valorize neglected feedstocks such as biomass and recycled plastics to obtain valuable platform chemicals. The recent work of our group's member has demonstrated the first example of a vanadium-catalyzed C-C bond cleavage in representative lignin model compounds under mild conditions and by utilizing visible light. Improving on the original catalyst design, we will show that the meticulous optimization of ligand's electronic properties can dramatically enhance the performance of the corresponding catalyst. A library of vanadium complexes with significant improvement in catalytic rate has been prepared, and the catalysts have been extensively characterized by various spectroscopic techniques. The development of faster catalysts has also enabled us to utilize operationally more convenient light-emitting diodes (LEDs) in our photocatalytic studies. Furthermore, the knowledge gained from computational DFT studies enabled us to easily expand the scope of our research to aliphatic alcohol substrates other than lignin models. We have been able to apply our photocatalytic system to successfully target C-C bonds in proximity of alcohol groups in over a dozen different substrates. Finally, we will discuss our findings on the photophysical properties of our new vanadium photocatalysts and introduce our work on translating this unique reactivity to a heterogeneous system.

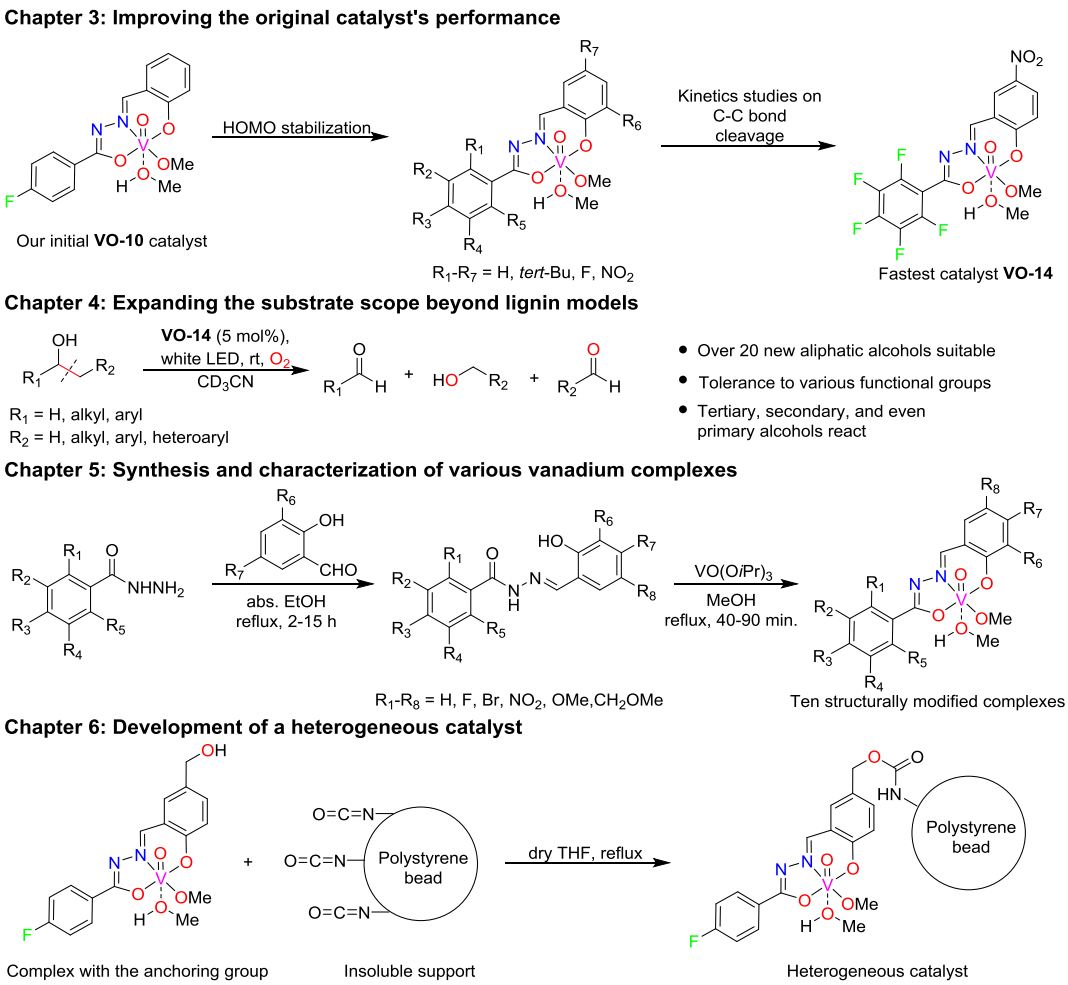

Scheme 2.19. Graphical representation of the research aspects covered in the following chapters.

References

1. Roque, J. B.; Kuroda, Y.; Gottemann, L. T.; Sarpong, R. *Science* **2018**, *361*, 171–174.

2. Zhou, Z. Z.; Liu, M.; Lv, L.; Li, C. J. *Angew. Chem. Int. Ed*. **2018**, *57*, 2616–2620.

3. Chen, P. H.; Billett, B. A.; Tsukamoto, T.; Dong, G. *ACS Catal*. **2017**, *7*, 1340−1360.

4. For selected examples on TM catalyzed C-C bond cleavage in strained rings see: (a) Noyori, R.; Kumagai, Y.; Umeda, I.; Takaya, H. *J. Am. Chem. Soc*. **1972**, *94*, 4018−4020. (b) Trost, B. M.; Chan, D. M. T. *J. Am. Chem. Soc*. **1983**, *105*, 2315−2325. (c) Ogoshi, S.; Nagata, M.; Kurosawa, H. J. *Am. Chem. Soc*. **2006**, *128*, 5350−5351. (d) Shaw, M. H.; McCreanor, N. G.; Whittingham, W. G.; Bower, J. F. *J. Am. Chem. Soc*. **2015**, *137*, 463−468. (e) Murakami, M.; Amii, H.; Shigeto, K.; Ito, Y. *J. Am. Chem. Soc*. **1996**, *118*, 8285−8290. (f) Murakami, M.; Itahashi, T.; Ito, Y. *J. Am. Chem. Soc*. **2002**, *124*, 13976−13977. (g) Zhou, X.; Dong, G. *J. Am. Chem. Soc*. **2015**, *137*, 13715−13721. (h) Edelbach, B. L.; Lachicotte, R. J.; Jones, W. D. *Organometallics* **1999**, *18*, 4040−4049.

5. Wang, J.; Zheng, N. *Angew. Chem. Int. Ed*. **2015**, *54*, 1–5.

6. (a) Maity, S.; Zhu, M.; Shinabery, R. S.; Zheng, N. *Angew. Chem.Int. Ed*. **2012**, *51*, 222–226; *Angew. Chem*. **2012**, *124*, 226–230; (b) Nguyen, T. H.; Maity, S.; Zheng, N. *Beilstein J. Org. Chem*. **2014**, *10*, 975–980; (c) Nguyen, T. H.; Morris, S. A.; Zheng, N. *Adv. Synth. Catal*. **2014**, *356*, 2831–2837.

7. Yayla, H. G.; Wang, H.; Tarantino, K. T.; Orbe, H. S.; Knowles, R. R. *J. Am. Chem. Soc.* **2016**, *138*, 10794–10797.

8. Guo, J. J.; Hu, A.; Chen, Y.; Sun, J.; Tang, H.; Zuo, Z.; *Angew. Chem. Int. Ed*. **2016**, *55*, 1–5.

9. Wang, D.; Mao, J.; Zhu, C. *Chem. Sci*. **2018**, *9*, 5805–5809.

10. Corcoran, E. B.; Pirnot, M. T.; Lin, S.; Dreher, S. D.; DiRocco, D. A.; Davies, I. W.; Buchwald, S. L.; MacMillan, D. W. C. *Science* **2016**, *353*, 279−283.

11. Terrett, J.; Cuthbertson, J.; Shurtleff, V.; MacMillan, D. W. C. *Nature* **2015**, *524*, 330−334.

12. Shaw, M. H.; Shurtleff, V. W.; Terrett, J. A.; Cuthbertson, J. D.; MacMillan, D. W. C. *Science* **2016**, *352*, 1304−1308.

13. Johnston, C.; Smith, R.; Allmendinger, S.; MacMillan, D. W. C. *Nature* **2016**, *536*, 322−325.

14. Zuo, Z.; Cong, H.; Li, W.; Choi, J.; Fu, G. C.; MacMillan, D. W. C. *J. Am. Chem. Soc*. **2016**, *138*, 1832−1835.

15. Nawrat, C.; Jamison, C.; Slutskyy, Y.; MacMillan, D. W. C.; Overman, L. *J. Am. Chem. Soc.* **2015**, *137*, 11270−11273.

16. Zuo, Z.; Ahneman, D. T.; Chu, L.; Terrett, J. A.; Doyle, A. G.; MacMillan, D. W. C. *Science* **2014**, *345*, 437−440.

17. Liu, H.; Li, H.; Lu, J.; Zeng, S.; Wang, M.; Luo, N.; Xu, S.; Wang, F. *ACS Catal*. **2018**, *8*, 4761−4771.

18. da Silva, J. A. L.; Frausto da Silva, J. J. R.; Pombeiro, A. J. L. *Coord. Chem. Rev*. **2011**, *255*, 2232−2248.

19. (a) Jiang, N.; Ragauskas, A. J. *Tetrahedron Lett*. **2007**, *48*, 273−276. (b) Jiang, N.; Ragauskas, A. J. J. *Org. Chem*. **2007**, *72*, 7030−7033.

20. Ohde, C.; Limberg, C. *Chem. Eur. J*. **2010**, *16*, 6892−6899.

21. Hanson, S. K.; Wu, R.; Silks, L. A. *Org. Lett*. **2011**, *13*, 1908−1911.

22. Pawar, V. D.; Bettigeri, S.; Weng, S. S.; Kao, J. Q.; Chen, C. T. *J. Am. Chem. Soc.* **2006**, *128*, 6308−6309.

23. Radosevich, A.; Musich, C.; Toste, F. D. *J. Am. Chem. Soc*. **2005**, *127*, 1090−1091.

24. Weng, S. S.; Shen, M. W.; Kao, J. Q.; Munot, Y. S.; Chen, C. T. *Proc. Natl. Acad. Sci*. **2006**, *103*, 3522−3527.

25. Chen, C. T.; Kao, J. Q.; Salunke, S. B.; Lin, Y. H. *Org. Lett*. **2011**, *13*, 26−29.

26. (a) Collinson, S. R.; Thielemans, W. *Coord. Chem. Rev*. **2010**, *254*, 1854−1870. (b) Zakzeski, J.; Bruijnincx, P. C. A.; Jongerius, A. L.; Weckhuysen, B. M. *Chem. Rev*. **2010**, *110*, 3552−3599.

27. Son, S.; Toste, F. D. *Angew. Chem., Int. Ed*. **2010**, *49*, 3791−3794.

28. Chan, J. W. M.; Bauer, S.; Sorek, H.; Sreekumar, S.; Wang, K.; Toste, F. D. *ACS Catal*. **2013**, *3*, 1369−1377.

29. Sedai, B.; Diaz-Urrutia, C.; Baker, R. T.; Wu, R.; Silks, L. A.; Hanson, S. K. *ACS Catal*. **2011**, *1*, 794−804.

30. Hanson, S. K.; Wu, R.; Silks, L. A. *Angew. Chem*. **2012**, *124*, 1−5.

31. Zhang, G.; Scott, B. L.; Wu, R.; Silks, L. A.; Hanson, S. K. *Inorg. Chem*. **2012**, *51*, 7354−7361.

32. Sedai, B.; Diaz-Urrutia, C.; Baker, R. T.; Wu, R.; Silks, L. A.; Hanson, S. K. *ACS Catal*. **2013**, *3*, 3111−3122.

33. Jiang, Y.; Yan, L.; Yu, H.; Zhang, Q.; Fu, Y. *ACS Catal*., **2016**, *6*, 4399–4410.

34. Gazi, S.; Ng, W. K. H.; Ganguly, R.; Moeljadi, A. M. P.; Hirao, H.; Soo, H. S. *Chem. Sci*., **2015**, *6*, 7130–7142.

CHAPTER 3

KINETICS AND DFT STUDIES OF PHOTOREDOX CARBON-CARBON BOND CLEAVAGE REACTIONS

PREFACE

The content of this chapter has been reproduced from the article “Kinetics and DFT Studies of Photoredox Carbon−Carbon Bond Cleavage Reactions by Molecular Vanadium Catalysts under Ambient Conditions”, Gazi, S.; **Đokić**, **M**.; Moeljadi, A. M. P.; Ganguly, R.; Hirao, H.; Soo, H. S. *ACS Catal*. **2017**, *7*, 4682−4691, with permission of the American Chemical Society. H. S. S. and S. G. conceived the research. S. G. wrote the manuscript and conducted experiments along with M. Đ. S. G. and M. Đ. analyzed and interpreted the data. M. A. M. P. and H. H. performed computational studies and assisted in interpreting the results. R. G. performed the X-Ray crystallographic measurements.

3.1 Introduction

Photoredox catalysis has emerged as a versatile and selective method to utilize light energy to enable carbon-carbon bond formation reactions, despite the intermediacy of a highly reactive radical species.[1-10] In a number of seminal studies, transition metal and organic photosensitizers have been used to activate common substrates and generate transient radical species, which are occasionally coupled with another catalyst (often nickel-based) to create C-C or C-X (X = O, N, and S) bonds.[11-14] On the contrary, studies pertaining to selective photoredox aliphatic C-C bond scission reaction are scarce and have received limited attention. Most current protocols in photoredox bond cleavage chemistry include activation of the pre-functionalized alkyl or aryl halides, or the loss of stable and volatile CO_2 from carboxylates and their derivatives.[15-18] As a result, there have been few reports of C-C bond activation of aliphatic sp^3 carbons, especially by visible light at ambient temperatures and pressures despite its potential in enabling novel synthetic approaches for late-stage organic transformations or valorizing neglected resources such as biomass lignin or recycled plastics.[19-21]

As outlined in the previous chapters, our group has dedicated significant effort in creating constituents of artificial photosynthetic systems that would simultaneously generate solar fuels and solar chemicals.[22-24] The oxidative carbon-carbon bond cleavage reaction mediated by visible light-absorbing vanadium catalysts is a suitable oxidative half-reaction for the AP system, since it generates synthetically useful carbonyl compounds as products and can potentially provide electrons for the reductive half-reaction. This remarkably selective and unique reactivity was previously studied on several structurally distinct lignin model compounds using the original vanadium complex **VO-10** designed by Soo and co-workers.[24] It was shown through DFT studies that the vanadium complex can absorb visible light through a ligand-to-metal charge transfer and subsequently activate sp^3 C-C bond of aliphatic alcohols proximal to the hydroxy group under ambient conditions.[24] The calculations also showed that phenols inhibit the catalysis since the aliphatic C-C bond activation barrier in phenolic substrates is exceeding 30 kcal mol^{-1}.[24] Although the photocatalytic reactions with most of the lignin models proceeded with high substrate conversions and moderate to high product yields, a 300 W solar simulator was used in the experiments as the light source.[24]

To make this technology more affordable and operationally convenient, we have replaced the high-power solar simulator with a commercially available 48 W white LED. Unfortunately, the preliminary studies using the original vanadium photocatalyst and a white LED with a representative lignin model substrate revealed low substrate conversion and insignificant amounts of products. These results indicated a necessity for developing a faster catalyst that can perform a C-C bond cleavage with a satisfactory rate even under irradiation of a lower power LED.

In this chapter, we will showcase how drawing upon our prior DFT and experimental results led to a library of new and systematically designed vanadium(V) complexes that incorporate electron withdrawing groups (EWGs) on the specific sites of the ligand so as to increase the oxidative strength of the corresponding complexes. In addition, a new substrate that is structurally analogous to our previously used lignin model was synthesized as well. However, this substrate would not hydrolyze *in situ* to form phenolic by-products and is thus more suitable for comparing the catalytic properties of new catalysts. The photocatalytic experiments revealed that the aliphatic C-C bond cleaves 2.5-17 times faster in the new substrate compared to the lignin model used in earlier studies. Finally, by performing detailed kinetics studies, photochemical quantum yield measurements, and DFT calculations, we have identified the fastest catalyst in the library that is up to 7 times faster than our original photocatalyst and up to 15 times faster than the slowest catalyst in the series. This study has also provided us with valuable insights on the possible substrate scope expansion in our future research.

3.2 Design and Synthesis of New Photocatalysts

The DFT calculations previously conducted on our original vanadium photocatalyst **VO-10** supported by a redox non-innocent hydrazone-imidate ligand tautomer indicated that the highest occupied molecular orbital (HOMO) is mainly localized on its ligand **L-1**.[24] More specifically, the greater orbital amplitude was observed on carbon atoms labeled 2, 3, 5, and 7 of the fluorine-bearing aryl ring, and the carbons 8, 9, 11, and 12 of the salicylaldimine aryl ring (Figure 3.1b). In our group's prior work with photocatalyst **VO-10**, it was shown that after the homolytic C-C bond cleavage in aliphatic alcohols, one of the resulting unpaired electrons is transferred to the HOMO on the ligand that has been oxidized due to LMCT.[24] With this proposed mechanism in mind, we hypothesized that the C-C bond cleavage should proceed faster if the HOMO

is more stabilized (ie, lower in energy) provided that the electron transfer is the reaction's rate limiting step. To examine this hypothesis, we have prepared a series of vanadium complexes containing EWGs, mainly fluoro- and nitro-, at the ligand sites with highest orbital density of the HOMO to most effectively lower the HOMO energy level.

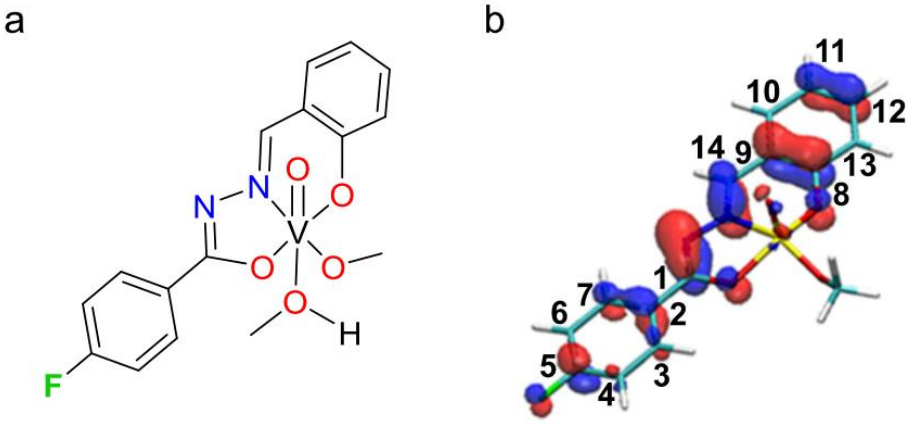

Figure 3.1. (a) Structure of our group's previously published catalyst **VO-10**, and (b) spatial distribution of the HOMO of **VO-10**.

Details regarding the synthesis and characterization of ligands and vanadium complexes are summarized in the experimental section. Briefly, ligands **L-1-6** were prepared by condensation reactions of corresponding hydrazides and substituted 2-hydroxybenzaldehydes by adopting our previously reported procedure and were isolated in high yields.[24,25] Subsequent treatment of the ligands with stoichiometric amounts of the vanadium precursor, vanadium(V) oxytriisopropoxide, resulted in the formation of vanadium complexes **VO-10-15**, also obtained in high yields and purity (Scheme 3.1).

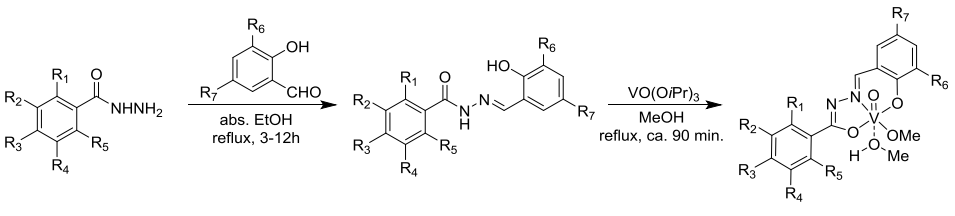

L-1: R_1,R_2,R_4,R_5,R_6,R_7=H; R_3=F;
L-2: R_1-R_7=H
L-3: R_1,R_2,R_4,R_5,R_7=H; R_3=F; R_6=*tert*-Bu
L-4: R_1-R_5=F; R_6,R_7=H
L-5: R_1-R_5=F; R_6=H; R_7=NO_2
L-6: R_1-R_5=F; R_6,R_7=NO_2

VO-10: R_1,R_2,R_4,R_5,R_6,R_7=H; R_3=F;
VO-11: R_1-R_7=H
VO-12: R_1,R_2,R_4,R_5,R_7=H; R_3=F; R_6=*tert*-Bu
VO-13: R_1-R_5=F; R_6,R_7=H
VO-14: R_1-R_5=F; R_6=H; R_7=NO_2
VO-15: R_1-R_5=F; R_6,R_7=NO_2

Scheme 3.1. Preparation of hydrazone-amide ligands (**L-1-6**) and the corresponding vanadium complexes (**VO-10-15**) investigated in this study.

Apart from complex **VO-10,** which is used as a benchmark in this study, all the remaining vanadium complexes are new compounds and have been extensively characterized by the means of NMR spectroscopy, mass spectrometry, and elemental analyses. Furthermore, single crystals of **VO-11** and **VO-13-15** suitable for X-ray diffraction analysis have been obtained by slow evaporation from methanol and the resulting X-ray crystallographic structures are depicted in Figure 3.2. Unfortunately, our numerous attempts to obtain single crystals of **VO-12** were unsuccessful, although significant structural differences between **VO-12** and the remaining complexes are not expected.

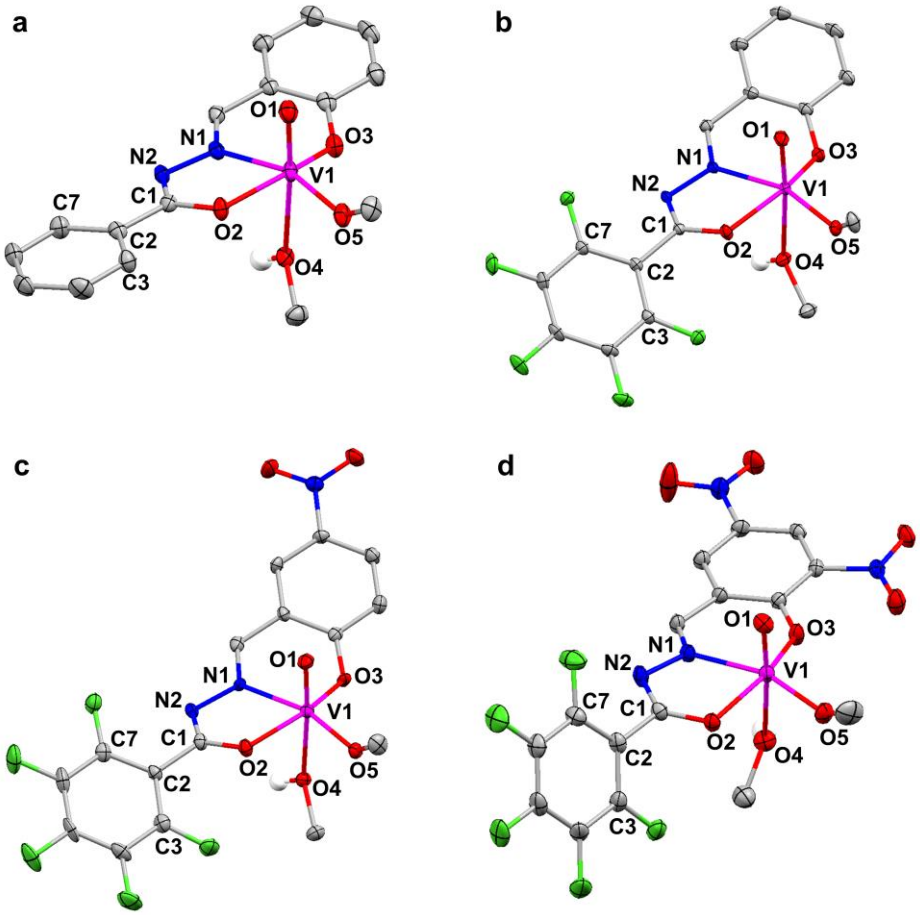

Figure 3.2. Oak Ridge thermal ellipsoid plots (ORTEPs) from X-ray diffraction experiments on (a) **VO-11**, (b) **VO-13**, (c) **VO-14**, and (d) **VO-15**. The thermal ellipsoids are at 50% probability. The vanadium, nitrogen, oxygen, and fluorine atoms are shown in pink, blue, red, and green, respectively. Hydrogen atoms (all except the one from methanol ligand) are omitted for clarity.

The X-ray diffraction analysis revealed that the complexes exhibit an octahedral geometry in the solid state with the equatorial methoxide and a weakly bound axial

methanol ligand, similarly to the structure of **VO-10** previously reported. The V-O bond distance of vanadium-methanol is longer than that of vanadium-methoxide, and the characteristic vanadium oxo V=O bond lengths for **VO-11**, **VO-13**, **VO-14**, and **VO-15** are found to be 1.5903(19), 1.5888(10), 1.581(2), and 1.5845(16) Å, which coincides with the values reported for V=O bonds of similar V^V oxo complexes.[26-28] Surprisingly, there does not seem to be a significant relation between the electron withdrawing properties of the ligands and the bond lengths. In addition, the fluorine-bearing aryl ring of the ligand is distorted from the equatorial plane to different extents in these vanadium complexes. The values for torsion angles (Ψ) of O2-C1-C2-C3 moiety in **VO-11**, **VO-13**, **VO-14**, and **VO-15**, are 1.2(3)°, 36.0(2)°, 34.6(5)°, and 53.9(3)° respectively. The distortion from planarity is likely caused to be by the steric influence of the ortho fluorine groups. Additional structural parameters of the vanadium complexes are summarized in the experimental procedures.

3.3 Substrates for Photocatalytic Carbon-Carbon Bond Cleavage

Following the preparation and characterization of our new vanadium complexes, we proceeded to examine their reactivity in photocatalytic C-C bond cleavage reactions. With the aim of comparing the relative reactivities of novel complexes, compounds **5** and **25** were chosen as suitable substrates. Compound **5** had been used as a substrate in our group's earlier work with catalyst **VO-10**, and it was later found to generate a phenolic secondary reaction product (**7**).[24] The photocatalytic C-C bond activation in **5** using **VO-10** proceeds with the initial formation of **20** and **21** as the main products, which were identified by ^{1}H NMR spectroscopy from the reaction mixture. However, subsequent *in situ* hydrolysis of **21** led to the formation of **22** and **7**, the latter being a phenolic compound that may irreversibly bind to **VO-10** and thus, inactivate it (Scheme 3.2, **Int-22**). The lower pK_a of phenol compared to aliphatic alcohol in **5** along with the higher aliphatic C-C bond activation barrier in phenolic substrates indicates that guaiacol would slowly poison the catalyst.

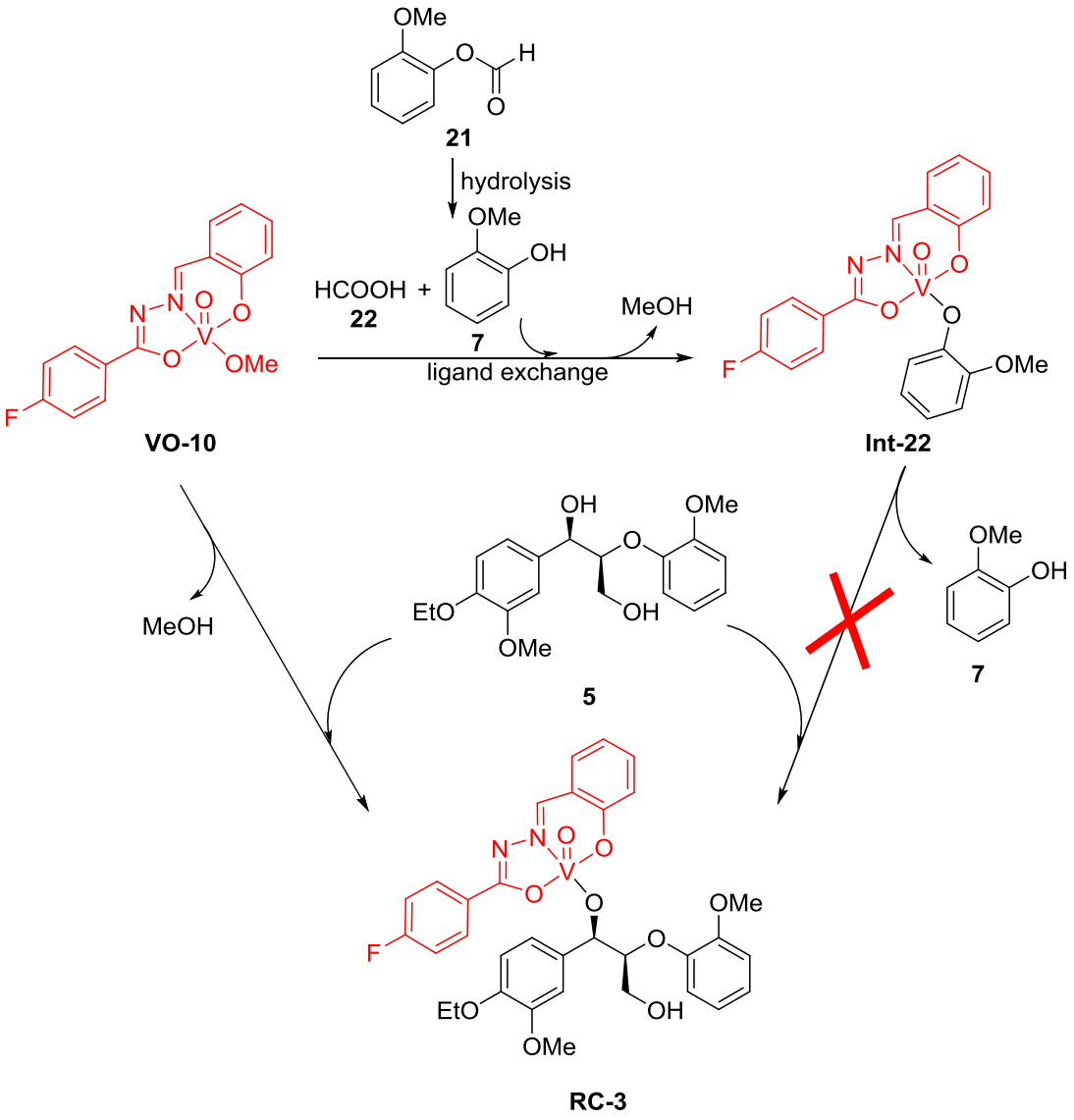

Scheme 3.2. Proposed catalyst deactivation pathway in reaction with **5** caused by the *in situ* hydrolysis of **21**.

Hoping to avoid this catalyst deactivation side-reaction and to facilitate our kinetics studies, we designed and synthesized substrate **25** as an alternative. We expected **25** to undergo a similar selective photocatalytic C-C bond activation reaction with new catalysts under identical reaction conditions, but it would generate a benzyl formate (**26**) instead of **21** (Scheme 3.3). Subsequent hydrolysis of **26** would then yield benzyl alcohol (**27**) in place of **7**, which should not competitively inhibit the catalysts.

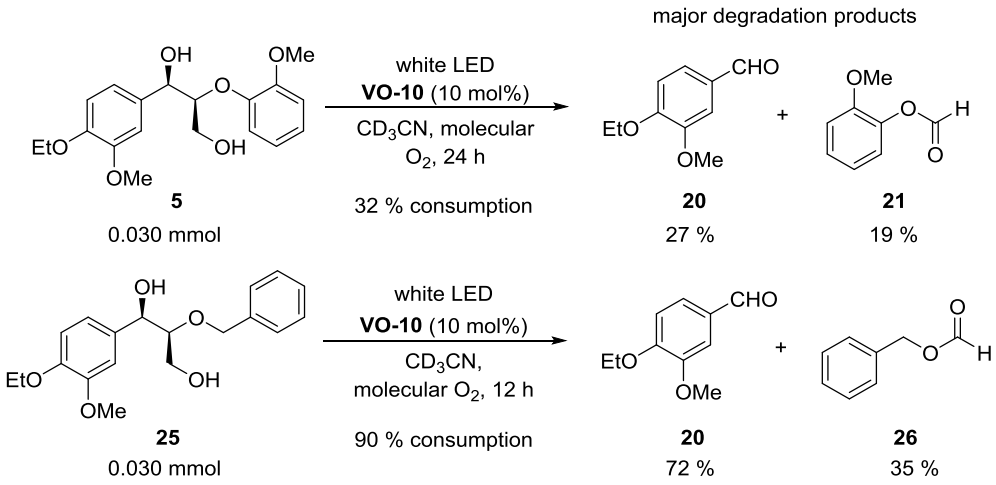

Scheme 3.3. Product distribution after selective C-C bond cleavage of **5** and **25** under visible light irradiation and ambient conditions.

Additionally, we anticipated that **25** might react faster than **5** since the transient radical species would be more effectively stabilized through hyperconjugation with a benzyloxy instead of phenoxy moiety, which was also supported by our new DFT calculations. Hence, **25** would be a more suitable substrate to provide insights into the intrinsic catalytic properties of our new complexes in shorter time and with fewer side-reactions than **5** under the photoredox catalytic conditions. Details regarding the synthesis and characterization of **25** are summarized in the experimental procedures. Briefly, **25** was prepared in a two-step synthesis starting with **20** and methyl 2-(benzyloxy)acetate (**28**). The first step consists of C-C bond formation *via* a nucleophilic attack of a carbanion generated from **28** on the aldehyde of **20** to yield **29**. The following reduction of methyl ester in **29** by $NaBH_4$ resulted in formation of primary alcohol **25**.

With the library of new complexes and two substrates in hands, we proceeded to optimize the photocatalytic reaction conditions with the previously reported **VO-10**, and identify the photolysis products of new substrate **25**. Instead of using a 300 W solar simulator that was employed in our group's previous work,[24] each photocatalytic degradation experiment was performed with an operationally more convenient and affordable 48 W LED as the white light source. The reactions were conducted in a sealed NMR tube with 30 μmol of substrate, 3 μmol of **VO-10** (10 mol %), and 30 μmol of 1,1,2,2-tetrachloroethylene as an inert internal standard in 0.6 mL of deuterated acetonitrile (CD_3CN) as the solvent. Continuous ambient conditions water circulation around the reaction vessel ensured that the temperature of the reaction mixture was below 30 °C. Furthermore, the reaction vessel was supplied with an oxygen balloon that

maintained 1 atm aerobic environment and minimized solvent evaporation over the course of photolysis. After 24 hours of visible light irradiation in the described setup, substrate conversion and product yields were determined by ^{1}H NMR spectroscopy (Figure 3.3). The product identities were verified by additional spectroscopic techniques (^{13}C NMR spectroscopy and HRMS) after silica gel chromatographic purification. Utilizing **VO-10** resulted in only about 32% of **5** being consumed (% relative to 1,1,2,2-tetrachloroethylene), while forming 27% of **20** and 19% of **21** *via* selective C-C bond cleavage (Table 3.1).

Table 3.1. Photocatalytic reaction of **5** with catalysts **VO-10-15**, distribution of products, and the product yields.

Catalyst	Consumption of substrate (%)	Distribution of the products and yields (%)			
	5	**20**	**21**	**7**	**22**
VO-10	32	27	19	10	11
VO-11	31	26	17	8	10
VO-12	22	15	10	4	5
VO-13	61	52	31	10	14
VO-14	76	68	51	14	16
VO-15	55	46	29	10	12

Remarkably, a significantly faster consumption of **25** under the same photocatalytic conditions was observed in only 12 hours of irradiation. Around 87% of **25** was converted to yield **20** (72%) and **26** (35%) as the major reaction products *via* an analogous C-C bond cleavage (Table 3.2). This result shows that **25** reacts faster than **5** with **VO-10** under the same photocatalytic conditions supporting our prior hypothesis.

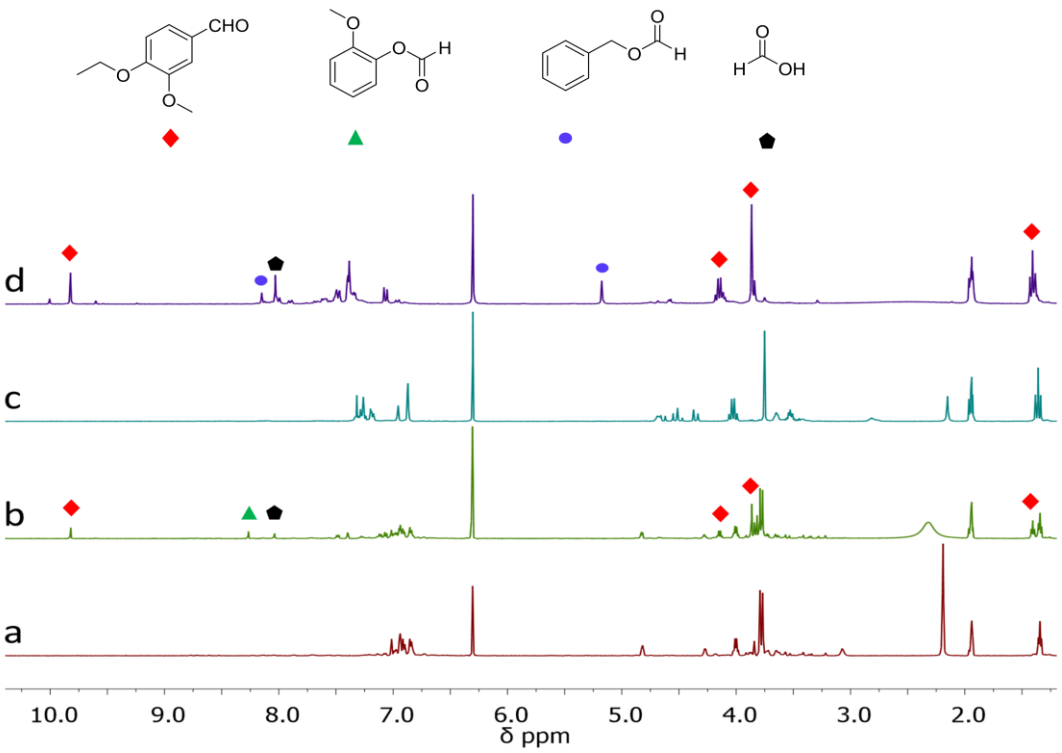

Figure 3.3. ^{1}H NMR spectra of a reaction mixture containing **5** (30.0 µmol), **VO-10** (3.0 µmol, 10 mol %), and an internal standard 1,1,2,2-tetrachloroethylene (30.0 µmol) in CD_3CN (a) before and (b) after 24 h of irradiation with a 48 W white LED. The ^{1}H NMR spectra of a reaction mixture containing **25** (30.0 µmol), **VO-10** (3.0 µmol, 10 mol %), and an internal standard 1,1,2,2-tetrachloroethylene (30.0 µmol) in CD_3CN (c) before and (d) after 12 h of irradiation with a 48 W white LED. Continuous room temperature water circulation through a transparent glass vessel around the NMR tube was used to maintain the temperatures below 30 °C during illumination. The peak at 6.30 ppm corresponds to the internal standard.

Table 3.2. Photocatalytic reaction of **25** with catalysts **VO-10-15**, distribution of products, and the product yields.

Catalyst	Consumption of substrate (%)	Distribution of the products and yields (%)				
	25	**20**	**26**	**27**	**2**	**22**
VO-10	87	72	35	18	14	36
VO-11	85	71	36	18	6	28
VO-12	84	70	33	19	8	32
VO-13	89	82	40	15	11	38
VO-14	93	88	54	21	12	33
VO-15	88	81	39	20	10	34

The control experiments with **25** were carried out in absence of vanadium catalysts under light irradiation, but also in the presence of selected catalysts (**VO-10**, **VO-12**, and **VO-14**) with heating at 80 °C in the dark. The ^{1}H NMR spectroscopy was utilized to monitor the reaction progress in the presence of 1,1,2,2-tetrachloroethylene as the internal standard under otherwise similar reaction conditions to the ones previously described. Only 7% of **25** reacted, and a trace amount (5%) of **20** was formed after 24 hours of visible light irradiation. On the other hand, thermal conditions gave rise to a ketone **32** (30%) derived from oxidation of benzylic alcohol of **25** only in the presence of 10 mol % of **VO-14** and after 24 hours, while **25** did not react in the presence of **VO-10** and **VO-11** at 80 °C. After establishing the conditions for selective photocatalytic C-C bond cleavage in **5** and **25**, we sought to identify the most reactive catalyst in the library by carefully monitoring the trends in activity with the substrates.

3.4 Kinetics Studies on the Photocatalytic C-C Bond Cleavage by Vanadium Complexes

In our kinetics studies, we performed a series of photocatalytic C-C bond cleavage reactions with **5** and **25** in presence of catalysts **VO-10-15**. Each experiment was conducted under the same conditions as described in the previous section and the measurements with each complex were repeated at least twice. The substrate conversion was monitored by ^{1}H NMR spectroscopy in 2 and 4 hours intervals and was determined with respect to the 1,1,2,2-tetrachloroethylene internal standard. The results show that among **VO-10-15**, their photocatalytic rates differ several-fold. Figure 3.4 depicts that **25** underwent C-C bond cleavage 3 to 17 times faster than **5** while displaying a prominent trend in catalytic rate between **VO-10-15**. More specifically, after 24 hours of visible light irradiation, only 22% of **5** was converted in presence of catalytic amount of **VO-12**, while the conversion reached 76% with the same amount of **VO-14**. On the other hand, conversion of **25** had reached maximum values, surpassing 80% with all the catalysts in only 12 hours, with most of them reaching steady substrate concentrations in only 8 hours of light irradiation. The observed nonlinear decrease in substrate concentration, C_t/C_0 (C_t is the substrate concentration at a given time t, and C_0 is the initial substrate concentration), indicated a first or higher order dependence of the rate law on the substrate. Consequently, in the plots of $\ln/(C_0/C_t)$ against time for both substrates, linear fits to the date provided reasonable agreement, indicating that the rate law has a first-order dependence on the substrate concentration since the oxidant O_2 is present in excessive amounts.

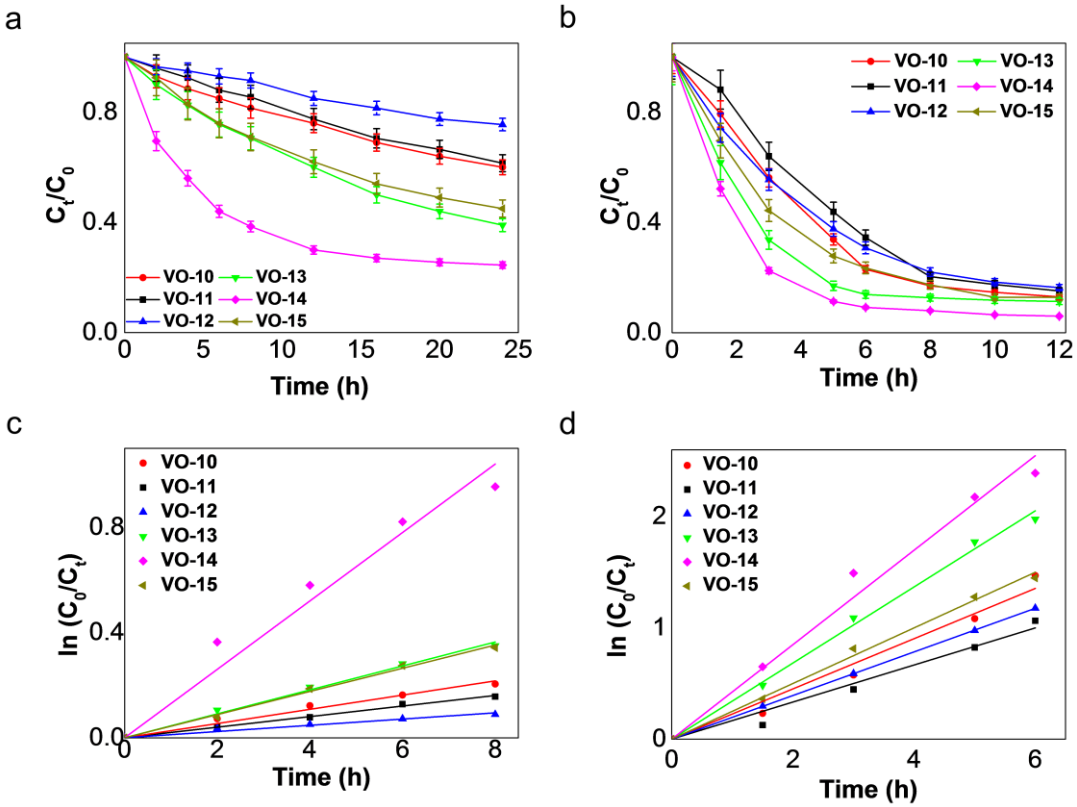

Figure 3.4. Kinetics plots for the decay of (a) **5** and (b) **25** during irradiation with photocatalysts **VO-10-15**, where C_t represents the substrate concentration at time t and C_0 is the initial concentration. The colored lines connecting the data points for each catalyst are meant as guides. Plots of $\ln(C_0/C_t)$ versus time (c) for **5** and (d) for **25** in the presence of different photocatalysts **VO-10-15**, where the slope of the best linear fit provides the pseudo-first-order rate constant k. In the figures, the data for each catalyst are represented as follows: **2a** (black squares), **2b** (red circles), **2c** (blue triangles), **2d** (green inverted triangles), **2e** (pink diamonds), and **2f** (olive tilted triangles).

Furthermore, we proceeded to examine the rate dependence on the catalyst by performing the kinetics experiments while varying the amount of the photocatalyst. In these experiments, the fastest catalyst **VO-14** was selected and its amount was varied from 2.5 to 15 mol% relative to the substrates, while the initial concentration of the substrates was fixed at 30.0 μmol. The obtained kinetics results are depicted in Figure 3.5 indicating that the concentration decay of **5** or **25** is enhanced with the increasing amount of **VO-14**. To calculate the initial rates at low substrate conversions (1.5 h for **5** and 1 h for **25**) for different concentrations of **VO-14**, reasonable linear fits to the plots of $\ln(C_0/C_t)$ against time could be made. The slight deviation from linearity in case of low concentrations of **VO-14** with substrate **5** could be the result of the overwhelming effect of hydrolysis byproduct, **7**, irreversibly coordinating to the catalyst, and thus inactivating it. The pseudo-first-order rate constants were then obtained for the

photoreactions of **5** or **25** with different concentrations of **VO-14** from the slope of the linear fits.

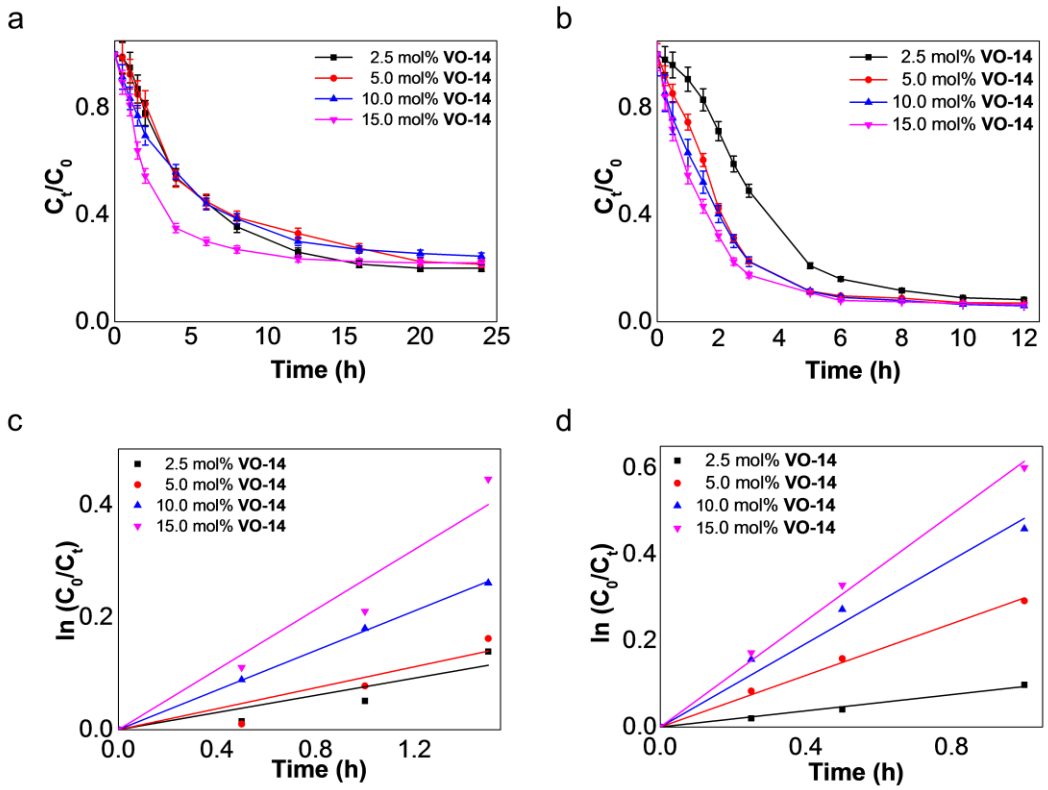

Figure 3.5. Kinetics plots for the decay of (a) **5** and (b) **25** during irradiation with different amounts of photocatalyst **VO-14**, where C_t represents substrate concentration at time t and C_0 is the initial concentration. The colored lines connecting the data points for different catalyst concentrations are meant as guides. Plots of $\ln(C_0/C_t)$ versus time for (c) **5** and (d) **25** in the presence of different amounts of **VO-14**, where the slope of the best linear fit provides the pseudo-first-order rate constant k. In the figures, the data for different catalyst concentrations are as follows: 2.50 mol% of **VO-14** (black squares), 5.0 mol% of **VO-14** (red circles), 10.0 mol% of **VO-14** (blue triangles), and 15.0 mol% of **VO-14** (pink inverted triangles).

The linear increase of pseudo-first-order rate constants with increasing amount of **VO-14** (Figure 3.6) concurs with the first order rate dependence on the catalyst concentration, with deviation from linearity appears to be slightly larger for **25** than for **5**, as indicated by the R^2 values (0.982 and 0.989, respectively) of the linear fits shown in Figure 3.6. Based on these plots, we have derived the second-order initial rate constants, $k_{2x,y}$ (2x = catalyst from **VO-10-15**, y = substrate **5** or **25**) from the slopes of the linear fits. From the above shown results, the rate equation for this photocatalytic C-C bond cleavage reaction can be expressed as the following:

$$\text{Rate} = k'[\mathbf{y}] = k_{2x,y}[\mathbf{2x}][\mathbf{y}] \quad (1)$$

pseudo-first-order rate constant, $k' = k_{2x,y}[\mathbf{2x}]$ (2)

The attained kinetics parameters for reactions of **5** and **25** in the presence of each catalyst are tabulated in Table 3.3.

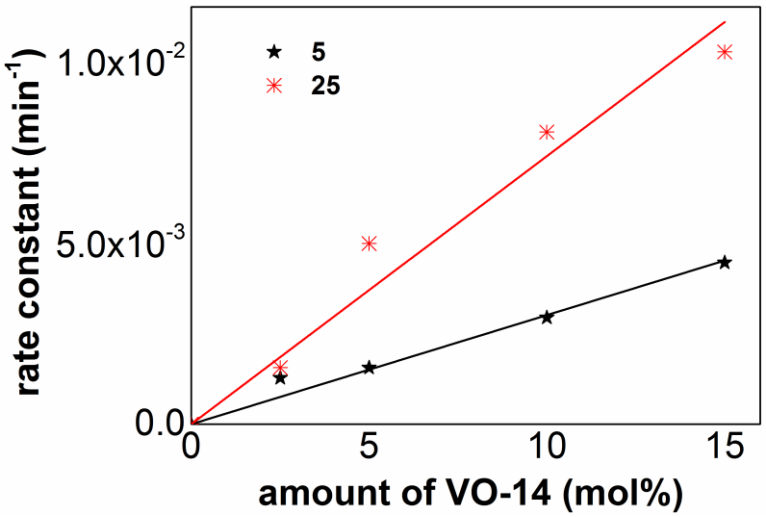

Figure 3.6. Almost linear increase in pseudo-first-order rate constant for the reactions of **5** and **25** with increasing concentrations of **VO-14**.

The kinetics studies revealed that the fastest catalyst for photodegradation of **5** is **VO-14**, which reacts with an initial second-order rate constant about 15 times higher than that of the slowest catalyst **VO-12**. Among all the catalysts used in the kinetics studies, the trend in decreasing order of reactivity with **5** is **VO-14** > **VO-13** ~ **VO-15** > **VO-10** > **VO-11** > **VO-12**. In the case of C-C bond cleavage in substrate **25**, **VO-14** is still the fastest catalyst with the initial second-order rate constant about 2.7-fold higher than that of the slowest catalyst, which is **VO-11** in place of **VO-12**. Due to its higher reactivity, **25** gave poorer differentiation in activity of **VO-10-15**, though a similar trend in initial second-order rate constants was observed as **VO-14** > **VO-13** > **VO-15** > **VO-10** ~ **VO-10** > **VO-11**. In addition to being the fastest catalyst, **VO-14** is also more robust and it exhibited slightly higher turnover numbers (TON), since up to about 93% of **25** reacted in its presence, while the reaction reached maximum at around 80% conversion of **25** in the presence of **VO-11** and **VO-12**, even after prolonging the reaction time.

Table 3.3. Kinetics parameters of **VO-10-15** for photocatalytic C-C bond cleavage in **5** and **25**.

Complex	Pseudo-first-order rate constant of consumption of substrates (k)		Second-order rate constant of reaction ($k_{2x,y}$)	
	k' for **5** (min^{-1})	k' for **25** (min^{-1})	k_{2x} for **5** ($M^{-1}min^{-1}$)	k_{2x} for **25** ($M^{-1}min^{-1}$)
VO-10	4.51×10^{-4}	3.76×10^{-3}	0.090	0.752
VO-11	3.35×10^{-4}	2.77×10^{-3}	0.067	0.554
VO-12	1.97×10^{-4}	3.26×10^{-3}	0.039	0.652
VO-13	7.59×10^{-4}	5.70×10^{-3}	0.152	1.140
VO-14	2.16×10^{-3}	7.07×10^{-3}	0.601	1.477
VO-15	7.34×10^{-4}	4.16×10^{-3}	0.147	0.832

Based on the findings of our kinetics studies, it appears that catalysts **VO-13-15**, which contain the pentafluoro moiety on the imidate part of the ligand, perform better in reactions with **5** and **25** than **VO-10-12**, which contain only one or no fluorine substituents at all. Yet, the effect of the nitro substituents on the aryl hydrazone part of the ligand is subtler. The kinetics studies revealed **VO-14** as the fastest catalyst, which contains only one electron-withdrawing nitro group on the ligand in the *para* position relative to the phenoxide. However, the incorporation of an additional nitro group *ortho* to the phenoxide in **VO-15** had a detrimental effect on the photocatalytic rate, since the activity became similar to (in case of **5**) or even slower (for **25**) than that of **VO-13**, which has no substituents on the aryl hydrazone motif. In addition, complexes **VO-10-12** with only one or no EWG substituents on the imidate part of the ligand reacted much slower with both substrates. Complex **VO-12** which contains an electron-donating and a sterically bulky *tert*-Bu group on the aryl hydrazone portion of the ligand displayed particularly slow reaction rates further supporting our initial hypothesis that introduction of EWGs at specific sites of the ligand is crucial for higher catalyst activity. Specifically, substitution at locations with greater orbital density in HOMO can be beneficial, otherwise steric or redox effects could slow down the catalytic activity, as in case of **VO-12** and **VO-15**, which have *ortho* substituents of opposite donor properties. Even

though we expected **VO-15** to be the fastest catalyst since it contains the greatest number of electron-withdrawing substituents and consequently, highest oxidizing strength, we suspect that the turnover could be limited by the regeneration of the catalyst.

The detailed kinetics studies performed here are in good agreement with the DFT studies of our group's earlier work, where the rate-determining step was suggested to be the photoinduced C-C bond cleavage reaction.[24] Consequently, there is a first-order dependence of the reaction rate separately on the catalyst and the substrate concentration, as well as a zero-order dependence on the O_2 concentration since the re-oxidation of the catalyst proceeds after the rate-determining step involving C-C bond cleavage. The kinetics studies helped us identify **VO-14** as the fastest catalyst that reacts up to 7 times faster than the original complex **VO-10** and up to 15 times faster than the slowest catalyst **VO-12** in our library of new vanadium complexes.

3.5 Electrochemical and DFT Studies

Our kinetics studies have helped us identify the fastest catalyst in the series and the results are in good agreement with our initial hypothesis that introduction of EWGs at specific sites of the ligand can stabilize the HOMO resulting in faster C-C bond activation. However, an unexpected find was that although **VO-15** possesses a greater number of EWGs, it is not the most reactive catalyst. Instead, complex **VO-14** with one nitro group less performs better than **VO-15**. As previously proposed by Soo and co-workers,[24] the catalyst undergoes a one electron reduction to vanadium(IV) during the photocatalysis and it must be reoxidized by aliphatic peroxides in the process to complete the catalytic cycle. Summarized in Table 3.4 are the calculated lowest unoccupied molecular orbital (LUMO) energies for complexes **VO-10-15**, and the LUMO of **VO-15** is the lowest in energy. The values indicate that the V^{IV} state is easily accessed in the case of **VO-15**. Therefore, the regeneration of V^{V} by one-electron reoxidation of the metal center is expected to be thermodynamically least favorable. This proposition is additionally supported by our observation that after light irradiation, reaction mixture changed color from dark red to green. In our group's previous work, the formation of intractable, green vanadium(IV) species was also observed.[24] Yet, the same phenomenon was not detected in case of **VO-10-14** suggesting that aerial regeneration of V^{V} for **VO-15** could be slower or hindered.

Table 3.4. Calculated HOMO and LUMO energies (in eV) of **VO-10-15**.

Complex	HOMO	LUMO
VO-10	-5.964	-3.300
VO-11	-5.916	-3.291
VO-12	-5.954	-3.269
VO-13	-5.970	-3.387
VO-14	-6.000	-3.577
VO-15	-6.098	-3.723

In addition to DFT calculations, cyclic voltammetry measurements (CV) were also employed to investigate whether the trends in catalytic rates of **VO-10-15** were to some extent due to higher redox potentials and thus increased oxidation strengths of the vanadium complexes. All the complexes displayed one reversible V^{V}/V^{IV} redox wave in the examined electrochemical window. The obtained voltammograms showing the first oxidative wave of **VO-10-15** are depicted in Figure 3.7 below with the resulting half-wave potentials ($E_{1/2}$) being summarized in Table 3.6 As expected, the CV results showed that complex **VO-15** with the largest number of EWGs possessed the highest redox potential (olive line, Figure 3.7.). On the other hand, catalyst **VO-12** with the electron-rich *tert*-Bu group exhibited the lowest redox potential (blue line, Figure 3.7). The trend in redox potentials coincided with the reduction in number of EWGs on the ligand and was found to be **VO-15** > **VO-14** > **VO-13** > **VO-10** ~ **VO-11** > **VO-12**. The *para*-fluorine substituent in **VO-10** may be too far away and not as electron-withdrawing as the mesomeric nitro groups to cause a substantial increase in redox potentials compared to **VO-11**. The trend in redox potentials determined by the CV measurements was in good agreement with the trend in reactivity and with the electronic energies of the LUMO in **VO-10-15** (Table 3.4) obtained by DFT calculations. The DFT calculations using Gaussian 09[29,30-34] indicate that **VO-15** has the lowest, while **VO-12** has the highest HOMO and LUMO energies in the series of complexes. The increase of both HOMO and LUMO energies in **VO-10-15** matches well with the trend from CV measurements: **VO-15** > **VO-14** > **VO-13** > **VO-10** ~ **VO-11** > **VO-12**.

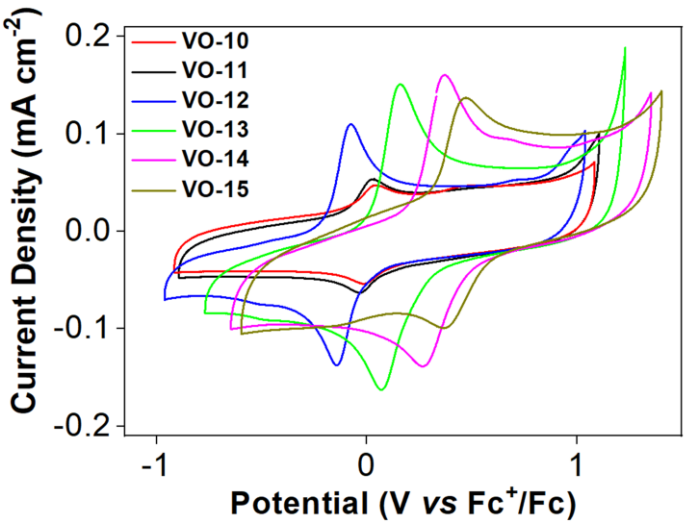

Figure 3.7. Cyclic voltammograms (CVs) of 1.0 mM of **VO-10** (red), **VO-11** (black), **VO-12** (blue), **VO-13** (green), **VO-14** (magenta), and **VO-15** (olive) in acetonitrile with 0.10 M *n*-Bu_4NPF_6 as electrolyte. The potentials are reported relative to the Fc^+/Fc redox couple. Decamethylferrocene (dmFc) was used as an internal standard to avoid overlapping redox waves with our complexes.

As suggested by both the electrochemical measurements and the calculated electronic properties, stronger oxidants **VO-13-15** are thermodynamically more favorable for the C-C bond cleavage with substrates **5** and **25** than **VO-10-12**, which contain fewer electron-withdrawing moieties. Furthermore, the DFT calculations revealed that, in the catalytic reactions with **VO-10-13**, the LMCT involved electronic transitions from HOMO-1 to LUMO, followed by a C-C bond cleavage in the T_1 state. In the cases of **VO-14** and **VO-15**, the LMCT is associated with the electronic transition from HOMO-2 to LUMO. Moreover, the DFT calculations suggest that the C-C bond activation in **25** should proceed faster than that in **5**. Utilizing prior calculations for **VO-10** with **5** as the benchmark,[24] the activation energies for the photocatalytic C-C bond cleavage of **25** with **VO-10-15** were lower by 2.9-9.3 kcal mol^{-1} in the S_1 state and by 4.3-8.9 kcal mol^{-1} in the T_1 state (Table 3.5).

Table 3.5. Activation energy from the ground state for the C-C bond cleavage photocatalyzed by **VO-10-15** *via* LMCT.

Complex	Substrate	$\Delta E^{\ddagger}$ (S_1) (kcal mol^{-1})	$\Delta E^{\ddagger}$ (T_1) (kcal mol^{-1})
VO-10	**5**	25.7	28.2
VO-10	**25**	20.1	23.1
VO-11	**25**	20.3	23.2
VO-12	**25**	22.8	23.9
VO-13	**25**	20.5	22.7
VO-14	**25**	16.4	19.6
VO-15	**25**	17.3	19.3

A probable reason for the lower activation energy for the C-C bond cleavage in **25** could be the greater stability of the radical species formed due to the homolytic bond cleavage. The C-C bond proximal to the benzyl alcohol in **25** may be weaker than the analogous bond in **5**, since the resultant radical for the former (**Int-23** in Scheme 3.4) should be stabilized by hyperconjugation more effectively.

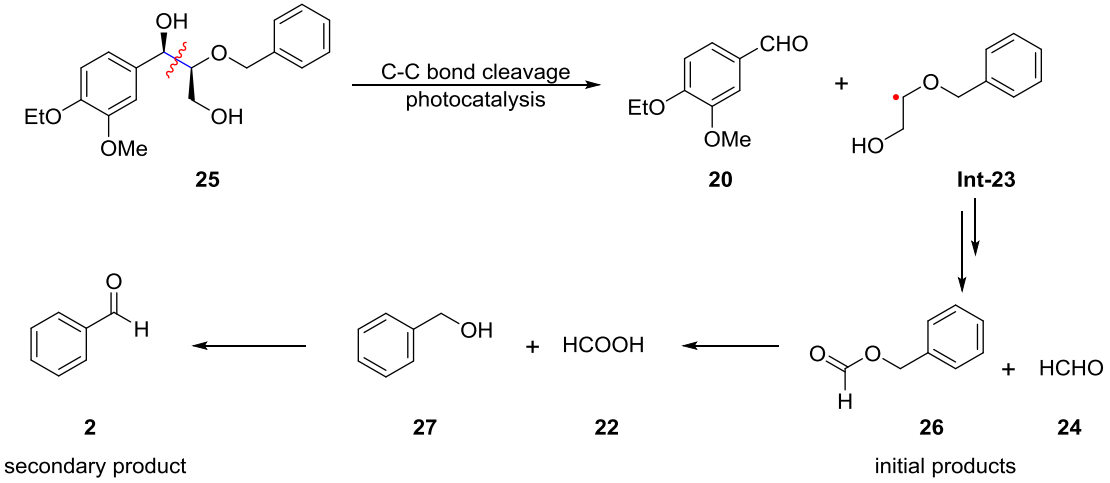

Scheme 3.4. C-C bond cleavage of **25** under visible light irradiation with white LED.

The two sp^3 hybridized pairs of the benzyloxy group in **Int-23** are likely more effective in distributing the spin density of the radical than a phenoxy group, which has one of its lone pairs taken up by the mesomeric interactions with the aryl ring. The formed radicals are then expected to react with molecular O_2, which possibly leads to the formation of **24** initially but eventually converts to the corresponding formate and other oxidized products. The ^{1}H NMR spectrum of the reaction mixture showed a characteristic peak at 9.60 ppm, which may be attributed to **24**, although it would probably be further oxidized or polymerized under the reaction conditions. Subsequent hydrolysis or oxidation of the formates may occur to give rise to **7** (in case of **5**) or **27** (for **25**) as secondary reaction products. Likewise, our calculations concur with the observed product distribution by ^{1}H NMR spectroscopy.

3.6 Photophysical and Quantum Yield Measurements

To better comprehend and explain the unique photocatalytic reactivity of **Vo-10-15**, we have also examined their photophysical properties. The UV-vis absorption spectra of **VO-15** depicted in Figure 3.8a all exhibit absorption bands in the visible region trailing up to about 500 nm and arising from LMCT transitions. Complexes **VO-10** and **VO-11** have almost identical LMCT absorption bands with the maxima located at about 396 nm, while **VO-12** and **VO-13** exhibit less light absorption above 396 nm. Remarkably, complexes **VO-14** and **VO-15** have the most blue-shifted LMCT bands with maxima around 355 nm (Figure 3.8a, inset). In addition, all the vanadium complexes **VO-10-15** exhibit emission when photoexcited at 370 nm in acetonitrile (Figure 3.8b).

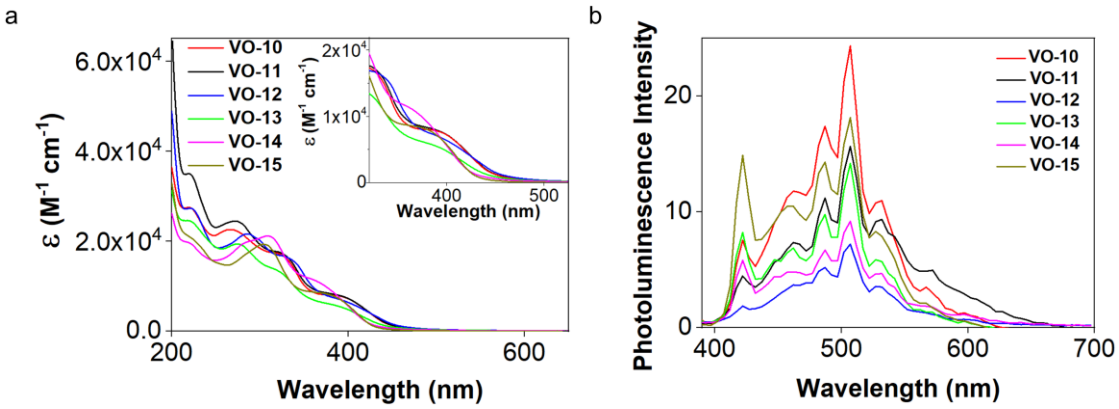

Figure 3.8. (a) UV-vis absorption spectra of 0.10 mM solutions **2a** (black), **2b** (red), **2c** (blue), **2d** (green), **2e** (magenta), and **2f** (olive) in MeCN. The inset shows the LMCT

band of the complexes. (b) Photoemission spectra of 0.50 mM solutions of **VO-15** with excitation at 370 nm in MeCN. The spectra have the same color scheme as part (a).

Since all the photocatalysts displayed similarities in their visible light absorption and emission profiles, quantum yield measurements were performed to determine if the fraction of light absorbed by **VO-10-15** had impact on the reaction rates. We employed the standard ferrioxalate as the chemical actinometer to determine the fraction of light absorbed by **VO-10-15** at 436 nm, and hence the quantum yield (Φ) of photocatalytic degradation of **5** and **25**. Details regarding the quantum yield measurements are described in the experimental section.[38,39] We chose 436 nm because the quantum yield of ferrioxalate for this wavelength is reported to be 1.11%, and the results of our measurements are summarized in Table 3.6.

Table 3.6. Redox potentials and quantum yields of **VO-10-15**.

Complex	Redox potentials ($E_{1/2}$) in V vs Fc^+/Fc	Quantum yield of consumption of substrates (Φ)	
		Φ for **5** (%)	Φ for **25** (%)
VO-10	0.008	0.42	2.13
VO-11	-0.007	0.28	1.76
VO-12	-0.110	0.18	2.17
VO-13	0.120	0.64	3.25
VO-14	0.320	1.60	3.79
VO-15	0.420	0.65	2.83

From the quantum yield measurements on photochemical conversion of **5**, catalyst **VO-14** showed the highest quantum efficiency (1.60%), while **VO-12** had the lowest quantum efficiency (0.18%). Complexes **VO-13** and **VO-15** showed comparable results (0.64% and 0.65% respectively). Likewise, in the case of **25**, complex **VO-14** demonstrated the highest quantum efficiency (3.79%), while **VO-11** had the poorest quantum efficiency (1.76%) although all the complexes displayed higher efficiencies for the C-C bond cleavage in **25**. Hence, the trend in photochemical quantum efficiencies for **VO-10-15** correlates well with their redox potentials and reaction rates in photocatalytic degradation of **5** and **25** under ambient aerobic conditions.

3.7 Conclusion

In summary, we have successfully prepared a library of new vanadium(V) oxo complexes (**VO-10-15**) as visible light active photocatalysts supported by redox noninnocent hydrazone-amide ligands (**L-1-6**). A catalytic amount of the complexes can induce a highly selective C-C bond cleavage in representative alcohol substrates **5** and **25** to yield valuable fine chemicals such as aryl aldehydes, aryl formates, and benzyl formates. These products are important building blocks in organic synthesis as they contain reactive formyl groups that can be further functionalized.

Our experimental studies identified **VO-14,** which contains more EWGs, as the most robust as well as the fastest catalyst for selective C-C bond cleavage reaction, up to 15 times faster than the slowest catalyst **VO-12**, which possesses electron-donating *tert*-butyl substituent on the ligand. In addition, both the kinetics and the DFT studies indicated that substrate **25** is 2.5-17 times more reactive than **5** toward C-C bond cleavage under our photocatalytic degradation conditions. Although **VO-15** exhibited the highest calculated and the electrochemically determined redox potential, it was found to be less reactive than **VO-14**. We propose that the regeneration of the V^{V} active catalyst from the V^{IV} resting state for **VO-15** is slower than that for **VO-14**, which reduces the overall reaction rate for **VO-15**. In our experimental and DFT investigations, the introduction of EWGs at specific locations on the ligand has been crucial in increasing the reaction yield and catalytic rate. The obtained results have provided us with significant insights for further substrate scope expansion since the higher stability of the intermediate radical species favors faster reactivity.

3.8 Experimental Procedures

3.8.1 General Information

The vanadium complexes and ligands were prepared under a N_2 atmosphere using standard Schlenk techniques. Other synthetic procedures were conducted under aerobic conditions unless stated otherwise. The chemicals used in the experiments were purchased from Sigma-Aldrich and were used as received. Deuterated solvents were purchased from Cambridge Isotope Laboratories and were used as received. The ^{1}H, ^{13}C, ^{19}F, and ^{51}V NMR spectroscopic data were obtained using Bruker AVANCE spectrometers operating at 300, 400, and 500 MHz. The resulting ^{1}H and ^{13}C NMR chemical shifts (δ reported in ppm) were referenced according to the residual solvent signal(s) ($CDCl_3$ = 7.26 ppm for ^{1}H and 77.2 ppm for ^{13}C; CD_3CN = 1.94 ppm for ^{1}H

and 118.3 ppm for ^{13}C; MeOD-d_4 = 3.31 ppm for ^{1}H and 49.2 ppm for ^{13}C; DMSO-d_6 = 2.50 ppm for ^{1}H and 39.52 ppm for ^{13}C). The ^{51}V NMR chemical shift was referenced relative to $V^{V}(O)(Cl)_3$ external standard (δ = 0.0 ppm). Crystallographic data were collected on a Bruker X8 CCD diffractometer. The structures were solved and refined using the Bruker SHELXTL software package. High-resolution electrospray ionization mass spectra (HR-ESIMS) were obtained using a Waters Q-TOF Premier mass spectrometer. Elemental analyses were performed with the Elementar vario MICRO cube analyzer. FT-IR spectroscopy measurements were carried out with a Shimadzu IRPrestige-21 FT-IR spectrometer. In a typical experiment, about 1.5 mg of the sample were mixed with about 30.0 mg of potassium bromide (KBr) to make a pellet. The pellets were made with a Specac Atlas manual hydraulic press 15T at 10 ton pressure. The FT-IR experiments were conducted in transmission mode with data collected from 400 to 4000 cm^{-1}

3.8.2 Synthetic Procedures and Spectroscopic Data

General procedure for the synthesis of ligands

In each reaction, to a stirring, heated solution of aryl hydrazide in absolute ethanol (EtOH) under N_2 was added a solution of the corresponding aryl aldehyde in EtOH dropwise. The reaction mixture was then stirred at reflux for a specific amount of time detailed below (between 2 and 15 h). The ligand was subsequently either precipitated out of the mixture or was obtained by removing the solvent under vacuum. The as-synthesized ligands were of sufficient purity to be used in the complexation reactions without any further purification.

4-Fluoro-*N*'-(2-hydroxybenzylidene)benzohydrazide (L-1)

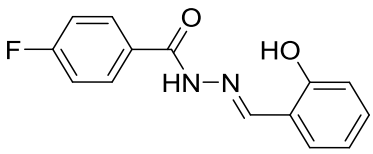

Following the previously reported procedure,[24] an EtOH solution of salicylaldehyde (1.22 g, 10 mmol in 5 mL of EtOH) was added to a solution of 4-fluorobenzohydrazide (1.54 g, 10 mmol in 15 mL of EtOH) and stirred. After ca. 12 h, the corresponding ligand **L-1** was obtained (2.32 g, 90% yield). ^{1}H NMR (DMSO–d_6, 300 MHz): δ = 6.89 – 6.95 (m, 2 H), 7.30 (t, J = 6.0 Hz, 1 H), 7.38 (t, J = 9.0 Hz, 2 H), 7.55 (d, J = 6 Hz, 1 H), 8.00

– 8.05 (m, 2 H), 8.64 (s, 1 H), 11.26 (s, 1 H), 12.12 (s, 1 H) ppm. $^{13}C\{^{1}H\}$ NMR (DMSO–d_6, 100 MHz): δ = 115.6, 116.4, 118.7, 119.4, 129.3, 129.5, 130.4, 131.4, 148.3, 157.5, 161.8, 164.3 ppm. $^{19}F\{^{1}H\}$ NMR (DMSO–d_6, 282.40 MHz): δ = –108.01 ppm. HRMS (ESI+, m/z) calculated for $C_{14}H_{12}FN_2O_2$ $[M+H]^+$ m/z = 259.0883, found 259.0885. Elemental analysis for $C_{14}H_{11}FN_2O_2$ calculated: C, 65.11; H, 4.29; N, 10.85%; found: C, 64.78; H, 4.20; N, 11.11%. IR (cm^{-1}): 3207 (ν_{O-H}), 3026 (ν_{N-H}), 1643 ($\nu_{C=N}$). The obtained values coincide with the reported data.[24]

***N'*-(2-hydroxybenzylidene)benzohydrazide (L-2)**

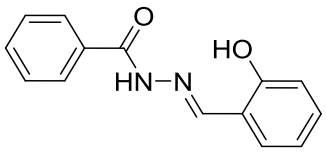

An EtOH solution of salicylaldehyde (0.122 g, 1.0 mmol, in 2 mL EtOH) was added to a solution of benzohydrazide (0.136 g, 1.0 mmol in 5 mL of EtOH) and stirred. After 3 h, the corresponding ligand **L-2** was obtained (0.236 g, 98% yield). ^{1}H NMR (DMSO-d_6, 400 MHz): δ = 6.91-6.96 (m, 2 H), 7.30 (t, J = 8.3 Hz, 1 H), 7.52-7.63 (m, 4 H), 7.95 (d, J = 7.2 Hz, 2 H), 8.66 (s, 1 H), 11.33 (s, 1 H), 12.13 (s, 1 H) ppm. $^{13}C\{^{1}H\}$ NMR (DMSO-d_6, 100 MHz): δ = 116.4, 118.7, 119.4, 127.7, 128.6, 129.6, 131.4, 132.0, 132.8, 148.4, 157.5, 162.9 ppm. HRMS (ESI+, m/z) calculated for $C_{14}H_{13}N_2O_2$ $[M+H]^+$ m/z = 241.0977, found 241.0986. Elemental analysis for $C_{14}H_{12}N_2O_2$ calculated: C, 69.99; H, 5.03; N, 11.66%; found: C, 69.81; H, 5.13; N, 11.48%. IR (cm^{-1}): 3269 (ν_{O-H}), 3057 (ν_{N-H}), 1672 ($\nu_{C=N}$).

***N'*-(3-(tert-butyl)-2-hydroxybenzylidene)-4-fluorobenzohydrazide (L-3)**

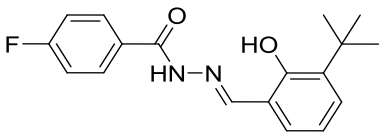

An EtOH solution of 3-(*tert*-butyl)-2-hydroxybenzaldehyde (0.178 g, 1.0 mmol in 2 mL EtOH) was added to a solution of 4-fluorobenzohydrazide (0.154 g, 1.0 mmol in 5 mL of EtOH) and stirred. After 12 h, the corresponding ligand **L-3** was obtained (0.305 g, 97% yield). ^{1}H NMR (DMSO-d_6, 400 MHz): δ = 1.41 (s, 9 H), 6.89 (t, 1 H, J = 7.7 Hz), 7.30 (dd, 2 H, J = 3.6, 7.7 Hz), 7.41 (t, 2 H, J = 8.8 Hz), 8.03 (dd, 2 H, J = 5.5, 8.8 Hz), 8.57 (s, 1 H), 12.25 (s, 1 H), 12.44 (s, 1 H) ppm. $^{13}C\{^{1}H\}$ NMR (DMSO-d_6, 100

MHz): δ = 29.2, 34.5, 115.6 (d, J = 21.8 Hz), 117.6, 118.7, 128.5, 129.0 (d, J = 2.8 Hz), 129.5, 130.4 (d, J = 9.1 Hz), 136.4, 150.9, 157.0, 161.7, 164.4 (d, J = 248.5 Hz) ppm. $^{19}F\{^{1}H\}$ NMR (DMSO-d_6, 376.50 Hz): δ = -107.8 ppm. HRMS (ESI+, *m/z*) calculated for $C_{18}H_{20}N_2O_2F$ $[M+H]^+$ *m/z* = 315.1509, found 315.1515. Elemental analysis for $C_{18}H_{19}N_2O_2F$ calculated: C, 68.77; H, 6.09; N, 8.91%; found: C, 68.48; H, 6.30; N, 9.22%. IR (cm^{-1}): 3188 (ν_{O-H}), 3026 (ν_{N-H}), 1656 ($\nu_{C=N}$).

2,3,4,5,6-Pentafluoro-*N'*-(2-hydroxybenzylidene)benzohydrazide (L-4)

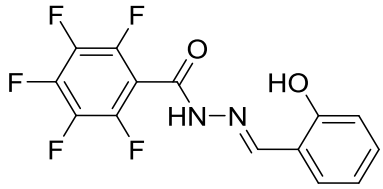

An EtOH solution of 2-hydroxybenzaldehyde (0.122 g, 1.0 mmol, in 2 mL EtOH) was added to a solution of 2,3,4,5,6-pentafluorobenzohydrazide (0.226 g, 1.0 mmol in 5 mL of EtOH) and stirred. After 4 h, the corresponding ligand **L-4** was obtained (0.325 g, 98% yield). ^{1}H NMR (CD_3CN, 300 MHz): δ = 6.96-7.00 (m, 2 H), 7.36-7.41 (m, 2 H), 8.34 (s, 1 H), 10.48 (s, 1 H), 11.07 (s, 1 H) ppm. $^{13}C\{^{1}H\}$ NMR ($(CD_3)_2CO$, 100 MHz): δ = 117.7, 118.4, 120.3, 132.3, 133.1, 137.4 (m), 139.8 (m), 142.8 (m), 144.0 (m), 145.2 (m), 146.5 (m), 152.9, 158.3, 159.6 ppm. $^{19}F\{^{1}H\}$ NMR (CD_3CN, 282.40 Hz): δ = -162.4 (m, 2 F), -152.5 (tt, 1 F, J = 3.2, 20.0 Hz), -142.1 (m, 2 F) ppm. HRMS (ESI+, *m/z*) calculated for $C_{14}H_8N_2O_2F_5$ $[M+H]^+$ *m/z* = 331.0506, found 331.0504. Elemental analysis for $C_{14}H_7N_2O_2F_5$ calculated: C, 50.92; H, 2.14; N, 8.48%; found: C, 50.81; H, 2.20; N, 8.67%. IR (cm^{-1}): 3205 (ν_{O-H}), 3047 (ν_{N-H}), 1678 ($\nu_{C=N}$).

2,3,4,5,6-Pentafluoro-*N'*-(2-hydroxy-5-nitrobenzylidene)benzohydrazide (L-5)

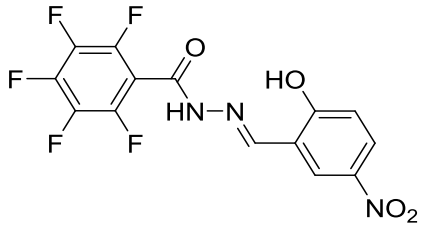

An EtOH solution of 2-hydroxy-5-nitrobenzaldehyde (0.167 g, 1.0 mmol, in 2 mL EtOH) was added to a solution of 2,3,4,5,6-pentafluorobenzohydrazide (0.226 g, 1.0 mmol in 5 mL of EtOH) and stirred. After 4 h, the corresponding ligand **L-5** was obtained (0.360 g, 96% yield). ^{1}H NMR (CD_3CN, 300 MHz): δ = 7.12 (d, 1 H, J = 9.2

Hz), 8.22 (dd, 1 H, *J* = 2.8, 9.2 Hz), 8.40 (d, 1 H, *J* = 2.8 Hz), 8.45 (s, 1 H), 10.77 (s, 1 H), 12.13 (s, 1 H) ppm. $^{13}C\{^{1}H\}$ NMR ($(CD_3)_2CO$, 100 MHz): δ = 118.1, 118.7, 127.9, 128.0, 137.4 (m), 139.9 (m), 141.5, 142.3 (m), 144.0 (m), 144.9 (m), 146.5 (m), 150.7, 163.0, 164.5 ppm. $^{19}F\{^{1}H\}$ NMR (CD_3CN, 282.40 Hz): δ = -162.3 (m, 2 F), -152.1 (tt, 1 F, *J* = 3.4, 20.0 Hz), -141.9 (m, 2 F) ppm. HRMS (ESI+, *m/z*) calculated for $C_{14}H_7N_3O_4F_5$ $[M+H]^+$ *m/z* = 376.0357, found 376.0357. Elemental analysis for $C_{14}H_6N_3O_4F_5$ calculated: C, 44.82; H, 1.61; N, 11.20%; found: C, 44.74; H, 1.94; N, 11.05%. IR (cm^{-1}): 3257 (ν_{O-H}), 3107 (ν_{N-H}), 1672 ($\nu_{C=N}$), 1328 (ν_{NO2}).

2,3,4,5,6-Pentafluoro-*N'*-(2-hydroxy-3,5-dinitrobenzylidene)-benzohydrazide (L-6)

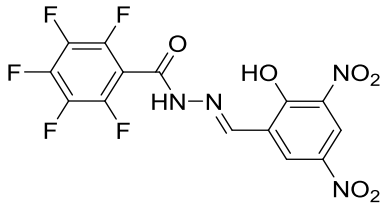

An EtOH solution of 2-hydroxy-3,5-dinitrobenzaldehyde (0.212 g, 1.0 mmol, in 2 mL EtOH) was added to a solution of 2,3,4,5,6-pentafluorobenzohydrazide (0.226 g, 1.0 mmol in 5 mL of EtOH) and stirred. After 4 h, the corresponding ligand **L-6** was obtained (0.410 g, 98% yield). ^{1}H NMR (CD_3CN, 300 MHz): δ = 8.59 (s, 1 H), 8.73 (d, 1 H, *J* = 2.8 Hz), 8.84 (d, 1 H, *J* = 2.8 Hz) ppm. $^{13}C\{^{1}H\}$ NMR ($(CD_3)_2CO$), 100 MHz): δ = 123.1, 123.5, 128.3, 130.5, 137.5 (m), 140.0 (m), 141.1, 142.6 (m), 144.2 (m), 145.1 (m), 146.7 (m), 148.7, 157.3, 158.0 ppm. $^{19}F\{^{1}H\}$ NMR (CD_3CN, 282.40 Hz): δ = -161.4 (m, 2 F), 150.9 (tt, 1 F, *J* = 2.6, 20.0 Hz), -140.9 (m, 2 F) ppm. HRMS (ESI+, *m/z*) calculated for $C_{14}H_6N_4O_6F_5$ $[M+H]^+$ *m/z* = 421.0208, found 421.0216. Elemental analysis for $C_{14}H_5N_4O_6F_5$ calculated: C, 40.02; H, 1.20; N, 13.33%; found: C, 39.93; H, 1.49; N, 13.17%. IR (cm^{-1}): 3190 (ν_{O-H}), 3088 (ν_{N-H}), 1691 ($\nu_{C=N}$), 1332 (ν_{NO2}).

General procedure for the synthesis of vanadium oxo complexes

In each reaction, to a heated, stirring solution of the ligand in methanol (MeOH) was added the vanadium(V) precursor, $VO(O\textit{i}Pr)_3$, under N_2, which led to an immediate change of the reaction color from brown to dark red. The reaction mixture was stirred under reflux for ca. 90 min. Subsequently, the solvent was removed under vacuum and

the remaining dark solid product was obtained. The solid was then re-dissolved in methanol and filtered before finally obtaining the complex by solvent evaporation.

Vanadium oxo complex VO-10

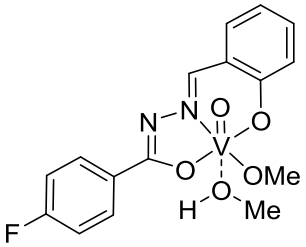

According to the previously reported procedure,[24] to a stirring solution of **L-1** (0.258 g, 1.0 mmol in 20 mL of MeOH) was added $VO(OiPr)_3$ (227 μL, 1.0 mmol). After ca. 90 min. the corresponding vanadium complex **VO-10** was obtained (0.248 g, 70% yield). ^{1}H NMR (MeOD, 300 MHz): δ = 6.94 – 7.04 (m, 2 H), 7.20 (t, J = 9.0 Hz, 2 H), 7.50 (t, J = 7.2 Hz, 1 H), 7.61 (d, J = 7.8 Hz, 1 H), 8.12 – 8.17 (m, 2 H), 8.75 (s, 1 H) ppm. ^{13}C{^{1}H} NMR (MeOD–d_4, 100 MHz): δ = 116.4, 116.6, 117.9, 121.6, 121.9, 132.1, 132.2, 133.8, 135.5, 154.1, 165.2, 167.7 ppm. ^{19}F{^{1}H} NMR (MeOD–d_4, 282.40 MHz): δ = –110.6 ppm. ^{51}V NMR (MeOD–d_4, 105.15 MHz): δ = –548.7 ppm. HRMS (ESI+, m/z) calculated for $C_{15}H_{12}FN_2O_4V$ $[M]^+$ m/z = 354.0221, found 354.0205. Elemental analyses for $C_{15}H_{12}FN_2O_4V$ calculated: C, 50.86; H, 3.41; N, 7.91%; found: C, 50.54; H, 3.09; N, 8.34%. IR (cm^{-1}): 3196 (ν_{O-H}), 1610 ($\nu_{C=N}$), 999 ($\nu_{V=O}$). The obtained values coincide with the reported data.[24]

Vanadium oxo complex VO-11

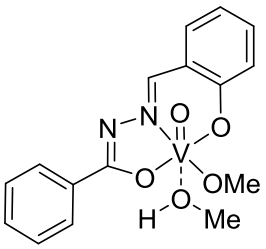

To a MeOH solution of **L-2** (0.120 g, 0.50 mmol in 5 mL of MeOH) was added $VO(OiPr)_3$ (118 μL, 0.50 mmol). After 90 min., the corresponding vanadium complex **VO-11** was obtained (0.160 g, 95% yield). ^{1}H NMR (MeOD-d_4, 400 MHz): δ = 6.96 (d, J = 8.2 Hz, 1 H), 7.02 (t, J = 7.9 Hz, 1 H), 7.45-7.55 (m, 4 H), 7.62 (dd, J = 7.8, 1.6 Hz, 1 H), 8.10-8.12 (m, 2 H), 8.77 (s, 1 H) ppm. ^{13}C{^{1}H} NMR (MeOD-d_4, 100 MHz): δ = 117.7, 121.4, 121.8, 129.5, 129.6, 132.6, 133.7, 134.4, 135.4, 153.9, 160.8, 166.0 ppm.

^{51}V NMR (MeOD-d_4, 105.25 MHz): δ = -547.9 ppm. HRMS (ESI+, m/z) calculated for $C_{15}H_{14}N_2O_4V$ $[M+H]^+$ m/z = 337.0393, found 337.0398. Elemental analysis for $C_{15}H_{13}N_2O_4V$ calculated: C, 53.59; H, 3.90; N, 8.33%; found: C, 53.89; H, 3.92; N, 8.14%. IR (cm^{-1}): 3352 (ν_{O-H}), 1598 ($\nu_{C=N}$), 999 ($\nu_{V=O}$).

Vanadium oxo complex VO-12

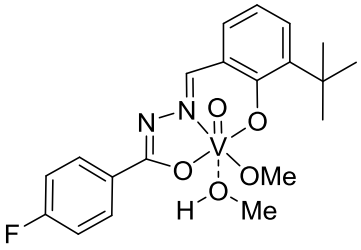

To a stirring solution of **L-3** (0.157 g, 0.50 mmol in 5 mL of MeOH) was added $VO(OiPr)_3$ (118 µL, 0.50 mmol). After ca. 90 min. the corresponding vanadium complex **VO-12** was obtained (0.155 g, 75.6% yield). ^{1}H NMR (MeOD-d_4, 400 MHz): δ = 1.50 (s, 9 H), 6.98 (t, 1 H, J = 7.7 Hz), 7.20 (t, 2 H, J = 8.8 Hz), 7.49 (d, 1 H, J = 6.9 Hz), 7.57 (d, 1 H, J = 7.0 Hz), 8.16 (dd, 2 H, J = 5.6, 8.7 Hz), 8.75 (s, 1 H) ppm. ^{13}C{^{1}H} NMR (MeOD-d_4, 100 MHz): δ = 30.2, 36.1, 116.3 (d, J = 22 Hz), 121.4, 122.2, 128.8, 131.9 (d, J = 9.1 Hz), 132.0, 132.6, 133.5, 138.7, 154.4, 164.7, 166.3 (d, J = 248.6 Hz) ppm. ^{19}F{^{1}H} NMR (MeOD-d_4, 376.50 MHz): δ = -110.8 ppm. ^{51}V NMR (MeOD-d_4, 105.25 MHz): δ = -551.2 ppm. HRMS (ESI+, m/z) calculated for $C_{19}H_{21}N_2O_4FV$ $[M+H]^+$ m/z = 411.0925, found 411.0930. Elemental analysis for $C_{19}H_{20}N_2O_4FV$ calculated: C, 55.62; H, 4.91; N, 6.83%; found: C, 55.45; H, 5.01; N, 7.13%. IR (cm^{-1}): 1604 ($\nu_{C=N}$), 1004 ($\nu_{V=O}$).

Vanadium oxo complex VO-13

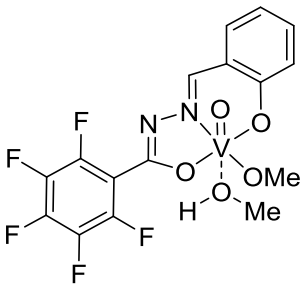

To a MeOH solution of **L-4** (0.165 g, 0.50 mmol in 5 mL of MeOH) was added $VO(OiPr)_3$ (118 µL, 0.50 mmol). After 90 min., the corresponding vanadium complex **VO-13** was obtained (0.192 g, 90% yield). ^{1}H NMR (MeOD-d_4, 300 MHz): δ = 6.96 (d,

1 H, *J* = 8.3 Hz), 7.03 (t, 1 H, *J* = 7.4 Hz), 7.56 (t, 1 H, *J* = 7.6 Hz), 7.64 (d, 1 H, *J* = 7.5 Hz), 8.77 (s, 1 H) ppm. $^{13}C\{^{1}H\}$ NMR (MeOD-*d*$_4$, 100 MHz): δ = 117.8, 121.3, 121.6, 134.2, 136.1, 137.9 (m), 140.4 (m), 142.3 (m), 144.9 (m), 145.4 (m), 147.9 (m), 156.3, 164.5, 165.6 ppm. $^{19}F\{^{1}H\}$ NMR (MeOD-*d*$_4$, 282.40 MHz): δ = -164.3 (m, 2 F), -154.5 (tt, 1 F, *J* = 2.8, 20.1 Hz), -140.5 (m, 2 F) ppm. ^{51}V NMR (MeOD-*d*$_4$, 105.25 MHz): δ = -553.6 ppm. HRMS (ESI+, *m/z*) calculated for $C_{15}H_9N_2O_4F_5V$ $[M+H]^+$ *m/z* = 426.9922, found 426.9924. Elemental analysis for $C_{15}H_8N_2O_4F_5V$ calculated: C, 42.28; H, 1.89; N, 6.57%; found: C, 42.33; H, 2.00; N, 6.45%. IR (cm^{-1}): 3448 (ν_{O-H}), 1606 ($\nu_{C=N}$), 991 ($\nu_{V=O}$).

Vanadium oxo complex VO-14

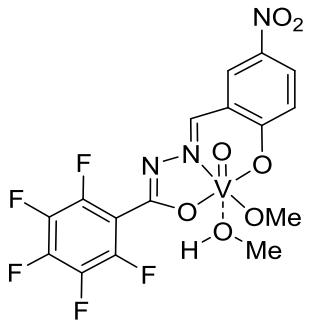

To a MeOH solution of **L-5** (0.187 g, 0.50 mmol in 5 mL of MeOH) was added $VO(OiPr)_3$ (118 μL, 0.50 mmol). After 90 min., the corresponding vanadium complex **VO-14** was obtained (0.225 g, 95% yield). ^{1}H NMR (MeOD-*d*$_4$, 400 MHz): δ = 7.08 (d, 1 H, *J* = 9.2 Hz), 8.38 (dd, 1 H, *J* = 2.9, 9.2Hz), 8.65 (d, 1 H, *J* = 2.8 Hz), 8.91 (s, 1 H) ppm. $^{13}C\{^{1}H\}$ NMR (MeOD-*d*$_4$, 100 MHz): δ = 119.5, 120.9, 130.4, 130.5, 137.9 (m), 140.5 (m), 141.7, 142.5 (m), 145.0 (m), 145.4 (m), 147.9 (m), 155.6, 165.3, 169.3 ppm. $^{19}F\{^{1}H\}$ NMR (MeOD-*d*$_4$, 376.50 Hz): δ = -164.2 (m, 2 F), -154.1 (tt, 1 F, *J* = 3.2, 20.1 Hz), -140.3 (m, 2 F) ppm. ^{51}V NMR (MeOD-*d*$_4$, 105.25 MHz): δ = -556.4 ppm. HRMS (ESI+, *m/z*) calculated for $C_{15}H_8N_3O_6F_5V$ $[M+H]^+$ *m/z* = 471.9773, found 471.9769. Elemental analysis for $C_{15}H_7N_3O_6F_5V$ calculated: C, 38.24; H, 1.50; N, 8.92%; found: C, 37.90; H, 1.92; N, 8.75%. IR (cm^{-1}): 3442 (ν_{O-H}), 1608 ($\nu_{C=N}$), 1338 (ν_{NO2}), 995 ($\nu_{V=O}$).

Vanadium oxo complex VO-15

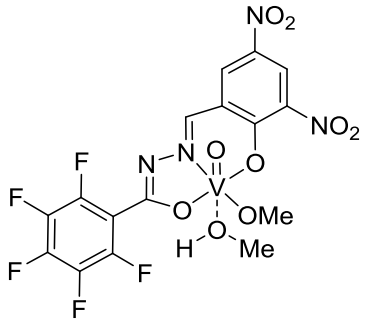

To a MeOH solution of **L-6** (0.210 g, 0.50 mmol in 5 mL of MeOH) was added $VO(OiPr)_3$ (118 μL, 0.50 mmol). After 90 min., the corresponding vanadium complex **VO-15** was obtained (0.232 g, 90% yield). ^{1}H NMR (MeOD-*d*$_4$, 400 MHz): δ = 8.85 (d, 1 H, *J* = 2.8 Hz), 8.95 (d, 1 H, *J* = 2.8 Hz), 9.01 (s, 1 H) ppm. ^{13}C{^{1}H} NMR (MeOD-*d*$_4$, 100 MHz): δ = 124.4, 125.8, 133.7, 138.0 (m), 139.5, 140.1, 140.5 (m), 142.7 (m), 145.2 (m), 145.4 (m), 148.0 (m), 155.0, 161.1, 166.0 ppm. ^{19}F{^{1}H} NMR (MeOD-*d*$_4$, 282.40 MHz): δ = -164.1 (m, 2 F), -153.7 (tt, 1 F, *J* = 3.4, 20.1 Hz), -140.1 (m, 2 F) ppm. ^{51}V NMR (MeOD-*d*$_4$, 105.25 MHz): δ = -543.8 ppm. HRMS (ESI+, *m/z*) calculated for $C_{15}H_7N_4O_8F_5V$ $[M+H]^+$ *m/z* = 516.9624, found 516.9622. Elemental analysis for $C_{15}H_6N_4O_8F_5V$ calculated: C, 34.90; H, 1.17; N, 10.85%; found: C, 34.72; H, 1.07; N, 10.70%. IR (cm^{-1}): 3415 (ν_{O-H}), 1608 ($\nu_{C=N}$), 1344 (ν_{NO2}), 993 ($\nu_{V=O}$).

Synthesis of the lignin model compound 5

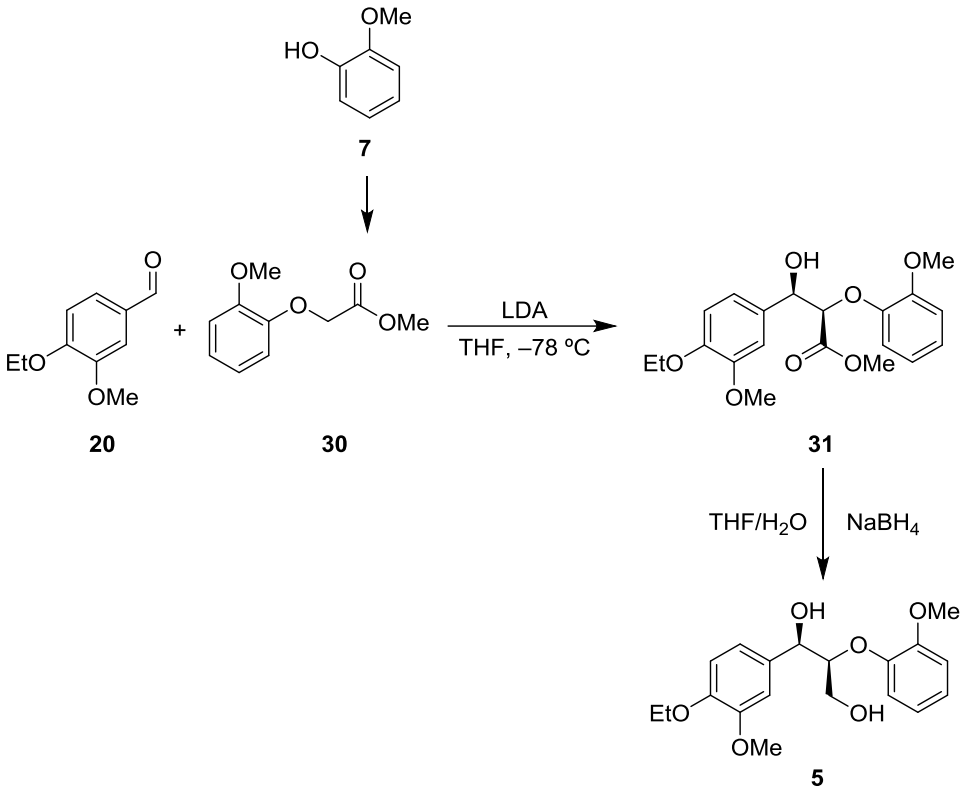

Scheme 3.5. Synthetic pathway for preparation of **5**.

The lignin model compound **5** used in this study was prepared by following the previously reported procedure.[27] In short, a C-C bond formation between **20** and methyl(methoxyphenoxy)acetate (**30**) resulted in the formation of methyl ester **31**, which is finally reduced by $NaBH_4$ to provide **5**. The product identity was confirmed by NMR spectroscopy and HR-MS. ^{1}H NMR (CD_3CN, 300 MHz): δ = 1.34 (t, J = 6.9 Hz, 3 H), 3.06 (t, J = 6.9 Hz, 1 H), 3.60 – 3.75 (m, 2 H), 3.77 (s, 3 H), 3.79 (s, 3 H), 4.01 (q, J = 6.9 Hz, 2 H), 4.25 – 4.30 (m, 1 H), 4.82 (t, J= 4.8 Hz, 1 H), 6.81 – 7.02 (m, 7 H) ppm. HRMS (ESI+, *m/z*) calculated for $C_{19}H_{25}O_6$ $[M + H]^+$ *m/z* = 349.1651, found 349.1656. The values match the reported data.[27]

Synthesis of the lignin model compound 25

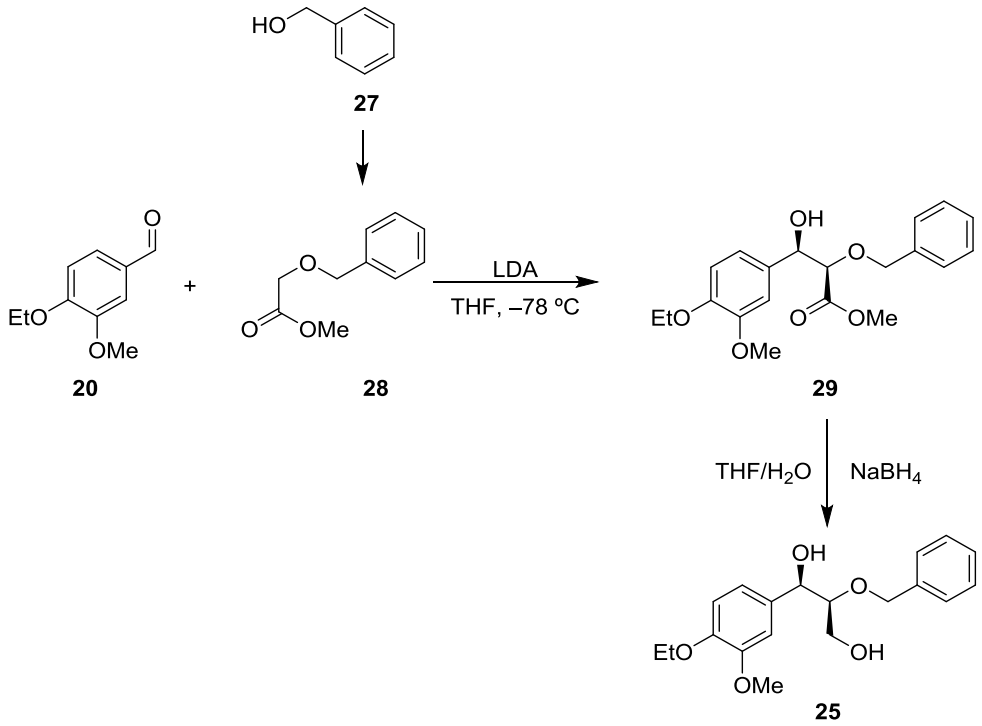

Scheme 3.6. Synthetic pathway for preparation of **25**.

The lignin model compound **25** was synthesized by modifying the previously reported procedure.[27] In the modified procedure, instead of **7**, we used **27**. The product was purified by flash column chromatography on silica gel with *n*-hexane:ethyl acetate (EtOAc) (5:2). The isolated **25** was a colorless viscous liquid. The product identity was confirmed by NMR spectroscopy and HRMS. ^{1}H NMR (CD_3CN, 300 MHz): δ = 1.36 (t, 3 H, J = 7.0 Hz), 3.39-3.58 (m, 2 H), 3.64-3.66 (m, 1 H), 3.75 (s, 3 H), 4.03 (q, 2 H, J = 7.0 Hz), 4.35 (d, 1 H, J = 11.5 Hz), 4.51 (t, 1 H, 12.1 Hz), 4.62-4.69 (m, 1 H), 6.30 (s, 2 H), 6.87-6.96 (m, 3 H), 7.17-7.34 (m, 5 H) ppm. ^{13}C{^{1}H} NMR (CD_3CN, 300 MHz): δ = 15.3, 56.4, 62.5, 65.2, 73.1, 74.4, 84.5, 111.9, 113.6, 120.3, 128.4, 128.8, 129.2, 136.2, 140.0, 148.8, 150.1 ppm. HRMS (ESI+, *m/z*) calculated for $C_{19}H_{25}O_5$ $[M+H]^+$ *m/z* = 333.1702, found 333.1708.

3.8.3 Kinetics Studies on Photodegradation of Lignin Models with Vanadium Catalysts

General procedure for the photodegradation of the lignin model compound 5

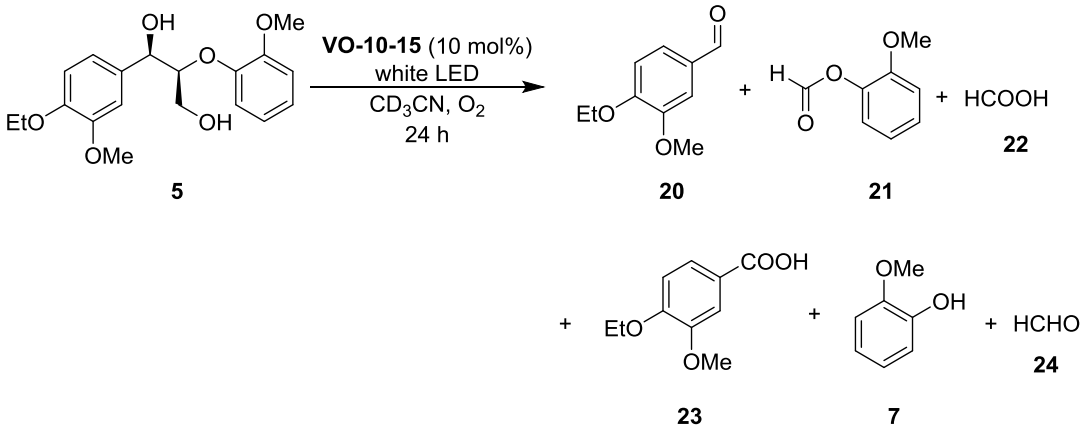

Scheme 3.7. Photocatalytic degradation of **5** with **VO-10-15**.

Photodegradation experiments were carried out in an NMR tube. In a typical procedure, **5** (0.011 g, 0.030 mmol) and the vanadium catalyst (10 mol%, 1.1-1.5 mg of **VO-10-15**) were dissolved in CD_3CN (0.50 mL) and 1,1,2,2-tetrachloroethane (3.2 μL, 0.032 mmol) was added as an internal standard to calculate the conversion and yield of the products. The NMR tube was fitted with a needle and a balloon of pure O_2 that ensured 1 atm of O_2 throughout the experiment. The reaction mixture was irradiated up to 24 h under white LED light (48 W) and ambient temperatures. A continuous water circulator was used to maintain the reaction temperatures below 30 °C. The light irradiation was briefly stopped every 2 or 4 h and the NMR tube containing the reaction mixture was used in the NMR spectroscopic experiments to monitor the reaction progress and kinetics. Reaction products, other than **21**, were identified by ^{1}H NMR spectroscopy by comparing the peaks from the reaction mixture's ^{1}H NMR spectrum to those of the commercially available samples. Compound **21** was identified in our group's previous work by independent synthesis.[24]

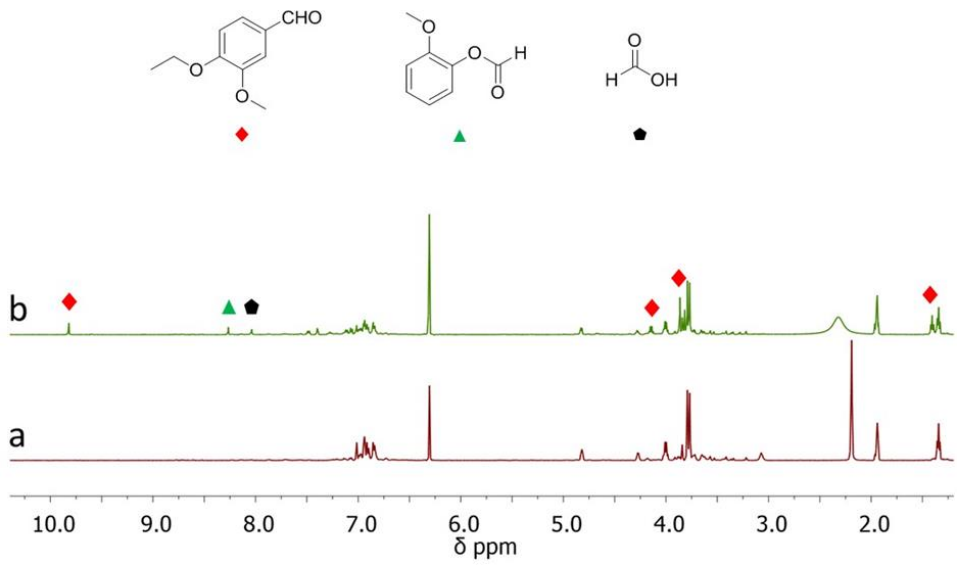

Figure 3.9. The ^{1}H NMR spectra of the reaction solution containing **5** (30.0 μmol), **VO-10** (3.0 μmol, 10 mol%), and the internal standard 1,1,2,2-tetrachloroethane (30.0 μmol) in CD_3CN a) before and b) after 24 h of irradiation with a 48 W white LED. The peak at 6.30 ppm corresponds to the internal standard.

General procedure for the photodegradation of the lignin model compound 25

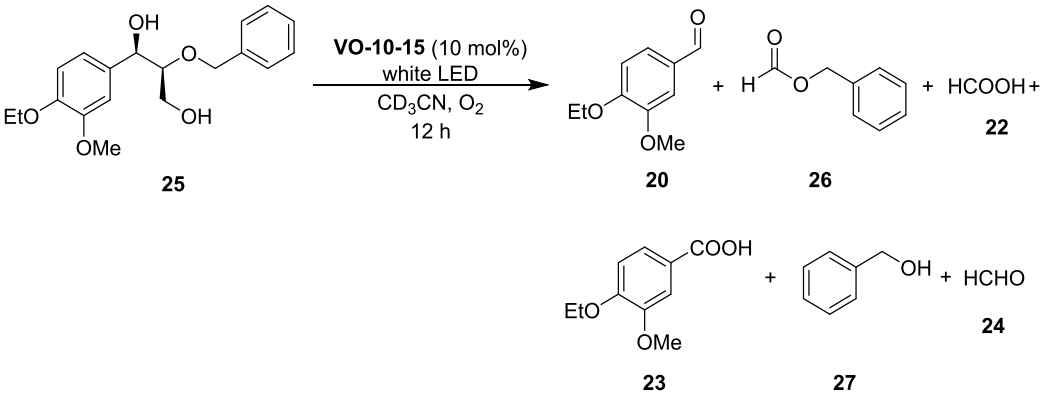

Scheme 3.8. Photocatalytic degradation of **25** with **VO-10-15**.

Photodegradation experiments were carried out in an NMR tube. In a typical procedure, **25** (0.010 g, 0.030 mmol) and the vanadium catalyst (10 mol%, 1.1-1.5 mg of **VO-10-15**) were dissolved in CD_3CN (0.50 mL) and 1,1,2,2-tetrachloroethane (3.2 μL, 0.030 mmol) was added as an internal standard to calculate the conversion and yield of the products. The NMR tube was fitted with a needle and a balloon of pure O_2 that ensured 1 atm of O_2 throughout the experiment. The reaction mixture was irradiated up to 12 h under white LED light (48 W) and ambient temperatures. A continuous water circulator was used to maintain the reaction temperatures below 30 °C. The light irradiation was briefly stopped every 1.5 or 2 h and the NMR tube containing the

reaction mixture was used in the NMR spectroscopic experiments to monitor the reaction progress and kinetics. The identity of the degradation product **26** was confirmed by NMR spectroscopy after isolation by preparatory silica gel thin layer chromatography (TLC) (eluent: EtOAc/*n*-hexane 2:3) and independent synthesis. ^{1}H NMR ($CDCl_3$, 400 MHz): δ = 5.22 (s, 2 H), 7.33-7.40 (m, 5 H), 8.15 (s, 1 H) ppm. $^{13}C\{^{1}H\}$ NMR ($CDCl_3$, 100 MHz): δ = 65.6, 128.3, 128.4, 128.6, 135.2, 160.7 ppm. The identities of other reaction products were verified by comparison of the ^{1}H NMR spectrum of the reaction mixture with those of the commercially available samples.

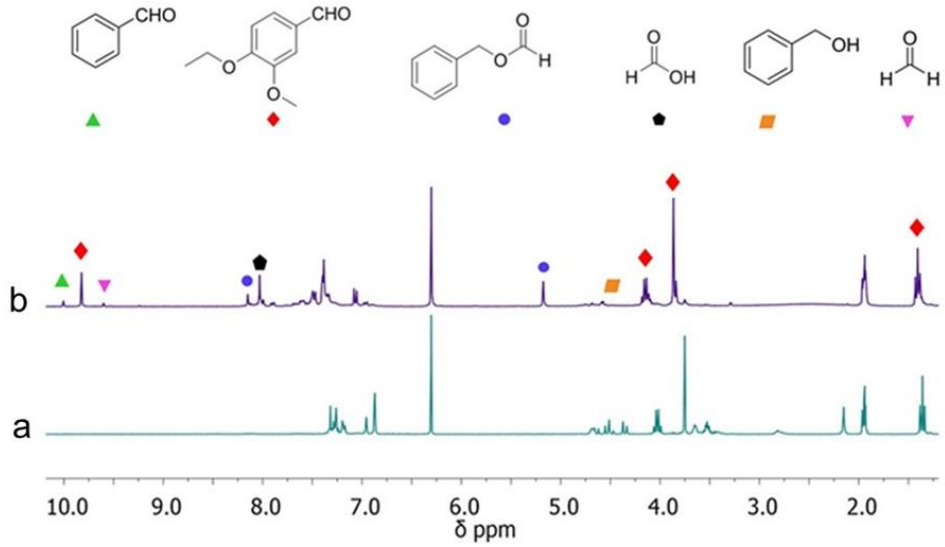

Figure 3.10. The ^{1}H NMR spectra of the reaction solution containing **25** (30.0 μmol), **VO-10** (3.0 μmol, 10 mol%), and the internal standard 1,1,2,2-tetrachloroethane (30.0 μmol) in CD_3CN a) before and b) after 12 h of irradiation with a 48 W white LED. The peak at 6.30 ppm corresponds to the internal standard.

General procedure for the control reaction of irradiating 25 in the absence of catalysts

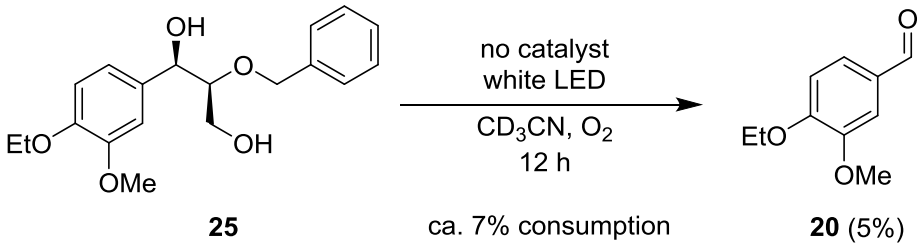

Scheme 3.9. Control reaction of irradiating **25** in the absence of catalyst under otherwise identical reaction conditions.

Each of these control experiments was carried out in an NMR tube. In a typical procedure, **25** (0.010 g, 0.030 mmol) was dissolved in CD_3CN (0.50 mL) in the absence of any vanadium catalyst, and 1,1,2,2-tetrachloroethane (3.2 μL, 0.040 mmol) was added as an internal standard to calculate the conversions and yields of the products. The NMR tube was sealed and then fitted with a needle and a balloon of pure O_2 to ensure that the solution remained under 1 atm of O_2 throughout the experiment. The reaction mixture was irradiated up to 24 h with a white LED (48 W) at ambient temperatures. A continuous water circulator was used to maintain the reaction temperatures below 30 °C. After 24 h, around 7% of **25** was consumed as observed by ^{1}H NMR spectroscopy.

General procedure for the thermal reaction of 25 in the dark in the presence of selected catalysts

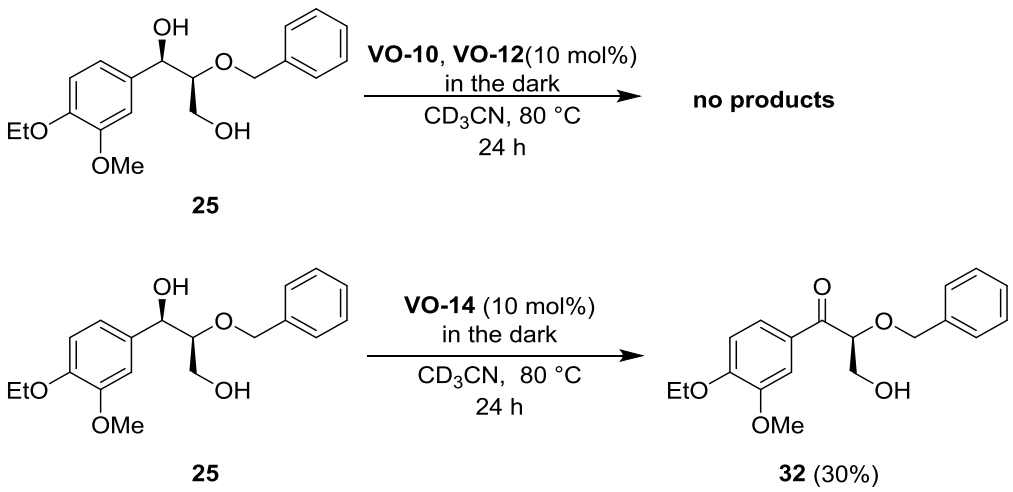

Scheme 3.10. Control reactions by heating **25** at 80 ºC in the dark with selected vanadium catalysts.

Each of these thermal control experiments was carried out in an NMR tube. In a typical procedure, **25** (0.010 g, 0.030 mmol) was dissolved in CD_3CN (0.50 mL) along with **VO-10**, **VO-12**, or **VO-14** (10 mol%, 1.1-1.5 mg), and 1,1,2,2-tetrachloroethane (3.2 μL, 0.040 mmol) was added as an internal standard to calculate the conversions and yields of the products. The NMR tube was sealed and then fitted with a needle and a balloon of air to ensure that the solution remained under atmospheric pressure throughout the experiment. Air was used to ensure a fair comparison with the conversion of **25** from the previous report.[1] The reaction mixtures were heated at 80 °C in the dark up to 24 h with catalysts **VO-10**, **VO-12**, and **VO-14**. After 24 h, only the reaction

mixture with **VO-14** showed the presence of the ketone **32** (30%) due to oxidation of the benzylic alcohol, based on the ^{1}H NMR spectroscopy. The identity of **32** was confirmed by HR-MS after isolation from the reaction mixture by preparative silica gel thin-layer chromatography with the eluent system EtOAc:*n*-hexane in a ratio of 2:3. ^{1}H NMR (CD_3CN, 500 MHz): δ = 1.40 (t, *J* = 7.0 Hz, 3 H), 3.78-3.88 (m, 5 H), 4.13 (q, *J* = 7.0 Hz, 2 H), 4.52 (d, *J* = 11.5 Hz, 1 H), 4.61 (d, *J* = 11.5 Hz, 1 H), 4.87 (dd, *J* = 5.9, 4.2 Hz, 1 H), 6.98 (d, *J* = 8.5 Hz, 1 H), 7.23-7.34 (m, 5 H), 7.53 (d, *J* = 2.0 Hz, 1 H), 7.67 (dd, *J* = 8.5, 2.0 Hz, 1 H) ppm. HRMS (ESI+, *m/z*) calculated for $C_{19}H_{23}O_5$ $[M+H]^+$ *m/z* = 331.1545, found 331.1556.

3.8.4 Electrochemical Studies

The CV experiments were conducted using a Biologic SP-300 potentiostat with 1.0 mM solutions of the sample and 0.10 M *n*-Bu_4NPF_6 as the electrolyte in acetonitrile (MeCN) at a scan rate of 100 mV s^{-1}. A standard three-electrode electrochemical cell was used with a glassy carbon working electrode (3.0 mm in diameter from BAS), a Pt wire as the counter electrode, and another Pt wire as a pseudoreference electrode. The potentials were measured in the presence of dmFc as an internal reference (-0.48 V with respect to Fc^+/Fc). Before each experiment, the working electrode (glassy carbon) was polished using a 0.05 μm alumina suspension on a polishing pad, followed by sonication in deionized water for 10 min and dried in air. In each experiment, the solutions were prepared by bubbling Ar through the solvents for 10 min.

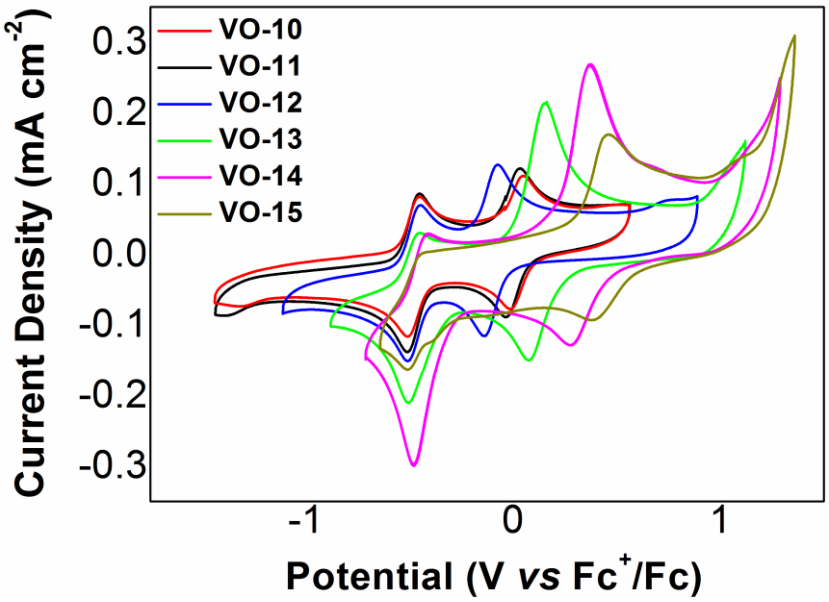

Figure 3.11. Cyclic voltammograms of **VO-10-15** in the presence of dmFc as the internal standard. The reversible dmFc wave is set to -0.48 V vs. Fc^{+}/Fc.

3.8.5 Quantum Yield Measurements

Potassium ferrioxalate, $K_3[Fe(OX)_3]\cdot 3H_2O$, is generally used as a standard chemical actinometer for determining the quantum yield in any photochemical reaction under visible light.[38,39] Initially, the rate of formation of the Fe^{2+} from $K_3[Fe(OX)_3]\cdot 3H_2O$ complex upon visible light irradiation (with 48 W white LED) was measured. In a typical experiment, 0.60 mL of an aqueous reaction mixture containing 6.0 mM of $K_3[Fe(OX)_3]\cdot 3H_2O$ complex and 20 mM of the 1,10-phenanthroline was irradiated in a dry NMR tube under visible light with 48 W white LED. The UV-vis absorption spectrum of the reaction mixture was recorded before and after different irradiation times. The rate of formation of the $[Fe(Phen)_3]^{2+}$ was calculated. Since the quantum yield of $K_3[Fe(OX)_3]$ in water is reported to be 1.11% at 436 nm, the quantum yields for our photocatalytic processes were determined at 436 nm.

The quantum yields were calculated using the equation: $\phi_2 = (f_1 \cdot \phi_1 \cdot r_2) / (f_2 \cdot r_1)$, where ϕ_1 = the known quantum yield of any photoreaction 1, r_1 = rate of reaction 1, f_1 = fraction of light absorbed by the photoactive species used in reaction 1, r_2 = rate of reaction 2, f_2 = fraction of light absorbed by the photoactive species used in reaction 2, and ϕ_2 = quantum yield of the photoreaction 2 to be determined. The fraction of light absorbed by the photoactive species, $f = (1\text{-}10^{-A})$, where A = absorbance.

Results:

$K_3[Fe(OX)_3]$

The rate of change in absorbance at 510 nm (Figure 3.12.b) due to the formation of $[Fe(Phen)_3]^{2+}$ is 0.220 s^{-1} / 0.60 mL of solution. Since the molar extinction coefficient of $[Fe(Phen)_3]^{2+}$ at 510 nm is 1.12 x 10^4 M^{-1} cm^{-1} and the absorption path length 0.20 cm, the rate of the formation of the complex $[Fe(Phen)_3]^{2+}$ is calculated as 9.86 x 10^{-5} M s^{-1} / 0.60 mL of solution which is equivalent to 5.91 x 10^{-5} mmol s^{-1}.

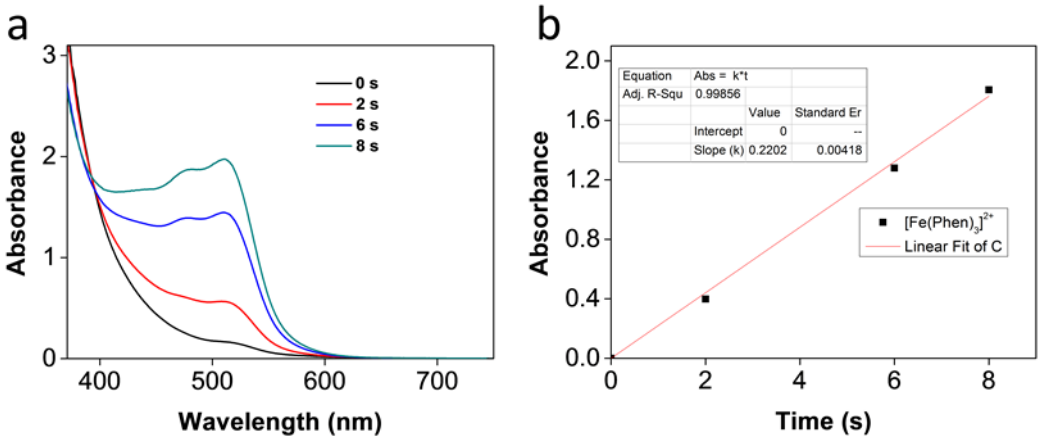

Figure 3.12. (a) UV-Vis absorption spectra of the complex $[Fe(phen)_3]^{2+}$ formed after different visible light irradiation times (white LED) of a 0.60 mL aqueous solution containing 6.0 mM of $K_3[Fe(OX)_3]\cdot 3H_2O$ and 20 mM of 1,10-phenanthroline. (b) Kinetics determined by plotting of absorbance at 510 nm versus irradiation time in seconds.

For $K_3[Fe(OX)_3]$ the rate, r_1 = 5.91 x 10^{-5} mmol s^{-1}. Since the absorbance at 436 nm is 0.60 for 0.20 cm path length, the 0.40 cm of inner diameter of NMR tube will result in a 0.40 cm path length, so the absorbance will be 1.2. The fraction of light absorbed, $f_1 = (1\text{-}10^{-A}) = 0.93$. The quantum yield of $K_3[Fe(OX)_3]$ is reported to be ϕ_1 = 1.11%, at 436 nm.

Lignin model **5**

For all the experiments, a 0.60 mL CD_3CN solution containing **5** (0.030 mmol, 50 mM) with the vanadium catalyst (0.0030 mmol, 5.0 mM) was irradiated under white light LED (48 W) in presence of the internal standard (1,1,2,2-tetrachloroethane) in an NMR tube. For quantum yield calculations, the initial rate was used. For **5**, the initial rate appeared to remain almost constant up to at least 4 h.

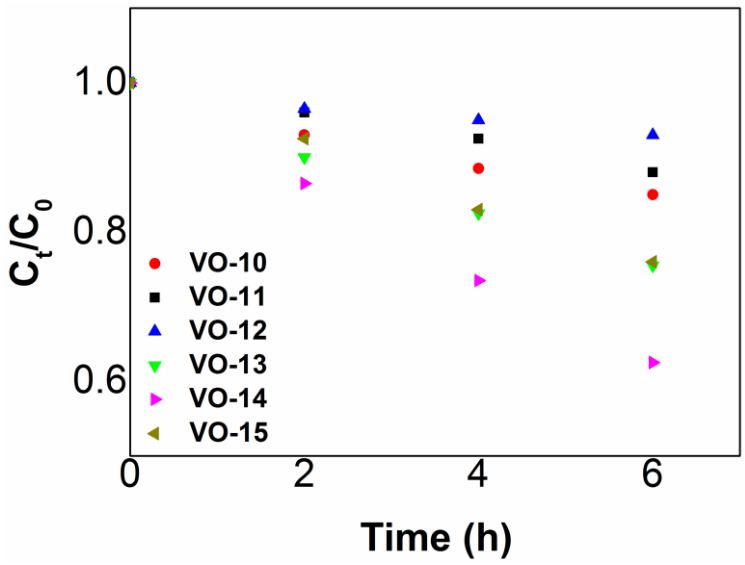

Figure 3.13. Plot of C_t/C_0 versus time (h) for the consumption of **5** in the presence of a catalytic amount (10 mol%) of different complexes under visible light irradiation with white LED.

Calculations:

For $K_3[Fe(OX)_3]$

Rate, $r_1 = 5.91 \times 10^{-5}$ mmol s^{-1}; fraction of light absorbed, $f_1 = (1\text{-}10^{-A}) = 0.93$. The quantum yield of $K_3[Fe(OX)_3]$ is reported to be $\phi_1 = 1.11\%$, at 436 nm.

The rate, $r_{\mathbf{VO\text{-}10}} = 2.39 \times 10^{-7}$ mmol s^{-1}, the fraction of light absorbed, $f_{\mathbf{VO\text{-}10}} = (1\text{-}10^{-A}) = 0.99$, since the absorbance at 436 nm of the 5.0 mM of **VO-10** with path length 0.40 cm is more than 2.0. The quantum yield, $\phi_{\mathbf{VO\text{-}10}}$ = to be determined

$\phi_{\mathbf{VO\text{-}10}} = (f_1 \cdot \phi_1 \cdot r_{\mathbf{VO\text{-}10}}) / (f_{\mathbf{VO\text{-}10}} \cdot r_1) = (0.93 \times 1.11 \times 2.39 \times 10^{-7}$ mmol $s^{-1}) / (0.99 \times 5.91 \times 10^{-5}$ mmol $s^{-1}) = 0.42\%$

Rate, $r_{\mathbf{VO\text{-}11}} = 1.56 \times 10^{-7}$ mmol s^{-1}; fraction of light absorbed, $f_{\mathbf{VO\text{-}11}} = (1\text{-}10^{-A}) = 0.99$, since the absorbance at 436 nm of the 5.0 mM of **VO-11** with path length 0.40 cm is more than 2.0. The quantum yield, $\phi_{\mathbf{VO\text{-}11}}$, to be determined is defined as the following:

$\phi_{\mathbf{VO\text{-}11}} = (f_1 \cdot \phi_1 \cdot r_{\mathbf{VO\text{-}11}}) / (f_{\mathbf{VO\text{-}11}} \cdot r_1) = (0.93 \times 1.11 \times 1.56 \times 10^{-7}$ mmol $s^{-1}) / (0.99 \times 5.91 \times 10^{-5}$ mmol $s^{-1}) = 0.28\%$

The rate, $r_{\mathbf{VO\text{-}12}}$ = 1.04 x 10^{-7} mmol s^{-1}, the fraction of light absorbed, $f_{\mathbf{VO\text{-}12}}$ = (1-10^{-A}) = 0.99, since the absorbance at 436 nm of the 5.0 mM of **VO-12** with path length 0.40 cm is more than 2.0. The quantum yield, $\phi_{\mathbf{VO\text{-}12}}$ = to be determined

$\phi_{\mathbf{VO\text{-}12}} = (f_1 \cdot \phi_1 \cdot r_{\mathbf{VO\text{-}12}}) / (f_{\mathbf{VO\text{-}12}} \cdot r_1)$ = (0.93 x 1.11 x 1.04 x 10^{-7} mmol s^{-1}) / (0.99 x 5.91 x 10^{-5} mmol s^{-1}) = 0.18%

The rate, $r_{\mathbf{VO\text{-}13}}$ = 3.64 x 10^{-7} mmol s^{-1}, the fraction of light absorbed, $f_{\mathbf{VO\text{-}13}}$ = (1-10^{-A}) = 0.99, since the absorbance at 436 nm of the 5.0 mM of **VO-13** with path length 0.40 cm is more than 2.0. The quantum yield, $\phi_{\mathbf{VO\text{-}13}}$ = to be determined

$\phi_{\mathbf{VO\text{-}13}} = (f_1 \cdot \phi_1 \cdot r_{\mathbf{VO\text{-}13}}) / (f_{\mathbf{VO\text{-}13}} \cdot r_1)$ = (0.93 x 1.11 x 3.64 x 10^{-7} mmol s^{-1}) / (0.99 x 5.91 x 10^{-5} mmol s^{-1}) = 0.64%

The rate, $r_{\mathbf{VO\text{-}14}}$ = 9.16 x 10^{-7} mmol s^{-1}, the fraction of light absorbed, $f_{\mathbf{VO\text{-}14}}$ = (1-10^{-A}) = 0.99, since the absorbance at 436 nm of the 5 mM of **VO-14** with path length 0.40 cm is 1.92. The quantum yield, $\phi_{\mathbf{VO\text{-}14}}$ = to be determined

$\phi_{\mathbf{VO\text{-}14}} = (f_1 \cdot \phi_1 \cdot r_{\mathbf{VO\text{-}14}}) / (f_{\mathbf{VO\text{-}14}} \cdot r_1)$ = (0.93 x 1.11 x 9.16 x 10^{-7} mmol s^{-1}) / (0.99 x 5.91 x 10^{-5} mmol s^{-1}) = 1.60 %

The rate, $r_{\mathbf{VO\text{-}15}}$ = 3.54 x 10^{-7} mmol s^{-1}, the fraction of light absorbed, $f_{\mathbf{VO\text{-}15}}$ = (1-10^{-A}) = 0.99, since the absorbance at 436 nm of the 5.0 mM of **VO-15** with path length 0.40 cm is 1.36. The quantum yield, $\phi_{\mathbf{VO\text{-}15}}$ = to be determined

$\phi_{\mathbf{VO\text{-}15}} = (f_1 \cdot \phi_1 \cdot r_{\mathbf{VO\text{-}15}}) / (f_{\mathbf{VO\text{-}15}} \cdot r_1)$ = (0.93 x 1.11 x 3.54 x 10^{-7} mmol s^{-1}) / (0.95 x 5.91 x 10^{-5} mmol s^{-1}) = 0.65%

Lignin model **25**

For all the experiments, a 0.60 mL CD_3CN solution containing **25** (0.030 mmol, 50 mM) with the vanadium catalyst (0.0030 mmol, 5.0 mM) was irradiated under white light LED (48 W) in presence of the internal standard (1,1,2,2-tetrachloroethane) in an NMR tube. For quantum yield calculations, the initial rate was used. For **25**, the initial rate appeared to remain almost constant up to at least 3 h.

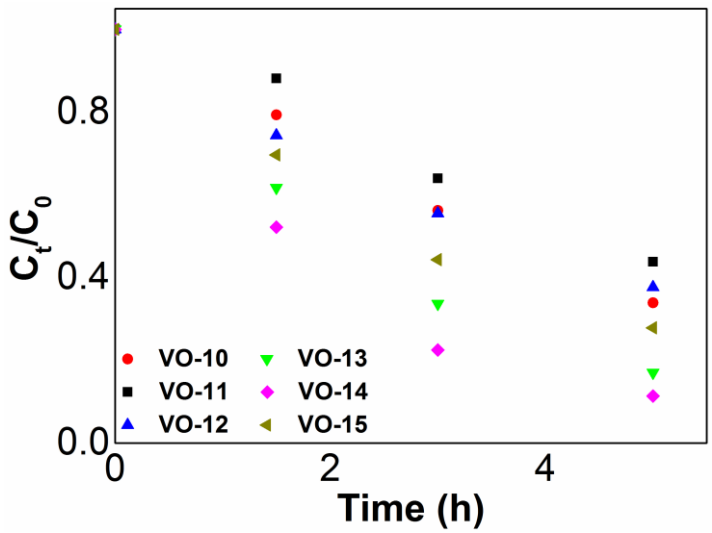

Figure 3.14. Plot of C_t/C_0 versus time (h) for the consumption of **25** in the presence of a catalytic amount (10 mol%) of different complexes under visible light irradiation with white LED.

Calculations:

For $K_3[Fe(OX)_3]$

The rate, $r_1 = 5.91 \times 10^{-5}$ mmol s^{-1}, the fraction of light absorbed, $f_1 = (1\text{-}10^{-A}) = 0.93$. The quantum yield of $K_3[Fe(OX)_3]$ is reported to be $\phi_1 = 1.11\%$, at 436 nm.

The rate, $r_{\mathbf{VO\text{-}10}} = 1.21 \times 10^{-6}$ mmol s^{-1}, the fraction of light absorbed, $f_{\mathbf{VO\text{-}10}} = (1\text{-}10^{-A}) = 0.99$, since the absorbance at 436 nm of the 5.0 mM of **VO-10** with path length 0.40 cm is more than 2.0. The quantum yield, $\phi_{\mathbf{VO\text{-}10}}$ = to be determined

$\phi_{\mathbf{VO\text{-}10}} = (f_1 \cdot \phi_1 \cdot r_{\mathbf{VO\text{-}10}}) / (f_{\mathbf{VO\text{-}10}} \cdot r_1) = (0.93 \times 1.11 \times 1.21 \times 10^{-6}$ mmol $s^{-1}) / (0.99 \times 5.91 \times 10^{-5}$ mmol $s^{-1}) = 2.13\%$

The rate, $r_{\mathbf{VO\text{-}11}} = 1.0 \times 10^{-6}$ mmol s^{-1}, the fraction of light absorbed, $f_{\mathbf{VO\text{-}11}} = (1\text{-}10^{-A}) = 0.99$, since the absorbance at 436 nm of the 5.0 mM of **VO-11** with path length 0.40 cm is more than 2.0. The quantum yield, $\phi_{\mathbf{VO\text{-}11}}$ = to be determined

$\phi_{\mathbf{VO\text{-}11}} = (f_1 \cdot \phi_1 \cdot r_{\mathbf{VO\text{-}11}}) / (f_{\mathbf{VO\text{-}11}} \cdot r_1) = (0.93 \times 1.11 \times 1.0 \times 10^{-6}$ mmol $s^{-1}) / (0.99 \times 5.91 \times 10^{-5}$ mmol $s^{-1}) = 1.76\%$

The rate, $r_{\mathbf{VO\text{-}12}} = 1.23 \times 10^{-6}$ mmol s^{-1}, the fraction of light absorbed, $f_{\mathbf{VO\text{-}12}} = (1\text{-}10^{-A}) = 0.99$, since the absorbance at 436 nm of the 5.0 mM of **VO-12** with path length 0.40 cm is more than 2.0. The quantum yield, $\phi_{\mathbf{VO\text{-}12}}$ = to be determined

$\phi_{VO\text{-}12}$ = ($f_1 \cdot \phi_1 \cdot r_{VO\text{-}12}$) / ($f_{VO\text{-}12} \cdot r_1$) = (0.93 x 1.11 x 1.23 x 10^{-6} mmol s^{-1}) / (0.99 x 5.91 x 10^{-5} mmol s^{-1}) = 2.17%

The rate, $r_{VO\text{-}13}$ = 1.84 x 10^{-6} mmol s^{-1}, the fraction of light absorbed, $f_{VO\text{-}13}$ = ($1\text{-}10^{-A}$) = 0.99, since the absorbance at 436 nm of the 5.0 mM of **VO-13** with path length 0.40 cm is more than 2.0. The quantum yield, $\phi_{VO\text{-}13}$ = to be determined

$\phi_{VO\text{-}13}$ = ($f_1 . \phi_1 . r_{VO\text{-}13}$) / ($f_{VO\text{-}13} . r_1$) = (0.93 x 1.11 x 1.84 x 10^{-6} mmol s^{-1}) / (0.99 x 5.91 x 10^{-5} mmol s^{-1}) = 3.25%

The rate, $r_{VO\text{-}14}$ = 2.15 x 10^{-6} mmol s^{-1}, the fraction of light absorbed, $f_{VO\text{-}14}$ = ($1\text{-}10^{-A}$) = 0.99, since the absorbance at 436 nm of the 5.0 mM of **VO-14** with path length 0.40 cm is more than 2.0. The quantum yield, $\phi_{VO\text{-}14}$ = to be determined.

$\phi_{VO\text{-}14}$ = ($f_1 \cdot \phi_1 \cdot r_{VO\text{-}14}$) / ($f_{VO\text{-}14} \cdot r_1$) = (0.93 x 1.11 x 2.15 x 10^{-6} mmol s^{-1}) / (0.99 x 5.91 x 10^{-5} mmol s^{-1}) = 3.79%

The rate, $r_{VO\text{-}15}$ = 1.54 x 10^{-6} mmol s^{-1}, the fraction of light absorbed, $f_{VO\text{-}15}$ = ($1\text{-}10^{-A}$) = 0.90, since the absorbance at 436 nm of the 5.0 mM of **VO-15** with path length 0.40 cm is 1.0. The quantum yield, $\phi_{VO\text{-}15}$ = to be determined

$\phi_{VO\text{-}15}$ = ($f_1 \cdot \phi_1 \cdot r_{VO\text{-}15}$) / ($f_{VO\text{-}15} \cdot r_1$) = (0.93 x 1.11 x 1.54 x 10^{-6} mmol s^{-1}) / (0.95 x 5.91 x 10^{-5} mmol s^{-1}) = 2.83%

3.8.6 UV-vis and Photoluminescence Spectroscopic Studies

The UV-vis spectroscopic studies were performed on the vanadium complexes and their corresponding ligands using a Shimadzu UV-3600 UV-vis-NIR spectrophotometer. For this purpose, 0.10 mM MeCN solutions of the complexes and ligands were prepared. The resulting spectra are shown below.

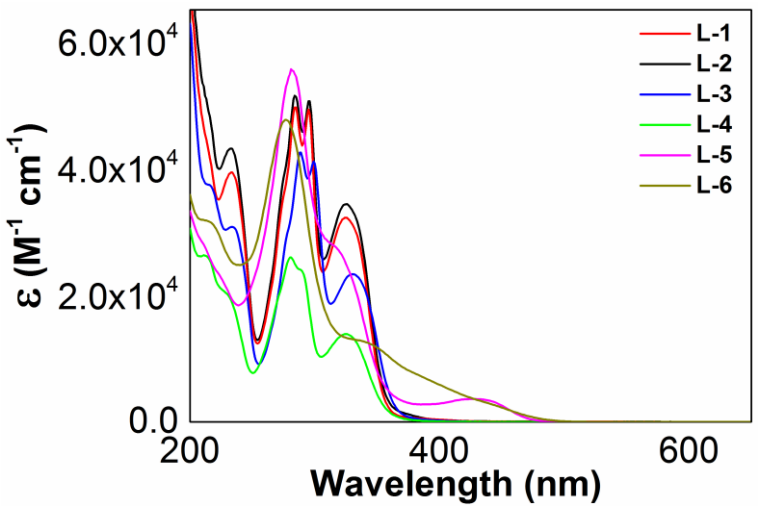

Figure 3.15. The UV-Vis spectra of the 0.10 mM MeCN solutions of **L-1-6** with a 0.50 cm path length cuvette.

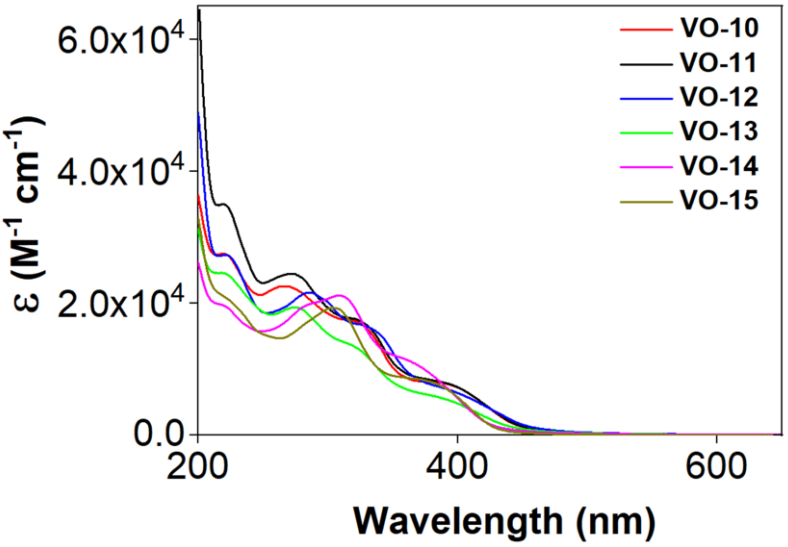

Figure 3.16. The UV-Vis spectra of the 0.10 mM MeCN solutions of **VO-10-15** with a 0.50 cm path length cuvette.

The steady-state photoluminescence spectroscopic measurements were performed with a Varian Cary Eclipse fluorescence spectrophotometer on 0.50 mM solutions of **VO-10-15** in MeCN. The resulting spectra are shown below.

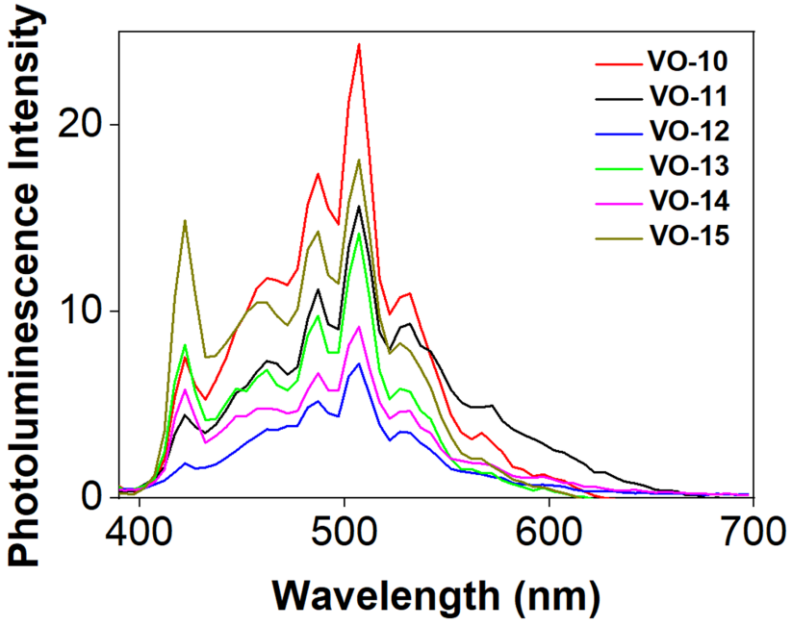

Figure 3.17. The photoluminescence spectra of 0.50 mM MeCN solutions of **VO-10-15**, each collected in a 0.50 cm path length cuvette with an excitation wavelength of 370 nm.

3.8.7 DFT Computational Data

Computational DFT studies were performed using the Gaussian09 software package.[29] The geometry optimization and frequency calculations were initially carried out at the UB3LYP/6-31G* level in the gas phase.[30-32] Subsequently, single-point energy calculations with the 6-311+G(d,p) basis set in a solvent phase were performed on the optimized geometry in order to obtain refined energy data. The effect of acetonitrile as a solvent was included using the IEFPCM-SCRF model.[33] Zero-point vibrational energies (ZPEs) were obtained from frequency calculations and were included as a correction to the refined energy data. The presence of an imaginary vibrational frequency was used to identify a stationary geometry as the transition state (TS) structure. The MOLEKEL software package was used to visualize the spatial distributions of selected molecular orbitals from single-point energy calculation results.[34]

We considered the photocatalytic C-C bond cleavage step of substrate **25** using catalysts **VO-10-15** according to the proposed mechanism shown in Figure 3.18 below. To simplify the computational model, the ethoxy substituent in substrate **25** was replaced with a methoxy group. Both singlet and triplet pathways were considered.

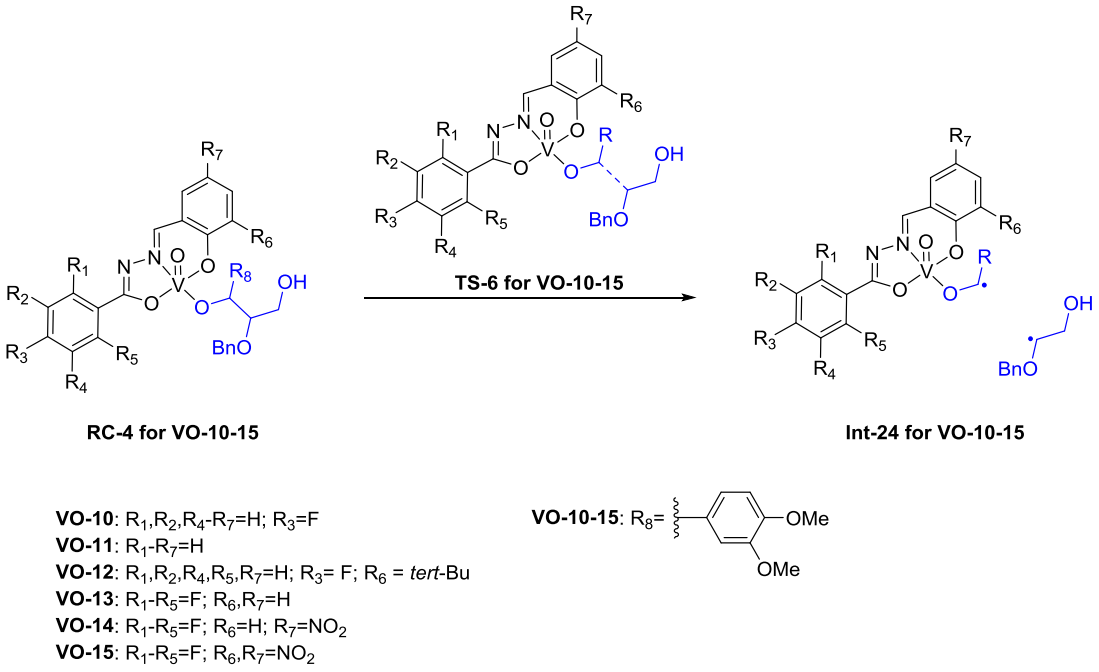

Figure 3.18. Photocatalytic C-C bond cleavage step of **25**.

Raw energy data:

Table 3.7. Raw energy data of **RC-4**, **TS-6**, **Int-24** for photocatalytic C-C bond cleavage in **25** with **VO-10-15** *via* singlet or triplet pathways for optimized geometries of **VO-10-15**.

Catalyst	Structure	E_{gas}(B1) [hartree]	ZPE [hartree]	E_{SCRF}(B2) [hartree]
VO-10	^{1}RC-4	-2992.680934	0.575673	-2993.321518
	^{1}TS-6	-2992.629983	0.571024	-2993.284953
	^{1}Int-24	-2992.630001	0.570797	-2993.285600
	^{3}RC-4	-2992.634511	0.572714	-2993.284567
	^{3}TS-6	-2992.627707	0.571839	-2993.281115
	^{3}Int-24	-2992.629392	0.570412	-2993.285515
VO-11	^{1}RC-4	-2893.447232	0.583947	-2894.052389
	^{1}TS-6	-2893.396032	0.579306	-2894.015564
	^{1}Int-24	-2893.396055	0.579069	-2894.016219
	^{3}RC-4	-2893.400625	0.581023	-2894.015507
	^{3}TS-6	-2893.393746	0.580115	-2894.011736
	^{3}Int-24	-2893.395454	0.578685	-2894.016148
VO-12	^{1}RC-4	-3149.932202	0.688917	-3150.612809
	^{1}TS-6	-3149.880210	0.684148	-3150.573505
	^{1}Int-24	-3149.880360	0.683620	-3150.574615
	^{3}RC-4	-3149.880435	0.683217	-3150.577165
	^{3}TS-6	-3149.878397	0.684805	-3150.572354
	^{3}Int-24	-3149.889219	0.685956	-3150.580218
VO-13	^{1}RC-4	-3389.568903	0.542421	-3390.347426
	^{1}TS-6	-3389.519284	0.537631	-3390.310811
	^{1}Int-24	-3389.519927	0.537373	-3390.311003
	^{3}RC-4	-3389.521121	0.539173	-3390.308161
	^{3}TS-6	-3389.517358	0.538409	-3390.308038
	^{3}Int-24	-3389.519744	0.537111	-3390.310800
VO-14	^{1}RC-4	-3594.070028	0.544767	-3594.914284
	^{1}TS-6	-3594.025492	0.540371	-3594.883788
	^{1}Int-24	-3594.025560	0.540034	-3594.884551
	^{3}RC-4	-3594.023575	0.541586	-3594.880568
	^{3}TS-6	-3594.022566	0.540960	-3594.879263
	^{3}Int-24	-3594.024153	0.539633	-3594.881441
VO-15	^{1}RC-4	-3798.557377	0.547036	-3799.465193
	^{1}TS-6	-3798.518211	0.542648	-3799.435571
	^{1}Int-24	-3798.518285	0.542338	-3799.435592
	^{3}RC-4	-3798.518119	0.542142	-3799.435239
	^{3}TS-6	-3798.516081	0.543518	-3799.433203
	^{3}Int-24	-3798.516580	0.543951	-3799.434532

Table 3.8. Frontier orbital energy levels of **VO-10-15**.

Catalyst	HOMO-3 [hartree]	HOMO-2 [hartree]	HOMO-1 [hartree]	HOMO [hartree]	LUMO [hartree]
VO-10	-0.25432	-0.25268	-0.23563	-0.21917	-0.12127
VO-11	-0.25432	-0.25260	-0.23576	-0.21908	-0.12096
VO-12	-0.25235	-0.24841	-0.23526	-0.21882	-0.12013
VO-13	-0.26001	-0.25304	-0.24360	-0.21939	-0.12447
VO-14	-0.26390	-0.25696	-0.25356	-0.22048	-0.13147
VO-15	-0.26260	-0.25896	-0.25318	-0.22408	-0.13682

3.8.8 X-Ray Crystallographic Analysis

Single crystals of suitable dimensions of complexes **VO-11** and **VO-13-15** were obtained by slow evaporation from MeOH. The crystals were then mounted on a quartz fiber and the X-Ray intensity data were measured on a Bruker X8 APEX system. Data were processed and corrected for Lorentz and polarization effects with SAINT[35] and for absorption effects with SADABS.[36] Structural solution and refinement were carried out with the SHELXTL suite of programs.[37] The structures were solved by direct method and refined for all data by full-matrix least-squares methods on F^2. All non-hydrogen atoms were subjected to anisotropic refinement. The hydrogen atoms were generated geometrically and allowed to ride on their respective parent atoms; they were assigned appropriate isotopic thermal parameters. Additional crystallographic parameters for each structure are tabulated in the Appendix. Furthermore, the structures can be accessed from the Cambridge Crystallographic Data Center (CCDC) using the following codes: **VO-11** (CCDC 1531640), **VO-13** (CCDC 1531642), **VO-14** (CCDC 1531641), and **VO-15** (CCDC 1531643).

References

1. Cuthbertson, J.; MacMillan, D. W. C. *Nature* **2015**, *519*, 74−77.

2. Zuo, Z.; Ahneman, D. T.; Chu, L.; Terrett, J. A.; Doyle, A. G.; MacMillan, D. W. C. *Science* **2014**, *345*, 437−440.

3. Pirnot, M. T.; Rankic, D. A.; Martin, D. B. C.; MacMillan, D. W. C. *Science* **2013**, *339*, 1593−1596.

4. Devery, J. J., III; Douglas, J.; Nguyen, J.; Cole, K.; Flowers Ii, R.; Stephenson, C. R. J. *Chem. Sci.* **2015**, *6*, 537−541.

5. Furst, L.; Narayanam, J. M.; Stephenson, C. R. *Angew. Chem., Int. Ed.* **2011**, *50*, 9655−9659.

6. Wei, G.; Zhang, C.; Bureš, F.; Ye, X.; Tan, C.-H.; Jiang, Z. *ACS Catal.* **2016**, *6*, 3708−3712.

7. Levin, M.; Kim, S.; Toste, F. D. *ACS Cent. Sci.* **2016**, *2*, 293−301.

8. Amador, A.; Sherbrook, E.; Yoon, T. *J. Am. Chem. Soc.* **2016**, *138*, 4722−4725.

9. Xiao, Q.; Sarina, S.; Bo, A.; Jia, J.; Liu, H.; Arnold, D.; Huang, Y.; Wu, H.; Zhu, H. *ACS Catal.* **2014**, *4*, 1725−1734.

10. Ding, W.; Lu, L. Q.; Liu, J.; Liu, D.; Song, H. T.; Xiao, W. J. *J. Org. Chem.* **2016**, *81*, 7237−7243.

11. Corcoran, E. B.; Pirnot, M. T.; Lin, S.; Dreher, S. D.; DiRocco, D. A.; Davies, I. W.; Buchwald, S. L.; MacMillan, D. W. C. *Science* **2016**, *353*, 279−283.

12. Terrett, J.; Cuthbertson, J.; Shurtleff, V.; MacMillan, D. W. C. *Nature* **2015**, *524*, 330−334.

13. Shaw, M. H.; Shurtleff, V. W.; Terrett, J. A.; Cuthbertson, J. D.; MacMillan, D. W. C. *Science* **2016**, *352*, 1304−1308.

14. Luo, J.; Zhang, J. *ACS Catal.* **2016**, *6*, 873−877.

15. Johnston, C.; Smith, R.; Allmendinger, S.; MacMillan, D. W. C. *Nature* **2016**, *536*, 322−325.

16. Zuo, Z.; Cong, H.; Li, W.; Choi, J.; Fu, G. C.; MacMillan, D. W. C. *J. Am. Chem. Soc.* **2016**, *138*, 1832−1835.

17. Nawrat, C.; Jamison, C.; Slutskyy, Y.; MacMillan, D. W. C.; Overman, L. *J. Am. Chem. Soc.* **2015**, *137*, 11270−11273.

18. Douglas, J.; Sevrin, M.; Stephenson, C. R. J. *Org. Process Res. Dev.* **2016**, *20*, 1134−1147.

19. Lee, S.; Fung, H.; Feng, S.; Chan, K. *Organometallics* **2016**, *35*, 2480−2487.

20. Sun, H.; Yang, C.; Gao, F.; Li, Z.; Xia, W. *Org. Lett.* **2013**, *15*, 624−627.

21. Cai, S.; Zhao, X.; Wang, X.; Liu, Q.; Li, Z.; Wang, D. Z. *Angew. Chem., Int. Ed.* **2012**, *51*, 8050−8053.

22. Das, S. P.; Ganguly, R.; Li, Y.; Soo, H. S. *Dalton Trans.* **2016**, *45*, 13556−13564.

23. Shao, H.; Muduli, S.; Tran, P.; Soo, H. S. *Chem. Commun.* **2016**, *52*, 2948−2951.

24. Gazi, S.; Hung Ng, W.; Ganguly, R.; Putra Moeljadi, A.; Hirao, H.; Soo, H. S. *Chem. Sci.* **2015**, *6*, 7130−7142.

25. Wang, L.; Qin, W.; Tang, X.; Dou, W.; Liu, W. *J. Phys. Chem. A* **2011,** *115*, 1609−1616.

26. Zhang, G.; Scott, B. L.; Wu, R.; Silks, L. A. P.; Hanson, S. K. *Inorg. Chem.* **2012**, *51*, 7354−7361.

27. Sun, S.; Toste, D. *Angew. Chem. Int. Ed*. **2010**, *49*, 3791−3794.

28. Hanson, S. K.; Baker, R. T.; Gordon, J. C.; Scott, B. L.; Sutton, A. D.; Thorn, D. L.; *J. Am. Chem. Soc*. **2009**, *131*, 428−429.

29. *Gaussian 09, Revision D.01*, Frisch, M. J.; Trucks, G. W.; Schlegel, H. B.; Scuseria, G. E.; Robb, M. A.; Cheeseman, J. R.; Scalmani, G.; Barone, V.; Mennucci, B.; Petersson, G. A.; Nakatsuji, H.; Caricato, M.; Li, X.; Hratchian, H. P.; Izmaylov, A. F.; Bloino, J.; Zheng, G.; Sonnenberg, J. L.; Hada, M.; Ehara, M.; Toyota, K.; Fukuda, R.; Hasegawa, J.; Ishida, M.; Nakajima, T.; Honda, Y.; Kitao, O.; Nakai, H.; Vreven, T.; Montgomery, J. A., Jr.; Peralta, J. E.; Ogliaro, F.; Bearpark, M.; Heyd, J. J.; Brothers, E.; Kudin, K. N.; Staroverov, V. N.; Kobayashi, R.; Normand, J.; Raghavachari, K.; Rendell, A.; Burant, J. C.; Iyengar, S. S.; Tomasi, J.; Cossi, M.; Rega, N.; Millam, M. J.; Klene, M.; Knox, J. E.; Cross, J. B.; Bakken, V.; Adamo, C.; Jaramillo, J.; Gomperts, R.; Stratmann, R. E.; Yazyev, O.; Austin, A. J.; Cammi, R.; Pomelli, C.; Ochterski, J. W.; Martin, R. L.; Morokuma, K.; Zakrzewski, V. G.; Voth, G. A.; Salvador, P.; Dannenberg, J. J.; Dapprich, S.; Daniels, A. D.; Farkas, Ö.; Foresman, J. B.; Ortiz, J. V.; Cioslowski, J.; Fox, D. J. Gaussian, Inc., Wallingford CT, 2009.

30. (a) Becke, A. D. *J. Chem. Phys.* **1993**, *98*, 5648−5652. (b) Lee, C.; Yang, W.; Parr, R. G. *Phys. Rev. B* **1988**, *37*, 785−789. (c) Vosko, S. H.; Wilk, L.; Nusair, M. *Can. J. Phys.* **1980**, *58*, 1200−1211.

31. (a) Grimme, S.; Ehrlich, S.; Goerigk, L. *J. Comput. Chem.* **2011**, *32*, 1456−1465. (b) Grimme, S.; Antony, J.; Ehrlich, S.; Krieg, H. *J. Chem. Phys*. **2010**, *132*, 154104−154119. (c) Johnson, E. R.; Becke, A. D. *J. Chem. Phys.* **2006**, *124*,

174104−174109. (d) Becke, A. D.; Johnson, E. R. *J. Chem. Phys.* **2005**, *123*, 154101−154109. (e) Johnson, E. R.; Becke, A. D. *J. Chem. Phys.* **2005**, *123*, 024101−024107.

32. (a) Hehre, W. J.; Radom, L.; Schleyer, P. v. R.; Pople, J. *Ab Initio Molecular Orbital Theory;* Wiley-Interscience: New York, 1986. (b) Clark, T.; Chandrasekhar, J.; Spitznagel, G. W.; Schleyer, P. v. R. *J. Comput. Chem*. **1983**, *4*, 294−301. (c) Krishnan, R.; Binkley, J. S.; Seeger, R.; Pople, J. A. *J. Chem. Phys.* **1980**, *72*, 650−654. (d) Hariharan, P. C.; Pople, J. A. *Theor. Chim. Acta* **1973**, *28*, 213−222.

33. Tomasi, J.; Mennucci, B.; Cammi, R. *Chem. Rev*. **2005**, *105*, 2999−3094.

34. Varetto, U. *Molekel 5.4.0.8;* Swiss National Supercomputing Center: Manno, Switzerland, 2009.

35. SAINT+ version 6.22a; Bruker AXS Inc.: Madison, WI, **2001**.

36. Sheldrick, G. M. SADABS; **1996**.

37. SHELXTL version 5.1; Bruker AXS Inc.: Madison, WI, **1997**.

38. Hatchard, C. G.; Parker, C. A. *Proc. R. Soc., Ser. A* **1956**, *235*, 518−536.

39. Kuhn, H. J.; Braslavsky, S. E.; Schmidt, R. *Pure Appl. Chem.* **2004**, *76*, 2105−2146.

CHAPTER 4

PHOTOREDOX CARBON-CARBON BOND OXYGENATION OF SMALL MOLECULAR ALCOHOLS

PREFACE

The content of this chapter is a part of the manuscript that is currently in preparation. The authors include Gazi, S.; Đokić, M.; Chin, K. F., Ng, P. R.; Soo, H. S. G. S. and S. H. S. conceived the project. Đ. M. performed photocatalytic experiments, and analyzed the data. C. K. F. conducted synthetic procedures for the preparation of non-commercially available substrates. N. P. R. assisted with optimizations of reaction conditions.

4.1 Introduction

Selective, catalytic C-C single bond cleavage is a continuing pursuit in synthetic chemistry due to its potential as a powerful tool in the late-stage functionalization or recycling of intricate small and macromolecules. Some of the challenges include the poor selectivity of C-C bond activation over reactions with other functional groups, the lack of thermodynamically compensating bond formation processes, and the kinetic inertness of the non-polar C-C bond. Therefore, most of the earlier studies on C-C bond activation chemistry have relied on TM catalyzed release of ring strain in small cyclic organic molecules such as cyclopropane, and cyclobutane rings under thermal conditions,[1-12] with only a few recent instances of C-C bond activations in larger, unstrained systems.[13,14] Besides the work of MacMillan and co-workers on tandem C-C bond cleavage and C-C bond formation *via* decarboxylation,[15-17] only a small number of reports have described the incidental C-C activation in reaction intermediates and substrates.[18-20] However, the use of photoredox catalysis in C-C activation of commercial small molecules or especially macromolecules remains scarce.

We have previously demonstrated that our vanadium catalysts are able to induce a highly selective C-C bond cleavage in representative β-O-4-containing lignin model substrates under visible light irradiation and ambient conditions.[21,22] Furthermore, the extensive kinetics and DFT studies helped us reveal the fastest catalyst and have provided us with insights in substrate scope expansion.[22] Here, we draw upon our previous findings to apply our unique chemistry to a broad range of small molecular, commercially available alcohols as suitable substrates. Aided by the results of mechanistic substrate screening, we have been able to expand our research scope to over 20 aliphatic alcohols, some of which containing heteroatoms, fused rings, or distinct steric hindrance. Surprisingly, in some instances, the initially formed oxygenated product would undergo a subsequent C-C bond cleavage *in situ*, indicating possibility of a cascade-type bond cleavage in certain alcohols.

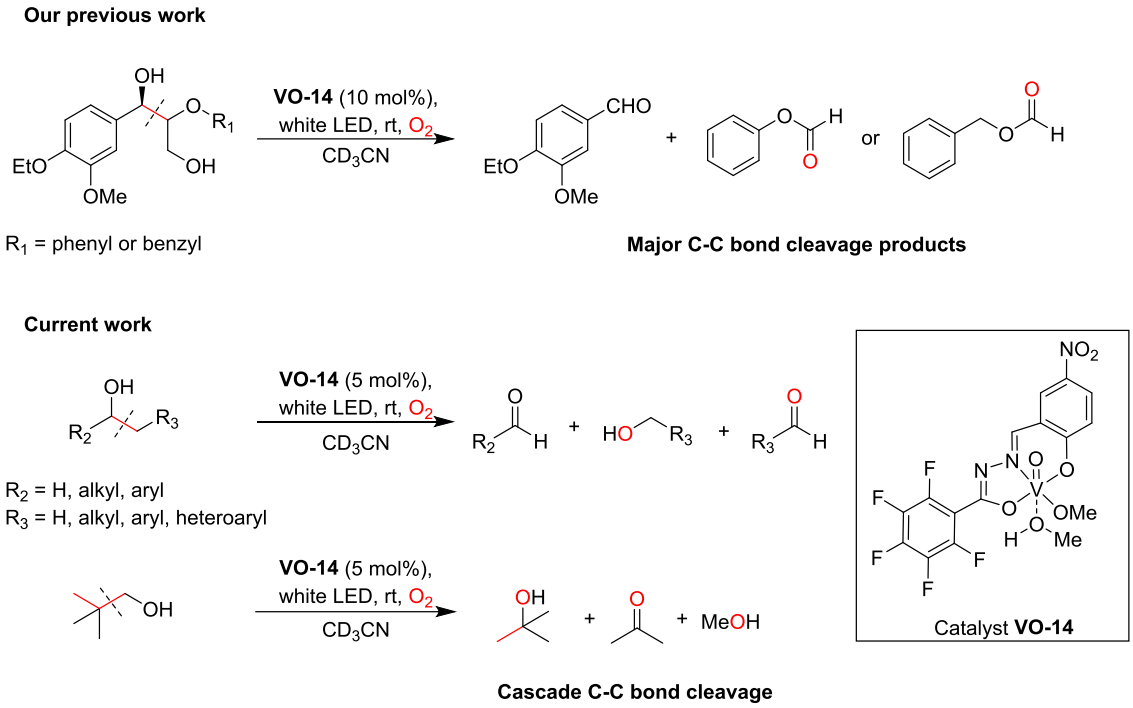

Scheme 4.1. Expanding the substrate scope of photocatalytic C-C bond cleavage beyond *β*-O-4 lignin models to commercially available alcohols.

4.2 Reactivity with Small Aliphatic Alcohols

Guided by the results from our prior work on lignin models **5** and **25**, we hypothesized that alcohol substrates which generate more stabilized radicals (ie, benzyl or tertiary) upon C-C bond cleavage, should react significantly faster than the ones that generate less stable primary or methyl radicals. Our initial substrate screening started with 1-phenylpropan-2-ol (**33**), a commercially available pharmaceutical intermediate and flavor ingredient. Gratifyingly, the substrate readily underwent C-C bond cleavage reaching 89% conversion within six hours in the presence of catalytic amounts of catalyst **VO-14**. The main products of the reaction should be **27** from oxidation by the O_2 in air and acetaldehyde (**34**), which were obtained in moderate yields of 32% and 47%, respectively, as derived from the ^{1}H NMR spectrum of the reaction mixture (Table 4.1, Entry 1). However, the subsequent *in situ* oxidation of benzyl alcohol led to **2** in substantial amounts as well (34%). In addition, a small amount of 1,2-diphenylethane (**35**) arising from the reaction of two benzyl radicals was detected as well.

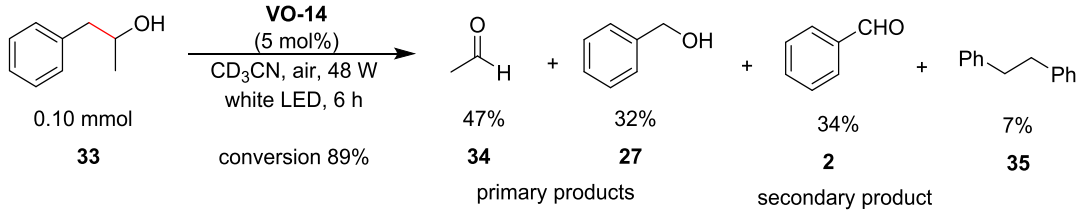

Scheme 4.2. Reactivity and product distribution of **33** with **VO-14**.

To prevent the over-oxidation of **27** and preserve the selectivity of the reaction, a number of hydrogen atom transfer (HAT) agents were examined as possible antioxidants to inhibit reactive oxygen species (ROS) that arose from the use of air. These antioxidants include triphenylmethane, 9,10-dihydroantracene (9,10-DHA), and 1,4-cyclohexadiene (1,4-CHD), and their effects on selectivity are summarized in Table 4.1. (Entries 2-5). It was found that both 9,10-DHA and 1,4-CHD provided the best results in minimizing the over-oxidation of **27**, while maintaining quantitative conversion and respectable primary product yields (Table 4.1, Entries 3 and 5). However, due to its limited solubility in MeCN, 9,10-DHA was replaced with 1,4-CHD as our optimal HAT agent. Moreover, reaction time had to be prolonged from 6 to 14 hours to ensure high conversion while still preserving high selectivity. Additional parameters that we screened include the use of O_2 instead of air, the catalyst loading, and the catalysts in our existing library, which have been summarized in Table 4.1. (Entries 6-13). As established in our prior studies with lignin models, **VO-14** was the fastest catalyst for photocatalytic C-C bond cleavage of **33** as well (Table 4.1, Entries 5, 11-13). Furthermore, **33** prove to be a more suitable substrate allowing us to reduce the catalyst loading from 10 to 5 mol% while still achieving high substrate conversion and product yields under reasonable reaction time (Table 4.1, Entries 5 and 10). In addition, the use of oxygen-containing balloon or open-air environments did not cause a drastic change in conversions and product distributions (Table 4.1, Entries 5 and 6) since in both cases the essential O_2 is present in excessive amounts. Control experiments conducted in the absence of catalyst, light, and air also confirm that each of these is vital. Furthermore, control experiments conducted at 80 °C without catalyst (Table 4.1, Entry 8), and without light (Table 4.1, Entry 7) both showed no significant C-C bond cleavage or alcohol oxidation products. These optimization and control experiments are tabulated in the experimental section.

Table 4.1. Screening of different HAT additives to maximize the primary C-C cleavage products in **33**. The optimized reaction conditions are emboldened. Product yields were determined by ^{1}H NMR spectroscopy with 1,1,2,2-tetrachloroethane as the internal standard.

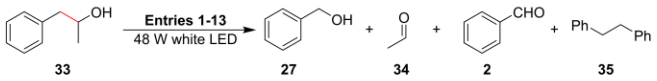

33 **27** **34** **2** **35**

Entry	HAT agents (eq.)	Catalyst (mol % loading)	Environment (air or O_2)	Reaction time (h)	Substrate conversion (%)	Distribution of products (%)			
						27	**34**	**2**	**35**
1	-	**VO-14** (5.0)	air	6	89	32	47	34	7
2	Ph_3CH (1.5)	**VO-14** (5.0)	air	14	71	33	38	10	7
3	9,10-DHA (1. 5)	**VO-14** (5.0)	air	14	>95	58	82	10	6
4	1,4-CHD (1.5)	**VO-14** (5.0)	air	14	>95	56	68	16	6
5	**1,4-CHD (4.0)**	**VO-14 (5.0)**	**air**	**14**	**>95**	**60**	**90**	**11**	**6**
6	1,4-CHD (4.0)	**VO-14** (5.0)	O_2	10	89	53	69	11	6
7	1,4-CHD (4.0)	-	air	14	-	-	-	-	-
8	1,4-CHD (4.0)	**VO-14** (5.0)	O_2	24	-	-	-	-	-
9	1,4-CHD (4.0)	**VO-14** (2.5)	air	14	81	51	64	9	3
10	1,4-CHD (4.0)	**VO-14** (10)	air	14	>95	56	90	10	3
11	1,4-CHD (4.0)	**VO-11** (5.0)	air	14	80	60	62	7	2
12	1,4-CHD (4.0)	**VO-12** (5.0)	air	14	64	44	56	12	2
13	1,4-CHD (4.0)	**VO-15** (5.0)	air	14	>95	55	76	25	3

With the optimized reaction conditions in hand, we proceeded to explore the functional group tolerance and the effects of various substituents on the reactivity and product distribution. For this purpose, we employed a mechanism-based substrate screening method recently reported by Glorius and co-workers.[23] Instead of synthesizing all the derivatives of **33** that contain different functional groups, the corresponding benzene derivative was added to the reaction mixture in stoichiometric amounts. The photocatalyzed C-C bond cleavage reactions proceeded with essentially quantitative conversions and moderate to high yields of the aldehyde and alcohol products in presence of a broad range of substituted benzenes (Figure 4.1.). Electron-donating groups such as methyl and methoxy, and electron-withdrawing functionalities including esters, halogens, nitro, and nitrile were all tolerated, although when benzonitrile and nitrobenzene were introduced (Figure 4.1., Entries 4 and 5), the substrate conversions reached >90% only after longer reaction times of 24 h. Notably, the feasibility of halogenated aromatic compounds offers the opportunity of subsequent functionalization with traditional transition metal-catalyzed coupling chemistry. Even though anilines were found to inhibit the catalyst, with no improvements to the conversions after

prolonged reaction times, the amine could be easily protected by a *tert*-butyloxycarbonyl (Boc) group and the reaction proceeded smoothly (Figure 4.1., Entry 8).

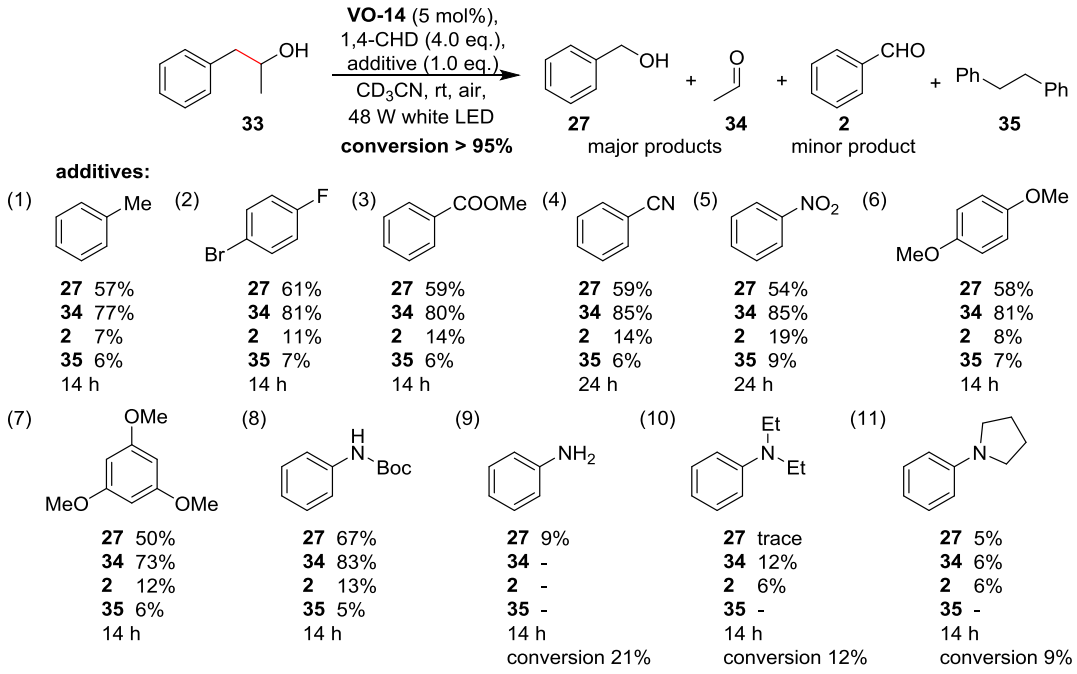

Figure 4.1. Mechanistic screening of substrates proposed by Glorius *et al.*[23] Substituted benzenes (Entries 1-11) displayed different effects on the rate and product distribution of photocatalytic C-C bond cleavage in **33** when added in stoichiometric amounts. Product yields were determined by ^{1}H NMR spectroscopy with 1,1,2,2-tetrachloroethane as the internal standard.

Guided by the insights from the mechanism-based screening, we then examined the reactivity of structural analogs of **33**. We hypothesized that substrates which also generate stabilized benzyl radicals upon C-C bond cleavage should undergo facile photocatalytic reactions. To test this assumption, we prepared substrate **36** (Figure 4.2., Entry 1) and used its derivatives to rapidly expand the substrate library by introducing various functionalities on one of its aryl rings. Gratifyingly, **36** was fully converted into **27** and **2** within 14 h, and the over 100% yield of **2** likely arose from *in situ* over-oxidation of **27**. In additional, as anticipated from the results of the mechanistic screening, electron-withdrawing substituents hindered the reactivity and led to longer reaction times, but quantitative conversion was still achievable (Figure 4.2., substrates **37**-**39**, **43**-**45**). Likewise, substrates with electron-donating methyl and methoxy groups at the *para*, *meta*, and even the sterically demanding *ortho* positions reacted readily to provide moderate to high yields of the expected products under the standard conditions

(Figure 4.2., substrates **40**-**42**). Additionally, all the substrates **36**-**45** yielded small amounts (less than 10%) of **35** arising from the reaction of two benzyl radicals.

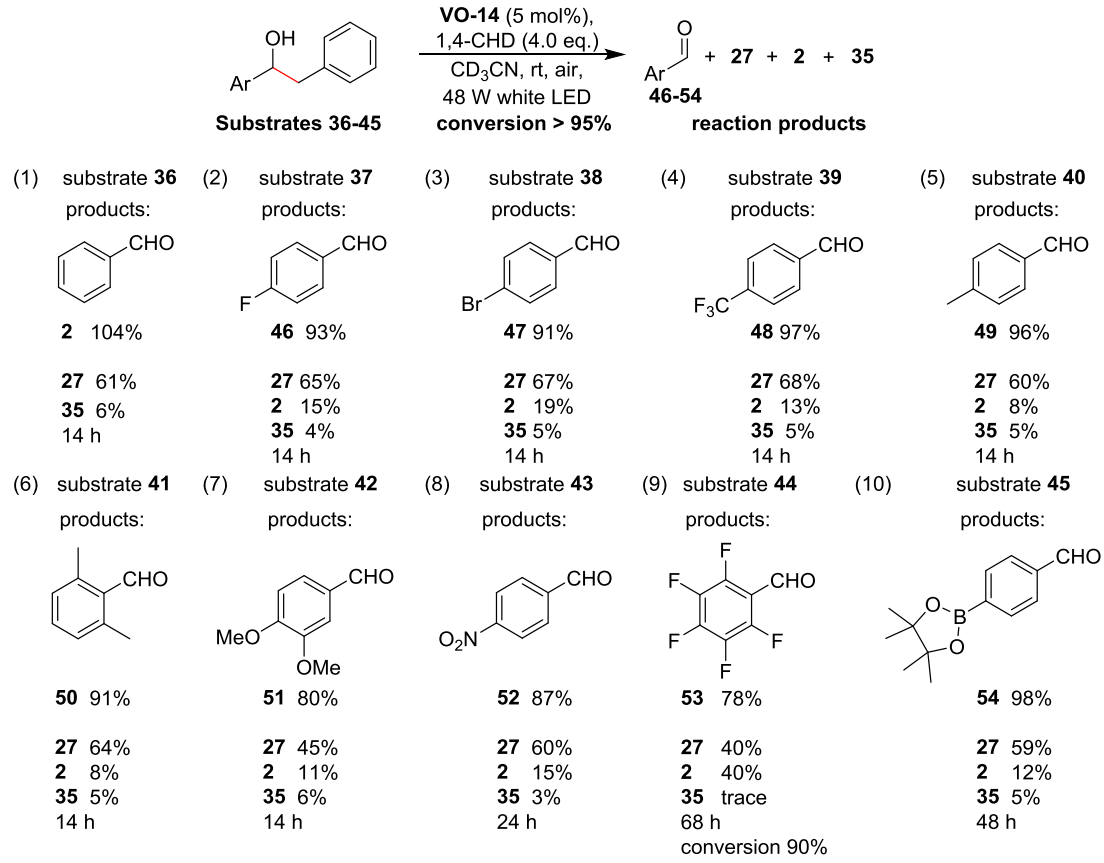

Figure 4.2. Effects of different functional groups on the rate and product distribution of photocatalytic C-C bond cleavage in a modifiable substrate **36** and its structural analogues. Product yields were determined by ^{1}H NMR spectroscopy with 1,1,2,2-tetrachloroethane as the internal standard.

Furthermore, we chose substrates **55** and **56** (a primary, and a tertiary alcohol, respectively), which would likewise generate benzyl radicals, and the reactions achieved high conversions within 14 and 30 h, respectively (Figure 4.3., Entries 1 and 2), despite the steric hindrance expected from the latter. We then proceeded to investigate substrates that incorporated more demanding steric functionalities, heterocycles, and polyaromatics. The reaction with substrates containing mesityl, 2,4,6-triisopropylphenyl, and 4-*tert*-butylphenyl substituents (Figure 4.3., substrates **58**-**60**, respectively) reached full conversion and moderate product yields within 14 h indicating that the steric bulk does not cause significant interference. Primary alcohol substrates with electron-deficient fluoro and electron-donating methoxy groups were suitable as well, confirming that branching on the alcohol carbon was not critical in this reaction

(Fig. 4.3., substrates **57** and **61**). Likewise, the presence of sulfur in 2-(thiophen-3-yl)ethan-1-ol (Figure 4.3., substrate **62**) and fused aryl rings in 2-(naphthalen-1-yl)ethan-1-ol (Figure 4.3., substrate **63**) were well tolerated with high conversions and reasonable yields. In instances of primary alcohol substrates, small amounts of **24** were detected in the ^{1}H NMR spectra of the reaction mixtures (characteristic peak at 9.60 ppm in CD_3CN) and were quantified with respect to the 1,1,2,2-tetrachloroethylene internal standard. The quantified amounts were significantly lower than expected based on high substrate conversions, which could have resulted from most of **24** either polymerizing or precipitating out from the reaction mixtures under our reaction conditions. Given that the major reaction products are known or commercially available compounds, their identities were confirmed by HR-MS and ^{1}H NMR spectroscopy by comparing the positions of characteristic peaks (ppm values) with their literature known values.

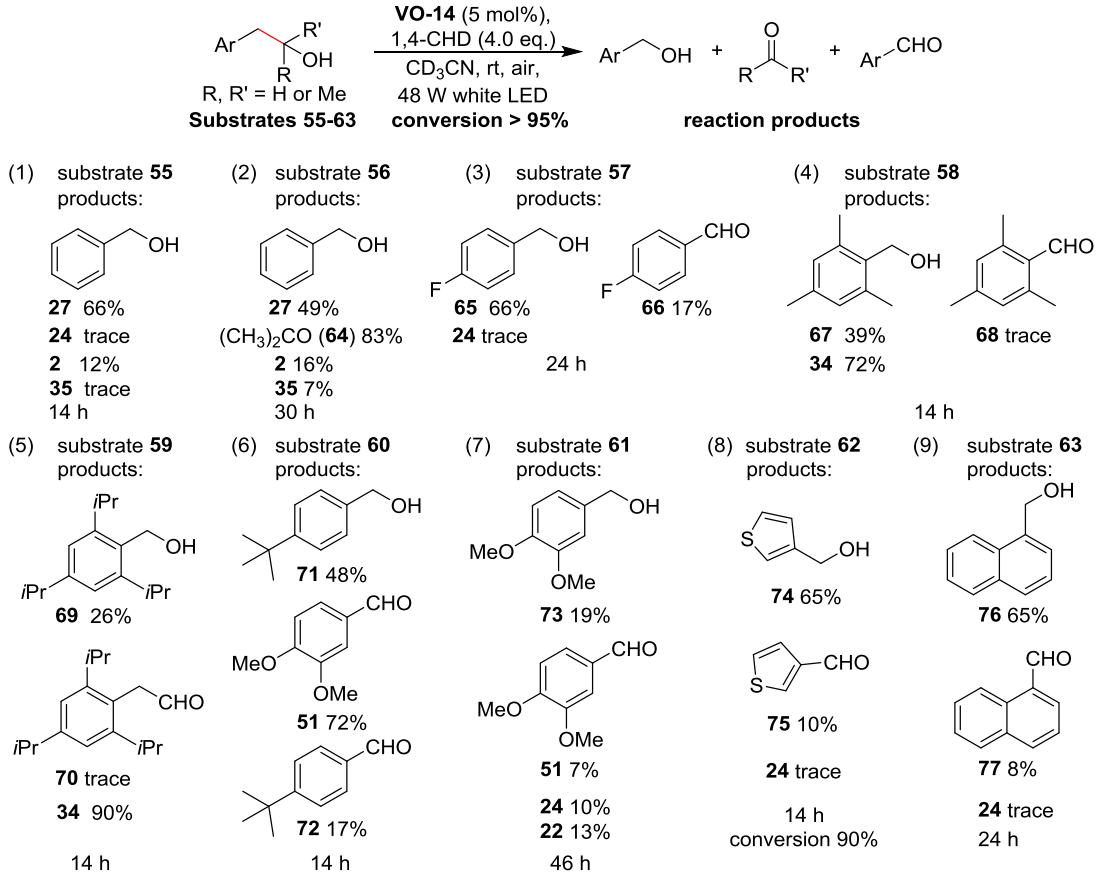

Figure 4.3. Photocatalytic C-C bond cleavage in numerous aliphatic alcohol substrates. Examples include sterically demanding substrates **58**-**60**, as well as the presence of a heteroatom in **62** and fused rings in **63.**

Lastly, apart from the substrates that generate stabilized benzyl radicals upon C-C bond cleavage, we were intent on expanding this unique reaction to readily available,

unactivated, acyclic and aliphatic alcohols that would generate less stable, tertiary, secondary, or even primary radicals. Gratifyingly, substrates that led to these progressively less stable radicals proceeded (Figure 4.4., substrates **78**-**81**), although the reaction times also gradually increased with concomitant reduction in conversion. Note that some of the products from these shorter-chain alcohols, such as propionaldehyde (**87**), acetone (**64**), and methanol are volatile. Under prolonged irradiation with our setup, these compounds would evaporate at room temperature, partly accounting for the diminished yields despite the relatively high conversions. Similarly, as with other substrates, conversions, product yields and identities were determined by the means of ^{1}H NMR spectroscopy. Remarkably, for **81**, we observed that in the absence of the 1,4-CHD antioxidant, one of the primary products, 1-propanol (**88**), appeared to have undergone a subsequent C-C bond cleavage *in situ* to generate ethanol. This surprising cascade C-C bond activation was also apparent in **78**, even in the presence of the HAT agent. The initially formed *tert*-butanol (**84**) underwent a second cleavage to finally yield **64** and methanol. To exclude the possibility of the intermediacy of singlet oxygen ($^1O_2$) generated by energy transfer from **VO-14**, we used the allyl alcohols, **82** and **83** as substrates (Figure 4.4., Entries 5 and 6). Allylic alcohols are known to react with $^1O_2$ to produce hydroperoxides or epoxides *via* ene type reactions.[24] However, in the presence of **VO-14** at low conversions, we detected mainly C-C bond cleavage products, and small amounts of carbonyl products, indicating that $^1O_2$ was unlikely to be the predominant active species.

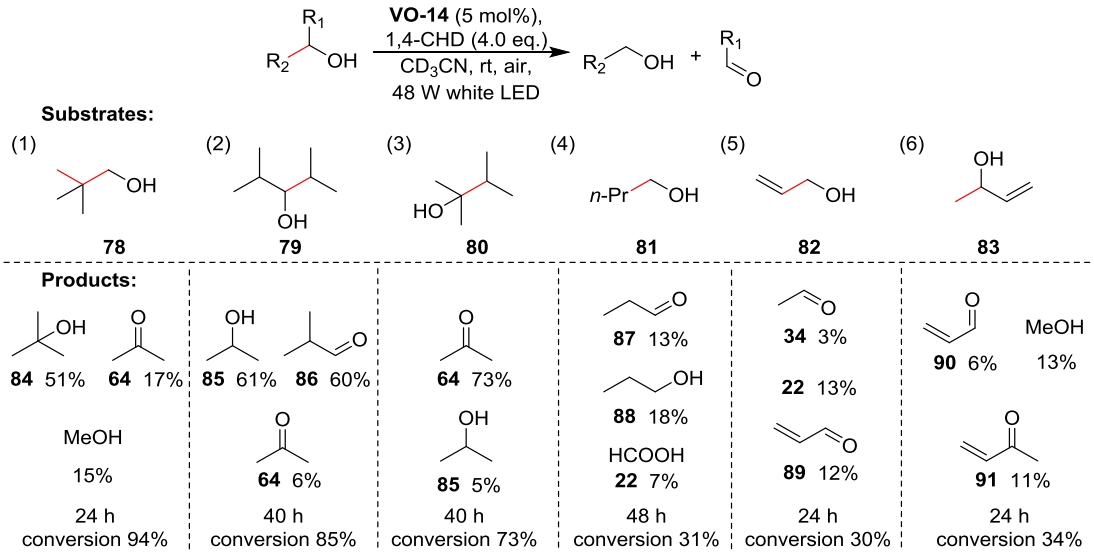

Figure 4.4. Reactivity of simple, commercially available alcohols. Substrates **78** and **81** indicate a possibility for cascade C-C bond cleavage, whereas **82** and **83** suggest the absence of $^1O_2$ related reactions.

4.3 Conclusion

In retrospect, we have been able to extend the scope of our photocatalytic C-C bond cleavage reaction to over 20 aliphatic alcohol substrates other than lignin models. The initial substrate **33** enabled us to optimize the reaction conditions towards the more selective product distribution. We discovered that adding a moderate excess of a HAT agent 1,4-CHD would prevent *in situ* oxidation of **27** to **2**, and thus improve the reaction's selectivity. Subsequently, we utilized the mechanistic screening of substrates, and concluded that the EWG-containing substrates had a detrimental effect on the reaction's rate. Furthermore, free amine groups were found to be incompatible with our catalytic system, but the reactions with carbamate-protected amines proceeded well.

A structural analogue of **33** was then used to rapidly increase the library of substrates and examine the effects of various functionalities on product distribution and reaction's rate. In accordance with the prior mechanistic screening, the electron-deficient substrates slowed down the reaction, although all the reactions proceeded with satisfactory conversions. Finally, we have performed a selective C-C bond cleavage in simple, commercially available tertiary, secondary, and even primary alcohols. Though the reactions were significantly sluggish in case of primary alcohols, the observed second C-C bond cleavage is a remarkable finding that will be explored in future studies

regarding the possibility of a cascade-type C-C bond activation in more specific substrates.

4.4 Experimental Procedures

4.4.1 General Information

The vanadium complexes and ligands were prepared under a N_2 atmosphere using standard Schlenk techniques according to the procedures described in the previous chapter. Other synthetic procedures were conducted under aerobic conditions unless stated otherwise. The chemicals used in the experiments were purchased from Sigma-Aldrich and were used as received. Deuterated solvents were purchased from Cambridge Isotope Laboratories and were used as received. The ^{1}H, ^{13}C, ^{19}F, and ^{11}B NMR spectroscopic data were obtained using Bruker AVANCE spectrometers operating at 300, 400, and 500 MHz. The resulting ^{1}H and ^{13}C NMR chemical shifts (δ reported in ppm) were referenced according to the residual solvent signal(s) ($CDCl_3$ = 7.26 ppm for ^{1}H and 77.2 ppm for ^{13}C; CD_3CN = 1.94 ppm for ^{1}H and 118.3 ppm for ^{13}C; MeOD-d_4 = 3.31 ppm for ^{1}H and 49.2 ppm for ^{13}C; DMSO-d_6 = 2.50 ppm for ^{1}H and 39.52 ppm for ^{13}C). The ^{11}B NMR chemical shifts were referenced relative to BF_3 external standard (δ = 0.0 ppm). High-resolution electrospray ionization mass spectra (HR-ESIMS) were obtained using a Waters Q-TOF Premier mass spectrometer.

4.4.2 Syntheses and Characterizations of Substrates

Synthesis of *tert*-Butylphenyl carbamate (92)

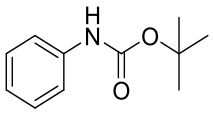

Compound *tert*-butyl phenylcarbamate (*N*-Boc-aniline) (**92**) was prepared in accordance with the reported procedure.[25] To a stirring solution of aniline (0.24 g, 2.5 mmol) in 2.5 mL of water was added di-*tert*-butyl dicarbonate (0.60 g, 2.8 mmol). After stirring for ca. 30 min. at room temperature, white solids started to form. The solids were collected by decanting off the supernatant water, washed with excess of water, and dried under reduced pressure to obtain the desired compound. The yield was 0.44 g of a white solid (95%). ^{1}H NMR (CD_3CN, 400 MHz): δ = 1.49 (s, 9 H), 6.99-7.03 (m, 1 H), 7.25-

7.30 (m, 2 H), 7.40 (dd, J = 0.9, 8.6 Hz, 2 H), 7.48 (bs, 1 H) ppm. $^{13}C\{^{1}H\}$ NMR (CD_3CN, 100 MHz): δ = 28.0, 79.9, 118.9, 123.0, 129.2, 139.7, 153.5 ppm.

General procedure for the synthesis of substrates 36-39, **44**, and **45**

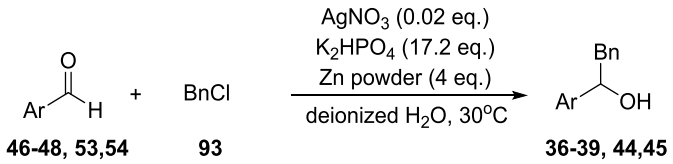

Scheme 4.3. Synthetic pathway for the preparation of substrates **36-39**, **44**, and **45**.

The substrates **36-39**, **44**, and **45** were synthesized by following the adopted general procedure.[26] To a clear solution of $AgNO_3$ (0.020 eq.) and K_2HPO_4 (17.2 eq.) in deionized water at 30 °C, aryl aldehyde (**46-48**, **53**,**54**) (1.0 eq.) and benzyl chloride (**93**) (1.5 eq.) were added together. Under vigorous stirring, zinc powder (4.0 eq.) was added portion-wise over 10 minutes. After the reaction was completed (progress was monitored by TLC), the mixture was acidified with 2.0 M $HCl_{(aq)}$ and extracted with EtOAc thrice. The combined organic layers were washed with brine, dried over anhydrous Na_2SO_4, and concentrated under reduced pressure to obtain the crude product. Subsequent purification was performed by flash column chromatography on silica gel with *n*-hexane and EtOAc as eluents. Yields of the pure products obtained ranged from 45 to 72%.

1,2-Diphenylethan-1-ol (36)

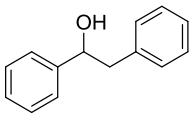

Compound **36** was prepared in accordance with the procedure described above using **2** as precursor. The product was isolated as a white solid (0.287 g, yield 72%). ^{1}H NMR (CD_3CN, 300 MHz): δ = 2.97 (d, J = 6.8 Hz, 2 H), 3.24 (d, J = 4.3 Hz, 1 H), 4.82-4.88 (m, 1 H), 7.16-7.35 (m, 10 H) ppm. $^{13}C\{^{1}H\}$ NMR ($CDCl_3$, 100 MHz): δ = 46.0, 75.3, 125.9, 126.6, 127.6, 128.4, 128.5, 129.5, 138.0, 143.8 ppm. The NMR spectroscopic data match the reported values.[27]

1-(4-Fluorophenyl)-2-phenylethan-1-ol (37)

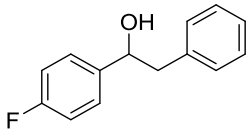

Compound **37** was prepared following the described procedure using 4-fluorobenzaldehyde (**46**) as precursor. The product was isolated as a pale yellow solid (0.248 g, yield 57%). ^{1}H NMR (CD_3CN, 300 MHz): δ = 2.94-2.96 (m, 2 H), 3.30 (d, J = 4.1 Hz, 1 H), 4.85 (dd, J = 6.7, 10.5 Hz, 1 H), 7.01-7.34 (m, 9 H) ppm. ^{13}C{^{1}H} NMR ($CDCl_3$, 100 MHz): δ = 46.2, 74.8, 115.3 (d, J = 21.2 Hz), 126.8, 127.7 (d, J = 8.0 Hz), 128.6, 129.6, 137.8, 139.6 (d, J = 3.0 Hz), 162.3 (d, J = 244 Hz) ppm. ^{19}F{^{1}H} NMR ($CDCl_3$, 376.5 MHz): δ = -115.0 ppm. The NMR spectroscopic data match the reported values.[27]

1-(4-Bromophenyl)-2-phenylethan-1-ol (38)

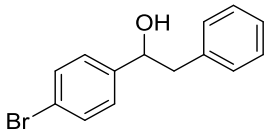

Compound **38** was prepared following the procedure described earlier using 4-bromobenzaldeyhde (**47**) as precursor. The product was isolated as a pale yellow solid (0.395 g, yield 71%). ^{1}H NMR ($CDCl_3$, 300 MHz): δ = 2.24 (s, 1 H), 2.92-3.02 (m, 2 H), 4.83 (t, J = 6.4 Hz, 1 H), 7.16-7.21 (m, 4 H), 7.24-7.36 (m, 3 H), 7.46-7.48 (m, 2 H) ppm. ^{13}C{^{1}H} NMR ($CDCl_3$, 100 MHz): δ = 45.8, 74.5, 121.2, 126.6, 127.6, 128.4, 129.4, 131.3, 137.4, 142.6 ppm. The NMR spectroscopic data match the reported values.[27]

2-Phenyl-1-(4-(trifluoromethyl)phenyl)ethan-1-ol (39)

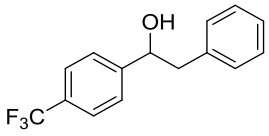

Compound **39** was prepared according to the previously described procedure using 4-(trifluoromethyl)benzaldehyde (**48**) as precursor. The final product was isolated as a white solid (0.354 g, yield 67%). ^{1}H NMR ($CDCl_3$, 400 MHz): δ = 2.97 (d, J = 6.7 Hz, 2 H), 3.45 (d, J = 4.2 Hz, 1 H), 4.95 (m, 1 H), 7.16-7.28 (m, 5 H), 7.49 (d, J = 8.4 Hz, 2 H), 7.62 (d, J = 8.2 Hz, 2 H) ppm. ^{13}C{^{1}H} NMR ($CDCl_3$, 100 MHz): δ = 46.1, 74.2,

122.8, 125.3 (q, J = 3.7 Hz), 126.2, 126.9, 128.6, 129.5, 129.9, 137.3, 147.6 ppm. $^{19}F\{^{1}H\}$ NMR ($CDCl_3$, 376.5 MHz): δ = -62.4 ppm. The NMR spectroscopic data match the reported values.[28]

2-Phenyl-1-(p-tolyl)ethan-1-ol (40)

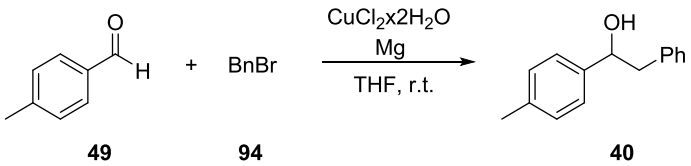

Scheme 4.4. Preparation of substrate **40**.

Compound **40** was prepared by adopting a reported procedure.[29] To a stirring mixture of 4-methylbenzaldehyde (**49**), benzyl bromide (**94**), and $CuCl_2{\cdot}2H_2O$ in tetrahydrofuran (THF) were added Mg turnings. The mixture was stirred at ambient temperature and reaction's progress was monitored by TLC. After the reaction was completed, the reaction mixture was treated successively with 20 mL of H_2O and EtOAc, stirred for 10 minutes more, and then filtered. The filtrate was treated with 50 mL of 2% $HCl_{(aq)}$ to dissolve a small number of suspended particles. The organic layer was separated, and the aqueous layer was extracted with EtOAc thrice (20 mL x 3). The combined organic layers were washed with H_2O, brine, and then dried over anhydrous Na_2SO_4. Removal of the solvent under reduced pressure yielded the crude product. Subsequent purification was performed by flash column chromatography on silica gel using *n*-hexane/EtOAc mixture as eluent. The pure product was isolated as a colorless oil (0.162 g, yield 38%). ^{1}H NMR (CD_3CN, 300 MHz): δ = 2.30 (s, 3 H), 2.94 (d, J = 6.8 Hz, 2 H), 3.17 (d, J = 4.3 Hz, 1 H), 4.80 (m, 1 H), 7.04-7.32 (m, 9 H) ppm. $^{13}C\{^{1}H\}$ NMR ($CDCl_3$, 100 MHz): δ = 21.2, 46.1, 75.3, 126.0, 126.6, 128.6, 129.2, 129.6, 137.3, 138.3, 141.0 ppm. The NMR spectroscopic data match the reported values.[27]

Procedure for the synthesis of substrates 41, **42**, and **60**

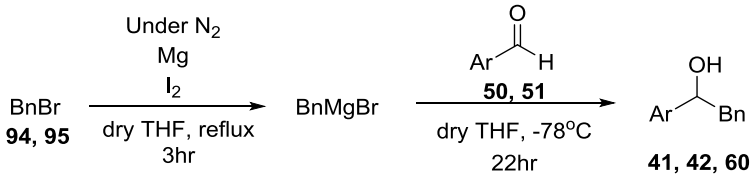

Scheme 4.5. Synthetic route for the preparation of substrates **41**, **42**, and **60**.

Substrates **41**, **42**, and **60** were prepared by using the general procedure. Under a N_2 atmosphere, to an oven-dried two-neck round bottom flask fitted with a reflux condenser, Mg (1.2 eq.) was added, followed by the addition of anhydrous THF and iodine (1-2 crystals). The mixture was stirred at reflux for five minutes and then **94** or 4-*tert*-butylbenzyl bromide (**95**) (1 eq.) was added dropwise. The reaction mixture was warmed up until it began to reflux, and discoloration was observed. The addition of **94** was maintained at that rate. After the complete addition, the reaction was maintained at reflux for three hours. The reaction mixture was subsequently cooled down to room temperature, and then further down to -78 °C using an acetone/dry ice bath. The mixture was then stirred at -78 °C for 10 minutes. Subsequently, the corresponding aryl aldehyde (1.0 eq. diluted with anhydrous THF) was added dropwise into the reaction mixture at -78 °C. After complete addition, the acetone/dry ice bath was removed, and the reaction mixture gradually warmed up to room temperature. The progress of the reaction was monitored by TLC. After the reaction was completed, saturated aqueous NH_4Cl solution was added dropwise into the reaction mixture. The aqueous layer was then extracted with EtOAc thrice. The combined organic layers were washed with brine, dried over anhydrous Na_2SO_4, and concentrated under reduced pressure to yield the crude product. Subsequent purification was performed by flash column chromatography on silica gel with solutions of *n*-hexane and EtOAc as eluents.

1-(2,6-Dimethylphenyl)-2-phenylethan-1-ol (41)

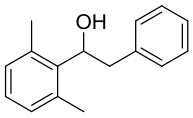

Compound **41** was synthesized by following the procedure described above with **94** and 2,6-dimethylbenzaldehyde (**50**) as precursors. The pure product was isolated as a colorless oil (0.455 g, yield 40%). ^{1}H NMR (CD_3CN, 300 MHz): δ = 2.38 (s, 6 H), 3.00 (dd, *J* = 6.1, 13.3 Hz, 1 H), 3.17 (dd, *J* = 8.7, 12.9 Hz, 2 H), 5.26-5.32 (m, 1 H), 6.95-7.05 (m, 3 H), 7.18-7.28 (m, 5 H) ppm. $^{13}C\{^1H\}$ NMR ($CDCl_3$, 100 MHz): δ = 20.8, 42.2, 72.8, 126.5, 127.1, 128.5, 129.4, 129.5, 136.1, 138.6, 138.7 ppm. HRMS (ESI+, *m/z*) calculated for $C_{16}H_{19}O$ $[M+H]^+$ *m/z* = 227.1436, found 227. 1427.

1-(3,4-Dimethoxyphenyl)-2-phenylethan-1-ol (42)

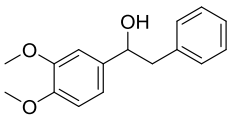

Compound **42** was synthesized by following the procedure described above with **94** and 3,4-dimethoxybenzaldehyde (**51**) as precursors. The product was isolated as a white solid (1.55 g, yield 60%). ^{1}H NMR (CD_3CN, 300 MHz): δ = 2.96 (d, 2 H, J = 5.4 Hz), 3.23 (d, 1 H, J = 4.2 Hz), 3.76 (s, 3 H), 3.77 (s, 3 H), 4.76-4.82 (m, 1 H), 6.83 (s, 2 H), 6.90 (s, 1 H), 7.18-7.28 (m, 5 H) ppm. ^{13}C{1H} NMR (CD_3CN, 75.47 MHz): δ = 46.5, 56.2, 56.3, 75.4, 110.9, 112.2, 119.1, 126.9, 129.0, 130.5, 138.6, 140.1, 149.2, 149.9 ppm. HRMS (ESI+, *m/z*) calculated for $C_{16}H_{19}O_3$ $[M+H]^+$ *m/z* = 259.1334, found 259.1335.

Synthesis of 1-(4-nitrophenyl)-2-phenylethan-1-ol (43)

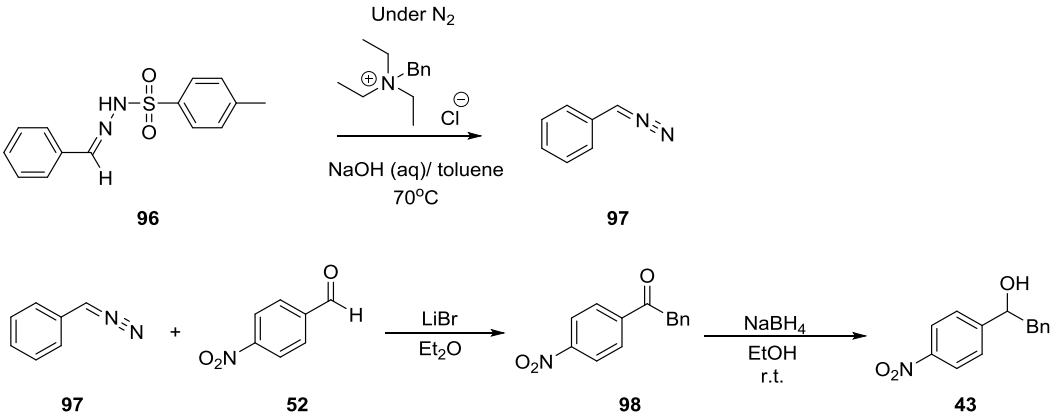

Scheme 4.6. Synthetic steps leading to the formation of substrate **43**.

Compound **21** was prepared according to a reported procedure.[30-32] Precursor compound **96** was prepared in accordance with a reported procedure.[33] Precursor **96** (2.9 mmol, 1.0 eq.) was dissolved in 20 mL toluene and was slowly added to a solution of benzyltriethylammonium chloride (0.44 mmol, 0.15 eq.) in 8.2 mL of aqueous NaOH (14% w/w) under a N_2 atmosphere. The reaction mixture was heated to 70 °C and maintained at that temperature with stirring for two hours. A progressive red coloration of the solution was observed. After cooling the mixture to room temperature, the organic layer was quickly separated from the aqueous layer, washed twice with 10 mL of water, and dried over anhydrous Na_2SO_4. Removal of toluene under reduced pressure yielded intermediate **97**, which was used in the next step without further purification.

To a stirred mixture of **52** (2.92 mmol, 1.0 eq.) and LiBr (29.2 mmol, 10 eq.) in 20 mL of Et_2O cooled in an ice-salt bath (-5 °C) was added a diluted solution of **97** (2.92 mmol, 1.0 eq.) in 20 mL toluene through a dropping funnel (note: the reaction flask was protected from light with Al-foil). The mixture was slowly warmed up to room temperature and stirred overnight. Subsequently, deionized water was added, and the organic layer was separated and dried over anhydrous $MgSO_4$. The solvent was then removed under reduced pressure, yielding the crude product. Purification of the crude product was performed by flash column chromatography on silica gel using 6:1 *n*-hexane/EtOAc as eluent to afford **98** as colorless oil (0.32 g, 45% yield).

To a solution of **98** (1.3 mmol) in EtOH (6 mL) was slowly added $NaBH_4$ (2.6 mmol, 2.0 eq.). The resulting clear solution was stirred at room temperature and monitored by TLC. After the reaction was completed, saturated aqueous NH_4Cl was added dropwise into the reaction mixture. The aqueous layer was then extracted with EtOAc thrice. The combined organic layers were washed with brine and concentrated under reduced pressure to yield the crude product. Purification of the crude material was performed by flash column chromatography on silica gel using 6:1 *n*-hexane/EtOAc as eluent to afford **43** as a white solid (0.31 g, 97% yield). ^{1}H NMR (CD_3CN, 300 MHz): δ = 2.98 (d, J = 6.8 Hz, 2 H), 3.55 (d, J = 4.2 Hz, 1 H), 5.00 (m, 1 H), 7.15-7.28 (m, 5 H), 7.52 (d, J = 8.5 Hz, 2 H), 8.13-8.16 (m, 2 H) ppm. ^{13}C{^{1}H} NMR ($CDCl_3$, 100 MHz): δ = 46.0, 74.3, 123.6, 126.6, 127.0, 128.7, 129.5, 136.7, 147.3, 150.9 ppm. The NMR spectroscopic data match the reported values.[34]

1-(Perfluorophenyl)-2-phenylethan-1-ol (44)

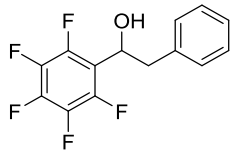

Compound **44** was prepared following the described procedure using 2,3,4,5,6-pentafluorobenzaldehyde (**53**) as precursor. The product was isolated as a white solid (0.342 g, yield 59%).^{1}H NMR (CD_3CN, 300 MHz): δ = 3.08 (dd, J = 7.7, 13.3 Hz, 1 H), 3.28 (dd, J = 7.4, 13.3 Hz, 1 H), 3.84 (d, J = 5.4 Hz, 1 H), 5.22 (dd, J = 7.4, 12.7 Hz, 1 H), 7.15-7.28 (m, 5 H) ppm. ^{13}C{^{1}H} NMR ($CDCl_3$, 100 MHz): δ = 43.1, 67.4, 116.2 (t, J = 13.2 Hz), 127.2, 128.8, 129.1, 136.3, 138.7 (m), 139.3 (m), 141.7 (m), 143.5 (m),

146.0 (m) ppm. $^{19}F\{^{1}H\}$ (CD_3CN, 282.4 MHz): δ = -165.1-(-164.9) (m, 2 F), -158.3 (tt, J = 1.0, 20.1 Hz, 1 F) -144.7-(-144.6) (m, 2 F) ppm. The NMR spectroscopic data match the reported values.[35]

2-Phenyl-1-(4-(4,4,5,5-tetramethyl-1,3,2-dioxaborolan-2-yl)phenyl)ethan-1-ol (45)

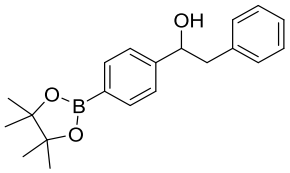

Compound **45** was prepared according to the procedure described above by using 4-(4,4,5,5-tetramethyl-1,3,2-dioxaborolan-2-yl)benzaldehyde (**54**) as precursor. The product was isolated as a white solid (0.147 g, yield 45%). ^{1}H NMR (CD_3CN, 300 MHz): δ = 1.32 (s, 12 H), 2.95 (d, J = 6.7 Hz, 2 H), 3.30 (d, J = 4.3 Hz, 1 H), 4.86 (m, 1 H), 7.15-7.25 (m, 5 H), 7.33 (d, J = 7.8 Hz, 2 H), 7.65 (d, J = 7.8 Hz, 2 H) ppm. $^{13}C\{^{1}H\}$ NMR (CD_3CN, 100 MHz): δ = 24.8, 46.0, 75.3, 83.8, 125.2, 126.6, 128.5, 129.5, 134.9, 137.9, 146.9 ppm. ^{11}B NMR (CD_3CN, 128 MHz): δ = 36.2 ppm. HRMS (ESI+, *m/z*) calculated for $C_{20}H_{26}BO_3$ $[M+H]^+$ *m/z* = 325.1975, found 325. 1973.

Synthesis of substrates 58 and 59

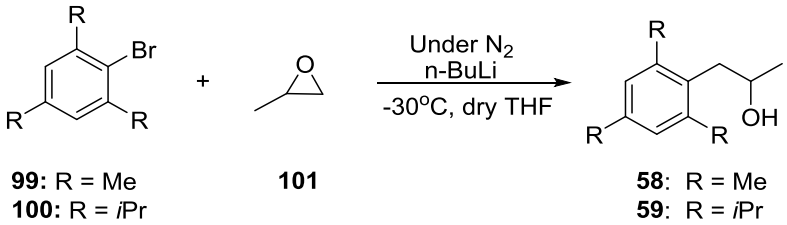

Scheme 4.7. Procedure for the preparation of substrates **58** and **59**.

Compounds 1-mesitylpropan-2-ol (**58**) and 1-(2,4,6-triisopropylphenyl)propan-2-ol (**59**) were prepared by adapting a reported procedure.[36] To a stirred solution of 2-bromo-1,3,5-trimethylbenzene (**99**) or 2-bromo-1,3,5-triisopropylbenzene (**100**) (2.0 mmol) in anhydrous THF (10 mL) at -30 °C was added *n*-butyllithium (2.2 mmol). The solution was stirred for 30 min at -30 °C, and then propylene oxide (**101**) (2.0 mmol) was added. The solution was then allowed to warm up to room temperature and was stirred for an additional hour. The reaction was subsequently quenched by the addition of saturated NH_4Cl (10 mL), and then diethyl ether (30 mL) was added. The combined organic layers

were washed with water and dried with anhydrous $MgSO_4$. Finally, the solvent was removed under reduced pressure to yield crude products, which were purified by flash column chromatography on silica (eluent: petroleum ether/EtOAc 2:1) to give rise to the pure **58** or **59** (yields 55 and 75%, respectively).

1-Mesitylpropan-2-ol (58)

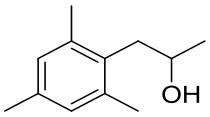

Compound **58** was prepared by following the procedure described above with **99** as a precursor. After the purification, **58** was isolated as a colorless liquid (0.195 g, yield 55%). ^{1}H NMR ($CDCl_3$, 300 MHz): δ = 1.30 (d, J = 6.3 Hz, 3 H), 1.60 (s, 1 H), 2.27 (s, 3 H), 2.33 (s, 6 H), 2.72-2.88 (m, 2 H), 4.01-4.07 (m, 1 H), 6.87 (s, 2 H) ppm. ^{13}C{^{1}H} NMR ($CDCl_3$, 75.47 MHz): δ = 20.4, 20.7, 23.2, 38.7, 67.8, 129.1, 132.3, 135.6, 137.0 ppm. HRMS (ESI+, *m/z*) calculated for $C_{12}H_{19}O$ $[M+H]^+$ *m/z* = 179.1436, found 179. 1435.

1-(2,4,6-Triisopropylphenyl)propan-2-ol (59)

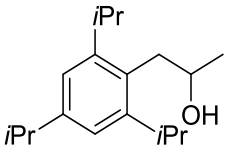

Compound **59** was prepared by following the procedure described above with **100** as a precursor. After the purification, **59** was isolated as a colorless oil (0.391 g, yield 75%). ^{1}H NMR ($CDCl_3$, 500 MHz): δ = 1.20-1.29 (m, 18 H), 1.33 (d, J = 6.1 Hz, 3 H), 1.59 (s, 1 H), 2.83-2.93 (m, 3 H), 3.27-3.32 (m, 2 H), 3.95-3.99 (m, 1 H), 7.02 (s, 2 H) ppm. ^{13}C{^{1}H} NMR ($CDCl_3$, 126 MHz): δ = 23.0, 23.9, 24.0, 24.2, 24.4, 29.3, 34.1, 36.6, 69.1, 121.1, 129.1, 146.9, 147.7 ppm. HRMS (ESI+, *m/z*) calculated for $C_{18}H_{31}O$ $[M+H]^+$ *m/z* = 263.2375, found 263. 2367.

2-(4-(*Tert*-butyl)phenyl)-1-(3,4-dimethoxyphenyl)ethan-1-ol (60)

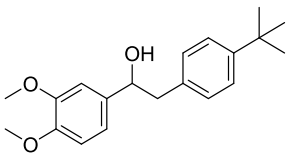

Compound **60** was synthesized by following the procedure described above with **95** and **51** as precursors. The product was isolated as a pale yellow solid (1.55 g, yield 55%). ^{1}H NMR (CD_3CN, 300 MHz): δ = 1.29 (s, 9 H), 2.92 (d, J = 6.6 Hz, 2 H), 3.74 (s, 3 H), 3.77 (s, 3 H), 4.77 (t, 1 H, J = 6.6 Hz), 6.86 (s, 3 H), 7.11 (d, J = 8.1 Hz, 2 H,, 7.30 (d, J = 8.1 Hz, 2 H) ppm. ^{13}C{1H} NMR (CD_3CN, 75.47 MHz): δ = 31.6, 34.9, 45.9, 56.2, 56.3, 75.4, 110.9, 112.3, 119.0, 125.9, 130.2, 137.1, 138.8 149.2, 149.7, 149.8 ppm. HRMS (ESI+, *m/z*) calculated for $C_{20}H_{27}O_3$ $[M+H]^+$ *m/z* = 315.1960, found 315.1963.

4.4.3 Optimization of Photoreaction Conditions

Examining the effects of the atmospheric and oxygen environments on the reaction

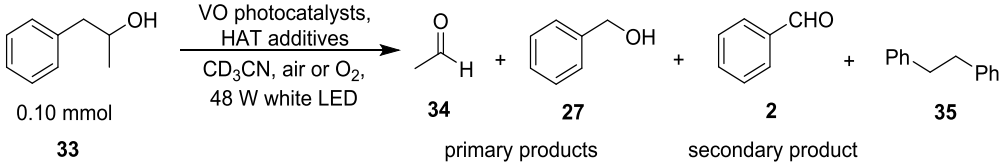

Scheme 4.8. Exemplary substrate used for optimizing various reaction conditions.

The photocatalytic experiments were carried out in NMR tubes. In a typical procedure, **33** (0.10 mmol, 14 μL), **VO-14** (5.0 μmol, 2.4 mg), and 1,4-CHD (0.40 mmol, 40 μL) were dissolved in CD_3CN (0.50 mL), and 1,1,2,2-tetrachloroethane (0.10 mmol, 10.6 μL) was added as an internal standard to aid calculations of the conversion and yield of the products. The NMR tube was fitted with a needle to supply air or oxygen gas from a balloon into the reaction vessel throughout the experiment. The reaction mixture was irradiated with white LEDs (48 W) at ambient temperatures. A continuous water circulator was used to maintain the reaction temperatures below 30 °C. The NMR tube containing the reaction mixture was monitored at specific time intervals by ^{1}H NMR spectroscopy before and after irradiation, to follow the progress of the reaction. The reaction products were identified by ^{1}H NMR spectroscopy by comparing the peaks from the reaction mixture's ^{1}H NMR spectrum to those of the commercially available compounds, where available. The results are summarized in the table below.

Table 4 2. Effects of air and oxygen environments on substrate conversion and product distribution. The optimal conditions are emboldened.

Entry	Reaction time (h)	Catalyst (mol%)	Environment	Substrate conversion (%)	Distribution of products (%)			
					34	**27**	**2**	**35**
1	4	**VO-14** (5)	air	59	46	33	2	4
2	8	**VO-14** (5)	air	84	65	50	8	4
3	10	**VO-14** (5)	air	92	68	54	10	4
4	**14**	**VO-14 (5)**	**air**	**>95**	**90**	**60**	**11**	**6**
5	4	**VO-14** (5)	O_2	63	55	40	4	4
6	8	**VO-14** (5)	O_2	81	64	51	8	5
7	10	**VO-14** (5)	O_2	89	69	53	11	5
8[a]	24	**VO-14** (5)	O_2	10	-	-	-	-

[a] Reaction was conducted at 80 °C in the absence of light.

Varying the catalyst loading

Photocatalytic experiments were carried out in NMR tubes. In an exemplary experiment, **33** (0.10 mmol, 14 μL), **VO-14** (0-15.0 μmol, 0-7.2 mg), and 1,4-CHD (0.40 mmol, 40 μL) were dissolved in CD_3CN (0.50 mL), and 1,1,2,2-tetrachloroethane (0.10 mmol, 10.6 μL) was added as an internal standard to calculate the conversion and yield of the products. The NMR tube was fitted with a needle to supply air into the reaction vessel throughout the experiment, while minimizing evaporation of the solvent. The reaction mixture was irradiated with white LEDs (48 W) at ambient temperatures. A continuous water circulator was used to maintain the reaction temperatures below 30 °C. The NMR tube containing the reaction mixture was used in the NMR spectroscopic experiments before and after 14 h of irradiation to allow us to monitor the progress of the reaction. The reaction products were identified by ^{1}H NMR spectroscopy by comparing the peaks from the reaction mixture's ^{1}H NMR spectrum to those of the commercially available compounds. The results are summarized in the table below.

Table 4.3. Effects of various catalyst loadings on substrate conversion and product distribution. The optimal conditions are emboldened.

Entry	Reaction time (h)	Catalyst (mol%)	Substrate conversion (%)	Distribution of products (%)			
				34	**27**	**2**	**35**
1	14	**VO-14** (0.0)	-	-	-	-	-
2[a]	24	**VO-14** (0.0)	-	-	-	-	-
3	14	**VO-14** (2.5)	81	64	51	9	3
4	**14**	**VO-14 (5.0)**	**>95**	**90**	**60**	**11**	**6**
5	14	**VO-14** (10)	>95	90	56	10	3
6	14	**VO-14** (15)	>95	91	54	14	5

[a] Reaction was conducted at 80 °C.

Screening of vanadium catalysts

Photocatalytic experiments were carried out in NMR tubes. In a typical experiment, **33** (0.10 mmol, 14 μL), the vanadium catalyst (**VO-10-15**, 5.0 μmol, 1.7-2.6 mg), and 1,4-CHD (0.40 mmol, 40 μL) were dissolved in CD_3CN (0.50 mL), and 1,1,2,2-tetrachloroethane (0.10 mmol, 10.6 μL) was added as an internal standard to calculate the conversion and yield of the products. The NMR tube was fitted with a needle to supply air into the reaction vessel throughout the experiment. The reaction mixture was irradiated with white LEDs (48 W) at ambient temperatures. A continuous water circulator was used to maintain the reaction temperatures below 30 °C. The NMR tube containing the reaction mixture was used in the NMR spectroscopic experiments before and after 14 h of light irradiation to allow us to monitor the progress of the reaction. The reaction products were identified by ^{1}H NMR spectroscopy by comparing the peaks from the reaction mixture's ^{1}H NMR spectrum to those of the commercially available compounds. The results are summarized in the table below.

Table 4.4. Effects of different catalysts on substrate conversion and product distribution. The optimal conditions are emboldened.

Entry	Reaction time (h)	Catalyst (mol%)	Substrate conversion (%)	Distribution of products (%)			
				34	**27**	**2**	**35**
1	14	**VO-10** (5.0)	85	70	63	8	4
2	14	**VO-11** (5.0)	80	62	60	7	2
3	14	**VO-12** (5.0)	64	56	44	12	2
4	14	**VO-13** (5.0)	93	74	63	10	4
5	**14**	**VO-14 (5.0)**	**>95**	**90**	**60**	**11**	**6**
6	14	**VO-15** (5.0)	>95	76	55	25	3

4.4.4 Identification of reaction products

Products of the photocatalytic C-C bond cleavage reactions are known compounds, and their identities have been confirmed by ^{1}H NMR spectroscopy and HR-MS. The characteristic ^{1}H NMR signals of the products have been compared with those of the commercially available compounds to confirm their identities. The HR-MS values are summarized below.

4-Fluorobenzaldehyde (46)

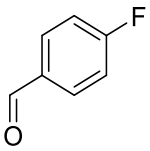

HRMS (ESI+, *m/z*) calculated for C_7H_6FO $[M+H]^+$ *m/z* = 125.0403, found 125.0405.

4-Bromobenzaldehyde (47)

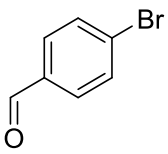

HRMS (ESI+, *m/z*) calculated for C_7H_6BrO $[M+H]^+$ *m/z* = 184.9602, found 184.9598.

4-(Trifluoromethyl)benzaldehyde (48)

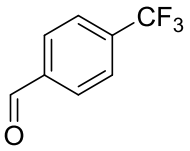

HRMS (ESI+, *m/z*) calculated for $C_8H_6F_3O$ $[M+H]^+$ *m/z* = 175.0371, found 175.0374.

4-Methylbenzaldehyde (49)

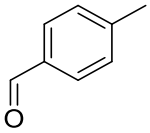

HRMS (ESI+, *m/z*) calculated for C_8H_9O $[M+H]^+$ *m/z* = 121.0653, found 121.0654.

2,6-Dimethylbenzaldehyde (50)

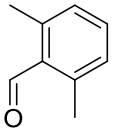

HRMS (ESI+, *m/z*) calculated for $C_9H_{11}O$ $[M+H]^+$ *m/z* = 135.0810, found 135.0813.

3,4-Dimethoxybenzaldehyde (51)

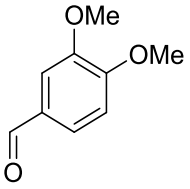

HMRS (ESI+, *m/z*) calculated for $C_9H_{11}O_3$ $[M+H]^+$ *m/z* = 167.0708, found 167.0713.

4-Nitrobenzaldehyde (52)

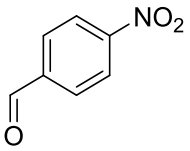

HRMS (ESI+, *m/z*) calculated for $C_7H_6NO_3$ $[M+H]^+$ *m/z* = 152.0348, found 152.0349.

2,3,4,5,6-Pentafluorobenzaldehyde (53)

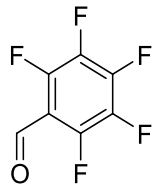

HRMS (ESI+, *m/z*) calculated for $C_7H_2F_5O$ $[M+H]^+$ *m/z* = 197.0026, found 197.0027.

4-(4,4,5,5-Tetramethyl-1,3,2-dioxaborolan-2-yl)benzaldehyde (54)

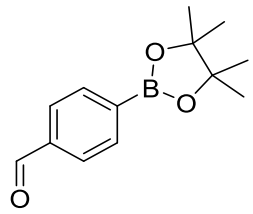

HRMS (ESI+, *m/z*) calculated for $C_{13}H_{18}O_3B$ $[M+H]^+$ *m/z* = 233.1349, found 233.1358.

Mesitylmethanol (67)

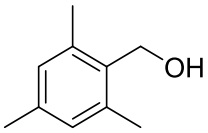

HMRS (ESI+, *m/z*) calculated for $C_{10}H_{15}O$ $[M+H]^+$ *m/z* = 151.1123, found 151.1125.

2,4,6-Trimethylbenzaldehyde (68)

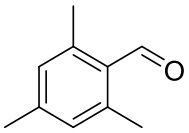

HRMS (ESI+, *m/z*) calculated for $C_{10}H_{13}O$ $[M+H]^+$ *m/z* = 149.0966, found 149.0972.

(2,4,6-Triisopropylphenyl)methanol (69)

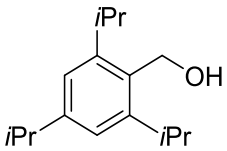

HMRS (ESI+, *m/z*) calculated for $C_{16}H_{27}O$ $[M+H]^+$ *m/z* = 235.2062, found 235.2057.

2,4,6-Triisopropylbenzaldehyde (70)

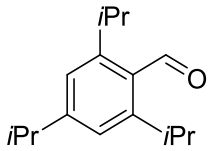

HMRS (ESI+, *m/z*) calculated for $C_{16}H_{25}O$ $[M+H]^+$ *m/z* = 233.1905, found 233.1904.

(4-(*Tert*-butyl)phenyl)methanol (71)

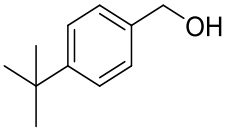

HRMS (ESI+, *m/z*) calculated for $C_{11}H_{17}O$ $[M+H]^+$ *m/z* = 165.1279, found 165.1274.

4-(*Tert*-butyl)benzaldehyde (72)

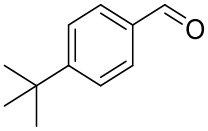

HRMS (ESI+, *m/z*) calculated for $C_{11}H_{15}O$ $[M+H]^+$ *m/z* = 163.1123, found 163.1127.

(3,4-Dimethoxyphenyl)methanol (73)

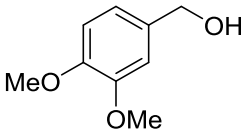

HRMS (ESI+, *m/z*) calculated for $C_9H_{13}O_3$ $[M+H]^+$ *m/z* = 169.0865, found 169.0866.

Tiophen-3-ylmethanol (74)

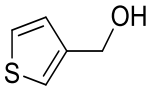

HRMS (ESI+, *m/z*) calculated for C_5H_7OS $[M+H]+$ *m/z* = 115.0218, found 115.0224.

Tiophene-3-carbaldehyde (75)

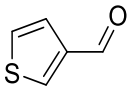

HRMS (ESI+, *m/z*) calculated for C_5H_5OS $[M+H]^+$ *m/z* = 113.0061, found 113.0059.

Naphtalen-1-ylmethanol (76)

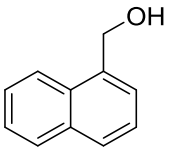

HRMS (ESI+, *m/z*) calculated for $C_{11}H_{11}O$ $[M+H]^+$ *m/z* = 159.0810, found 159.0814.

1-Naphtaldehyde (77)

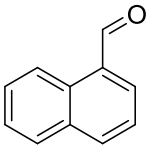

HRMS (ESI+, *m/z*) calculated for $C_{11}H_9O$ $[M+H]^+$ *m/z* = 157.0653, found 157.0654.

References

1. Chen, P. H.; Billett, B. A.; Tsukamoto, T.; Dong, G. *ACS Catal*. **2017**, *7*, 1340−1360.

2. Noyori, R.; Kumagai, Y.; Umeda, I.; Takaya, H. *J. Am. Chem. Soc*. **1972**, *94*, 4018−4020.

3. Trost, B. M.; Chan, D. M. T. *J. Am. Chem. Soc*. **1983**, *105*, 2315−2325.

4. Ogoshi, S.; Nagata, M.; Kurosawa, H. *J. Am. Chem. Soc*. **2006**, *128*, 5350−5351.

5. Shaw, M. H.; McCreanor, N. G.; Whittingham, W. G.; Bower, J. F. *J. Am. Chem. Soc*. **2015**, *137*, 463−468.

6. Bart, S. C.; Chirik, P. *J. Am. Chem. Soc*. **2003**, *125*, 886–887.

7. Murakami, M.; Itahashi, T.; Ito, Y. *J. Am. Chem. Soc*. **2002**, *124*, 13976−13977.

8. Zhou, X.; Dong, G. *J. Am. Chem. Soc*. **2015**, *137*, 13715−13721.

9. Edelbach, B. L.; Lachicotte, R. J.; Jones, W. D. *Organometallics* **1999**, *18*, 4040−4049.

10. Wang, J.; Zheng, N. *Angew. Chem. Int. Ed*. **2015**, *54*, 1–5.

11. Maity, S.; Zhu, M.; Shinabery, R. S.; Zheng, N. *Angew. Chem.Int. Ed*. **2012**, *51*, 222–226.

12. Yayla, H. G.; Wang, H.; Tarantino, K. T.; Orbe, H. S.; Knowles, R. R. *J. Am. Chem. Soc.* **2016**, *138*, 10794−10797.

13. Guo, J. J.; Hu, A.; Chen, Y.; Sun, J.; Tang, H.; Zuo, Z.; *Angew. Chem. Int. Ed*. **2016**, *55*, 1–5.

14. Wang, D.; Mao, J.; Zhu, C. *Chem. Sci*. **2018**, *9*, 5805–5809.

15. Corcoran, E. B.; Pirnot, M. T.; Lin, S.; Dreher, S. D.; DiRocco, D. A.; Davies, I. W.; Buchwald, S. L.; MacMillan, D. W. C. *Science* **2016**, *353*, 279−283.

16. Terrett, J.; Cuthbertson, J.; Shurtleff, V.; MacMillan, D. W. C. *Nature* **2015**, *524*, 330−334.

17. Shaw, M. H.; Shurtleff, V. W.; Terrett, J. A.; Cuthbertson, J. D.; MacMillan, D. W. C. *Science* **2016**, *352*, 1304−1308.

18. Zhu, S.; Das, A.; Bui, L.; Zhou, H.; Curran, D. P.; Rueping, M. *J. Am. Chem. Soc.* **2013**, *135*, 1823–1829.

19. Nakajima, K.; Nojima, S.; Nishibayashi, Y. *Angew. Chem. Int. Ed*. **2016**, *55*, 14106–14110.

20. Xia, Y.; Lu, G.; Liu, P.; Dong, G. *Nature* **2016**, *539*, 546–550.

21. Gazi, S.; Hung Ng, W.; Ganguly, R.; Putra Moeljadi, A.; Hirao, H.; Soo, H. S. *Chem. Sci*. **2015**, *6*, 7130−7142.

22. Gazi, S.; Đokić, M.; Moeljadi, A. M. P.; Ganguly, R.; Hirao, H.; Soo, H. S. *ACS Catal*. **2017**, *7*, 4682−4691.

23. Hopkinson, M. N.; Gomez-Suarez, A.; Teders, M.; Sahoo, B.; Glorius, F. *Angew. Chem. Int. Ed*. **2016**, *55*, 4361−4366.

24. Clennan, E. L.; Zhang, D.; Singleton, J. *Photochem. Photobiol*. **2006**, *82*, 1226−1232.

25. Chankeshwara, S. V.; Chakraborti, A. K. *Org. Lett*. **2006**, *8*, 3259−3262.

26. Bieber, L. W., Storch, E. C., Malvestiti, I., da Silva, M. F. *Tetrahedron Lett*. **1998**, *39*, 9393−9396.

27. Su, Y., Sun, X., Wu, D., Jiao, N. *Angew. Chem. Int. Ed*. **2013**, *52*, 9808− 9812.

28. Lovinger, G., J., Aparece, M. D., Morken, J. P. *J. Am. Chem. Soc*. **2017**, *139*, 3153−3160.

29. Chattopadhyay, A., Dubey, A., Goswami D. *Arkivoc* **2010**, 137−145.

30. Rasolofonjatovo, E., Treguier, B., Provot, O., Hamze, A., Morvan, E., Brion, J. D., Alami, M. *Tetrahedron Lett*. **2011**, *52*, 1136−1140.

31. Loeschorn, C. A., Nakajima, M., McCloskey, P. J., Anselme, J. P. *J. Org. Chem*. **1983**, *48*, 4407−4410.

32. Easton, C.J., Ivory, A. J., Smith, C. A. *J. Chem. Soc., Perkin Trans. 2*, **1997**, *0*, 503−508.

33. Crespin, L., Biancalana, L., Morack, T., Blakemore, D. C., Ley, S. V. *Org. Lett*. **2017**, *19*, 1084−1087.

34. Noyce, D. S., Hartter, D. R., Miles, F. B. *J. Am. Chem. Soc*. **1968**, *90*, 3794−3796.

35. Terent'ev, A. B., Vasil'eva, T. T., Ambartsumyan, A. A., Chakovskaya, O. V., Mysova, N. E., Kochetkov, K. A. *Russ. J. Org. Chem*. **2009**, *45*, 1181−1184.

36. Allan, G. R. and Carnell, A. J. *J. Org. Chem*. **2001**, *66*, 6495−6497.

CHAPTER 5

SYNTHESIS, CHARACTERIZATION, AND PHOTOPHYSICAL STUDIES OF VANADIUM COMPLEXES

PREFACE

The content of this chapter is a part of the manuscript that is currently in preparation. The authors include Đokić, M.; Gazi, S.; Ganguly, R.; Li, Y.; Soo, H. S. Đ. M. and S. H. S. concieved the research. Đ. M. performed synthetic procedures, and analyzed the data. G. S. provided assistance with photoluminescence measurements. G. R. and L. Y. performed X-Ray crystallographic experiments and provided the data.

5.1 Introduction

Visible light photoredox catalysis has lately received renewed attention as a useful approach towards selective bond activations of organic molecules.[1-10] Recent reports in the field mainly focus on catalytic C-C bond formation reactions by utilizing expensive ruthenium or iridium polypyridyl photosensitizers.[1] Although well explored in the fields of water-splitting, DSSCs, OLEDs, as polymerization initiators etc.,[11-21] these complexes and their analogues were rarely employed in the organic synthesis. Even less observed was the presence of redox photocatalysts in selective C-C bond cleavage reactions, despite their potential useful application in valorization of feedstock such as lignin and recycled plastics. Driven by the recent developments in the field of photoredox catalysis, we were interested in uncovering practical, earth abundant and easily prepared molecular photocatalysts that can mediate C-C bond cleavage reactions with high selectivity.

As discussed in previous chapters, our group has been active in developing affordable, and easily prepared redox photocatalysts for selective C-C bond activations. Based on the original catalyst's design,[22] our subsequent studies revealed that modifying the ligand by introducing EWGs (mainly, nitro and fluoro) stabilizes the HOMO, which leads to the increase of the rate of the catalytic reaction.[23] In addition, the kinetics studies helped us identify the fastest catalyst in the series,[23] which was then successfully employed for selective photocatalytic C-C bond cleavage in over 20 aliphatic alcohols.

In this chapter, we present ten new vanadium(V) oxo complexes that predominantly contain nitro, fluoro or bromo substituents at precise ligand positions, as well as several examples of the electron-rich complexes. Detailed comparative structural and photophysical studies reveal differences in light-absorbing, and emitting properties of these molecular vanadium species. The obtained results provided insights into the possibility of fine-tuning the ligand scaffold to achieve desired properties of the consequential complexes.

5.2 Synthesis and Characterization of Vanadium Complexes

The new vanadium-oxo complexes (**VO-16-25**) were prepared from their corresponding ligands (**L-7-16**) as shown in Scheme 5.1 The detailed syntheses of **L-7-16** and **VO-16-25** can be found in the experimental section. Generally, the ligands were

prepared by the condensation of a suitably derivatized salicylaldehyde with the corresponding benzohydrazone according to our previously reported procedure,[22,23] and were obtained in high yields (50-98%). Subsequently, the as-synthesized ligands were mixed with $VO(OiPr)_3$, which resulted in the formation of the vanadium oxo complexes, also collected in high yields (66-97%). The compounds were then characterized extensively by NMR spectroscopy, high-resolution mass spectrometry (HR-MS), and elemental analysis. In addition, all vanadium complexes formed single crystals suitable for X-ray crystallographic analysis.

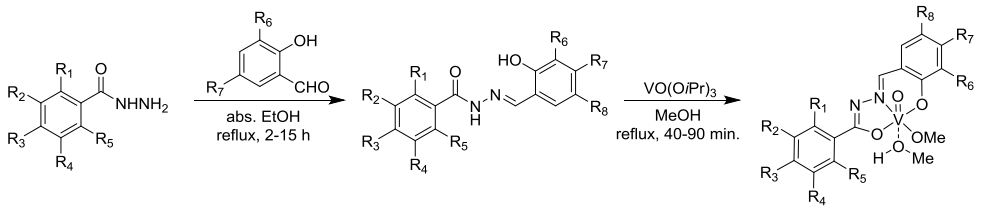

L-7: R_1-R_5,R_7=H; R_6,R_8=NO_2
L-8: R_1,R_2,R_4,R_5,R_7=H; R_3,R_6,R_8=NO_2
L-9: R_1,R_2,R_4-R_7=H; R_3=F; R_8=NO_2
L-10: R_1,R_2,R_4,R_5,R_7=H; R_3=F; R_6,R_8=NO_2
L-11: R_1,R_3,R_5-R_7=H; R_2,R_4=F; R_8=NO_2
L-12: R_1,R_3,R_5,R_7=H; R_2,R_4=F; R_6,R_8=NO_2
L-13: R_1,R_2,R_4-R_7=H; R_3=F; R_8=CH_2OCH_3
L-14: R_1-R_6,R_8=H, R_7=OCH_3
L-15: R_1,R_2,R_4-R_6,R_8=H, R_3=F, R_7=OCH_3
L-16: R_1,R_2,R_4,R_5,R_7=H; R_3,R_6,R_8=Br

VO-16: R_1-R_5,R_7=H; R_6,R_8=NO_2
VO-17: R_1,R_2,R_4,R_5,R_7=H; R_3,R_6,R_8=NO_2
VO-18: R_1,R_2,R_4-R_7=H; R_3=F; R_8=NO_2
VO-19: R_1,R_2,R_4,R_5,R_7=H; R_3=F; R_6,R_8=NO_2
VO-20: R_1,R_3,R_5-R_7=H; R_2,R_4=F; R_8=NO_2
VO-21: R_1,R_3,R_5,R_7=H; R_2,R_4=F; R_6,R_8=NO_2
VO-22: R_1,R_2,R_4-R_7=H; R_3=F; R_8=CH_2OCH_3
VO-23: R_1-R_6,R_8=H, R_7=OCH_3
VO-24: R_1,R_2,R_4-R_6,R_8=H, R_3=F, R_7=OCH_3
VO-25: R_1,R_2,R_4,R_5,R_7=H; R_3,R_6,R_8=Br

Scheme 5.1. Synthesis of vanadium complexes (**VO-16-25**) and corresponding ligands (**L-7-16**).

The X-ray crystallographic analyses revealed that the solid-state structures of **VO-16-22** and **VO-25** each exhibit octahedral geometry with an equatorial methoxide and an axial methanol bound to the vanadium center as reported for our similar vanadium(V) oxo complexes.[22,23] Surprisingly, the structures of **VO-23** and **VO-24** showed pentacoordinate, distorted square pyramidal geometries with no axial methanol ligand. This feature is unique to these two electron-rich complexes and has not been observed in any other of our vanadium(V) oxo compounds. The solid-state structures of the complexes are depicted in the Figure 5.1 Moreover, structures of **VO-16** and **VO-19** show that four and two asymmetric units are present within the crystal's unit cell, respectively. This phenomenon was not observed with crystal structures of our previously reported vanadium complexes. Nonetheless, in all the crystal structures, the bond length of the oxo V=O bond is in the typical range of 1.58-1.60 Å,[22-26] and does not seem to be strongly correlated to the electronic properties of the substituents on the ligand (methoxy, nitro, fluoro, bromo). Among all the complexes, **VO-17** is the most

electron deficient and thus, some of the bonds within the vanadium's inner coordination sphere are the most elongated in comparison with the same bonds of other complexes in the series. For instance, the vanadium-oxo V1-O1 bond is found to be the longest at 1.599(3) Å. Similar V1-O1 bond length was found only in **VO-23** (1.596(2) Å) and **VO18** (1.5952(14) Å). In other complexes, the bond averaged at 1.584-1.586 Å. The slight elongation was also observed for the V1-N1 bond, which measured 2.143(3) Å, and for the V1-O5 bond, which was found to be 1.773(2) Å. The same V1-O5 bond length was found with the complex **VO-20**. Interestingly, the V1-O2 bond in **VO-17** was found to be the shortest in our series of complexes and was only 1.917(2) Å. Furthermore, the V1-O3 bond was found to be 1.903(2) Å and is similar in length to the one of di-nitro-bearing complexes **VO-19** and **VO-21**. On the other hand, the V1-O4 bond was 2.280(2) Å and is within the range of 2.242-2.380 Å in the other complexes.

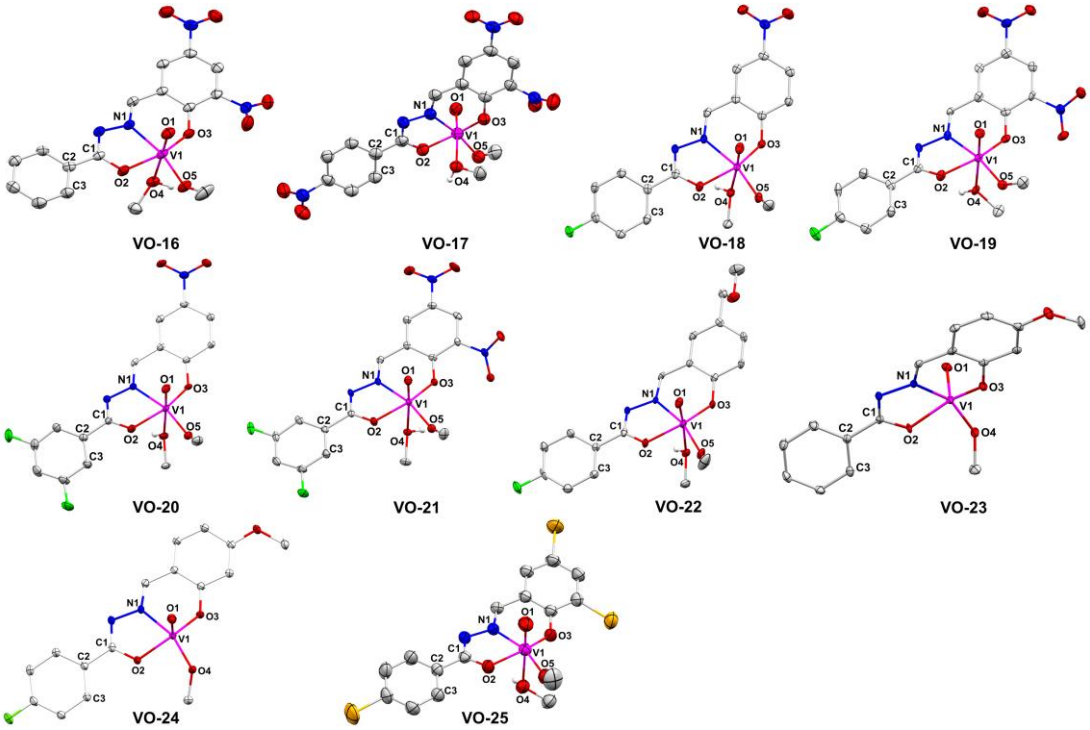

Figure 5.1. The crystal structures of complexes **VO-16-25**. The hydrogen atoms and uncoordinated solvent molecules (in the cases of **VO-16**, **VO-17**, and **VO-21**) were omitted for clarity. The thermal ellipsoids are at 50% probability. In the cases of **VO-16** and **VO-19**, only one of the asymmetric units is shown for each complex. The vanadium, nitrogen, oxygen, fluorine, bromine, and carbon atoms are shown in pink, blue, red, green, orange, and gray respectively.

In addition to characteristic bond lengths, the distortion from the equatorial plane of the aryl ring of the ligand's imidate arm was examined as well. The torsion angle (Ψ) of O2-C1-C2-C3 moiety varies significantly in the series of complexes **VO-16-25**. The

angle's values fall within a range of 1.0-23.6° with the minimum being present in one of the asymmetric units of **VO-16** (1.0(4))°, and the largest in **VO-18** (23.6(2))°. Complex **VO-16,** which exhibits four asymmetric units in the crystal unit, shows a significant variation of the dihedral angle values. The values for the four asymmetric units are: 1.0(4), 6.4(5), 20.9(4), and 21.3(4)°. The structures of the asymmetric units are shown in the experimental procedures section in more detail. In the case of our previously reported complexes that contain the pentafluoroaryl moiety, we found that the torsion angle values were significantly higher (34.56-53.92°). However, in the absence of this moiety and its steric factors, the distortion from the equatorial plane was expected to be much smaller, as it was found in complexes **VO-16-25**.

5.3 Photophysical Studies

To examine the light-absorbing properties of the vanadium complexes, UV-vis spectroscopic studies were conducted using 0.10 mM MeOH and MeCN solutions of **VO-16-25**. Two different solvents were used to examine the possible solvatochromism of the new vanadium complexes. As one of the solvents used in the UV-vis studies, MeOH was chosen due to its ability to dissolve most of the complexes well, while MeCN was chosen since it is the optimal solvent for our photocatalytic C-C bond cleavage studies. The obtained spectra are shown in the Figures 5.2 and 5.3 below. In addition, the UV-vis absorption spectra of ligands **L-7-16** are summarized in the experimental procedures.

Interestingly, change of solvent did cause a difference in the absorption of light of these vanadium complexes. To provide a clearer comparison of their light-absorbing properties, the complexes have been grouped into two subsets (**VO-16-21** and **VO-22-25**) based on the ligand-bearing substituents. Critically, each of the complexes exhibit a band centered between 380-400 nm that extends to 450-500 nm, which we have previously attributed to a LMCT by DFT calculations.[22,23] On the other hand, the absorption bands in the UV region resulted from intra-ligand charge transfer processes commonly observed in Schiff-base ligands.[27] From the UV-vis spectra of MeOH solutions (Figure 5.2) of **VO-16-25** it can be observed that the nitro- and fluoro-bearing complexes (**VO-16-21**) have significantly higher ε values ($M^{-1}cm^{-1}$) than the complexes with the different type of substituents (**VO-22-25**). Moreover, complexes **VO-16**, **VO-17**, **VO-19**, and **VO-21** have similar absorption profiles and their LMCT bands are

centered around 380 nm. Within the subset, similar absorption profiles are found between complexes **VO-18** and **VO-20**. The similarities in light-absorbing patterns are consistent with the type of substituents present within the complexes. For instance, complexes **VO-16**, **VO-17**, **VO-19**, and **VO-21** all have two nitro-groups and a varying number of fluoro-groups, while complexes **VO-18** and **VO-20** have only one nitro-group along with one or two floro-substituents, respectively.

On the other hand, complexes **VO-22-25** clearly show less visible-light absorption than their nitro- and fluoro-containing counterparts. Within the subset **VO-22-25**, complexes **VO-23** and **VO-24** have the highest ε values and their absorption profiles are almost identical. This similarity is due to the presence of a methoxy-substituent in both complexes, while one fluoro-group present only in **VO-24** is not able to cause any major impact on the light absorption profile of the complex. The LMCT bands within the subset are centered roughly around 400 nm, which indicates a slight red-shift in comparison with the LMCT band positions of the **VO-16-21**.

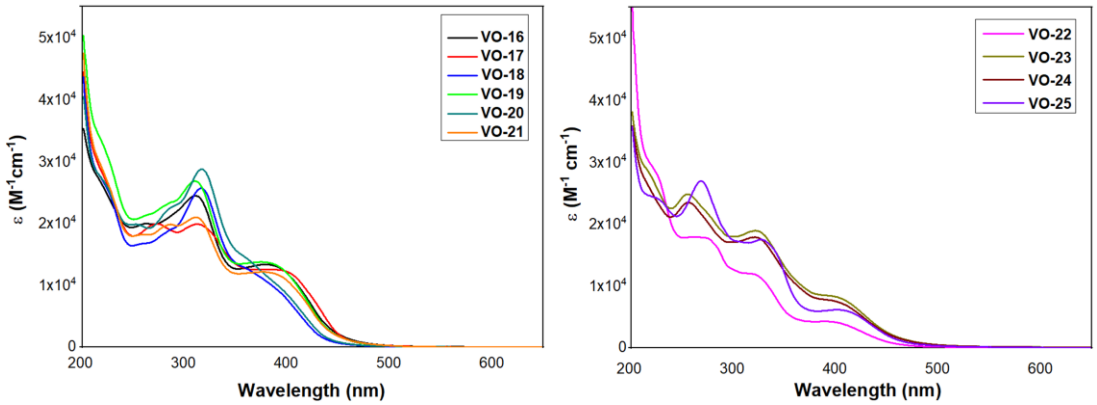

Figure 5.2. The UV-vis absorption spectra of 0.10 mM MeOH solutions of **VO-16** (black), **VO-17** (red), **VO-18** (blue), **VO-19** (green), **VO-20** (teal), and **VO-21** (orange) (left), and **VO-22** (pink), **VO-23** (olive), **VO-24** (burgundy), and **VO-25** (violet) (right).

In contrast, MeCN solutions of **VO-16-25** of the same concentrations are shown in Figure 5.3. Due to limited solubility, complexes **VO-18** and **VO-25** were not completely dissolved, which could have led to light diffraction off the suspended, fine particles and caused the UV-vis spectra to show abnormal absorption above 500 nm. In addition, the UV-vis spectra of **VO-16-21** and **VO-22-25** showed the LMCT bands centered at around the same wavelengths as in MeOH, but with the unexpected decrease in ε values of about 1000 units or more for each complex in **VO-16-21** subset and the increase of ε for roughly the same amount for complexes **VO-22-25**.

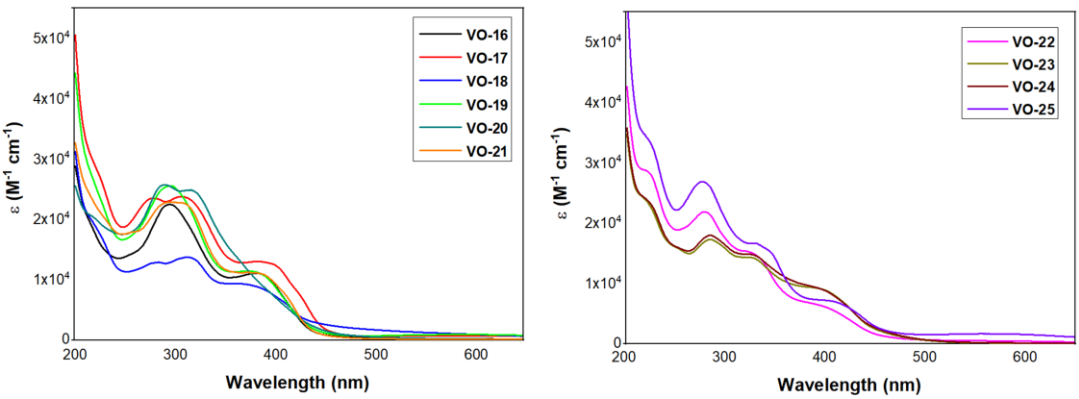

Figure 5.3. The UV-vis absorption spectra of 0.10 mM MeCN solutions of **VO-16** (black), **VO-17** (red), **VO-18** (blue), **VO-19** (green), **VO-20** (teal), and **VO-21** (orange) (left), and **VO-22** (pink), **VO-23** (olive), **VO-24** (burgundy), and **VO-25** (violet) (right).

The UV-vis spectra of both MeOH and MeCN solutions clearly indicate that nitro substitution on the ligand increases ε and hence, the light-absorbing properties of the corresponding vanadium complex. In fact, **VO-16**, **VO-17**, **VO-19**, and **VO-21** showed the highest ε values, suggesting that the presence of multiple nitro groups leads to the highest amount of visible light absorption. Although ε values of the nitro-containing complexes were higher in MeOH, this solvent could not be used in the photocatalytic C-C bond cleavage studies as it would competitively prevent the substrate from effectively coordinating to the vanadium center.

In addition to comparing the light-absorbing properties of vanadium complexes within our library, comparison with vanadium complexes supported by different types of ligands could give additional useful information regarding our ligand designs. In a previous report, Soo and co-workers have examined the light absorbing properties of a vanadium(V) complex reported by Toste *et al*. (**VO-26**) and a commercially available vanadium(V) oxytripropoxide (**VO-27**) in MeCN solutions and compared them with the light-absorption of **VO-10**.[22] In addition, a vanadium(IV) compound, vanadyl acetylacetonate (**VO-28**) was examined as well.[22]

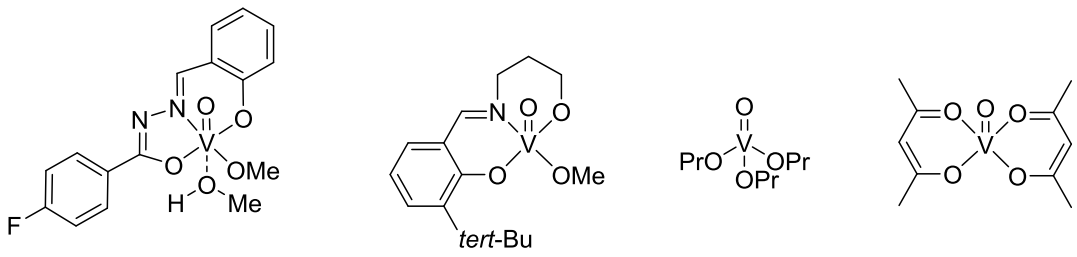

Figure 5.4. Various oxovanadium complexes examined for different light-absorbing properties in a report by Soo *et al*.

As shown in Figure 5.5 below, other vanadium(V) complexes, especially **VO-27**, absorb significantly less light in the visible region compared to **VO-10**.[22] Furthermore, the vanadium(IV) species **VO-28** shows much less visible-light absorption than any of the examined vanadium(V) complexes.[22]

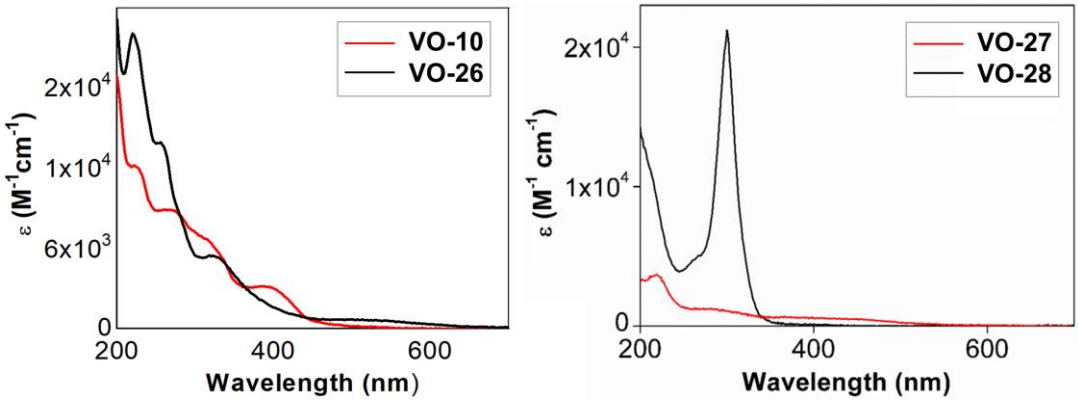

Figure 5.5. Comparison of UV-vis spectra of vanadium complexes with different ligand types. UV-vis spectra of 0.10 mM MeCN solutions of **VO-10** and **VO-26** (left), and **VO-27** and **VO-28** (right). Figure has ben adapted from reference 22.

These results suggest that among the series of vanadium(V) complexes, those that are supported with highly conjugated ligand systems tend to absorb more visible light through LMCT. The LMCT bands observed in our vanadium complexes are hence much more prominent than in other vanadium(V) species. Furthermore, the LMCT seems to be critical for visible-light absorption, since the vanadium(IV) **VO-28** complex displayed drastically lower visible-light absorption than vanadium(V) compounds.

Aside from their light-absorbing properties, our vanadium complexes display weak emission when photoexcited at 375 nm. This unusual characteristic among molecular vanadium(V) oxo compounds was probed by steady-state photoluminescence (PL)

spectroscopy and the resulting spectra of MeOH (Figure 5.6) and MeCN (Figure 5.7) solutions are depicted below.

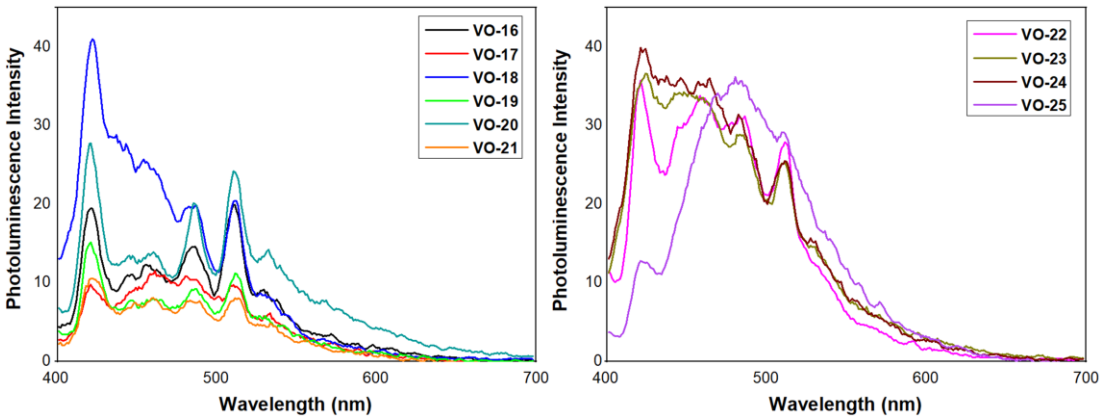

Figure 5.6. The photoemission spectra of 0.10 mM MeOH solutions of **VO-16** (black), **VO-17** (red), **VO-18** (blue), **VO-19** (green), **VO-20** (teal), and **VO-21** (orange) (left), and **VO-22** (pink), **VO-23** (olive), **VO-24** (burgundy), and **VO-25** (violet) (right) with excitation at 375 nm.

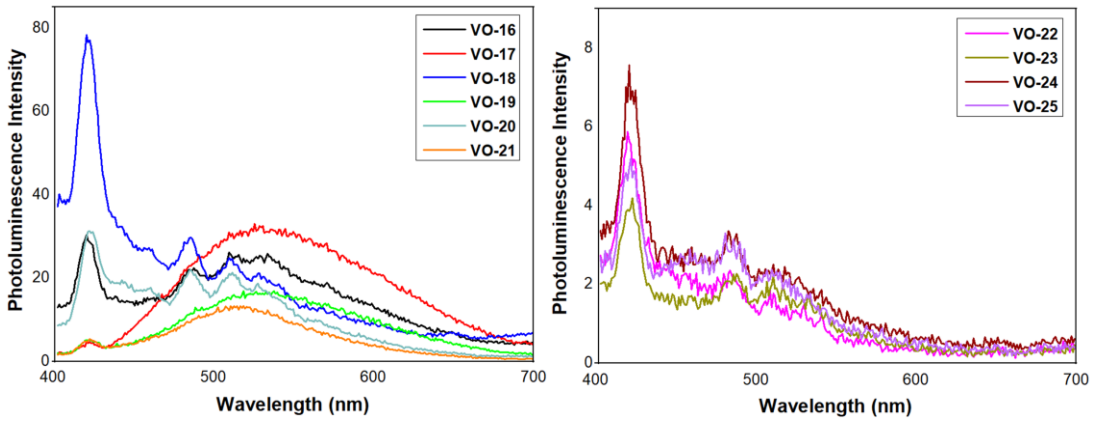

Figure 5.7.The photoemission spectra of 0.10 mM MeCN solutions of **VO-16** (black), **VO-17** (red), **VO-18** (blue), **VO-19** (green), **VO-20** (teal), and **VO-21** (orange) (left), and **VO-22** (pink), **VO-23** (olive), **VO-24** (burgundy), and **VO-25** (violet) (right) with excitation at 375 nm.

Both MeOH and MeCN solutions of **VO-16-25** displayed PL signal starting from 410 nm and well into the visible region. The PL signal at around 420 nm is present in all the complexes and is believed to originate from the phenyl groups of the ligand, as reported in the literature.[28] Furthermore, **VO-16-25** exhibited broad emissions ranging from ca. 450-600 nm. Similar emission profiles were observed with our previously reported vanadium(V) oxo complexes **VO-10-15** bearing pentafluoro, nitro, and *tert*-Bu substituents on their ligand.[23] In case of MeOH solutions, **VO-16-21** with electron-deficient ligands exhibited almost identical emission profiles, coinciding with the type

of substituents present in these complexes (Figure 5.6, left). Likewise, **VO-22-25** displayed very similar emission profiles within the subset, although the broad emission band centered at ca. 480 nm became more apparent (Figure 5.6, right).

In the case of MeCN solutions of **VO-16-21** (Figure 5.7, left), similar emission profiles were retained within the group, though **VO-17**, **VO-19**, and **VO-21** exhibited significantly broadened emission from 450-650 nm, which was slightly red-shifted in the case of **VO-17**. On the other hand, **VO-22-25** subset (Figure, 5.7. right) showed increased emission around 420 nm, while the broad band typically ranging from 450-600 nm became less prominent. The results thus indicate that the choice of solvent affected the emission, especially in the case of electron-rich complexes **VO-22-24** and bromo-substituted **VO-25**.

5.4 Photocatalytic Reactivity Towards C-C Bond Cleavage

After having synthesized and thoroughly characterized ten new vanadium complexes, we moved on to investigate their photocatalytic properties for C-C bond activation in hope of uncovering an even faster catalyst than our previously reported complex **VO-14**. In order to facilitate the screening of reactivities of new catalysts, we have employed **33** as the ideal substrate along with the formerly optimized reaction conditions that would minimize any side-reactions. The results of photocatalytic reactions with **VO-16-25** are summarized in Table 5.1 below.

Table 5.1. Comparing the reactivities of catalysts **VO-16-25** with **33** under our optimal reaction conditions with our fastest catalyst **VO-14**.

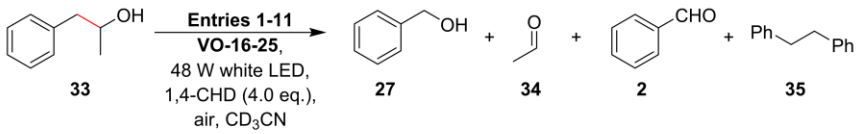

33 27 34 2 35

Entry	Catalyst (mol%)	Reaction time (h)	Substrate conversion (%)	Distribution of products (%)			
				27	**34**	**2**	**35**
1	**VO-14 (5.0)**	**14**	**>95**	**60**	**90**	**11**	**6**
2	**VO-16** (5.0)	18	>95	54	69	14	3
3	**VO-17** (5.0)	18	90	50	66	14	2
4	**VO-18** (5.0)	32	70	48	56	5	5
5	**VO-19** (5.0)	32	90	52	62	10	3
6	**VO-20** (5.0)	16	95	55	70	9	4
7	**VO-21** (5.0)	16	90	43	58	14	trace
8	**VO-22** (5.0)	24	95	73	74	17	3
9	**VO-23** (5.0)	44	88	57	54	22	trace
10	**VO-24** (5.0)	44	90	52	53	24	trace
11	**VO-25** (5.0)	24	78	47	50	14	trace

Judging from the reaction times needed to reach full substrate conversions, unfortunately, no catalyst in the series of ten structurally modified complexes outperformed **VO-14** (Table 5.1, Entry 1). Catalysts **VO-16** and **VO-17**, both bearing only strong electron-withdrawing NO_2 groups at specific ligand positions achieved >95 and 90% conversions, respectively, in 18 h (Table 5.1, Entries 2 and 3), compared to 14 h required for **VO-14** to achieve full substrate conversion. Furthermore, when a combination of difluoro- and mono- or dinitro substituents was used in catalysts **VO-20** and **VO-21**, substrate conversions of 95 and 90%, respectively, were achieved in 16 h (Table 5.1, Entries 6 and 7). On the other hand, ligand substitutions with only one fluoro- but one or two nitro groups in **VO-18** and **VO-19** (Table 5.1, Entries 4 and 5) resulted in significantly longer reaction times required to achieve higher conversions. This result could also stem from the fact that these complexes displayed poor solubility in MeCN throughout the photoreaction.

In contrast to complexes containing strong EWGs, catalyst **VO-25** with moderately electron-withdrawing bromo-substituents exhibited 78% conversion in 24 h (Table 5.1, Entry 11), but also displayed poor solubility in the reaction medium. Additionally, catalyst **VO-22** with no prominent electron-withdrawing or donating substituents showed 95% substrate conversion in 24 h (Table 5.1, Entry 8). Finally, catalysts **VO-23** and **VO-24** with similar substitutions on the ligand including strong electron-donating methoxy group exhibited almost identical reactivities that were significantly hindered compared to all the other complexes in the series (Table 5.1, Entries 9 and 10). In addition, **VO-23** and **VO-24** generated the most of **2** from over-oxidation of **27**, most likely due to slow reactivities and prolonged reaction times.

Overall, different reactivities of oxovanadium photocatalysts **VO-16-25** are well correlated with our prior hypothesis that HOMO stabilization by strong EWGs at specific positions on the ligand can enhance the reactivity. However, although some ligand designs might offer better HOMO stabilization due to the presence of numerous NO_2 groups on the ligand, it should be noted that insolubility of such systems can also become a significant problem and hinder their otherwise expected high reactivity.

5.5 Conclusion

In conclusion, ten new vanadium(V) oxo complexes with different ligand substitutions, both electron-donating and withdrawing, were synthesized and thoroughly characterized. Crystallographic analysis revealed some remarkable structural properties, previously not observed with this type of vanadium complexes. Some of these include pentacoordinate complexes with electron-rich ligands, or appearance of asymmetric units in the crystal's unit for electron-deficient complexes.

Furthermore, the UV-vis absorption spectroscopy revealed that similar ligand substitution patterns led to almost identical light-absorption profiles of the resultant complexes, while the electronic properties of the substituents affected the molar absorptivity values. Specifically, complexes with electron-deficient ligands generally exhibited higher ε values compared to their electron-rich counterparts. Though the trends among complexes remained similar, different solvents affected the ε values, indicating a certain level of solvatochromism.

Additionally, all the examined complexes showed photoluminescence when photoexcited at 375 nm. Though limited in intensity, this fascinating characteristic has not been observed in other molecular vanadium complexes. Similarly, emission profiles closely follow the trends in ligand substitution as well.

Finally, the newly prepared complexes were screened for photocatalytic reactivity towards C-C bond cleavage with our model substrate and under optimized reaction conditions. Although all the complexes exhibited photocatalytic properties, we were not able to identify an improved catalyst that would outperform **VO-14** as the fastest catalyst in our library. This finding, however, could stem from the fact that a number of catalysts among **VO-16-25** displayed limited solubility in the reaction medium, thus indicating the importance of appropriately modifying the ligand backbone towards HOMO stabilization as well as achieving good solubility.

5.6 Experimental Procedures

5.6.1 General Information

The vanadium complexes and ligands were prepared under a N_2 atmosphere using standard Schlenk techniques. Other synthetic procedures were conducted under aerobic conditions unless stated otherwise. The chemicals used in the experiments were purchased from Sigma-Aldrich and were used as received. Deuterated solvents were purchased from Cambridge Isotope Laboratories and were used as received. The ^{1}H, ^{13}C, ^{19}F, and ^{51}V NMR spectroscopic data were obtained using Bruker AVANCE spectrometers operating at 300, 400, and 500 MHz. The resulting ^{1}H and ^{13}C NMR chemical shifts (δ reported in ppm) were referenced according to the residual solvent signal(s) ($CDCl_3$ = 7.26 ppm for ^{1}H and 77.2 ppm for ^{13}C; CD_3CN = 1.94 ppm for ^{1}H and 118.3 ppm for ^{13}C; MeOD-d_4 = 3.31 ppm for ^{1}H and 49.2 ppm for ^{13}C; DMSO-d_6 = 2.50 ppm for ^{1}H and 39.52 ppm for ^{13}C). The ^{51}V NMR chemical shift was referenced relative to V^{v} $(O)(Cl)_3$ external standard (δ = 0.0 ppm). Crystallographic data were collected on a Bruker X8 CCD diffractometer. The structures were solved and refined using the Bruker SHELXTL software package. High-resolution electrospray ionization mass spectra (HR-ESIMS) were obtained using a Waters Q-TOF Premier mass spectrometer. Elemental analyses were performed with the Elementar vario MICRO cube analyzer. The steady-state photoluminescence spectroscopic measurements were performed with a Varian Cary Eclipse fluorescence spectrophotometer. FT-IR

spectroscopy measurements were carried out with a Shimadzu IRPrestige-21 FT-IR spectrometer. In a typical experiment, about 1.5 mg of the sample were mixed with about 30.0 mg of potassium bromide (KBr) to make a pellet. The pellets were made with a Specac Atlas manual hydraulic press 15T at 10 ton pressure. The FT-IR experiments were conducted in transmission mode with data collected from 400 to 4000 cm^{-1}

5.6.2 Synthetic Procedures and Spectroscopic Data

General procedure for the synthesis of ligands

In each reaction, to a stirring, heated solution of aryl hydrazide in absolute EtOH under N_2 was added a solution of the corresponding aryl aldehyde in EtOH dropwise. The reaction mixture was then stirred at reflux for a specific amount of time detailed below (between 2 and 15 h). The ligand was subsequently either precipitated out of the mixture or was obtained by removing the solvent under vacuum. The as-synthesized ligands were of sufficient purity to be used in the complexation reactions without any further purification.

***N′*-(2-hydroxy-3,5-dinitrobenzylidene)benzohydrazide (L-7)**

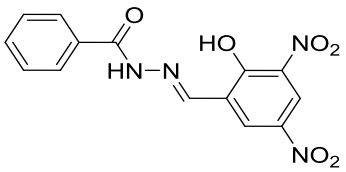

An EtOH solution of 3,5-dinitrosalicylaldehyde (0.212 g, 1.0 mmol in 2 mL EtOH) was added to a solution of benzohydrazide (0.136 g, 1.0 mmol in 5 mL of EtOH) and stirred. After 2 h, the corresponding ligand precipitated and was collected by filtration (0.257 g, 78% yield). ^{1}H NMR (DMSO-d_6, 400 MHz): δ = 7.57 (t, 2 H, J = 6.1 Hz), 7.65 (t, 1 H, J = 5.9 Hz), 7.97 (d, 2 H, J = 5.9 Hz), 8.76 (d, 1 H, J = 2.2 Hz), 8.80 (s, 1 H), 8.83 (d, 1 H, J = 2.2 Hz) ppm. ^{13}C{^{1}H} NMR (CD_3CN, 100 MHz): δ = 122.1, 122.6, 128.2, 129.3, 129.9, 132.3, 133.2, 137.9, 139.3, 146.3, 157.9, 164.0 ppm. HRMS (ESI+, m/z) calculated for $C_{14}H_{11}N_4O_6$ $[M+H]^+$ m/z = 331.0679, found 331.0677. IR (cm^{-1}): 3344 (ν_{O-H}), 3089 (ν_{N-H}), 1680 ($\nu_{C=N}$), 1340 (ν_{NO2}).

***N′*-(2-hydroxy-3,5-dinitrobenzylidene)-4-nitrobenzohydrazide (L-8)**

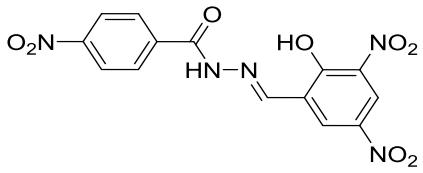

A solution of 2,4-dinitrosalicylaldehyde (0.106 g, 0.50 mmol in 3 mL of EtOH) was added dropwise to a solution of 4-nitrobenzohydrazide (0.090 g, 0.50 mmol in 2 mL of EtOH). After stirring for about 3 h, the product was obtained by filtration (0.175 g, 94% yield). ^{1}H NMR (DMSO-d_6, 500 MHz): δ = 8.20 (d, 2 H, J = 8.8 Hz), 8.40 (d, 2 H, J = 8.8 Hz), 8.75 (d, 1 H, J = 2.9 Hz), 8.81 (d, 1 H, J = 2.9 Hz), 8.83 (s, 1 H) ppm. ^{13}C{^{1}H} NMR (DMSO-d_6, 100 MHz): δ = 122.5, 123.1, 123.7, 128.2, 129.4, 137.2, 137.3, 137.7, 146.1, 149.6, 157.8, 161.6 ppm. HRMS (ESI+, *m*/*z*) calculated for $C_{14}H_{10}N_5O_8$ $[M+H]^+$ *m/z* = 376.0529, found 376.0536. IR (cm^{-1}): 3331 (ν_{O-H}), 3091 (ν_{N-H}), 1695 ($\nu_{C=N}$), 1342 (ν_{NO2}).

4-Fluoro-*N′*-*(*2-hydroxy-5-nitrobenzylidene)benzohydrazide (L-9)

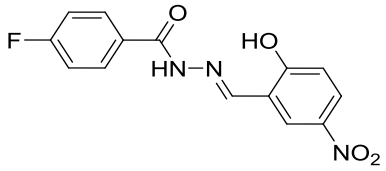

An EtOH solution of 2-hydroxy-5-nitrobenzaldehyde (0.069 g, 0.41 mmol in 1 mL of EtOH) was added dropwise to a solution of 4-fluorobenzohydrazide[1] (0.063 g, 0.41 mmol in 3 mL of EtOH) and stirred. After about 15 h, the resulting ligand precipitated out and was collected by filtration (0.11 g, 92% yield). ^{1}H NMR (DMSO–d_6, 400 MHz): δ = 7.11 (d, 1 H, J = 9.1 Hz), 7.39 (t, 2 H, J = 8.7 Hz), 8.03 (dd, 2 H, J = 5.8, 8.0 Hz), 8.17 (dd, 1 H, J = 2.6, 9.0 Hz), 8.59 (d, 1 H, J = 2.3 Hz), 8.73 (s, 1 H) ppm. ^{13}C{^{1}H} NMR (DMSO–d_6, 100 MHz): δ = 115.6 (d, J = 21.9 Hz), 117.1, 120.0, 123.7, 126.6, 129.2 (d, J = 2.5 Hz), 130.5 (d, J = 9.1 Hz), 139.9, 144.4, 162.0, 162.6, 164.4 (d, J = 248.4 Hz) ppm. ^{19}F{^{1}H} NMR (DMSO–d_6,376.50 MHz): δ = -107.8 ppm. HRMS (ESI+, *m/z*) calculated for $C_{14}H_{11}N_3O_4F$ $[M + H]^+$ *m/z* = 304.0734, found 304.0724. IR (cm^{-1}): 3305 (ν_{O-H}), 3082 (ν_{N-H}), 1635 ($\nu_{C=N}$), 1328 (ν_{NO2}).

4-Fluoro-*N′*-(2-hydroxy-3,5-dinitrobenzylidene)benzohydrazide (L-10)

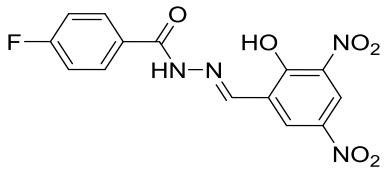

An EtOH solution of 2-hydroxy-3,5-dinitrobenzaldehyde (0.21 g, 1.0 mmol in 3 ml of EtOH) was added dropwise to a solution of 4-fluorobenzohydrazide (0.15 g, 1.0 mmol in 5 mL of EtOH). After about 15 h, the yellow precipitated ligand was collected by filtration (0.24 g, 71% yield). ^{1}H NMR (DMSO–d_6, 500 MHz): δ = 7.41 (t, 2 H, J = 8.7 Hz), 8.05 (dd, 2 H, J = 5.6, 8.5 Hz), 8.75 (d, 1 H, J = 2.8 Hz), 8.79 (s, 1 H), 8.81 (d, 1 H, J = 2.7 Hz) ppm. ^{13}C{^{1}H} NMR (DMSO–d_6, 100 MHz): δ = 115.7 (d, J = 21.7 Hz), 122.4, 123.1, 128.1 (d, J = 2.1 Hz), 128.6, 130.7 (d, J = 9.1 Hz), 136.8, 137.3, 145.4, 158.2, 162.1, 164.5 (d, J = 249.3 Hz). ^{19}F{^{1}H} NMR (DMSO–d_6, 376.50 MHz): δ = -107.3 ppm. HRMS (ESI+, *m/z*) calculated for $C_{14}H_{10}N_4O_6F$ $[M + H]^+$ *m/z* = 349.0584, found 349.0580. IR (cm^{-1}): 3307 ($\nu_{O\text{-}H}$), 3107 ($\nu_{N\text{-}H}$), 1678 ($\nu_{C=N}$), 1332 (ν_{NO2}).

3,5-Difluoro-*N'*-(2-hydroxy-5-nitrobenzylidene)benzohydrazide (L-11)

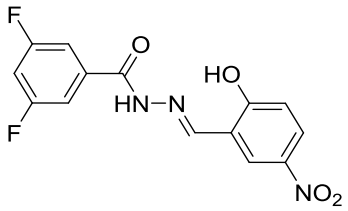

To a solution of 2,4-difluorobenzohydrazide (0.175 g, 1.0 mmol in 5 mL of EtOH) was added dropwise a solution of 2-hydroxy-5-nitrobenzaldehyde (0.165 g, 1.0 mmol in 2 mL of EtOH). After stirring for 3 h, the pale-yellow ligand was collected by filtration and dried under vacuum (0.282 g, 87.8% yield). ^{1}H NMR (DMSO–d_6, 400 MHz): δ = 7.12 (d, 1 H, J = 9.1 Hz), 7.56 (tt, 1 H, J = 2.3, 9.1 Hz), 7.67 (dd, 2 H, J = 2.0, 8.1 Hz), 8.19 (dd, 1 H, J = 2.9, 9.1 Hz), 8.61 (d, 1 H, J = 2.9 Hz), 8.75 (s, 1 H), 12.28 (s, 2 H) ppm. ^{13}C{^{1}H} NMR (DMSO–d_6, 100 MHz): δ = 107.5 (t, J = 25.7 Hz), 111.2 (m), 117.1, 120.0, 123.4, 126.8, 136.2 (t, J = 8.6 Hz), 140.0, 144.8, 160.6 (t, J = 2.8 Hz), 162.1 (dd, J = 12.7, 246.0 Hz), 162.6 ppm. ^{19}F{^{1}H} NMR (DMSO–d_6, 376.50 MHz): δ = -108.5 ppm. HRMS (ESI+, *m/z*) calculated for $C_{14}H_{10}N_3O_4F_2$ $[M + H]^+$ *m/z* = 322.0639, found 322.0641. IR (cm^{-1}): 3311 ($\nu_{O\text{-}H}$), 3084 ($\nu_{N\text{-}H}$), 1668 ($\nu_{C=N}$), 1330 (ν_{NO2}).

3,5-Difluoro-*N'*-(2-hydroxy-3,5-dinitrobenzylidene)benzohydrazide (L-12)

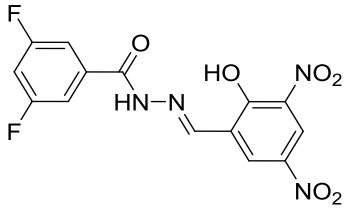

To a stirring solution of 2,4-difluorobenzohydrazide (0.172 g, 1.0 mmol in 5 mL EtOH) was added dropwise, a suspension of 2-hydroxy-3,5-dinitrobenzaldehyde (0.212 g, 1.0 mmol in 2 mL of EtOH). After stirring for 3 h, the dark yellow product was collected by filtration and dried in vacuum (0.294 g, 80% yield). ^{1}H NMR (DMSO–d_6, 400 MHz): δ = 7.57 (tt, 1 H, J = 2.3, 9.2 Hz), 7.67 (dd, 2 H, J = 2.0, 8.0 Hz), 8.74 (d, 1 H, J = 2.9 Hz), 8.79 (s, 1 H), 8.81 (d, 1 H, J = 2.9 Hz) ppm. ^{13}C{^{1}H} NMR (DMSO–d_6, 100 MHz): δ = 107.8 (t, J = 25.8 Hz), 111.3 (m), 122.6, 123.3, 128.0, 135.5 (t, J = 8.7 Hz), 137.0, 137.3, 145.8, 158.0, 160.7 (t, J = 2.6 Hz), 162.4 (dd, J = 12.7, 246.1 Hz). ^{19}F{^{1}H} NMR (CD_3CN, 282.40 MHz): δ = -109.0 ppm. HRMS (ESI+, *m/z*) calculated for $C_{14}H_9N_4O_6F_2$ $[M + H]^+$ *m/z* = 367.0490, found 367.0487. IR (cm^{-1}): 3207 (ν_{O-H}), 3091 (ν_{N-H}), 1672 ($\nu_{C=N}$), 1330 (ν_{NO2}).

4-Fluoro-*N′*-(2-hydroxy-5-(methoxymethyl)benzylidene)benzohydrazide (L-13)

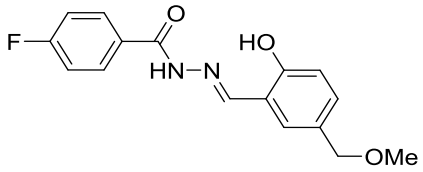

A solution of 2-hydroxy-5-(methoxymethyl)benzaldehyde (0.830 g, 5.0 mmol in 5 mL of EtOH) was added to a solution of 4-fluorobenzohydrazide (0.770 g, 5.0 mmol in 10 mL of EtOH). After stirring for about 15 h, the solvent was removed in vacuum yielding the final product (0.750 g, 50% yield). ^{1}H NMR (DMSO-d_6, 500 MHz): δ = 3.27 (s, 3 H), 4.34 (s, 2 H), 6.91 (d, 1 H, J = 8.3 Hz), 7.25 (d, 1 H, J = 6.6 Hz), 7.38 (t, 2 H, J = 8.8 Hz), 7.54 (s, 1 H), 8.01 (dd, 2 H, J = 5.6, 8.5 Hz), 8.64 (s, 1 H), 11.14 (s, 1 H), 12.10 (s, 1 H) ppm. ^{13}C{^{1}H} NMR (DMSO-d_6, 100 MHz): δ = 57.2, 73.1, 115.5 (d, J = 21.8 Hz), 116.3, 118.5, 128.5, 129.2, 129.4 (d, J = 2.7 Hz), 130.4 (d, J = 9.1 Hz), 131.2, 147.7, 156.8, 161.8, 164.3 (d, J = 248.1 Hz) ppm. ^{19}F{^{1}H} NMR (DMSO-d_6, 376.50 MHz): δ = -108.4 ppm. HRMS (ESI+, *m/z*) calculated for $C_{16}H_{16}N_2O_3F$ $[M+H]^+$ *m/z* = 303.1145, found 303.1143. IR (cm^{-1}): 3199 (ν_{O-H}), 3037 (ν_{N-H}), 1674 ($\nu_{C=N}$).

***N′*-(2-hydroxy-4-methoxybenzylidene)benzohydrazide (L-14)**

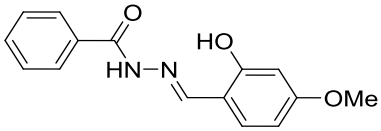

To a solution of benzohydrazide (0.136 g, 1.0 mmol in 5 mL EtOH) was added dropwise, a solution of 2-hydroxy-4-methoxybenzaldehyde (0.152 g, 1.0 mmol in 2 mL EtOH). After 2.5 h, the ligand was obtained by removing the solvent under vacuum and was further dried (0.244 g, 90.4% yield). ^{1}H NMR (DMSO-d_6, 400 MHz): δ = 3.76 (s, 3 H), 6.49-6.54 (m, 2 H), 7.41 (d, 1 H, J = 8.6 Hz), 7.51-7.61 (m, 3 H), 7.90 (m, 2 H), 8.54 (s, 1 H), 11.63 (s, 1 H), 12.02 (s, 1 H) ppm. ^{13}C{^{1}H} NMR (DMSO-d_6, 100 MHz): δ = 55.5, 101.4, 106.7, 112.0, 127.8, 128.8, 131.4, 132.2, 133.0, 149.2, 159.6, 162.3, 163.0 ppm. HRMS (ESI+, *m/z*) calculated for $C_{15}H_{15}N_2O_3$ $[M+H]^+$ *m/z* = 271.1083, found 271.1087. IR (cm^{-1}): 3226 (ν_{O-H}), 3030 (ν_{N-H}), 1633 ($\nu_{C=N}$).

4-Fluoro-*N'*-(2-hydroxy-4-methoxybenzylidene)benzohydrazide (L-15)

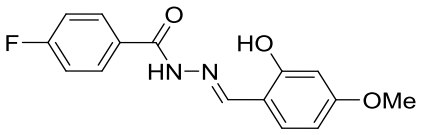

A solution of 2-hydroxy-4-methoxybenzaldehyde (0.031 g, 0.20 mmol in 1 mL EtOH) was added dropwise to a solution of 4-fluorobenzohydrazide (0.031 g, 0.20 mmol in 1mL EtOH). After about 3 h, the ligand was obtained by removing the solvent under reduced pressure (0.057 g, 98% yield). ^{1}H NMR (DMSO-d_6, 400 MHz): δ = 3.78 (s, 3 H), 6.50-6.54 (m, 2 H), 7.36-7.45 (m, 3 H), 8.00 (dd, 2 H, J = 5.5, 8.7 Hz), 8.54 (s, 1 H), 11.59 (s, 1 H), 12.01 (s, 1 H) ppm. ^{13}C{^{1}H} NMR (DMSO-d_6, 100 MHz): δ = 55.3, 101.2, 106.5, 111.7, 115.5 (d, J = 21.7 Hz), 129.4 (d, J = 2.8 Hz), 130.3 (d, J = 9.0 Hz), 131.1, 148.8, 159.4, 161.5, 162.1, 164.2 (d, J = 247.8 Hz) ppm. ^{19}F{^{1}H} NMR (DMSO-d_6, 376.50): δ = -107.5 ppm. HRMS (ESI+, *m/z*) calculated for $C_{15}H_{14}N_2O_3F$ $[M+H]^+$ *m/z* = 289.0988, found 289.0993. IR (cm^{-1}): 3232 (ν_{O-H}), 3080 (ν_{N-H}), 1643 ($\nu_{C=N}$).

4-Bromo-*N'*-(3,5-dibromo-2-hydroxybenzylidene)benzohydrazide (L-16)

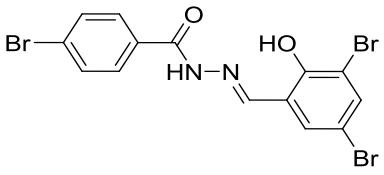

A solution of 3,5-dibromo-2-hydroxybenzaldehyde (0.280 g, 1.0 mmol in 2 mL of EtOH) was added dropwise to a stirring solution of 4-bromobenzohydrazide (0.215 g, 1.0 mmol in 5 mL of EtOH). The reaction mixture was then stirred at reflux for 6 h, and subsequently, the ligand was obtained by removing the solvent under reduced pressure (0.460 g, 96% yield). ^{1}H NMR (DMSO-d_6, 300 MHz): δ = 7.71-7.83 (m, 4 H), 7.90 (d, 2 H, J = 8.4 Hz), 8.53 (s, 1 H), 12.59 (s, 1 H), 12.66 (s, 1 H) ppm. ^{13}C{^{1}H} NMR (DMSO-d_6, 75.5 MHz): δ = 110.2, 111.0, 120.7, 126.0, 129.6, 131.0, 131.5, 131.9, 135.4, 147.1, 153.5, 161.9 ppm. HRMS (ESI+, *m/z*) calculated for $C_{14}H_{10}N_2O_2{}^{79}Br_2{}^{81}Br$ $[M+H]^+$ *m/z* = 476.8272, found 476.8290. IR (cm^{-1}): 3217 (ν_{O-H}), 3051 (ν_{N-H}), 1656 ($\nu_{C=N}$).

General procedure for the synthesis of vanadium oxo complexes

In each reaction, to a heated, stirring solution of the ligand in MeOH was added the vanadium(V) precursor, VO(O*i*Pr)$_3$, under N_2, which led to an immediate change of the reaction color from brown to dark red. The reaction mixture was stirred under reflux for ca. 90 min. Subsequently, the solvent was removed under vacuum and the remaining dark solid product was obtained. The solid was then re-dissolved in methanol and filtered before finally obtaining the complex by solvent evaporation.

Vanadium oxo complex VO-16

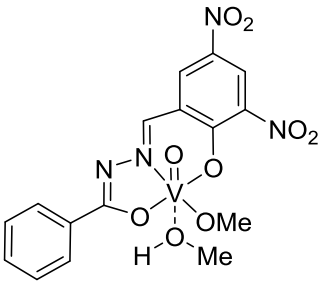

The reaction of **L-7** (0.165 g, 0.50 mmol in 5 mL of MeOH) and VO(OiPr)$_3$ (118 µL, 0.50 mmol) gave the corresponding vanadium complex after about 90 min (0.207 g, 97% yield). ^{1}H NMR (MeOD-d_4, 400 MHz): δ = 7.53 (dt, 3 H, J = 7.3, 30.8 Hz), 8.13 (m, 2 H), 8.85 (d, 1 H, J = 2.8 Hz), 8.91 (d, 1 H, J = 2.8 Hz), 8.97 (s, 1 H) ppm. ^{13}C{^{1}H} NMR (DMSO-d_6, 100 MHz): δ = 123.3, 124.1, 128.4, 128.8, 129.9, 132.1, 132.6, 137.3, 138.3, 150.8, 158.9, 171.9 ppm. ^{51}V NMR (MeOD-d_4, 105.25 MHz): δ = -546.9 ppm. HRMS (ESI+, *m/z*) calculated for $C_{15}H_{12}N_4O_8V$ $[M+H]^+$ *m/z* = 427.0095, found 427.0103. Elemental analysis calculated for $C_{15}H_{11}N_4O_8V{\cdot}CH_3OH$: C, 41.94; H, 3.30;

N, 12.23%; found: C, 41.23; H, 2.92; N, 12.30%. IR (cm^{-1}): 3400 (ν_{O-H}), 1620 ($\nu_{C=N}$), 1340 (ν_{NO2}), 1029 ($\nu_{V=O}$).

Vanadium oxo complex VO-17

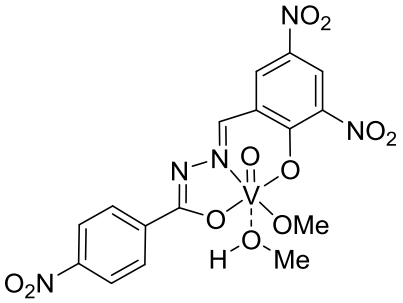

The reaction of **L-8** (0.095 g, 0.25 mmol in 2 mL of MeOH) and $VO(OiPr)_3$ (59 µL, 0.25 mmol) gave the corresponding vanadium complex after about 90 min (0.11 g, 92% yield).^{1}H NMR (MeOD-d_4, 400 MHz): δ = 8.36 (s, 4 H), 8.89 (d, 1 H, J = 2.0 Hz), 8.93 (d, 1 H, J = 2.4 Hz), 9.05 (s, 1 H) ppm. ^{51}V NMR (MeOD-d_4, 105.25 MHz): δ = -548.4 ppm. HRMS (ESI+, *m/z*) calculated for $C_{15}H_{11}N_5O_{10}V$ $[M+H]^+$ *m/z* = 471.9946, found 471.9935. IR (cm^{-1}): 3362 (ν_{O-H}), 1620 ($\nu_{C=N}$), 1350 (ν_{NO2}), 979 ($\nu_{V=O}$).

Vanadium oxo complex VO-18

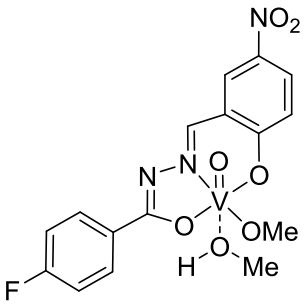

The reaction of **L-9** (0.067 g, 0.22 mmol in 5 mL of MeOH) and $VO(OiPr)_3$ (59 µL, 0.025 mmol) resulted in the corresponding complex after about 40 min (0.070 g, 71% yield). ^{1}H NMR (MeOD–d_4, 400 MHz): δ = 7.06 (d, J = 9.2 Hz, 1 H), 7.21 (t, J = 8.8 Hz, 2 H), 8.15-8.18 (m, 2 H), 8.35 (dd, J = 2.8, 9.2 Hz, 1 H), 8.62 (d, J = 2.8 Hz, 1 H), 8.87 (s, 1 H) ppm. ^{19}F{^{1}H} NMR (MeOD–d_4, 376.50 MHz): δ = -110.2 ppm. ^{51}V NMR (MeOD-d_4, 105.25 MHz): δ = -550.0 ppm. HRMS (ESI+, *m/z*) calculated for $C_{15}H_{12}N_3O_6FV$ $[M + H]^+$ *m/z* = 400.0150, found 400.0136. IR (cm^{-1}): 3444 (ν_{O-H}), 1604 ($\nu_{C=N}$), 1338 (ν_{NO2}), 952 ($\nu_{V=O}$).

Vanadium oxo complex VO-19

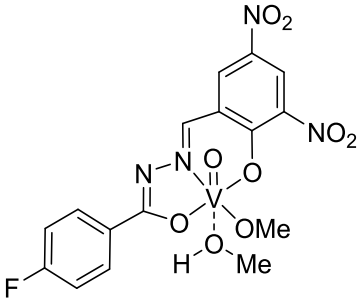

The reaction of **L-10** (0.075 g, 0.22 mmol) and $VO(OiPr)_3$ (55 µL, 0.23 mmol) gave the corresponding vanadium complex after about 40 min (0.073 g, 66% yield). ^{1}H NMR (MeOD–*d*$_4$, 400 MHz): δ = 7.23 (t, 2 H, *J* = 8.7 Hz), 8.18 (dd, 2 H, *J* = 5.6, 8.7 Hz), 8.85 (d, 1 H, *J* = 2.8 Hz), 8.91 (d, 1 H, *J* = 2.8 Hz), 8.96 (s, 1 H) ppm. ^{13}C{^{1}H} NMR ($(CD_3)_2CO$, 100 MHz): δ = 116.6 (d, *J* = 22.0 Hz), 124.6, 125.1, 127.6, 132.3 (d, *J* = 9.0 Hz), 133.1, 139.2, 139.8, 152.8, 160.4, 166.2 (d, *J* = 249.4 Hz), 173.1 ppm. ^{19}F{^{1}H} NMR (MeOD–*d*$_4$, 376.50 MHz): δ = -109.6 ppm. ^{51}V NMR (MeOD-*d*$_4$, 105.25 MHz): δ = -547.1 ppm. HRMS (ESI+, *m/z*) calculated for $C_{15}H_{11}N_4O_8FV$ $[M + H]^+$ *m/z* = 445.0001, found 445.0013. Elemental analysis calculated for $C_{15}H_{10}N_4O_8FV$: C, 40.56; H, 2.27; N, 12.61%; found: C, 40.85; H, 2.48; N, 12.71%. IR (cm^{-1}): 3354 (ν_{O-H}), 1616 ($\nu_{C=N}$), 1342 (ν_{NO2}), 981 ($\nu_{V=O}$).

Vanadium oxo complex VO-20

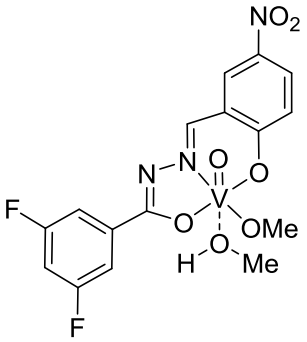

The reaction of **L-11** (0.160 g, 0.50 mmol in 5 mL of MeOH) and $VO(OiPr)_3$ (118 µL, 0.50 mmol) led to the corresponding complex in about 90 min (0.203 g, 97% yield). ^{1}H NMR (MeOD–*d*$_4$, 400 MHz): δ = 7.08 (d, 1 H, *J* = 9.2 Hz), 7.16 (tt, 1 H, *J* = 2.4, 8.8 Hz), 7.68 (dd, 2 H, *J* = 2.2, 8.2 Hz), 8.37 (dd, 1 H, *J* = 2.8, 9.2 Hz), 8.64 (d, 1 H, *J* = 2.8 Hz), 8.92 (s, 1 H) ppm. ^{19}F{^{1}H} NMR (MeOD–*d*$_4$, 376.50 MHz): δ = -111.1 ppm. ^{51}V NMR (MeOD-*d*$_4$, 105.25 MHz): δ = -551.3 ppm. HRMS (ESI+, *m/z*) calculated for $C_{15}H_{11}N_3O_6F_2V$ $[M + H]^+$ *m/z* = 418.0056, found 418.0069. Elemental analysis

calculated for $C_{15}H_{10}N_3O_6F_2V$: C, 43.18; H, 2.42; N, 10.07%; found: C, 42.84; H, 2.65; N, 9.69%. IR (cm^{-1}): 3421 (ν_{O-H}), 1610 ($\nu_{C=N}$), 1338 (ν_{NO2}), 995 ($\nu_{V=O}$).

Vanadium oxo complex VO-21

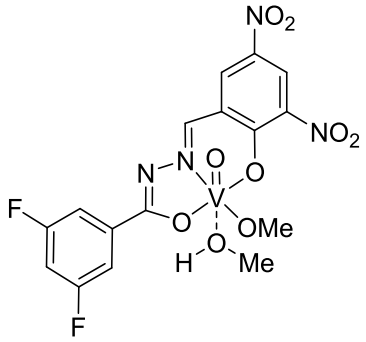

The reaction of **L-12** (0.183 g, 0.50 mmol in 10 mL of MeOH) and $VO(OiPr)_3$ (118 µL, 0.50 mmol) resulted in the corresponding complex after about 90 min (0.225 g, 97% yield). ^{1}H NMR (MeOD–*d*$_4$, 400 MHz): δ = 7.18 (t, 1 H, *J* = 8.9 Hz), 7.68 (d, 2 H, *J* = 6.0 Hz), 8.85 (s, 1 H), 8.91 (s, 1 H), 8.99 (s, 1 H) ppm. ^{19}F{^{1}H} NMR (MeOD–*d*$_4$, 376.50 MHz): δ = -110.8 ppm. ^{51}V NMR (MeOD-*d*$_4$, 105.25 MHz): δ = -548.3 ppm. HRMS (ESI+, *m/z*) calculated for $C_{15}H_{10}N_4O_8F_2V$ $[M + H]^+$ *m/z* = 462.9906, found 462.9906. Elemental analysis calculated for $C_{15}H_9N_4O_8F_2V$: C, 38.98; H, 1.96; N, 12.12%; found: C, 38.83; H, 1.35; N, 12.18%. IR (cm^{-1}): 3311 (ν_{O-H}), 1616 ($\nu_{C=N}$), 1342 (ν_{NO2}), 989 ($\nu_{V=O}$).

Vanadium oxo complex VO-22

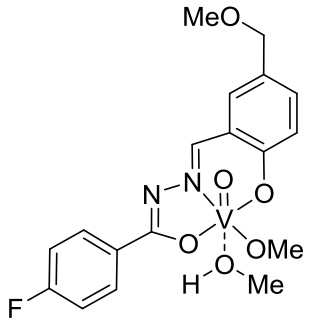

The reaction of **L-13** (0.150 g, 0.50 mmol in 5 mL of MeOH) and $VO(OiPr)_3$ (118 µL, 0.50 mmol) resulted in the corresponding complex after about 45 min (0.132 g, 66% yield). ^{1}H NMR (MeOD-*d*$_4$, 400 MHz): δ = 3.40 (s, 3 H), 4.46 (s, 2 H), 6.94 (d, 1 H, *J* = 8.4 Hz), 7.20 (t, 2 H, *J* = 8.8 Hz), 7.51 (dd, 1 H, *J* = 2.1, 8.5 Hz), 7.59 (d, 1 H, *J* = 1.9 Hz), 8.15 (dd, 2 H, *J* = 5.6, 8.8 Hz), 8.76 (s, 1 H) ppm. ^{13}C{^{1}H} NMR (MeOD-*d*$_4$, 100

MHz): δ = 58.2, 74.8, 116.3 (d, J = 22.0 Hz), 117.8, 121.5, 128.7 (m), 131.5, 132.0 (d, J = 8.9 Hz), 133.2, 135.4, 153.8, 166.3 (d, J = 248.8 Hz), 172.6 ppm. $^{19}F\{^{1}H\}$ NMR (MeOD-d_4, 376.50 MHz): δ = -110.7 ppm. ^{51}V NMR (MeOD-d_4, 105.25 MHz): δ = -546.4 ppm. HRMS (ESI+, *m/z*) calculated for $C_{17}H_{17}N_2O_5FV$ $[M+H]^+$ *m/z* = 399.0561, found 399.0554. Elemental analysis calculated for $C_{17}H_{16}N_2O_5FV$: C, 51.27; H, 4.05; N, 7.03%; found: C, 51.10; H, 4.16; N, 7.18%. IR (cm^{-1}): 3394 (ν_{O-H}), 1614 ($\nu_{C=N}$), 999 ($\nu_{V=O}$).

Vanadium oxo complex VO-23

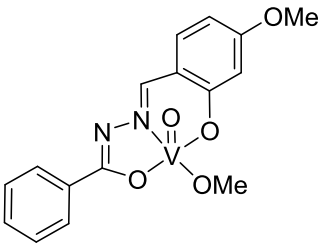

The reaction of **L-14** (0.135 g, 0.50 mmol in 5 mL MeOH) and $VO(OiPr)_3$ (118 µL, 0.50 mmol) resulted in the corresponding complex after about 2 h (0.177 g, 97% yield). ^{1}H NMR (MeOD-d_4, 400 MHz): δ = 3.88 (s, 3 H), 6.53 (d, 1 H, J = 2.2 Hz), 6.63 (dd, 1 H, J = 2.4, 8.7 Hz), 7.46 (t, 2 H, J = 7.3 Hz), 7.51 (dd, 2 H, J = 4.8, 8.7 Hz), 8.08 (d, 2 H, J = 6.9 Hz), 8.67 (s, 1 H) ppm. ^{51}V NMR (MeOD-d_4, 105.25 MHz): δ = -545.3 ppm. HRMS (ESI+, *m/z*) calculated for $C_{16}H_{16}N_2O_5V$ $[M+H]^+$ *m/z* = 367.0499, found 367.0491. Elemental analysis calculated for $C_{16}H_{15}N_2O_5V$: C, 52.47; H, 4.13; N, 7.65%; found: C, 52.75; H, 3.82; N, 7.89%. IR (cm^{-1}): 3446 (ν_{O-H}), 1591 ($\nu_{C=N}$), 995 ($\nu_{V=O}$).

Vanadium oxo complex VO-24

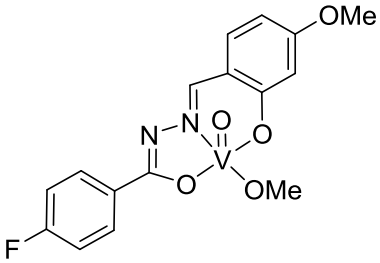

The reaction of **L-15** (0.030 g, 0.10 mmol in 1 mL MeOH) and $VO(OiPr)_3$ (24 µL, 0.10 mmol) resulted in the corresponding complex after about 2 h (0.035 g, 92% yield). ^{1}H NMR (MeOD-d_4, 400 MHz): δ = 3.87 (s, 3 H), 6.53 (d, 1 H, J = Hz), 6.63 (dd, 1 H, J = Hz), 7.19 (t, 2 H, J = 8.8 Hz), 7.51 (d, 1 H, J = 8.7 Hz), 8.10-8.14 (m, 2 H), 8.66 (s,

1 H) ppm.$^{19}F\{^{1}H\}$ NMR (MeOD-d_4, 376.50 MHz): δ = -111.1 ppm. ^{51}V NMR (MeOD-d_4, 105.25 MHz): δ = -545.3 ppm. HRMS (ESI+, *m/z*) calculated for $C_{16}H_{15}N_2O_5FV$ $[M+H]^+$ *m/z* = 385.0405, found 385.0415. IR (cm^{-1}): 3419 (ν_{O-H}), 1602 ($\nu_{C=N}$), 956 ($\nu_{V=O}$).

Vanadium oxo complex VO-25

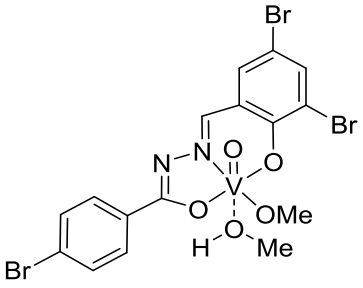

The reaction of **L-16** (0.238 g, 0.50 mmol in 5mL of MeOH) and $VO(OiPr)_3$ (118 µL, 0.50 mmol) resulted in the corresponding complex after ca. 90 min. (0.258 g, 90% yield). ^1H NMR (MeOD-d_4, 300 MHz): δ = 7.64 (d, 2 H, *J* = 8.4 Hz), 7.78 (s, 1 H), 7.89 (d, 1 H, *J* = 1.7 Hz), 8.01 (d, 2 H, *J* = 8.4 Hz), 8.73 (s, 1 H) ppm. ^{51}V NMR (MeOD-d_4, 105.25 MHz): δ = -544.9 ppm. HRMS (ESI+, *m/z*) calculated for $C_{15}H_{11}N_2O_4V^{79}Br_2{}^{81}Br$ $[M+H]^+$ *m/z* = 572.7688, found 572.7687. IR (cm^{-1}): 3404 (ν_{O-H}), 1601 ($\nu_{C=N}$), 1010 ($\nu_{V=O}$).

5.6.3 UV-vis Spectroscopic Studies

The UV-Vis spectroscopic studies were conducted using a Shimadzu UV 3600 UV-Vis-NIR spectrophotometer. For this purpose, 0.10 mM MeCN solutions of the ligands **L-7-16** were prepared. The UV-Vis analyses were performed using a 5 x 5 mm cuvette.

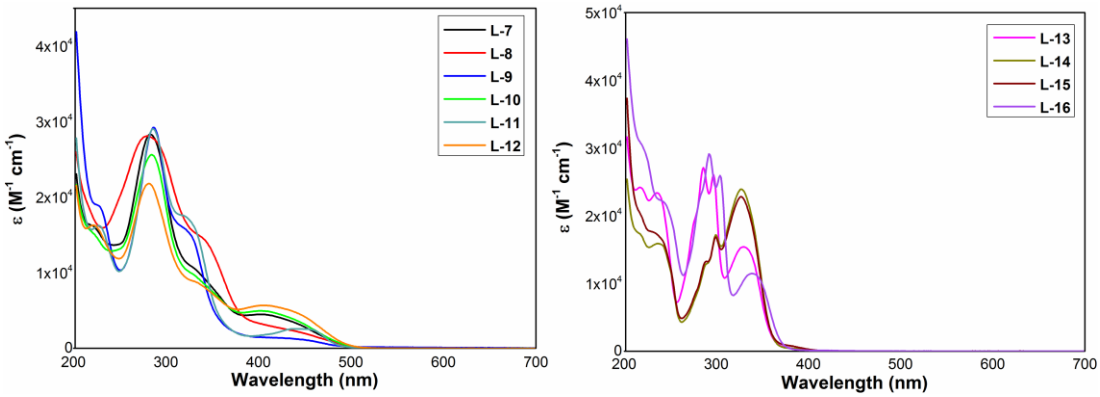

Figure 5.8. The UV-vis absorption spectra of 0.10 mM MeCN solutions of ligands **L-7** (black), **L-8** (red), **L-9** (blue), **L-10** (green), **L-11** (teal), and **L-12** (orange) (left), and **L-13** (pink), **L-14** (olive), **L-15** (burgundy), and **L-16** (violet) (right).

5.6.4 X-Ray Crystallographic Analysis

Single crystals of suitable dimensions of complexes **VO-16-25** were obtained by slow evaporation from MeOH. The crystals were then mounted on a quartz fiber and the X-Ray intensity data were measured on a Bruker X8 APEX system. Data were processed and corrected for Lorentz and polarization effects with SAINT[29] and for absorption effects with SADABS.[30] The structured were solved and refined with the SHELXTL suite of programs.[31] The structures were solved by direct method and refined for all data by full-matrix least-squares methods on F^2. All non-hydrogen atoms were subjected to anisotropic refinement. The hydrogen atoms were generated geometrically and allowed to ride on their respective parent atoms; they were assigned appropriate isotopic thermal parameters. Additional crystallographic parameters for each structure are tabulated in the Appendix.

References

1. (a) Cuthbertson, J.; MacMillan, D. W. C. *Nature* **2015**, *519*, 74−77. (b) Zuo, Z.; Ahneman, D. T.; Chu, L.; Terrett, J. A.; Doyle, A. G.; MacMillan, D. W. C. *Science* **2014**, *345*, 437−440. (c) Pirnot, M. T.; Rankic, D. A.; Martin, D. B. C.; MacMillan, D. W. C. *Science* **2013**, *339*, 1593−1596. (d) Corcoran, E. B.; Pirnot, M. T.; Lin, S.; Dreher, S. D.; DiRocco, D. A.; Davies, I. W.; Buchwald, S. L.; MacMillan, D. W. C. *Science* **2016**, *353*, 279−283. (e) Terrett, J.; Cuthbertson, J.; Shurtleff, V.; MacMillan, D. W. C. *Nature* **2015**, *524*, 330−334. (f) Shaw, M. H.; Shurtleff, V. W.; Terrett, J. A.; Cuthbertson, J. D.; MacMillan, D. W. C. *Science* **2016**, *352*, 1304−1308. (g) Johnston, C.; Smith, R.; Allmendinger, S.; MacMillan, D. W. C. *Nature* **2016**, *536*, 322−325. (h) Zuo, Z.; Cong, H.; Li, W.; Choi, J.; Fu, G. C.; MacMillan, D. W. C. *J. Am. Chem. Soc*. **2016**, *138*, 1832−1835. (i) Nawrat, C.; Jamison, C.; Slutskyy, Y.; MacMillan, D. W. C.; Overman, L. *J. Am. Chem. Soc*. **2015**, *137*, 11270−11273.

2. (a) Devery, J. J., III; Douglas, J.; Nguyen, J.; Cole, K.; Flowers Ii, R.; Stephenson, C. R. J. *Chem. Sci*. **2015**, *6*, 537−541. (b) Furst, L.; Narayanam, J. M.; Stephenson, C. R. *Angew. Chem., Int. Ed*. **2011**, *50*, 9655−9659. (c) Douglas, J.; Sevrin, M.; Stephenson, C. R. *J. Org. Process Res. Dev*. **2016**, *20*, 1134−1147.

3. Wang, J.; Zheng, N. *Angew. Chem. Int. Ed*. **2015**, *54*, 1–5.

4. (a) Maity, S.; Zhu, M.; Shinabery, R. S.; Zheng, N. *Angew. Chem.Int. Ed*. **2012**, *51*, 222–226. (b) Nguyen, T. H.; Maity, S.; Zheng, N. *Beilstein J. Org. Chem*. **2014**, *10*, 975–980; (c) Nguyen, T. H.; Morris, S. A.; Zheng, N. *Adv. Synth. Catal*. **2014**, *356*, 2831–2837.

5. Yayla, H. G.; Wang, H.; Tarantino, K. T.; Orbe, H. S.; Knowles, R. R. *J. Am. Chem. Soc.* **2016**, *138*, 10794–10797.

6. Guo, J. J.; Hu, A.; Chen, Y.; Sun, J.; Tang, H.; Zuo, Z.; *Angew. Chem. Int. Ed*. **2016**, *55*, 1–5.

7. Wang, D.; Mao, J.; Zhu, C. *Chem. Sci*. **2018**, *9*, 5805–5809.

8. Wei, G.; Zhang, C.; Bureš, F.; Ye, X.; Tan, C.-H.; Jiang, Z. *ACS Catal*. **2016**, *6*, 3708−3712.

9. Levin, M.; Kim, S.; Toste, F. D. *ACS Cent. Sci*. **2016**, *2*, 293−301.

10. Amador, A.; Sherbrook, E.; Yoon, T. *J. Am. Chem. Soc*. **2016**, *138*, 4722−4725.

11. Ashford, D. L.; Gish, M. K.; Vannucci, A. K.; Brennaman, M. K.; Templeton, J. L.; Papanikolas, J. M.; Meyer, T. J. *Chem. Rev*. **2015**, *115*, 13006–13049.

12. Pashaei, B.; Shahroosvand, H.; Graetzel, M.; Nazeeruddin, M. K. *Chem. Rev*., **2016**, *116*, 9485–9564.

13. Swierk, J. R.; Mallourk, T. E. *Chem. Soc. Rev*. **2013**, *42*, 2357–2387.

14. Li, G. C.; Swords, W. B.; Meyer, G. J. *J. Am. Chem. Soc*. **2017**, *139*, 14983–14991.

15. Brady, M. D.; Sampaio, R. N.; Wang, D. G.; Meyer, T. J.; Meyer, G. J. *J. Am. Chem. Soc.* **2017**, *139*, 15612–15615.

16. Visbal, R.; Gimeno, M. C. *Chem. Soc. Rev*. **2014**, *43*, 3551-3574.

17. Graetzel, M. *Acc. Chem. Res*. **2009**, *42*, 1788−1798.

18. Jou, J.-H.; Kumar, S.; Agrawal, A.; Li, T.-H.; Sahoo, S. *J. Mater. Chem. C* **2015**, *3*, 2974−3002.

19. Yam, V. W.-W.; Wong, K. M.-C.*Chem. Commun*. **2011**, *47*,11579−11592.

20. Yersin, H.; Rausch, A. F.; Czerwieniec, R.; Hofbeck, T.; Fischer, T. *Coord. Chem. Rev*. **2011**, *255*, 2622−2652.

21. Chi, Y.; Chou, P.-T. *Chem. Soc. Rev*. **2010**, *39*, 638−655.

22. Gazi, S.; Hung Ng, W.; Ganguly, R.; Putra Moeljadi, A.; Hirao, H.; Soo, H. S. *Chem. Sci*. **2015**, *6*, 7130−7142.

23. Gazi, S.; Đokić, M.; Moeljadi, A. M. P.; Ganguly, R.; Hirao, H.; Soo, H. S. *ACS Catal*. **2017**, *7*, 4682−4691.

24. Zhang, G.; Scott, B. L.; Wu, R.; Silks, L. A. P.; Hanson, S. K. *Inorg. Chem*. **2012**, *51*, 7354−7361.

25. Sun, S.; Toste, D. *Angew. Chem. Int. Ed*. **2010**, *49*, 3791−3794.

26. Hanson, S. K.; Baker, R. T.; Gordon, J. C.; Scott, B. L.; Sutton, A. D.; Thorn, D. L.; *J. Am. Chem. Soc*. **2009**, *131*, 428−429.

27. Wang, L.; Qin, W.; Tang, X.; Dou, W.; Liu, W. *J. Phys. Chem. A* **2011**, **115**, 1609–1616.

28. Perlepe, P. S.; Cunha-Silva, L.; Gagnon, K. J.; Teat, S. J.; Lampropoulos, C.; Escuer, A.; Stamatatos, T. C. *Inorg. Chem*. **2016**, *55*, 1270−1277.

29. SAINT+ version 6.22a; Bruker AXS Inc.: Madison, WI, **2001**.

30. Sheldrick, G. M. SADABS; **1996**.

31. SHELXTL version 5.1; Bruker AXS Inc.: Madison, WI, **1997**.

CHAPTER 6

CONCLUSION AND FUTURE WORK

6.1 Thesis Summary

Firstly, we have shown that the systematic modifications of the originally reported ligand **L-1** by the introduction of EWGs at ligand sites with highest HOMO density lead to the corresponding vanadium complexes with significantly improved catalytic rates compared to the previously reported **VO-10**. The detailed kinetics experiments helped us identify the fastest catalyst in the series, while the computational DFT studies yielded explanations for the enhanced reactivity of new catalysts.

With the optimal catalyst in our hands, we moved on to expand the scope of our photocatalytic system beyond lignin model compounds. Based on our prior DFT results, we started examining the reactivity of alcohols that would generate highly stabilized benzyl radicals upon C-C bond cleavage. The screening included more than 20 substrates and high tolerance to various functional groups was established. Subsequently, substrates which generate less stable tertiary, secondary, and even primary radicals were tested as well. Remarkably, in some cases, a second C-C bond cleavage of the newly formed alcohol product was observed, indicating a possibility of utilizing our technology to perform a cascade-type C-C bond activation in macromolecular alcohols.

Finally, the ease of preparation of hydrazone-amide ligands allowed us to quickly synthesize ten new vanadium complexes (**VO-16-25**) with different types of substitutions on the ligand moiety. Remarkably, complexes with electron-donating groups on the ligand exhibited unique pentacoordinate geometry in the solid state, which was verified by X-ray crystallographic analysis. Additional to distinct structural characteristics, the vanadium complexes display different photophysical characteristics, as well as different reactivities towards C-C bond activation. These findings suggest that various, desirable properties of the vanadium complexes can be achieved by carefully introducing the correct type of substituents at the specific sites on the ligand.

With the aim of investigating potential alternatives to water oxidation half-reaction that could be incorporated in AP systems for production of solar fuels and chemicals, we have showcased a noteworthy photocatalytic system comprising oxovanadium complexes that can induce highly selective C-C single bond scission in a number of aliphatic alcohols under mild conditions. As opposed to O_2 production from solar water splitting, our photocatalytic system can generate synthetically useful oxygenated

compounds that include desirable carbonyl and alcohol functionalities. Furthermore, the oxovanadium catalytic system could potentially serve as a source of electrons for a reductive half-reaction of an integrated AP unit that would generate solar fuels as well. In addition, as a part of the AP construct, our vanadium catalyst would also benefit from recyclability and would not be restricted by the choice of solvent. This possibility of converting our oxidative photocatalytic system into a complete AP unit is currently ongoing and the preliminary work regarding the translation of a molecular into a heterogeneous catalyst will be discussed in the following section.

6.2 Future Work

Although the vanadium complexes shown in preceding chapters have demonstrated unique reactivity towards C-C bond activation in a broad range of substrates under mild conditions, as molecular catalysts, they cannot be easily separated from the reaction products and reused in subsequent reactions. Furthermore, a considerable number of high-profile substrates are insoluble in acetonitrile, a solvent that readily dissolves most of our catalysts and was identified as the optimal solvent for our homogeneous photocatalytic conditions. In attempt to overcome these difficulties and make our catalytic system even more applicable, we have turned to developing heterogeneous systems by anchoring the vanadium complexes onto insoluble solid supports. Such systems should be easily separated from the reaction products by centrifuging and would potentially allow for a wider choice of solvents since the solubility of the catalyst would not limit the solvent choice anymore.

The vanadium complexes **VO-29** and **VO-30** (Figure 6.1) were developed with the intention of anchoring on various solid supports. Photocatalyst **VO-29** possesses an alcohol group on one of its aryl rings that can form chemical bonds with different surface groups of the solid support.[1] For instance, an isocyanate-functionalized polystyrene can react with the alcohol group of **VO-29** to form a carbamate bond and thus, incorporate the vanadium catalyst.[2-4]

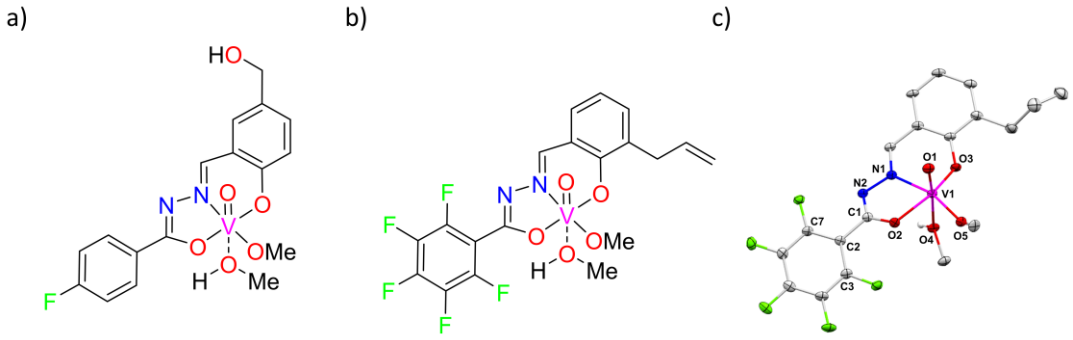

Figure 6.1. The proposed structures of (a) complex **VO-29** containing alcohol anchoring group, (b) **VO-30** with an alkene anchoring group, and (c) single crystal X-ray diffraction structure of **VO-30**. The vanadium, nitrogen, oxygen, and fluorine atoms are shown in pink, blue, red, and green, respectively.

To test this hypothesis, we have performed the reaction between the two materials and the reaction product was then thoroughly characterized by the means of Fourier transform infrared spectroscopy (FT-IR), X-ray photoelectron spectroscopy (XPS), and UV-visible diffuse reflectance spectroscopy (UV-vis DRS). Details regarding the chemical anchoring experiment are summarized in the experimental section. The initial FT-IR spectroscopic analyses revealed that the O=C=N- bond stretching frequency band (at ca. 2200 cm^{-1}) present in the sample of isocyanate-functionalized polystyrene (Figure 6.2a) has disappeared after the reaction, and that new bands around 1700 and 3500 cm^{-1} have appeared (Figure 6.2b). The positions of the new bands are consistent with the literature values of the C=O and -N-H stretching frequencies of the carbamate R-NH-C=O group.[3]

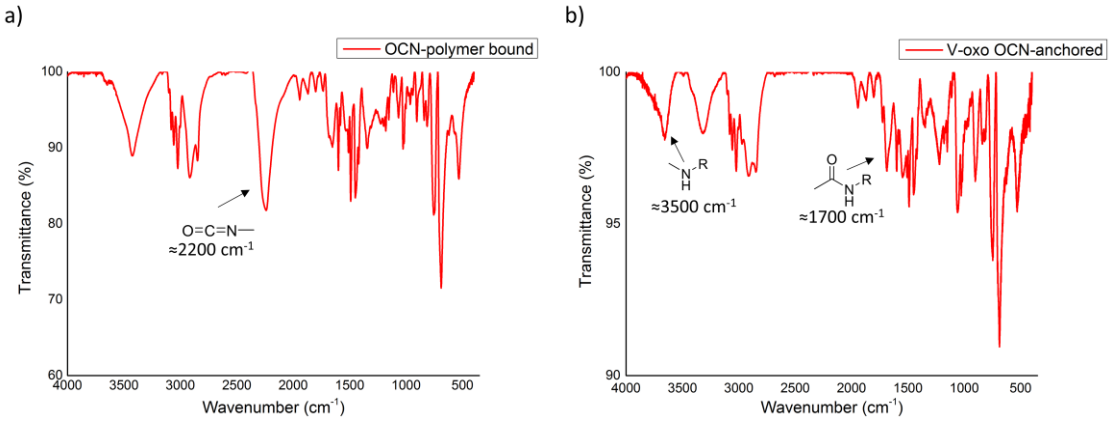

Figure 6.2. FT-IR spectra in transmittance mode of (a) isocyanate-functionlalized polystyrene, and (b) isocyanate-functionalized polystyrene after the anchoring reaction with **VO-29**. The most significant bond stretching frequencies are marked with arrows.

Additionally, the UV-vis DRS analysis showed a broad band around 480 nm that can be attributed to the LMCT band of vanadium catalysts,[5,6] while the spectrum of isocyanate-functionalized polystyrene showed the absence of such a peak at the same position (Figure 6.3).

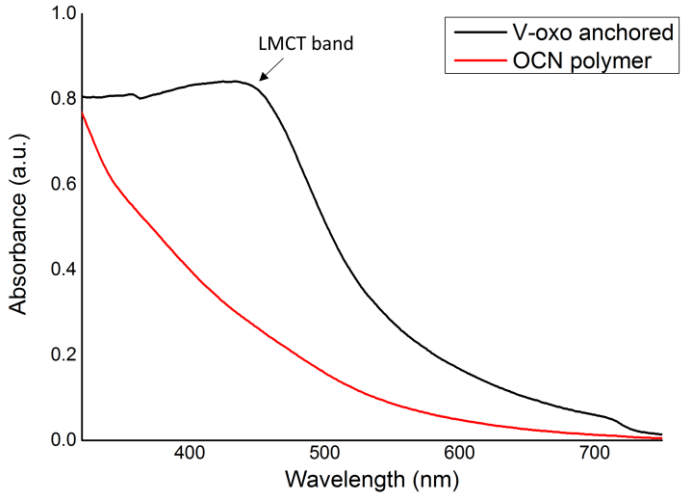

Figure 6.3. The UV-vis DRS spectra of isocyanate-functionalized polystyrene before (red line), and after anchoring with **VO-29** (black line) plotted as absorbance values. The arrow indicates the position of the LMCT band typical of our vanadium(V) complexes.

Finally, the XPS measurements verified the presence of vanadium on the surface of the composite material with the two peaks characteristic of V 2p core energy levels (Figure 6.4b).[7] Furthermore, the measured binding energy values for $2p_{3/2}$ and $2p_{1/2}$ core levels were 523 and 516 eV, respectively, indicating that V^V oxidation state should be retained after the anchoring.[7] All the performed characterization measurements have provided information which designate that the chemical anchoring between the alcohol group of **VO-29** and isocyanate of the polystyrene has occurred to a certain extent. The future work will also focus on determining the amount of the vanadium complex present on the polymer's surface.

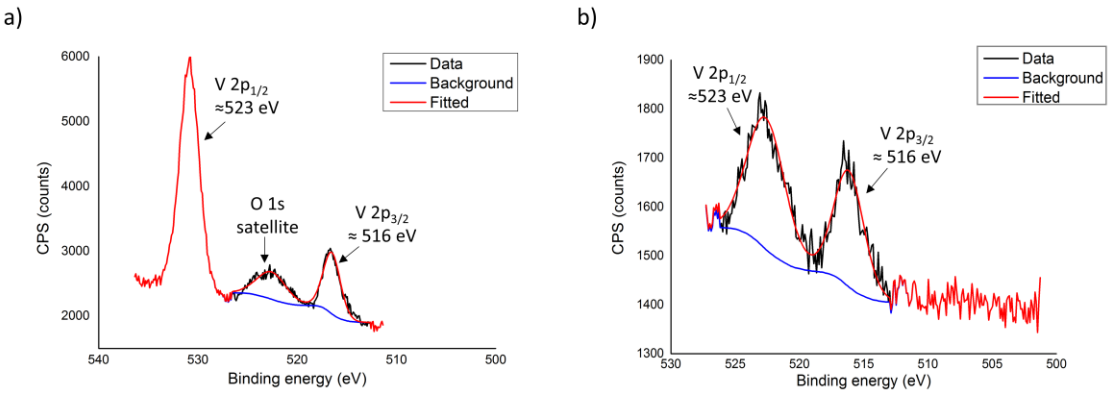

Figure 6.4. The XPS spectra of (a) vanadium complex **VO-29**, and (b) product of the anchoring reaction of **VO-29** onto isocyanate-functionalized polystyrene. The binding energies of vanadium 2p core levels are shown in the figure.

With the prepared composite at our disposal, we attempted to test its reactivity with our well-established substrate **33**. For the purpose of conducting the reaction, 10 mg of the composite material were suspended in 1 mL of CD_3CN, along with 14 μL of substrate (0.10 mmol), 40 μL of 1,4-CHD (0.40 mmol), and 10.6 μL (0.10 mmol) of 1,1,2,2-tetrachloroethane as internal standard. The reaction mixture was stirred in a vial fitted with a needle to supply aerobic atmosphere while being irradiated by white LEDs for 24 h. After 24 h of irradiation, the composite was removed by centrifuging, and the supernatant solution was used in ^{1}H NMR spectroscopic experiments to determine the product yields and substrate conversion. The preliminary results showed that after 24 h of irradiation there was ca. 25% substrate conversion and 13% of **34**, 7% of **27**, 13% of **2**, as well as 2% of **35** formation (Scheme 6.1). The experiments regarding the optimization of reaction conditions and a possibility of utilizing different solvents are currently ongoing.

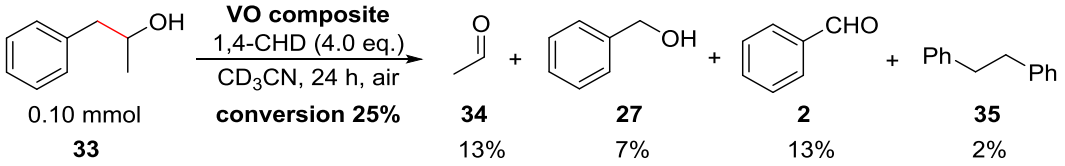

Scheme 6.1. Product distribution of C-C bond cleavage in **33** with a heterogeneous catalyst.

Another complex that was designed and prepared for anchoring on a solid support is **VO-30** that bears an alkene moiety on its ligand. The alkenes are known to react with surface -OH groups of metal oxides under thermal conditions resulting in a formation of the ether bonds.[8,9] Details regarding the synthesis of **VO-30** and its ligand are

described in the experimental section and the anchoring experiments involving **VO-30** and various metal oxides are currently being explored by our group.

In addition to developing a heterogeneous system, another aspect of our photocatalytic system that could be explored in the future is the possible functionalization of the transient alkyl radical generated upon C-C bond activation. In our current protocols, the aerobic oxygen binds to the alkyl radical leading to the formation of the alkyl peroxo radical, which subsequently transforms into an oxygenated product. However, if the transient radical could be successfully functionalized by other means, it would allow for a plethora of synthetically, and even medicinally useful products derived from alcohols by photoredox catalysis under exceptionally mild conditions and with inexpensive catalysts.

6.3 Experimental Procedures

6.3.1 General Information

The vanadium complexes and ligands were prepared under a N_2 atmosphere using standard Schlenk techniques. Other synthetic procedures were conducted under aerobic conditions unless stated otherwise. The chemicals used in the experiments were purchased from Sigma-Aldrich and were used as received. Deuterated solvents were purchased from Cambridge Isotope Laboratories and were used as received. The ^{1}H, ^{13}C, ^{19}F, and ^{51}V NMR spectroscopic data were obtained using Bruker AVANCE spectrometers operating at 300, 400, and 500 MHz. The resulting ^{1}H and ^{13}C NMR chemical shifts (δ reported in ppm) were referenced according to the residual solvent signal(s) ($CDCl_3$ = 7.26 ppm for ^{1}H and 77.2 ppm for ^{13}C; CD_3CN = 1.94 ppm for ^{1}H and 118.3 ppm for ^{13}C; MeOD-d_4 = 3.31 ppm for ^{1}H and 49.2 ppm for ^{13}C; DMSO-d_6 = 2.50 ppm for ^{1}H and 39.52 ppm for ^{13}C). The ^{51}V NMR chemical shift was referenced relative to V^{v} $(O)(Cl)_3$ external standard (δ = 0.0 ppm). Crystallographic data were collected on a Bruker X8 CCD diffractometer. The structures were solved and refined using the Bruker SHELXTL software package. High-resolution electrospray ionization mass spectra (HR-ESIMS) were obtained using a Waters Q-TOF Premier mass spectrometer. UV-visible diffuse reflectance spectra were collected with a Shimadzu UV-3600 UV-VIS-NIR spectrophotometer mounted with an ISR-3100 integrating sphere attachment. The sample was applied onto the surface of the barium sulfate powder that was packed on a sample holder of the ISR-3100 integrating sphere

attachment. Barium sulfate was used as a background reference. FT-IR spectroscopy measurements were carried out with Bruker Vertex 80v and Shimadzu IRPrestige-21 FT-IR spectrometers. In a typical experiment, about 1.5 mg of the sample were mixed with about 30.0 mg of potassium bromide (KBr) to make a pellet. The pellets were made with a Specac Atlas manual hydraulic press 15T at 10 ton pressure. The FT-IR experiments were conducted in transmission mode with data collected from 400 to 4000 cm^{-1}. XPS data were acquired using a Phoibos 100 spectrometer and a Mg X-ray source (SPECS, Germany) working at 12.5 kV equipped with dual Al/Mg anodes. The O 1s signal was also prominent in the XPS spectra due to the use of a carbon tape to attach samples onto the specimen plates.

6.3.2 Synthetic Procedures and Spectroscopic Data

General procedure for the synthesis of ligands

In each reaction, to a stirring, heated solution of aryl hydrazide in absolute EtOH under N_2 was added a solution of the corresponding aryl aldehyde in EtOH dropwise. The reaction mixture was then stirred at reflux for a specific amount of time detailed below (between 3 and 36 h). The ligand was subsequently either precipitated out of the mixture or was obtained by removing the solvent under vacuum. The as-synthesized ligands were of sufficient purity to be used in the complexation reactions without any further purification.

4-Fluoro-*N'*-(2-hydroxy-5-(hydroxymethyl)benzylidene)benzohydrazide (L-17)

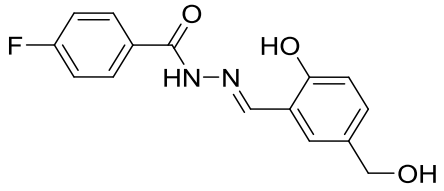

To a heated solution of 4-fluorobenzohydrazide (0.46 g, 2.9 mmol) in EtOH (20 mL) was added dropwise an EtOH solution of 2-hydroxy-5-(hydroxymethyl)benzaldehyde (0.45 g, 2.9 mmol in 10 mL of EtOH) and the mixture was stirred at reflux for 36 h. After the reaction was completed, the solvent was removed under reduced pressure and the crude product was obtained as brown solid. The crude was dissolved in EtOAc and precipitated with *n*-hexane to yield the ligand as a pale brown solid (0.60 g, 70% yield).

^{1}H NMR (DMSO-d_6, 500 MHz): δ = 4.43 (d, J = 5.4 Hz, 2 H), 5.11 (t, J = 5.6 Hz, 1 H), 6.89 (d, J = 8.3 Hz, 1 H), 7.24 (d, J = 8.4 Hz, 1 H), 7.38 (t, J = 8.7 Hz, 2 H), 7.51 (s, 1 H), 8.02 (dd, J = 5.6, 8.4 Hz, 2 H), 8.63 (s, 1 H), 11.06 (s, 1 H), 12.08 (s, 1 H) ppm. ^{13}C{^{1}H} NMR (DMSO-d_6, 100 MHz): δ = 62.4, 115.6 (d, J = 21.8 Hz), 116.1, 118.3, 127.4, 129.4 (d, J = 2.8 Hz), 130.1, 130.4 (d, J = 9.1 Hz), 133.4, 148.1, 156.3, 161.8, 163.7 (d, J = 248.0 Hz) ppm. ^{19}F{^{1}H} NMR (DMSO-d_6, 376.50 MHz): δ = -107.6 ppm. HRMS (ESI+, *m/z*) calculated for $C_{15}H_{14}FN_2O_3$ $[M+H]^+$ *m/z* = 289.0988, found 289.0994. IR (cm^{-1}): 3269 ($\nu_{O\text{-}H}$), 3035 ($\nu_{N\text{-}H}$), 1639 ($\nu_{C=N}$).

***N'*-(3-allyl-2-hydroxybenzylidene)-2,3,4,5,6-pentafluorobenzohydrazide (L-18)**

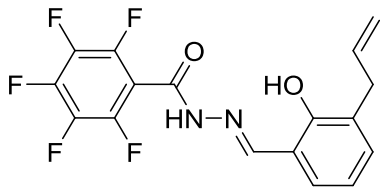

To a heated solution of 2,3,4,5,6-pentafluorobenzohydrazide (0.227 g, 1.0 mmol) in absolute EtOH (3 mL) was added dropwise an EtOH solution of 3-allyl-2-hydroxybenzaldehyde (147 μL, 1.0 mmol in 2 mL EtOH). The reaction mixture was stirred at reflux for 3 h. After the reaction was completed, the solvent was removed under reduced pressure, and the crude solid product was washed with *n*-hexane. The final product was isolated as a white solid (0.289 g, 78% yield). ^{1}H NMR (CD_3CN, 400 MHz): δ = 3.45 (d, J = 6.7 Hz, 2 H), 5.07 (m, 2 H), 6.04 (m, 1 H), 6.92 (m, 1 H), 7.26 (d, J = 7.6 Hz, 2 H), 8.34 (s, 1 H), 10.55 (bs, 1 H), 11.47 (s, 1 H) ppm. ^{13}C{^{1}H} NMR (CD_3CN, 100 MHz): δ = ppm. ^{19}F{^{1}H} NMR (CD_3CN, 282.40 MHz): δ = -161.8 (m, 2 F), -151.9 (t, J = 19.8 Hz, 1 F), -141.5 (m, 2 F) ppm. HRMS (ESI+, *m/z*) calculated for $C_{17}H_{12}F_5N_2O_2$ $[M+H]^+$ *m/z* = 371.0819, found 371.0822.

General procedure for the synthesis of vanadium oxo complexes

In each reaction, to a heated, stirring solution of the ligand in MeOH was added the vanadium(V) precursor, VO(O*i*Pr)$_3$, under N_2, which led to an immediate change of the reaction color from brown to dark red. The reaction mixture was stirred under reflux for ca. 90 min. Subsequently, the solvent was removed under vacuum and the remaining dark solid product was obtained. The solid was then re-dissolved in methanol and filtered before finally obtaining the complex by solvent evaporation.

Vanadium oxo complex VO-29

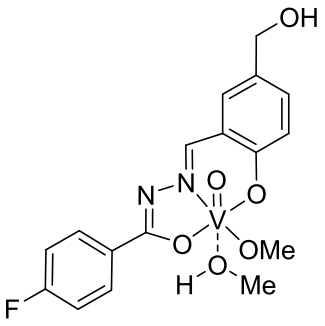

The reaction of **L-17** (0.15 g, 0.52 mmol) and $VO(OiPr)_3$ (114 μL, 0.52 mmol) resulted in the formation of the corresponding complex (0.38 g, 95% yield). ^{1}H NMR (MeOD-*d*$_4$, 400 MHz): δ = 4.61 (s, 2 H), 6.94 (d, *J* = 8.4 Hz, 1 H), 7.20 (t, *J* = 8.8 Hz, 2 H), 7.53 (dd, *J* = 2.1, 8.5 Hz, 1 H), 7.60 (d, *J* = 1.9 Hz, 1 H), 8.15 (m, 2 H), 8.76 (s, 1 H) ppm. ^{13}C{^{1}H} NMR (MeOD-*d*$_4$, 100 MHz): δ = 64.6, 116.4 (d, *J* = 29.3 Hz), 117.9, 121.6, 128.9, 132.1, 132.3 (d, *J* = 5.5 Hz), 134.8, 135.1, 154.1, 164.8, 168.1, 172.7 ppm. ^{19}F{^{1}H} NMR (MeOD-*d*$_4$, 376.50 MHz): δ = -110.7 ppm. ^{51}V NMR (MeOD-*d*$_4$, 105.25 MHz): δ = -545.8 ppm. HRMS (ESI+, *m/z*) calculated for $C_{16}H_{15}FN_2O_5V$ $[M+H]^+$ *m/z* = 385.0405, found 385.0399. IR (cm^{-1}): 3415 (ν_{O-H}), 1612 ($\nu_{C=N}$), 975 ($\nu_{V=O}$).

Vanadium oxo complex VO-30

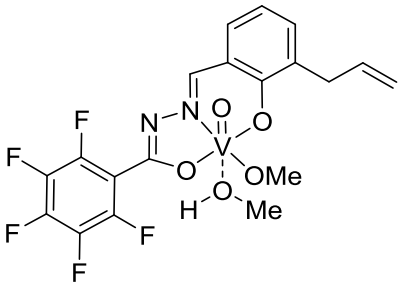

The reaction of **L-18** (0.185 g, 0.50 mmol in 5 mL of MeOH) and $VO(OiPr)_3$ (118 μL, 0.50 mmol) resulted in the formation of the corresponding complex (0.206 g, 88% yield). ^{1}H NMR (MeOD-*d*$_4$, 300 MHz): δ = 3.51 (m, 2 H), 5.10 (m, 2 H), 6.06 (m, 1 H), 6.99 (t, *J* = 7.6 Hz, 1 H), 7.50 (m, 2 H), 8.76 (s, 1 H) ppm. ^{13}C{^{1}H} NMR (MeOD-*d*$_4$, 100 MHz): δ = ppm. ^{19}F{^{1}H} NMR (MeOD-*d*$_4$, 282.40 MHz): δ = -164.5 (m, 2 F), -154.8 (tt, *J* = 3.0, 20.1 Hz, 1 F), -140.5 (m, 2 F) ppm. ^{51}V NMR (MeOD-*d*$_4$, 105.25 MHz): δ = -545.3 ppm. HRMS (ESI+, *m/z*) calculated for $C_{18}H_{13}F5N_2O_4V$ $[M+H]^+$ *m/z* = 467.0235, found 467.0224. IR (cm^{-1}): 3404 (ν_{O-H}), 1606 ($\nu_{C=N}$), 991 ($\nu_{V=O}$).

Procedure for the anchoring reaction of VO-29 on isocyanate-functionalized polystyrene

To a heated solution of **VO-29** (0.030 g, 0.080 mmol) in 5 mL of anhydrous THF was added 0.025 g (0.038-0.063 mmol) of isocyanate-functionalized polystyrene and the reaction mixture was stirred at reflux for 6 h. After the reaction, the suspension was filtered, solids were collected, and washed repeatedly with MeOH (3 x 5 mL), THF (3 x 5 mL), and then with MeCN (3 x 5 mL). The solid product was subsequently dried under reduced pressure yielding the desired product as a brownish solid (0.040 g).

6.3.3 X-Ray Crystallographic Analysis

Single crystals of suitable dimensions of complex **VO-30** were obtained by slow evaporation from MeOH. The crystals were mounted on a quartz fiber and the X-Ray intensity data were measured on a Bruker X8 APEX system. Data were processed and corrected for Lorentz and polarization effects with SAINT[10] and for absorption effects with SADABS.[11] The structure was solved and refined with the SHELXTL suite of programs.[12] The structure was solved by direct method and refined for all data by full-matrix least-squares methods on F^2. All non-hydrogen atoms were subjected to anisotropic refinement. The hydrogen atoms were generated geometrically and allowed to ride on their respective parent atoms; they were assigned appropriate isotopic thermal parameters. Additional crystallographic parameters of **VO-30** are tabulated in the Appendix.

References

1. Soo, H. S.; Gazi, S.; Đokić, M. Selective Carbon-Carbon Bond Cleavage by Earth Abundant Vanadium Compounds Under Visible Light Photocatalysis, WO/2016/126207, 2016.
2. Mikhaylov, V. N.; Sorokoumov, V. N.; Korvinson, K. A.; Novikov, A. S.; Balova, I. A. *Organometallics* **2016**, *35*, 1684−1697.
3. Carrara, C.; Sala, M. C.; Caneva, E.; Cauteruccio, S.; Licandro, E. *Org. Lett*. **2014**, *16*, 460−463.
4. Ou, B.; Li, D.; Liu, Q.; Zhou, Z.; Liao, B. *Mater. Chem. Phys*. **2012**, *135*, 1104−1107.
5. Gazi, S.; Ng, W. K. H.; Ganguly, R.; Moeljadi. A. M. P.; Hirao, H.; Soo, H. S. *Chem. Sci*. **2015**, *6*, 7130−7142.
6. Gazi, S.; Đokić, M.; Moeljadi, A. M. P.; Ganguly, R.; Hirao, H.; Soo, H. S. *ACS Catal*. **2017**, *7*, 4682−4691.
7. Biesinger, M. C.; Lau, L. W. M.; Gerson, A. R.; Smart, R. St. C. *App. Surf. Sci*. **2010**, *257*, 887−898.
8. Hanna, C. M.; Sanborn, C. D.; Ardo, S.; Yang, J. Y. *ACS Appl. Mater. Interfaces* **2018**, *10*, 13211−13217.
9. Pujari, S. P.; Scheres, L.; van Lagen, B.; Zuilhof, H. *Langmuir* **2013**, *29*, 10393−10404.
10. SAINT+ version 6.22a; Bruker AXS Inc.: Madison, WI, **2001**.
11. Sheldrick, G. M. SADABS; **1996**.
12. SHELXTL version 5.1; Bruker AXS Inc.: Madison, WI, **1997**.

APPENDIX

NMR Spectra of Compounds

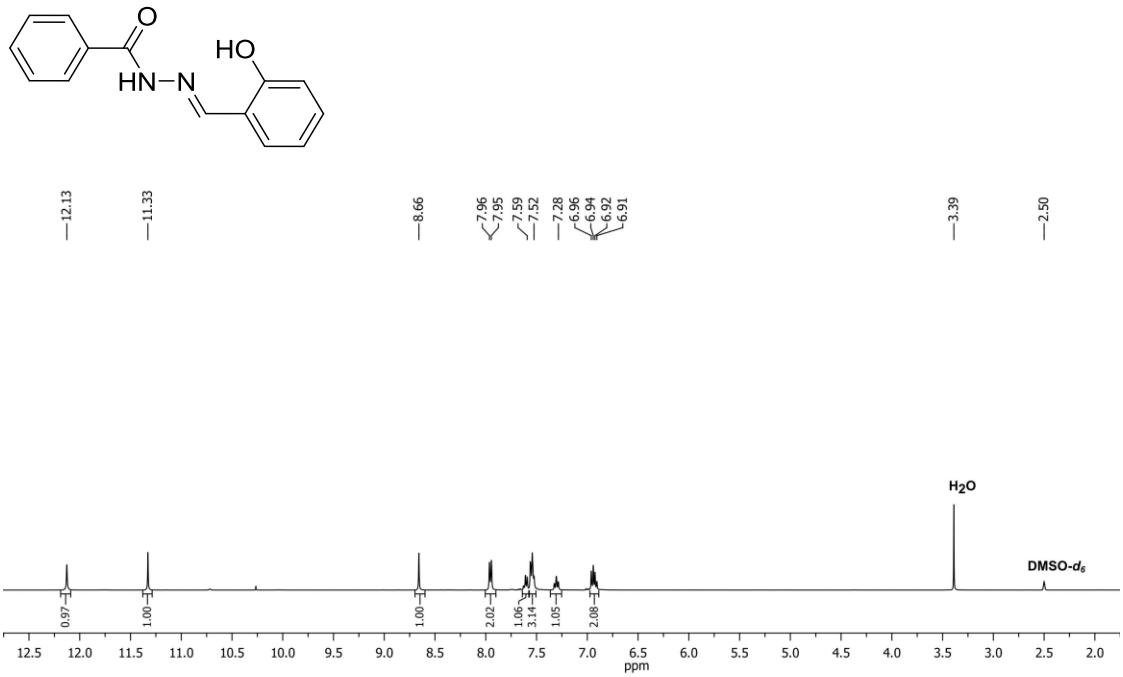

Figure A.1. The ^{1}H NMR spectrum of **L-2** (DMSO-d_6, 400 MHz).

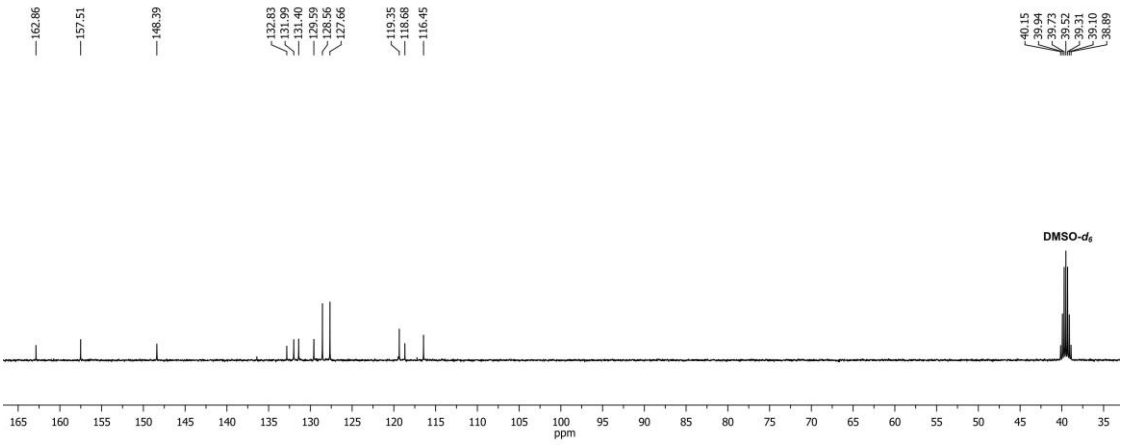

Figure A.2. The ^{13}C{^{1}H} NMR spectrum of **L-2** (DMSO-d_6, 100 MHz).

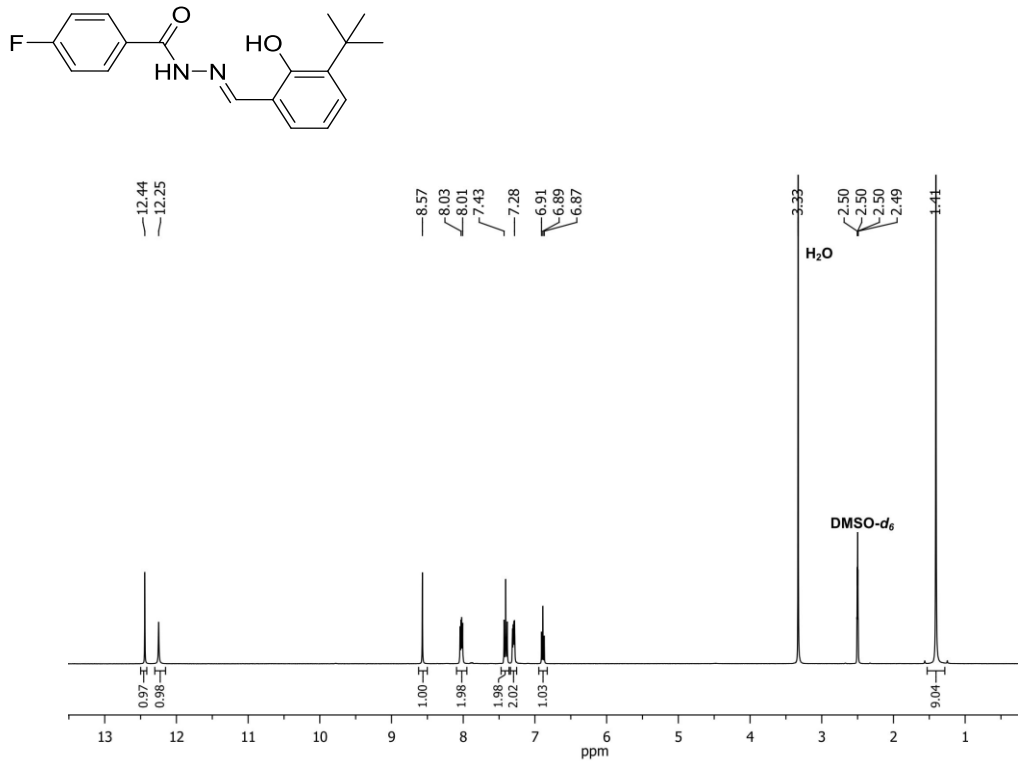

Figure A.3. The ^{1}H NMR spectrum of **L-3** (DMSO-d_6, 400 MHz).

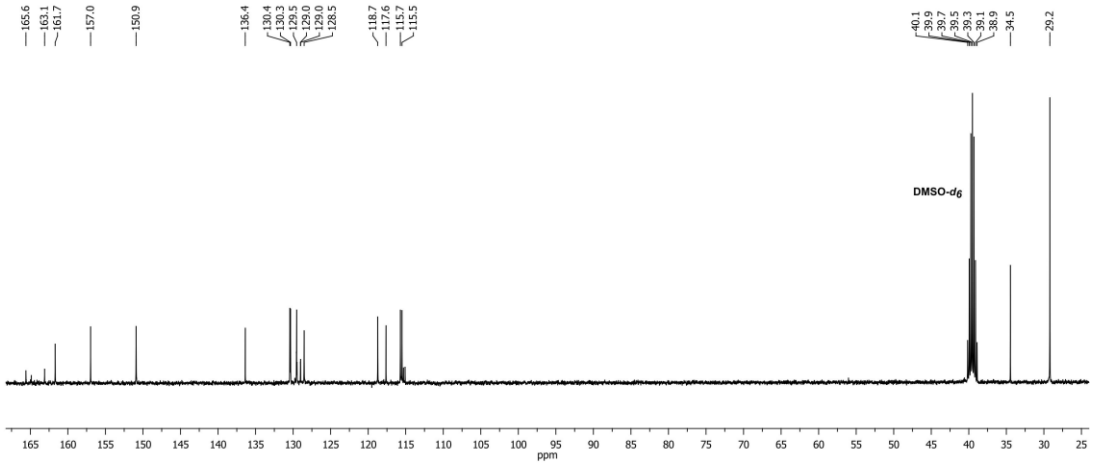

Figure A.4. The ^{13}C{^{1}H} NMR spectrum of **L-3** (DMSO-d_6, 100 MHz).

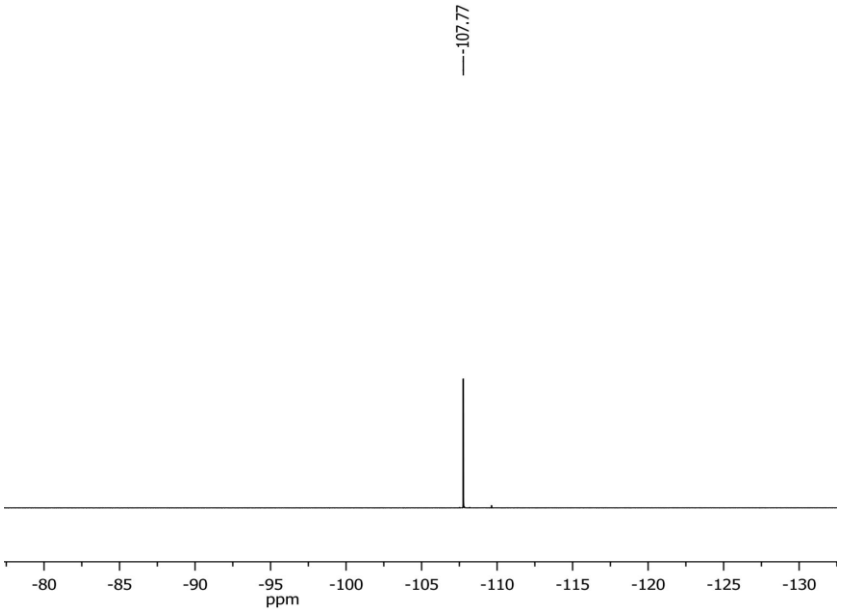

Figure A.5. The $^{19}F\{^{1}H\}$ NMR spectrum of **L-3** (DMSO-d_6, 376.50 MHz).

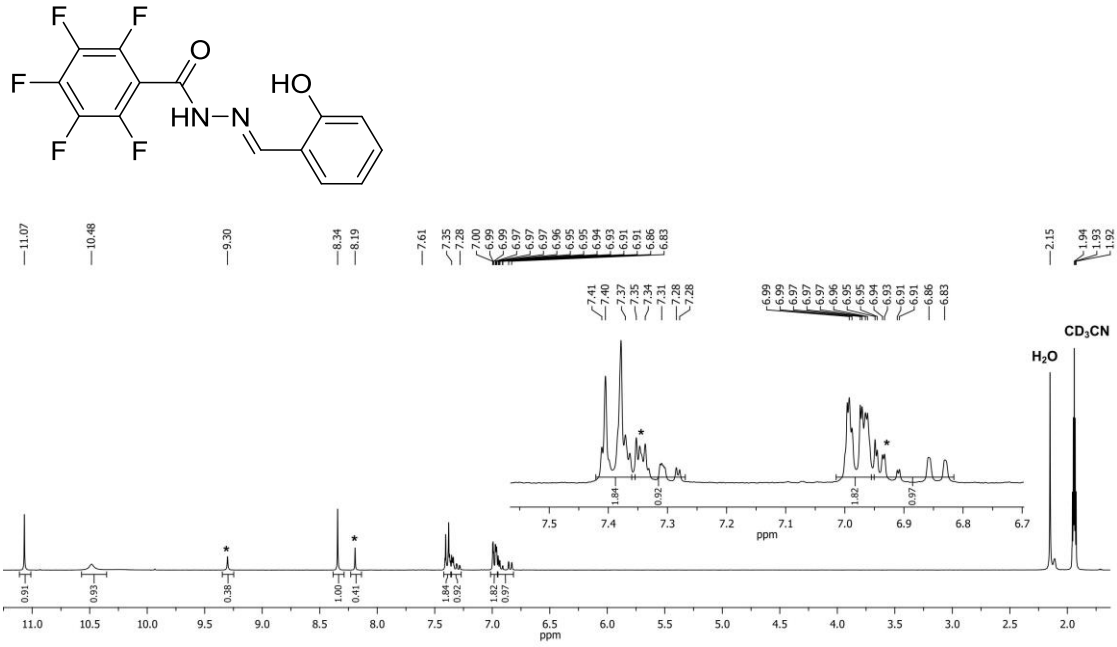

Figure A.6. The ^{1}H NMR spectrum of **L-4** (CD_3CN, 300 MHz). Peaks marked with asterisks correspond to the hydrazone-imidate form. The inset shows an expanded view of the aromatic region.

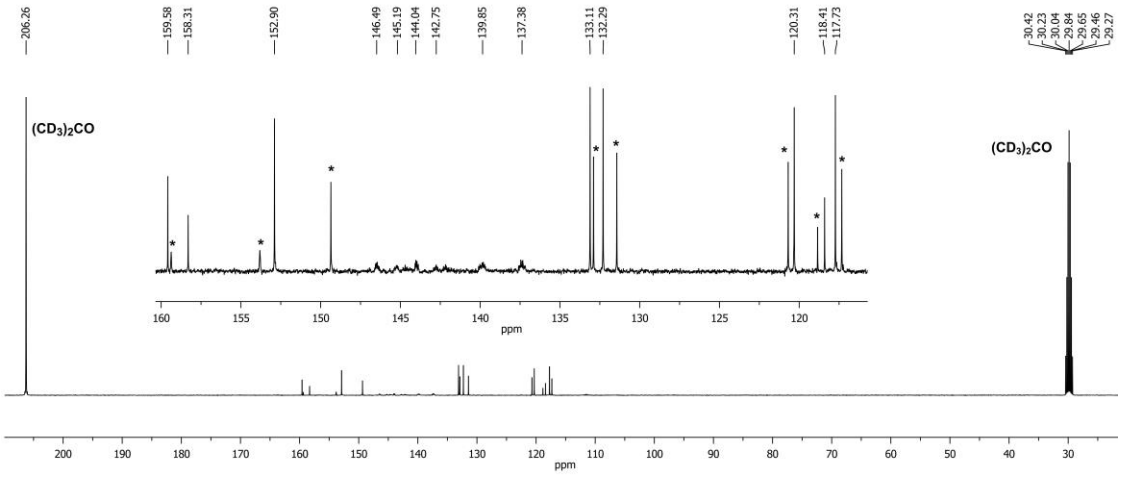

Figure A.7. The $^{13}C\{^{1}H\}$ NMR spectrum of **L-4** ($(CD_3)_2CO$, 100 MHz). Peaks marked with asterisks correspond to the hydrazone-imidate form. The inset shows the multiplets arising from the pentafluoro carbons coupling with ^{19}F nuclei more clearly.

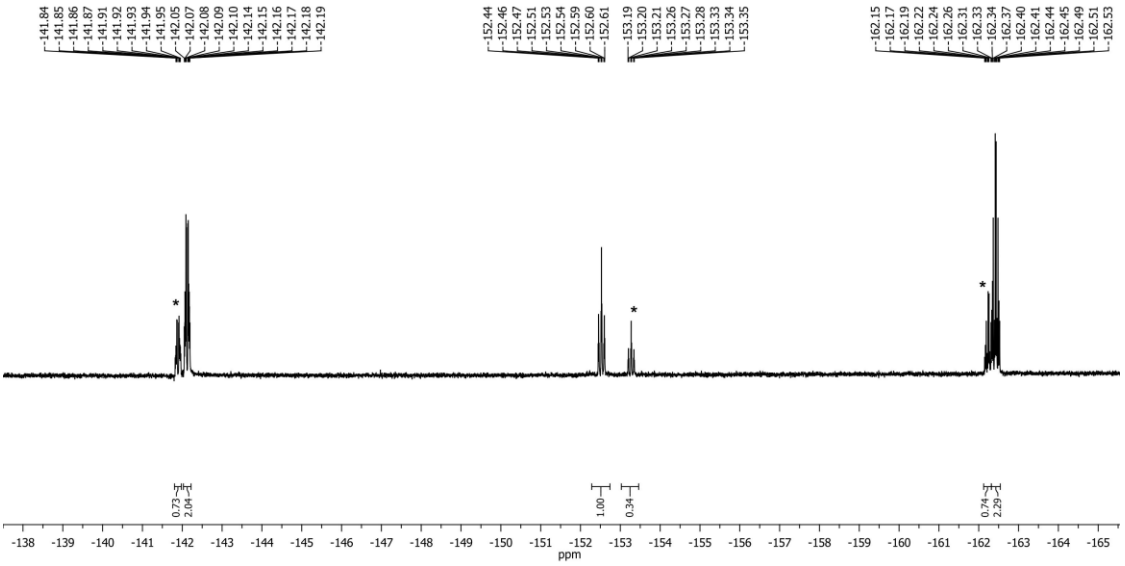

Figure A.8. The $^{19}F\{^{1}H\}$ NMR spectrum of **L-4** (CD_3CN, 282.40 MHz). Peaks marked with asterisks correspond to the hydrazone-imidate form.

Figure A.9. The ^{1}H NMR spectrum of **L-5** (CD_3CN, 300 MHz). Peaks marked with asterisks correspond to the hydrazone-imidate form. The inset shows an expanded view of the aromatic region.

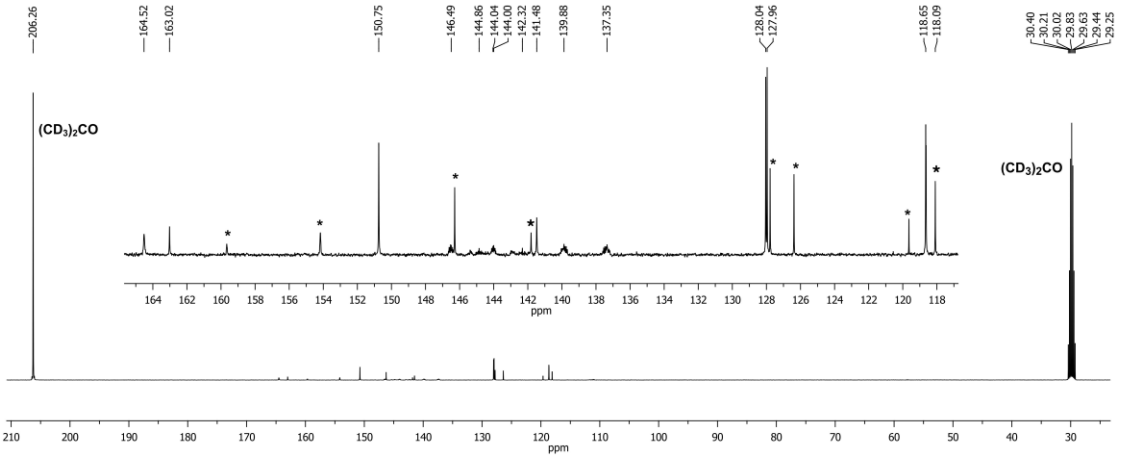

Figure A.10. The $^{13}C\{^{1}H\}$ NMR spectrum of **L-5** ($(CD_3)_2CO$, 100 MHz). Peaks marked with asterisks correspond to the hydrazone-imidate form. The inset shows the multiplets arising from the pentafluoro carbons coupling with ^{19}F nuclei more clearly.

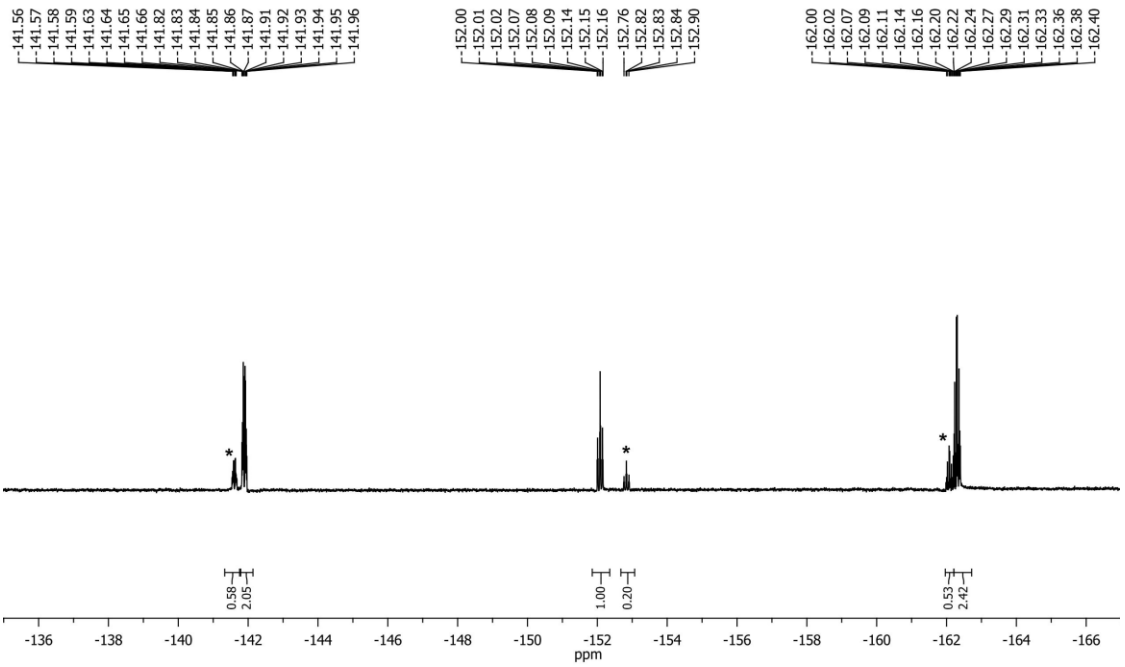

Figure A.11. The $^{19}F\{^{1}H\}$ NMR spectrum of **L-5** (CD_3CN, 282.40 MHz). Peaks marked with asterisks correspond to the hydrazone-imidate form.

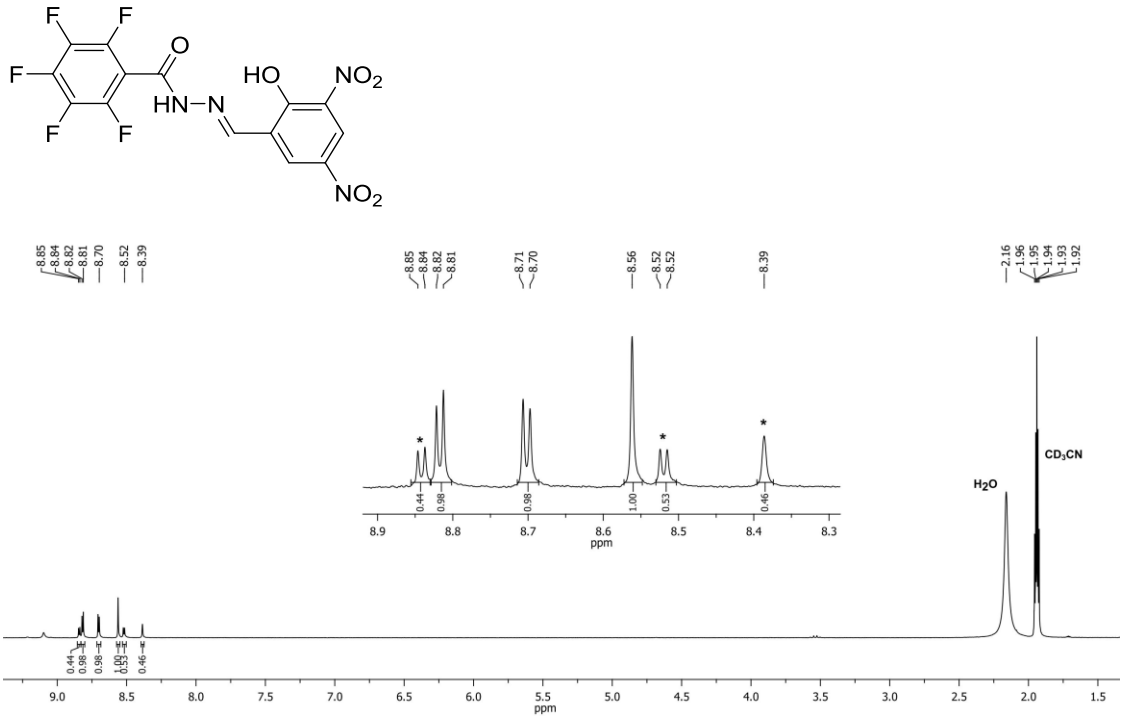

Figure A.12. The ^{1}H NMR spectrum of **L-6** (CD_3CN, 300 MHz). Peaks marked with asterisks correspond to the hydrazone-imidate form.

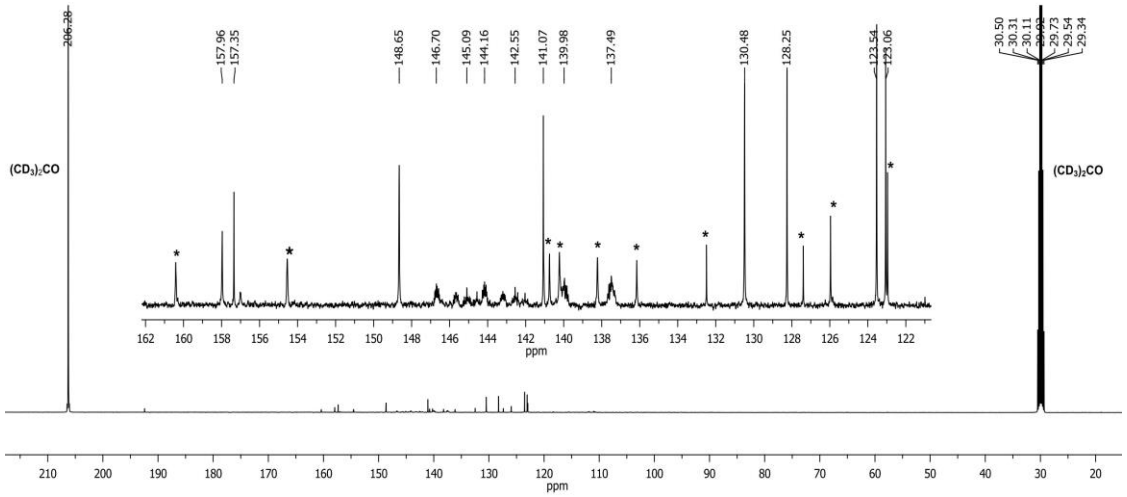

Figure A.13. The $^{13}C\{^{1}H\}$ NMR spectrum of **L-6** ($(CD_3)_2CO$, 100 MHz). Peaks marked with asterisks correspond to the hydrazone-imidate form. The inset shows the multiplets arising from coupling with ^{19}F nuclei for the pentafluoro carbons.

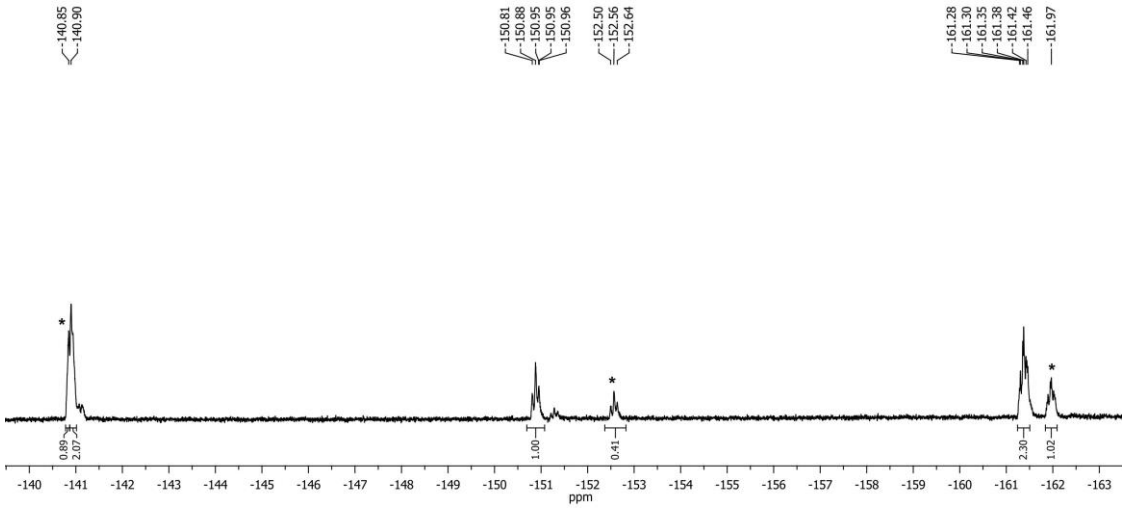

Figure A.14. The $^{19}F\{^{1}H\}$ NMR spectrum of **L-6** (CD3CN, 282.40 MHz). Peaks marked with asterisks correspond to the hydrazone-imidate form.

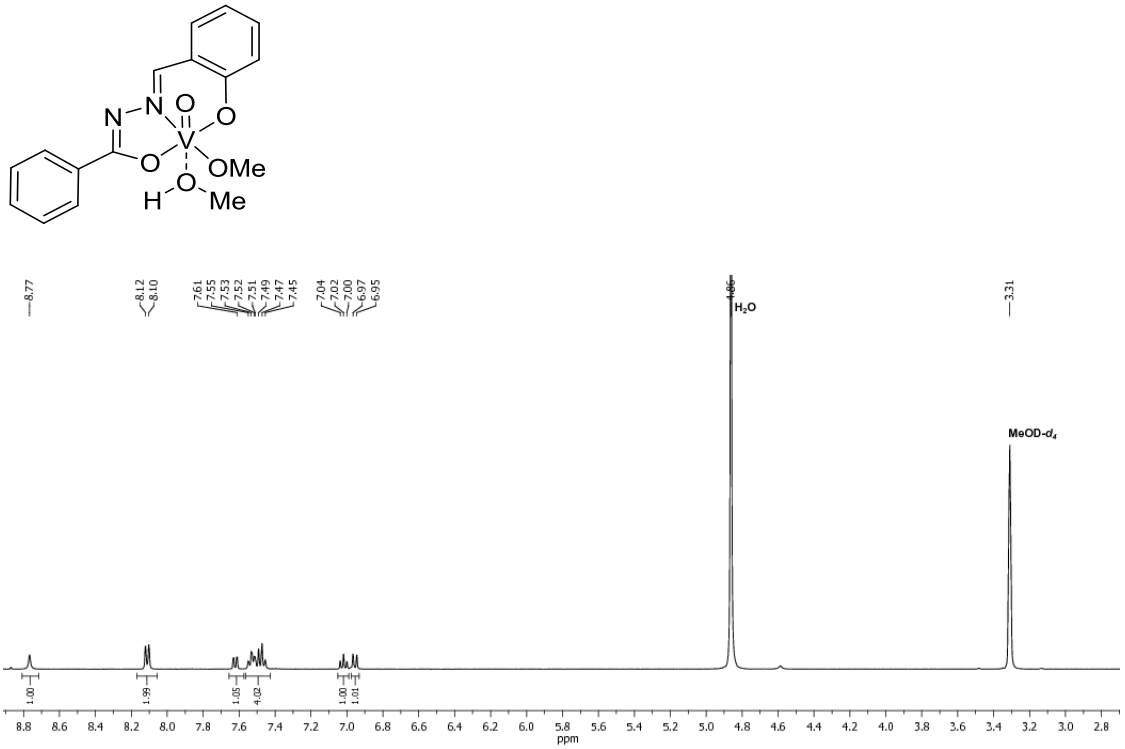

Figure A.15. The ^{1}H NMR spectrum of **VO-11** (MeOD-d_4, 400 MHz).

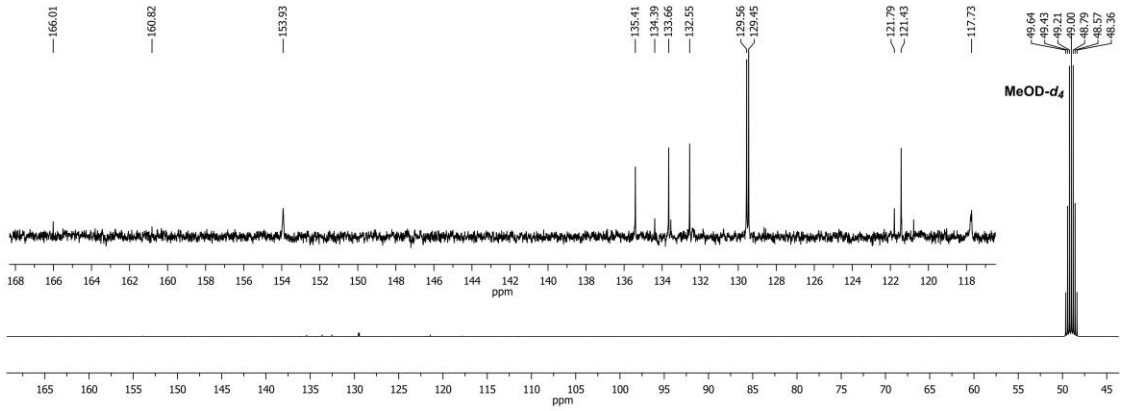

Figure A.16. The ^{13}C{^{1}H} NMR spectrum of **VO-11** (MeOD-d_4, 100 MHz). The inset shows the sp^2 hybridized carbon peaks more clearly.

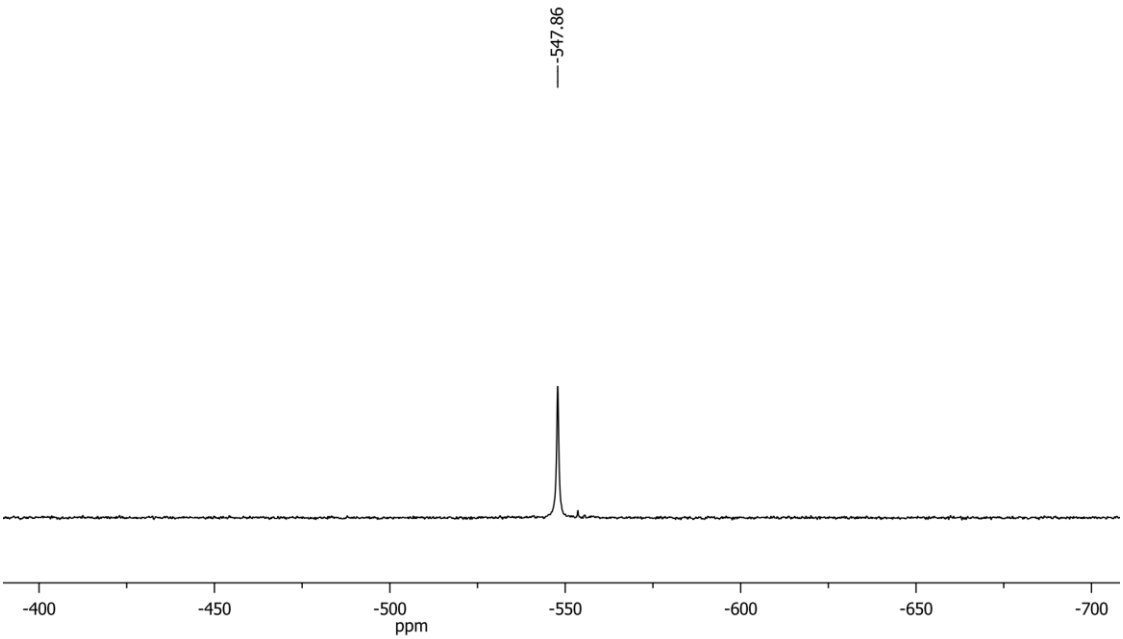

Figure A.17. The ^{51}V NMR spectrum of **VO-11** (MeOD-*d*$_4$, 105.25 MHz).

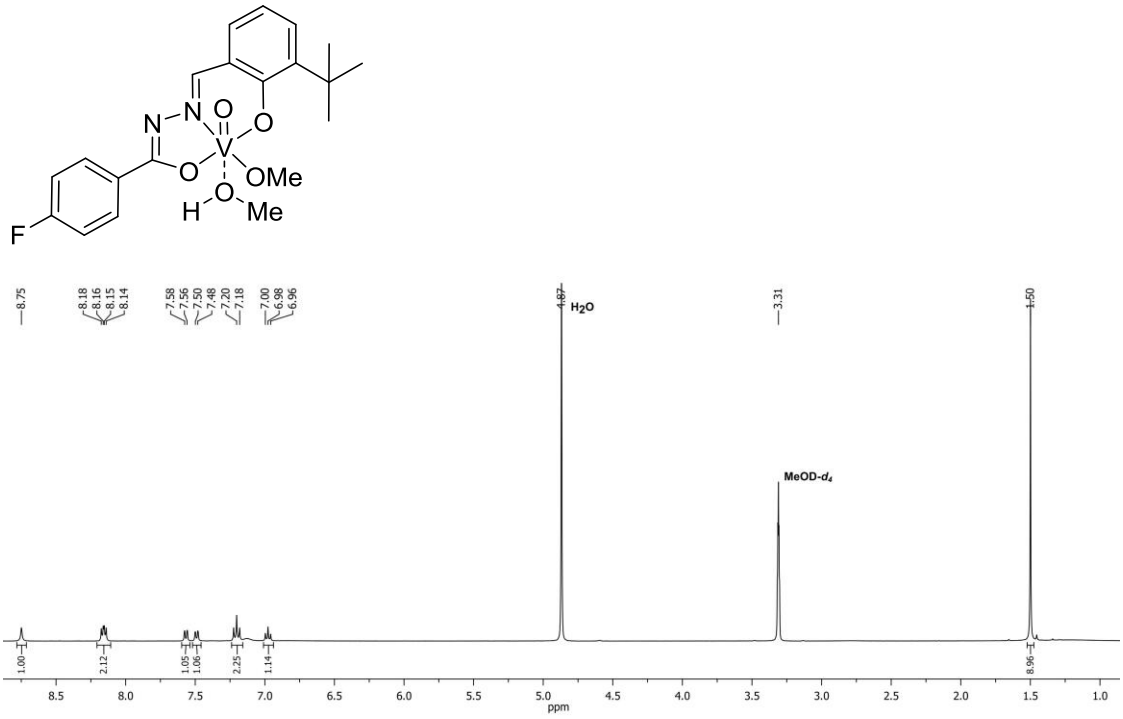

Figure A.18. The ^{1}H NMR spectrum of **VO-12** (MeOD-*d*$_4$, 400 MHz).

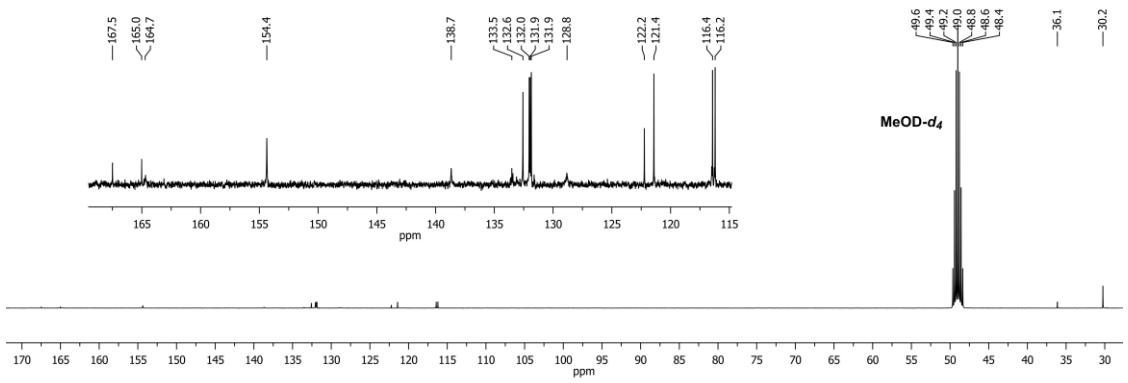

Figure A.19. The $^{13}C\{^{1}H\}$ NMR spectrum of **VO-12** (MeOD-d_4, 100 MHz). The inset shows the sp^2 hybridized carbon peaks more clearly.

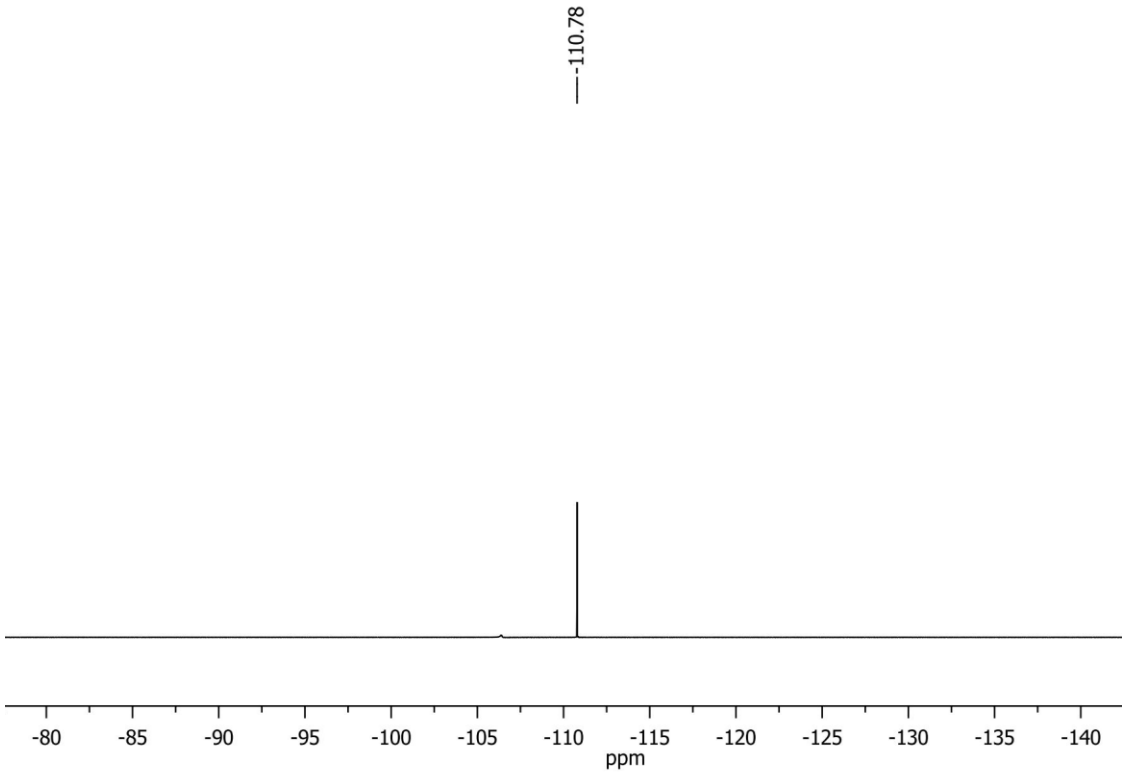

Figure A.20. The $^{19}F\{^{1}H\}$ NMR spectrum of **VO-12** (MeOD-d_4, 376.50 MHz).

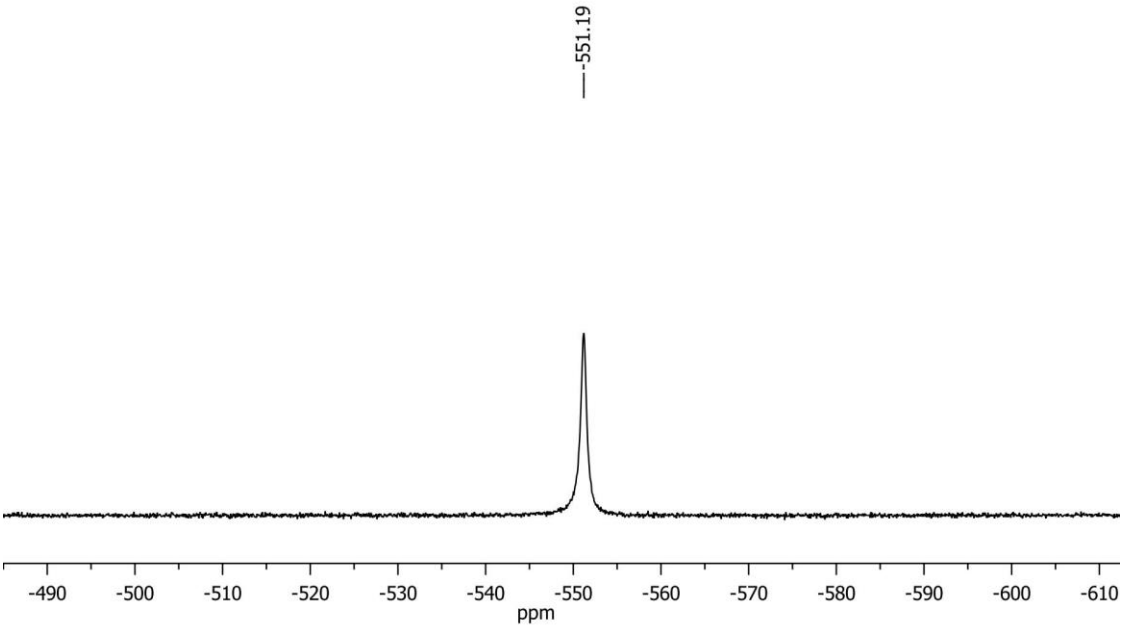

Figure A.21. The ^{51}V NMR spectrum of **VO-12** (MeOD-d_4, 105.25 MHz).

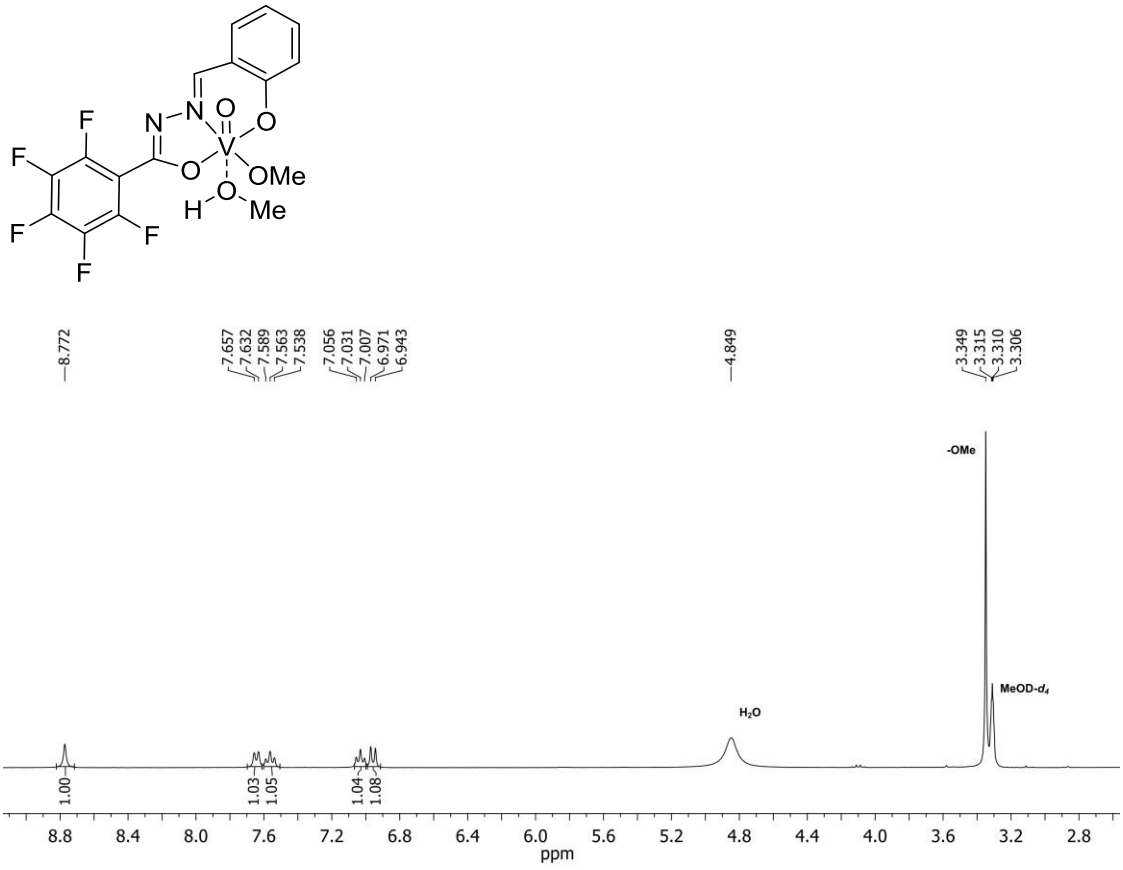

Figure A.22. The ^{1}H NMR spectrum of **VO-13** (MeOD-d_4, 300 MHz).

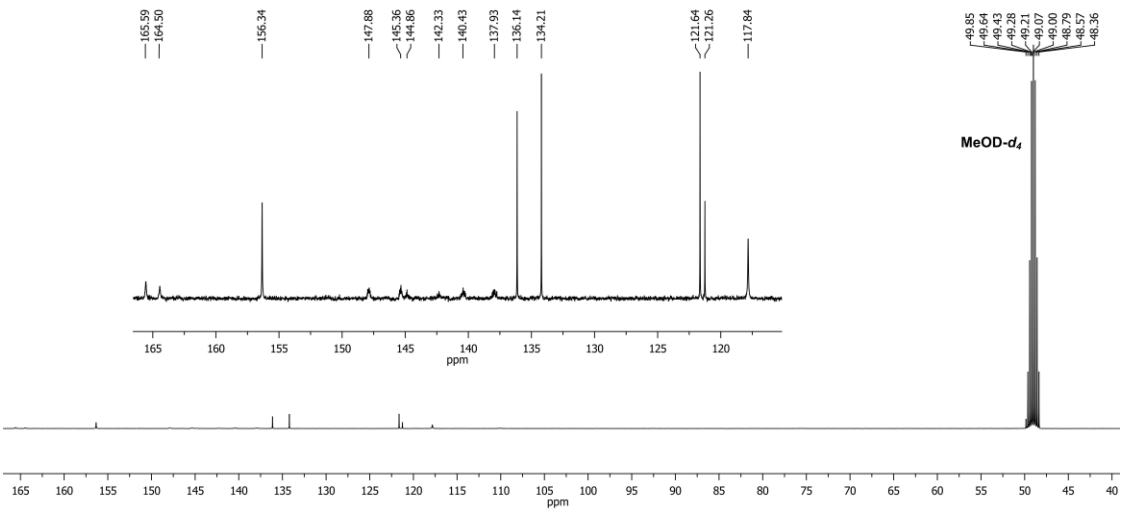

Figure A.23. The $^{13}C\{^{1}H\}$ NMR spectrum of **VO-13** (MeOD-d_4, 100 MHz). The inset shows the multiplets arising from the pentafluoro carbons coupling with ^{19}F nuclei, along with other peaks more clearly.

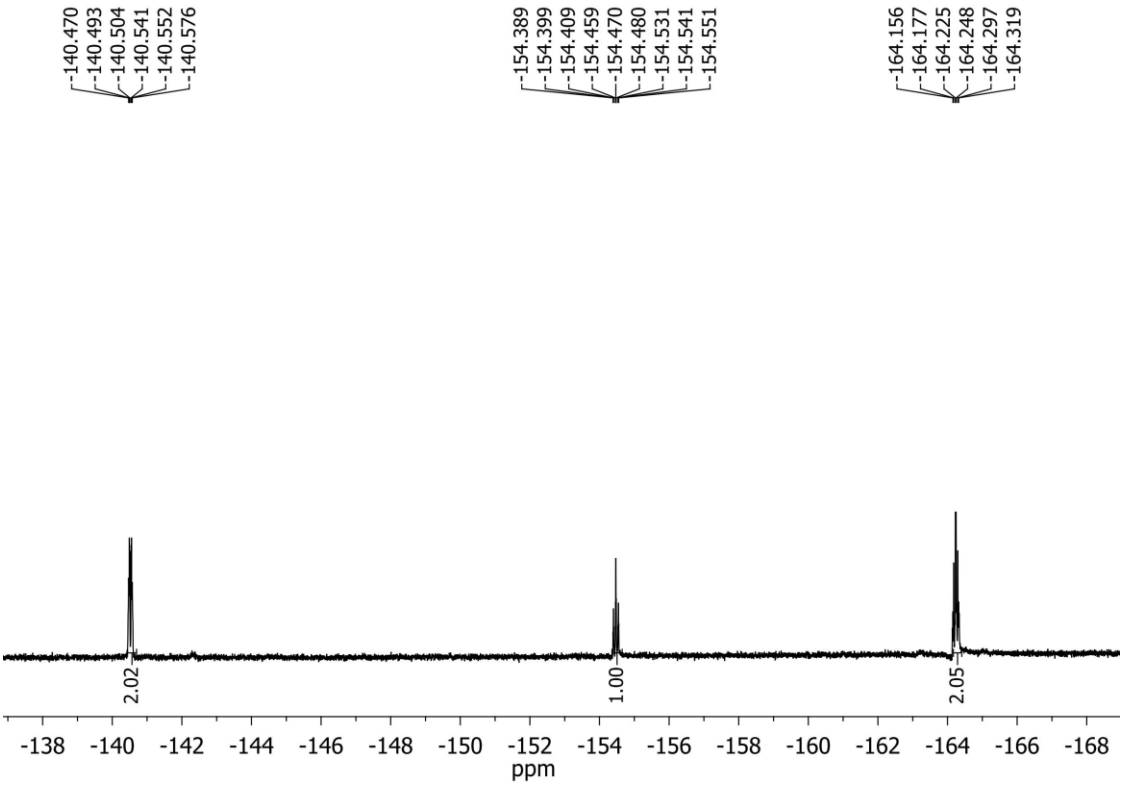

Figure A.24. The $^{19}F\{^{1}H\}$ NMR spectrum of **VO-13** (MeOD-d_4, 282.40 MHz).

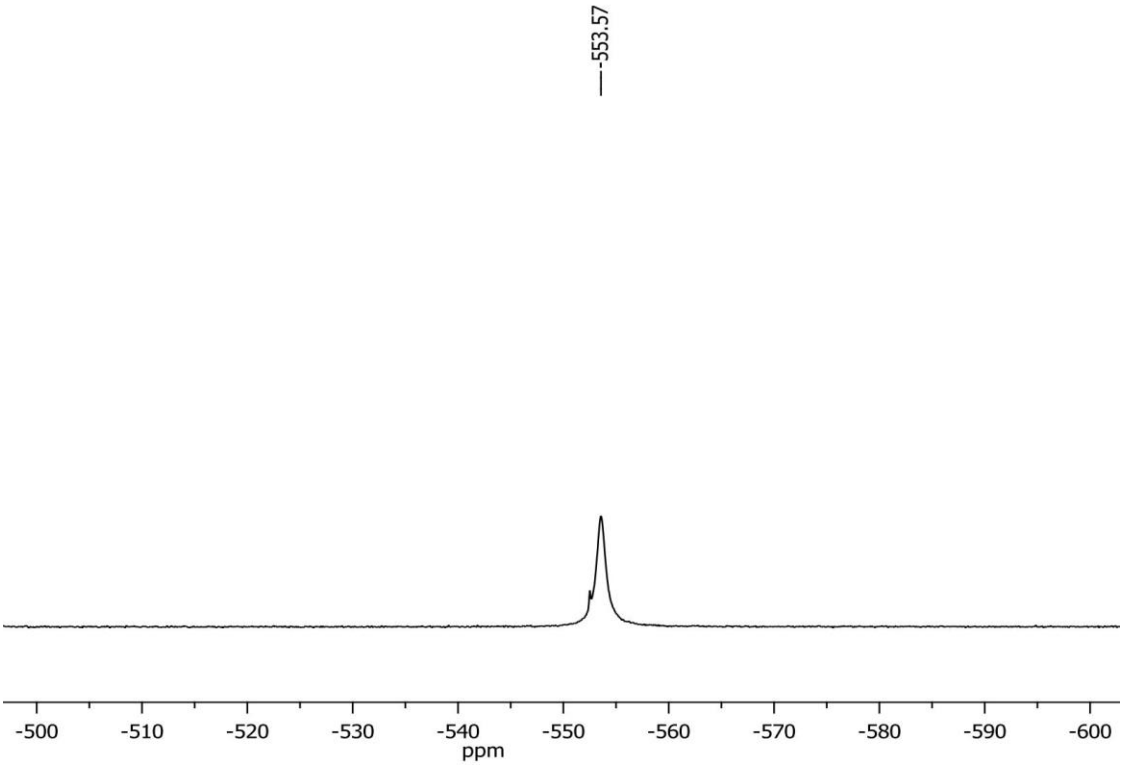

Figure A.25. The ^{51}V NMR spectrum of **VO-13** (MeOD-d_4, 105.25 MHz).

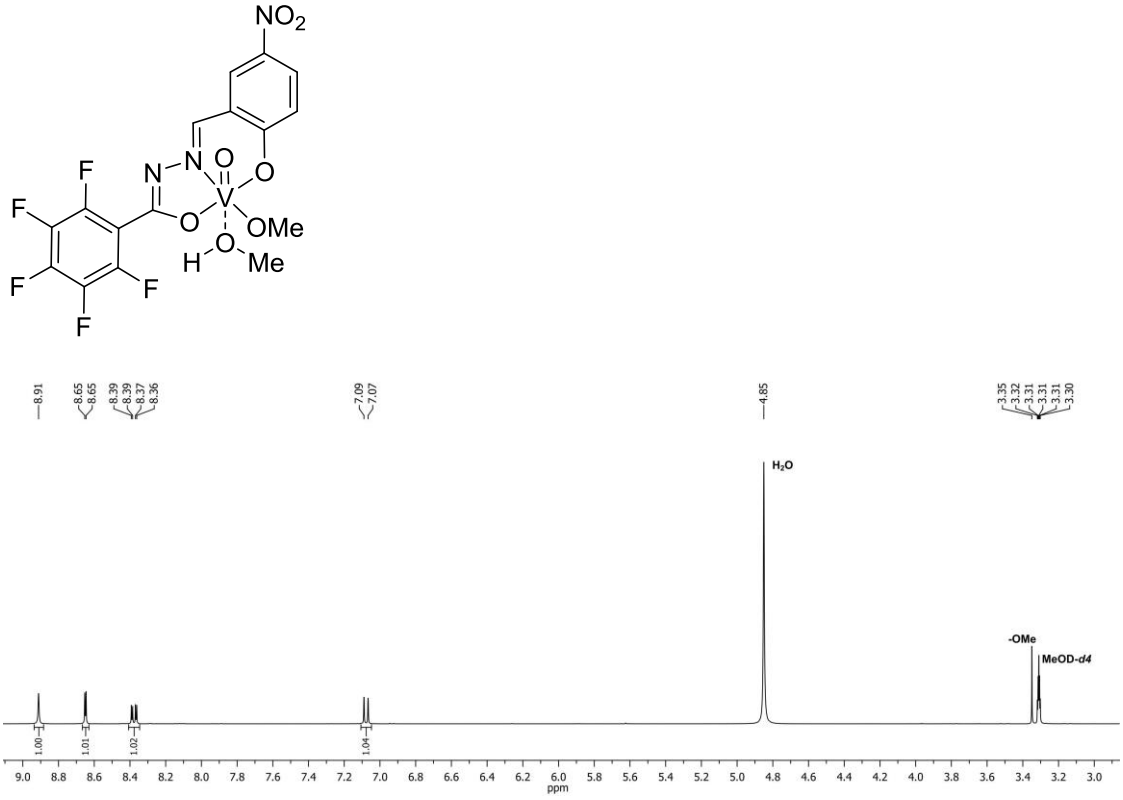

Figure A.26. The ^{1}H NMR spectrum of **VO-14** (MeOD-d_4, 400 MHz).

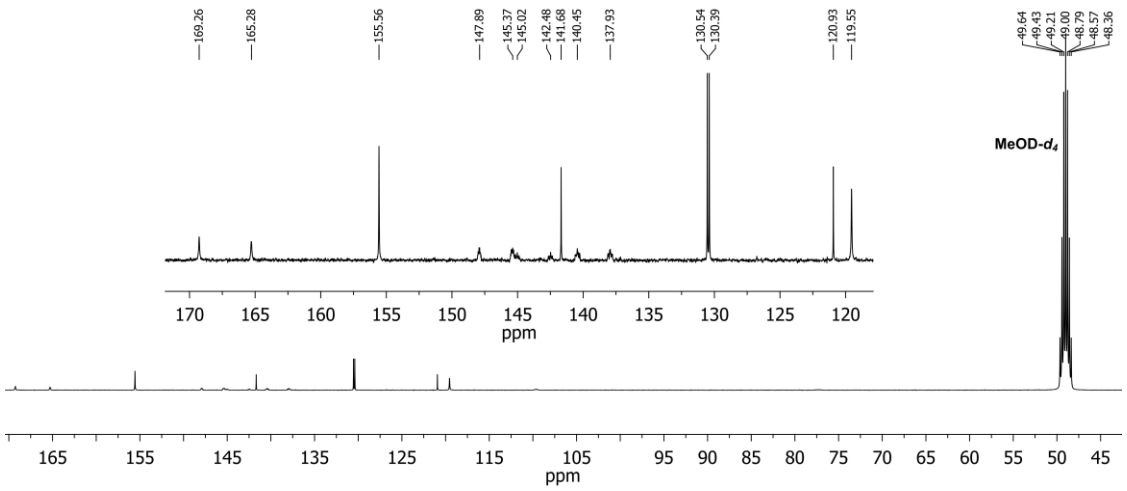

Figure A.27. The $^{13}C\{^{1}H\}$ NMR spectrum of **VO-14** (MeOD-d_4, 100 MHz). The inset shows the multiplets arising from the pentafluoro carbons coupling with ^{19}F nuclei, along with other peaks more clearly.

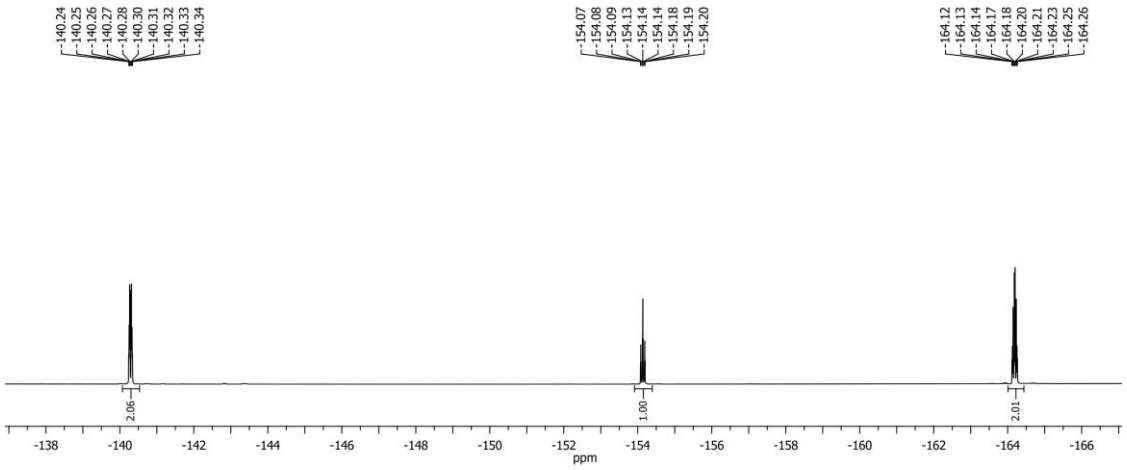

Figure A.28. The $^{19}F\{^{1}H\}$ NMR spectrum of **VO-14** (MeOD-d_4, 376.50 Hz).

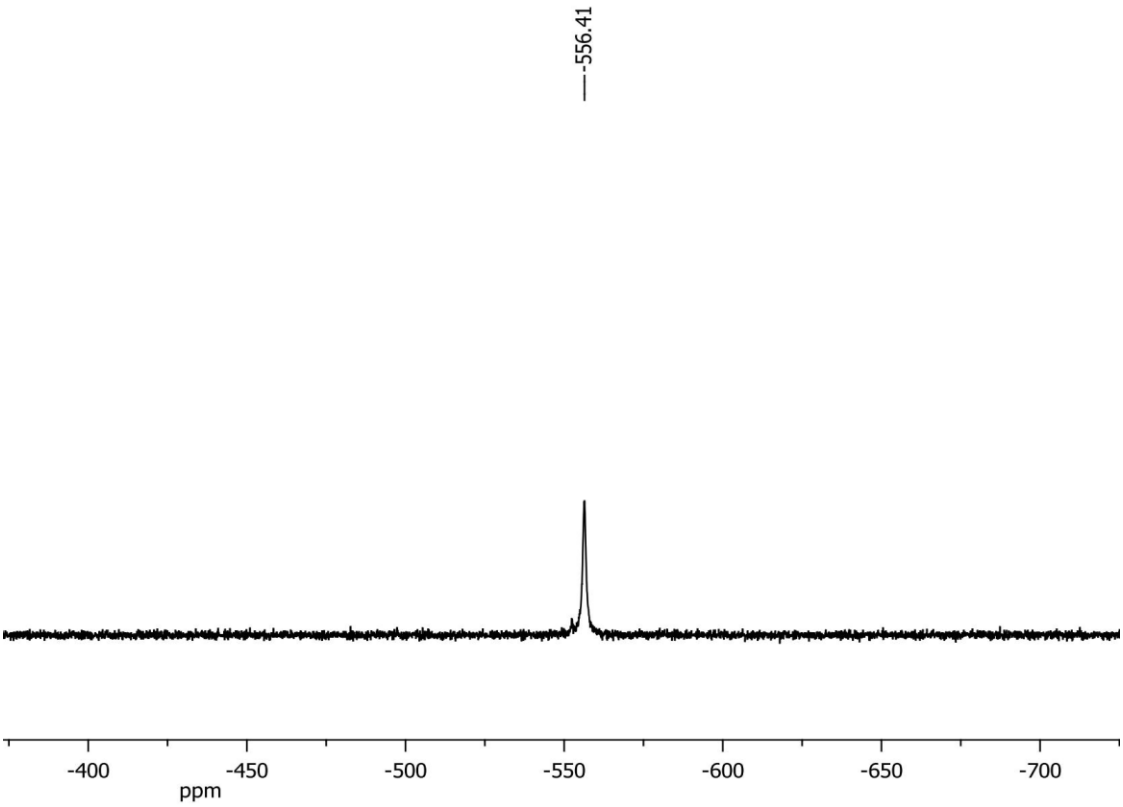

Figure A.29. The ^{51}V NMR spectrum of **VO-14** (MeOD-d_4, 105.25 MHz).

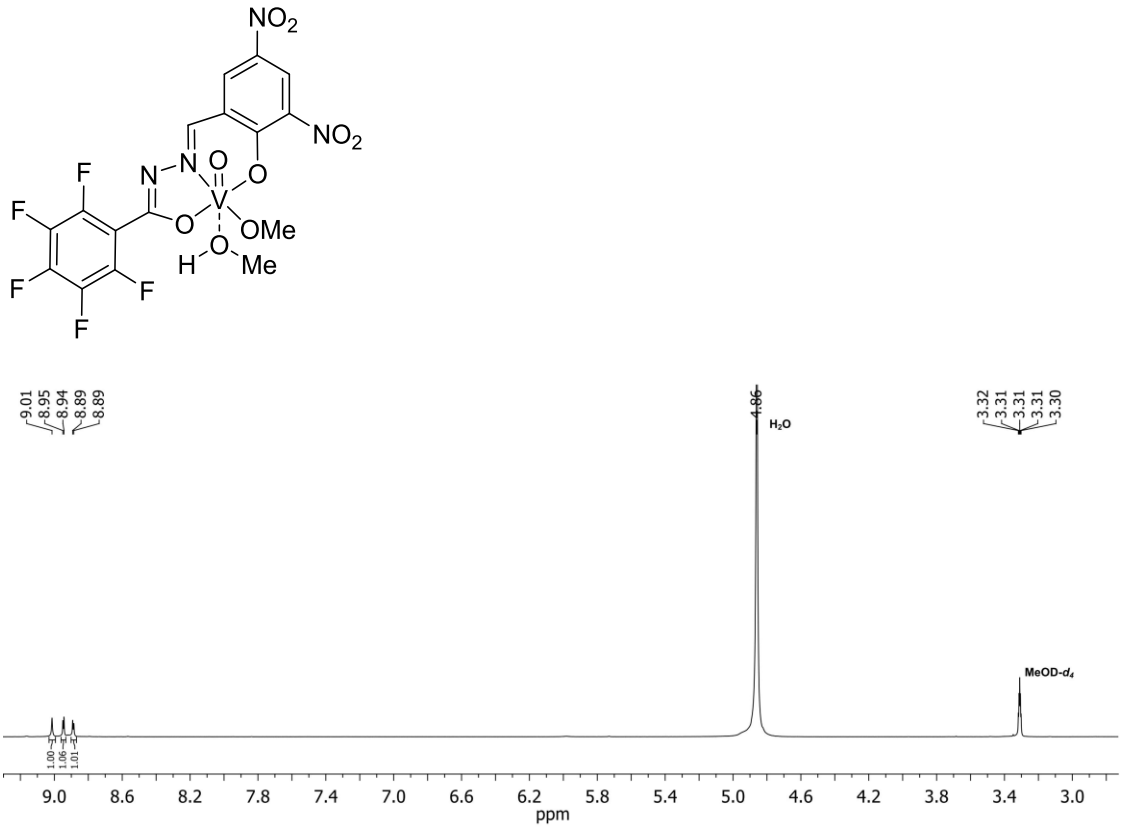

Figure A.30. The ^{1}H NMR spectrum of **VO-15** (MeOD-d_4, 400 MHz).

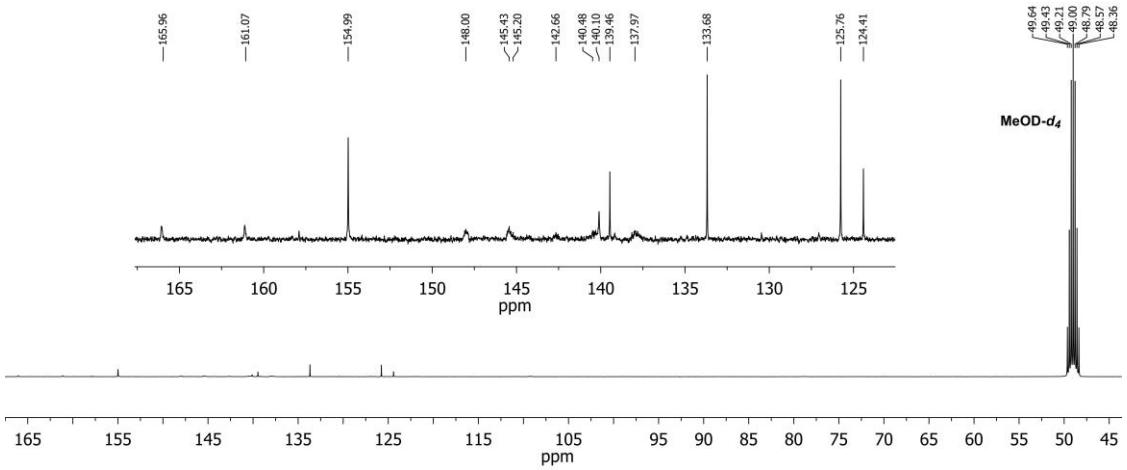

Figure A.31. The $^{13}C\{^{1}H\}$ NMR spectrum of **VO-15** (MeOD-d_4, 400 MHz). The inset shows the multiplets arising from the pentafluoro carbons coupling with ^{19}F nuclei, along with other peaks more clearly.

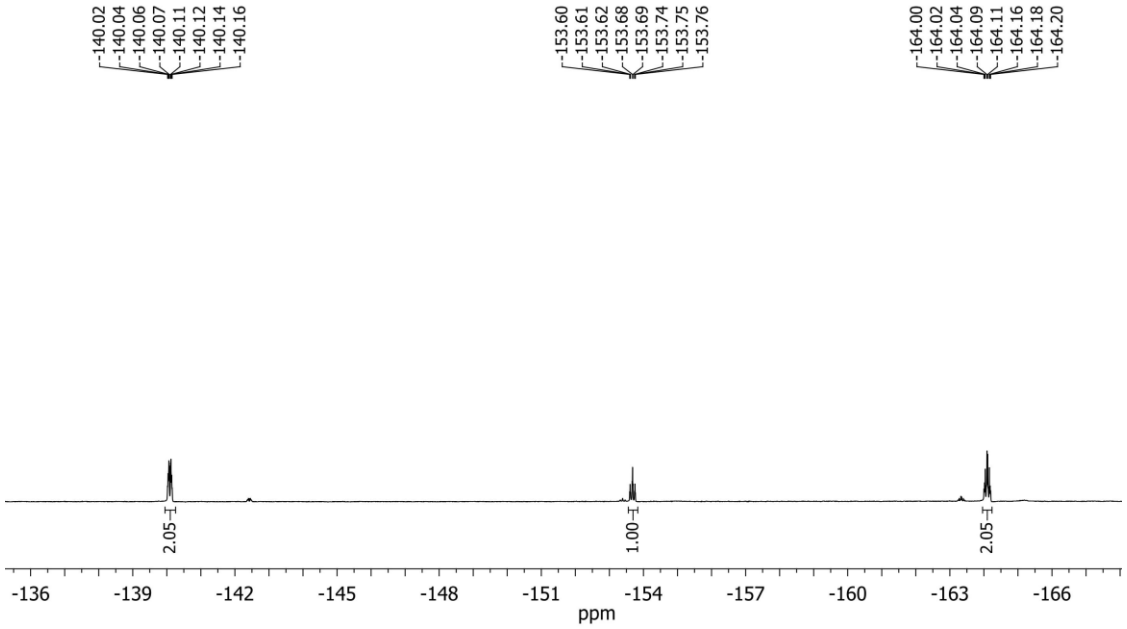

Figure A.32. The $^{19}F\{^{1}H\}$ NMR spectrum of **VO-15** (MeOD-d_4, 282.40 MHz).

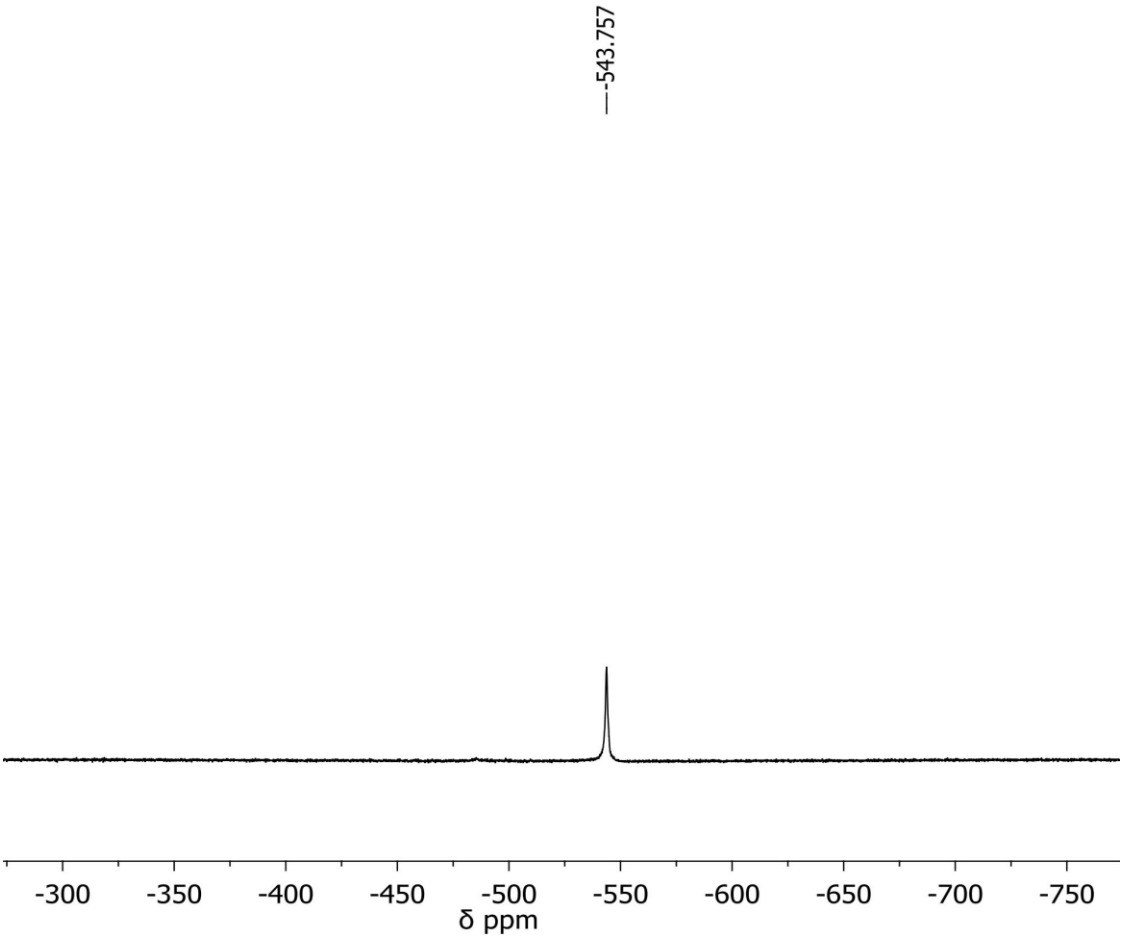

Figure A.33. The ^{51}V NMR spectrum of **VO-15** (MeOD-d_4, 105.25 MHz).

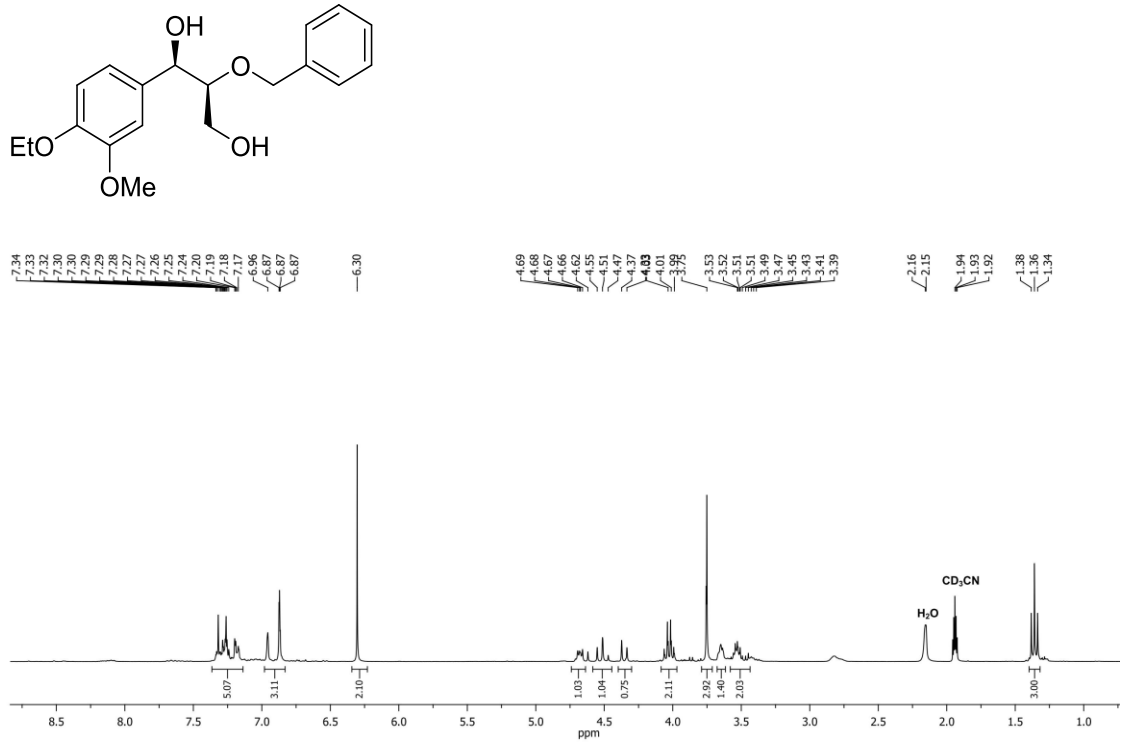

Figure A.34. The ^{1}H NMR spectrum of **25** (CD_3CN, 300 MHz).

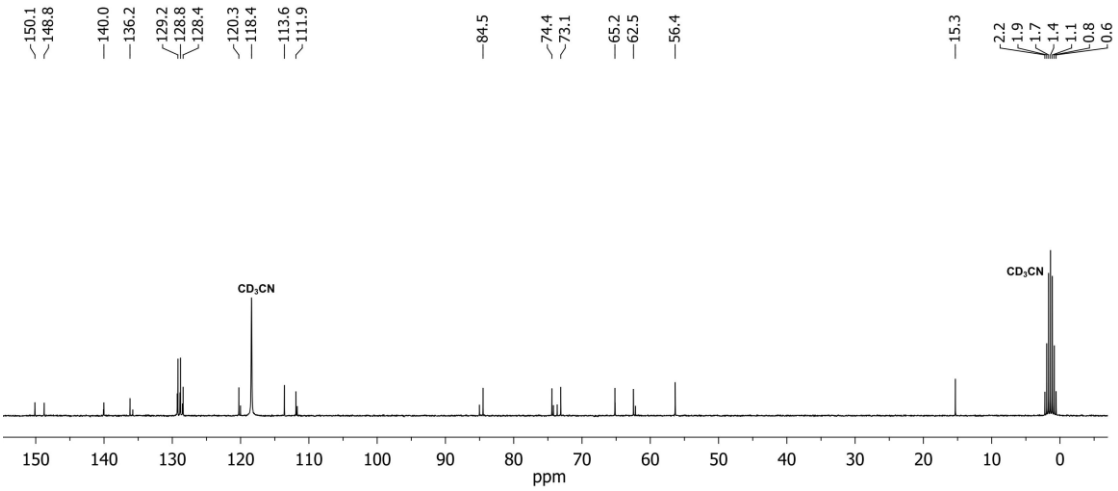

Figure A.35. The $^{13}C\{^{1}H\}$ NMR spectrum of **25** (CD_3CN, 75 MHz).

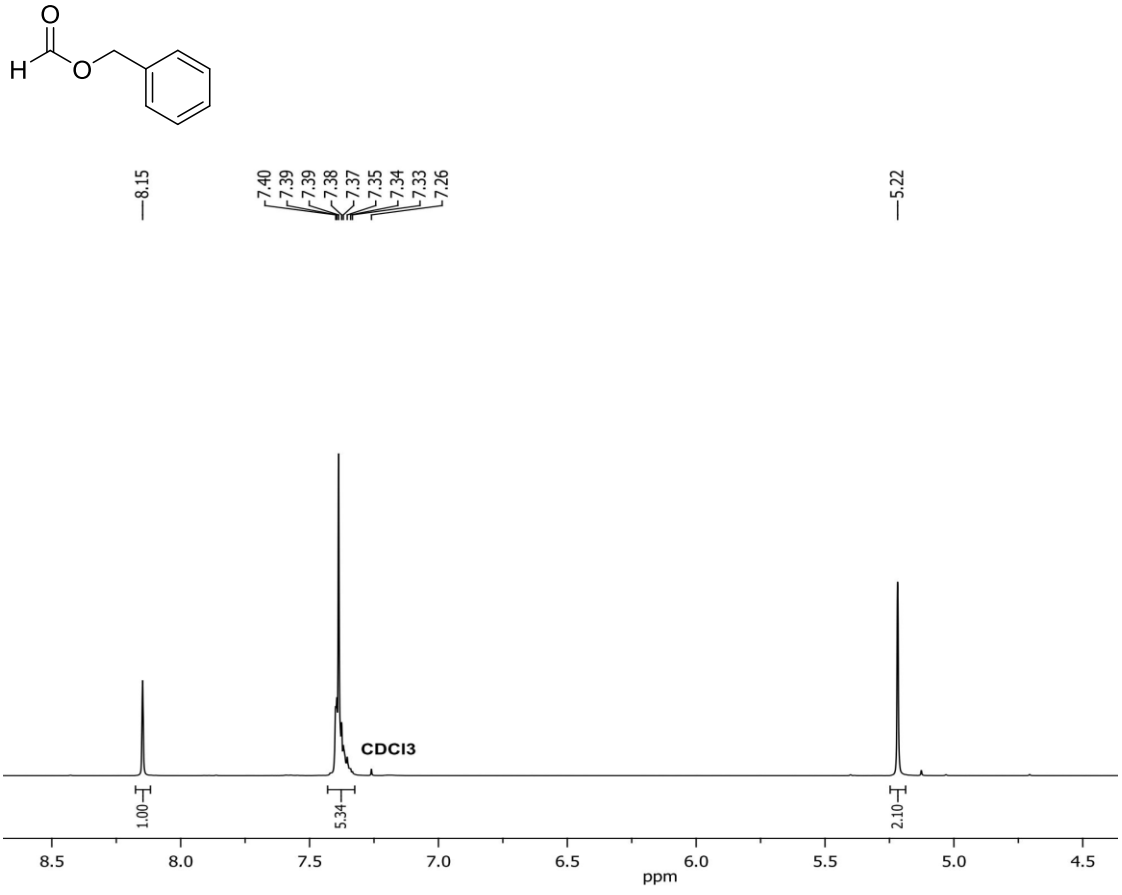

Figure A.36. The ^{1}H NMR spectrum of **26** ($CDCl_3$, 400 MHz).

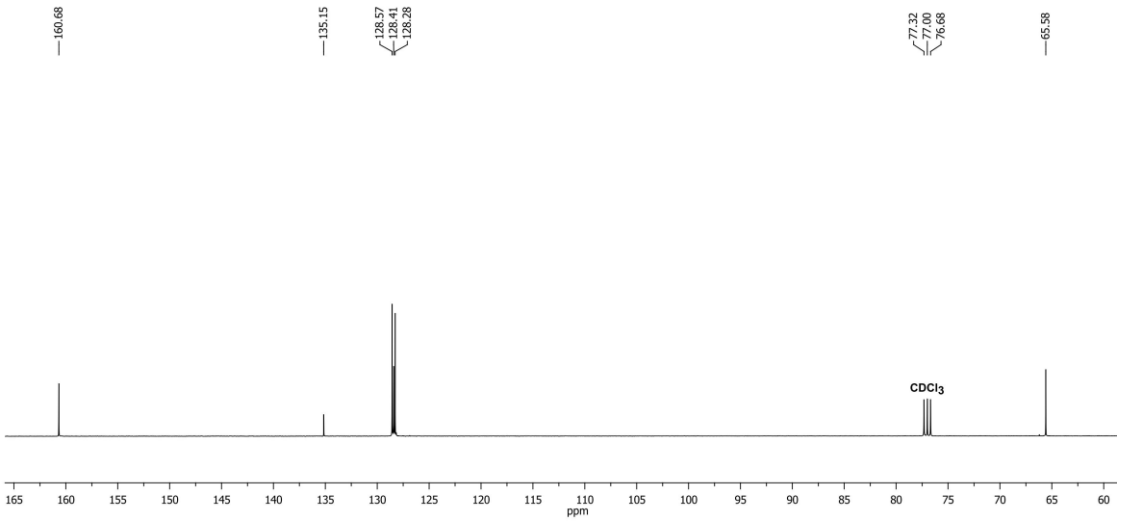

Figure A.37. The $^{13}C\{^{1}H\}$ NMR spectrum of **26** ($CDCl_3$, 100 MHz).

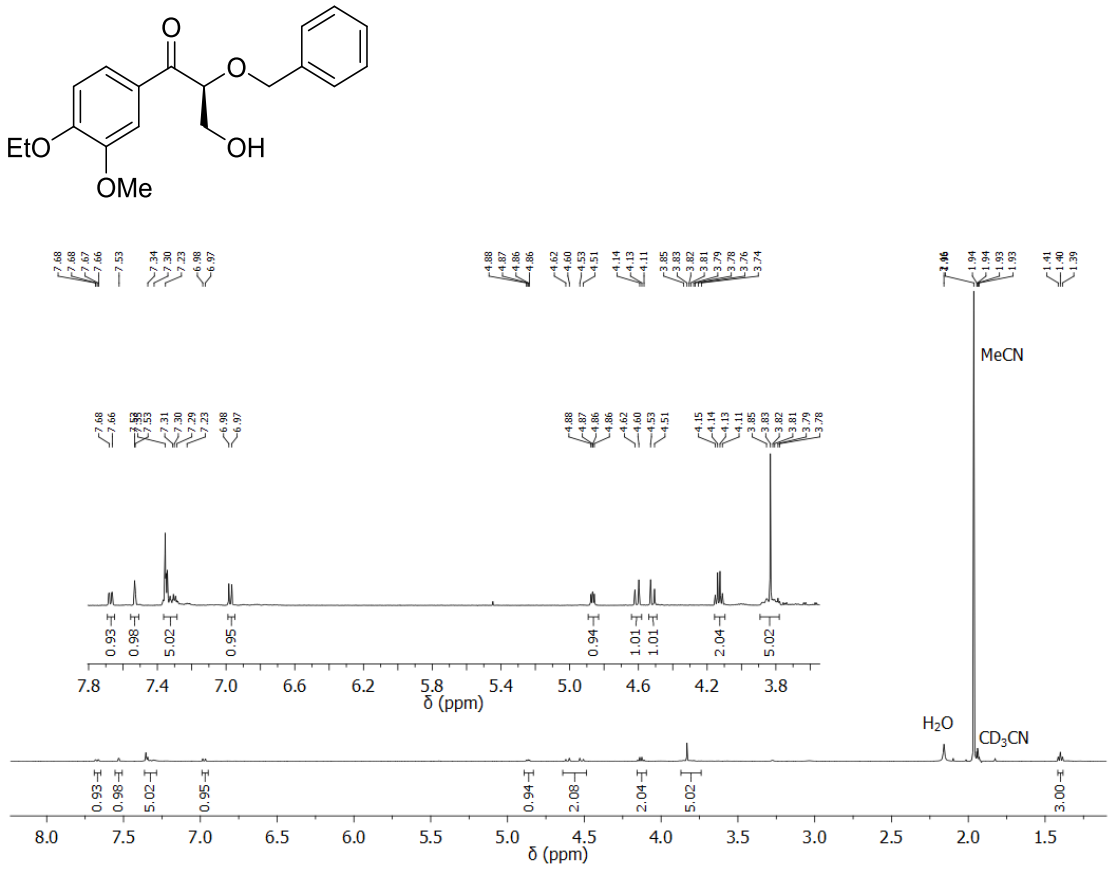

Figure A.38. The ^{1}H NMR spectrum of **32** (CD_3CN, 500 MHz) after isolation by preparatory thin-layer chromatography. The inset shows product peaks more clearly.

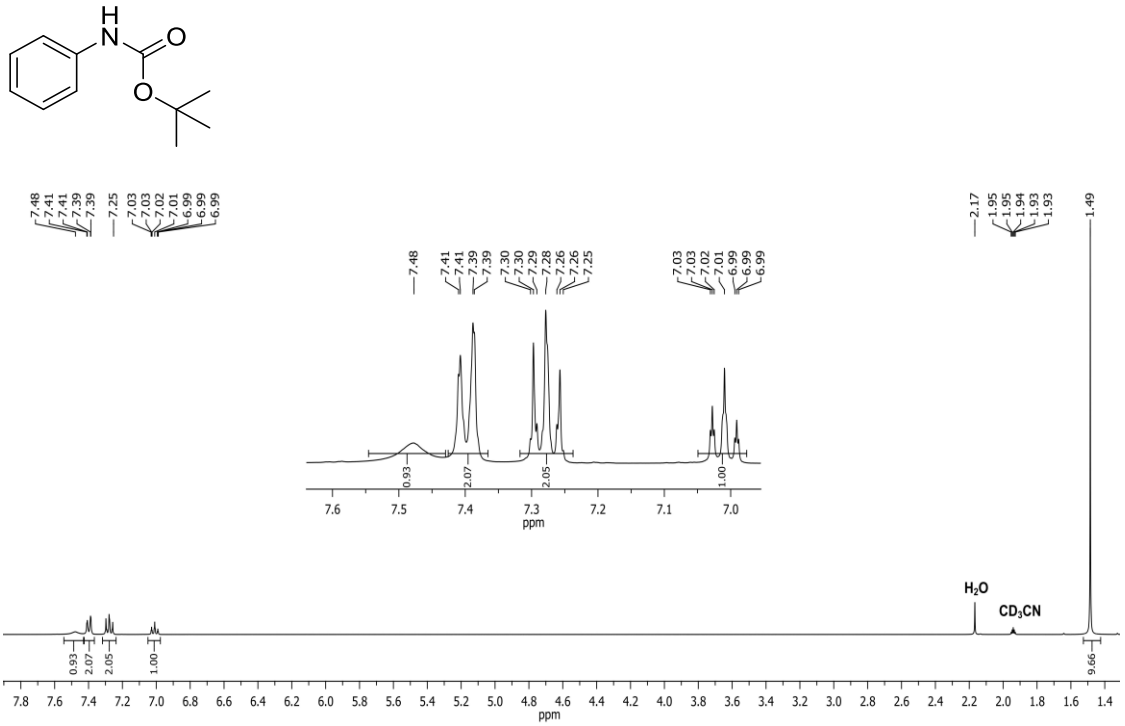

Figure A.39. The ^{1}H NMR spectrum of **92** (CD_3CN, 400 MHz)

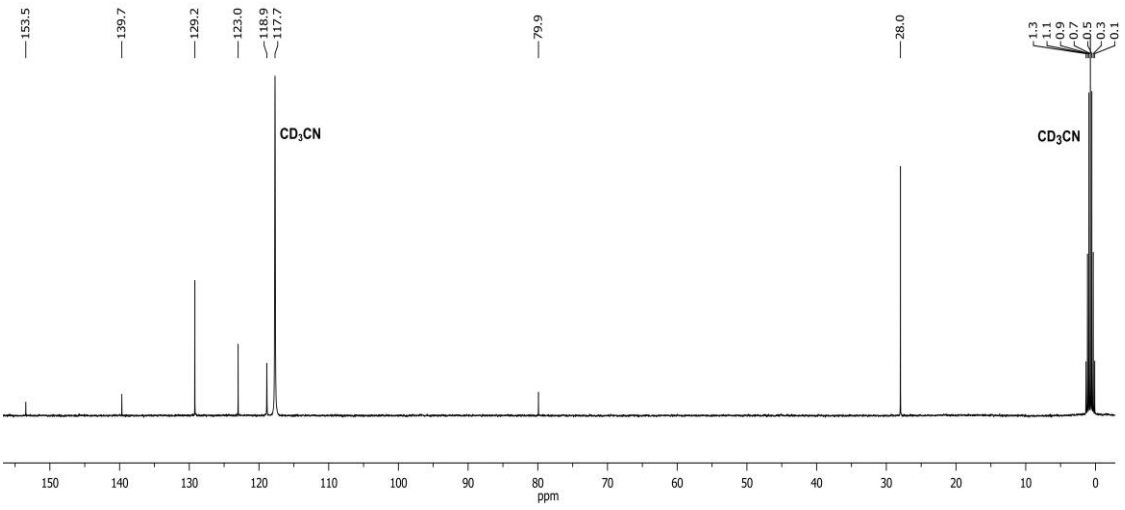

Figure A.40. The $^{13}C\{^{1}H\}$ NMR spectrum of **92** (CD_3CN, 100 MHz).

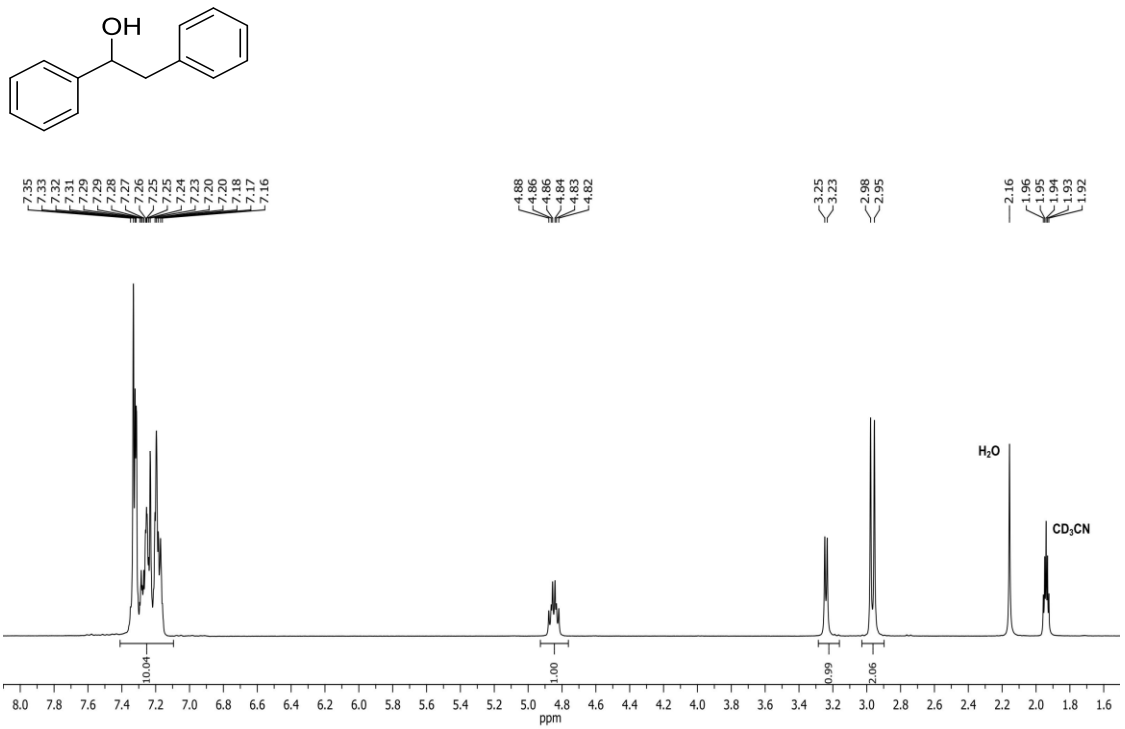

Figure A.41. The ^{1}H NMR spectrum of **36** (CD_3CN, 300 MHz).

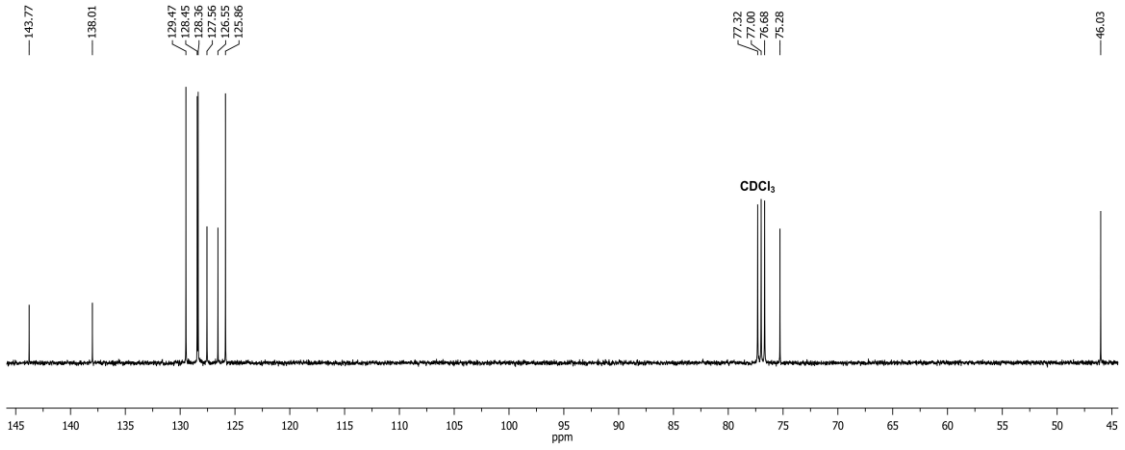

Figure A.42. The ^{13}C{^{1}H} NMR spectrum of **36** ($CDCl_3$, 100 MHz).

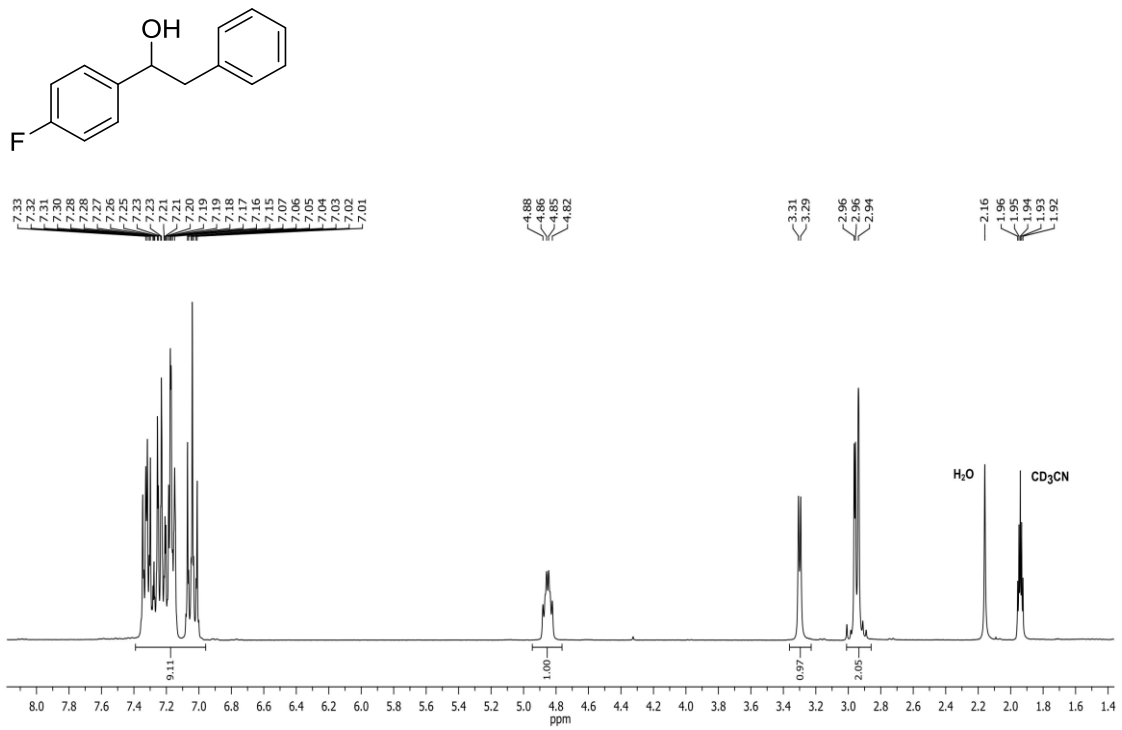

Figure A.43. The ^{1}H NMR spectrum of **37** (CD_3CN, 300 MHz).

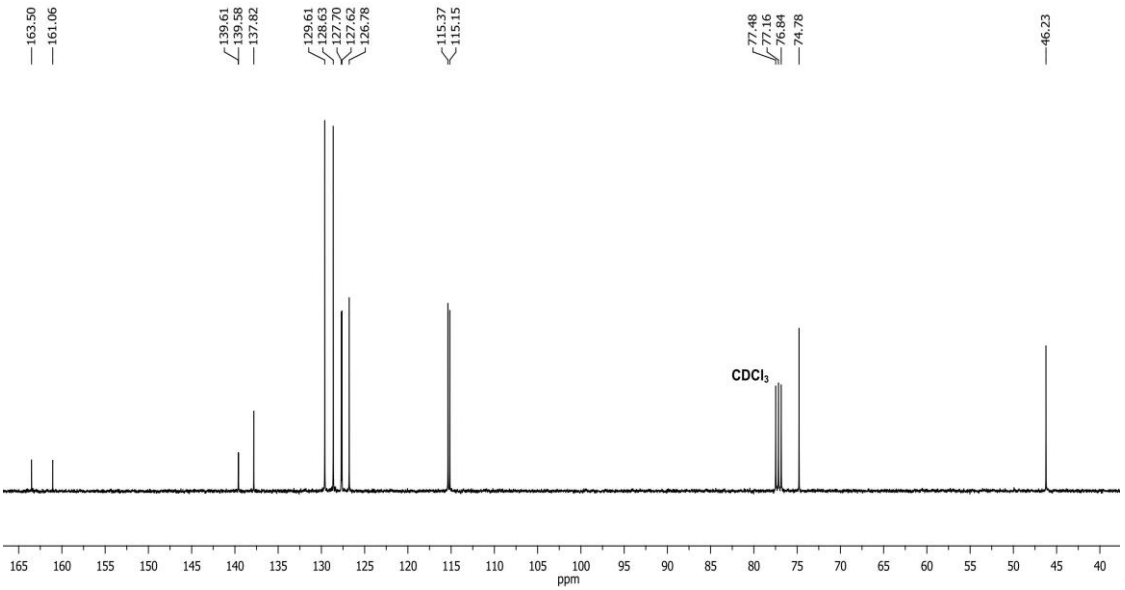

Figure A.44. The $^{13}C\{^{1}H\}$ NMR spectrum of **37** ($CDCl_3$, 100 MHz).

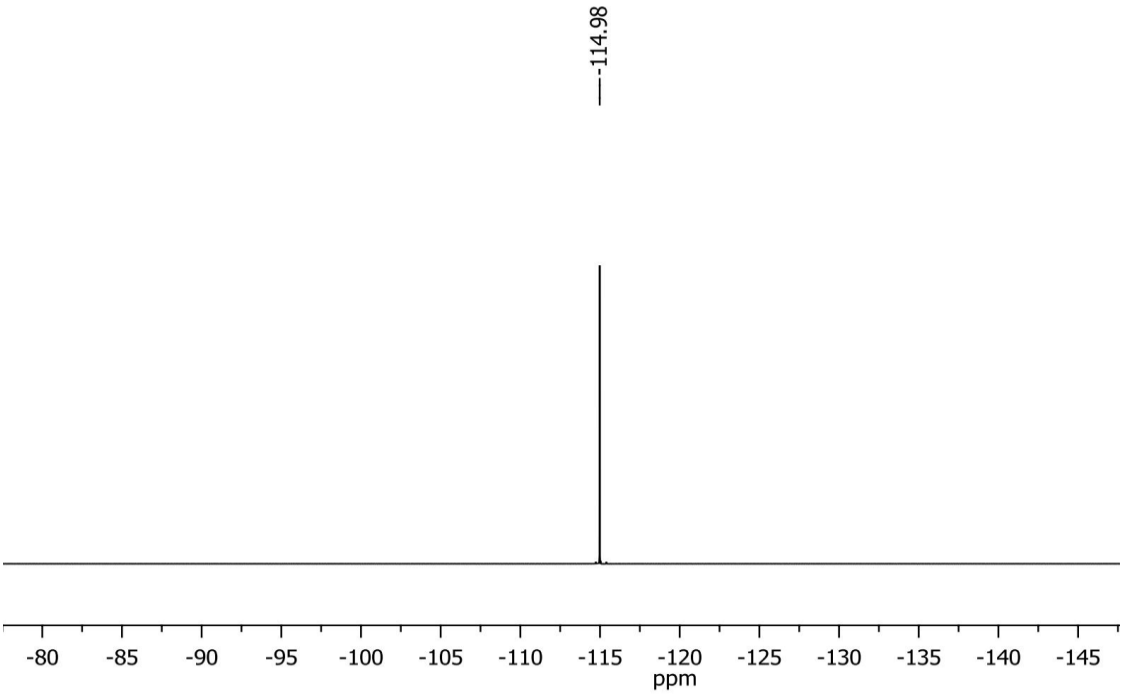

Figure A.45. The $^{19}F\{^{1}H\}$ NMR spectrum of **37** ($CDCl_3$, 376.5 MHz).

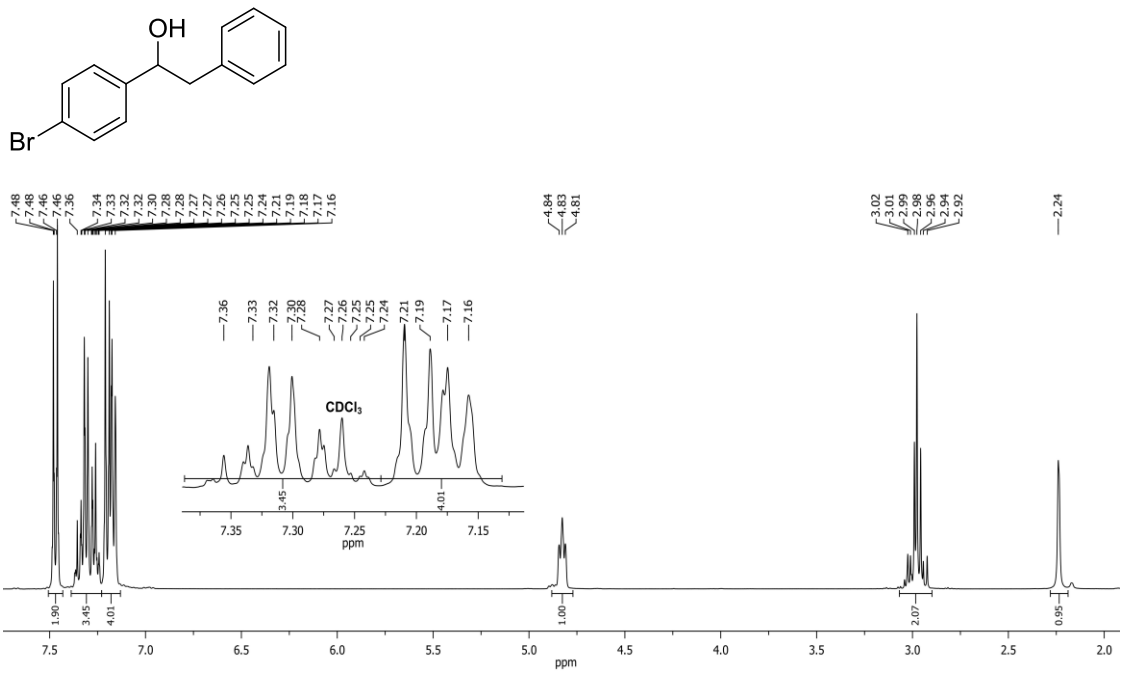

Figure A.46. The ^{1}H NMR spectrum of **38** ($CDCl_3$, 300 MHz).

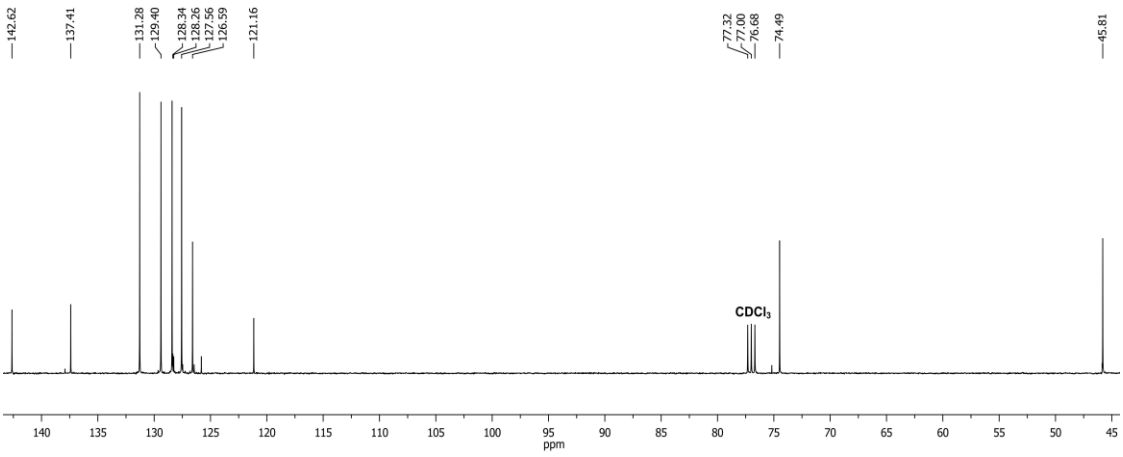

Figure A.47. The $^{13}C\{^{1}H\}$ NMR spectrum of **38** ($CDCl_3$, 100 MHz).

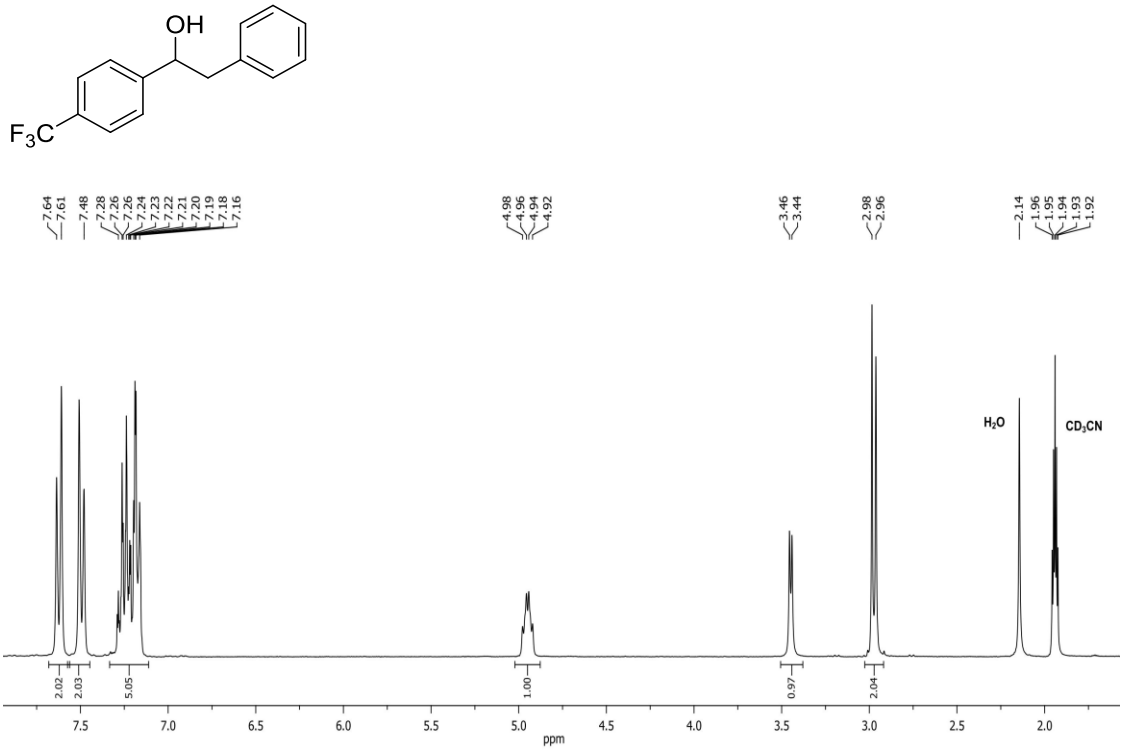

Figure A.48. The ^{1}H NMR spectrum of **39** (CD_3CN, 400 MHz).

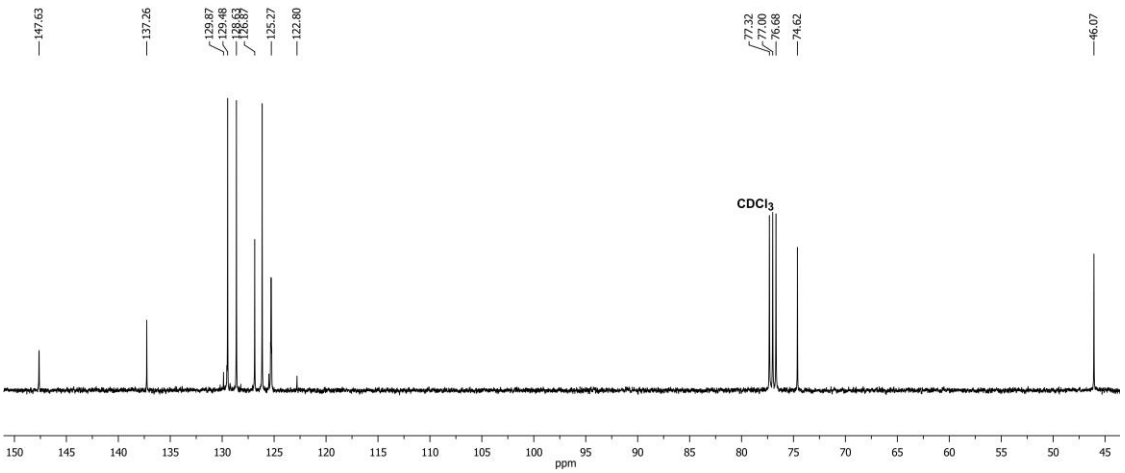

Figure A.49. The $^{13}C\{^{1}H\}$ NMR spectrum of **39** ($CDCl_3$, 100 MHz).

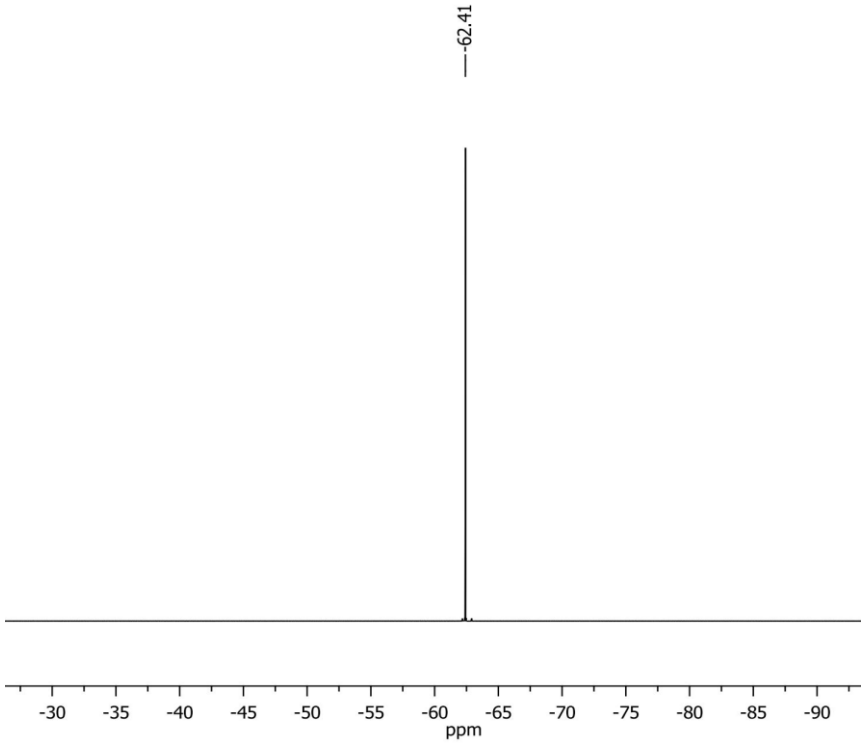

Figure A.50. The $^{19}F\{^{1}H\}$ NMR spectrum of **39** ($CDCl_3$, 376.5 MHz).

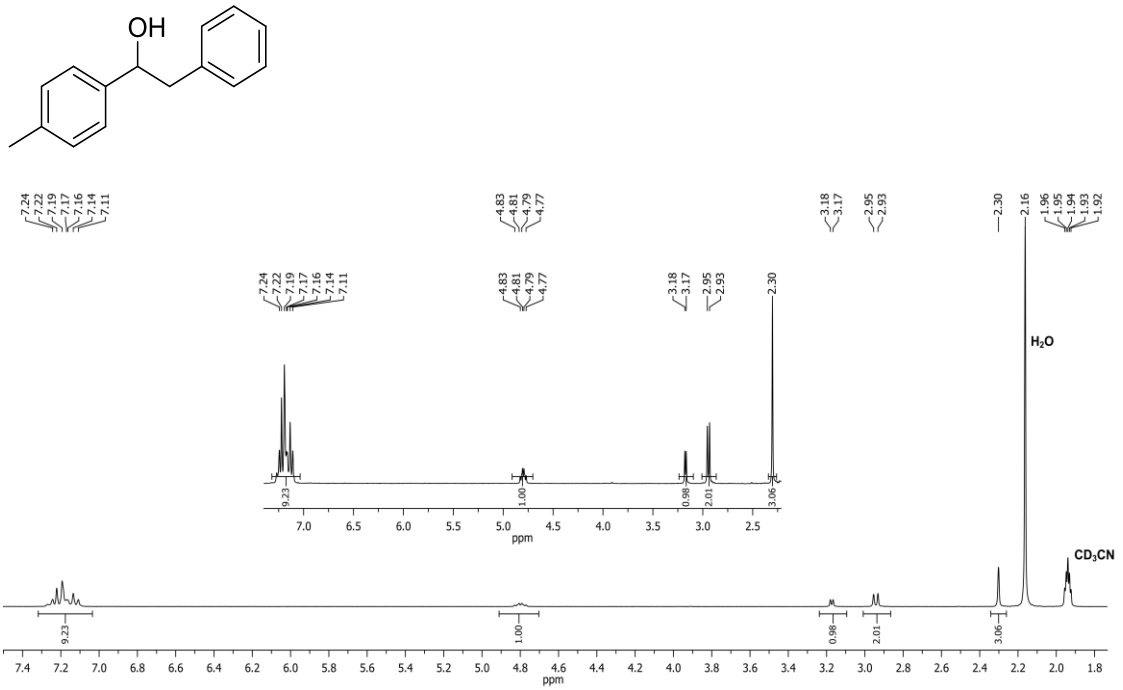

Figure A.51. The ^{1}H NMR spectrum of **40** (CD_3CN, 300 MHz).

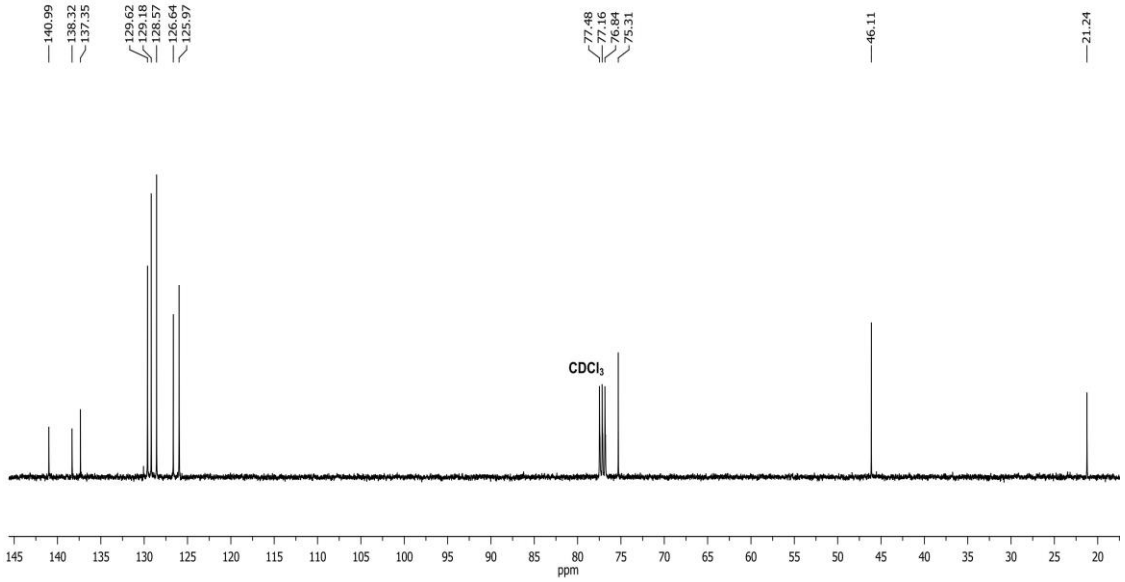

Figure A.52. The $^{13}C\{^{1}H\}$ NMR spectrum of **40** ($CDCl_3$, 100 MHz).

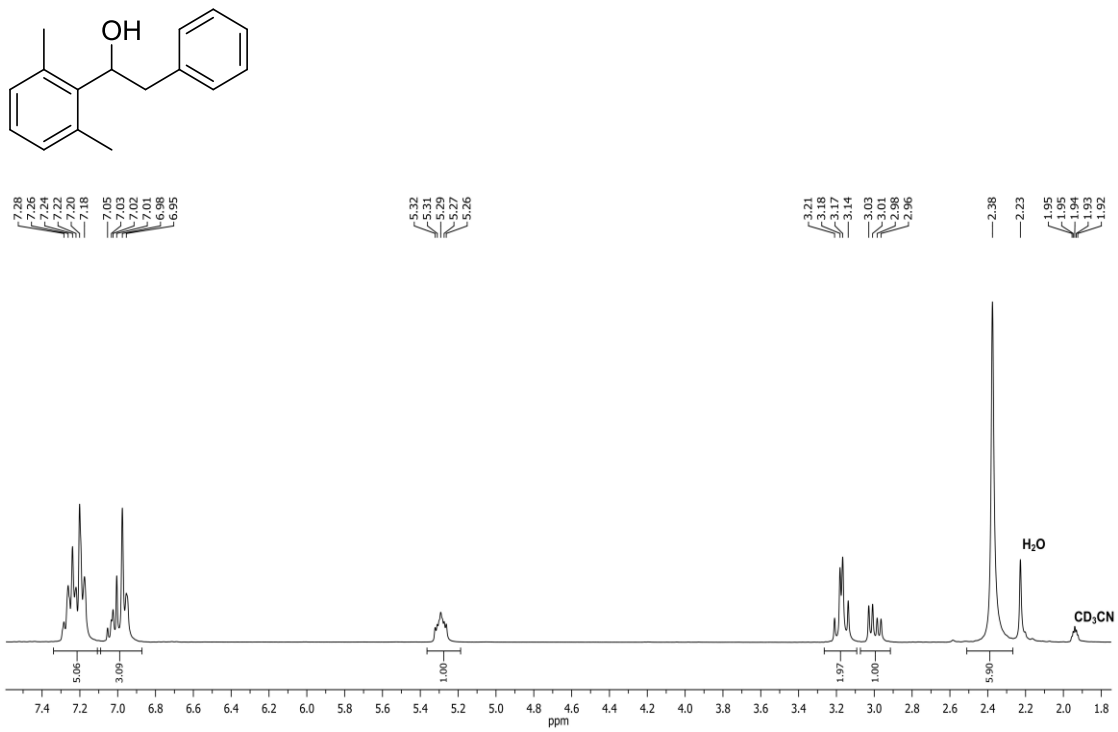

Figure A.53. The ^{1}H NMR spectrum of **41** (CD_3CN, 300 MHz).

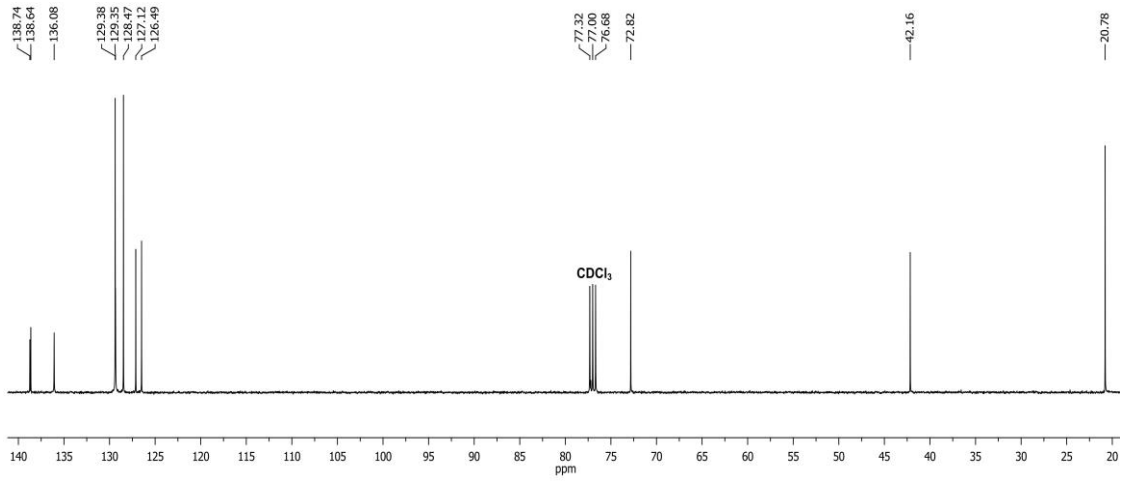

Figure A.54. The $^{13}C\{^{1}H\}$ NMR spectrum of **41** ($CDCl_3$, 100 MHz).

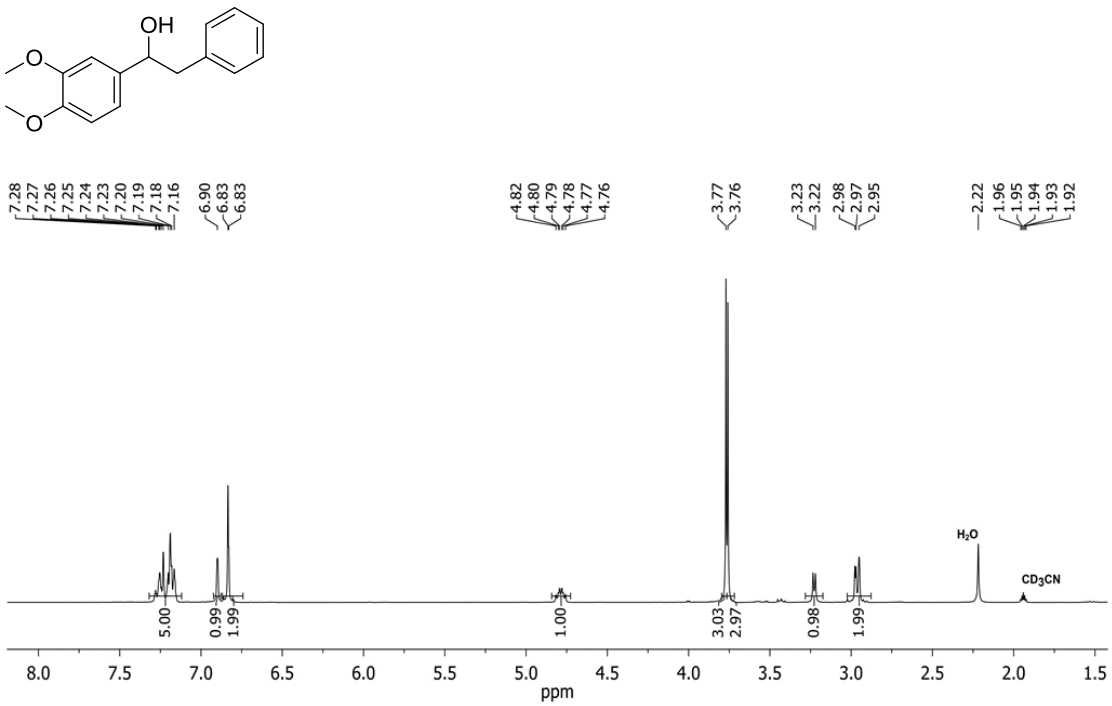

Figure A.55. The ^{1}H NMR spectrum of **42** (CD_3CN, 300 MHz).

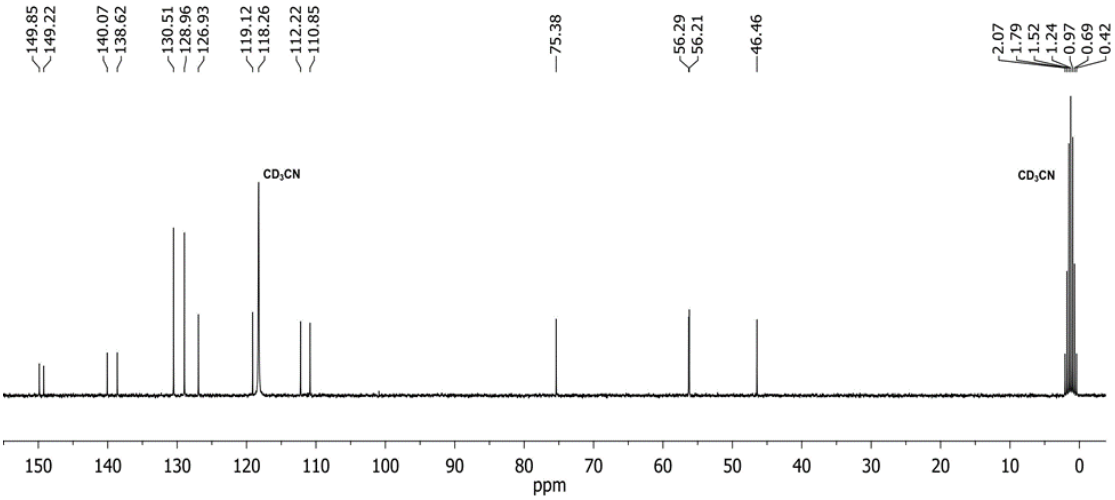

Figure A.56. The $^{13}C\{^{1}H\}$ NMR spectrum of **42** (CD_3CN, 75.47 MHz).

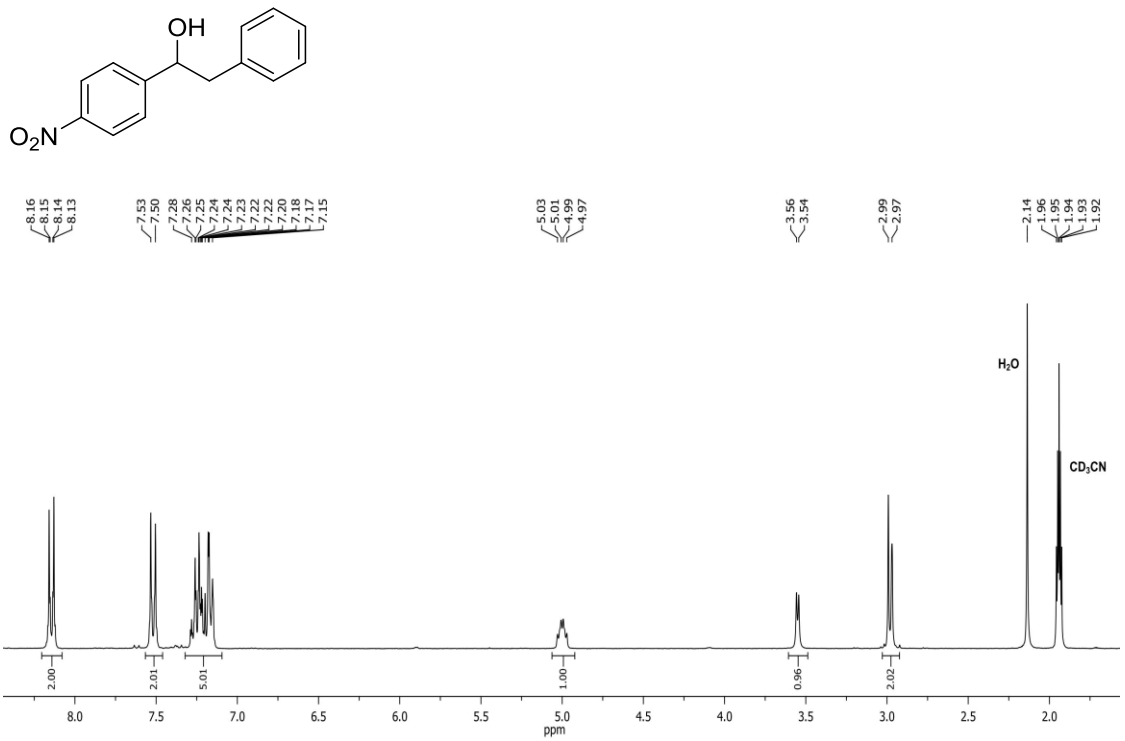

Figure A.57. The ^{1}H NMR spectrum of **43** (CD_3CN, 300 MHz).

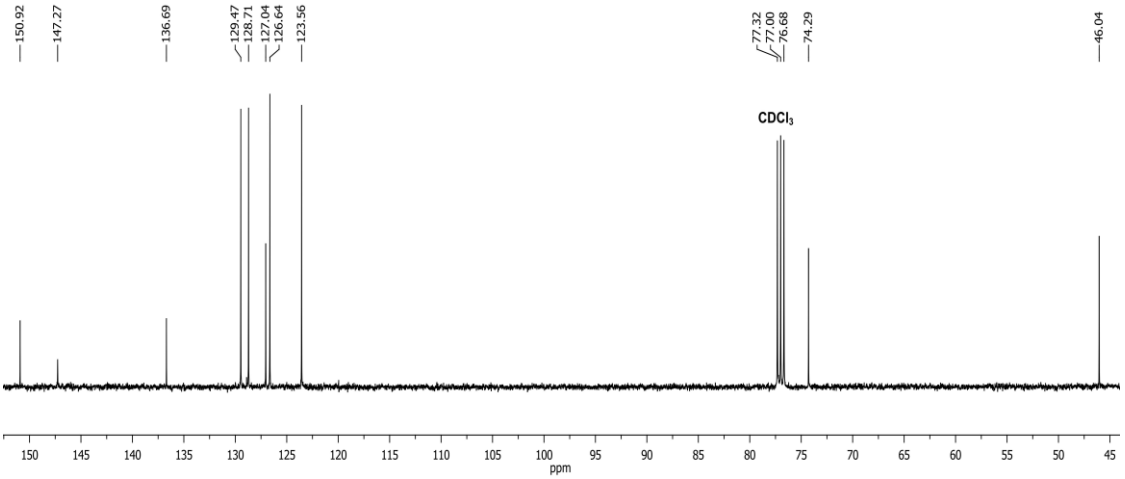

Figure A.58. The $^{13}C\{^{1}H\}$ NMR spectrum of **43** ($CDCl_3$, 100 MHz).

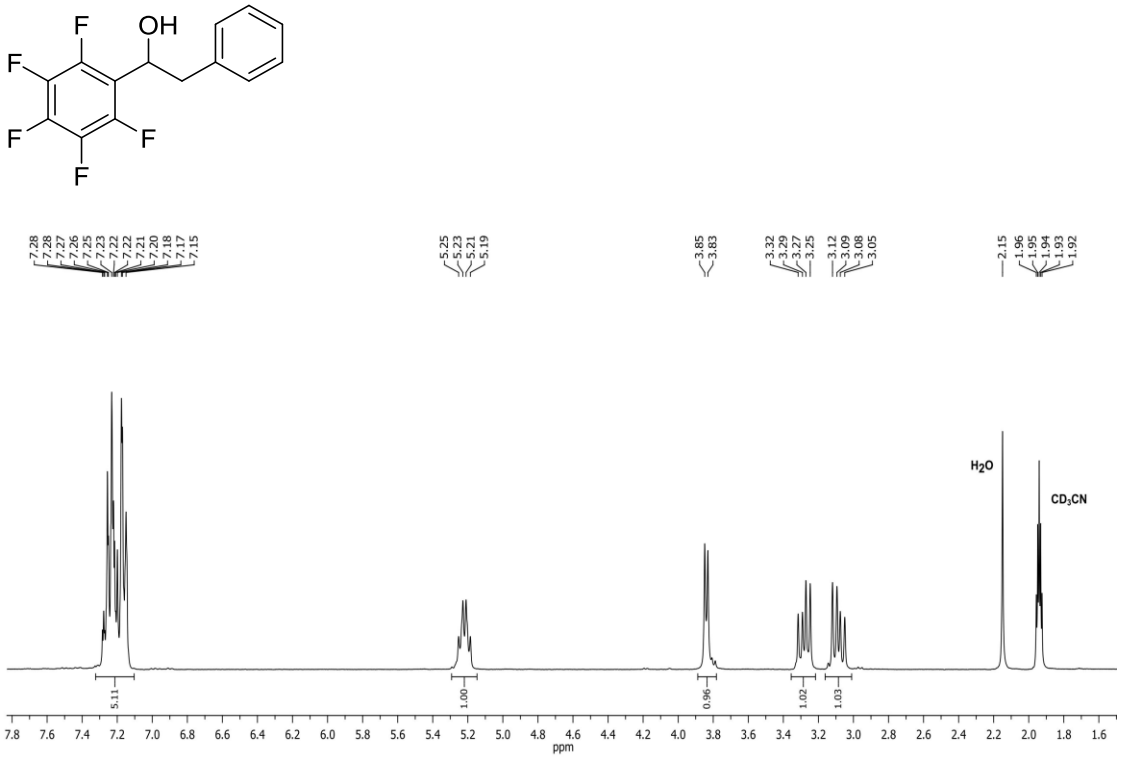

Figure A.59. The ^{1}H NMR spectrum of **44** (CD_3CN, 300 MHz).

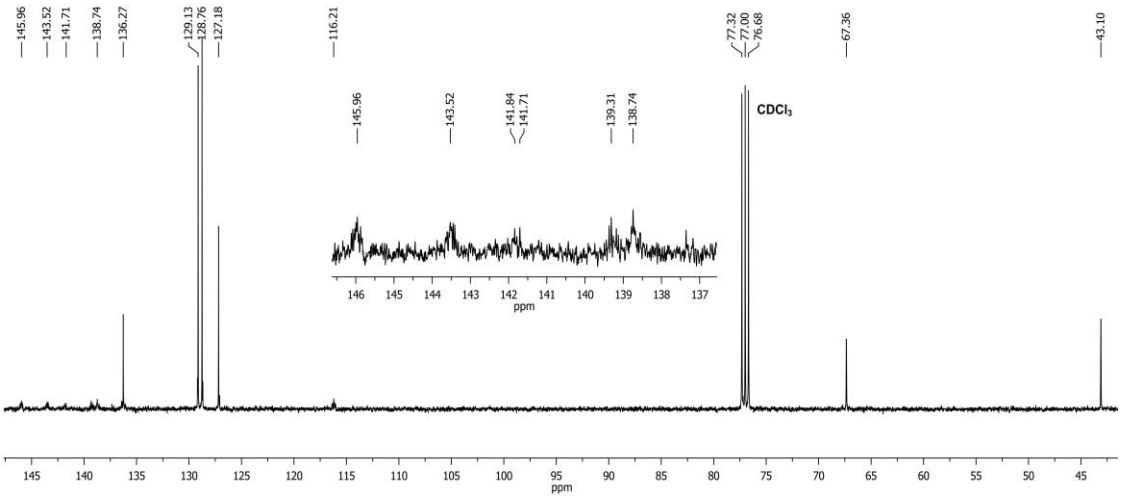

Figure A.60. The $^{13}C\{^{1}H\}$ NMR spectrum of **44** ($CDCl_3$, 100 MHz).

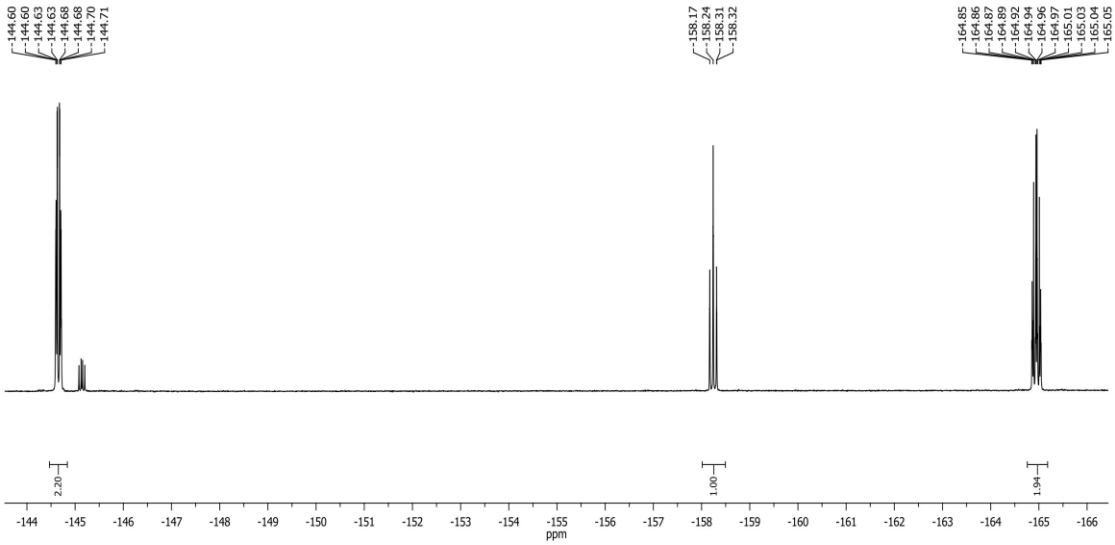

Figure A.61. The $^{19}F\{^{1}H\}$ NMR spectrum of **44** (CD_3CN, 282.4 MHz).

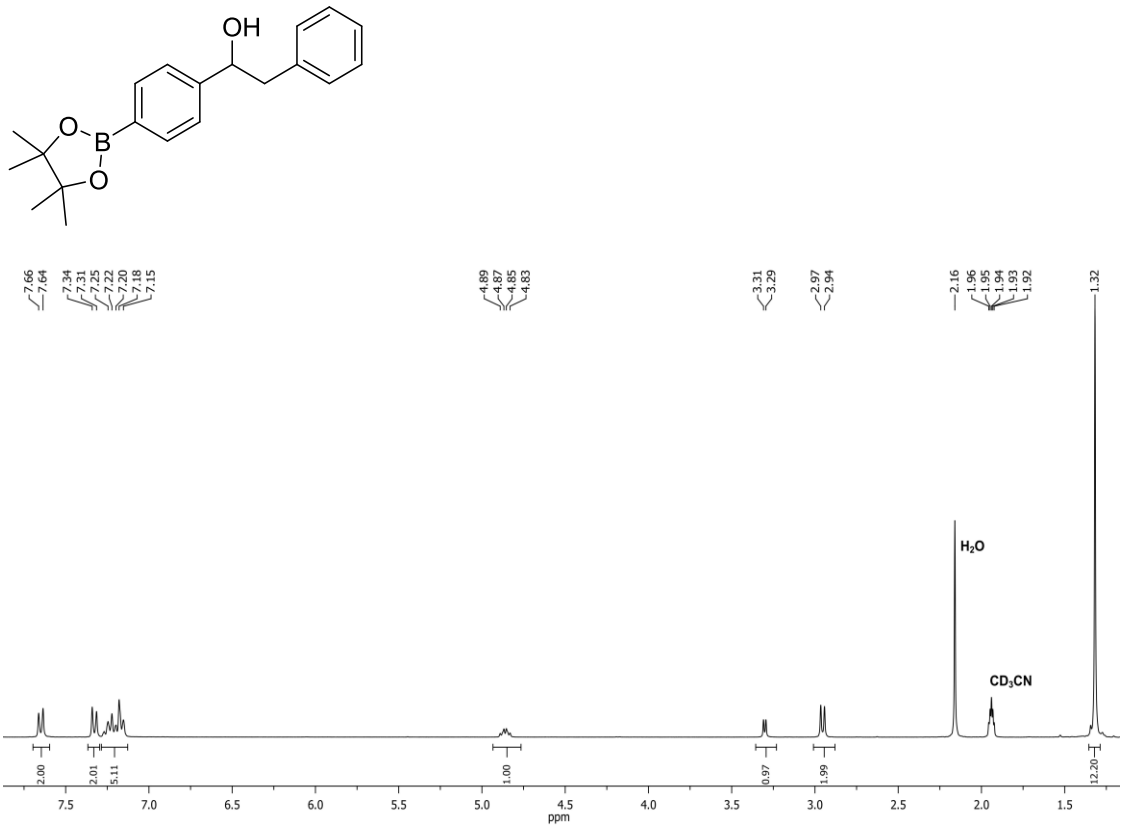

Figure A.62. The ^{1}H NMR spectrum of **45** (CD_3CN, 300 MHz).

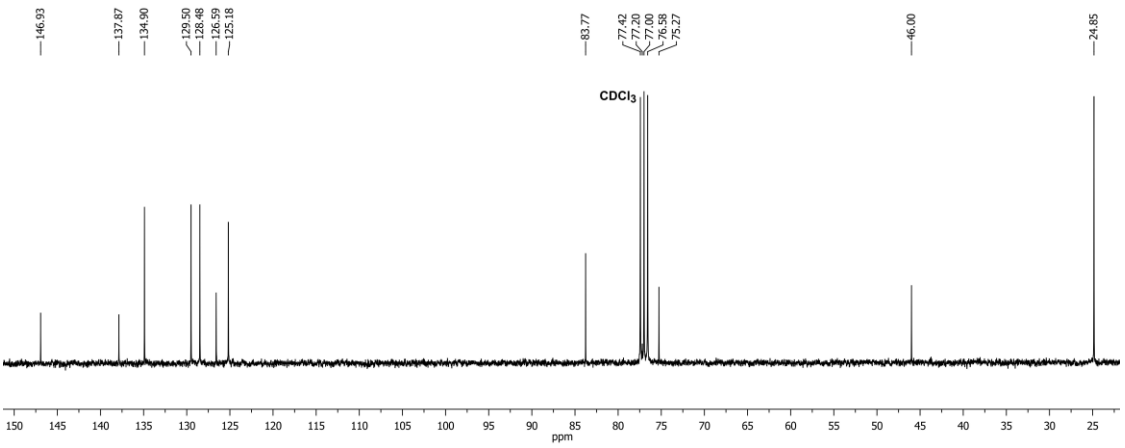

Figure A.63. The $^{13}C\{^{1}H\}$ NMR spectrum of **45** ($CDCl_3$, 100 MHz).

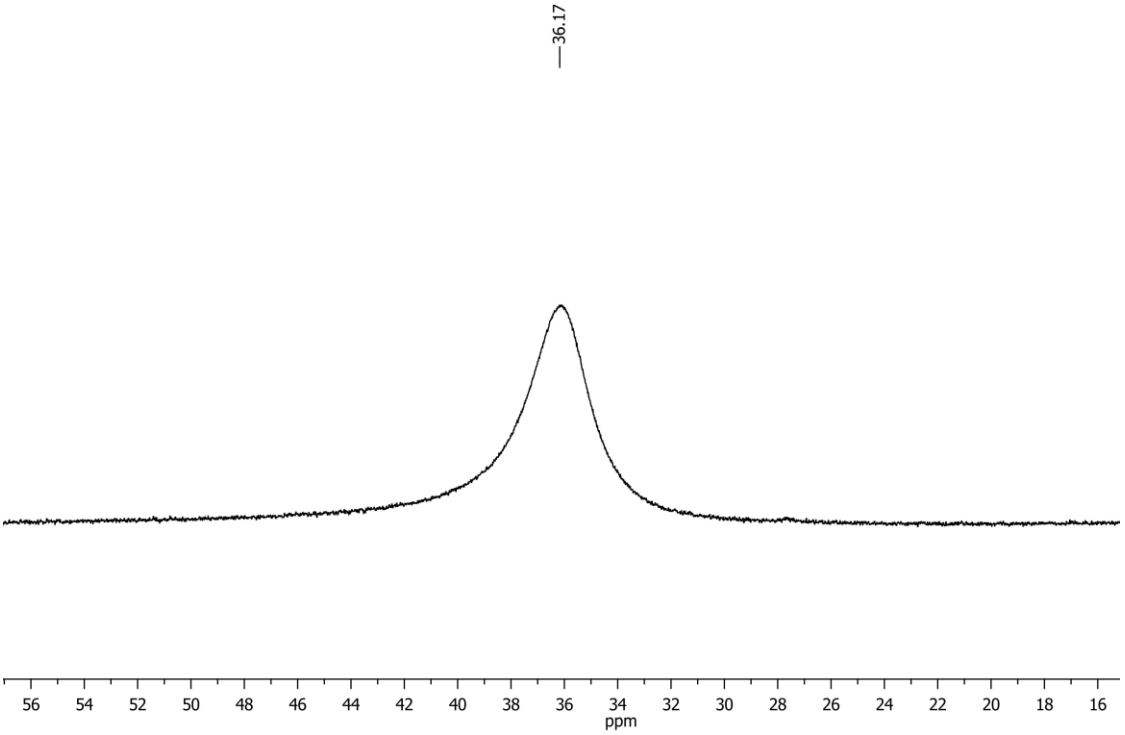

Figure A.64. The ^{11}B NMR spectrum of **45** (CD_3CN, 128 MHz).

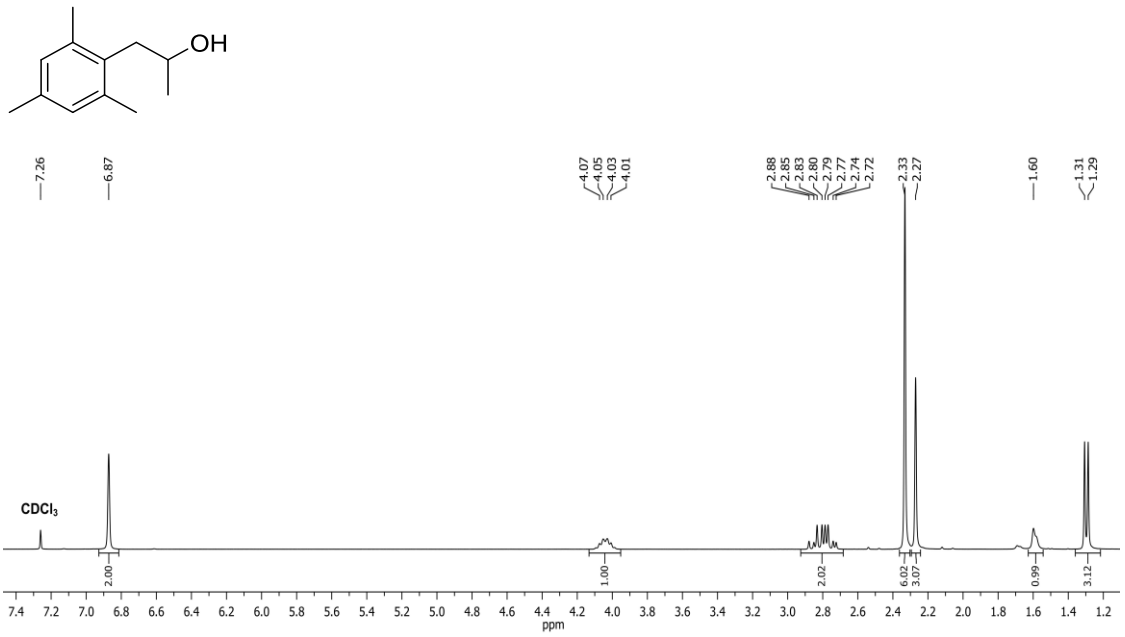

Figure A.65. The ^{1}H NMR spectrum of **58** ($CDCl_3$, 300 MHz).

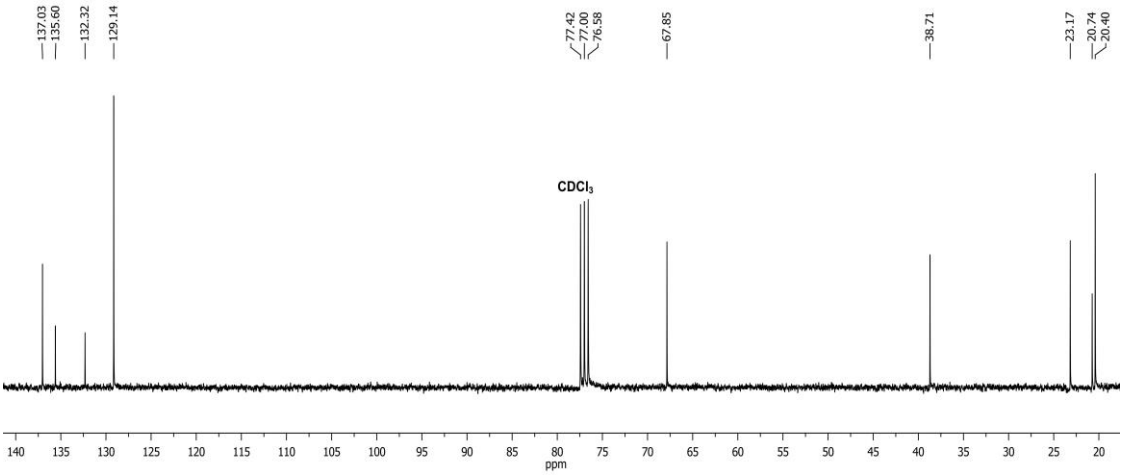

Figure A.66. The ^{13}C{^{1}H} NMR spectrum of **58** ($CDCl_3$, 75.46 MHz).

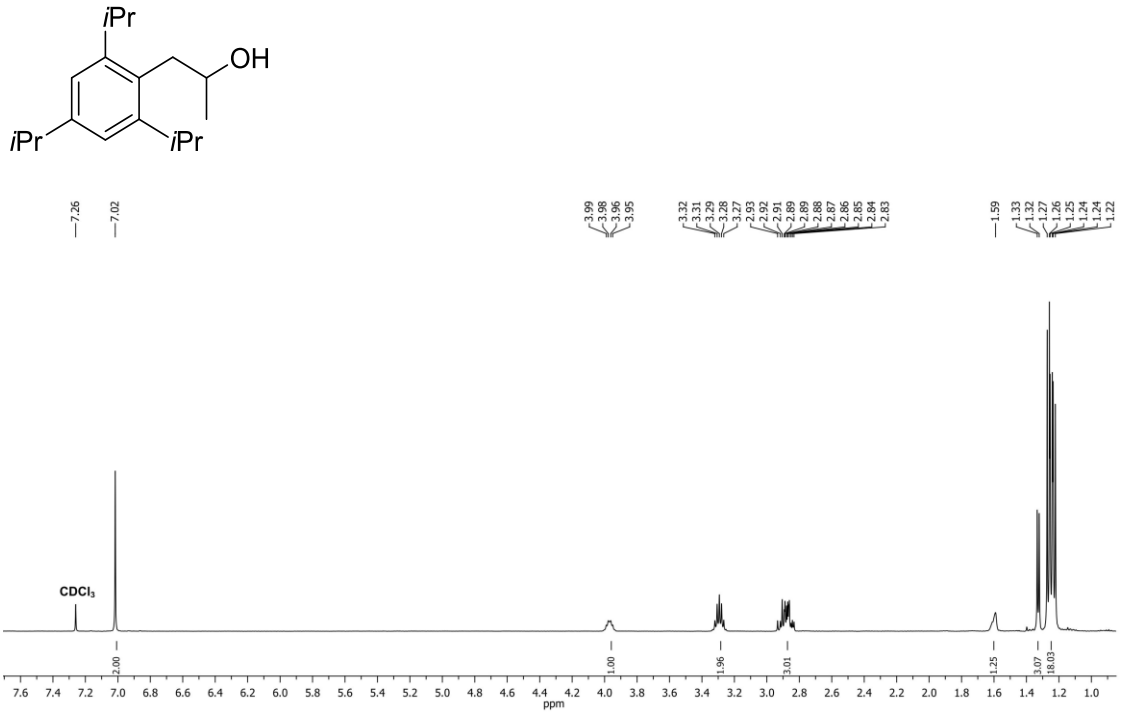

Figure A.67. The ^{1}H NMR spectrum of **59** ($CDCl_3$, 500 MHz).

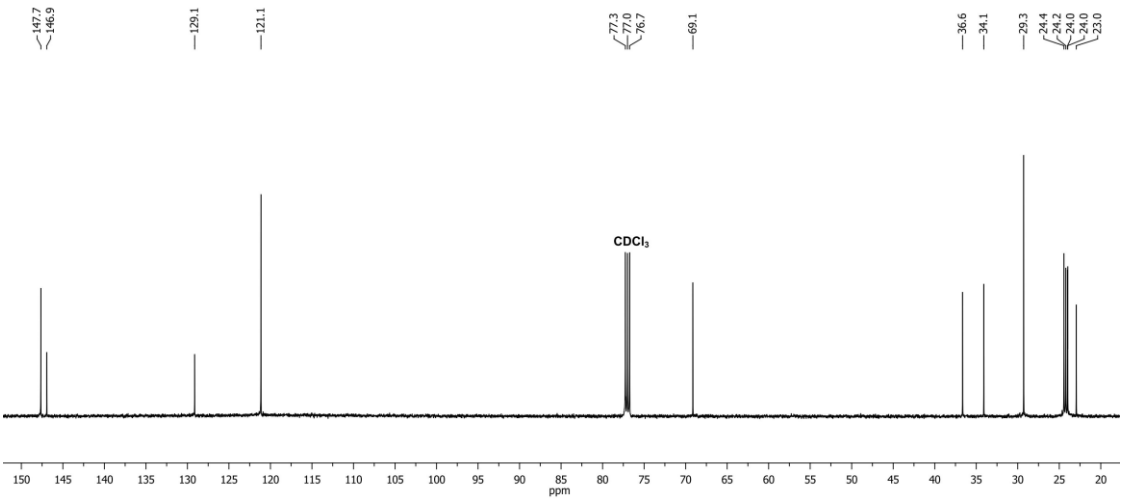

Figure A.68. The $^{13}C\{^{1}H\}$ NMR spectrum of **59** ($CDCl_3$, 126 MHz).

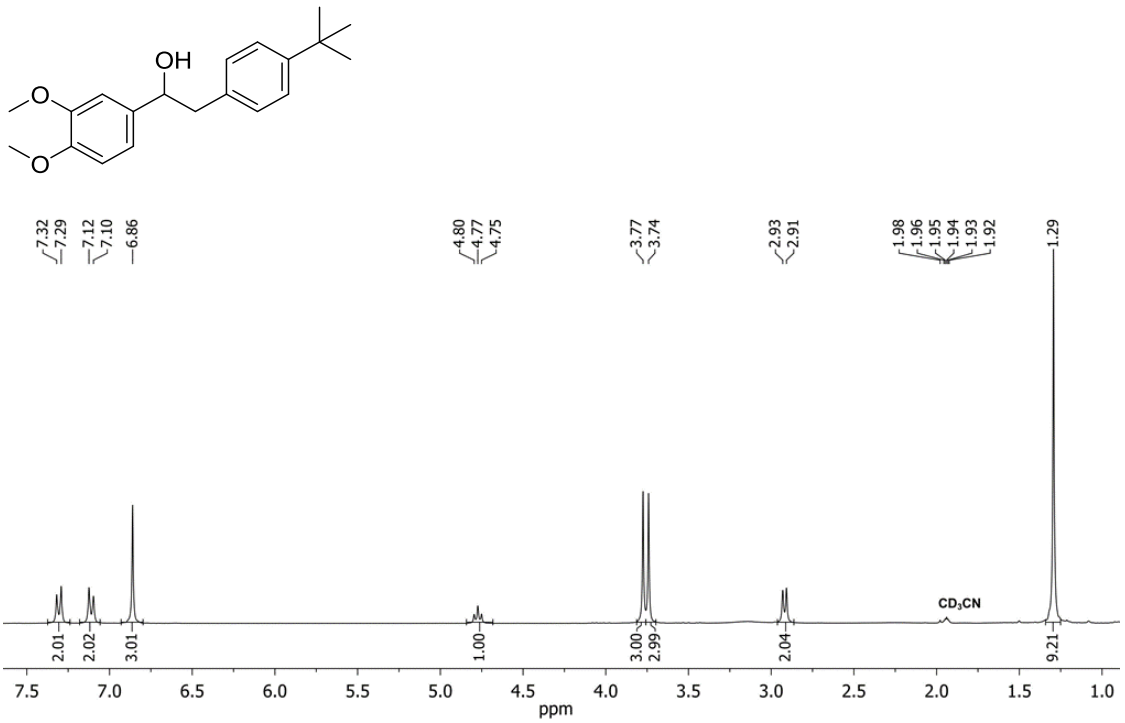

Figure A.69. The ^{1}H NMR spectrum of **60** (CD_3CN, 300 MHz).

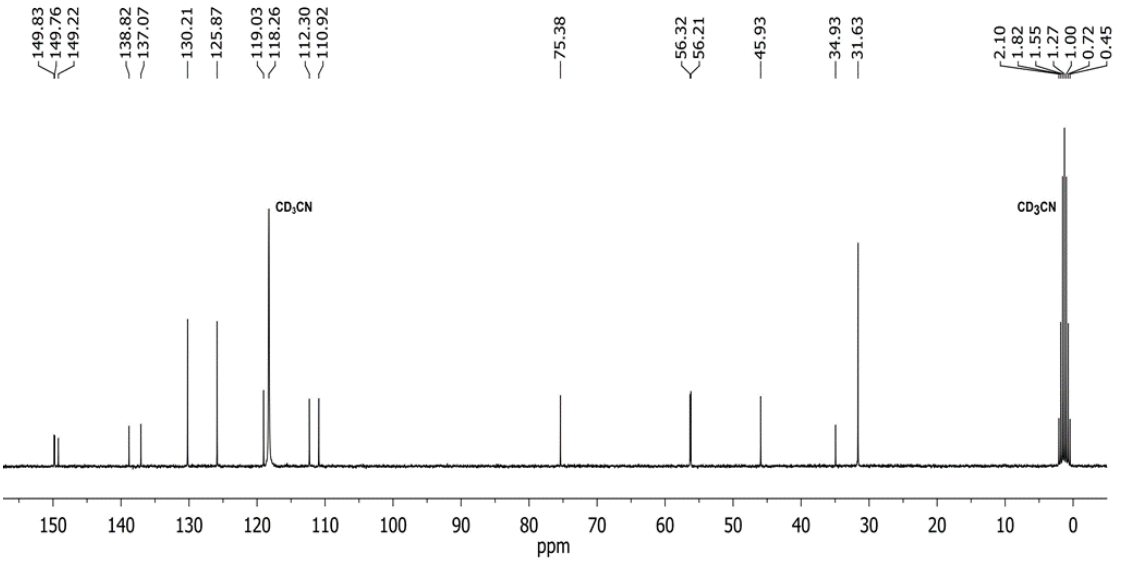

Figure A.70. The $^{13}C\{^{1}H\}$ NMR spectrum of **60** (CD_3CN, 75.47 MHz).

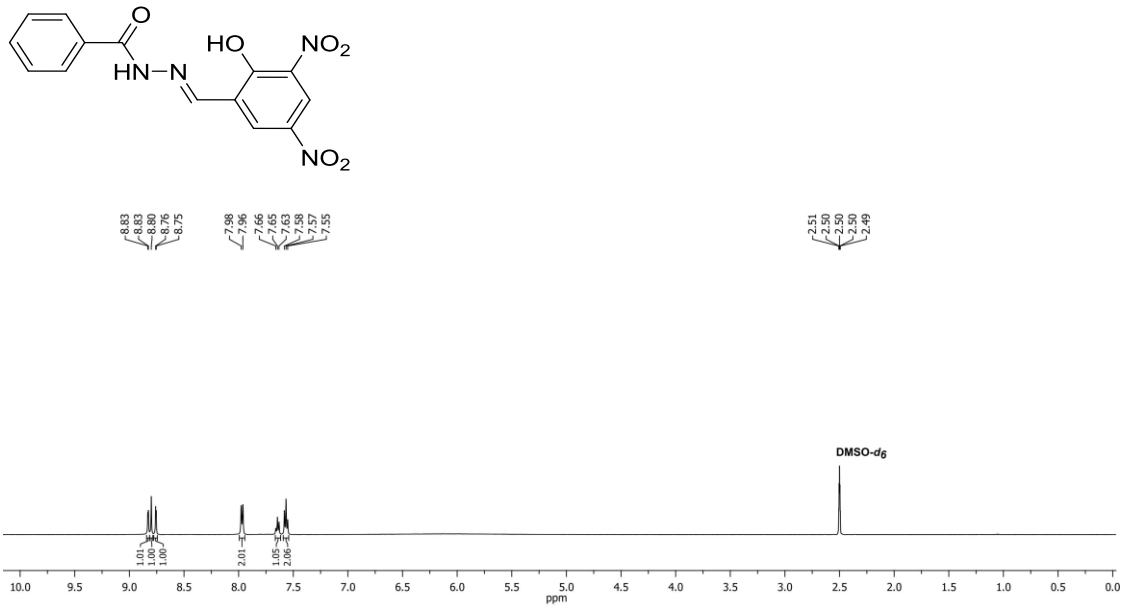

Figure A.71. The ^{1}H NMR spectrum of **L-7** (DMSO-d_6, 400 MHz).

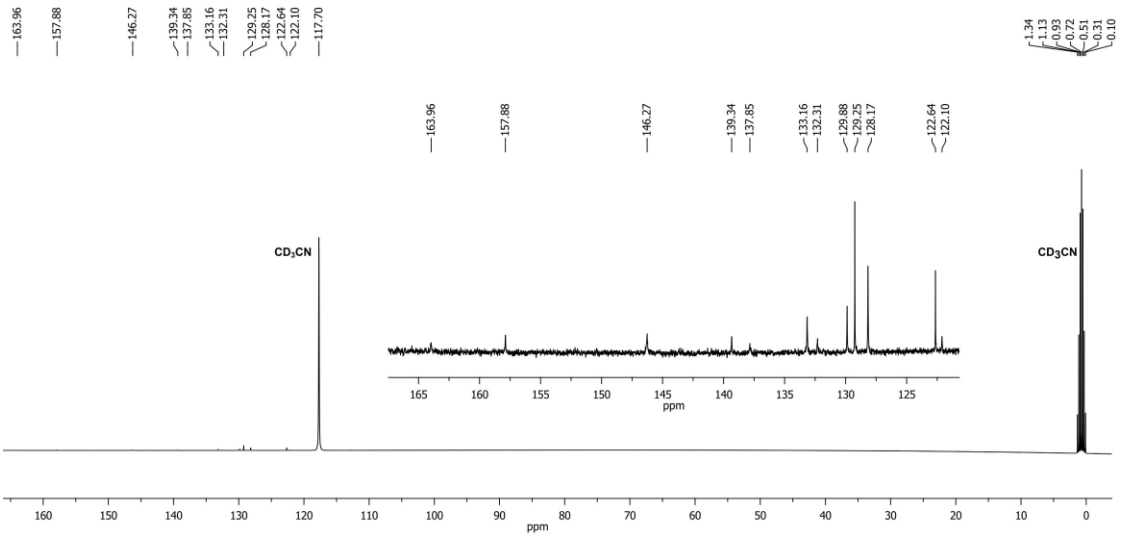

Figure A.72. The ^{13}C{^{1}H} NMR spectrum of **L-7** (CD_3CN, 100 MHz). The inset shows the ligand's carbon peaks more clearly.

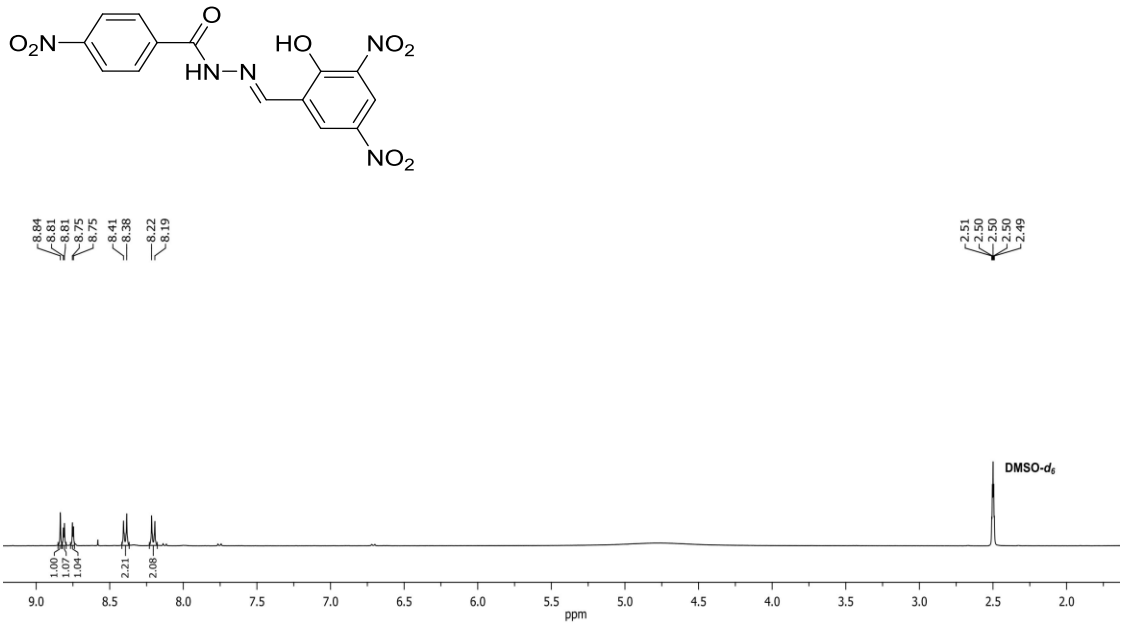

Figure A.73. The ^{1}H NMR spectrum of **L-8** (DMSO-d_6, 500 MHz).

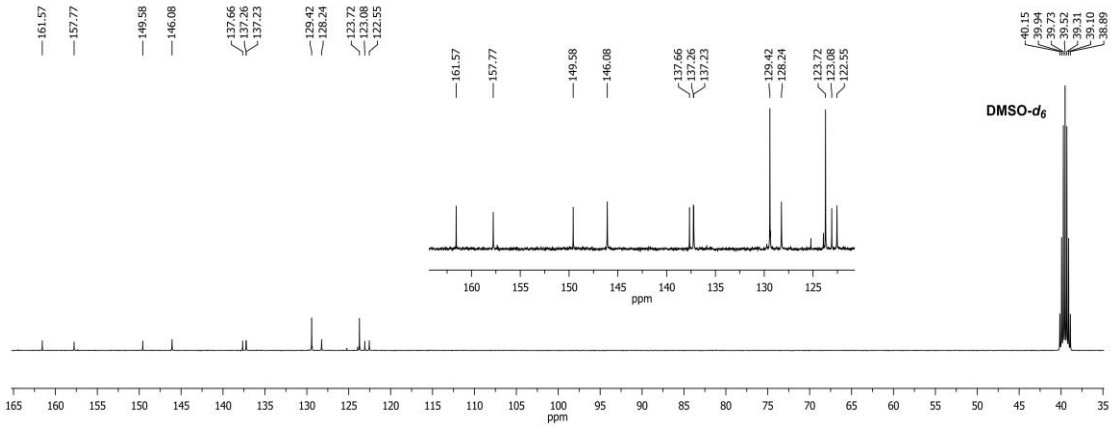

Figure A.74. The ^{13}C{^{1}H} NMR spectrum of **L-8** (DMSO-d_6, 100 MHz). The inset shows all signals more clearly.

Figure A.75. The ^{1}H NMR spectrum of **L-9** (DMSO-d_6, 400 MHz).

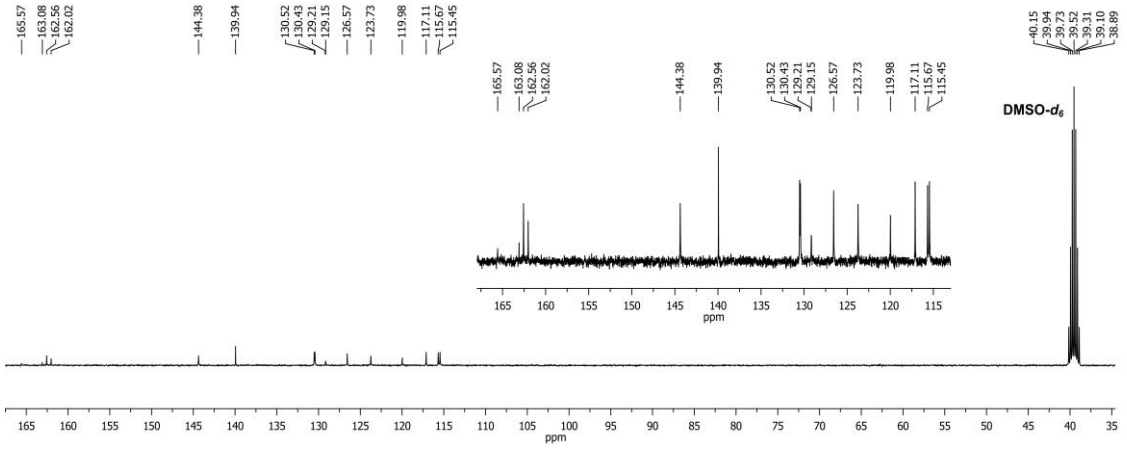

Figure A.76. The ^{13}C{^{1}H} NMR spectrum of **L-9** (DMSO-d_6, 100 MHz). The inset shows all signals more clearly.

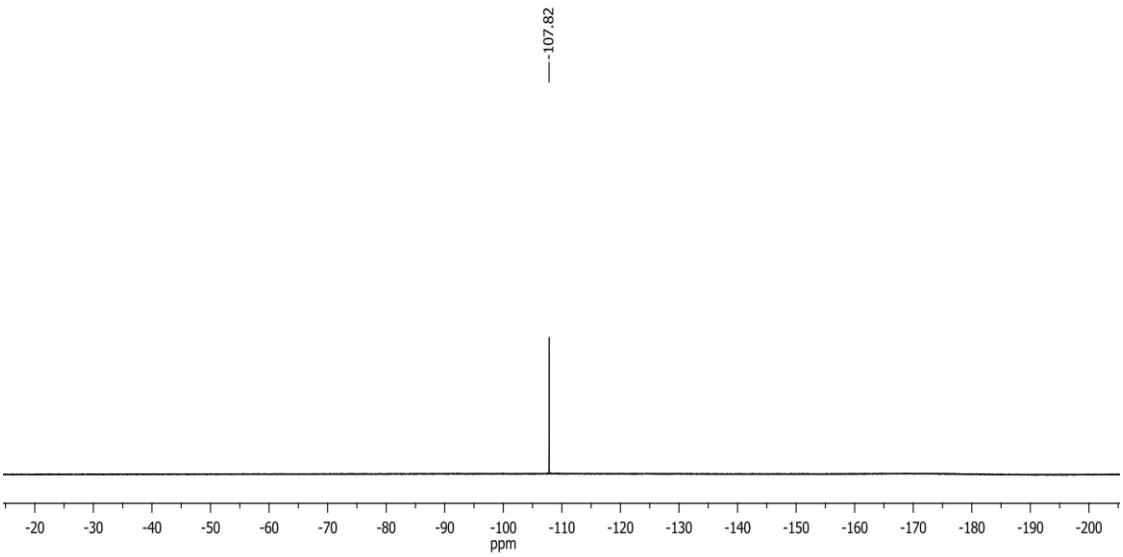

Figure A.77. The $^{19}F\{^{1}H\}$ NMR spectrum **L-9** (DMSO-d_6, 376.50 MHz).

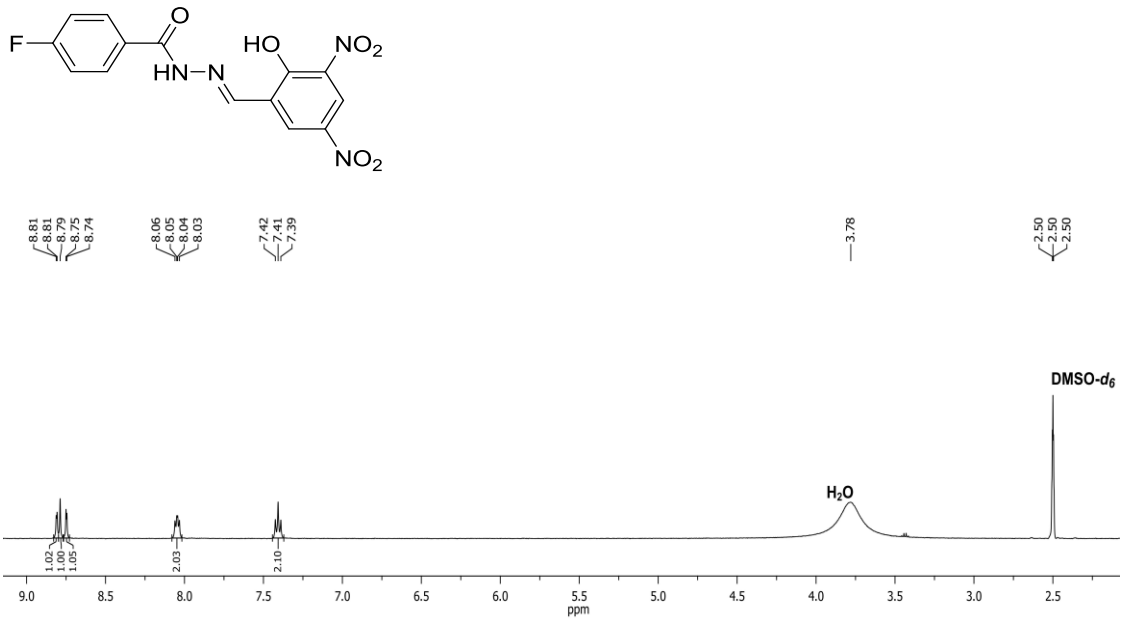

Figure A.78. The ^{1}H NMR spectrum of **L-10** (DMSO-d_6, 500 MHz).

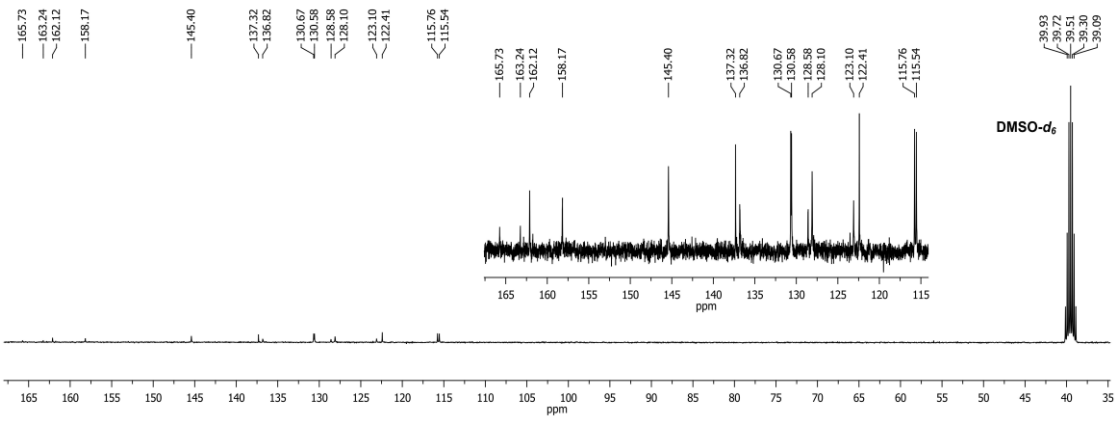

Figure A.79. The $^{13}C\{^{1}H\}$ NMR spectrum of **L-10** (DMSO-d_6, 100 MHz). The inset shows all the peaks more clearly.

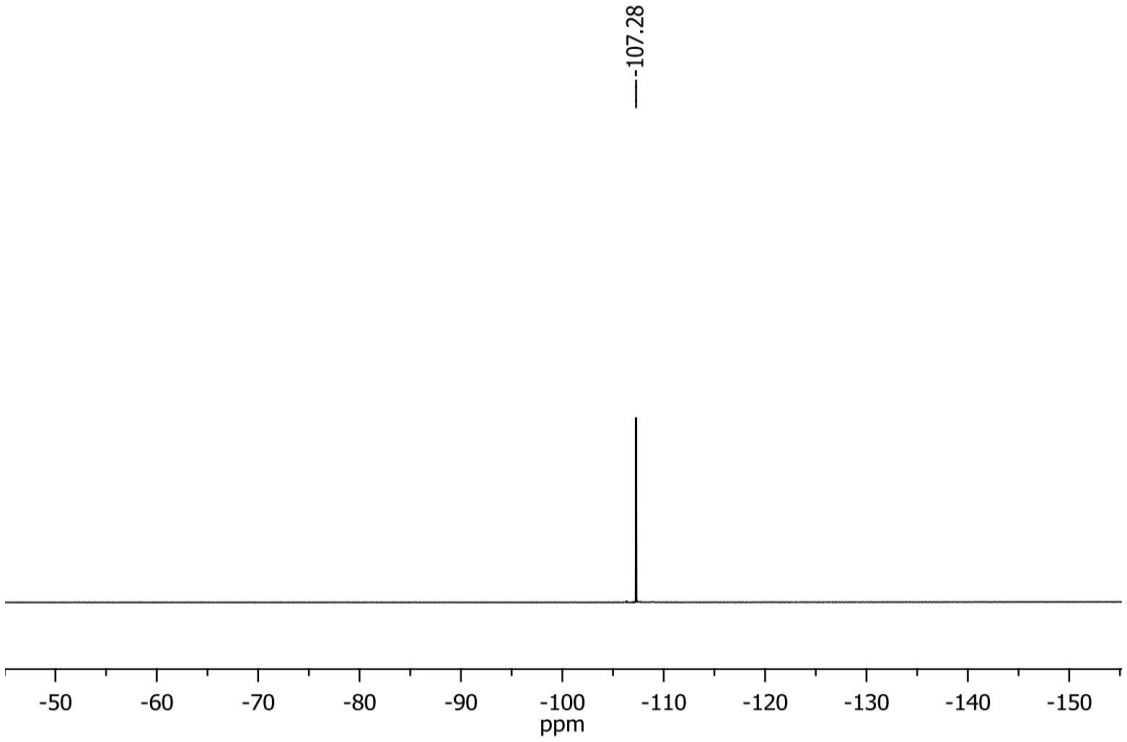

Figure A.80. The $^{19}F\{^{1}H\}$ NMR spectrum of **L-10** (DMSO-d_6, 376.50 MHz).

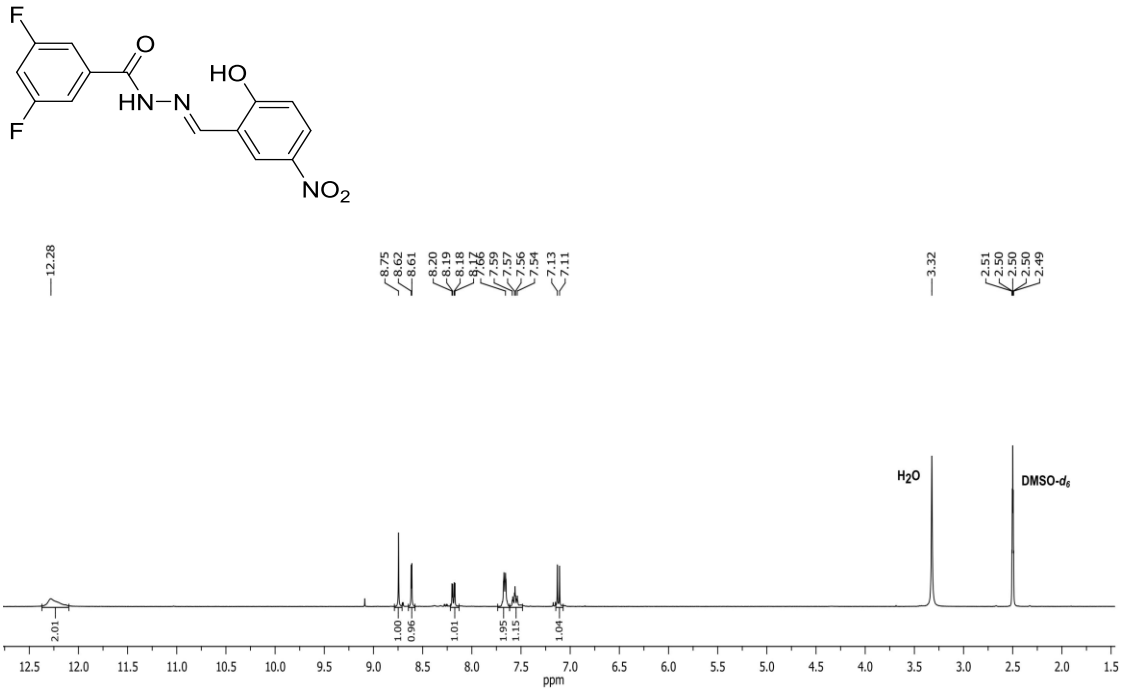

Figure A.81. The ^{1}H NMR spectrum of **L-11** (DMSO-d_6, 400 MHz).

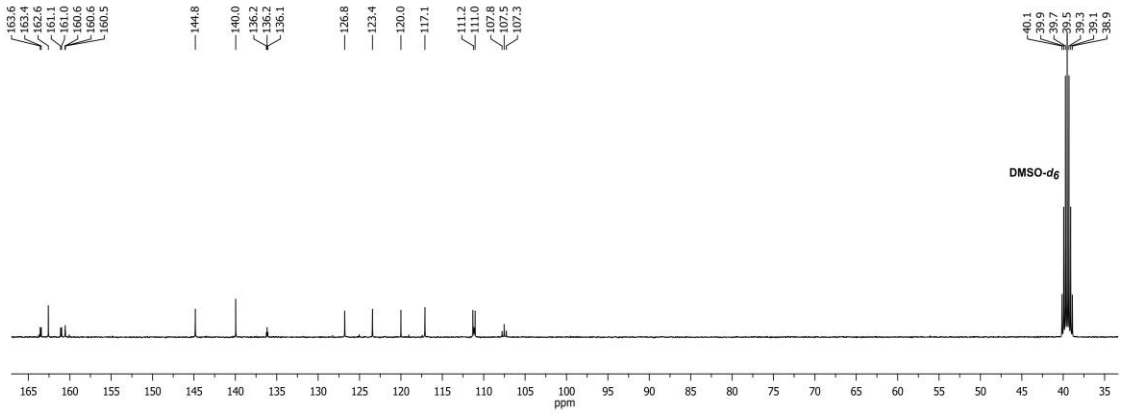

Figure A.82. The ^{13}C{^{1}H} NMR spectrum of **L-11** (DMSO-d_6, 100 MHz).

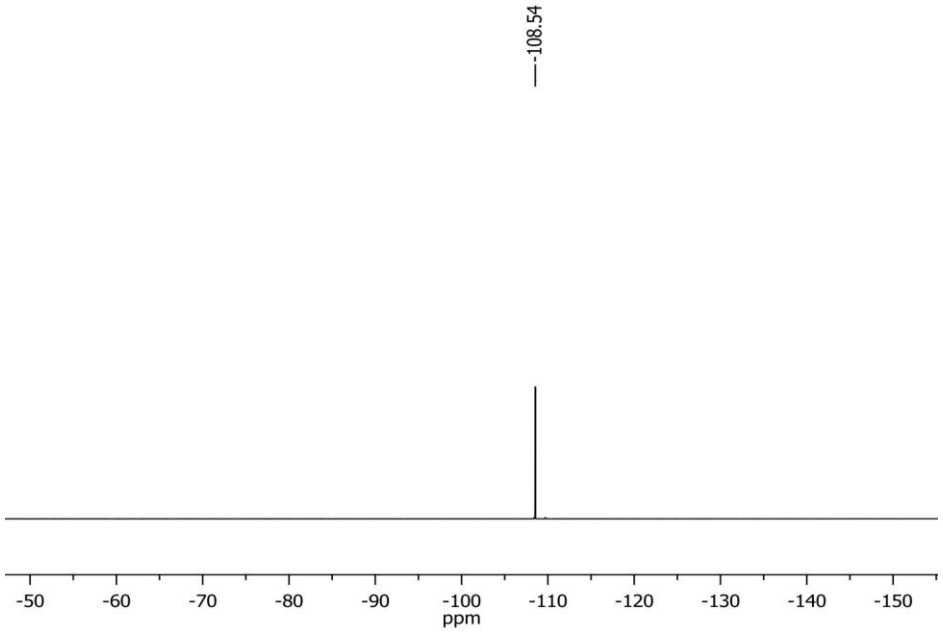

Figure A.83. The $^{19}F\{^{1}H\}$ NMR spectrum of **L-11** (DMSO-d_6, 376.50 MHz).

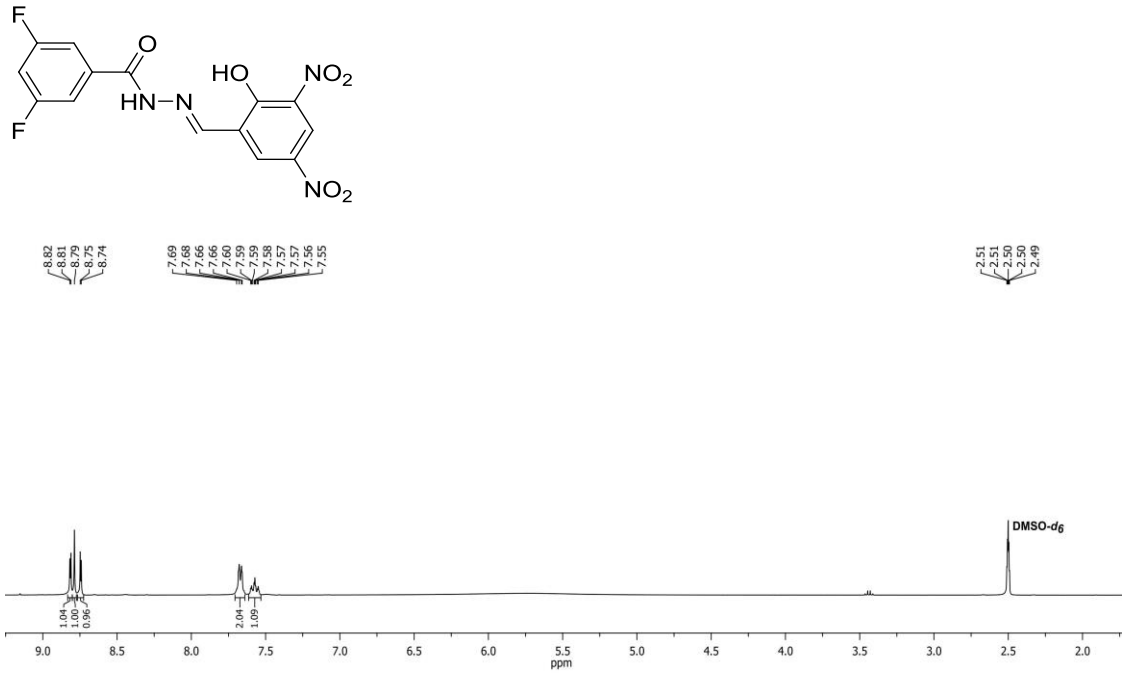

Figure A.84. The ^{1}H NMR spectrum of **L-12** (DMSO-d_6, 400 MHz).

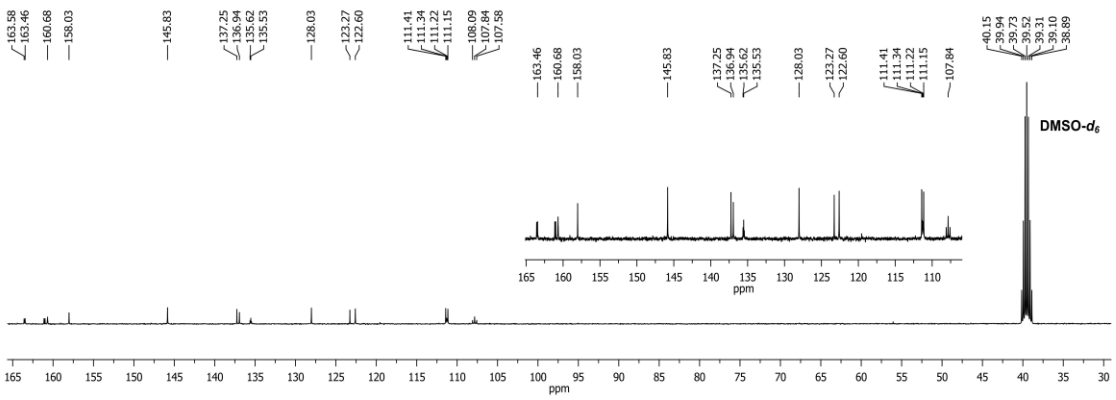

Figure A.85. The $^{13}C\{^{1}H\}$ NMR spectrum of **L-12** (DMSO-d_6, 100 MHz). The inset shows all signals more clearly.

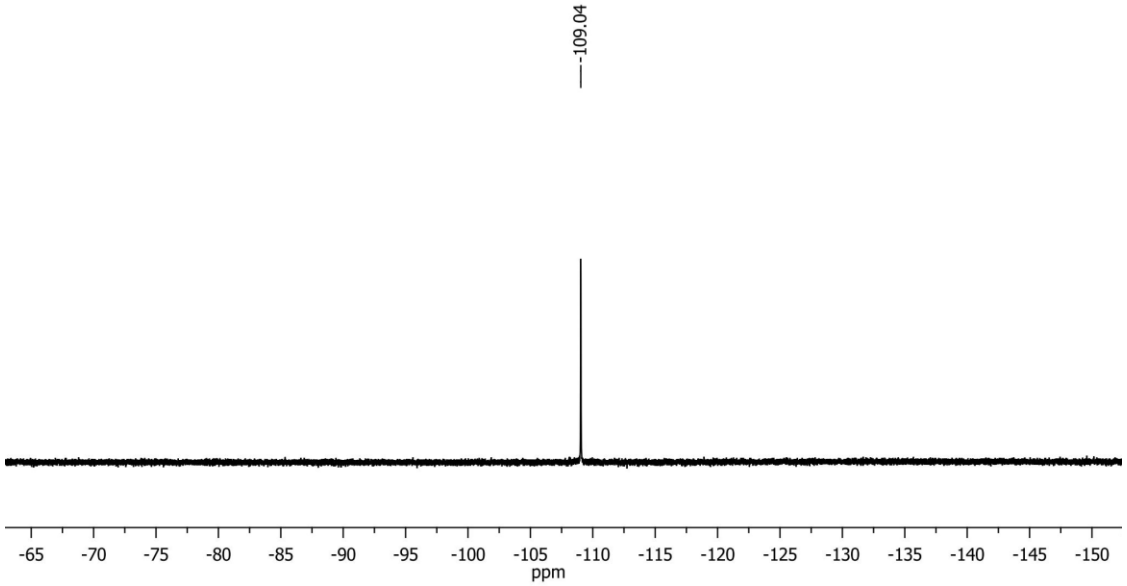

Figure A.86. The $^{19}F\{^{1}H\}$ NMR spectrum of **L-12** (CD_3CN, 282.40 MHz).

Figure A.87. The ^{1}H NMR spectrum of **L-13** (DMSO-d_6, 500 MHz).

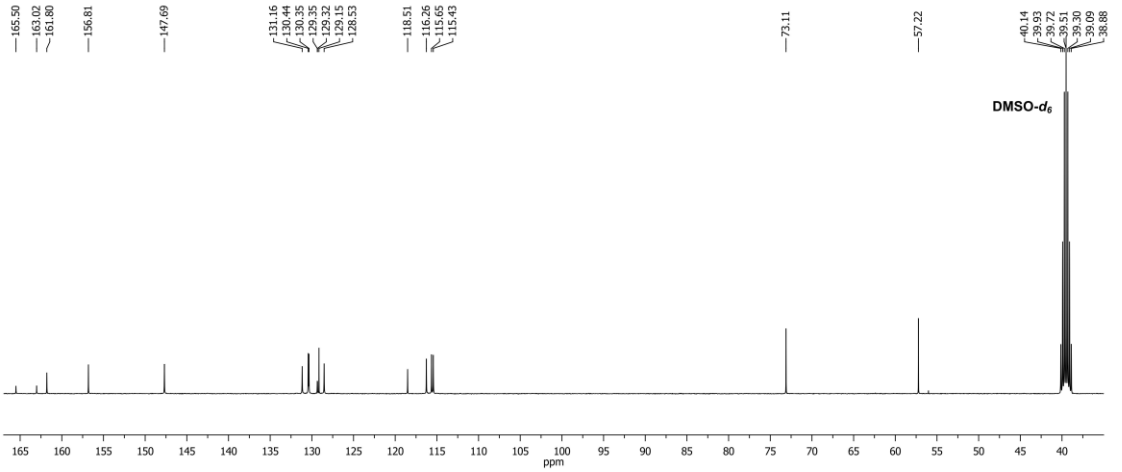

Figure A.88. The ^{13}C{^{1}H} NMR spectrum of **L-13** (DMSO-d_6, 100 MHz).

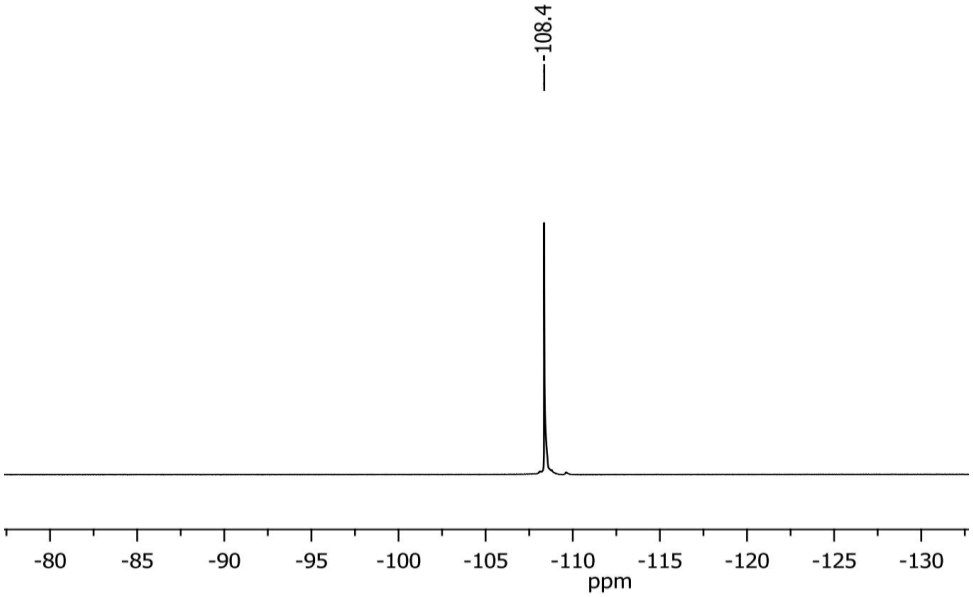

Figure A.89. The $^{19}F\{^{1}H\}$ NMR spectrum of **L-13** (DMSO-d_6, 376.50 MHz).

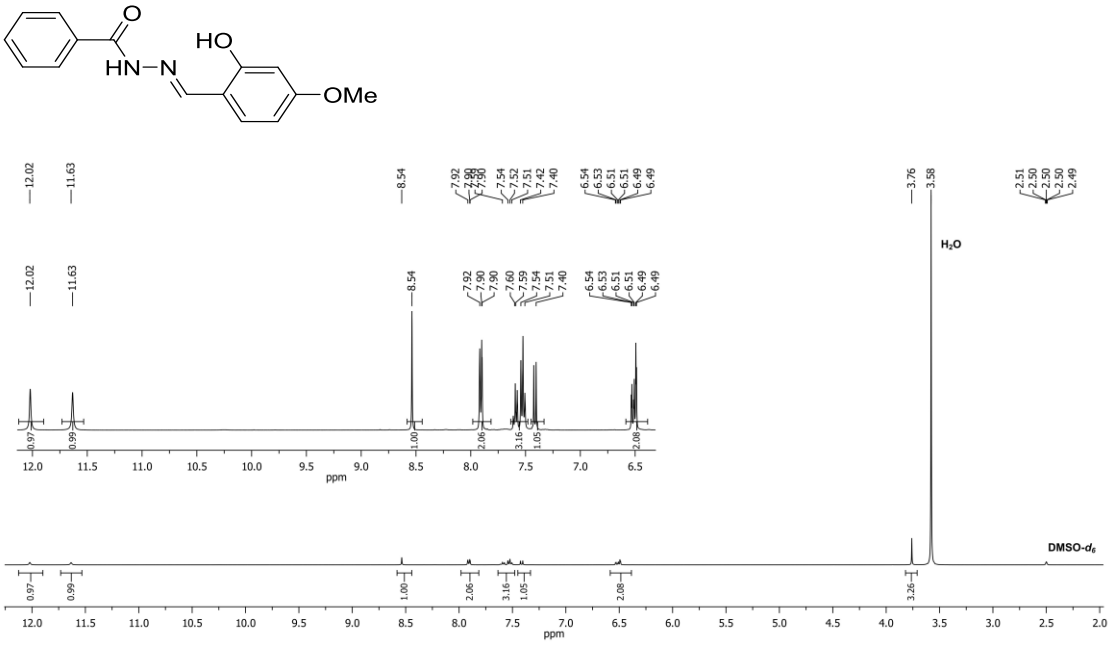

Figure A.90. The ^{1}H NMR spectrum of **L-14** (DMSO-d_6, 400 MHz). The inset shows all signals more clearly.

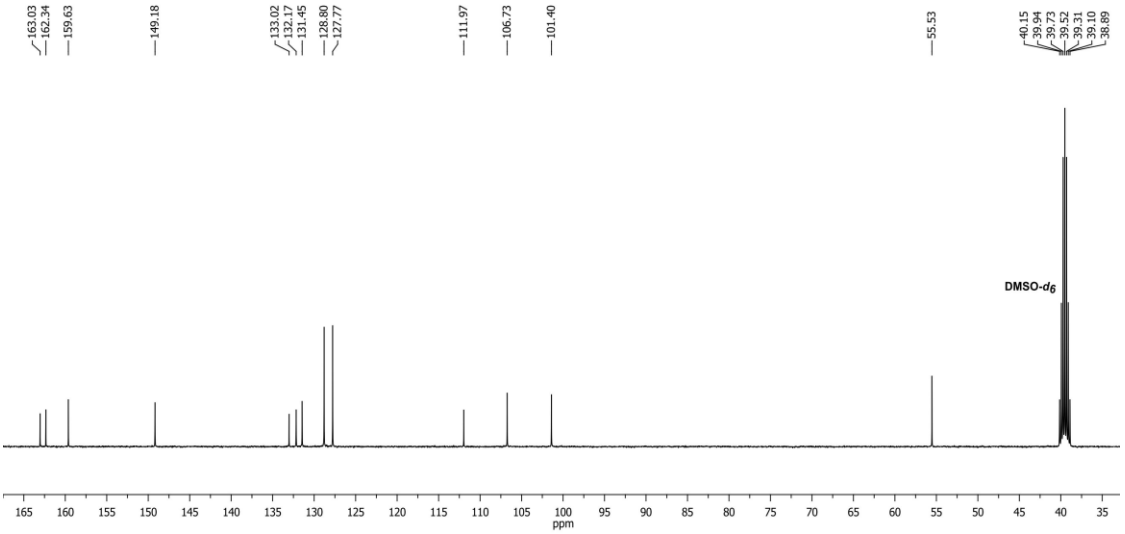

Figure A.91. The $^{13}C\{^{1}H\}$ NMR spectrum of **L-14** (DMSO-d_6, 100 MHz).

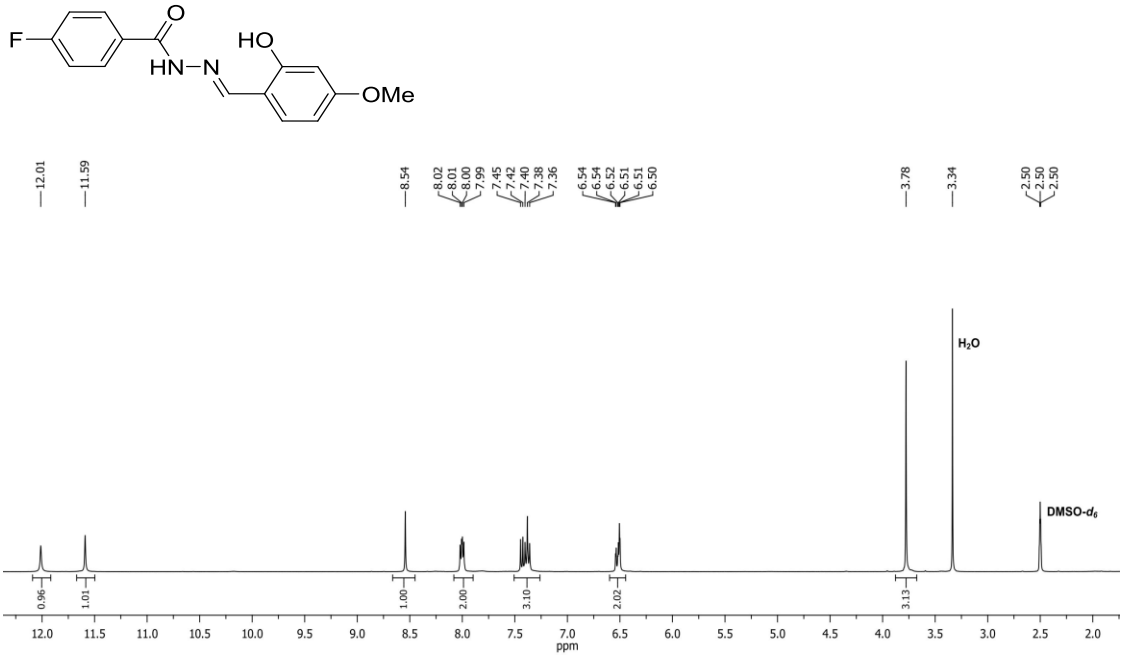

Figure A.92. The ^{1}H NMR spectrum of **L-15** (DMSO-d_6, 400 MHz).

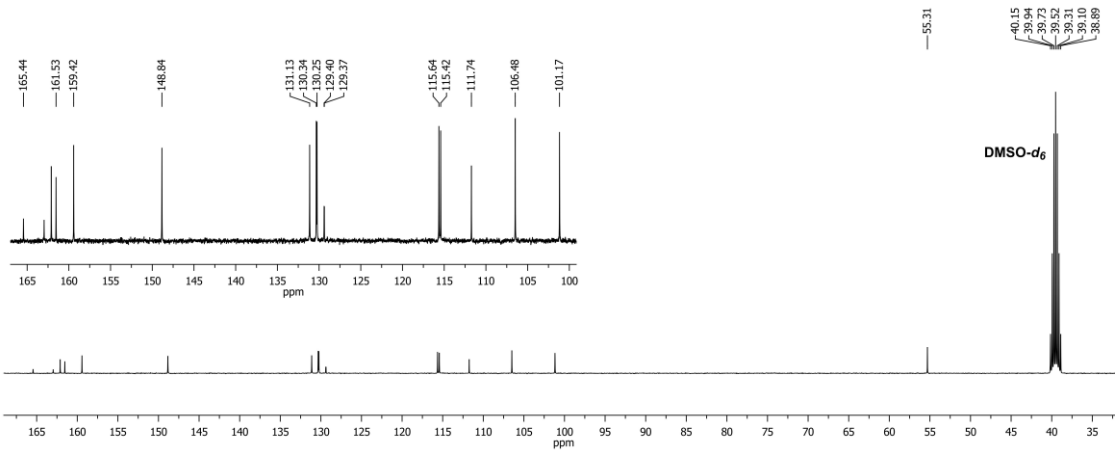

Figure A.93. The $^{13}C\{^{1}H\}$ NMR spectrum of **L-15** (DMSO-d_6, 100 MHz). The inset shows the signals more clearly.

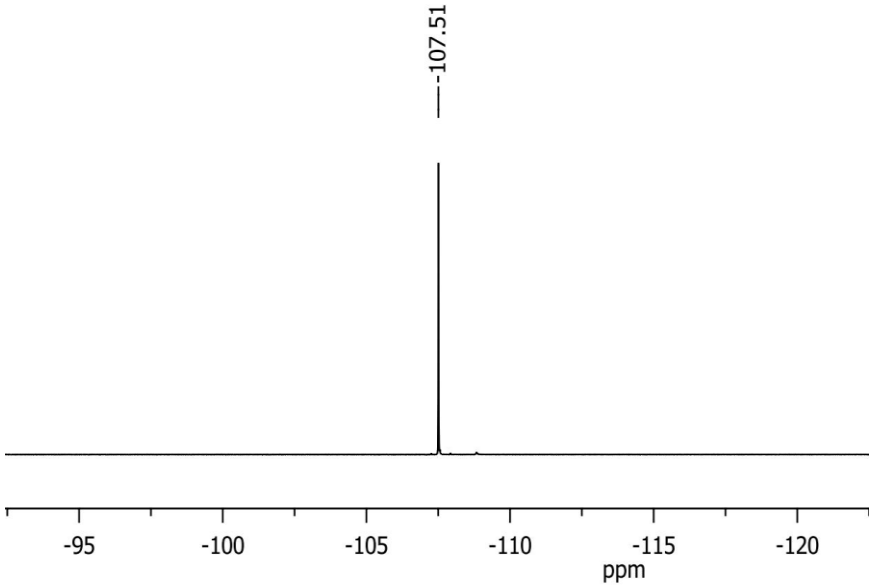

Figure A.94. The $^{19}F\{^{1}H\}$ NMR spectrum of **L-15** (DMSO-d_6, 376.50 MHz).

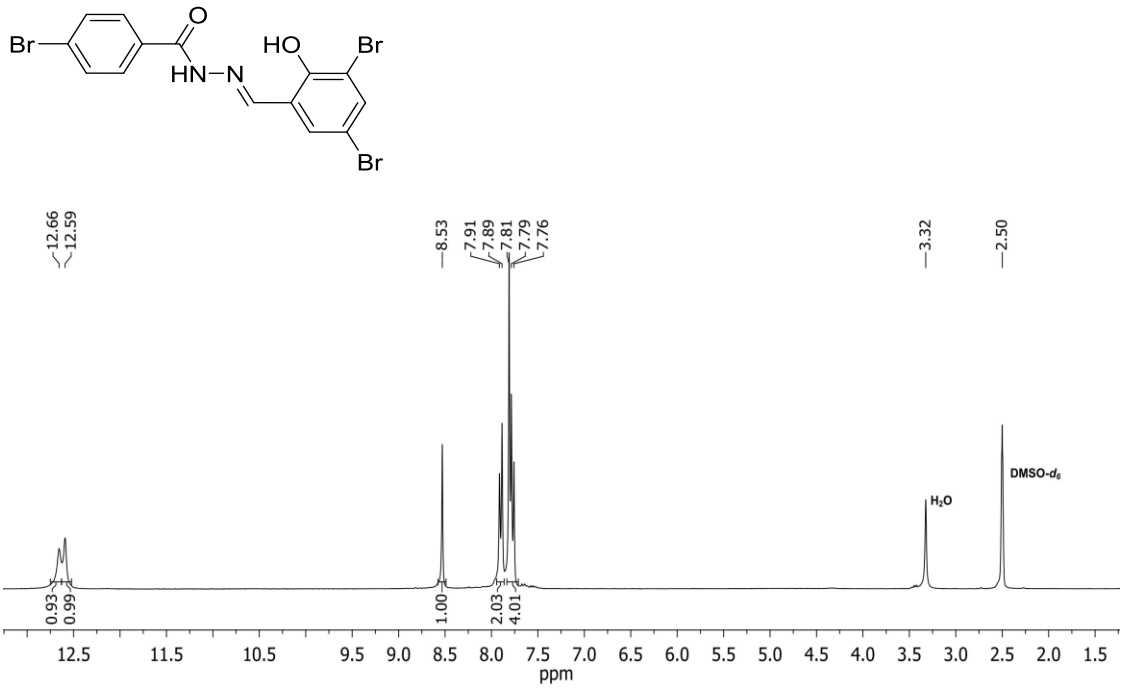

Figure A.95. The ^{1}H NMR spectrum of **L-16** (DMSO-d_6, 300 MHz).

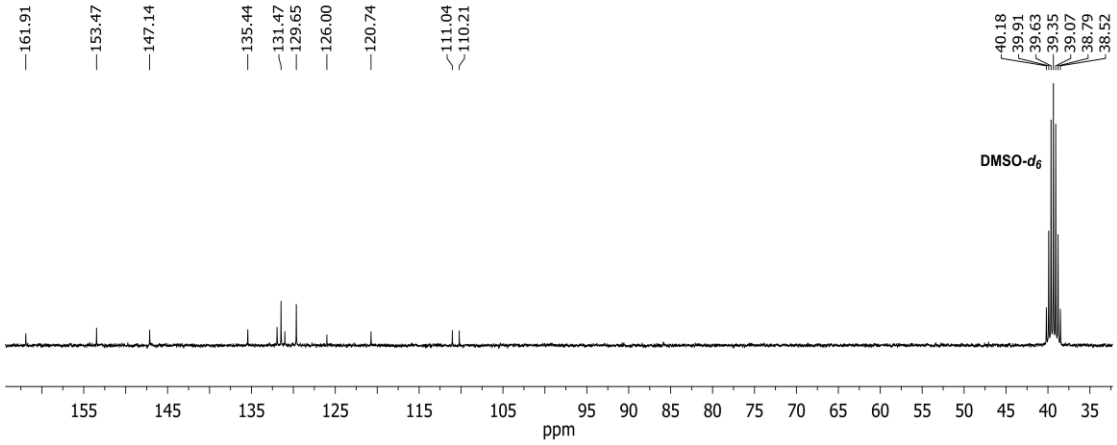

Figure A.96. The ^{13}C{^{1}H} NMR spectrum of **L-16** (DMSO-d_6, 75.5 MHz).

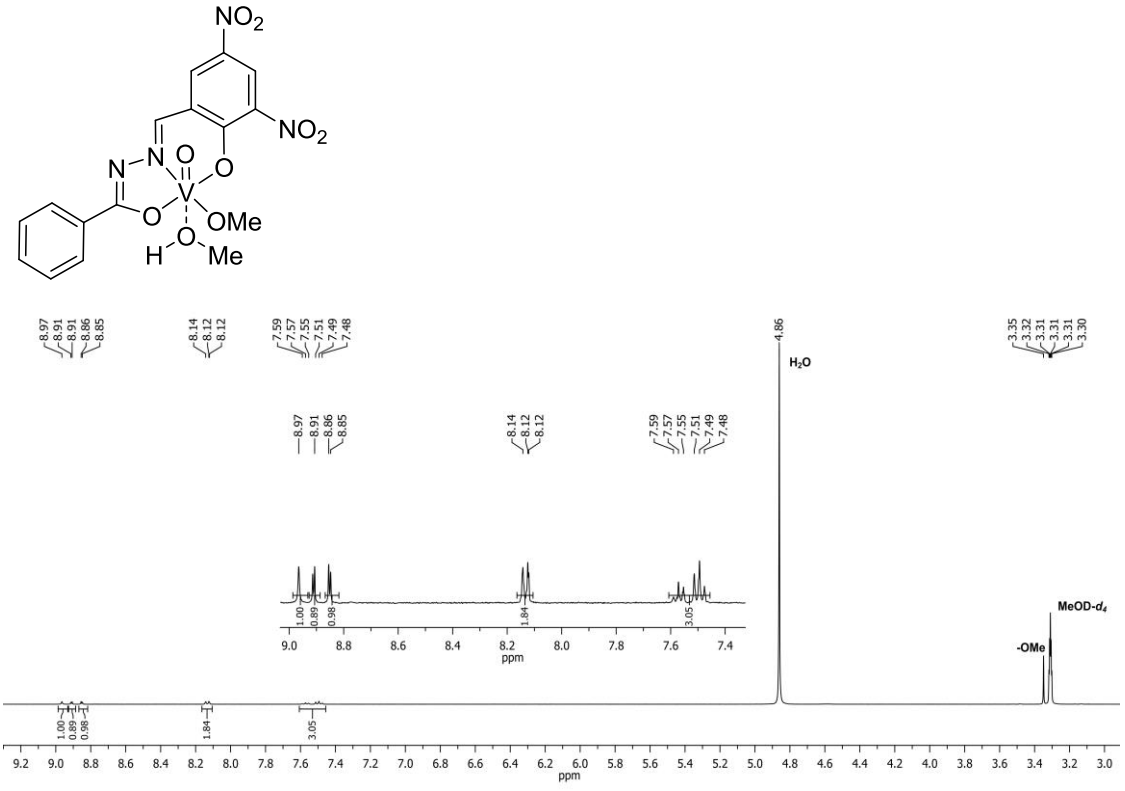

Figure A.97. The ^{1}H NMR spectrum of **VO-16** (MeOD-d_4, 400 MHz). The inset provides better clarity of the aromatic region.

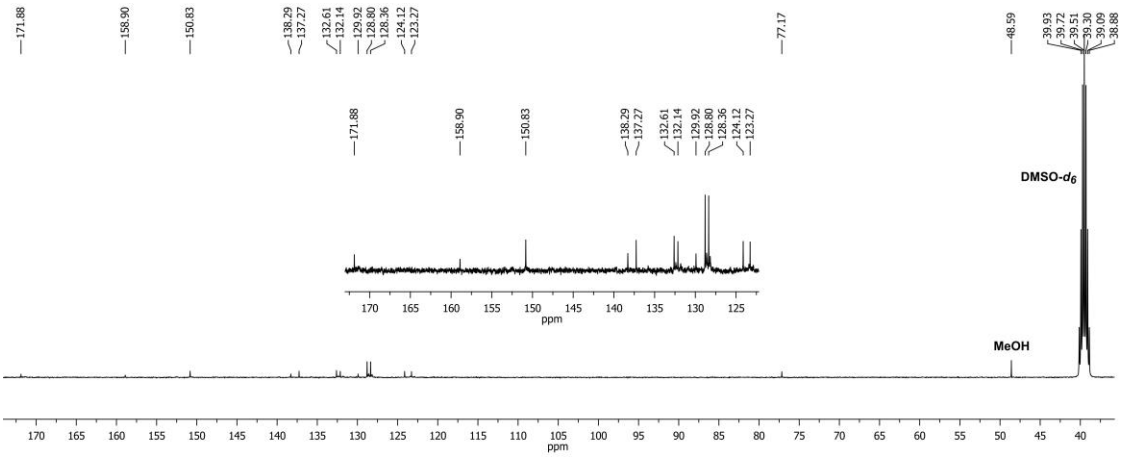

Figure A.98. The ^{13}C{^{1}H} NMR spectrum of **VO-16** (DMSO-d_6, 100 MHz). The inset shows carbon peaks of the complex more clearly.

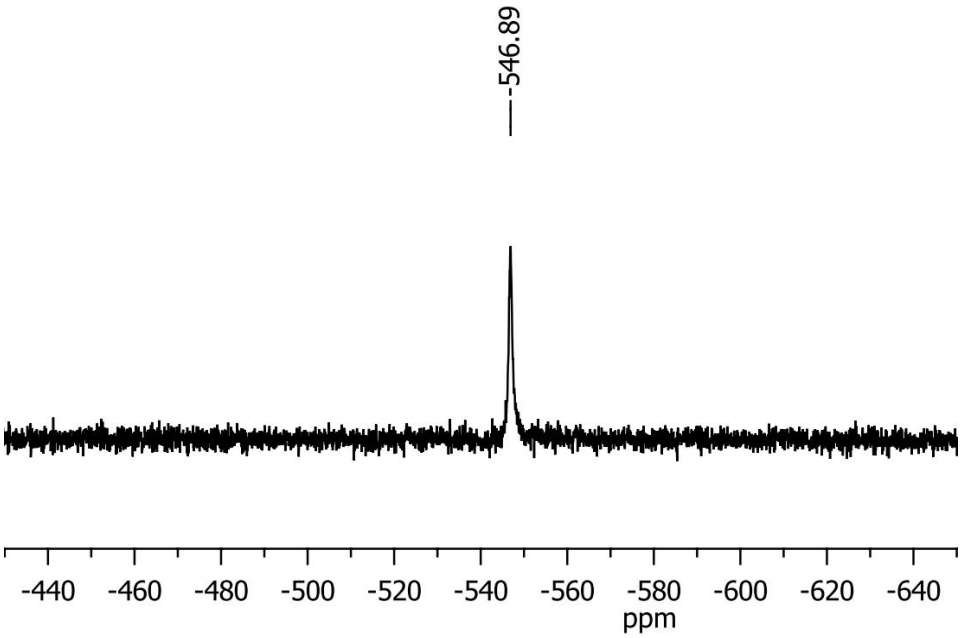

Figure A.99. The ^{51}V NMR spectrum of **VO-16** (MeOD-d_4, 105.25 MHz).

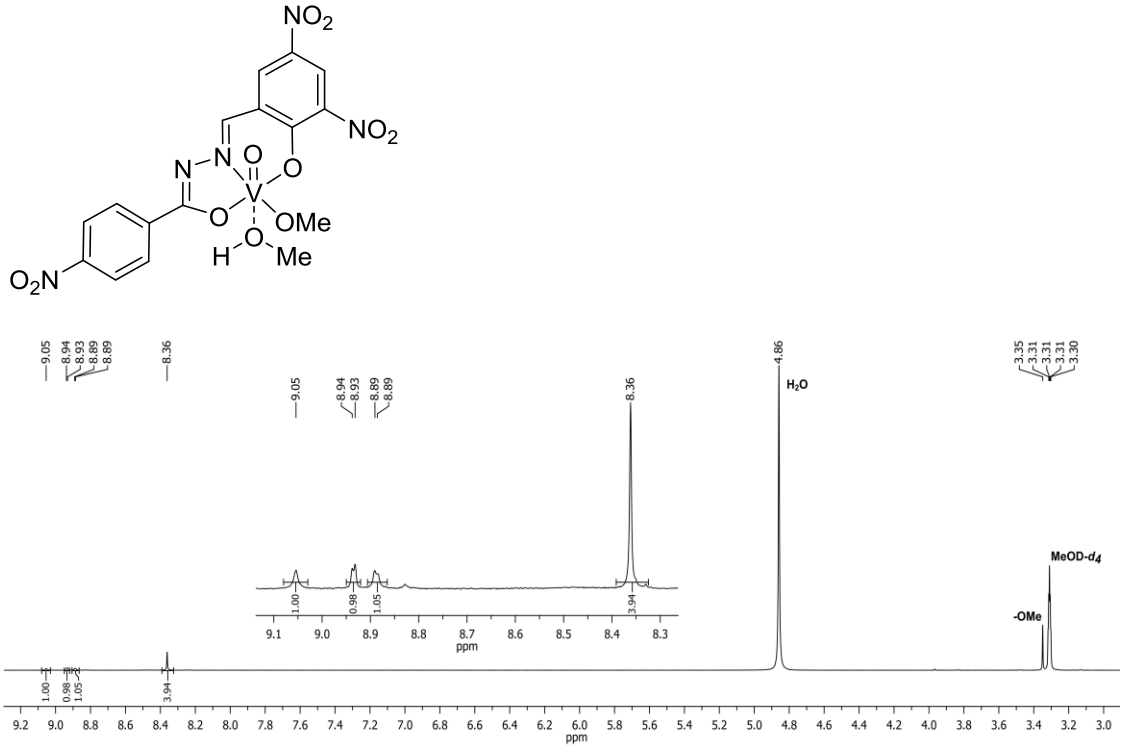

Figure A.100. The ^{1}H NMR spectrum of **VO-17** (MeOD-d_4, 400 MHz). The inset provides better clarity of the aromatic region.

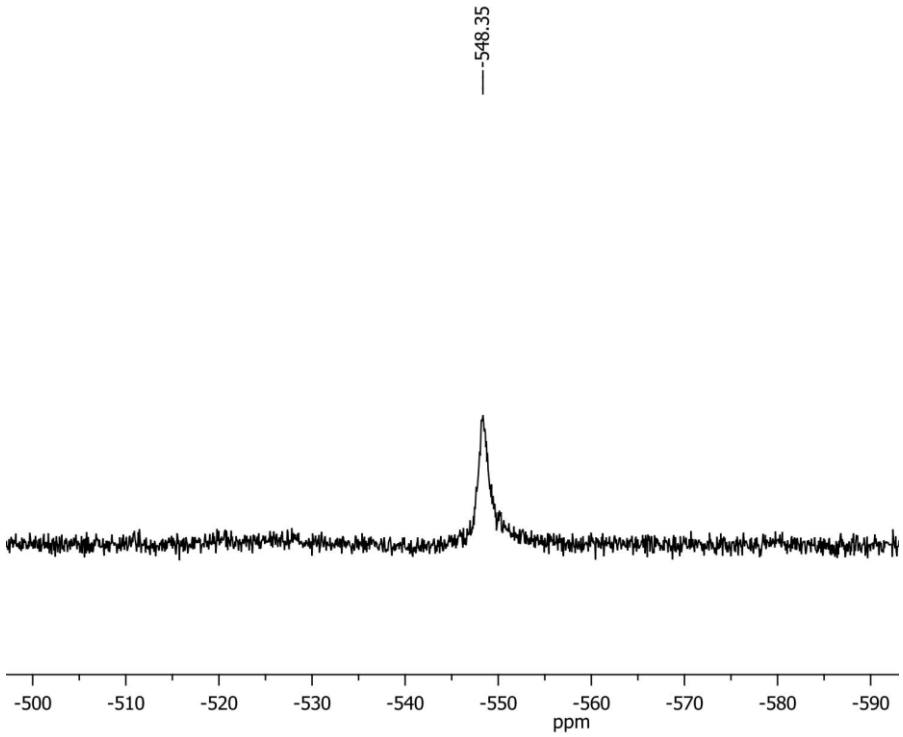

Figure A.101. The ^{51}V NMR spectrum of **VO-17** (MeOD-d_4, 105.25 MHz).

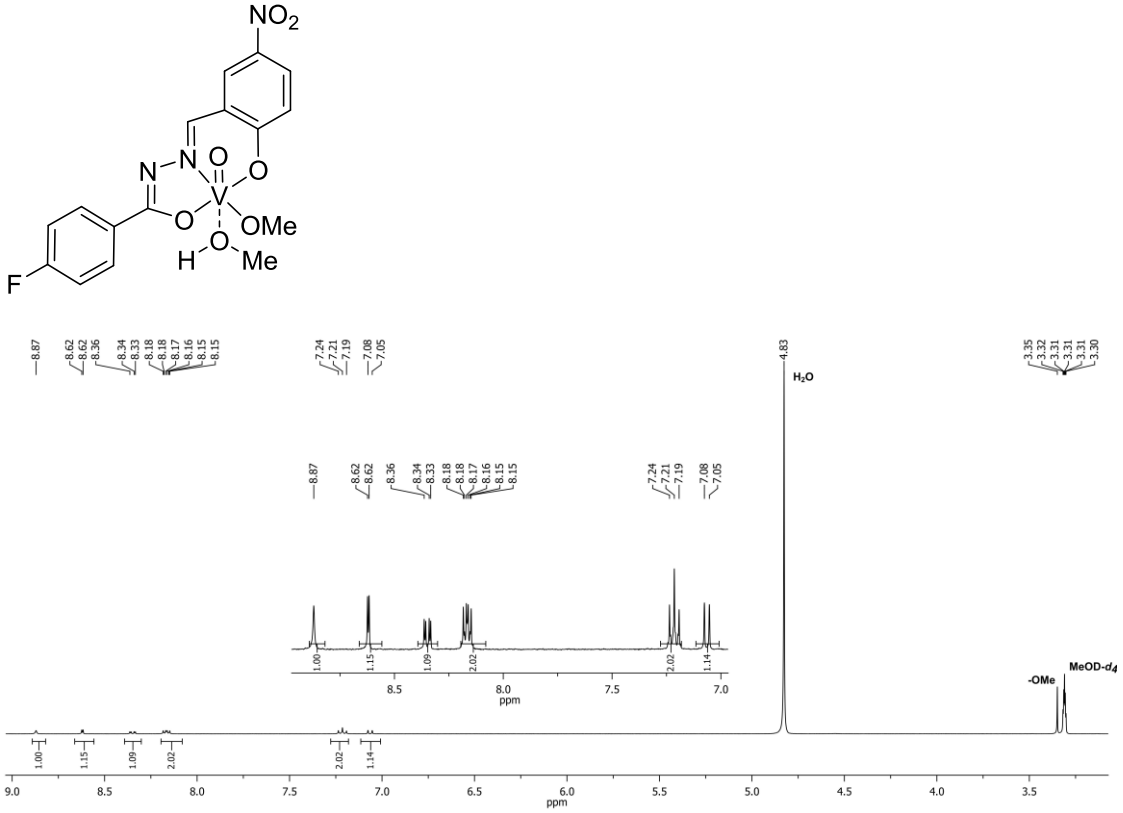

Figure A.102. The ^{1}H NMR spectrum of **VO-18** (MeOD-d_4, 400 MHz). The inset shows the aromatic region more clearly.

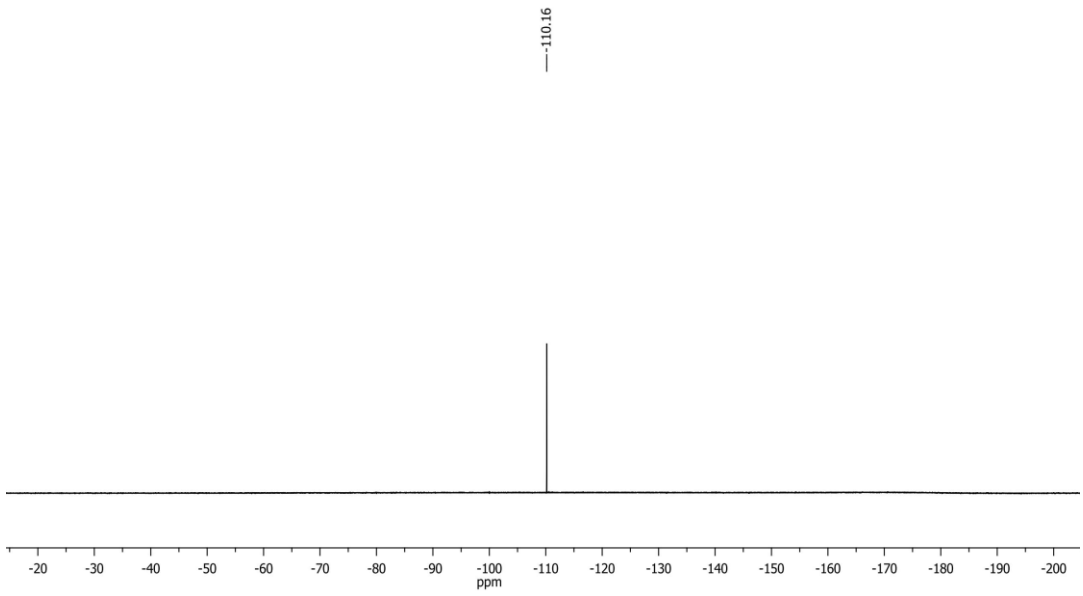

Figure A.103. The $^{19}F\{^{1}H\}$ NMR spectrum of **VO-18** (MeOD-d_4, 376.50).

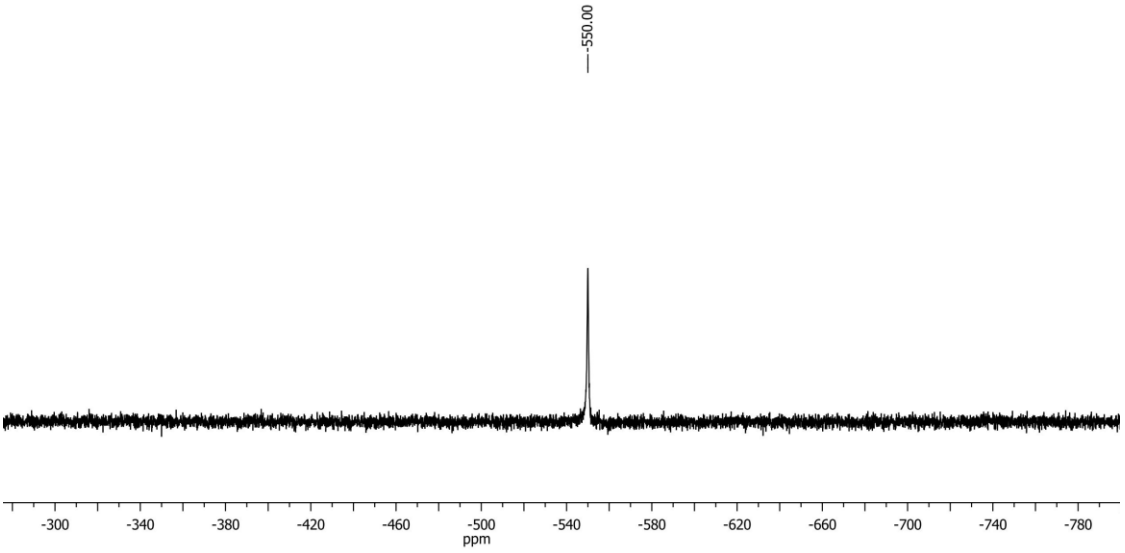

Figure A.104. The ^{51}V NMR spectrum of **VO-18** (MeOD-d_4, 105.25 MHz).

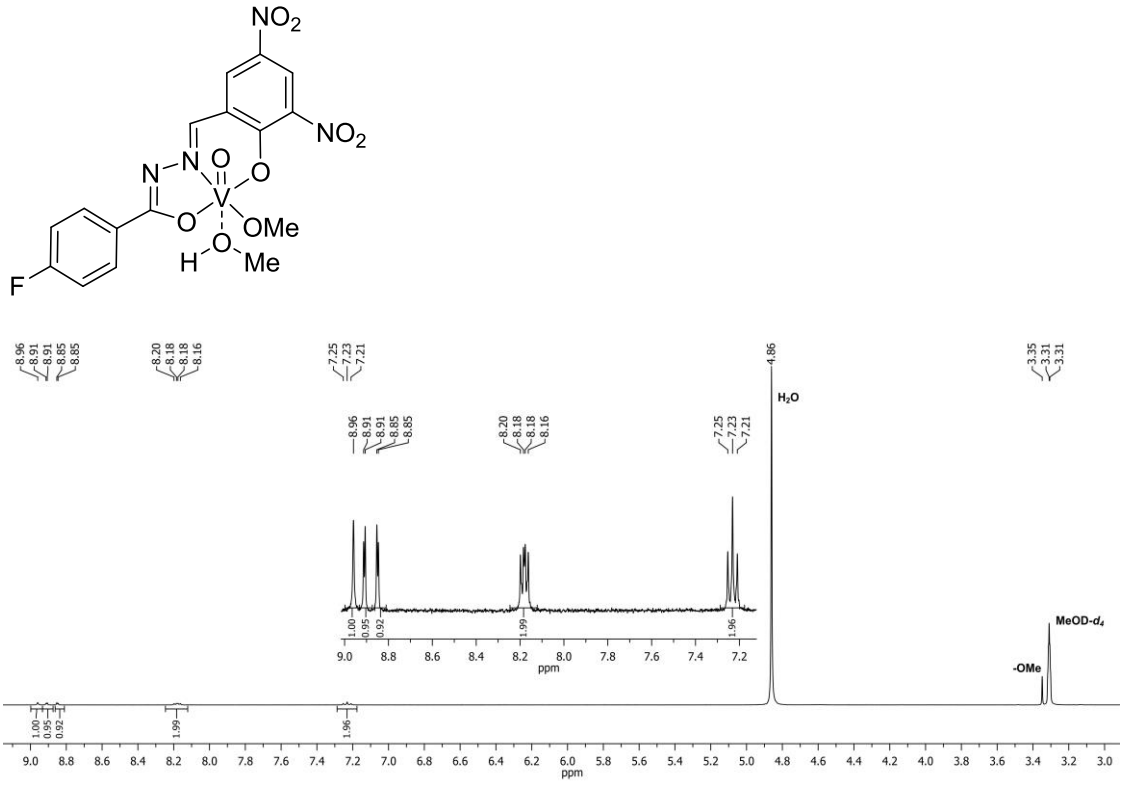

Figure A.105. The ^{1}H NMR spectrum of **VO-19** (MeOD-d_4, 400 MHz). The inset provides better clarity of the aromatic region.

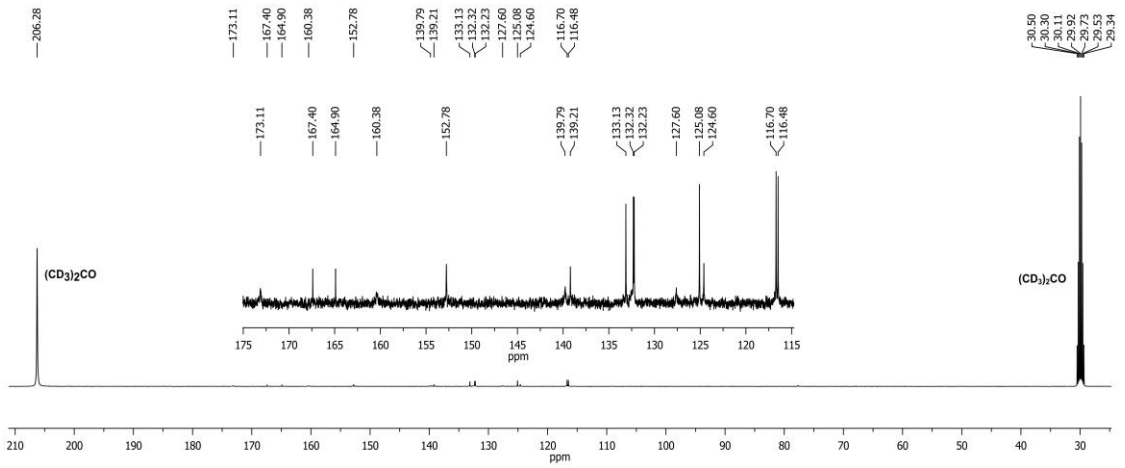

Figure A.106. The $^{13}C\{^{1}H\}$ NMR spectrum of **VO-19** ($(CD_3)_2CO$, 100 MHz). The inset provides better clarity of the carbons corresponding to the complex.

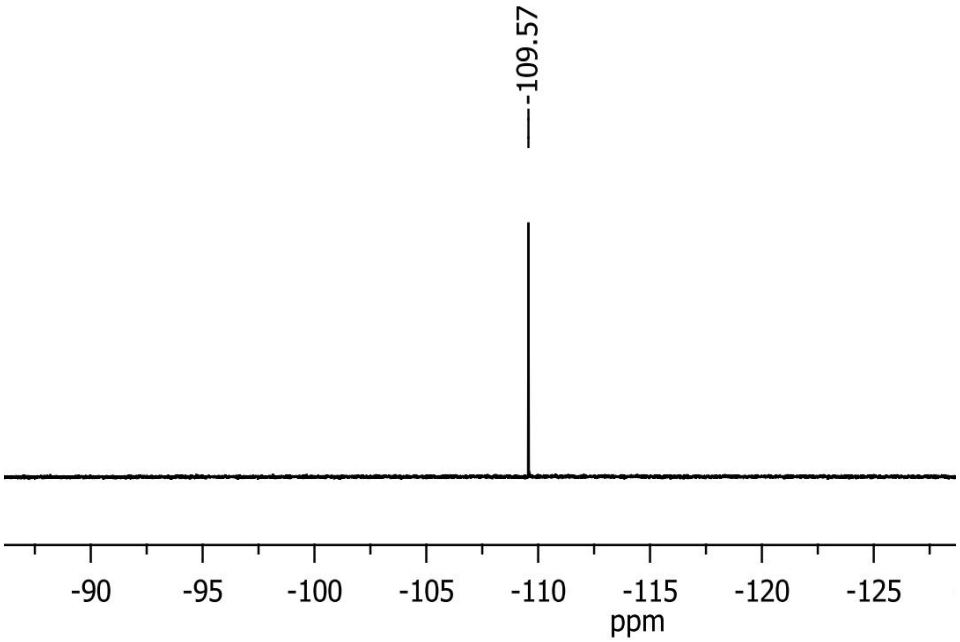

Figure A.107. The $^{19}F\{^{1}H\}$ NMR spectrum of **VO-19** (MeOD-d_4, 376.50 MHz).

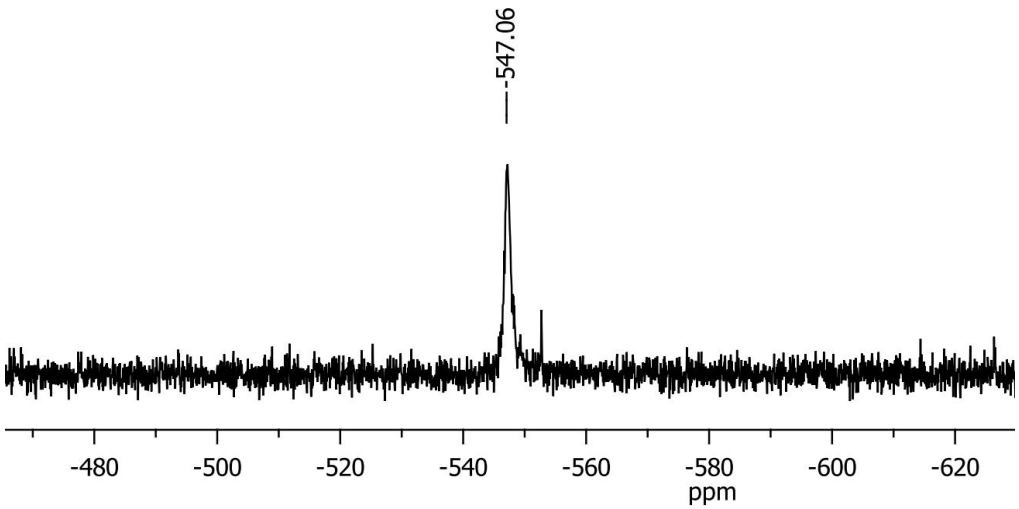

Figure A.108. The ^{51}V NMR spectrum of **VO-19** (MeOD-d_4, 105.25 MHz).

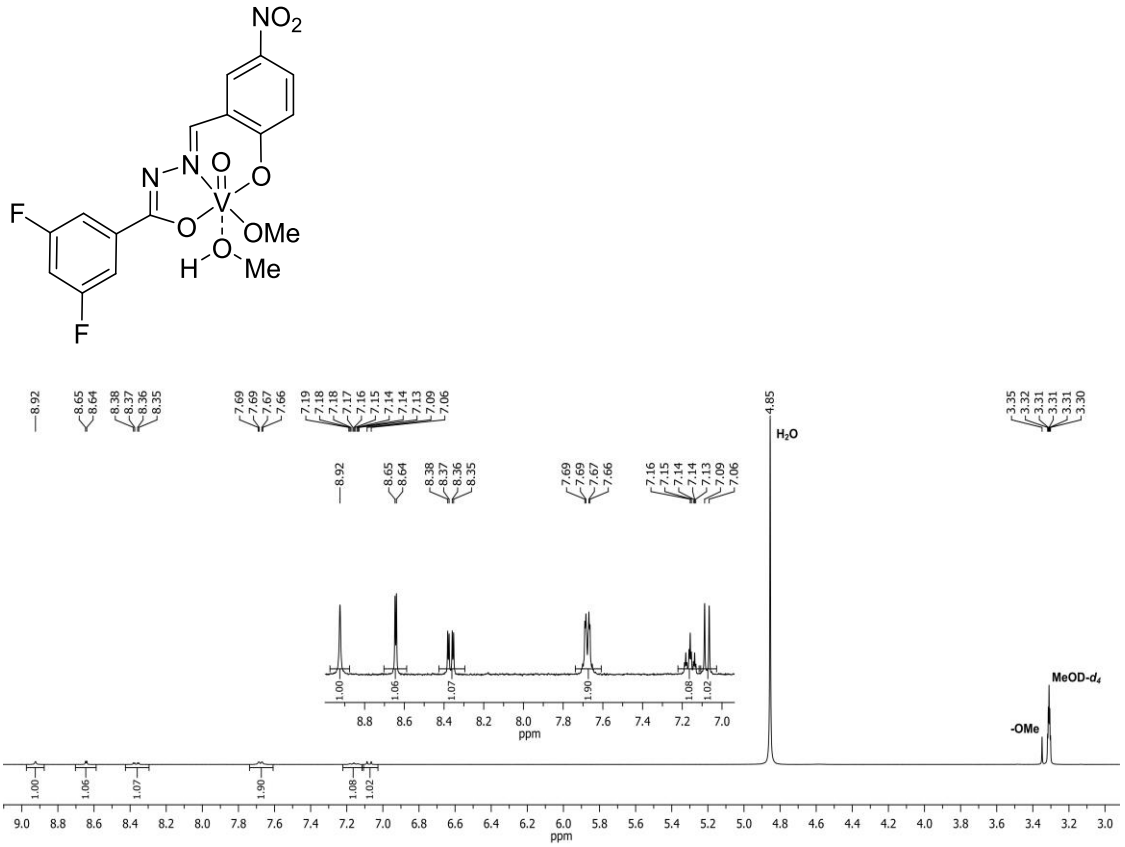

Figure A.109. The ^{1}H NMR spectrum of **VO-20** (MeOD-d_4, 400 MHz). The inset shows all the peaks more clearly.

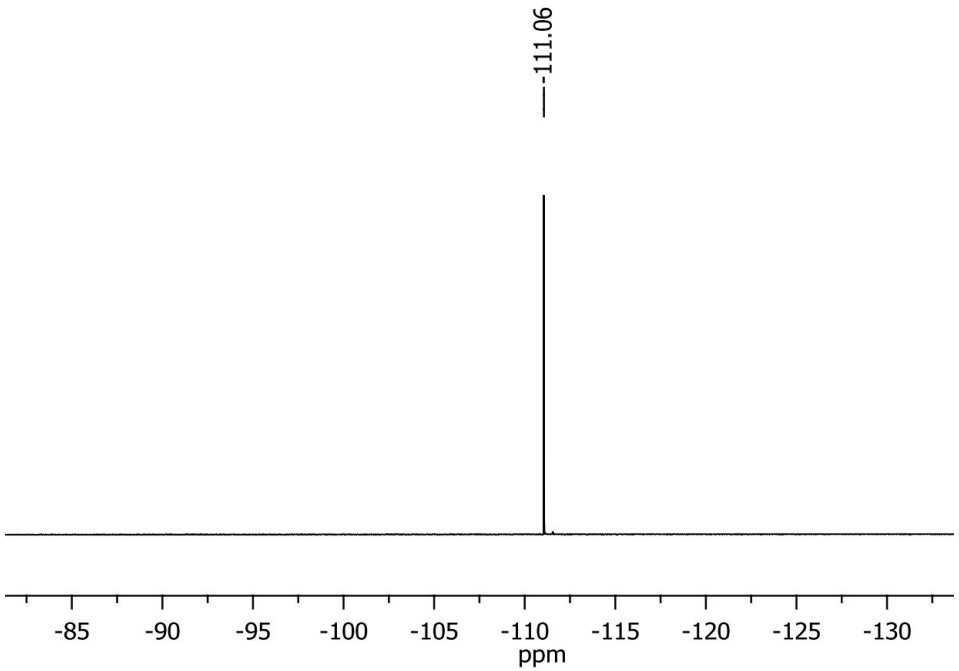

Figure A.110. The ^{19}F{^{1}H} NMR spectrum of **VO-20** (MeOD-d_4, 376.50 MHz).

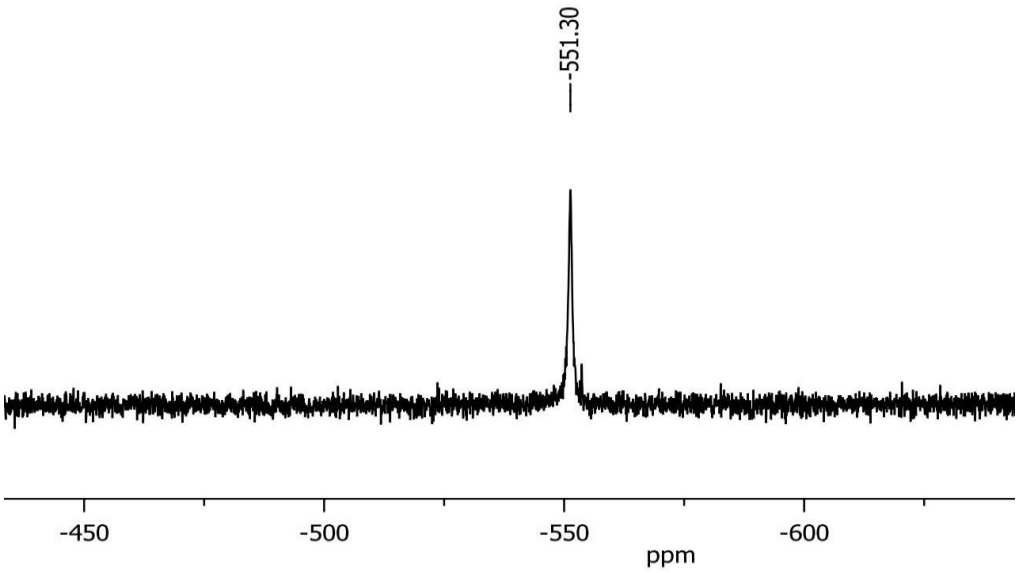

Figure A.111. The ^{51}V NMR spectrum of **VO-20** (MeOD-*d*$_4$, 105.25 MHz).

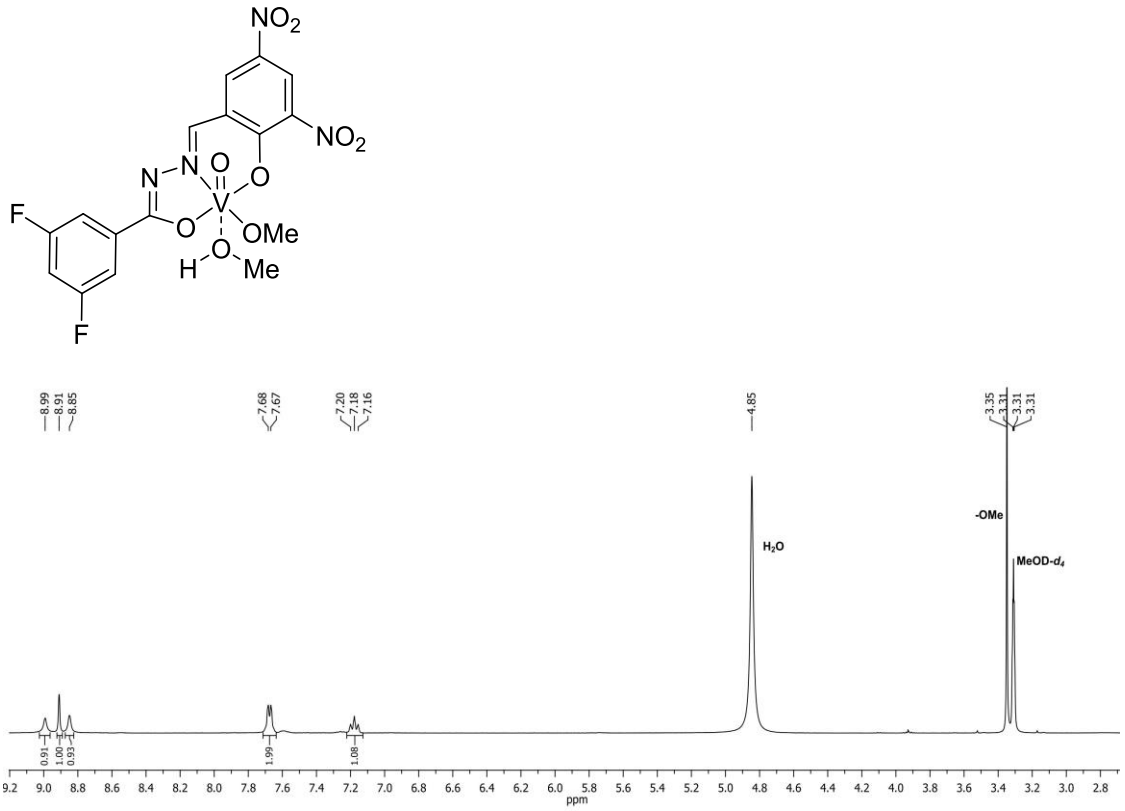

Figure A.112. The ^{1}H NMR spectrum of **VO-21** (MeOD-*d*$_4$, 400 MHz).

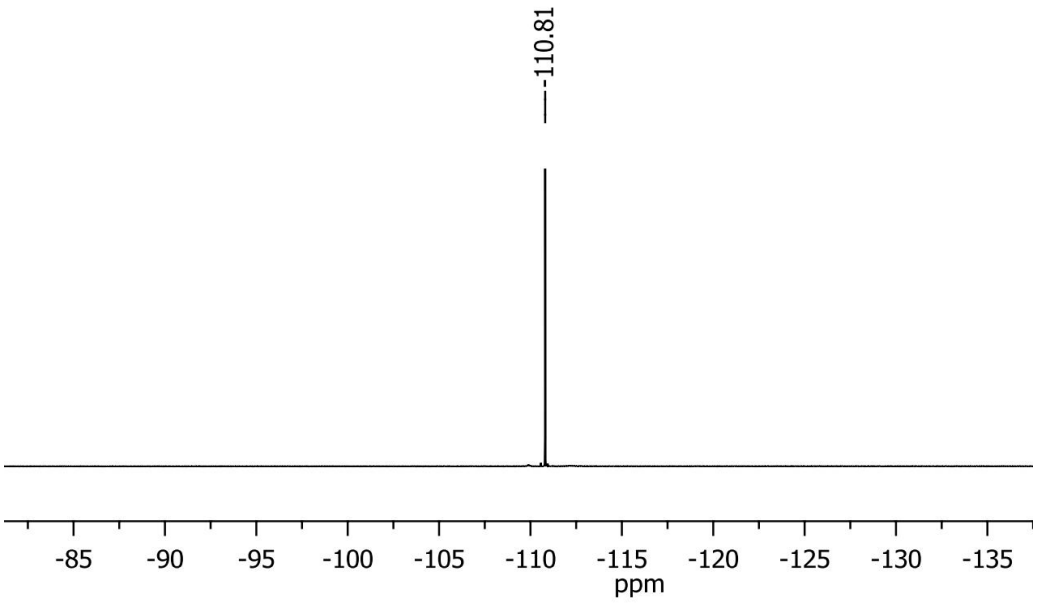

Figure A.113. The $^{19}F\{^{1}H\}$ NMR spectrum of **VO-21** (MeOD-d_4, 376.50 MHz).

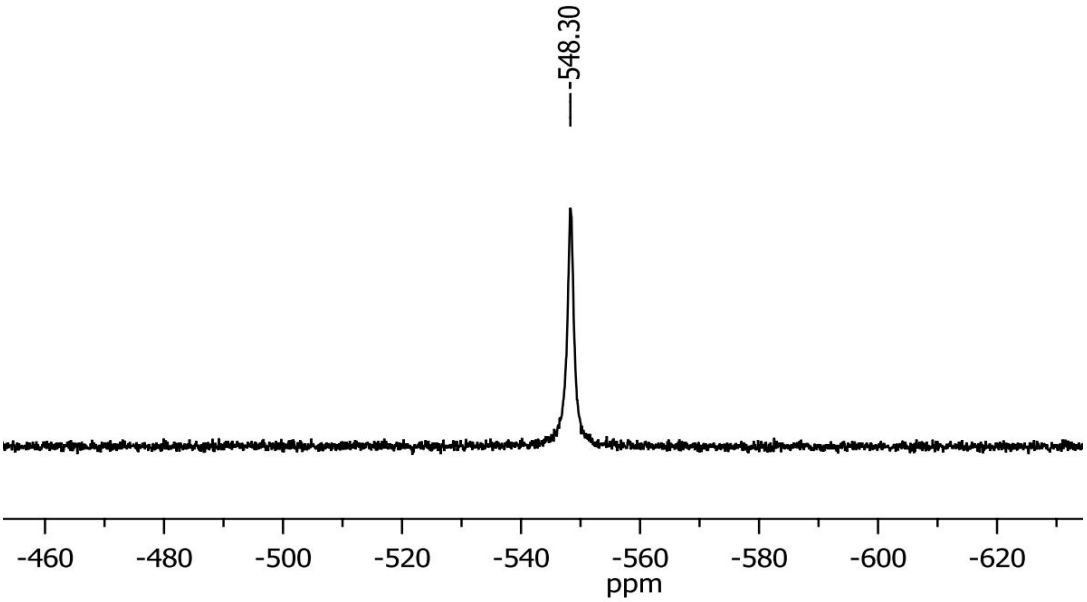

Figure A.114. The ^{51}V NMR spectrum of **VO-21** (MeOD-d_4, 105.25 MHz).

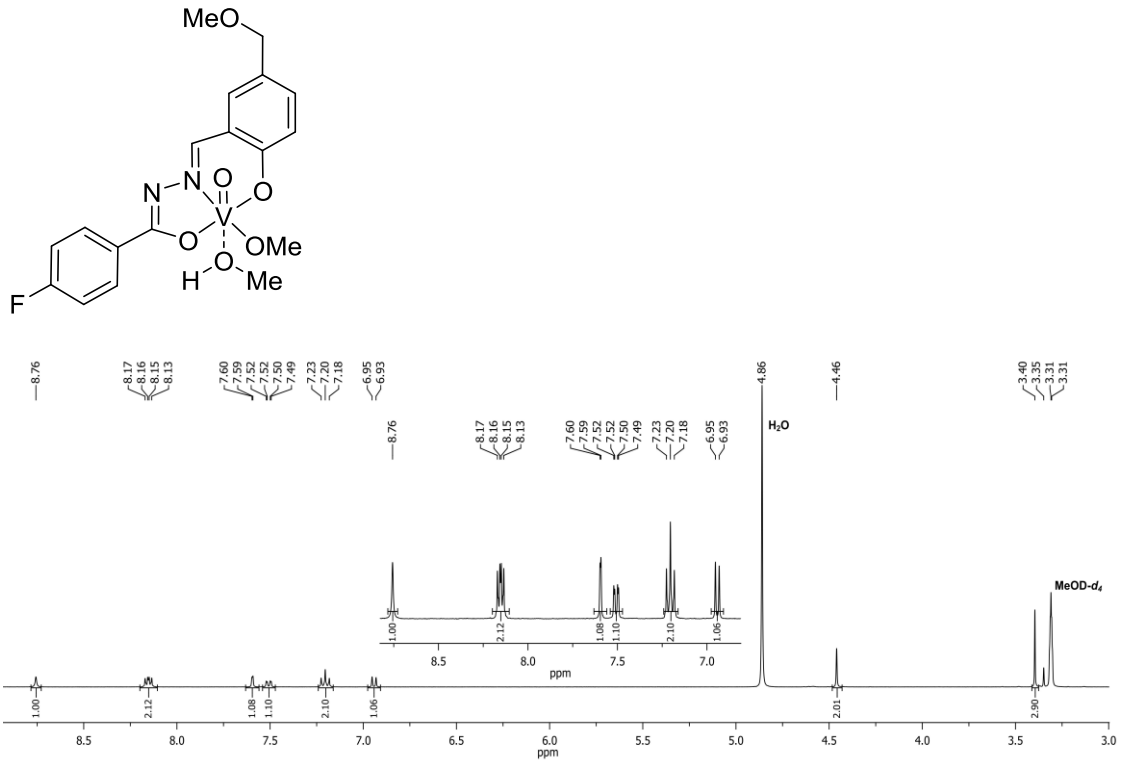

Figure A.115. The ^{1}H NMR spectrum of **VO-22** (MeOD-d_4, 400 MHz). The inset shows the aromatic region more clearly. The peak at 3.35 ppm originates from the –OMe group of methanol.

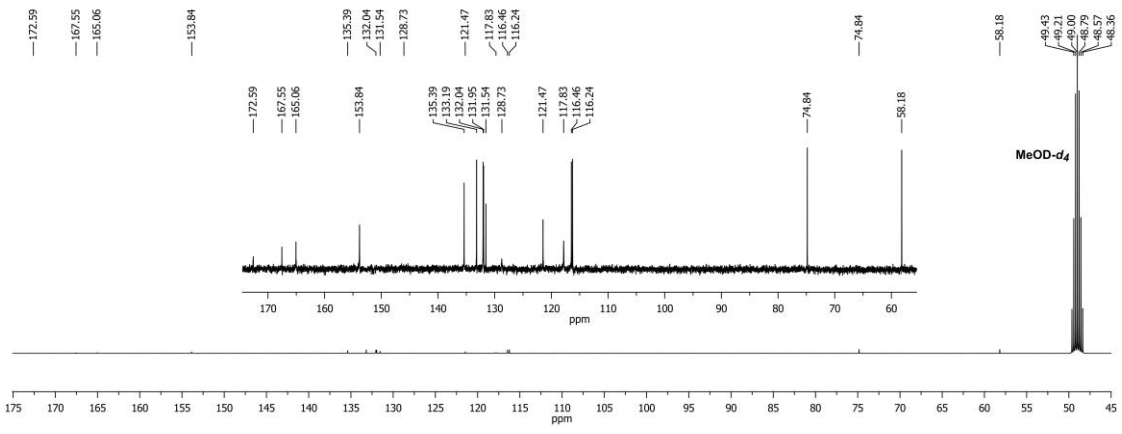

Figure A.116. The ^{13}C{^{1}H} NMR spectrum of **VO-22** (MeOD-d_4, 100 MHz). The inset shows the carbon peaks of the complex more clearly.

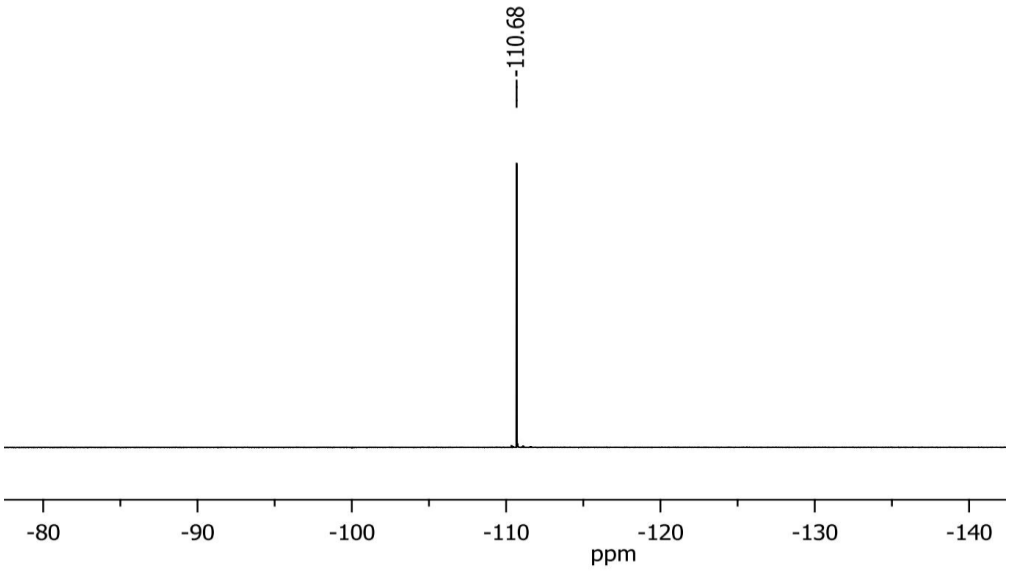

Figure A.117. The $^{19}F\{^{1}H\}$ NMR spectrum of **VO-22** (MeOD-d_4, 376.50 MHz).

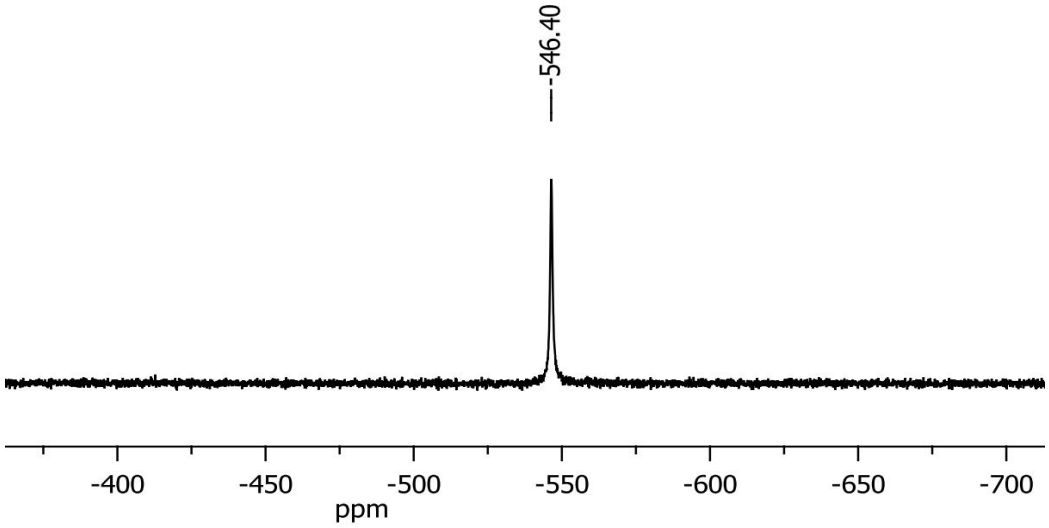

Figure A.118. The ^{51}V NMR spectrum of **VO-22** (MeOD-d_4, 105.25 MHz).

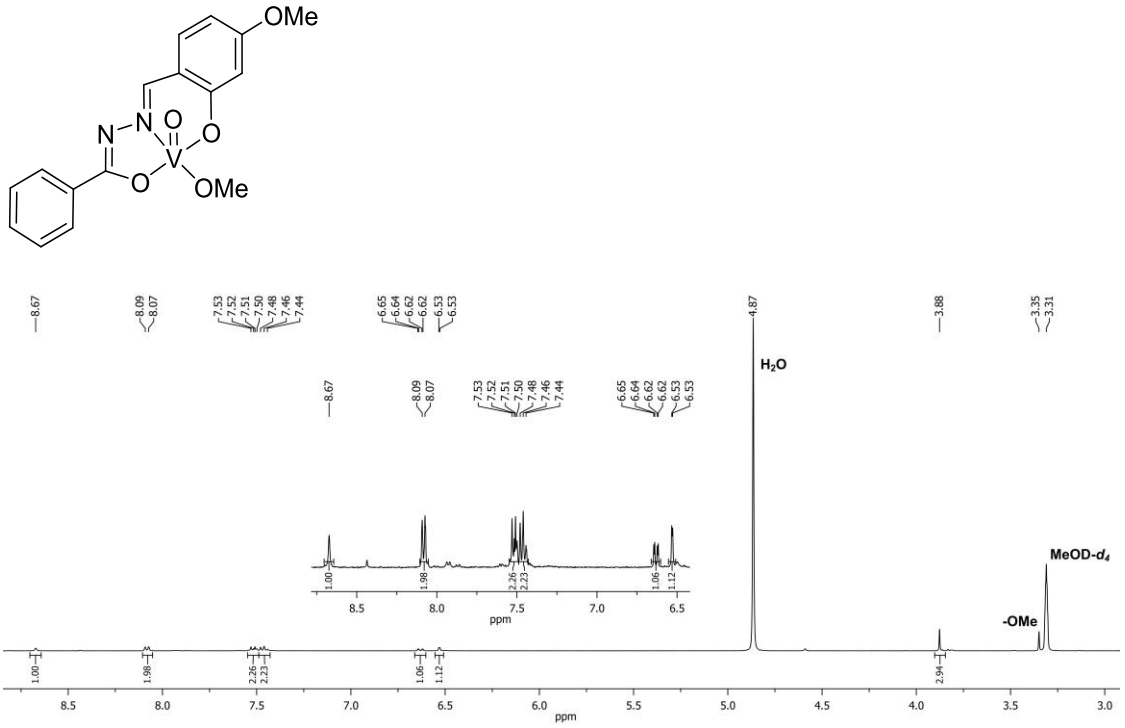

Figure A.119. The ^{1}H NMR spectrum of **VO-23** (MeOD-d_4, 400 MHz). The inset provides better clarity of the aromatic region.

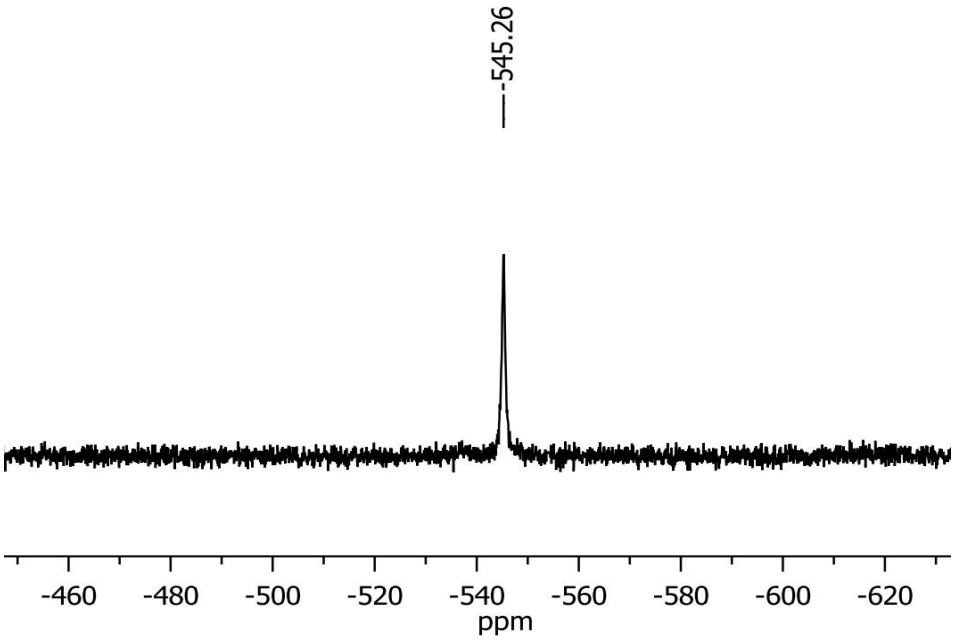

Figure A.120. The ^{51}V NMR spectrum of **VO-23** (MeOD-d_4, 105.25 MHz).

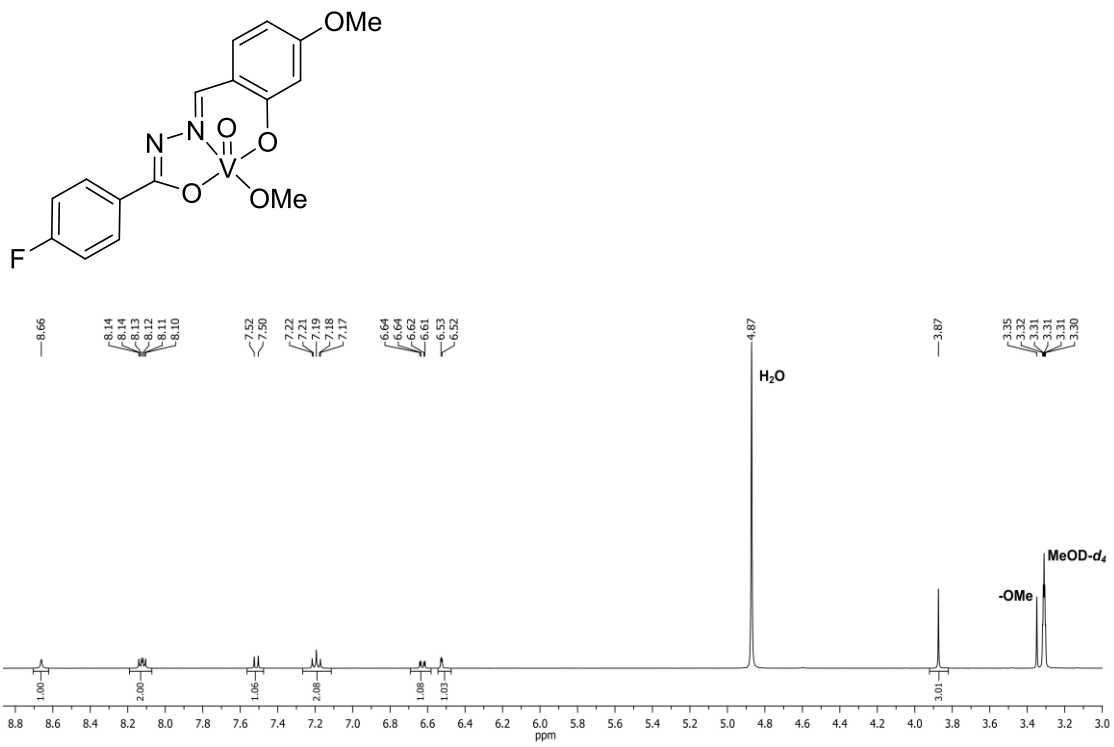

Figure A.121. The ^{1}H NMR spectrum of **VO-24** (MeOD-d_4, 400 MHz).

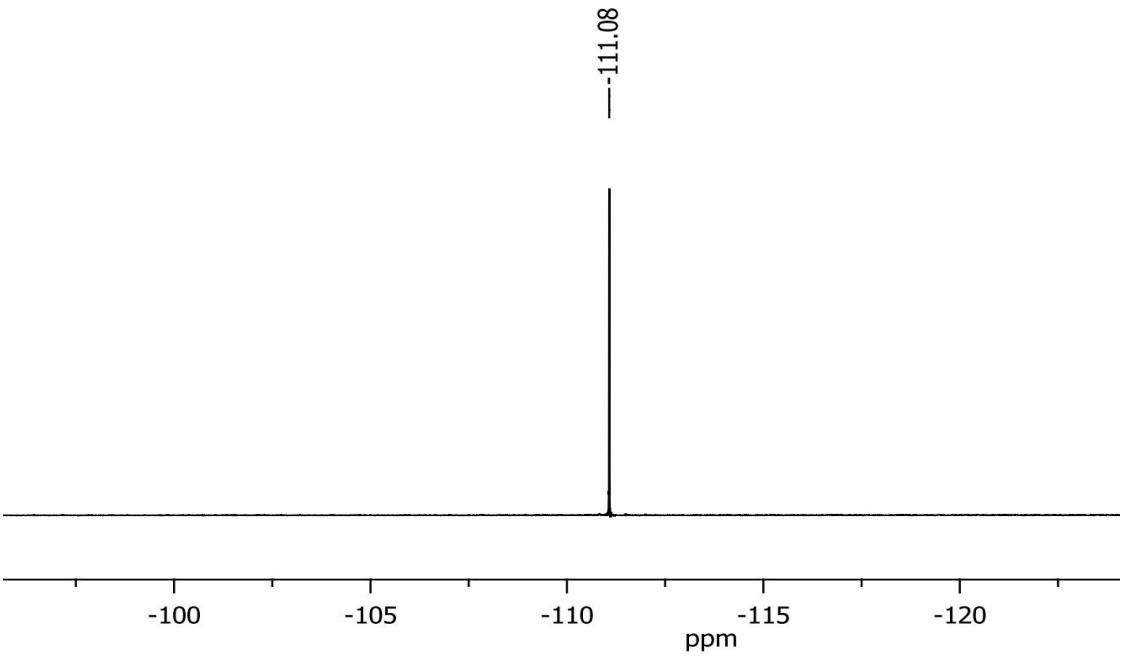

Figure A.122. The ^{19}F{^{1}H} NMR spectrum of **VO-24** (376.50 MHz).

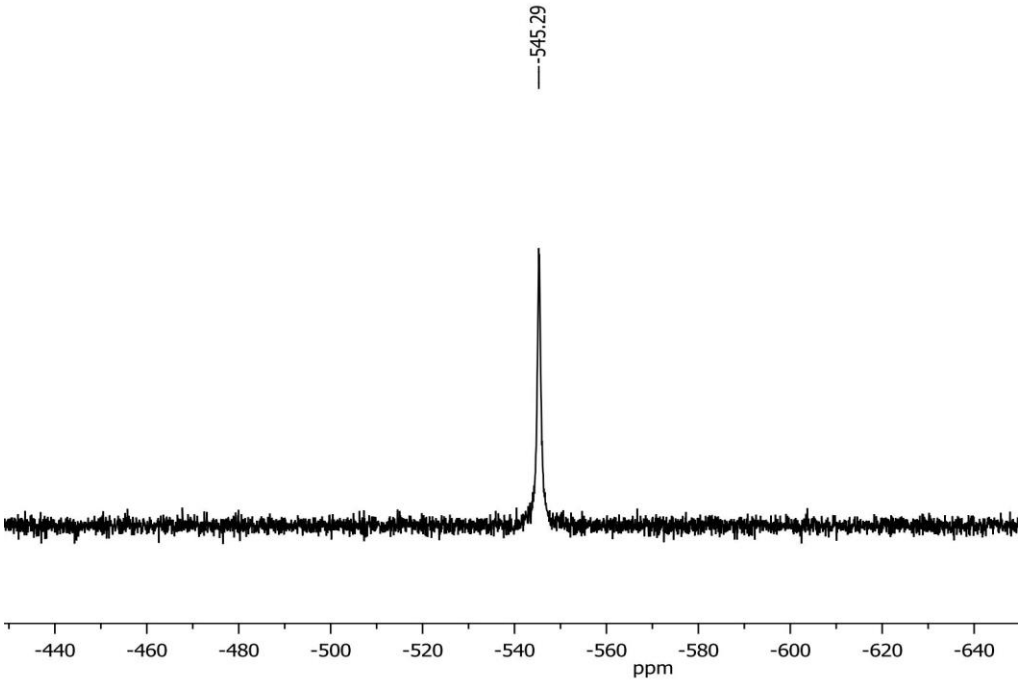

Figure A.123. The ^{51}V NMR spectrum of **VO-24** (MeOD-d_4, 105.25 MHz).

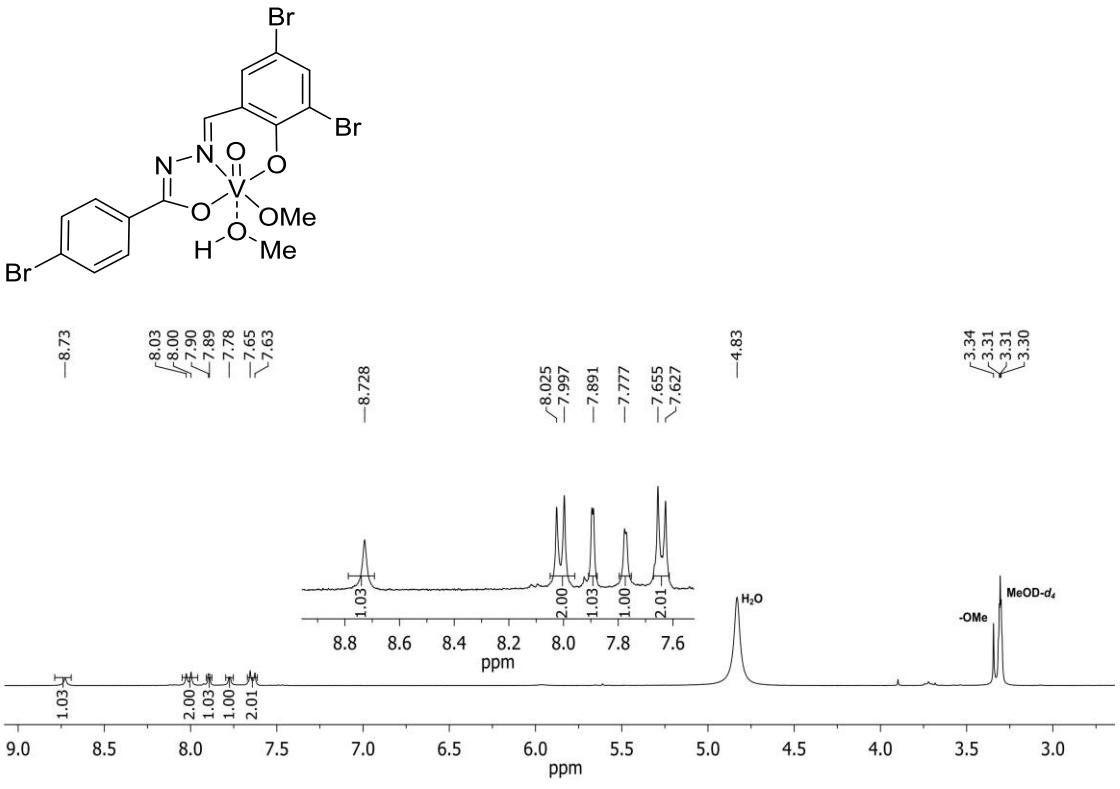

Figure A.124. The ^{1}H NMR spectrum of **VO-25** (MeOD-d_4, 300 MHz). The inset provides better clarity of the aromatic region.

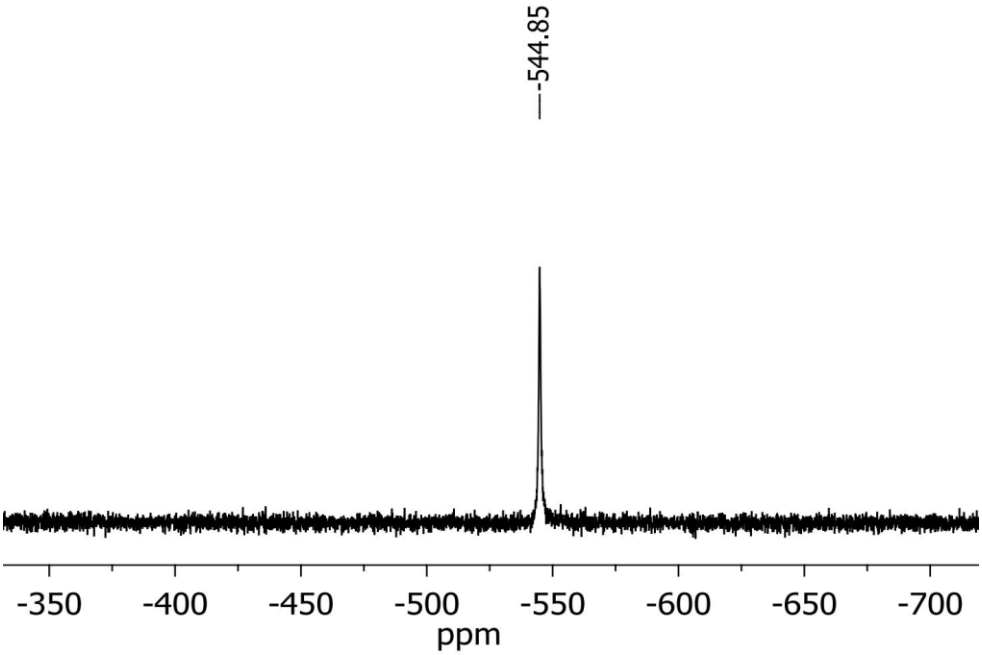

Figure A.125. The ^{51}V NMR spectrum of **VO-25** (MeOD-d_4, 105.25 MHz).

Figure A.126. The ^{1}H NMR spectrum of **L-17** (DMSO-d_6, 500 MHz).

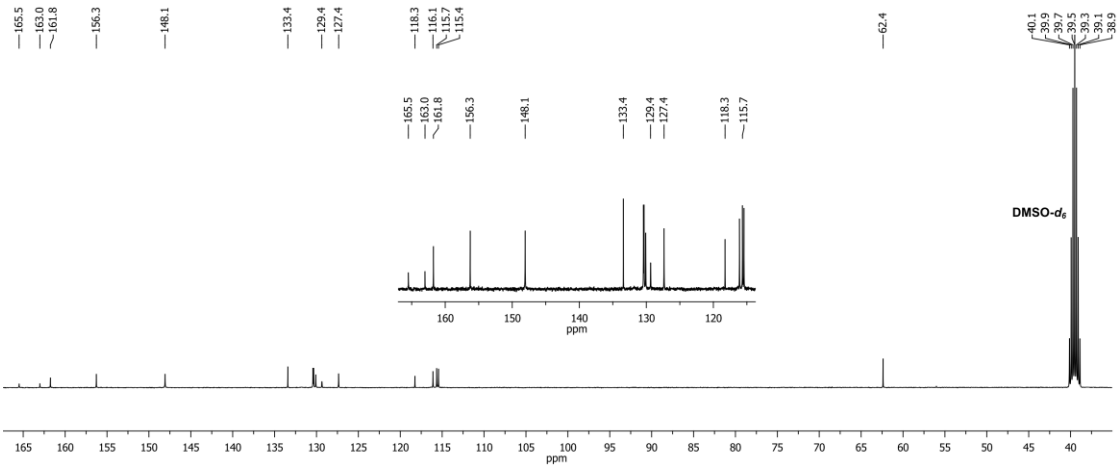

Figure A.127. The $^{13}C\{^{1}H\}$ NMR spectrum of **L-17** (DMSO-d_6, 100 MHz).

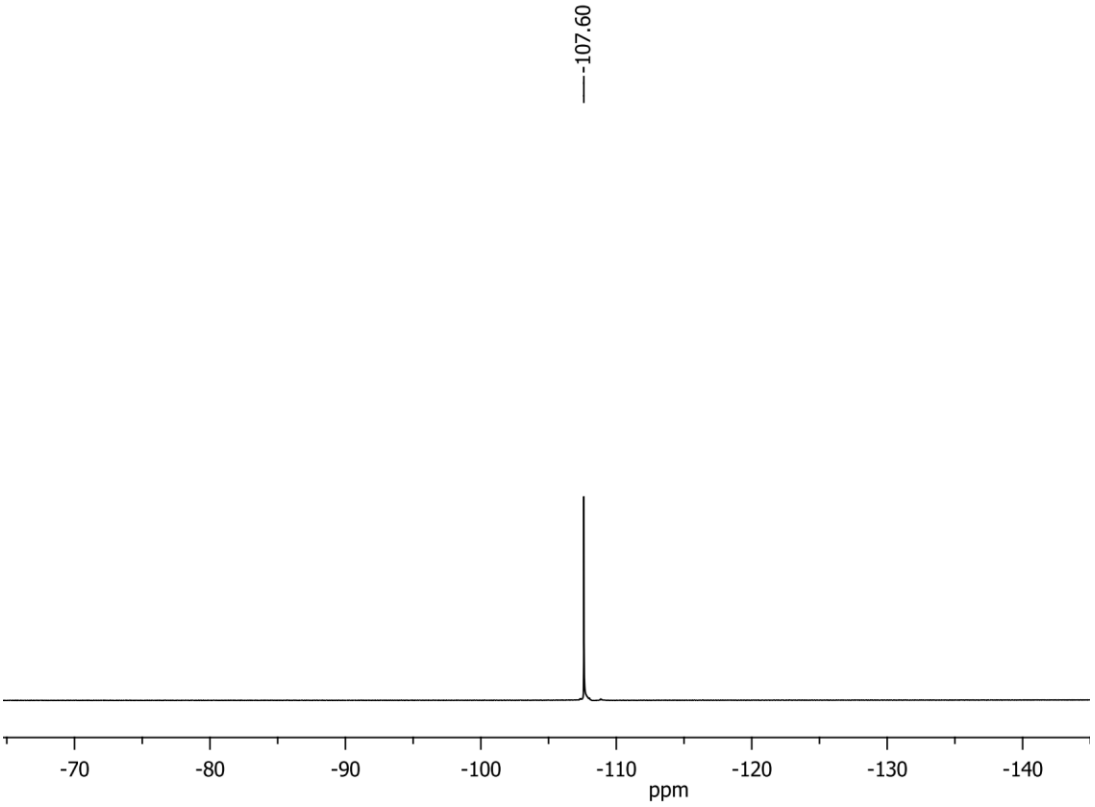

Figure A.128. The $^{19}F\{^{1}H\}$ NMR spectrum of **L-17** (DMSO-d_6, 376.50 MHz).

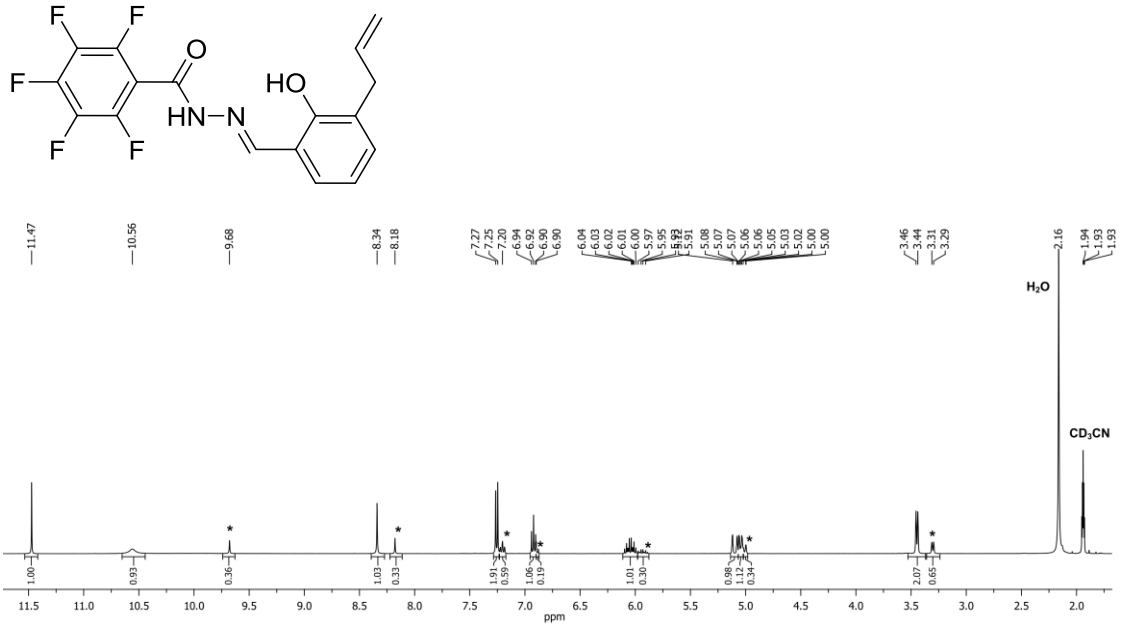

Figure A.129. The ^{1}H NMR spectrum of **L-18** (CD_3CN, 400 MHz). The peaks marked with asterisks correspond to the hydrazone-imidate form of the ligand.

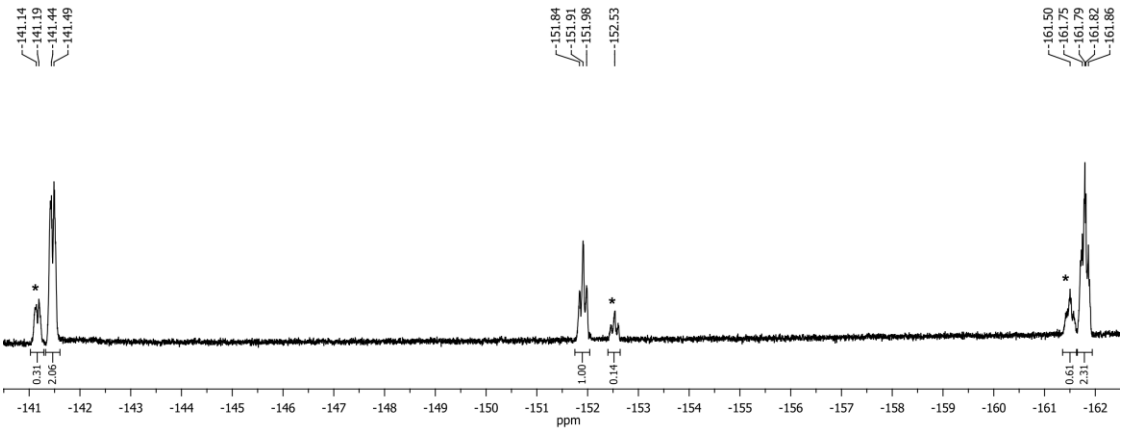

Figure A.130. The $^{19}F\{^{1}H\}$ NMR spectrum of **L-18** (CD_3CN, 282.40 MHz). The peaks marked with asterisks correspond to the hydrazone-imidate form of the ligand.

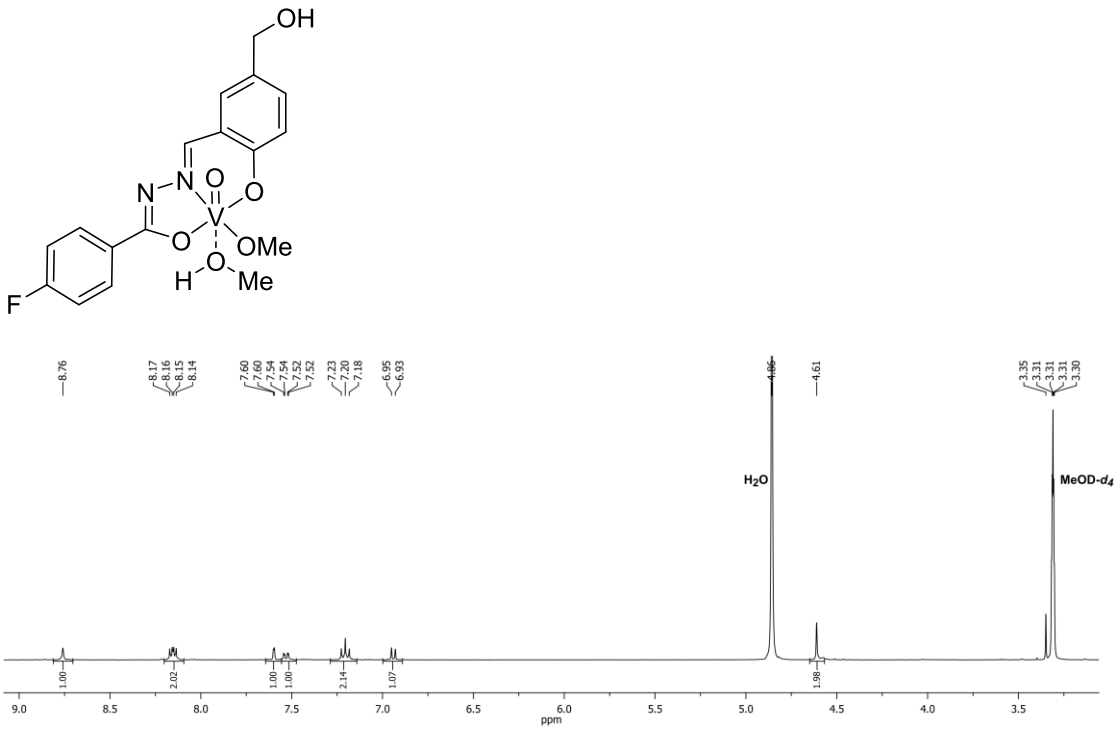

Figure A.131. The ^{1}H NMR spectrum of **VO-29** (MeOD-d_4, 400 MHz).

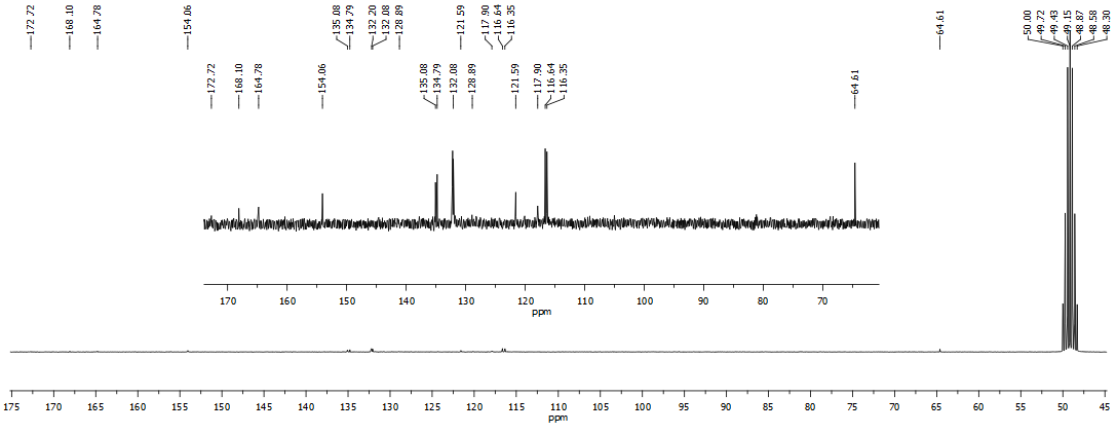

Figure A.132. The ^{13}C{^{1}H} NMR spectrum of **VO-29** (MeOD-d_4, 100 MHz). The inset shows all peaks more clearly.

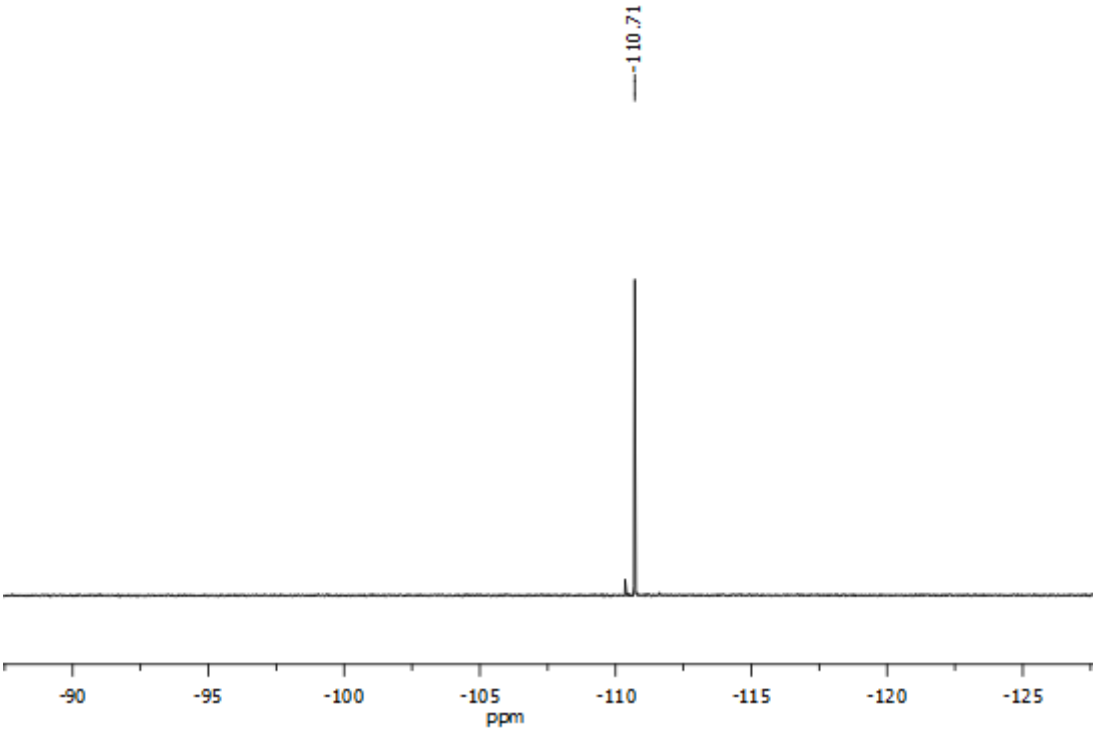

Figure A.133. The $^{19}F\{^{1}H\}$ NMR spectrum of **VO-29** (MeOD-d_4, 376.50 MHz).

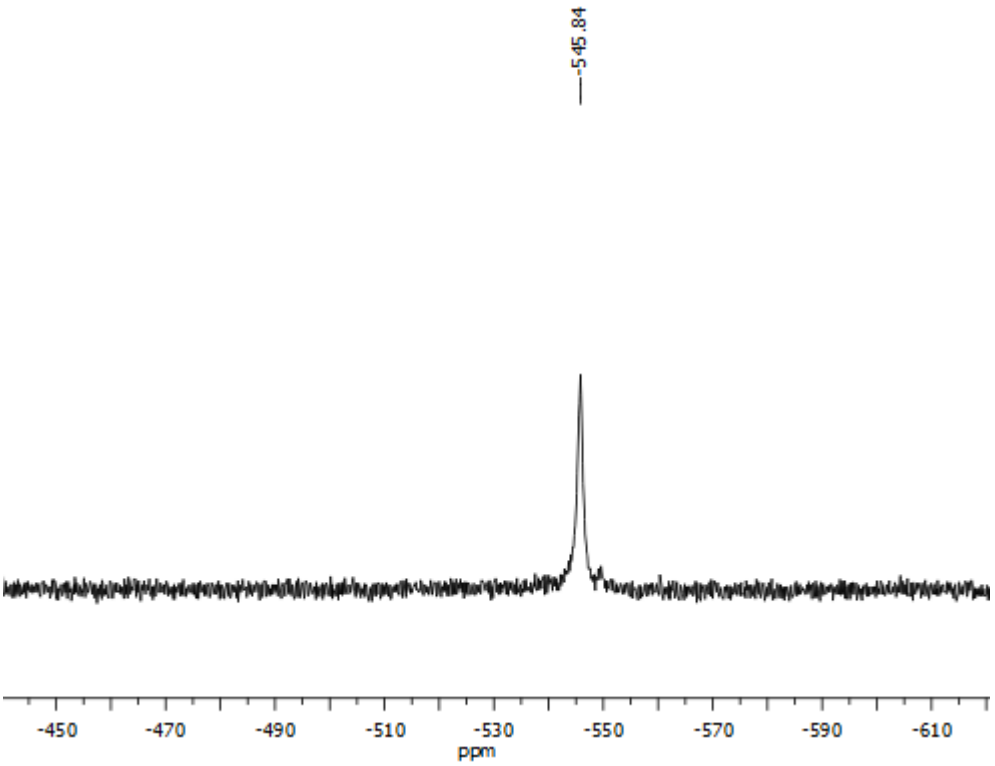

Figure A.134. The ^{51}V NMR spectrum of **VO-29** (MeOD-d_4, 105.25 MHz).

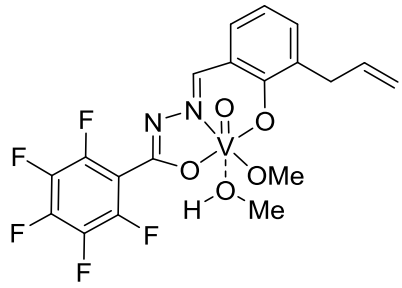

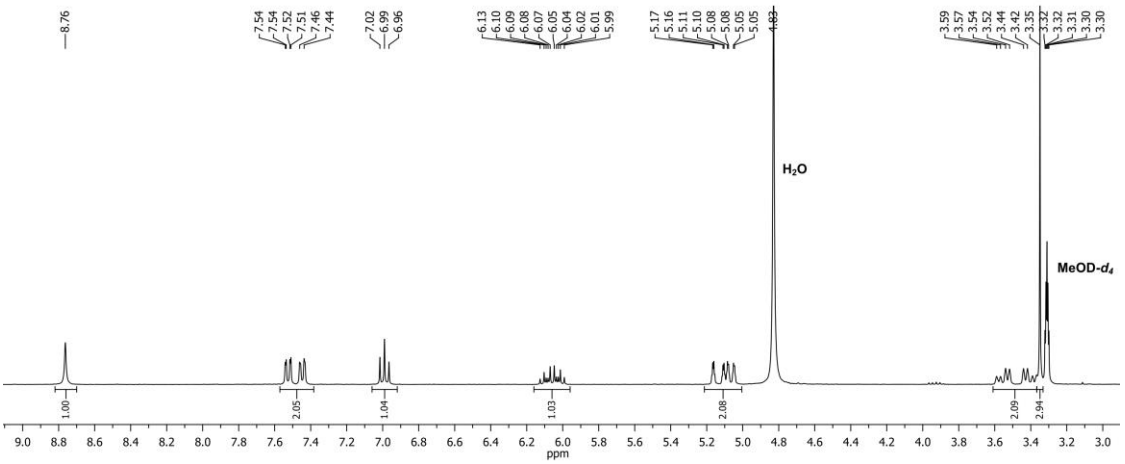

Figure A.135. The ^{1}H NMR spectrum of **VO-30** (MeOD-d_4, 400 MHz).

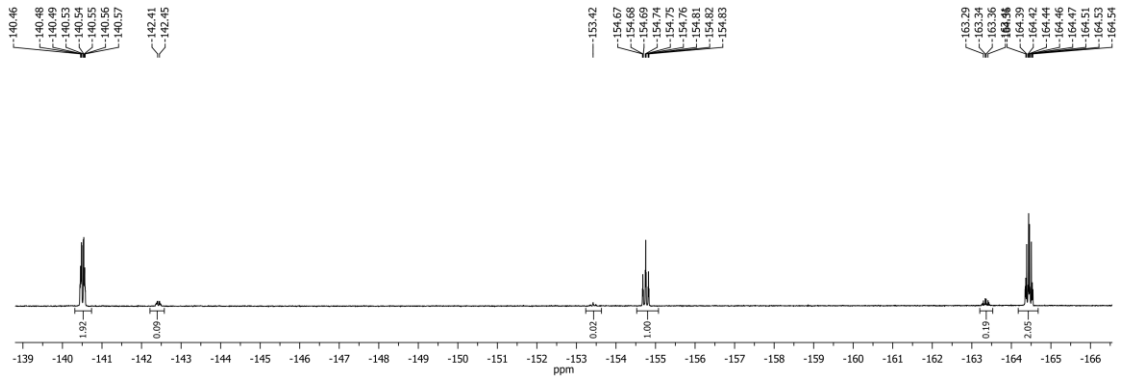

Figure A.136. The ^{19}F{^{1}H} NMR spectrum of **VO-30** (MeOD-d_4, 376.50 MHz).

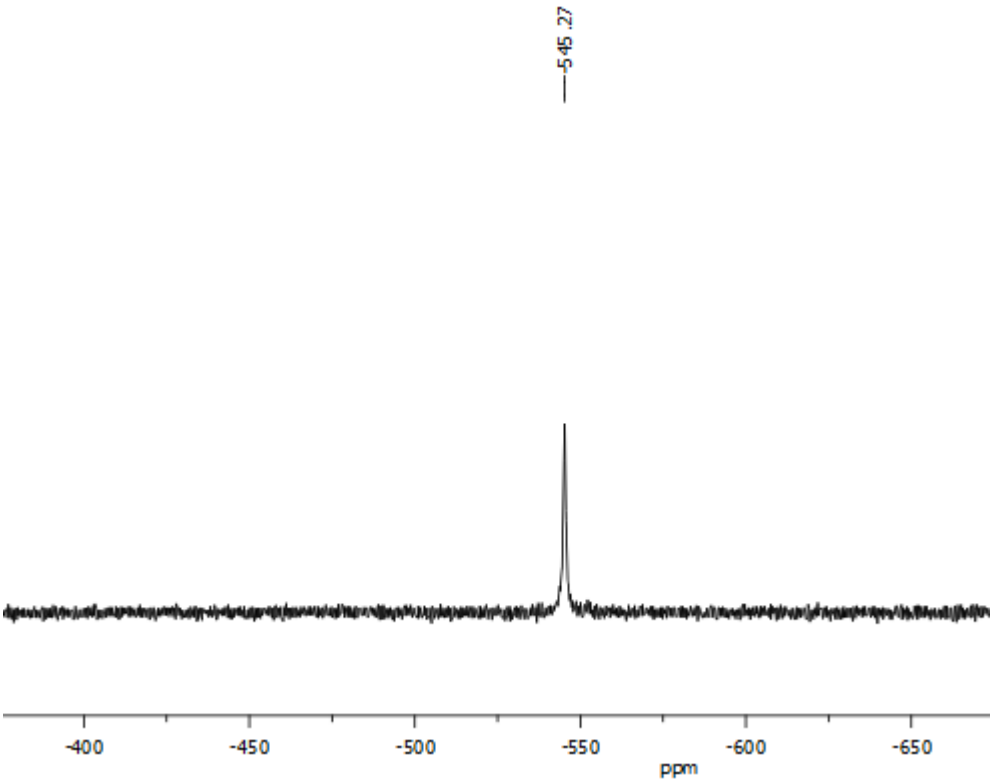

Figure A.137. The ^{51}V NMR spectrum of **VO-30** (MeOD-d_4, 105.25 MHz)

NMR Spectra of Reaction Products

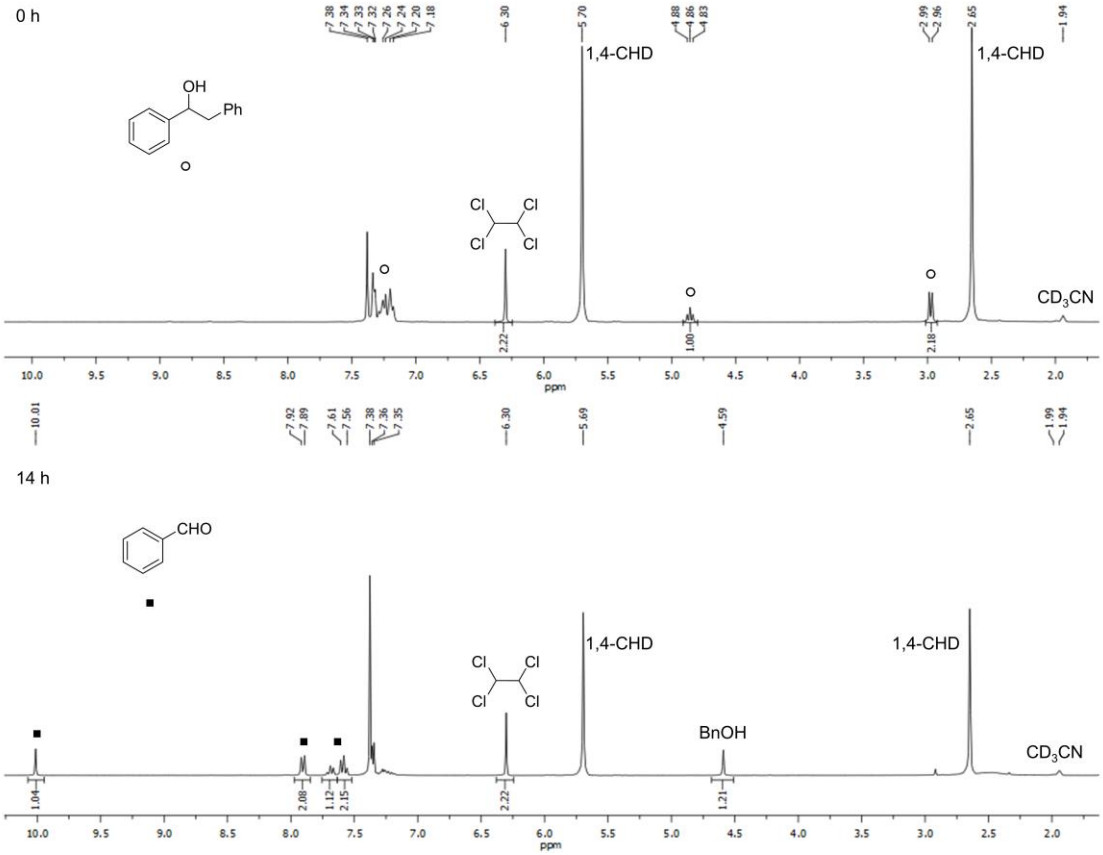

Figure A.138. The ^{1}H NMR spectra of the photoreaction with **36** before (top) and after (bottom) light irradiation. The peak at 2.91 ppm corresponds to product **35**.

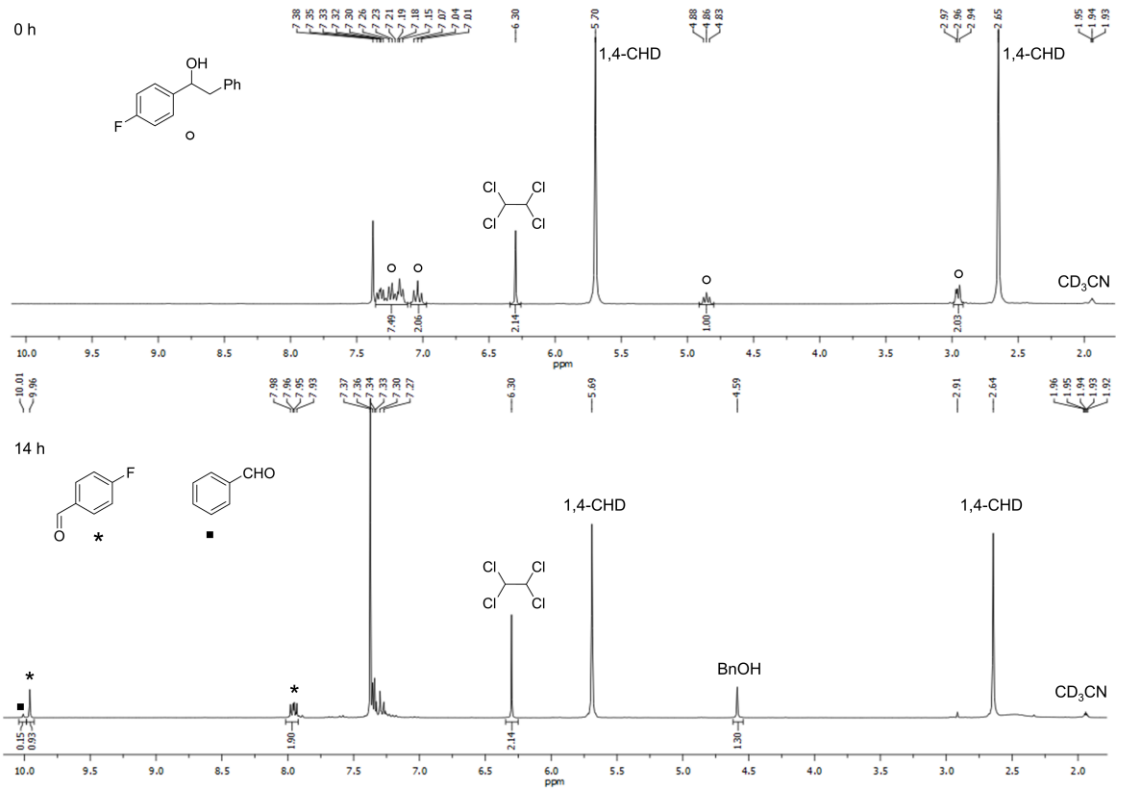

Figure A.139. The ^{1}H NMR spectra of the photoreaction with **37** before (top) and after (bottom) light irradiation. The peak at 2.91 ppm corresponds to product **35**.

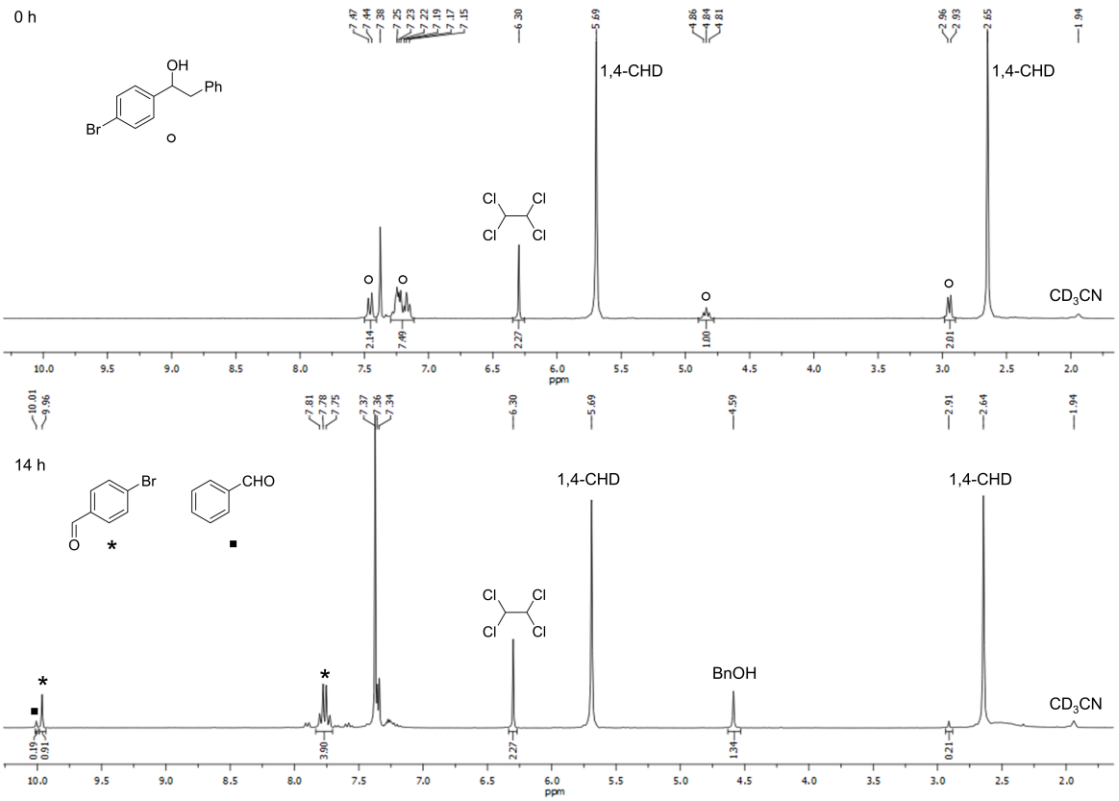

Figure A.140. The ^{1}H NMR spectra of the photoreaction with **38** before (top) and after (bottom) light irradiation. The peak at 2.91 ppm corresponds to product **35**.

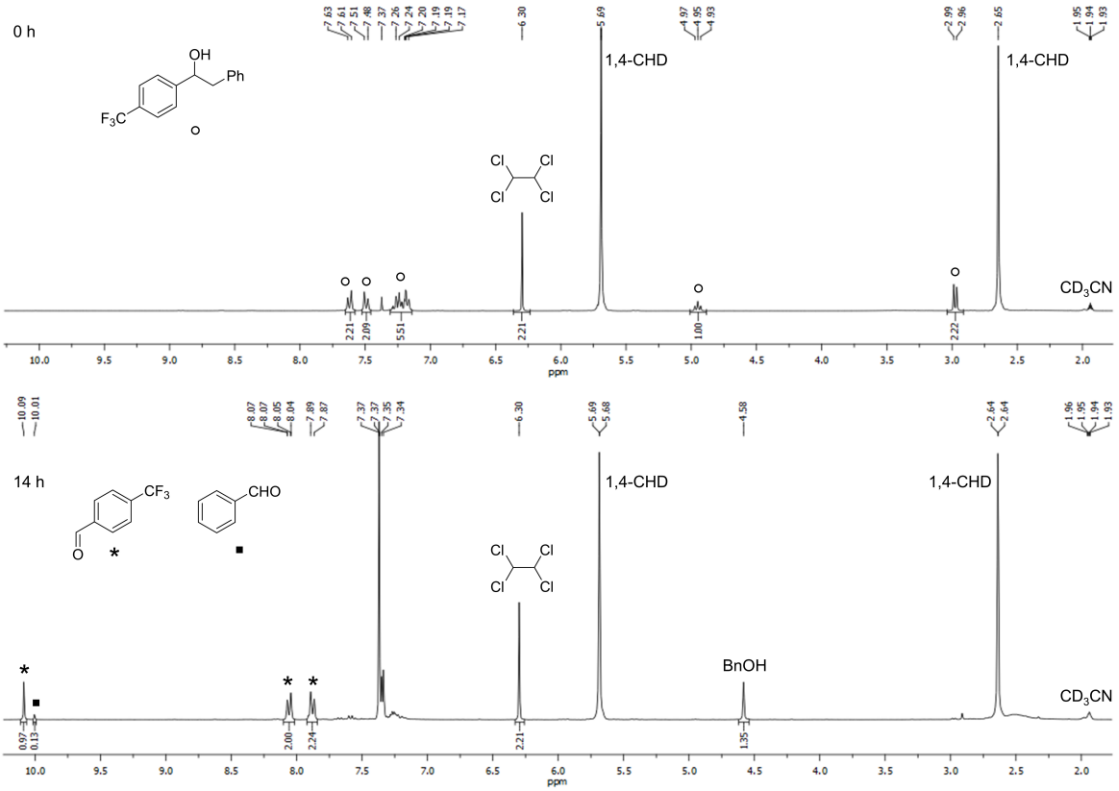

Figure A.141. The ^{1}H NMR spectra of the photoreaction with **39** before (top) and after (bottom) light irradiation. The peak at 2.91 ppm corresponds to product **35**.

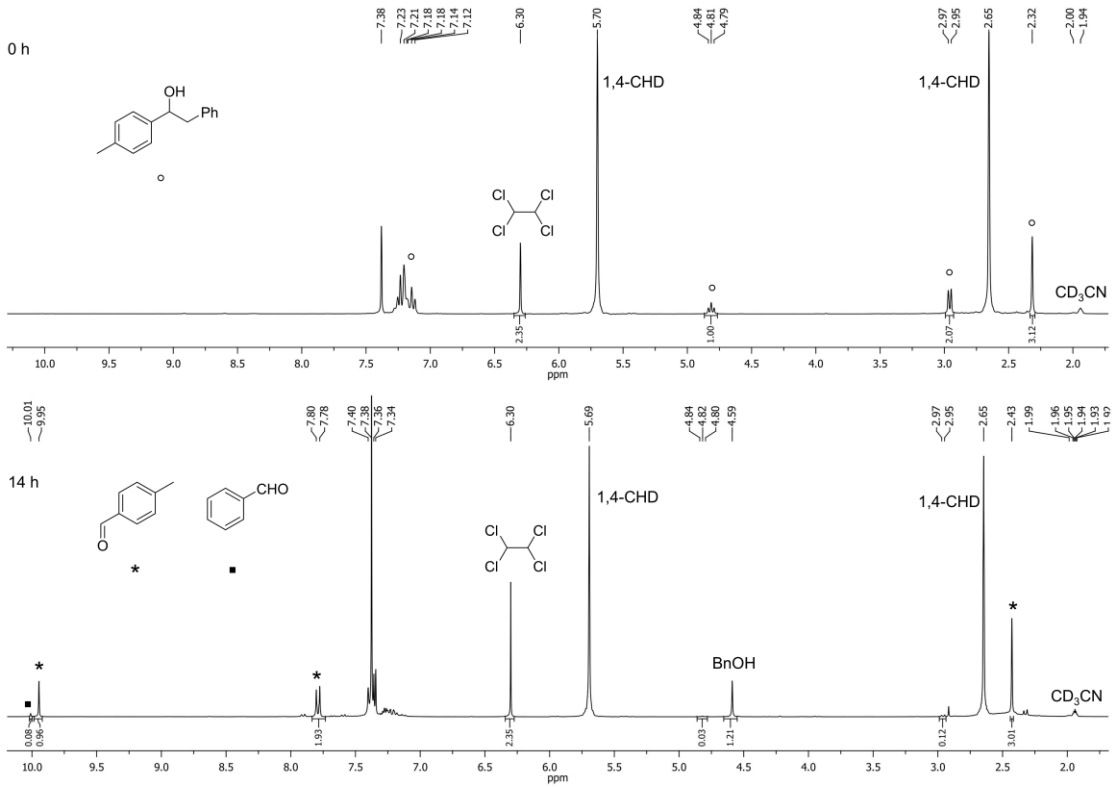

Figure A.142. The ^{1}H NMR spectra of the photoreaction with **40** before (top) and after (bottom) light irradiation. The peak at 2.91 ppm corresponds to product **35**.

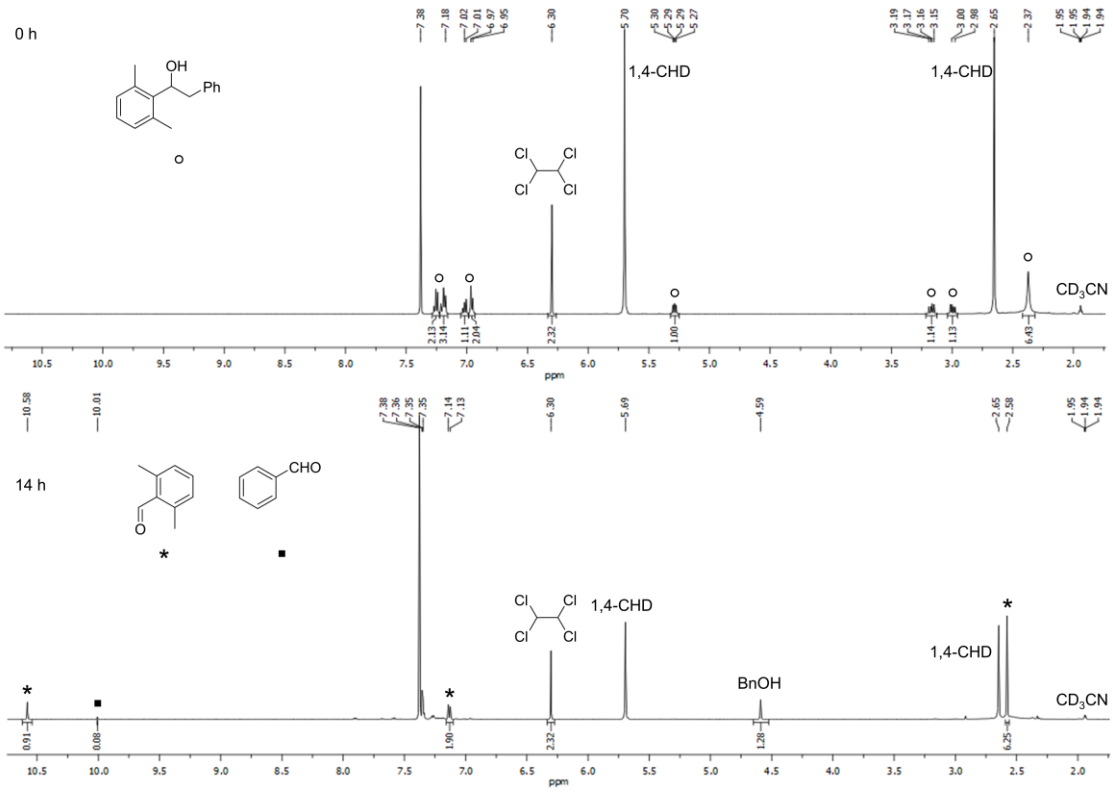

Figure A.143. The ^{1}H NMR spectra of the photoreaction with **41** before (top) and after (bottom) light irradiation. The peak at 2.91 ppm corresponds to product **35**.

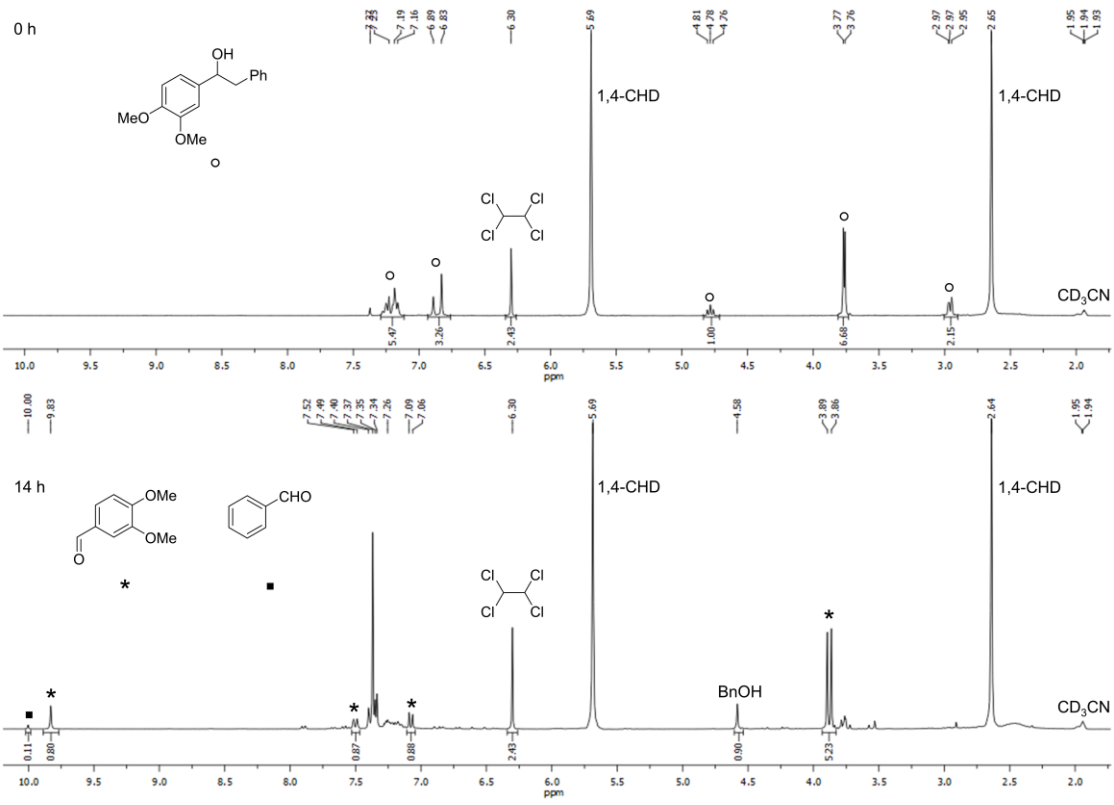

Figure A.144. The ^{1}H NMR spectra of the photoreaction with **42** before (top) and after (bottom) light irradiation. The peak at 2.91 ppm corresponds to product **35**.

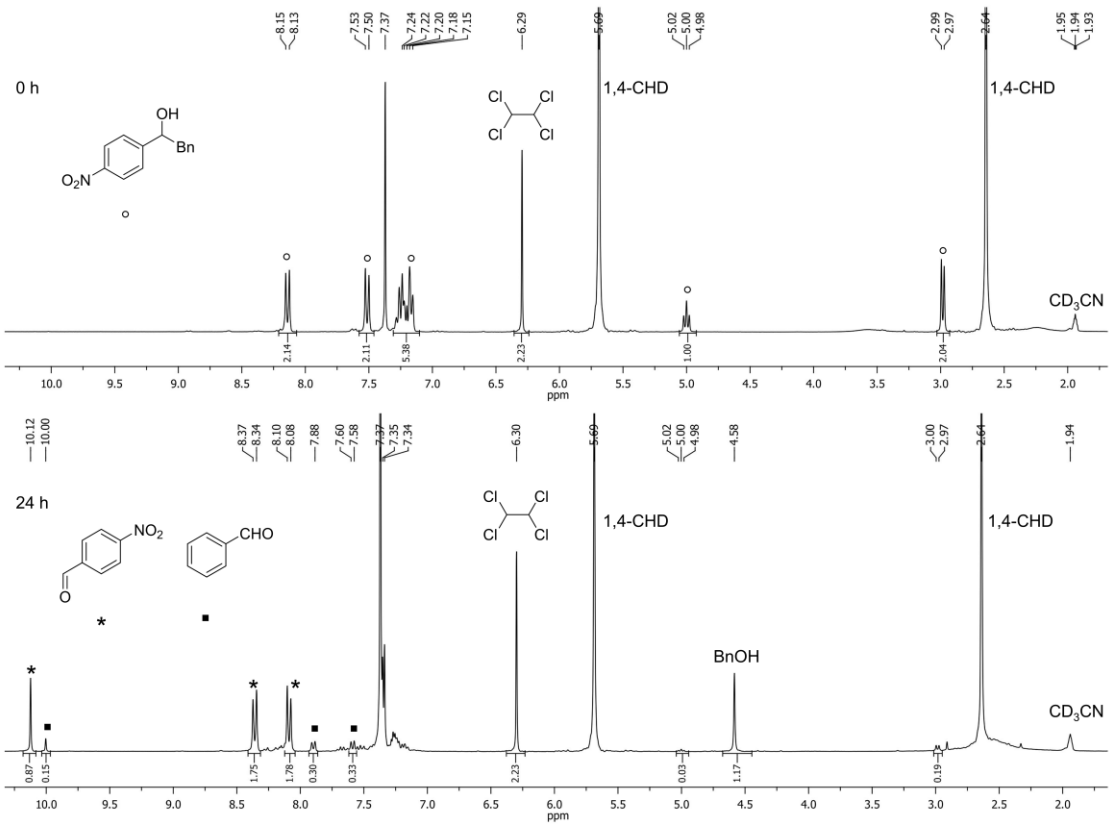

Figure A.145. The ^{1}H NMR spectra of the photoreaction with 4**3** before (top) and after (bottom) light irradiation. The peak at 2.91 ppm corresponds to product **35**.

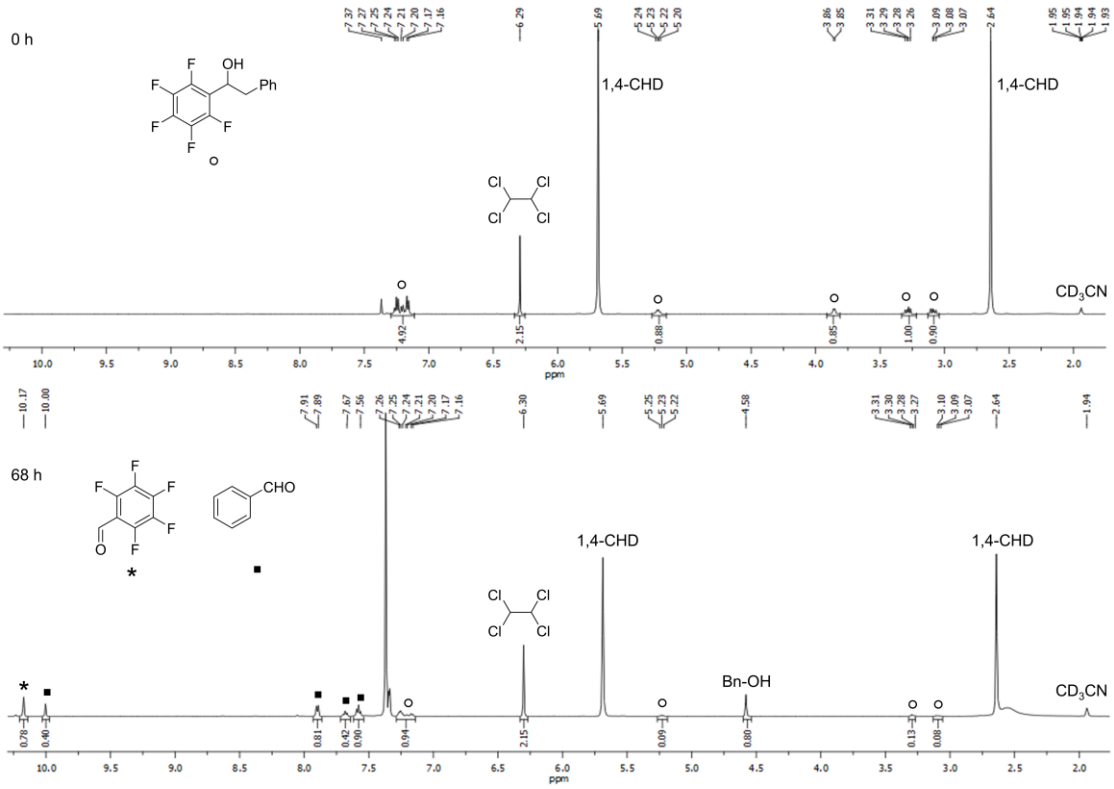

Figure A.146. The ^{1}H NMR spectra of the photoreaction with **44** before (top) and after (bottom) light irradiation. The peak at 2.91 ppm corresponds to product **35**.

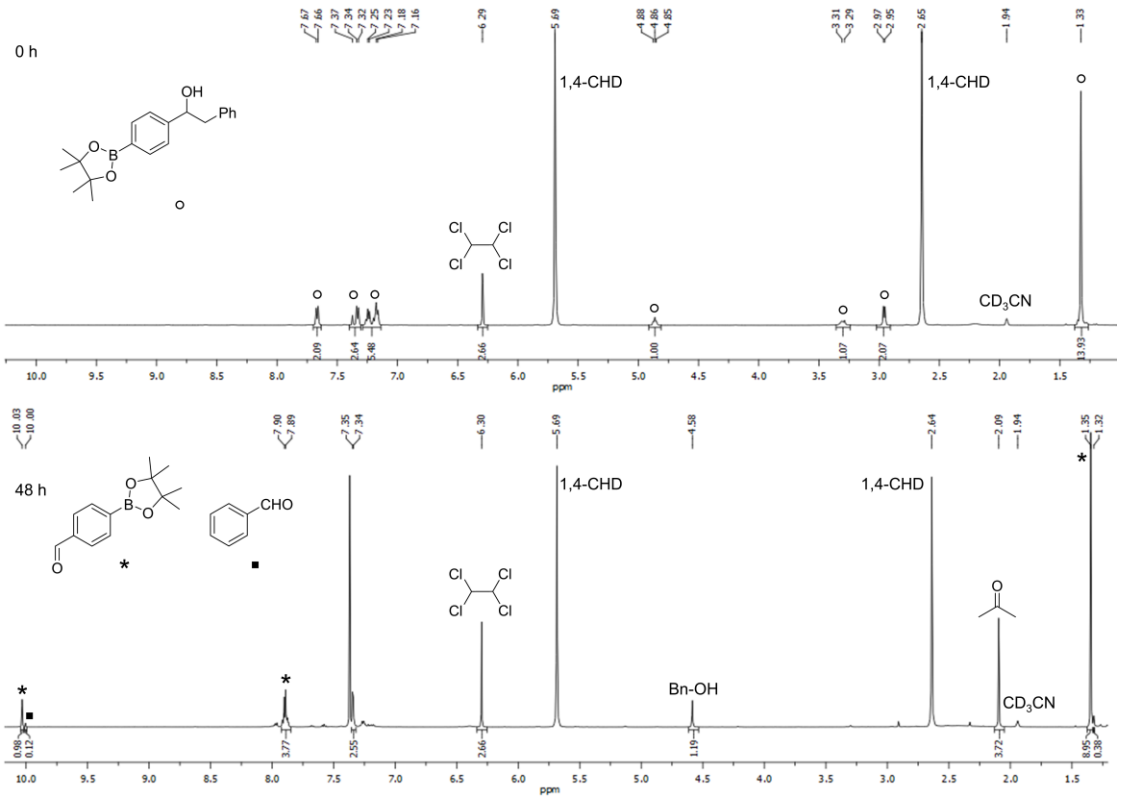

Figure A.147. The ^{1}H NMR spectra of the photoreaction with **45** before (top) and after (bottom) light irradiation. The peak at 2.91 ppm corresponds to **35**.

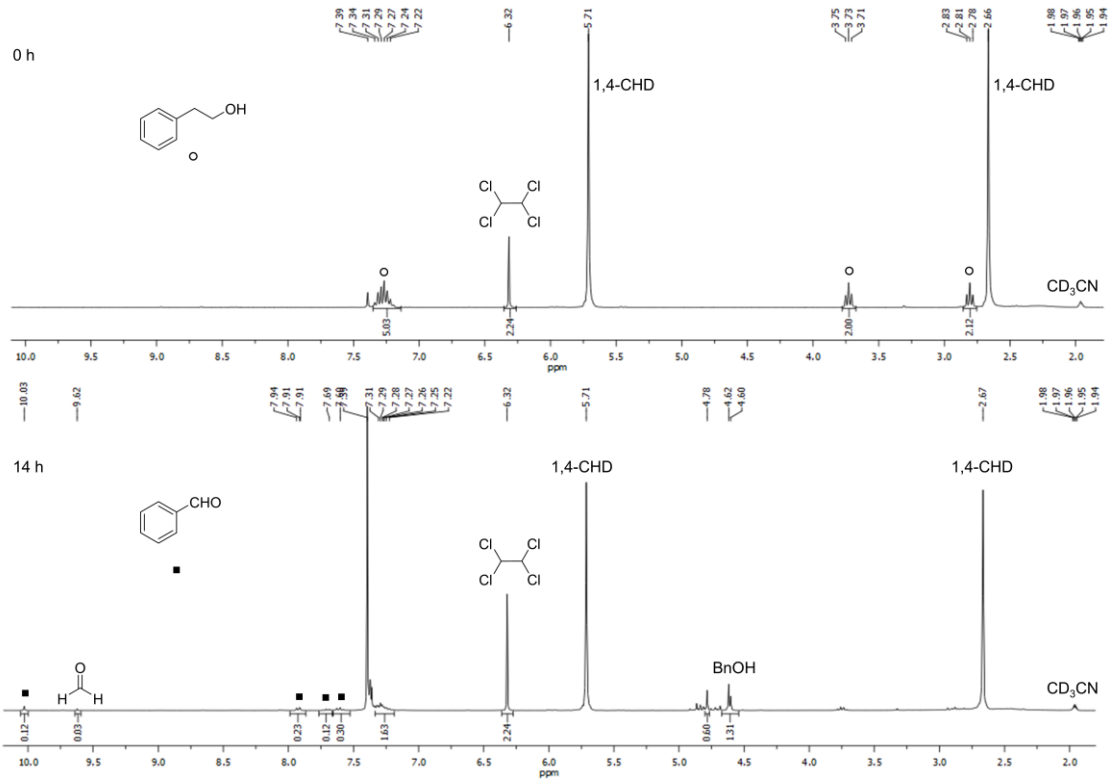

Figure A.148. The ^{1}H NMR spectra of the photoreaction with **55** before (top) and after (bottom) light irradiation.

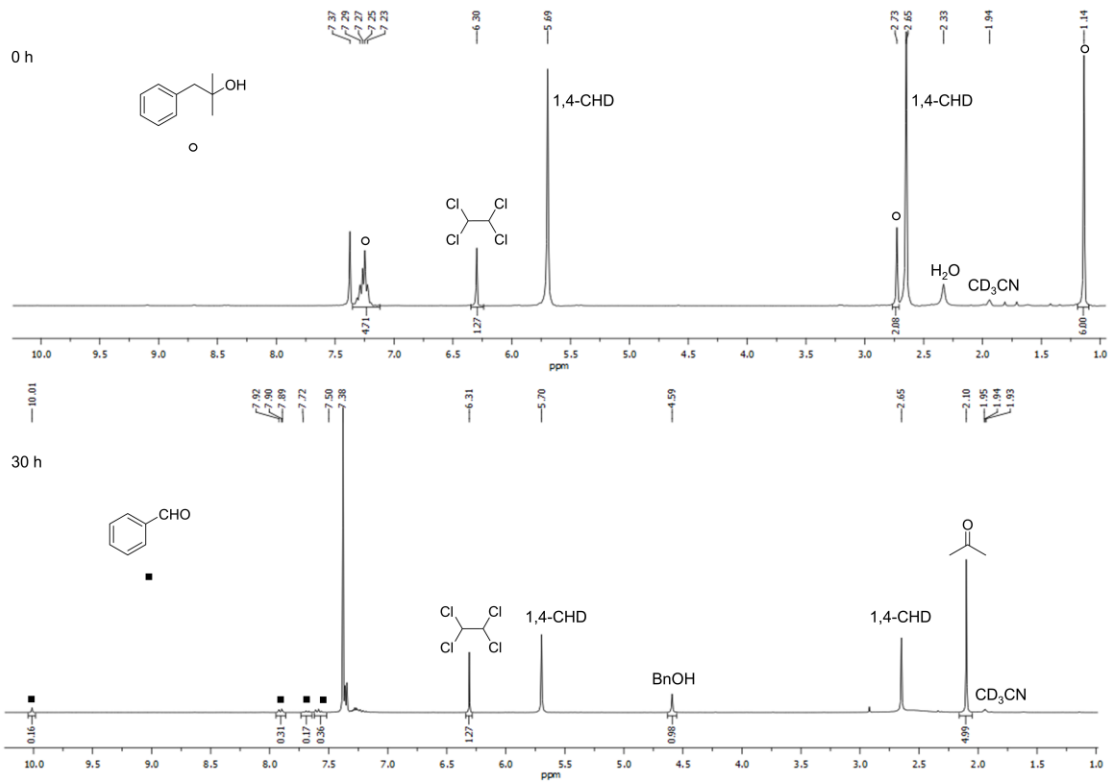

Figure A.149. The ^{1}H NMR spectra of the photoreaction with **56** before (top) and after (bottom) light irradiation. The peak at 2.91 ppm corresponds to **35**.

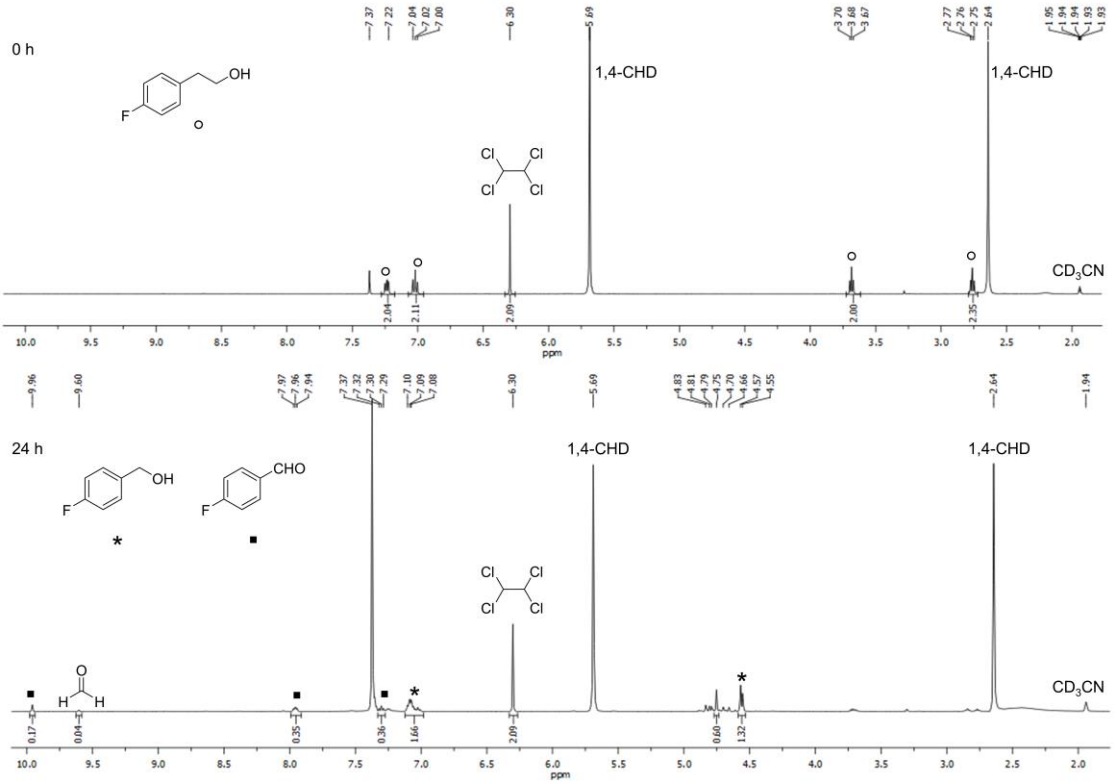

Figure A.150. The ^{1}H NMR spectra of the photoreaction with **57** before (top) and after (bottom) light irradiation.

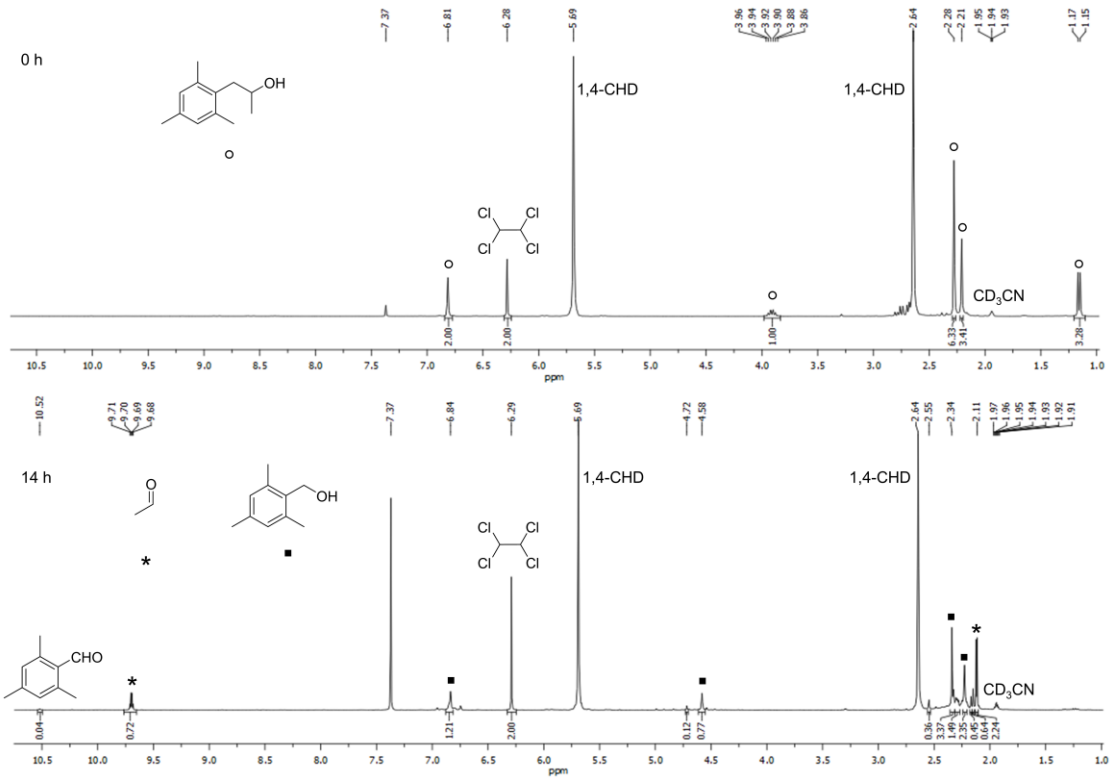

Figure A.151. The ^{1}H NMR spectra of the photoreaction with **58** before (top) and after (bottom) light irradiation.

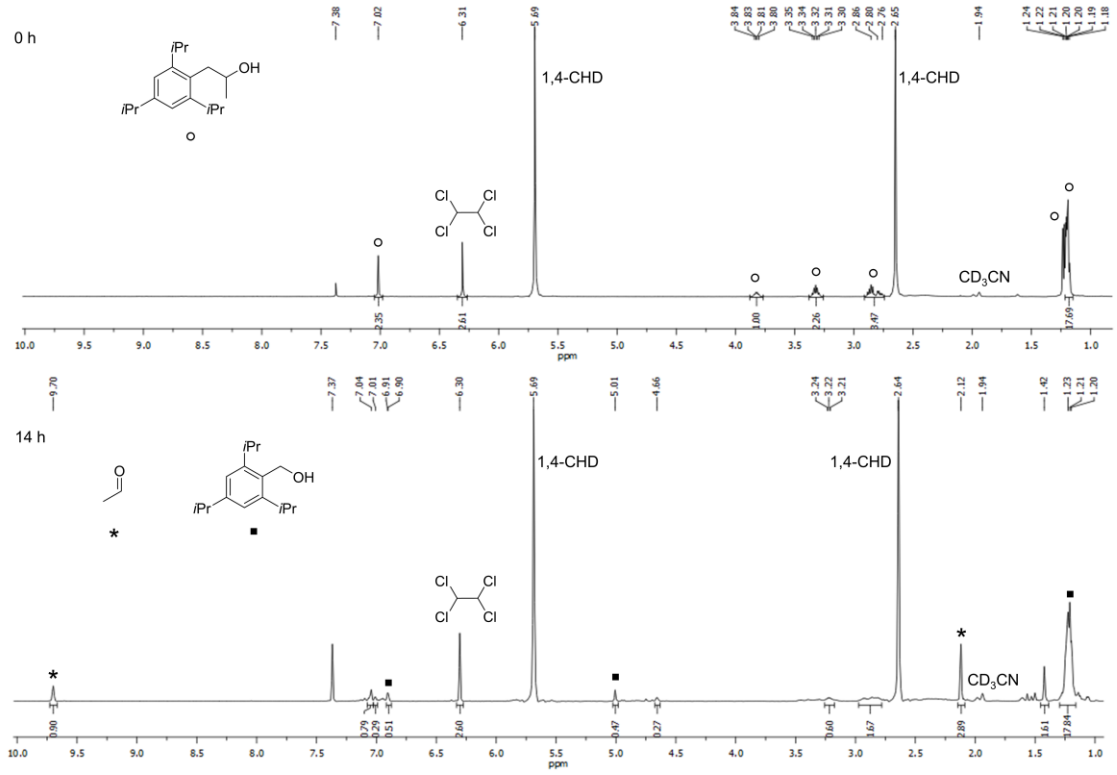

Figure A.152. The ^{1}H NMR spectra of the photoreaction with **59** before (top) and after (bottom) light irradiation.

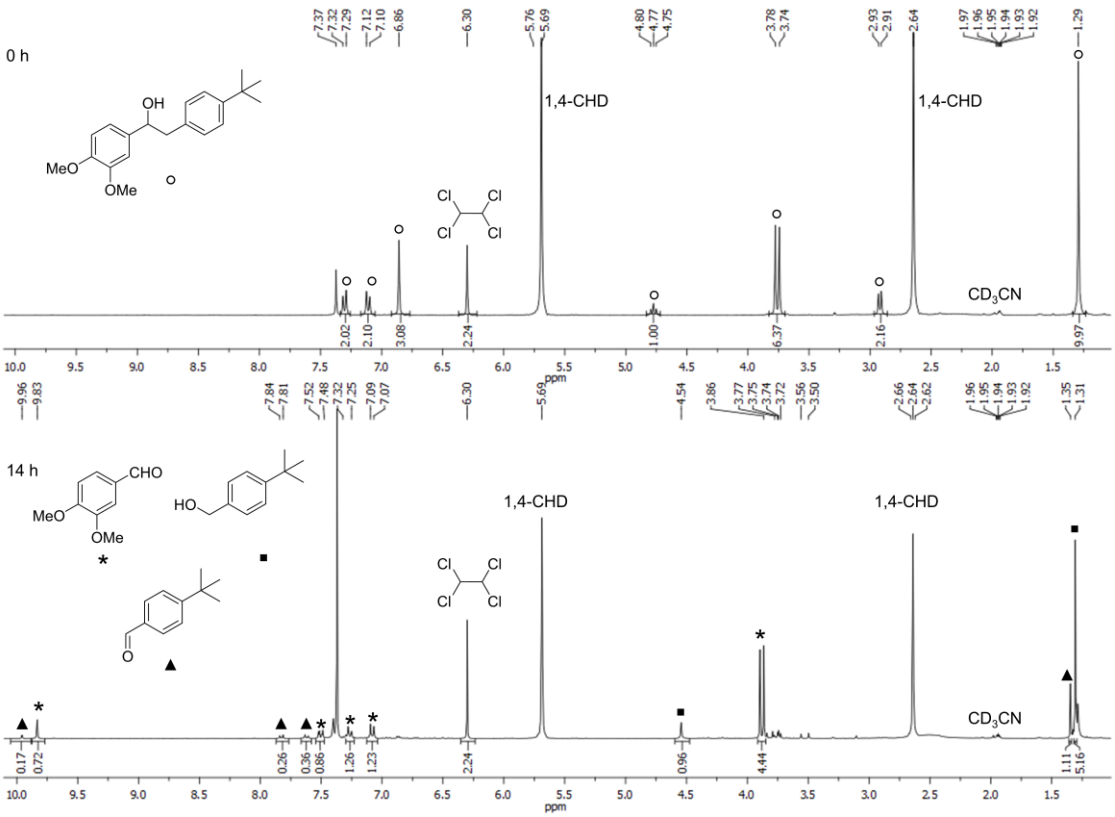

Figure A.153. The ^{1}H NMR spectra of the photoreaction with **60** before (top) and after (bottom) light irradiation.

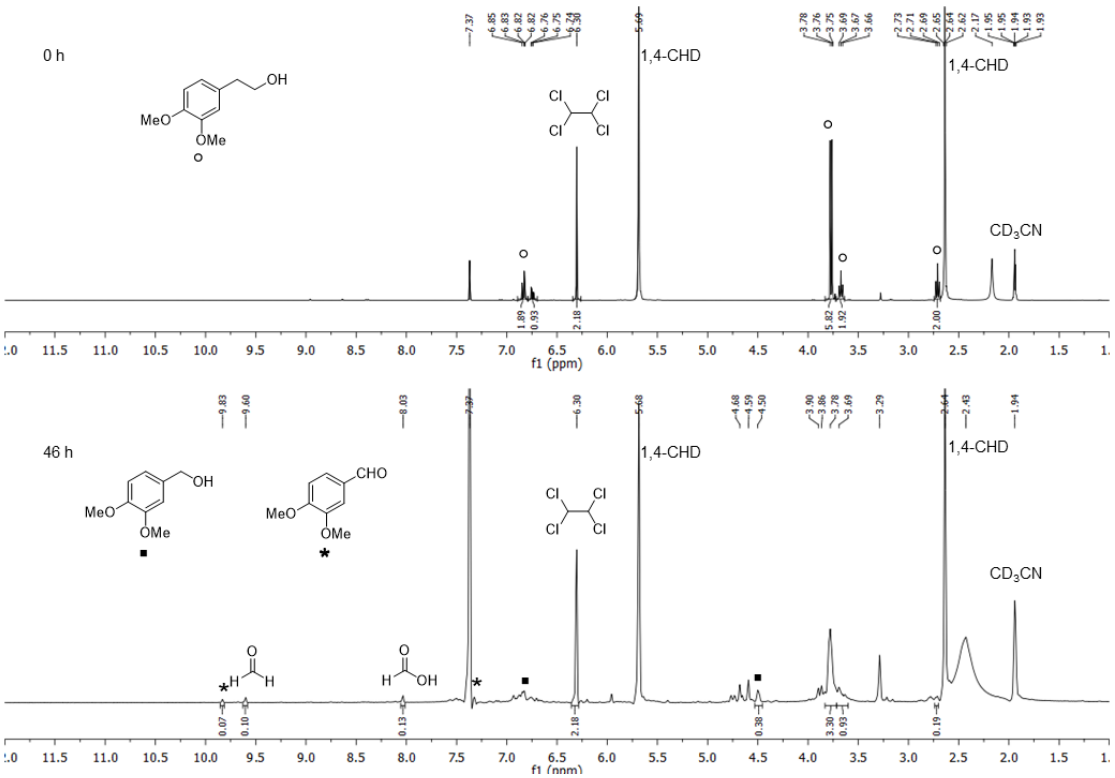

Figure A.154. The ^{1}H NMR spectra of the photoreaction with **61** before (top) and after (bottom) light irradiation. This reaction was performed on a 0.020 mmol scale and with a pure O_2 balloon to minimise side-reactions.

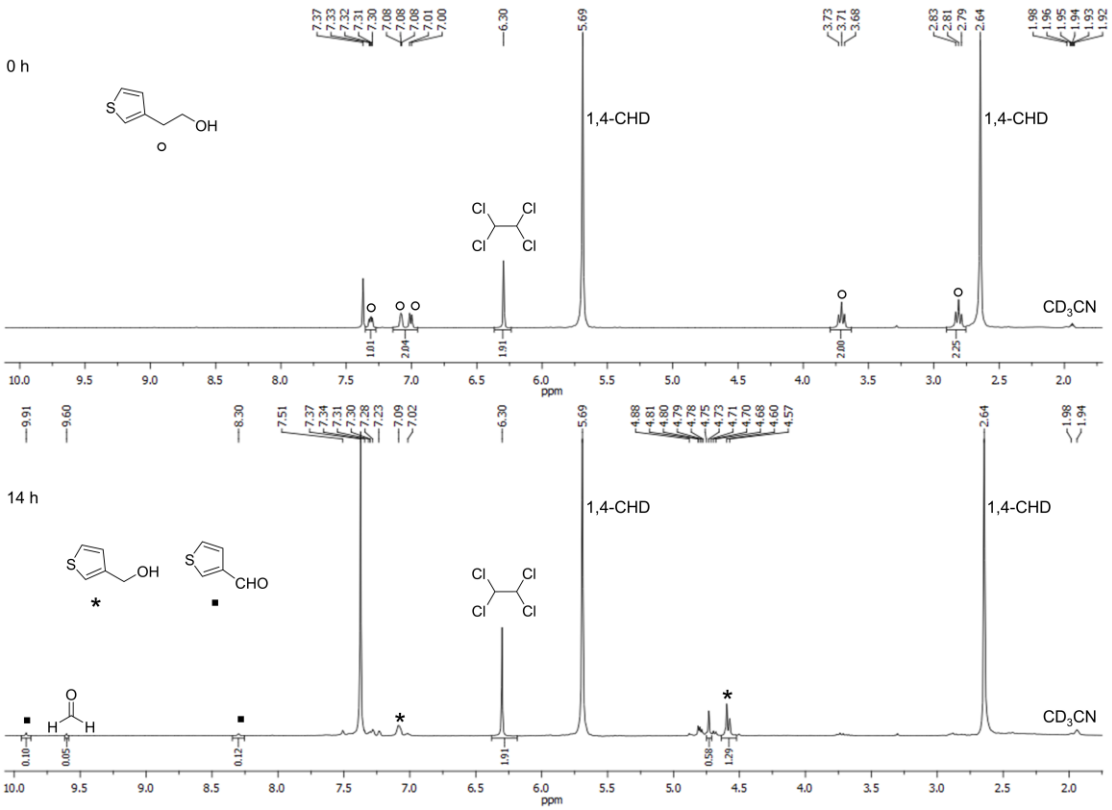

Figure A.155. The ^{1}H NMR spectra of the photoreaction with **62** before (top) and after (bottom) light irradiation.

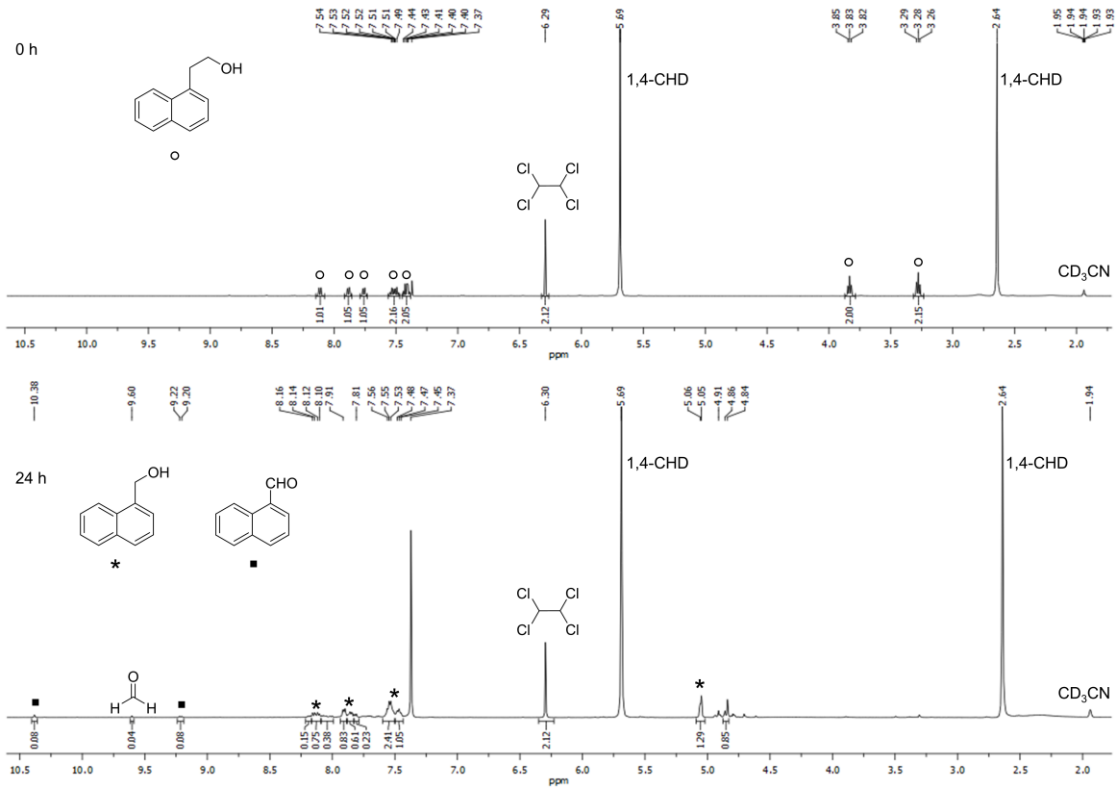

Figure A.156. The ^{1}H NMR spectra of the photoreaction with **63** before (top) and after (bottom) light irradiation.

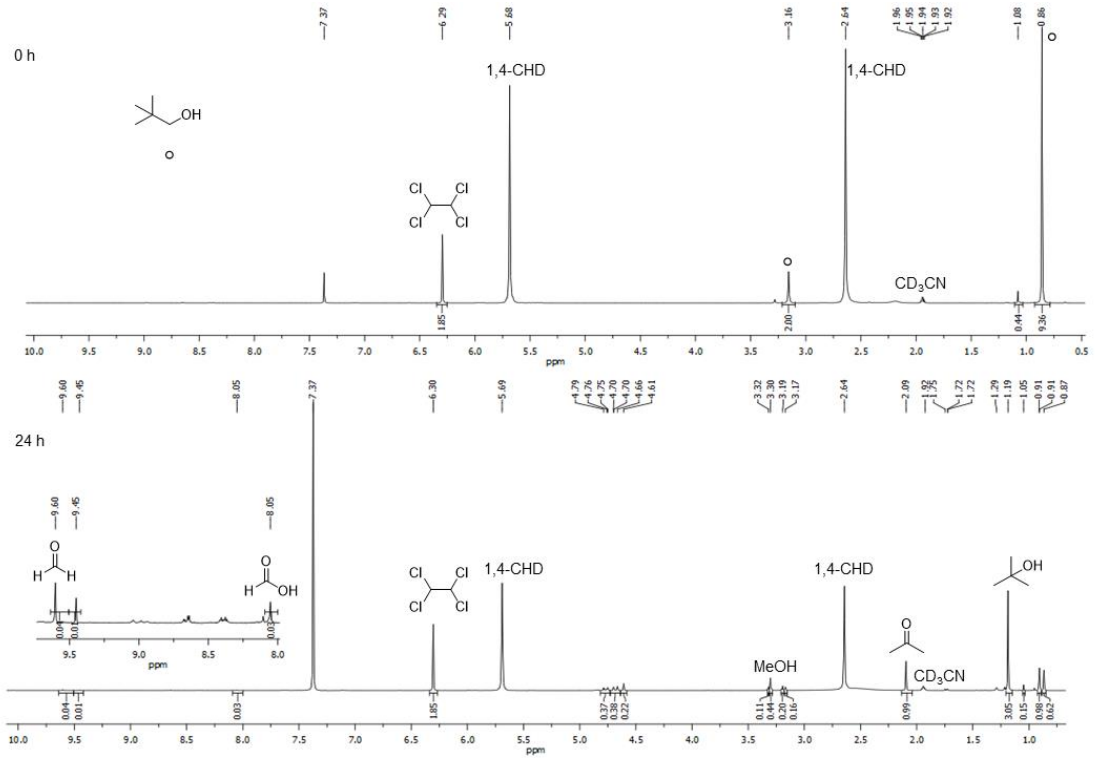

Figure A.157. The ^{1}H NMR spectra of the photoreaction with **78** before (top) and after (bottom) light irradiation. The inset shows the peaks corresponding to formic acid and formaldehyde more clearly.

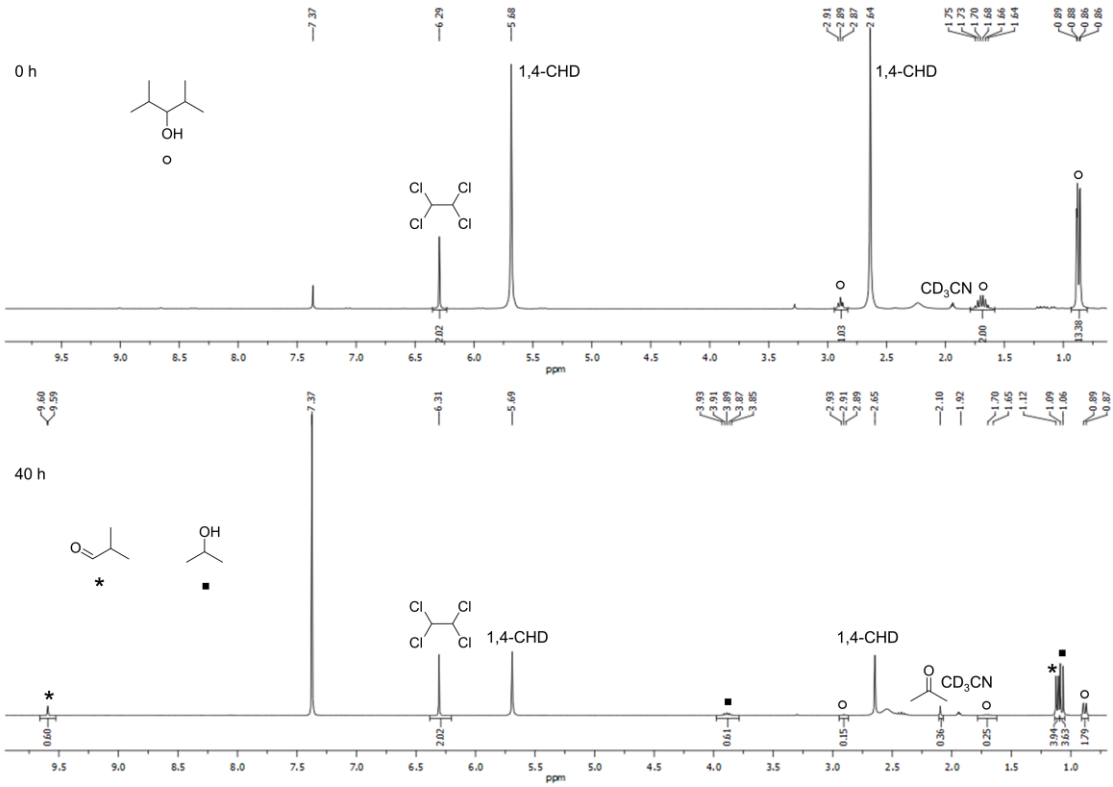

Figure A.158. The ^{1}H NMR spectra of the photoreaction with **79** before (top) and after (bottom) light irradiation.

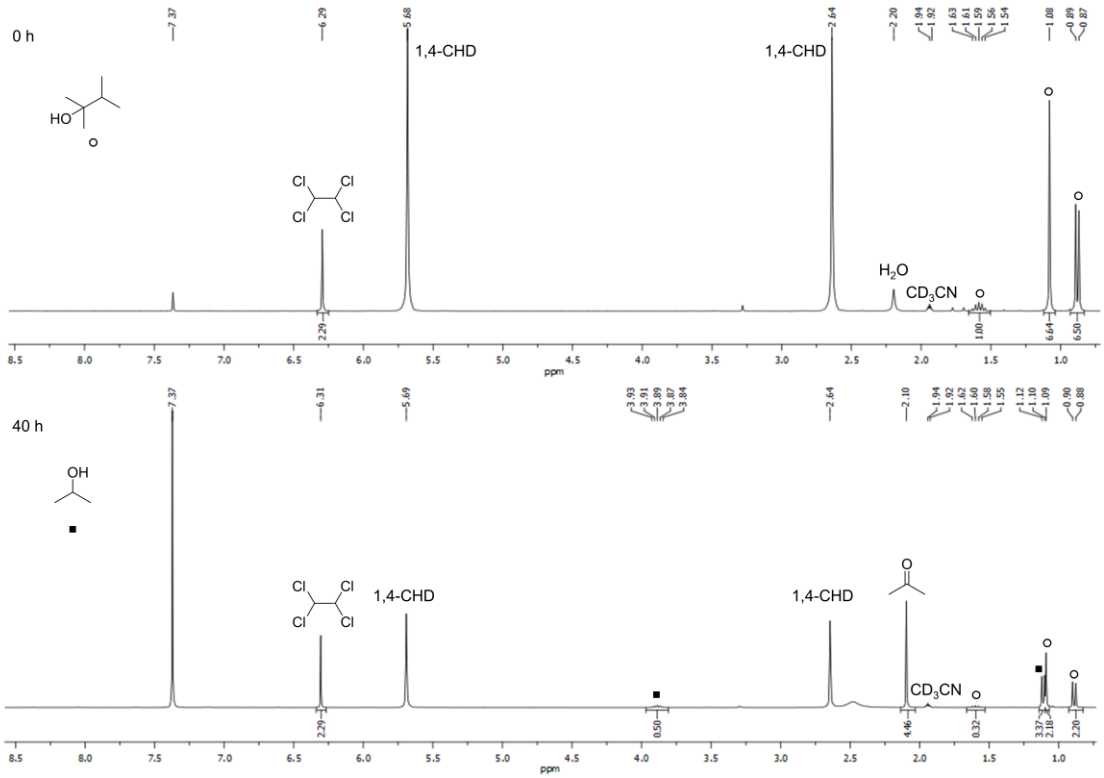

Figure A.159. The ^{1}H NMR spectra of the photoreaction with **80** before (top) and after (bottom) light irradiation.

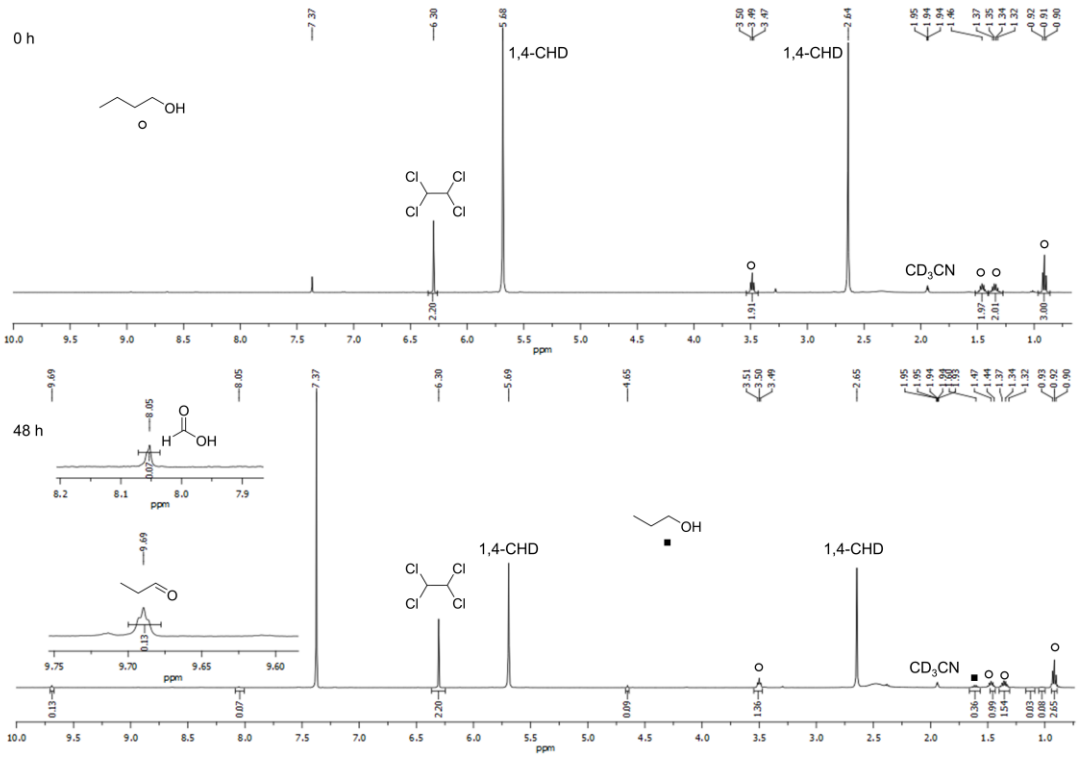

Figure A.160. The ^{1}H NMR spectra of the photoreaction with **81** before (top) and after (bottom) light irradiation. The inset shows the peaks corresponding to formic acid and propionaldehyde more clearly.

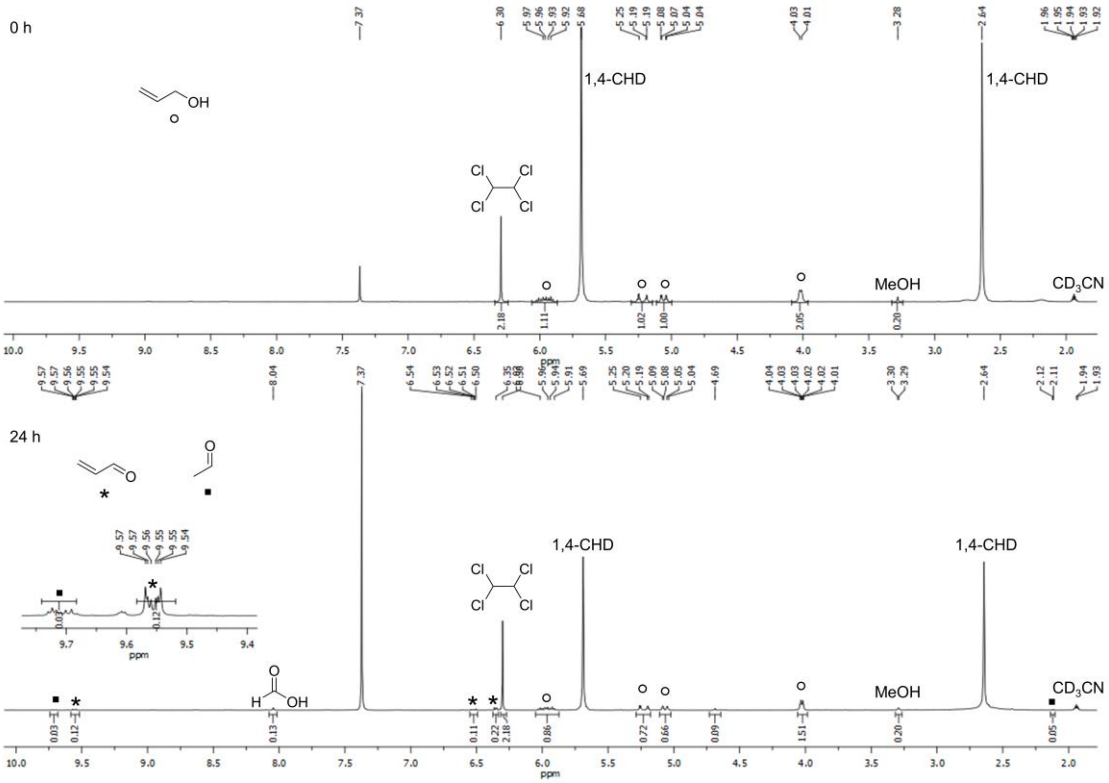

Figure A.161. The ^{1}H NMR spectra of the photoreaction with **82** before (top) and after (bottom) light irradiation. The inset shows the peaks corresponding to the aldehyde products more clearly.

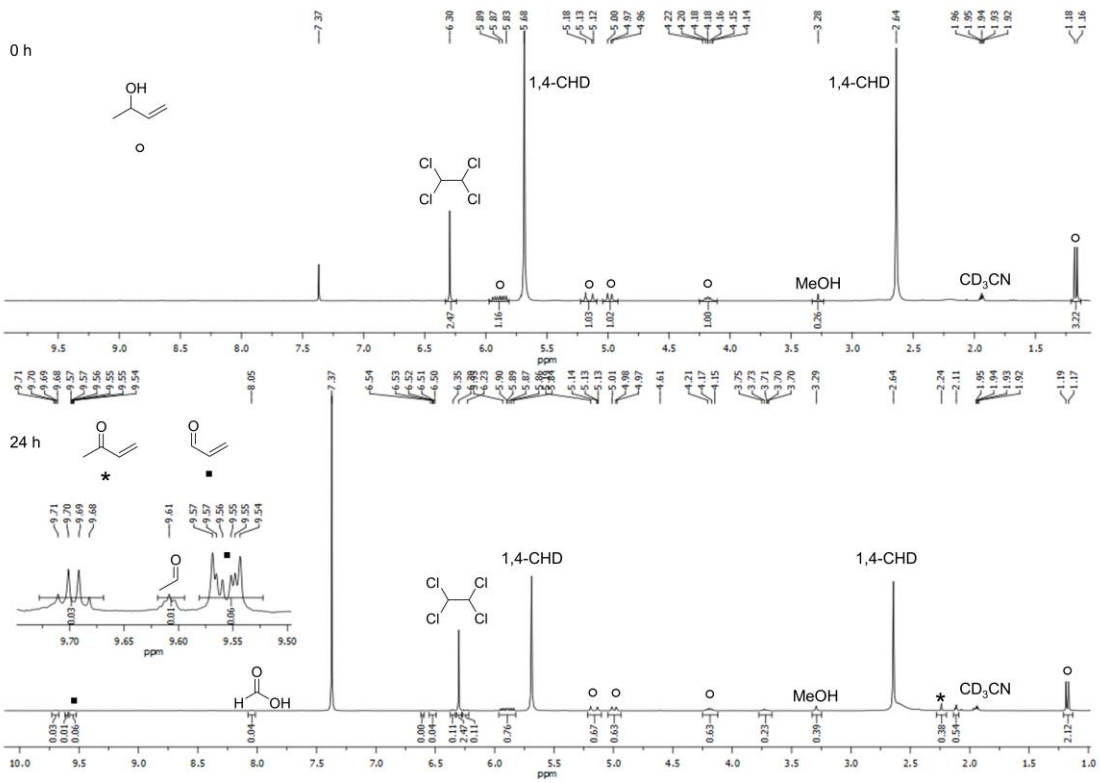

Figure A.162. The ^{1}H NMR spectra of the photoreaction with **83** before (top) and after (bottom) light irradiation. The inset shows the peaks corresponding to the aldehyde products more clearly.

X-Ray Crystallographic Data

Table A.1. Crystal and structure refinement data for complex **VO-11**.

Identification code	shs205s
Chemical formula	$C_{16}H_{17}N_2O_5V$
Formula weight	368.26 g/mol
Temperature	133(2) K
Wavelength	1.54178 Å
Crystal size	0.010 x 0.020 x 0.040 mm
Crystal habit	red block
Crystal system	monoclinic
Space group	P 2_1/c
Unit cell dimensions	a = 8.0417(2) Å α = 90° b = 16.8891(5) Å β = 103.445(2)° c = 12.0553(3) Å γ = 90°
Volume	1592.44(7) $Å^3$
Z	4
Density (calculated)	1.536 g/cm^3
Absorption coefficient	5.480 mm^{-1}
F(000)	760
Theta range for data collection	4.59 to 66.68°
Index ranges	-8<=h<=9, -19<=k<=19, -14<=l<=14
Reflections collected	9292
Independent reflections	2791 [R(int) = 0.0537]
Coverage of independent reflections	98.8%
Absorption correction	Multi-Scan
Max. and min. transmission	0.9470 and 0.8110
Structure solution technique	direct methods
Structure solution program	XT, VERSION 2013/1
Refinement method	Full-matrix least-squares on F^2
Refinement program	SHELXL-2014/7 (Sheldrick, 2014)
Function minimized	$\Sigma\ w(F_o^2 - F_c^2)^2$
Data / restraints / parameters	2791 / 0 / 222
Goodness-of-fit on F^2	1.103
Final R indices	2278 data; I>2σ(I) R1 = 0.0395, wR2 = 0.0988 all data R1 = 0.0518, wR2 = 0.1038
Weighting scheme	$w=1/[\sigma^2(F_o^2)+(0.0508P)^2]$ where $P=(F_o^2+2F_c^2)/3$
Largest diff. peak and hole	0.444 and -0.354 $eÅ^{-3}$
R.M.S. deviation from mean	0.066 $eÅ^{-3}$

Table A.2. Crystal and structure refinement data for complex **VO-13**.

Identification code	shs190
Chemical formula	$C_{16}H_{12}F_5N_2O_5V$
Formula weight	458.22 g/mol
Temperature	103(2) K
Wavelength	0.71073 Å
Crystal size	0.120 x 0.200 x 0.420 mm
Crystal habit	red block
Crystal system	triclinic
Space group	P -1
Unit cell dimensions	a = 7.7376(4) Å α = 77.527(3)° b = 10.3301(5) Å β = 71.110(2)° c = 11.7736(6) Å γ = 77.229(3)°
Volume	857.65(8) $Å^3$
Z	2
Density (calculated)	1.774 g/cm^3
Absorption coefficient	0.665 mm^{-1}
F(000)	460
Theta range for data collection	1.85 to 31.29°
Index ranges	-11<=h<=11, -15<=k<=15, -17<=l<=17
Reflections collected	26988
Independent reflections	5594 [R(int) = 0.0507]
Coverage of independent reflections	99.6%
Absorption correction	Multi-Scan
Max. and min. transmission	0.9240 and 0.7680
Structure solution technique	direct methods
Structure solution program	XS, VERSION 2013/1
Refinement method	Full-matrix least-squares on F^2
Refinement program	SHELXL-2014/7 (Sheldrick, 2014)
Function minimized	$\Sigma\ w(F_o^2 - F_c^2)^2$
Data / restraints / parameters	5594 / 0 / 267
Goodness-of-fit on F^2	1.043
Δ/σ_{max}	0.001
Final R indices	4860 data; I>2σ(I) R1 = 0.0324, wR2 = 0.0837 all data R1 = 0.0398, wR2 = 0.0882
Weighting scheme	$w=1/[\sigma^2(F_o^2)+(0.0395P)^2+0.3675P]$ where $P=(F_o^2+2F_c^2)/3$
Largest diff. peak and hole	0.704 and -0.557 $eÅ^{-3}$
R.M.S. deviation from mean	0.075 $eÅ^{-3}$

Table A.3. Crystal and structure refinement data for complex **VO-14**.

Identification code	shs191
Chemical formula	$C_{16}H_{11}F_5N_3O_7V$
Formula weight	503.22 g/mol
Temperature	103(2) K
Wavelength	0.71073 Å
Crystal size	0.020 x 0.060 x 0.180 mm
Crystal habit	red plate
Crystal system	triclinic
Space group	P -1
Unit cell dimensions	a = 7.8153(7) Å α = 78.955(7)° b = 11.0933(10) Å β = 85.104(7)° c = 11.0932(12) Å γ = 77.783(6)°
Volume	921.55(16) $Å^3$
Z	2
Density (calculated)	1.813 g/cm^3
Absorption coefficient	0.637 mm^{-1}
F(000)	504
Theta range for data collection	1.87 to 28.41°
Index ranges	-10<=h<=10, -14<=k<=14, -14<=l<=14
Reflections collected	15783
Independent reflections	4615 [R(int) = 0.1164]
Coverage of independent reflections	99.4%
Absorption correction	Multi-Scan
Max. and min. transmission	0.9870 and 0.8940
Structure solution technique	direct methods
Structure solution program	XS, VERSION 2013/1
Refinement method	Full-matrix least-squares on F^2
Refinement program	SHELXL-2014/7 (Sheldrick, 2014)
Function minimized	$\Sigma\ w(F_o^2 - F_c^2)^2$
Data / restraints / parameters	4615 / 0 / 294
Goodness-of-fit on F^2	0.981
Δ/σ_{max}	0.001
Final R indices	2669 data; I>2σ(I) R1 = 0.0548, wR2 = 0.0998 all data R1 = 0.1149, wR2 = 0.1218
Weighting scheme	$w=1/[\sigma^2(F_o^2)+(0.0343P)^2]$ where $P=(F_o^2+2F_c^2)/3$
Largest diff. peak and hole	0.454 and -0.760 $eÅ^{-3}$
R.M.S. deviation from mean	0.107 $eÅ^{-3}$

Table A.4. Crystal and structure refinement data for complex **VO-15**.

Identification code	shs174
Chemical formula	$C_{17}H_{14}F_5N_4O_{10}V$
Formula weight	580.26 g/mol
Temperature	153(2) K
Wavelength	0.71073 Å
Crystal size	0.180 x 0.240 x 0.280 mm
Crystal habit	red block
Crystal system	monoclinic
Space group	P 2_1/n
Unit cell dimensions	a = 14.0565(9) Å α = 90° b = 11.7664(7) Å β = 113.164(2)° c = 14.2345(10) Å γ = 90°
Volume	2164.5(2) $Å^3$
Z	4
Density (calculated)	1.781 g/cm^3
Absorption coefficient	0.566 mm^{-1}
F(000)	1168
Theta range for data collection	2.33 to 31.07°
Index ranges	-17<=h<=20, -17<=k<=17, -20<=l<=17
Reflections collected	40179
Independent reflections	6918 [R(int) = 0.0996]
Coverage of independent reflections	99.6%
Absorption correction	Multi-Scan
Max. and min. transmission	0.9050 and 0.8580
Structure solution technique	direct methods
Structure solution program	XS, VERSION 2013/1
Refinement method	Full-matrix least-squares on F^2
Refinement program	SHELXL-2014/7 (Sheldrick, 2014)
Function minimized	$\Sigma\ w(F_o^2 - F_c^2)^2$
Data / restraints / parameters	6918 / 0 / 341
Goodness-of-fit on F^2	1.002
Δ/σ_{max}	0.001
Final R indices	4668 data; I>2σ(I) R1 = 0.0483, wR2 = 0.1030 all data R1 = 0.0844, wR2 = 0.1236
Weighting scheme	$w=1/[\sigma^2(F_o^2)+(0.0337P)^2 +1.7738P]$ where $P=(F_o^2+2F_c^2)/3$
Largest diff. peak and hole	0.496 and -0.555 $eÅ^{-3}$
R.M.S. deviation from mean	0.085 $eÅ^{-3}$

Table A.5. Crystal and structure refinement data for **VO-16**.

Identification code	shs194s	
Chemical formula	$C_{65}H_{64}N_{16}O_{37}V_4$	
Formula weight	1865.08 g/mol	
Temperature	103(2) K	
Wavelength	1.54178 Å	
Crystal size	0.010 x 0.020 x 0.420 mm	
Crystal system	triclinic	
Space group	P -1	
Unit cell dimensions	a = 7.8518(2) Å	α = 95.1437(11)°
	b = 13.8041(3) Å	β = 95.0087(11)°
	c = 36.9524(7) Å	γ = 91.9535(11)°
Volume	3970.25(15) $Å^3$	
Z	2	
Density (calculated)	1.560 g/cm^3	
Absorption coefficient	4.730 mm^{-1}	
F(000)	1908	
Theta range for data collection	2.41 to 66.67°	
Index ranges	-8<=h<=9, -16<=k<=16, -43<=l<=43	
Reflections collected	76199	
Independent reflections	13949 [R(int) = 0.0546]	
Max. and min. transmissions	0.9540 and 0.2410	
Refinement method	Full-matrix least-squares on F^2	
Refinement program	SHELXL-2014/7 (Sheldrick, 2014)	
Function minimized	$\Sigma\, w(F_o^2 - F_c^2)^2$	
Data / restraints / parameters	13949 / 1300 / 1175	
Goodness-of-fit on F^2	1.070	
Δ/σ_{max}	0.002	
Final R indices	12817 data; I>2σ(I)	R1 = 0.0490, wR2 = 0.1170
	all data	R1 = 0.0528, wR2 = 0.1193
Weighting scheme	$w=1/[\sigma^2(F_o^2)+(0.0337P)^2+7.6363P]$ where $P=(F_o^2+2F_c^2)/3$	
Largest diff. peak and hole	0.965 and -0.606 $eÅ^{-3}$	
R.M.S. deviation from mean	0.068 $eÅ^{-3}$	

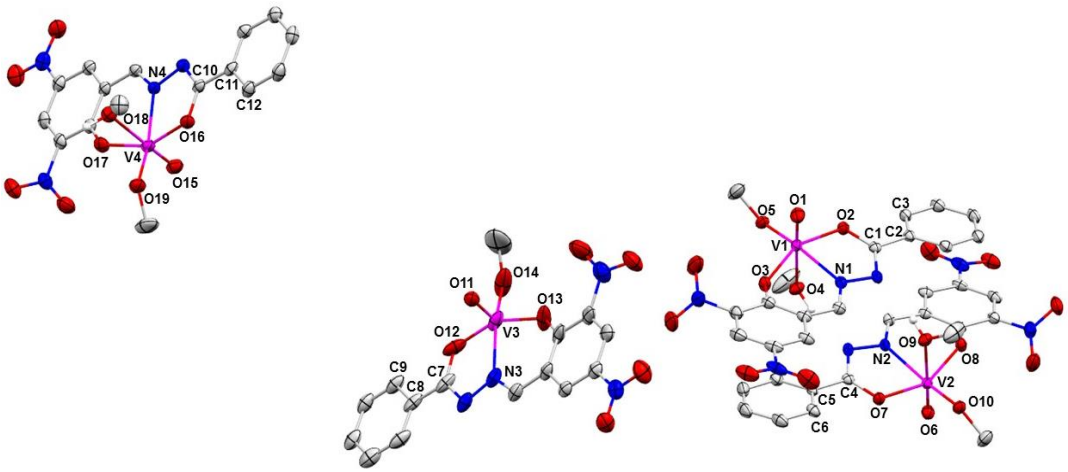

Figure A.163. Four asymmetric units of **VO-16** in the crystal cell. Hydrogen atoms and solvent molecules are omitted for clarity.

Table A.6. Crystal and structure refinement data for **VO-17**.

Identification code	cu_shs_195s_0m_5
Chemical formula	$C_{17}H_{18}N_5O_{12}V$
Formula weight	535.30 g/mol
Temperature	133(2) K
Wavelength	1.54178 Å
Crystal size	0.020 x 0.040 x 0.240 mm
Crystal habit	orange needle
Crystal system	triclinic
Space group	P -1
Unit cell dimensions	a = 7.0201(2) Å α = 110.0689(16)° b = 11.9058(4) Å β = 97.6241(17)° c = 14.1087(5) Å γ = 96.3340(17)°
Volume	1082.32(6) $Å^3$
Z	2
Density (calculated)	1.643 g/cm^3
Absorption coefficient	4.537 mm^{-1}
F(000)	548
Theta range for data collection	3.39 to 66.96°
Reflections collected	3799
Independent reflections	3799 [R(int) = 0.0616]
Coverage of independent reflections	98.1%
Absorption correction	Multi-Scan
Max. and min. transmission	0.9150 and 0.4090
Structure solution technique	direct methods
Structure solution program	XT, VERSION 2014/5
Refinement method	Full-matrix least-squares on F^2
Refinement program	SHELXL-2014/7 (Sheldrick, 2014)
Function minimized	$\Sigma\, w(F_o^2 - F_c^2)^2$
Data / restraints / parameters	3799 / 1 / 326
Goodness-of-fit on F^2	1.050
Final R indices	3447 data; $I>2\sigma(I)$ R1 = 0.0693, wR2 = 0.1740 all data R1 = 0.0724, wR2 = 0.1779
Weighting scheme	$w=1/[\sigma^2(F_o^2)+(0.1108P)^2+0.1505P]$ where $P=(F_o^2+2F_c^2)/3$
Largest diff. peak and hole	0.762 and -0.429 $eÅ^{-3}$
R.M.S. deviation from mean	0.124 $eÅ^{-3}$

Table A.7. Crystal and structure refinement data for **VO-18**.

Identification code	shs165s
Chemical formula	$C_{16}H_{15}FN_3O_7V$
Formula weight	431.25 g/mol
Temperature	103(2) K
Wavelength	1.54178 Å
Crystal size	0.020 x 0.040 x 0.420 mm
Crystal habit	red needle
Crystal system	monoclinic
Space group	P $2_1/c$
Unit cell dimensions	a = 11.2046(2) Å α = 90° b = 7.97740(10) Å β = 105.8546(7)° c = 20.2462(3) Å γ = 90°
Volume	1740.83(5) $Å^3$
Z	4
Density (calculated)	1.645 g/cm^3
Absorption coefficient	5.306 mm^{-1}
F(000)	880
Theta range for data collection	4.10 to 67.41°
Index ranges	-13<=h<=13, -9<=k<=9, -24<=l<=23
Reflections collected	15604
Independent reflections	3128 [R(int) = 0.0552]
Coverage of independent reflections	99.4%
Absorption correction	Multi-Scan
Max. and min. transmission	0.9010 and 0.2140
Structure solution technique	direct methods
Structure solution program	XS, VERSION 2013/1
Refinement method	Full-matrix least-squares on F^2
Refinement program	SHELXL-2014/7 (Sheldrick, 2014)
Function minimized	$\Sigma w(F_o^2 - F_c^2)^2$
Data / restraints / parameters	3128 / 0 / 259
Goodness-of-fit on F^2	1.079
Final R indices	2975 data; I>2σ(I) R1 = 0.0336, wR2 = 0.0921 all data R1 = 0.0351, wR2 = 0.0936
Weighting scheme	$w=1/[\sigma^2(F_o^2)+(0.0518P)^2+0.6730P]$ where $P=(F_o^2+2F_c^2)/3$
Largest diff. peak and hole	0.402 and -0.420 $eÅ^{-3}$
R.M.S. deviation from mean	0.064 $eÅ^{-3}$

Table A.8. Crystal and structure refinement data for **VO-19**.

Identification code	shs164s
Chemical formula	$C_{16}H_{14}FN_4O_9V$
Formula weight	476.25 g/mol
Temperature	103(2) K
Wavelength	1.54178 Å
Crystal size	0.010 x 0.020 x 0.220 mm
Crystal habit	red needle
Crystal system	triclinic
Space group	P -1
Unit cell dimensions	a = 7.8016(2) Å α = 92.8526(18)° b = 15.1489(4) Å β = 91.161(2)° c = 16.0022(4) Å γ = 97.375(2)°
Volume	1872.58(8) $Å^3$
Z	4
Density (calculated)	1.689 g/cm^3
Absorption coefficient	5.100 mm^{-1}
F(000)	968
Theta range for data collection	2.77 to 66.44°
Reflections collected	6405
Independent reflections	6405 [R(int) = 0.1823]
Coverage of independent reflections	97.3%
Absorption correction	Multi-Scan
Max. and min. transmission	0.9510 and 0.4000
Structure solution technique	direct methods
Structure solution program	XS, VERSION 2013/1
Refinement method	Full-matrix least-squares on F^2
Refinement program	SHELXL-2014/7 (Sheldrick, 2014)
Function minimized	$\Sigma\ w(F_o^2 - F_c^2)^2$
Data / restraints / parameters	6405 / 0 / 563
Goodness-of-fit on F^2	1.043
Final R indices	4475 data; $I>2\sigma(I)$ R1 = 0.1016, wR2 = 0.2271 all data R1 = 0.1581, wR2 = 0.2608
Weighting scheme	$w=1/[\sigma^2(F_o^2)+(0.1609P)^2]$ where $P=(F_o^2+2F_c^2)/3$
Absolute structure parameter	0.00(6)
Largest diff. peak and hole	1.279 and -1.510 $eÅ^{-3}$
R.M.S. deviation from mean	0.265 $eÅ^{-3}$

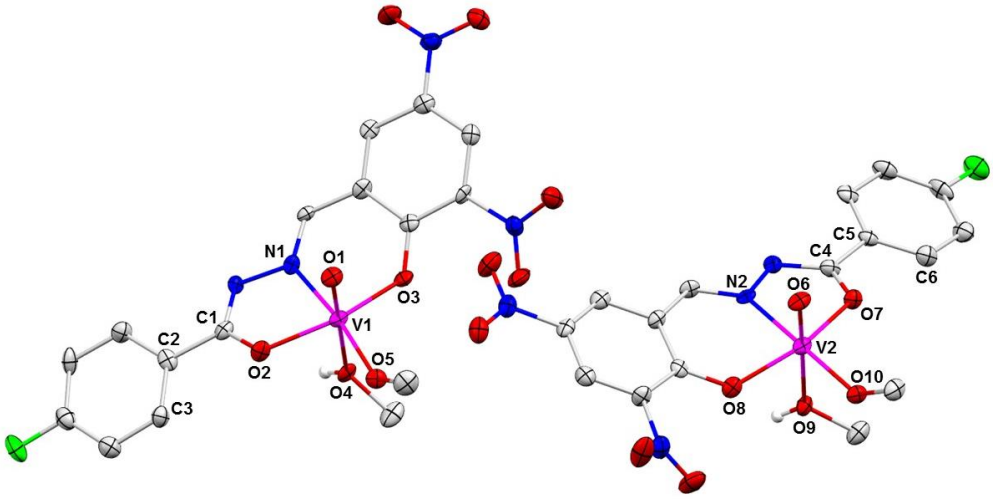

Figure A.164. Two asymmetric units in the crystal cell of **VO-19**. Hydrogen atoms are omitted for clarity.

Table A.9. Crystal and structure refinement data for **VO-20**.

Identification code	shs215s
Chemical formula	$C_{16}H_{14}F_2N_3O_7V$
Formula weight	449.24 g/mol
Temperature	103(2) K
Wavelength	1.54178 Å
Crystal size	0.010 x 0.040 x 0.100 mm
Crystal habit	red plate
Crystal system	triclinic
Space group	P -1
Unit cell dimensions	a = 7.7058(2) Å α = 79.765(3)° b = 10.7711(3) Å β = 83.602(2)° c = 11.3061(3) Å γ = 76.584(2)°
Volume	895.85(4) $Å^3$
Z	2
Density (calculated)	1.665 g/cm^3
Absorption coefficient	5.267 mm^{-1}
F(000)	456
Theta range for data collection	3.98 to 66.76°
Index ranges	-9<=h<=8, -12<=k<=12, -13<=l<=13
Reflections collected	9142
Independent reflections	3125 [R(int) = 0.0587]
Coverage of independent reflections	98.4%
Absorption correction	Multi-Scan
Max. and min. transmission	0.9490 and 0.6210
Structure solution technique	direct methods
Structure solution program	XS, VERSION 2013/1
Refinement method	Full-matrix least-squares on F^2
Refinement program	SHELXL-2014/7 (Sheldrick, 2014)
Function minimized	$\Sigma\ w(F_o^2 - F_c^2)^2$
Data / restraints / parameters	3125 / 0 / 267
Goodness-of-fit on F^2	1.030
Final R indices	2628 data; $I>2\sigma(I)$ R1 = 0.0431, wR2 = 0.1086 all data R1 = 0.0518, wR2 = 0.1135
Weighting scheme	$w=1/[\sigma^2(F_o^2)+(0.0644P)^2]$ where $P=(F_o^2+2F_c^2)/3$
Largest diff. peak and hole	0.408 and -0.393 $eÅ^{-3}$
R.M.S. deviation from mean	0.083 $eÅ^{-3}$

Table A.10. Crystal and structure refinement data for **VO-21**.

Identification code	shs203s
Chemical formula	$C_{17}H_{17}F_2N_4O_{10}V$
Formula weight	526.28 g/mol
Temperature	103(2) K
Wavelength	1.54178 Å
Crystal size	0.020 x 0.060 x 0.120 mm
Crystal habit	orange plate
Crystal system	triclinic
Space group	P -1
Unit cell dimensions	a = 6.85470(10) Å α = 68.8618(11)° b = 12.4917(2) Å β = 83.3484(11)° c = 13.1755(2) Å γ = 85.5873(11)°
Volume	1044.43(3) $Å^3$
Z	2
Density (calculated)	1.673 g/cm^3
Absorption coefficient	4.743 mm^{-1}
F(000)	536
Theta range for data collection	3.61 to 66.66°
Index ranges	-7<=h<=8, -14<=k<=14, -15<=l<=15
Reflections collected	10638
Independent reflections	3653 [R(int) = 0.0469]
Coverage of independent reflections	98.6%
Absorption correction	Multi-Scan
Max. and min. transmission	0.9110 and 0.6000
Structure solution technique	direct methods
Structure solution program	XS, VERSION 2013/1
Refinement method	Full-matrix least-squares on F^2
Refinement program	SHELXL-2014/7 (Sheldrick, 2014)
Function minimized	$\Sigma\, w(F_o^2 - F_c^2)^2$
Data / restraints / parameters	3653 / 0 / 314
Goodness-of-fit on F^2	1.037
Δ/σ_{max}	0.001
Final R indices	3247 data; I>2σ(I) R1 = 0.0404, wR2 = 0.1129 all data R1 = 0.0446, wR2 = 0.1158
Weighting scheme	$w=1/[\sigma^2(F_o^2)+(0.0770P)^2]$ where $P=(F_o^2+2F_c^2)/3$
Largest diff. peak and hole	0.441 and -0.428 $eÅ^{-3}$
R.M.S. deviation from mean	0.086 $eÅ^{-3}$

Table A.11. Crystal and structure refinement data for **VO-22**.

Identification code	shs146s
Chemical formula	$C_{18}H_{20}FN_2O_6V$
Formula weight	430.30 g/mol
Temperature	103(2) K
Wavelength	0.71073 Å
Crystal size	0.010 x 0.140 x 0.320 mm
Crystal habit	red plate
Crystal system	monoclinic
Space group	P $2_1/c$
Unit cell dimensions	a = 12.389(3) Å α = 90° b = 7.9459(15) Å β = 103.779(6)° c = 19.874(4) Å γ = 90°
Volume	1900.1(6) $Å^3$
Z	4
Density (calculated)	1.504 g/cm^3
Absorption coefficient	0.569 mm^{-1}
F(000)	888
Theta range for data collection	1.69 to 27.54°
Index ranges	-16<=h<=16, -10<=k<=10, -22<=l<=25
Reflections collected	15764
Independent reflections	4279 [R(int) = 0.1101]
Coverage of independent reflections	97.8%
Absorption correction	Multi-Scan
Max. and min. transmission	0.9940 and 0.8390
Structure solution technique	direct methods
Structure solution program	XS, VERSION 2013/1
Refinement method	Full-matrix least-squares on F^2
Refinement program	SHELXL-2014/7 (Sheldrick, 2014)
Function minimized	$\Sigma\ w(F_o^2 - F_c^2)^2$
Data / restraints / parameters	4279 / 0 / 259
Goodness-of-fit on F^2	0.986
Final R indices	2408 data; $I>2\sigma(I)$ R1 = 0.0589, wR2 = 0.1036 all data R1 = 0.1335, wR2 = 0.1295
Weighting scheme	$w=1/[\sigma^2(F_o^2)+(0.0480P)^2]$ where $P=(F_o^2+2F_c^2)/3$
Largest diff. peak and hole	0.451 and -0.492 $eÅ^{-3}$
R.M.S. deviation from mean	0.099 $eÅ^{-3}$

Table A.12. Crystal and structure refinement data for **VO-23**.

Identification code	shs231
Chemical formula	$C_{16}H_{15}N_2O_5V$
Formula weight	366.24 g/mol
Temperature	103(2) K
Wavelength	0.71073 Å
Crystal size	0.020 x 0.080 x 0.160 mm
Crystal habit	yellow plate
Crystal system	monoclinic
Space group	C c
Unit cell dimensions	a = 10.7553(6) Å α = 90° b = 21.5688(12) Å β = 127.434 (2)° c = 8.3497(4) Å γ = 90°
Volume	1538.05(15) $Å^3$
Z	4
Density (calculated)	1.582 g/cm^3
Absorption coefficient	0.675 mm^{-1}
F(000)	752
Theta range for data collection	1.89 to 31.00°
Index ranges	-15<=h<=14, -31<=k<=31, -12<=l<=11
Reflections collected	11404
Independent reflections	3440 [R(int) = 0.0809]
Coverage of independent reflections	99.8%
Absorption correction	Multi-Scan
Max. and min. transmission	0.9870 and 0.9000
Structure solution technique	direct methods
Structure solution program	XS, VERSION 2013/1
Refinement method	Full-matrix least-squares on F^2
Refinement program	SHELXL-2014/7 (Sheldrick, 2014)
Function minimized	$\Sigma\, w(F_o^2 - F_c^2)^2$
Data / restraints / parameters	3440 / 2 / 219
Goodness-of-fit on F^2	1.015
Final R indices	2684 data; I>2σ(I) R1 = 0.0462, wR2 = 0.0659 all data R1 = 0.0720, wR2 = 0.0723
Weighting scheme	$w=1/[\sigma^2(F_o^2)+(0.0177P)^2+0.3824P]$ where $P=(F_o^2+2F_c^2)/3$
Absolute structure parameter	0.05(2)

Largest diff. peak and hole	0.648 and -0.683 eÅ^{-3}
R.M.S. deviation from mean	0.103 eÅ^{-3}

Table A.13. Crystal and structure refinement data for **VO-24**.

Identification code	shs249m
Chemical formula	$C_{16}H_{14}FN_2O_5V$
Formula weight	384.23 g/mol
Temperature	100(2) K
Wavelength	0.71073 Å
Crystal size	0.085 x 0.304 x 0.341 mm
Crystal habit	red block
Crystal system	monoclinic
Space group	P 2_1/n
Unit cell dimensions	a = 10.7543(3) Å α = 90° b = 11.0189(3) Å β = 100.5998 (10)° c = 13.1808(4) Å γ = 90°
Volume	1535.28(8) $Å^3$
Z	4
Density (calculated)	1.662 g/cm^3
Absorption coefficient	0.689 mm^{-1}
F(000)	784
Theta range for data collection	2.43 to 30.98°
Index ranges	-15<=h<=15, -15<=k<=15, -19<=l<=18
Reflections collected	24603
Independent reflections	4855 [R(int) = 0.1052]
Coverage of independent reflections	99.3%
Absorption correction	Numerical Mu Calculated
Max. and min. transmission	0.9440 and 0.7990
Structure solution technique	direct methods
Structure solution program	XS, VERSION 2013/1
Refinement method	Full-matrix least-squares on F^2
Refinement program	SHELXL-2014/7 (Sheldrick, 2014)
Function minimized	$\Sigma\, w(F_o^2 - F_c^2)^2$
Data / restraints / parameters	4855 / 0 / 228
Goodness-of-fit on F^2	1.041
Δ/σ_{max}	0.001
Final R indices	3676 data; $I>2\sigma(I)$ R1 = 0.0690, wR2 = 0.1677 all data R1 = 0.0951, wR2 = 0.1902
Weighting scheme	$w=1/[\sigma^2(F_o^2)+(0.1051P)^2+1.3055P]$ where $P=(F_o^2+2F_c^2)/3$

Absolute structure parameter	0.05(2)
Largest diff. peak and hole	1.245 and -1.352 eÅ^{-3}
R.M.S. deviation from mean	0.141 eÅ^{-3}

Table A.14. Crystal and structure refinement data for **VO-25**.

Identification code	shs235m
Chemical formula	$C_{16}H_{14}Br_3N_2O_5V$
Formula weight	604.96 g/mol
Temperature	296(2) K
Wavelength	0.71073 Å
Crystal size	0.020 x 0.180 x 0.200 mm
Crystal habit	red plate
Crystal system	monoclinic
Space group	P 2_1/c
Unit cell dimensions	a = 11.2612(2) Å α = 90° b = 12.4044(3) Å β = 91.7283 (8)° c = 14.4856(3) Å γ = 90°
Volume	2022.55(7) $Å^3$
Z	4
Density (calculated)	1.987 g/cm^3
Absorption coefficient	6.446 mm^{-1}
F(000)	1168
Theta range for data collection	2.44 to 31.03°
Index ranges	-16<=h<=15, -17<=k<=17, -20<=l<=20
Reflections collected	61634
Independent reflections	6442 [R(int) = 0.0784]
Coverage of independent reflections	99.7%
Absorption correction	Multi-Scan
Max. and min. transmission	0.8820 and 0.3590
Structure solution technique	direct methods
Structure solution program	XS, VERSION 2013/1
Refinement method	Full-matrix least-squares on F^2
Refinement program	SHELXL-2014/7 (Sheldrick, 2014)
Function minimized	$\Sigma\ w(F_o^2 - F_c^2)^2$
Data / restraints / parameters	6442 / 0 / 246
Goodness-of-fit on F^2	1.030
Δ/σ_{max}	0.057
Final R indices	3462 data; I>2σ(I) R1 = 0.0382, wR2 = 0.0775 all data R1 = 0.1121, wR2 = 0.1096
Weighting scheme	$w=1/[\sigma^2(F_o^2)+(0.0338P)^2+2.9503P]$ where $P=(F_o^2+2F_c^2)/3$
Largest diff. peak and hole	0.775 and -0.949 $eÅ^{-3}$

R.M.S. deviation from mean 0.091 eÅ^{-3}

Table A.15. Crystal and structure refinement data for complex **VO-30**.

Identification code	shs309m
Chemical formula	$C_{19}H_{16}F5N_2O_5V$
Formula weight	498.28 g/mol
Temperature	100(2) K
Wavelength	0.71073 Å
Crystal size	0.060 x 0.300 x 0.320 mm
Crystal habit	brown plate
Crystal system	triclinic
Space group	P -1
Unit cell dimensions	a = 9.1540(3) Å α = 95.3703(13)° b = 10.4421(3) Å β = 98.4233(12)° c = 10.6666(3) Å γ = 97.3293(12)°
Volume	993.78(5) $Å^3$
Z	2
Density (calculated)	1.665 g/cm^3
Absorption coefficient	0.581 mm^{-1}
F(000)	504
Theta range for data collection	2.61 to 30.00°
Index ranges	-12<=h<=12, -14<=k<=14, -14<=l<=15
Reflections collected	22376
Independent reflections	5760 [R(int) = 0.0762]
Coverage of independent reflections	99.7%
Absorption correction	Multi-Scan
Max. and min. transmission	0.9660 and 0.8360
Structure solution technique	direct methods
Structure solution program	XT, VERSION 2014/5
Refinement method	Full-matrix least-squares on F^2
Refinement program	SHELXL-2016/6 (Sheldrick, 2016)
Function minimized	$\Sigma\, w(F_o^2 - F_c^2)^2$
Data / restraints / parameters	5760 / 1 / 295
Goodness-of-fit on F^2	1.007
Final R indices	4915 data; $I>2\sigma(I)$ R1 = 0.0576, wR2 = 0.1528 all data R1 = 0.0663, wR2 = 0.1628
Weighting scheme	$w=1/[\sigma^2(F_o^2)+(0.0992P)^2+0.6955P]$ where $P=(F_o^2+2F_c^2)/3$
Extinction coefficient	0.0360(70)

Largest diff. peak and hole	1.396 and -1.410 eÅ^{-3}
R.M.S. deviation from mean	0.116 eÅ^{-3}

FT-IR Data

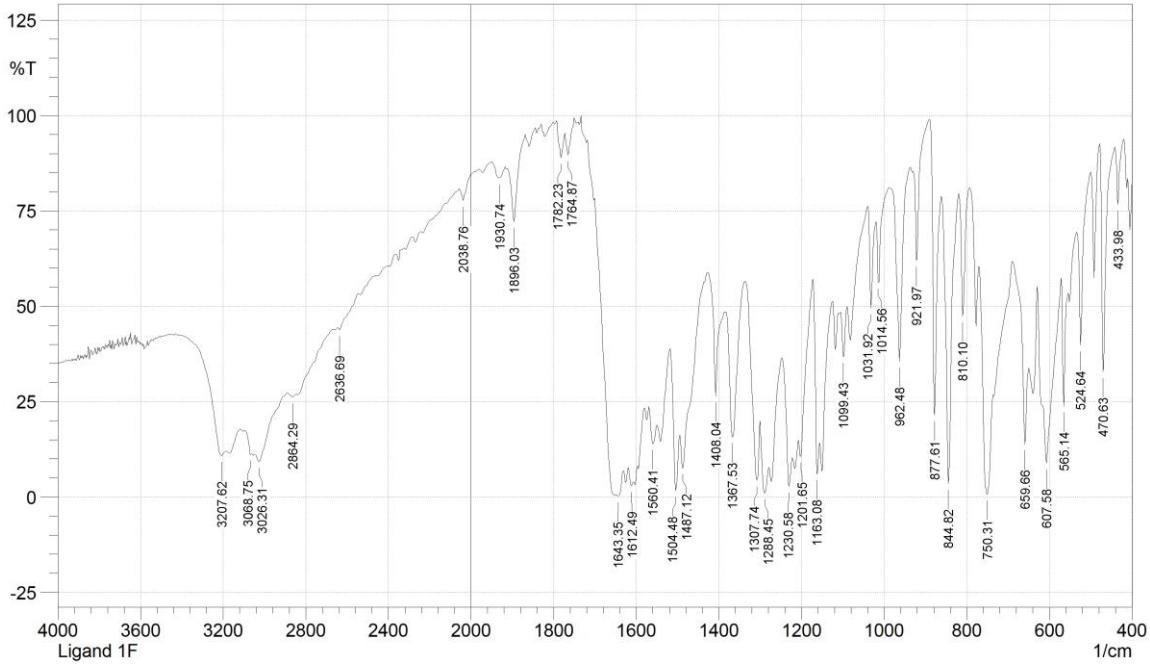

Figure A.165. The FT-IR spectrum of **L-1**.

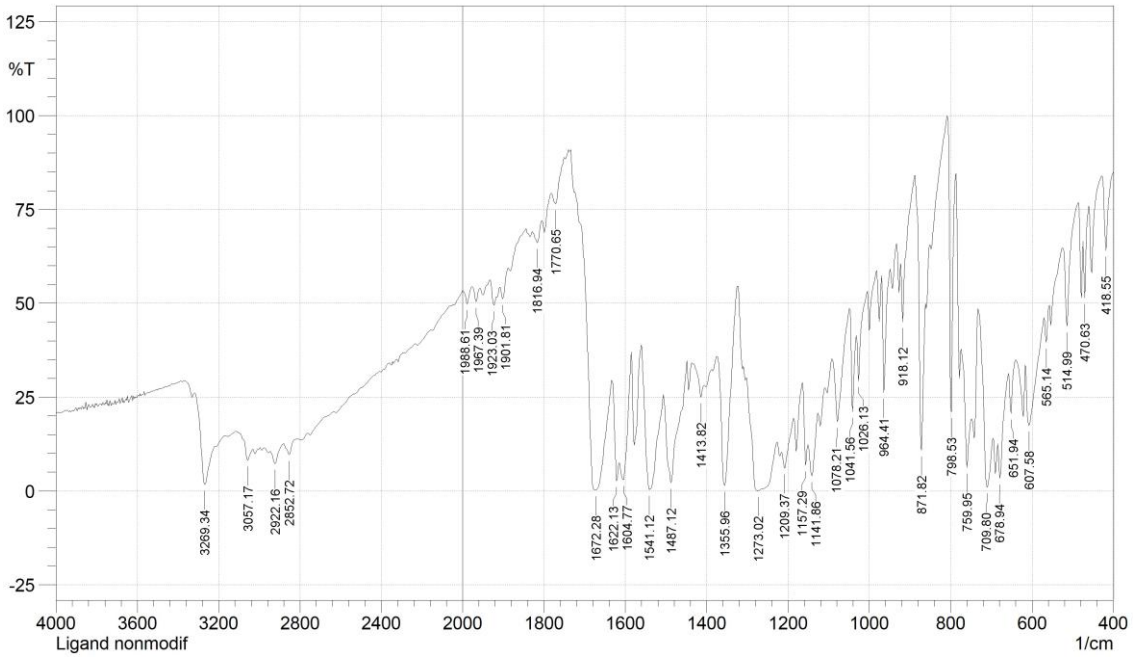

Figure A.166. The FT-IR spectrum of **L-2**.

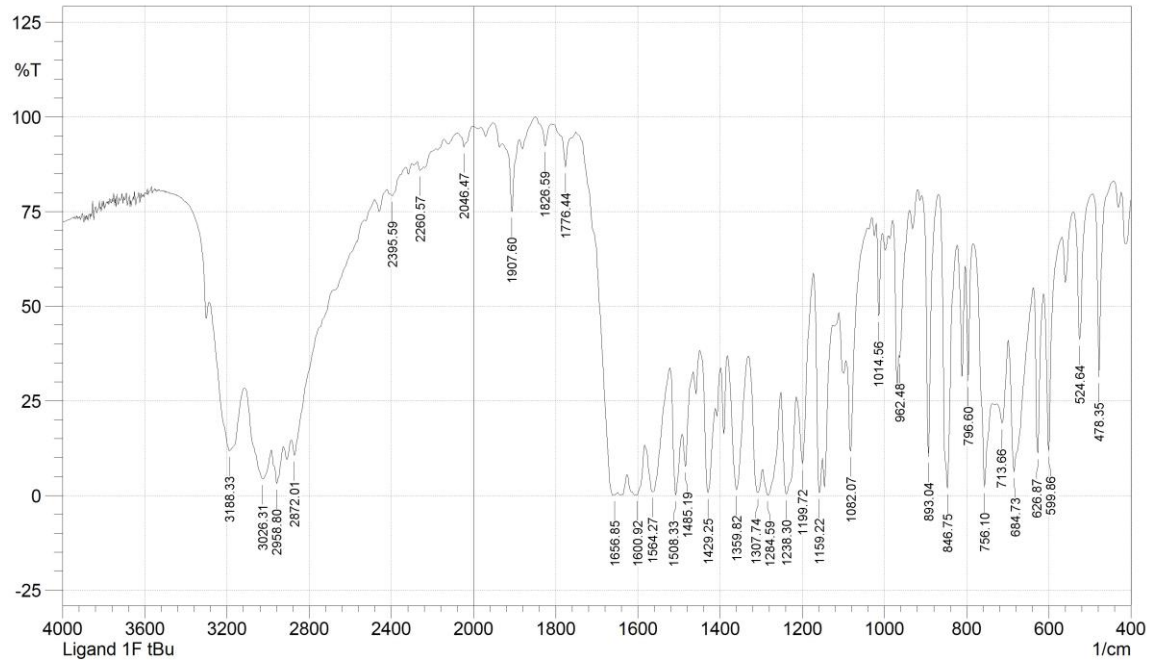

Figure A.167. The FT-IR spectrum of **L-3**.

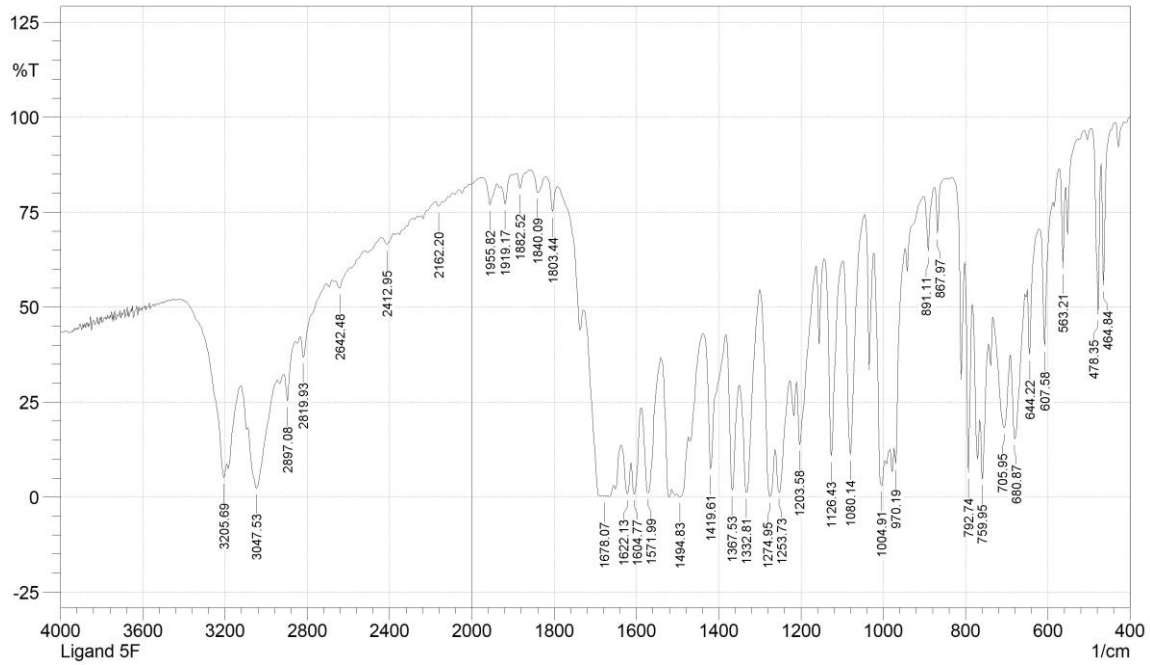

Figure A.168. The FT-IR spectrum of **L-4**.

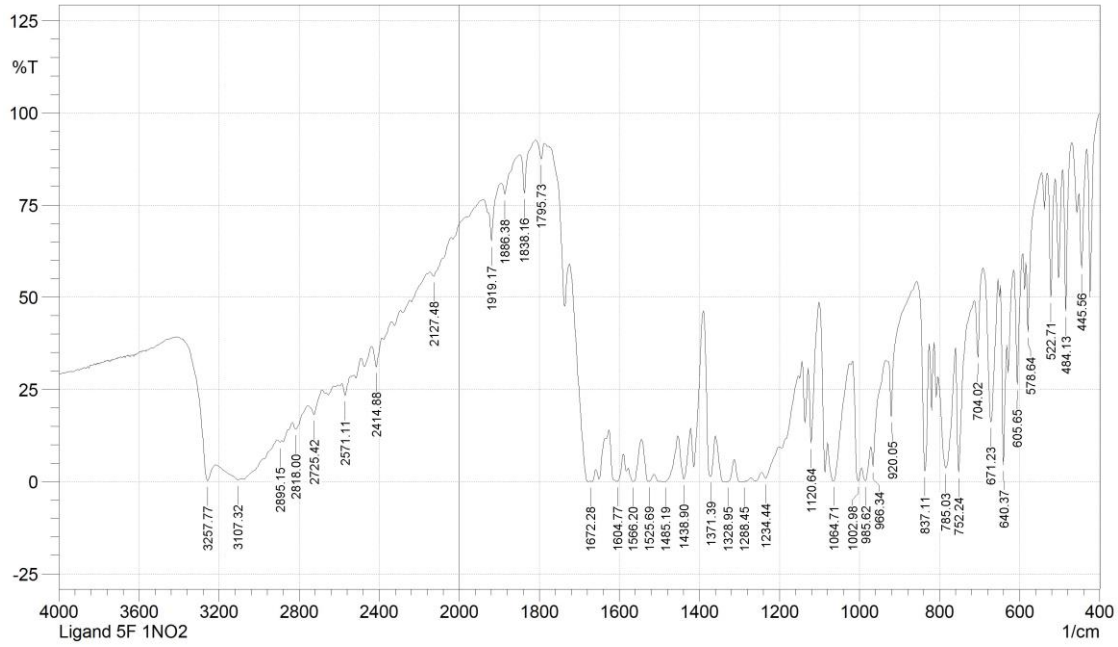

Figure A.169. The FT-IR spectrum of **L-5**.

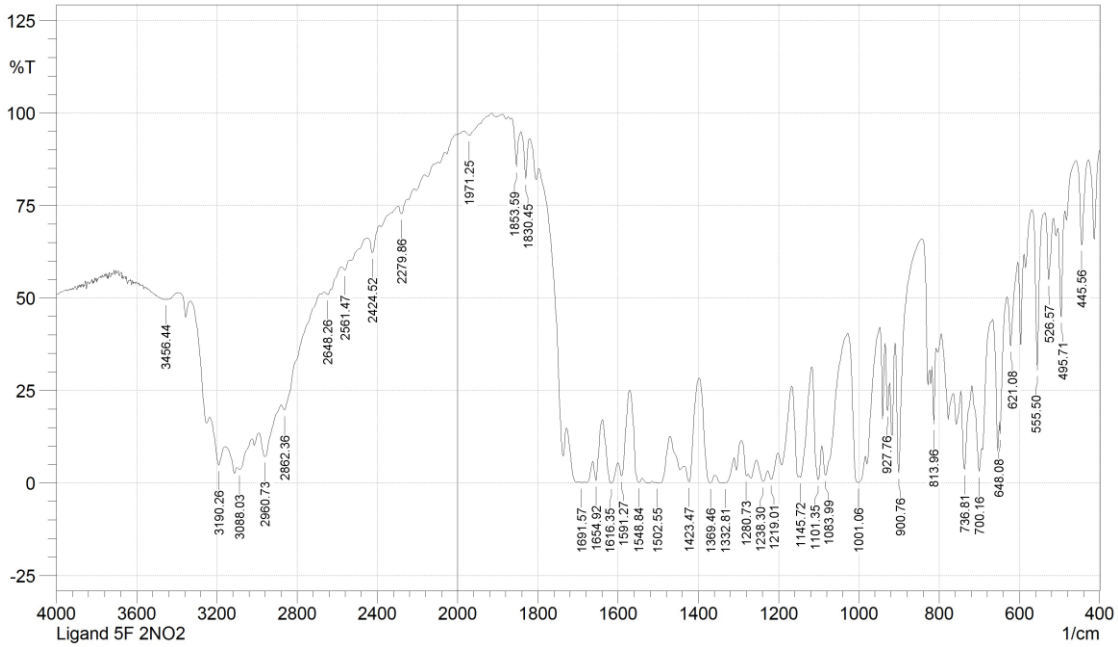

Figure A.170. The FT-IR spectrum of **L-6**.

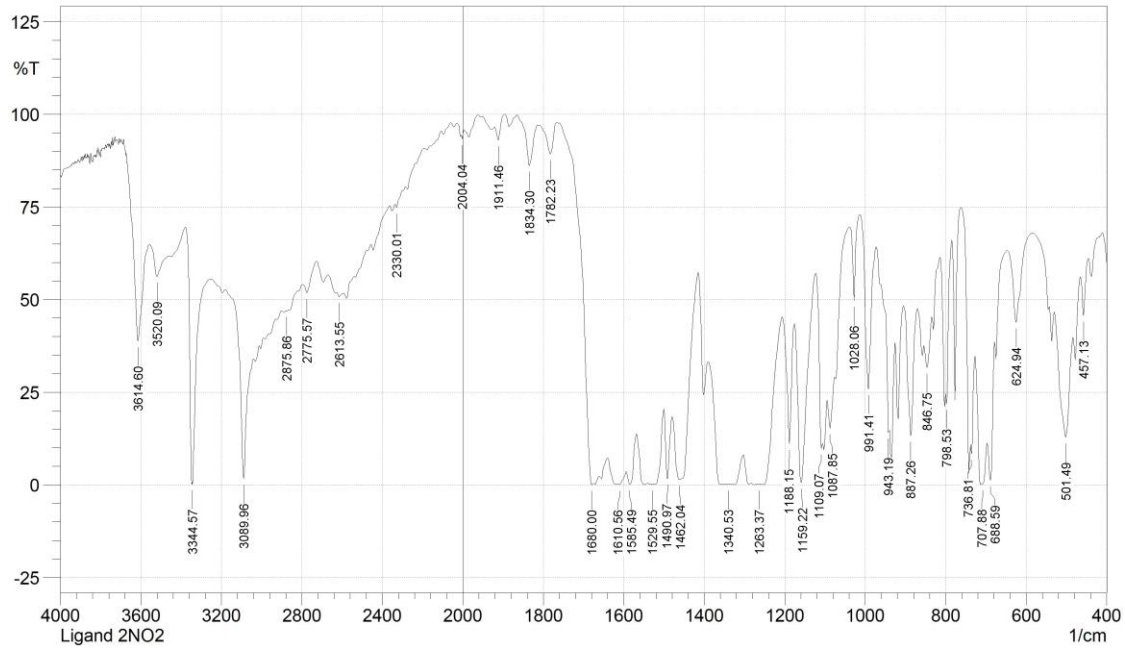

Figure A.171. The FT-IR spectrum of **L-7**.

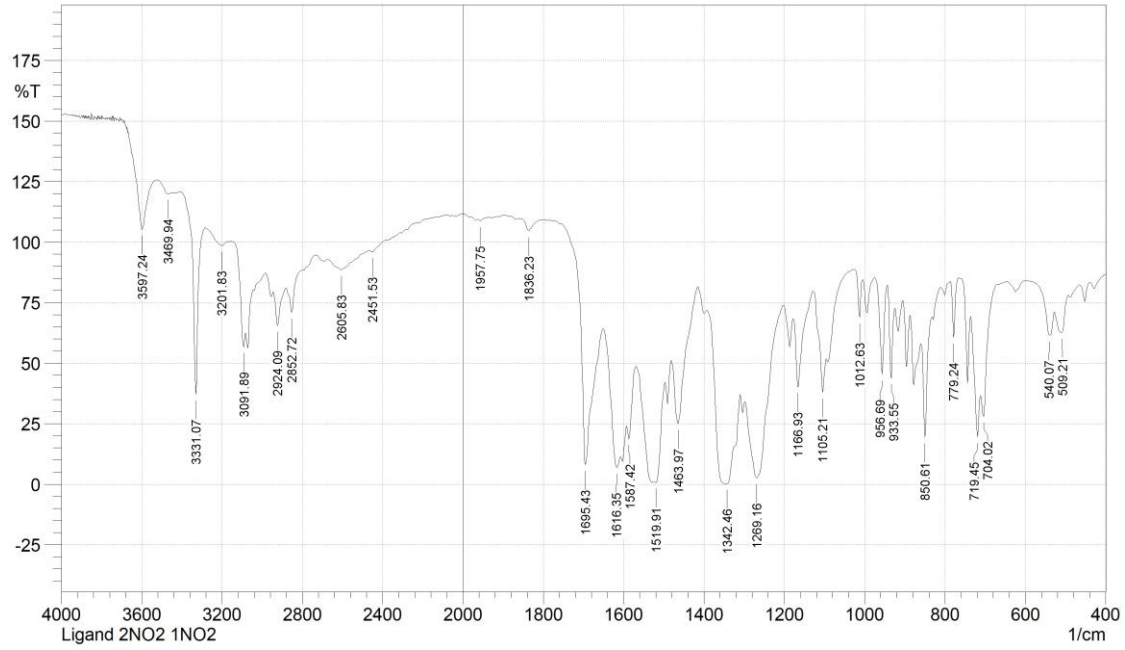

Figure A.172. The FT-IR spectrum of **L-8**.

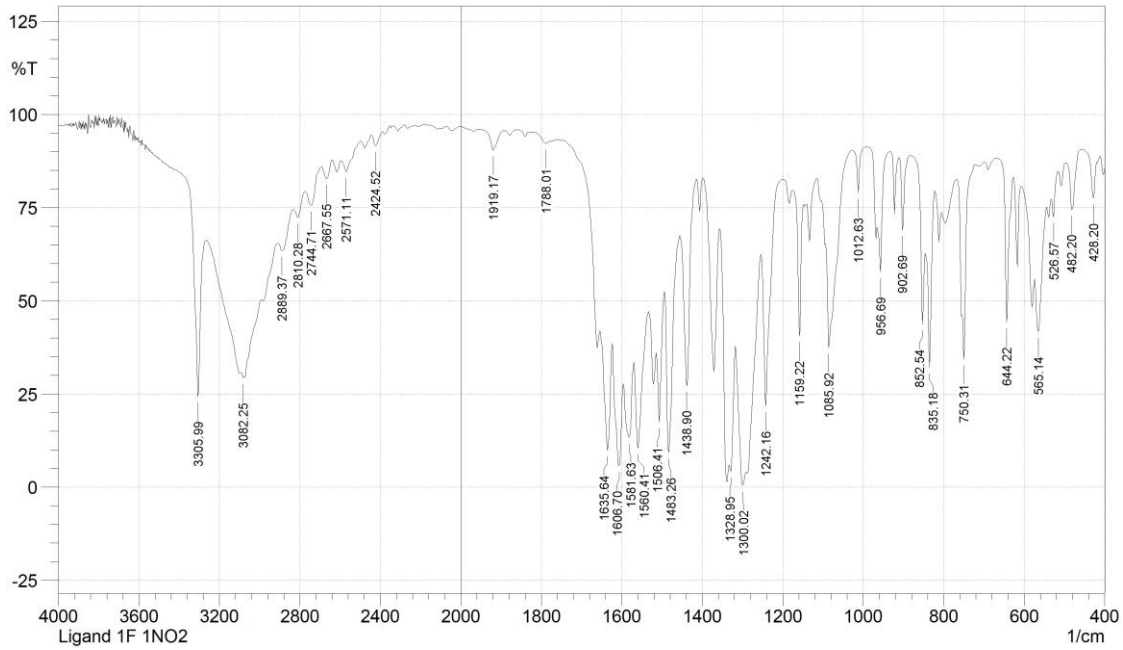

Figure A.173. The FT-IR spectrum of **L-9**.

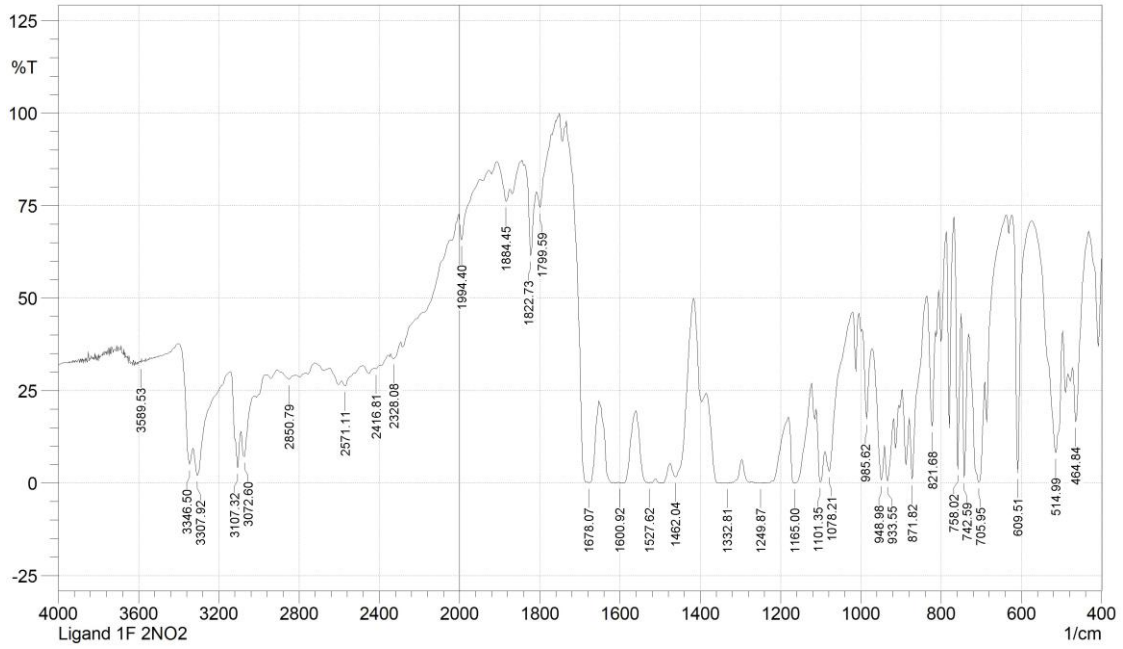

Figure A.174. The FT-IR spectrum of **L-10**.

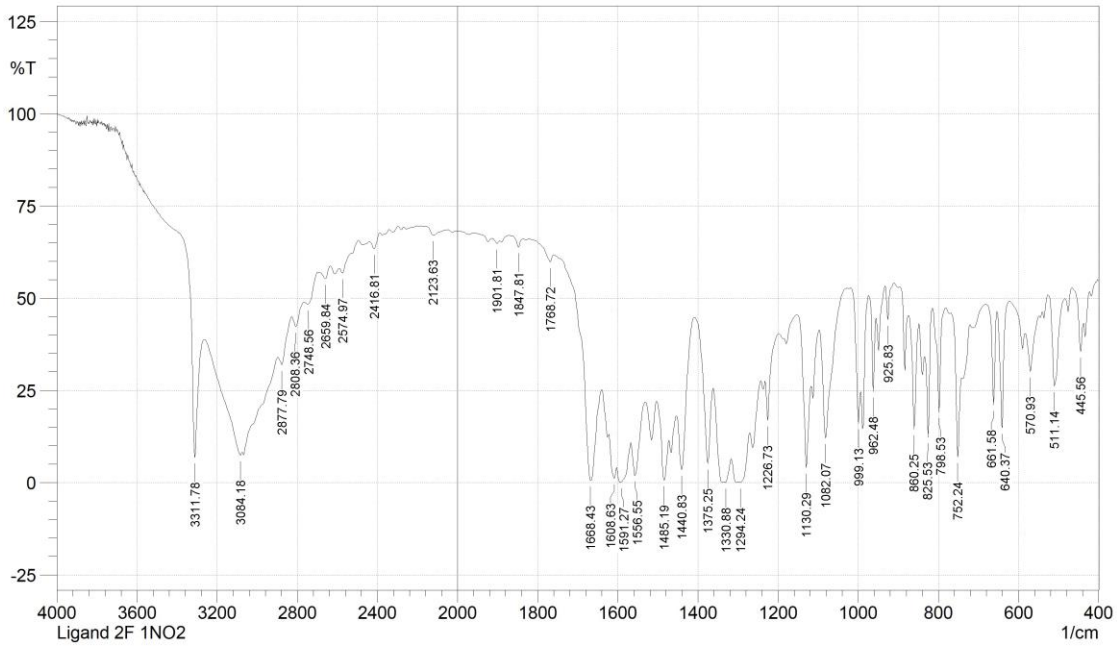

Figure A.175. The FT-IR spectrum of **L-11**.

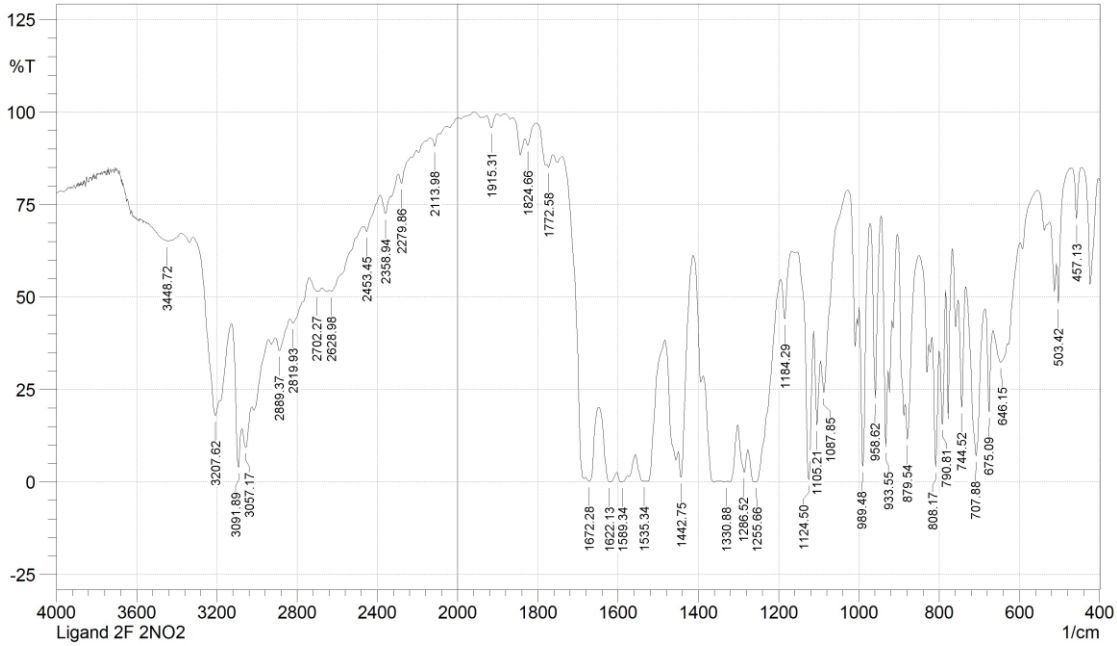

Figure A.176. The FT-IR spectrum of **L-12**.

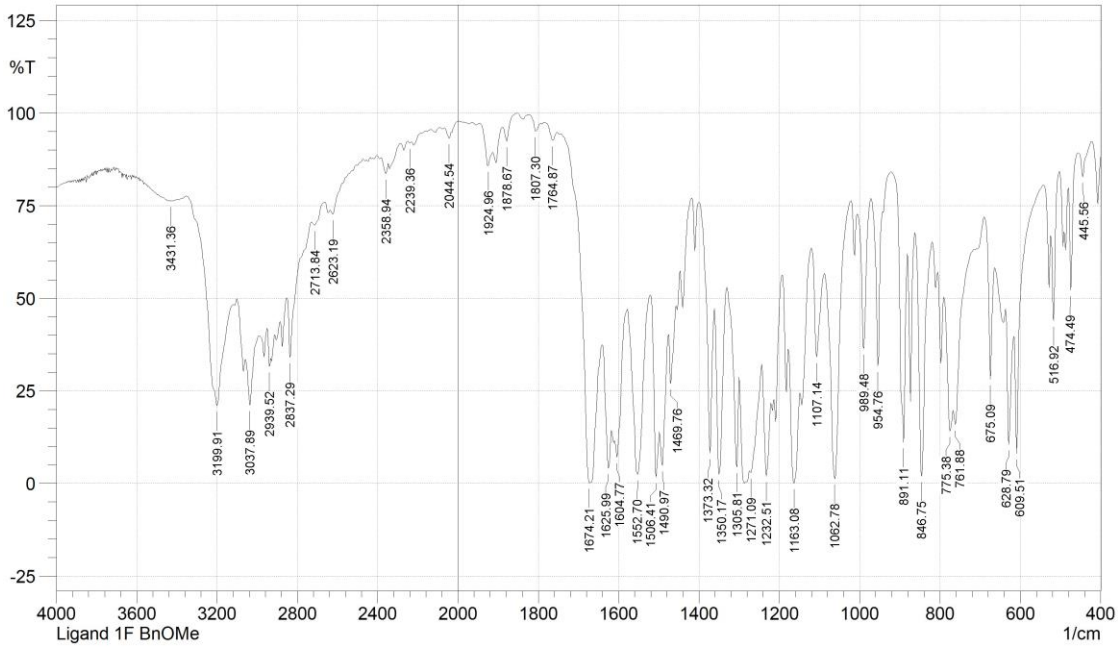

Figure A.177. The FT-IR spectrum of **L-13**.

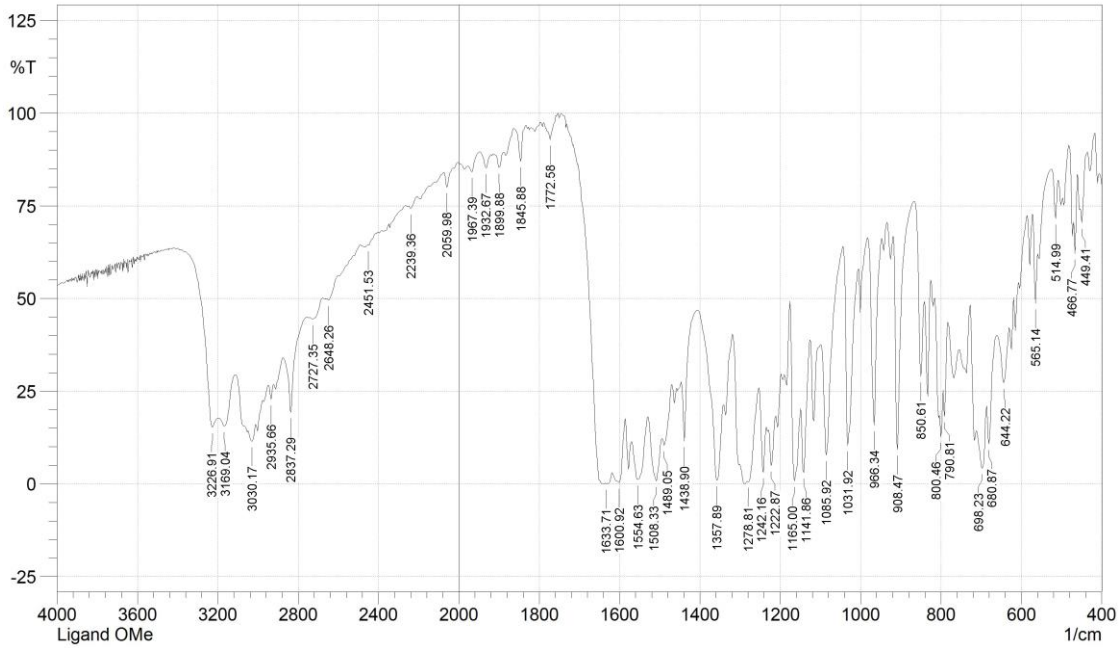

Figure A.178. The FT-IR spectrum of **L-14**.

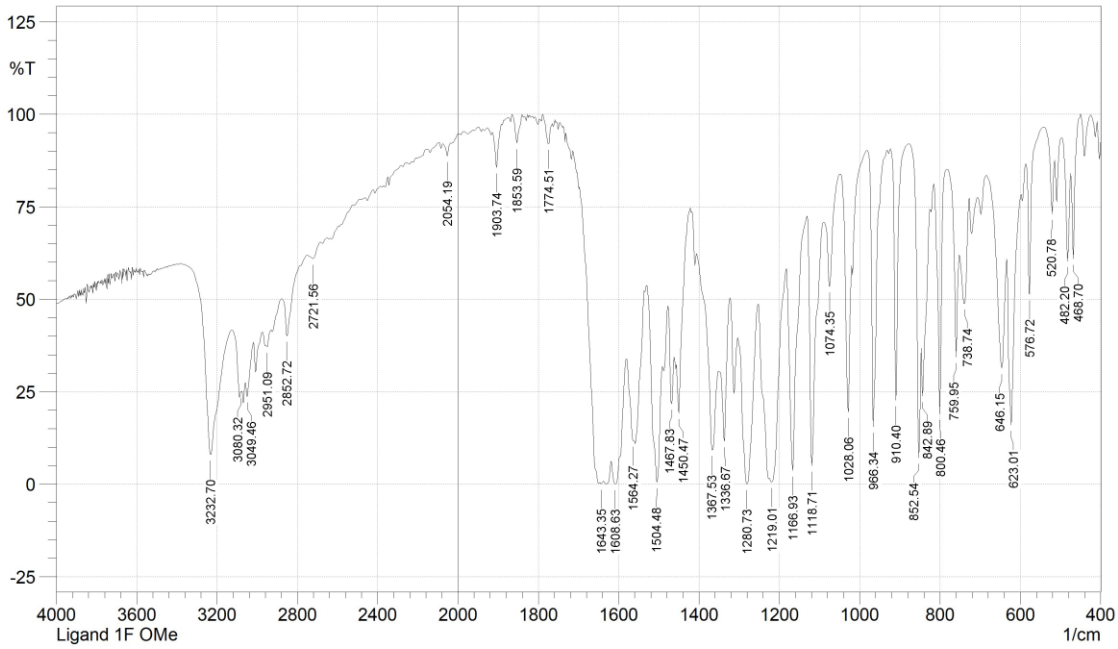

Figure A.179. The FT-IR spectrum of **L-15**.

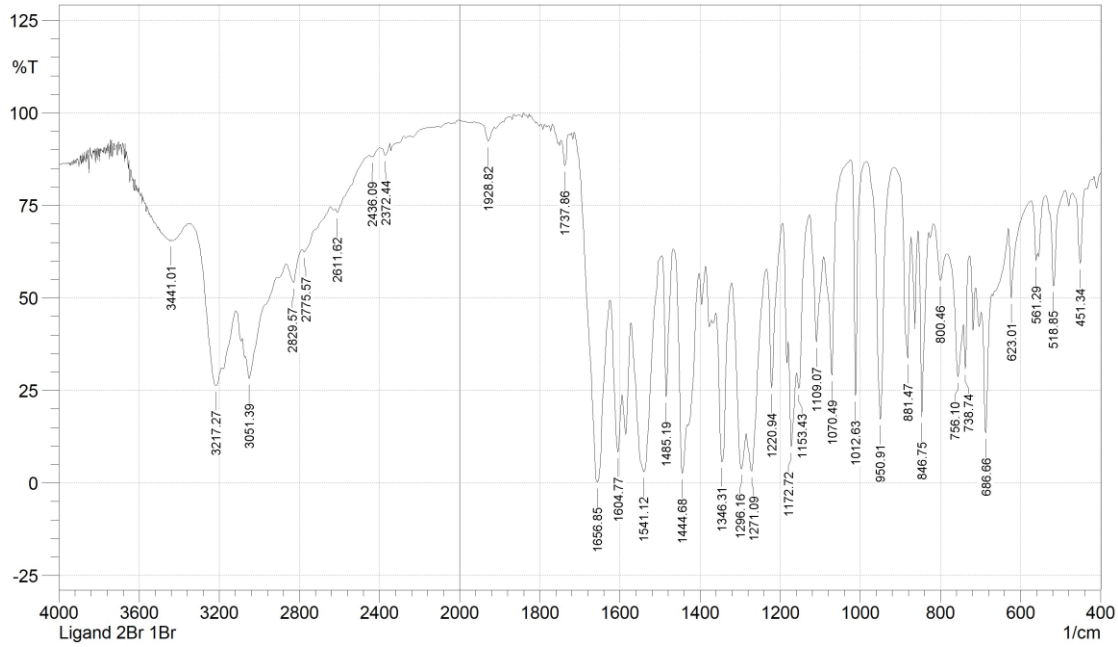

Figure A.180. The FT-IR spectrum of **L-16**.

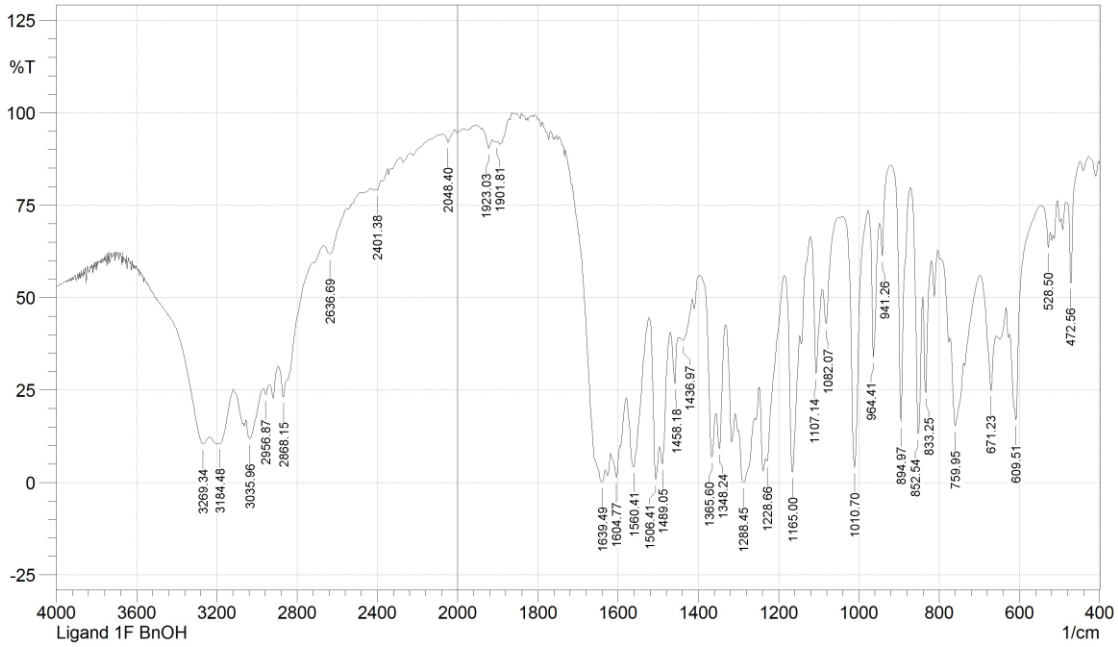

Figure A.181. The FT-IR spectrum of **L-17**.

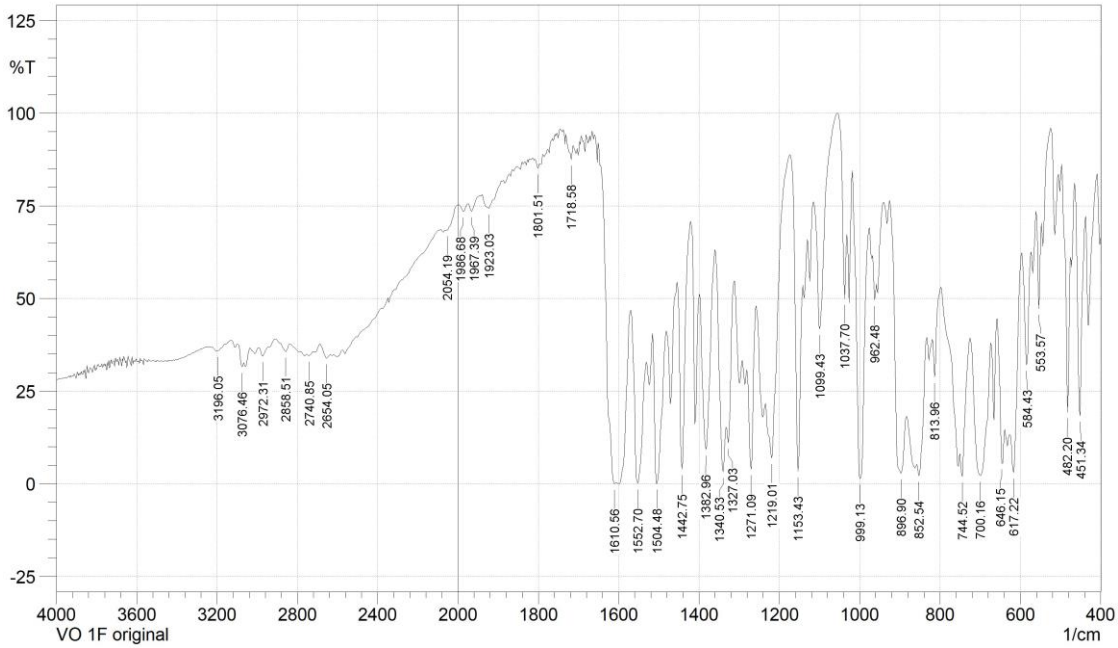

Figure A.182. The FT-IR spectrum of **VO-10**.

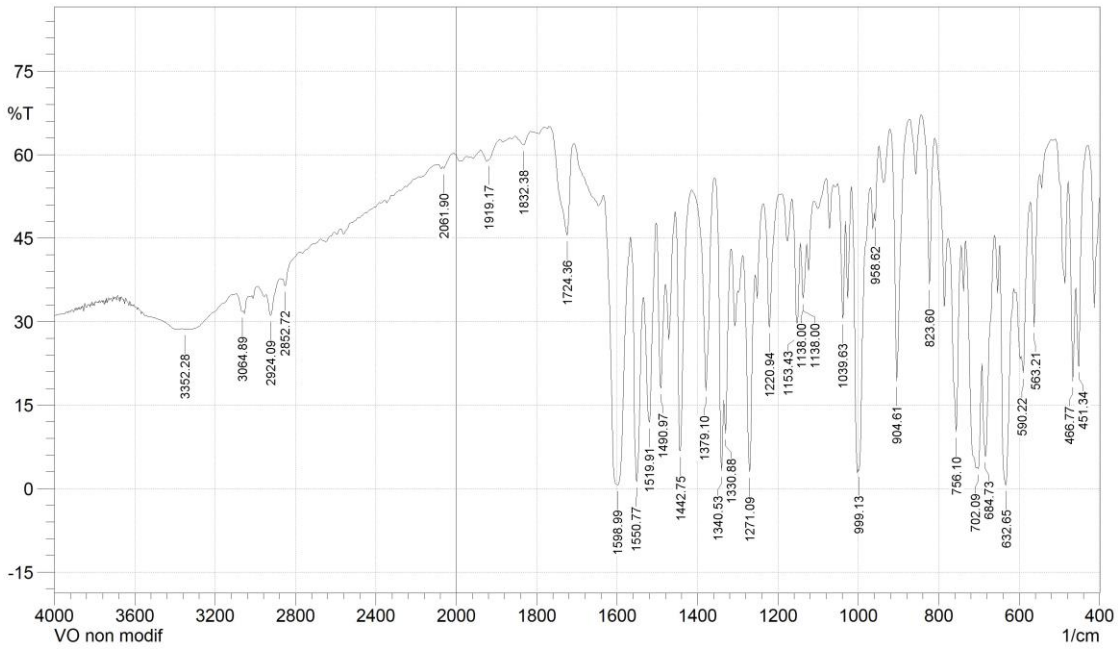

Figure A.183. The FT-IR spectrum of **VO-11**.

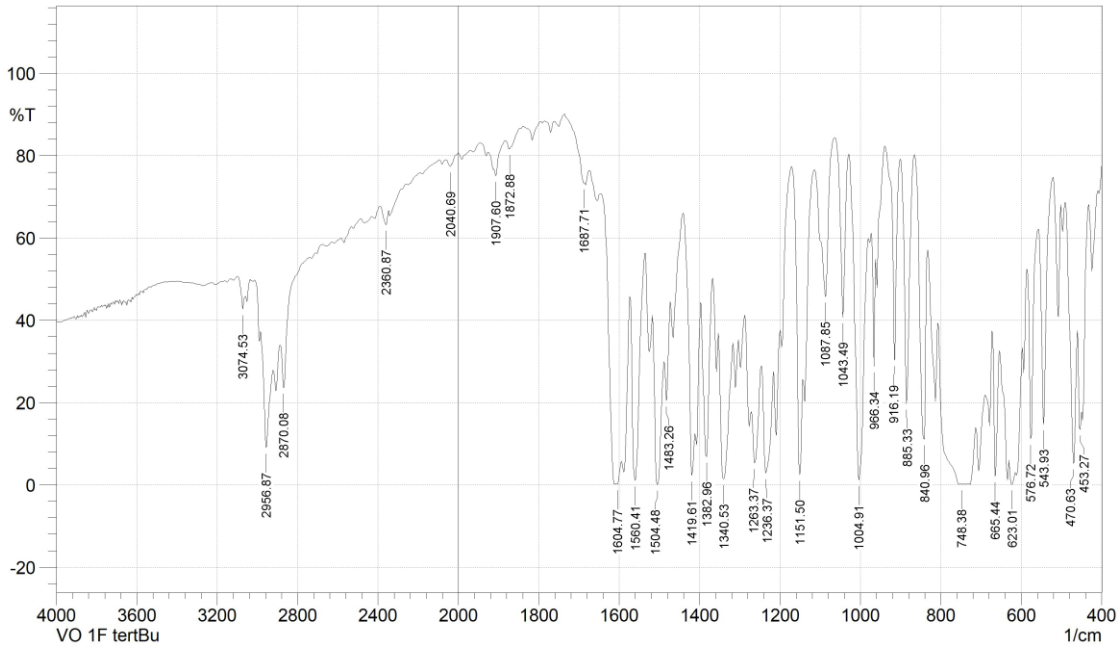

Figure A.184. The FT-IR spectrum of **VO-12**.

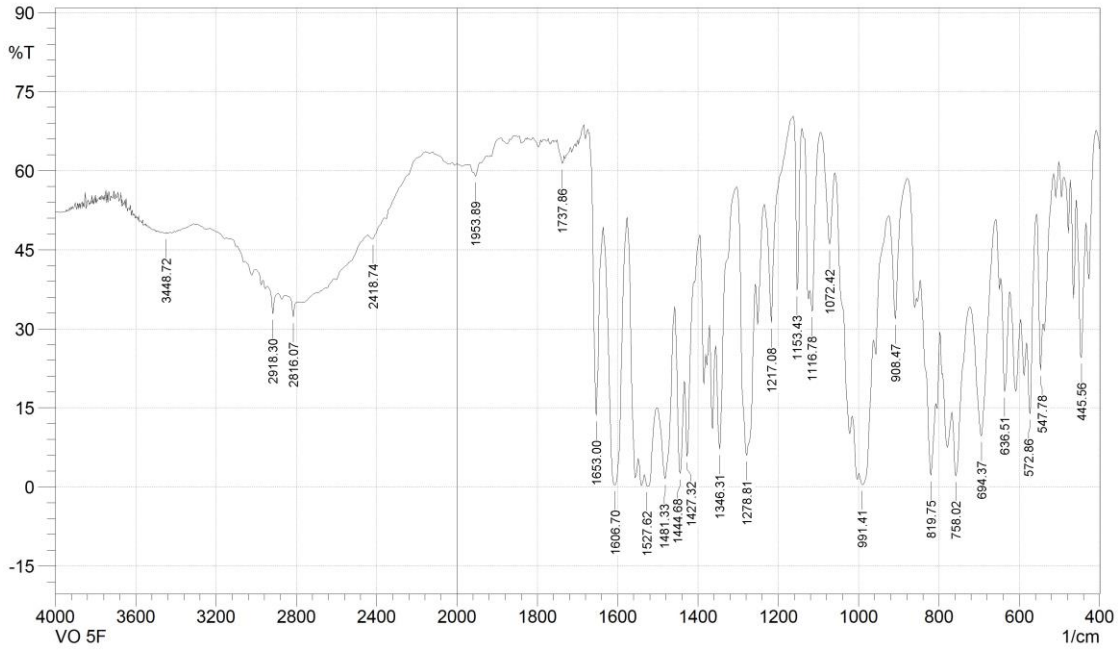

Figure A.185. The FT-IR spectrum of **VO-13**.

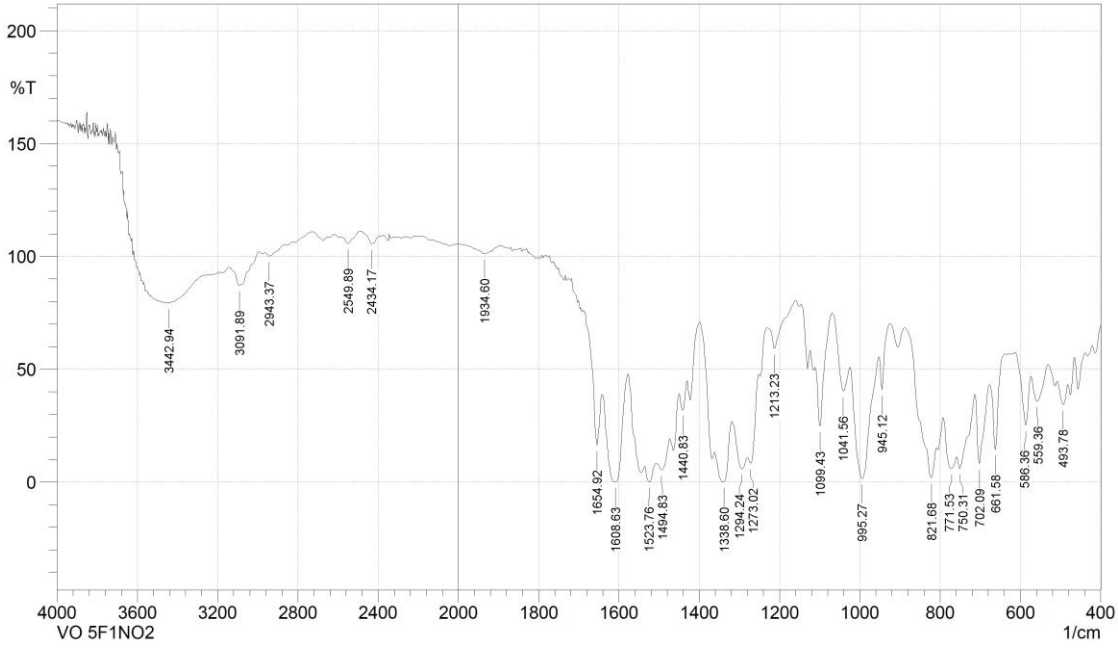

Figure A.186. The FT-IR spectrum of **VO-14**.

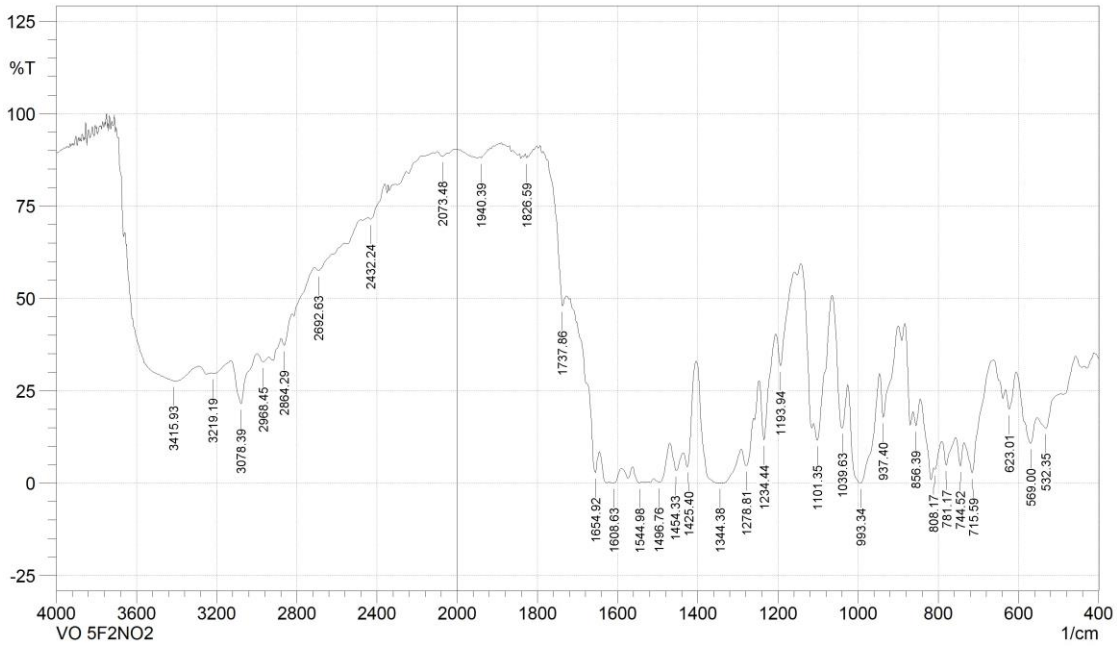

Figure A.187. The FT-IR spectrum of **VO-15**.

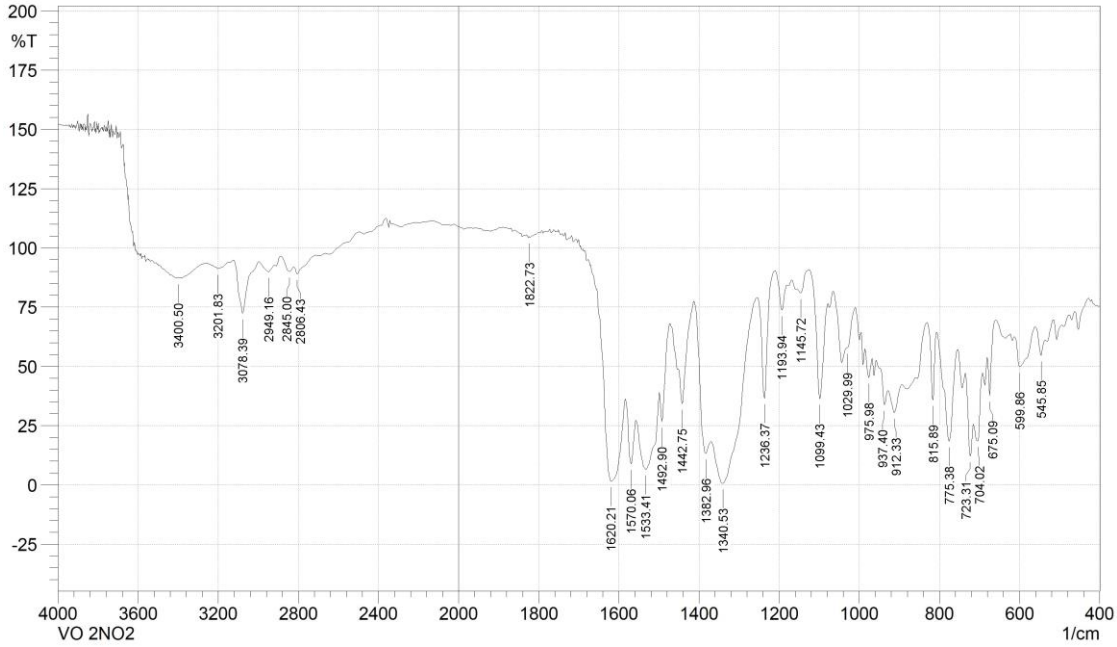

Figure A.188. The FT-IR spectrum of **VO-16**.

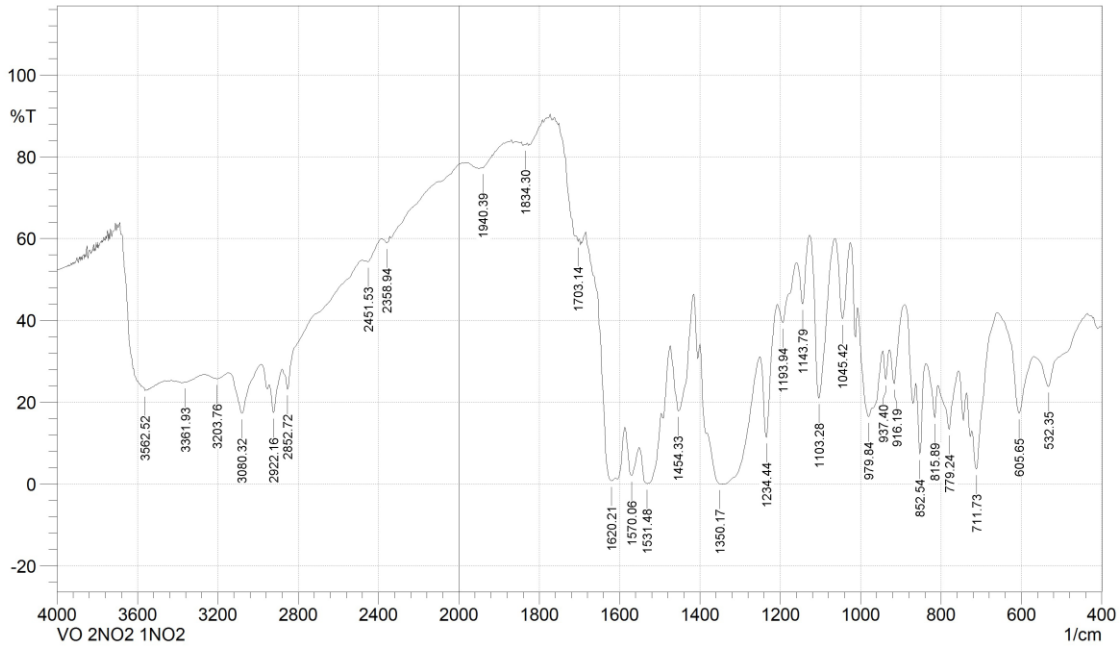

Figure A.189. The FT-IR spectrum of **VO-17**.

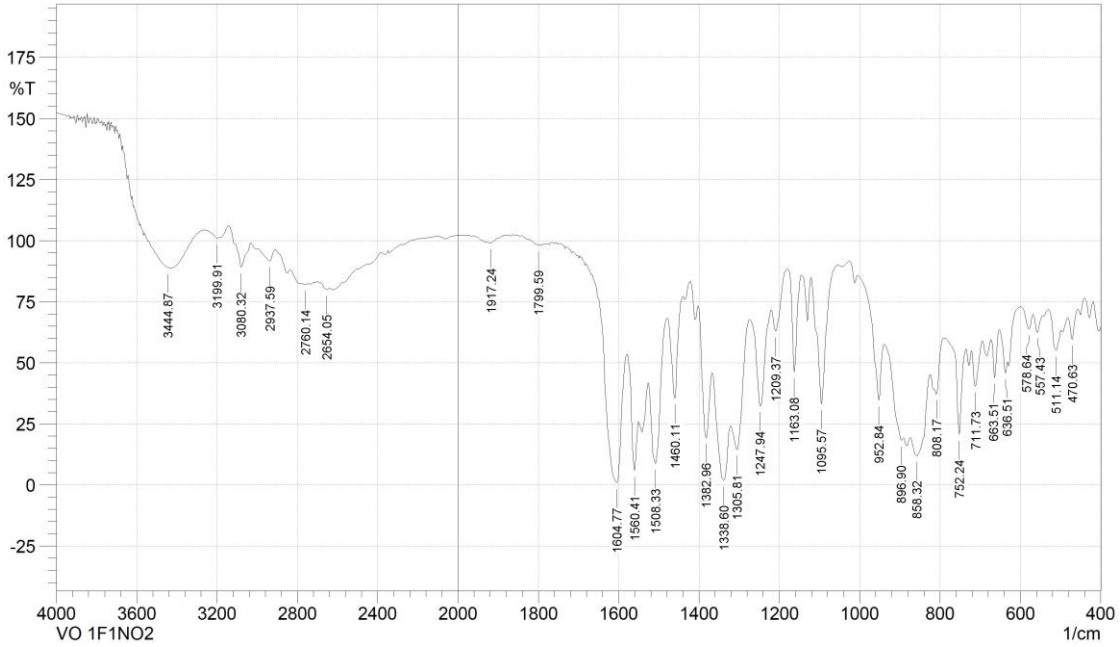

Figure A.190. The FT-IR spectrum of **VO-18**.

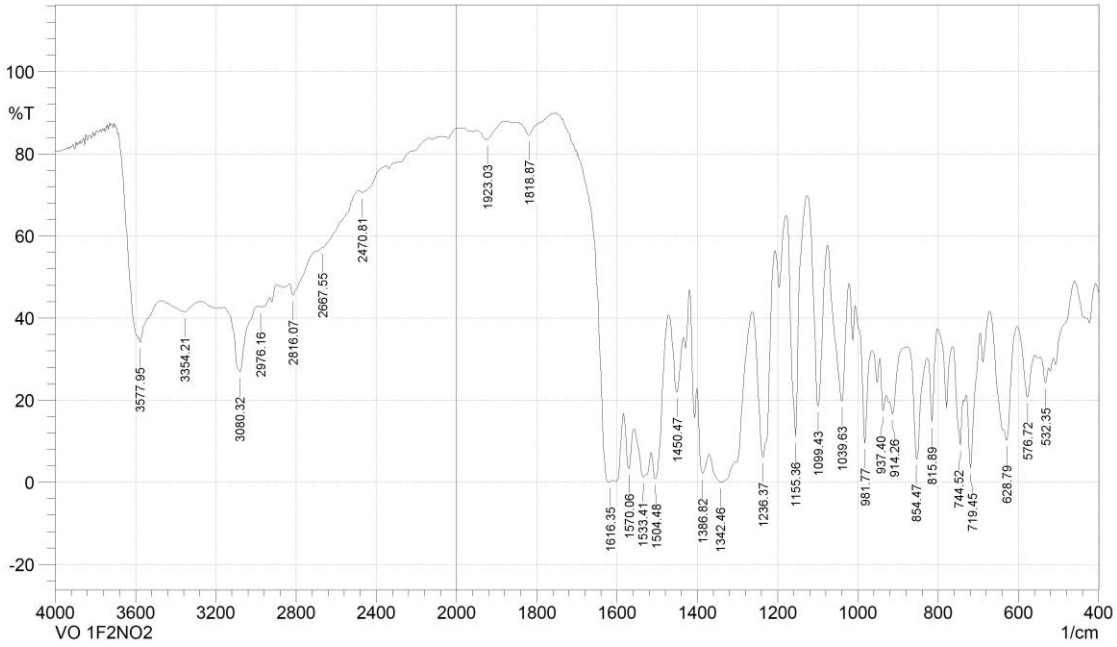

Figure A.191. The FT-IR spectrum of **VO-19**.

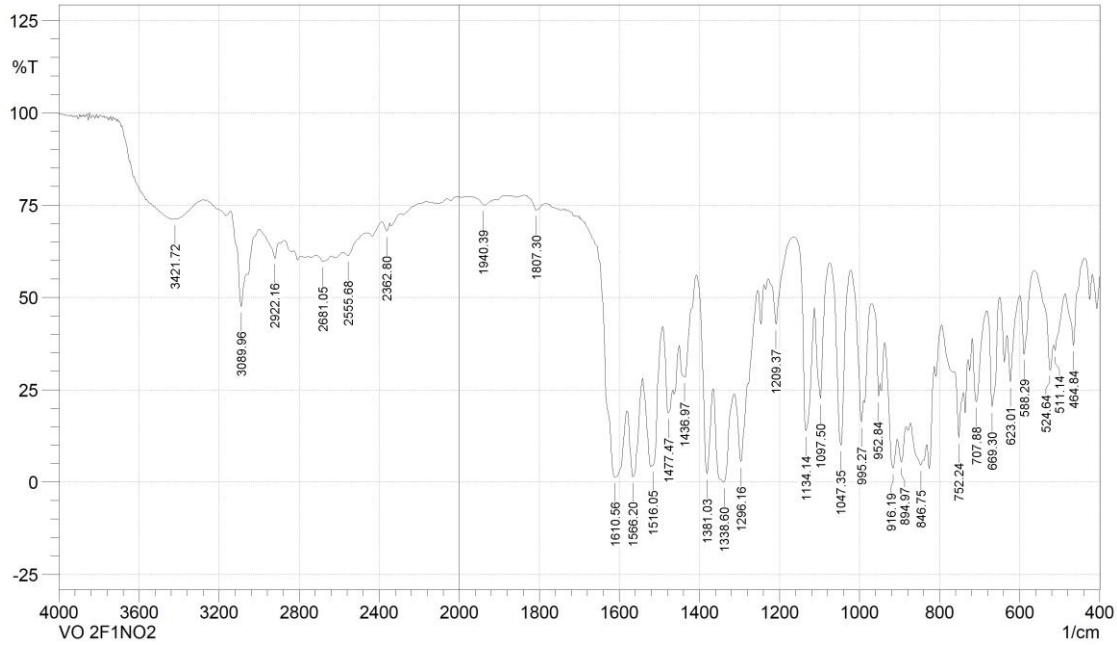

Figure A.192. The FT-IR spectrum of **VO-20**.

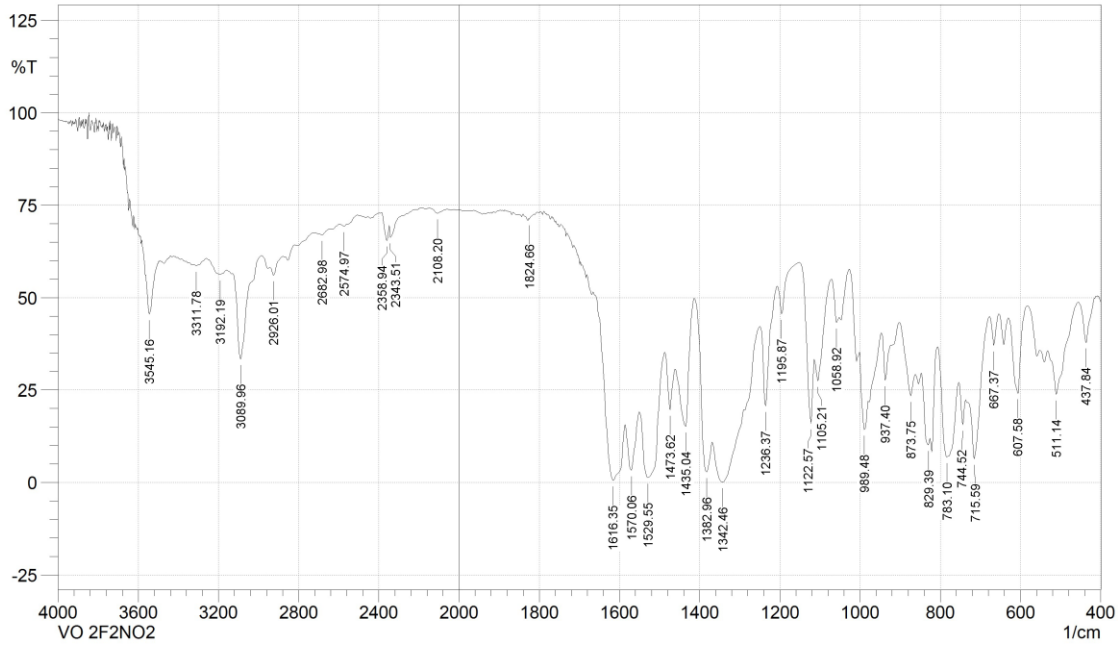

Figure A.193. The FT-IR spectrum of **VO-21**.

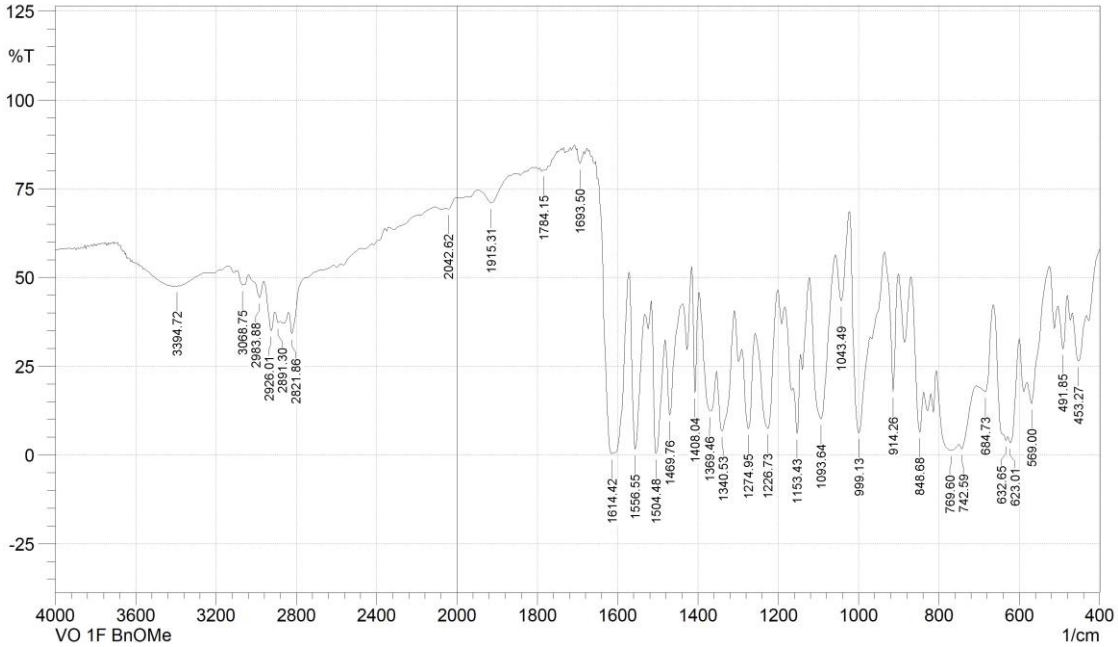

Figure A.194. The FT-IR spectrum of **VO-22**.

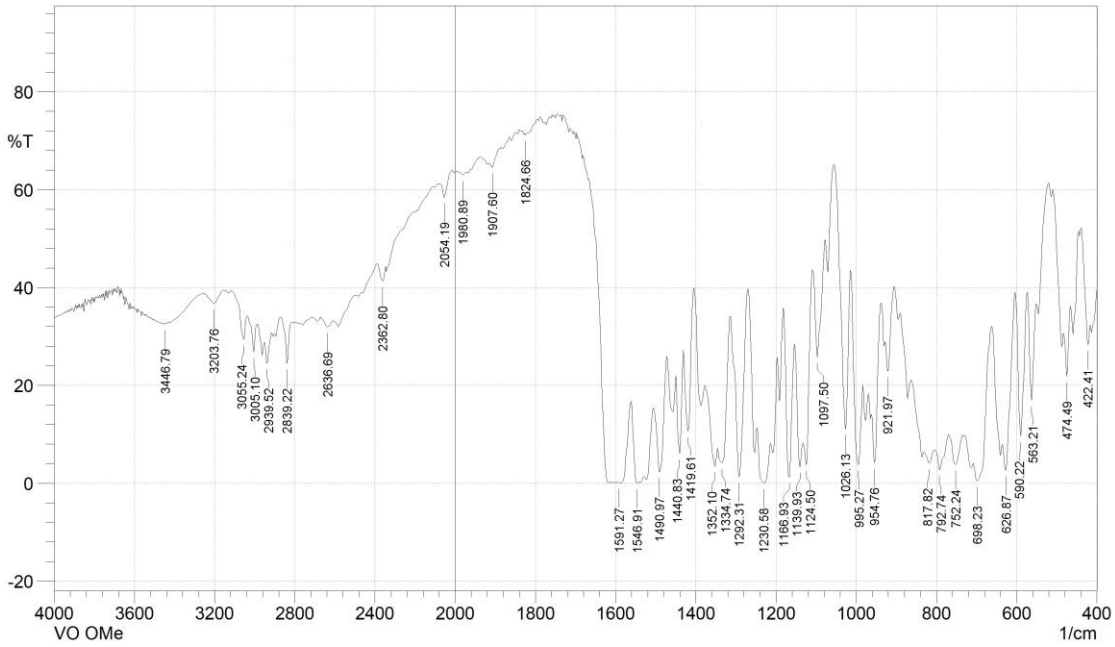

Figure A.195. The FT-IR spectrum of **VO-23**.

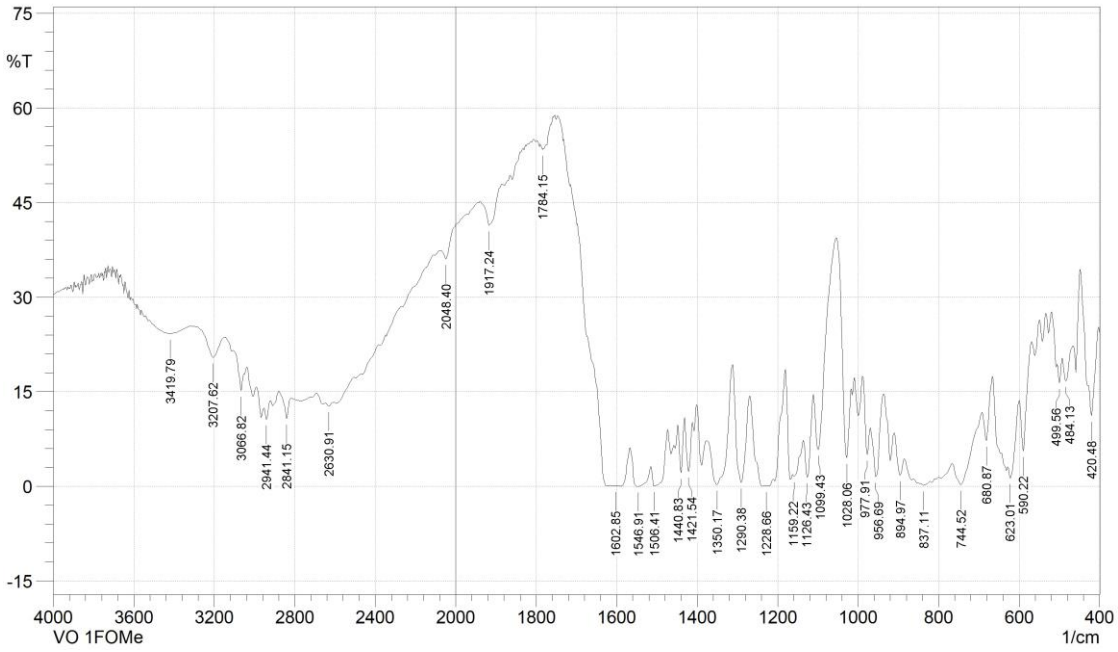

Figure A.196. The FT-IR spectrum of **VO-24**.

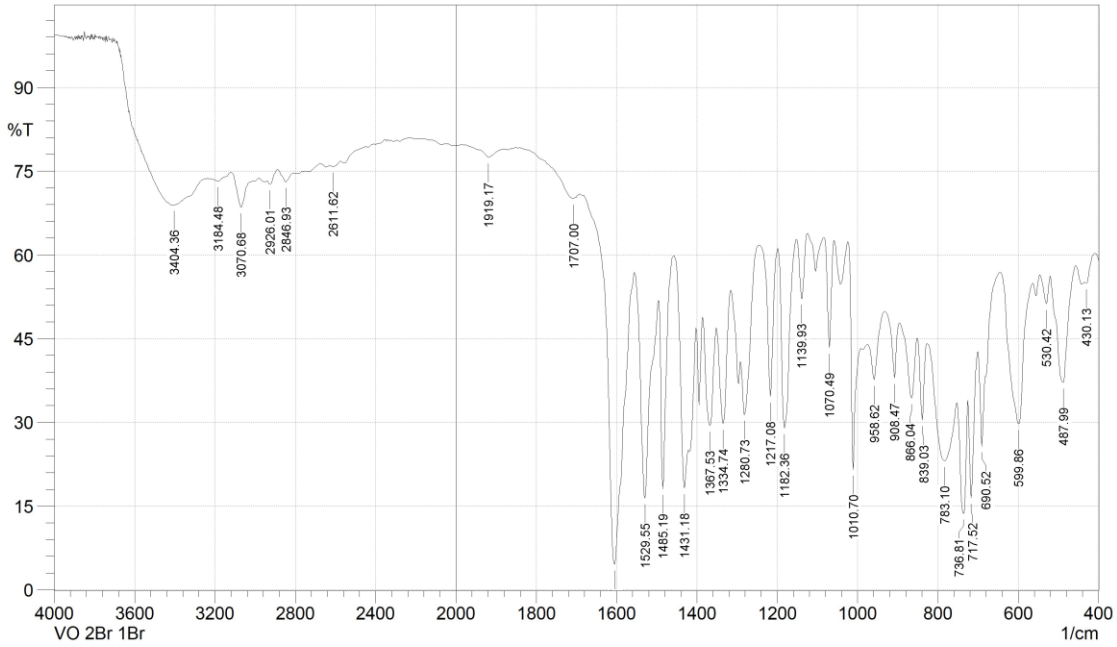

Figure A.197. The FT-IR spectrum of **VO-25**.

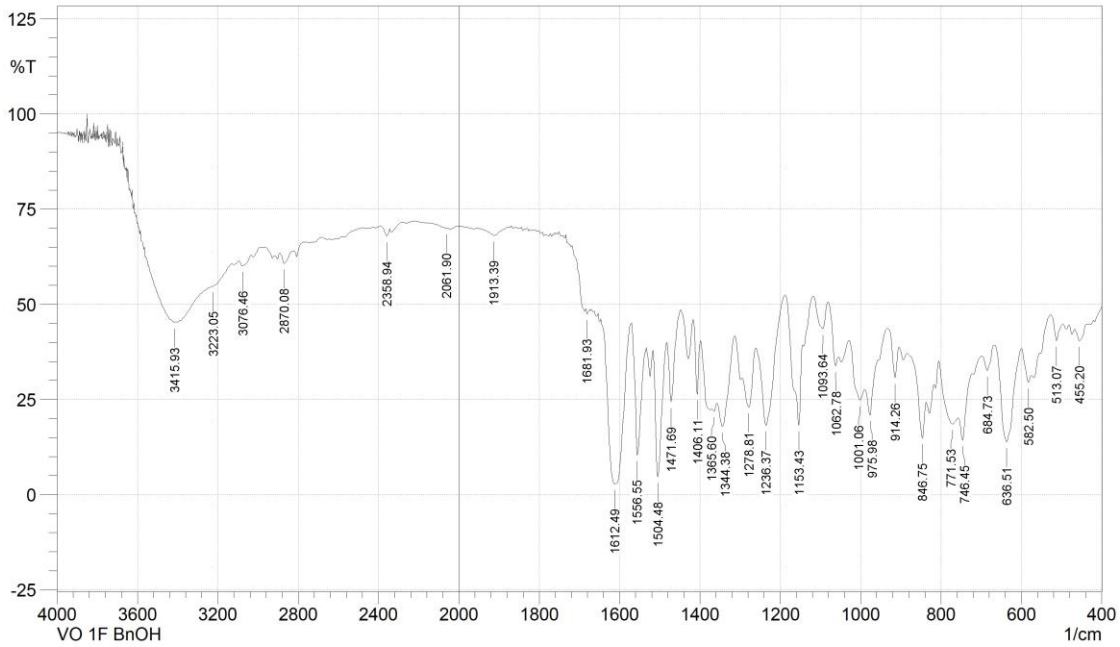

Figure A.198. The FT-IR spectrum of **VO-29**.

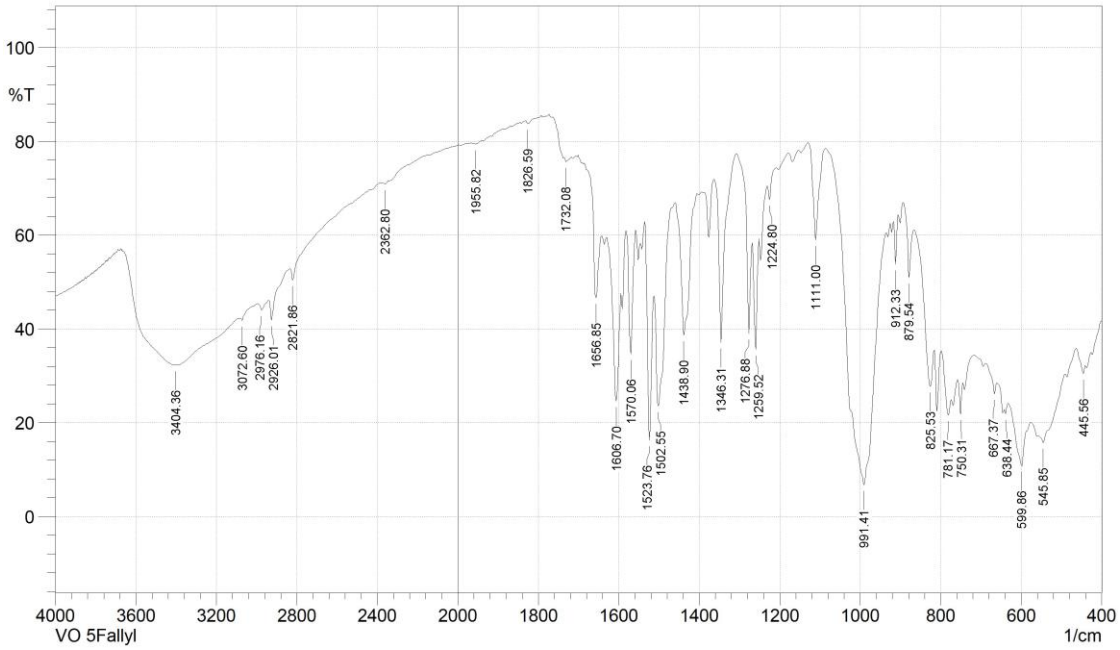

Figure A.199. The FT-IR spectrum of **VO-30**.